Investigation of Subgrade Moisture Flow

Caused by Hydro-Thermal Gradients

In Airfield Pavements

by

Pugazhvel Thirthar Palanivelu

A Dissertation Presented in Partial Fulfillment
of the Requirement for the Degree
Doctor of Philosphy

Approved July 2017 by the
Graduate Supervisory Committee:
Claudia Zapata, Chair
Edward Kavazanjian
Sandra Houston
Shane Underwood

ARIZONA STATE UNIVERSITY

August 2017

ABSTRACT

Recent research efforts have been directed to improve the quality of pavement design procedures by considering the transient nature of soil properties due to environmental and aging effects on pavement performance. The main purpose of this research study was to investigate the existence of subgrade soil moisture changes that may have arisen due to thermal and hydraulic gradients at the Atlantic City NAPTF and to evaluate their effect on the material stiffness and the California Bearing Ratio (CBR) strength parameter of the clay subgrade materials. Laboratory data showed that at the same water content, matric suction decreases with increasing temperature; and at the same suction, hydraulic conductivity increases with increasing temperature. Models developed, together with moisture/temperature data collected from 30 sensors installed in the test facility, yielded a maximum variation of suction in field of 155 psi and changes in hydraulic conductivity from 2.9E-9 m/s at 100% saturation to 8.1E-12 at 93% saturation. The maximum variation in temperature was found to be 20.8^{o}C at the shallower depth and decreased with depth; while a maximum variation in moisture content was found to be 3.7% for Dupont clay and 4.4% for County clay. Models developed that predicts CBR as a function of dry density and moisture content yielded a maximum variation of CBR of 2.4 for Dupont clay and 2.9 for County clay. Additionally, models were developed relating the temperature with the bulk stress and octahedral stress applied on the subgrade for dual gear, dual tandem and triple tandem gear types for different tire loads. It was found that as the temperature increases the stresses increase. A Modified Cary and Zapata model was used for predicting the resilient modulus(M_r) of the subgrade. Using the models developed and the temperature/moisture changes observed in the field, the variation of suction, bulk and

octahedral stresses were estimated, along with the resilient modulus for three different gear types. Results indicated that changes in M_r as large as 9 ksi occur in the soils studied due to the combined effect of external loads and environmental condition changes.

This work is dedicated to my dad Dr. Palanivelu, my mom Dr. Umadevi,

my family, my friends both in India and all over the world,

and the late Mr. Maria Perraira Achille Raj.

ACKNOWLEDGMENTS

This project was possible due to the funding and support of the Federal Aviation Administration under grant number 13-G-008 entitled "Investigation of Subgrade Moisture Flow in an Airfield Pavement". I would like to thank Dr. Navneet Garg for his support during the whole process and for providing valuable information to the project.

I would like to thank Dr. Claudia Zapata, for her continuous support and guidance both in academic and personal life throughout this long journey. I would like to thank my fellow students Yutong Lu, Joshuah Contreras and Rakshith Gowda who helped me in performing various experiments that contributed towards this study.

My deepest gratitude to Professor Dr. Matthew W. Witczak for his technical supervision of the work performed and for his patient guidance during the whole project. Without his support and guidance, this work could not have been accomplished. I would also like to express my gratitude towards Dr. Edward Kavanzanjian, Dr. Sandra Houston, Dr. Shane Underwood, Dr. Chris Lawrence and Dr. Jaewon Jang for all the knowledge shared during these years and for their contribution to my formation as a graduate student.

I would like to thank Mr. Peter Goguen, Mr Kenneth Witczak and Mr . Lefferey Long for their help and guidance in setting up and performing the experiments in ASU laboratory.

Lastly, I would like to thank all my fellow students, and friends who helped me in this long journey.

TABLE OF CONTENTS

Page

CHAPTER Page

CHAPTER Page

CHAPTER Page

CHAPTER Page

CHAPTER Page

CHAPTER Page

CHAPTER Page

CHAPTER Page

LIST OF TABLES

Table Page

Table Page

Table Page

Table Page

Table Page

Table Page

Table Page

Table Page

LIST OF FIGURES

Figure Page

Figure Page

Figure Page

Figure Page

Figure Page

Figure Page

Figure Page

Figure Page

Figure Page

Figure Page

Figure Page

Figure Page

Figure Page

Figure Page

Chapter 1. INTRODUCTION

The longevity and the performance of a pavement is one of the most important attributes considered by engineers during the airfield pavement design process. The design of an airfield pavement takes into account the material properties, the stress state and the environmental conditions that affect its longevity. The material properties can be characterized in terms of their strength and/or in terms of their stiffness. The resilient modulus (M_r) is a fundamental parameter used in the design of the pavements and it characterizes the soil in terms of its stiffness. The variability of the resilient modulus depends on different factors such as moisture content, dry density, number of load repetitions, the compaction energy, the compaction method used, the state of stress and environmental conditions in the field. Various models have been used to correlate the resilient modulus to the parameters mentioned above. Previously the design of the pavements was considered to be performed for the worst possible conditions for the particular site. However, recent studies (Dempsey et al, 1985; Barbour et al, 1995; Akesson et al, 2009) proved that environmental factors played an important role on pavement performance.

Historically, pavement design has considered environmental effects on pavement performance, but the approach has been mostly empirical. As part of a comprehensive study sponsored by the National Cooperative Highway Research Program (NCHRP 1-37), a new Mechanistic Empirical Pavement Design Guide (MEPDG) was developed, which is the foundation of the now available AASHTOWare Pavement ME Design software. As part of this software, the Enhanced Integrated Climatic Model (EICM) allows for the input, collection, characterization, and analysis, of environmental and material properties effects

on the stiffness of unbound materials. The outcome of the EICM has a significant impact in the final distress predictions provided by the guide. The approach incorporates unsaturated soil mechanics principles to analyze and predict the performance of the pavement. The EICM makes use of real time hydraulic gradients (gravimetric and capillary/suction) as drivers in the prediction of moisture flow in a pavement system under a specific set of boundary conditions, including groundwater table location and actual site climatic conditions.

In pavement performance test sections used to enhance/verify structural design models; it is common practice that the unbound material is compacted to a predefined soil moisture and density condition for a specified laboratory-compactive energy. This is accomplished so that estimates of the initial soil strength (CBR, k value) and resilient response can be deduced from laboratory-generated properties corresponding to the expected in-situ moisture-density achieved in the construction process. These values are also typically cross verified by field testing. Recently, Federal Aviation Administration (FAA) pavement research engineers have discovered and concluded that significant changes in unbound material strength have occurred, with time even during load performance studies (Zapata, 2013, Project Proposal). Based upon these findings; the research team hypothesized that these changes in moisture, and hence in-situ strength, can only be attributed to a function of in-situ soil moisture flow that is caused mainly by the development of thermal gradients within the test sections.

To study the validity and existence of soil moisture changes by thermal gradients induced by climate changes at the National Airport Pavement Test Facility (NAPTF), this study was initiated in 2013. The goal was to verify this phenomenon and eventually incorporate

it into all future NAPTF structural performance studies. Additionally, if this hypothesis was proven, verifiable models could be developed to predict these moisture changes; and a more accurate appraisal of the test section performance would be possible.

The coupled hydro-thermal behavior of unsaturated soil has taken on increasing importance in recent years due to its significance within a variety of emerging geotechnical problems. While several analytical models for the behavior of unsaturated soils under both hydraulic and thermal gradients are available, data for validating these models and for evaluating the relevant soil properties are very limited in the literature. In addition, laboratory test methods for characterizing the soil properties needed for these models are generally in the embryonic state.

This report details the development and execution of a laboratory and field testing program aimed at enhancing the accuracy of the prediction of real-time environment effects upon the changes in unbound material strength and the resilient (non-linear) moduli for use in the design and performance evaluation/ predictions of airfield pavement systems. Finally, this study provided a unique opportunity to verify moisture movement without the effect of groundwater table location or intake of water content from outside sources.

OBJECTIVES

The main purpose of this research study is to investigate the existence of subgrade soil moisture changes that may have arisen due to thermal and hydraulic gradients at the Atlantic City NAPTF and to evaluate their effect on the resilient modulus (material stiffness) and the California Bearing Ratio (CBR) strength parameter of the clay subgrade materials used at the facility. In order to accomplish this goal, the following tasks were pursued:

1) **Evaluation of the properties of the clay subgrade soils used in the airfield test facility when subjected to unsaturated conditions and temperature changes.** This objective was accomplished by testing two different fine-grained soils in the laboratory, which correspond to the subgrade layers at the facility. A range of soil properties, from simple index properties to advanced unsaturated hydraulic and thermal property responses were obtained. The laboratory testing program included the development of soil compaction curves for dry density and moisture content at three different compacting efforts; soil moisture retention properties and unsaturated hydraulic conductivity at different temperatures; thermal properties, as well as non-linear resilient modulus, CBR and vane shear tests.
2) **Evaluation of the effects of temperature and hydraulic gradients upon the moisture changes of the subgrade materials.** To accomplish this objective, the test facility was instrumented with moisture and temperature sensors to continuously collect data for a 3-year period.
3) **Comparison of the data obtained from the field investigation with hydro-thermal model results.** A sensitivity analysis to evaluate the relative importance of unsaturated soil properties and environmental conditions upon changes in moisture content under covered areas was performed.
4) **Prediction of changes in CBR and resilient modulus caused by in-situ moisture and temperature changes.** This objective was accomplished by developing relationships that predict the changes in CBR and M_r due to the coupled effect of temperature and moisture changes in the subgrade clay layers. Laboratory experiments and field collected data were used to accomplish this objective.

5) **Evaluation of effect of external loading conditions on CBR and Resilient Modulus of the subgrade material**. In order to achieve this objective, a relationship between the stress state parameters caused by external loading conditions with the temperature was developed. This relationship was used to predict the changes in the CBR and resilient modulus of the subgrade in the field.

DISSERTATION ORGANIZATION

Chapter 1 summarizes the objectives of this study and presents a general plan of work used to accomplish the goals. Chapter 2 presents a compilation of previous findings related to the goals of this study. That includes general descriptions of unbound material characterization tests; a brief introduction to the resilient modulus and the models previously used to predict the resilient modulus of the soil; and a general framework on the environmental effects on the resilient modulus of subgrade materials. It also introduces the reader to moisture flow modeling in non-isothermal conditions.

Chapter 3 presents the data collected in the NAPTF, including the test geometry, material used for its construction, historical compaction data, CBR and FWD records. Environmental and moisture information collected during this study is also presented in this chapter.

Chapter 4 deals with the soil properties collected in the laboratories at ASU. Test results from particle size analysis, Atterberg limits, soil classification, specific gravity, compaction, consolidation, swelling tests, unsaturated thermal and hydraulic properties of the two soils are presented in this chapter.

The CBR testing program and results are presented in Chapter 5. This chapter summarizes the CBR and vane shear test results and present a prediction model to obtain CBR based on compaction conditions and energy level. Chapter 6 shows the Multilayer Elastic theory analysis used to obtain the relationship of the bulk and the octahedral stress parameters with temperature on the asphalt layer. Chapter 7 provides a description of the resilient modulus testing, evaluation and analysis of the two clay subgrades at NAPTF. Chapter 8 presents the analysis of the moisture/temperature sensor data collected in the testing facility. It also constitutes the analysis performed on the data to study the variation of the temperature and moisture content in the field. Chapter 9 constitutes the analysis of variation in the unsaturated hydraulic properties, stress state parameters, CBR and resilient modulus of the subgrade materials caused due to the variation obtained in Chapter 8. Chapter 10 is a summary of the results of the moisture field conditions modeling study. This analysis includes a parametric study accomplished with a coupled moisture-temperature software package to assess the impact of the variation of hydro-thermal unsaturated soil properties on the prediction of moisture changes in the field. Chapter 11 summarizes the study and present the main conclusions obtained. Finally, Chapter 12 compiles a set of recommendations for future studies.

Chapter 2. LITERATURE REVIEW

This chapter summarizes the literature review needed in order to understand fundamental concepts of fluid flow in porous media and its implications for the analysis and design of pavement structures. Following, it is a session that presents the strength/stiffness properties used to characterize unbound materials in pavement engineering. The effect of environmental-related factors such as moisture and temperature, along with studies that predict fluid flow due to thermal gradients are presented in the next session. Finally, a general overview of techniques used to model moisture flow in unsaturated and non-isothermal conditions is presented. The summary presented in this chapter covers the following topics: 1) Characterization of CBR and Resilient Modulus of the soils; 2) thermal effects on unsaturated soil properties; 3) moisture effects on soil resilient modulus; 4) soil moisture variability under covered areas and its subsequent effect on the strength/response of the unbound pavement layers; 5) contribution of different factors to the variability of soil resilient modulus. And 6) hydro-thermal coupled models available to predict fluid flow.

CHARACTERIZATION OF PAVEMENT SUBGRADE MATERIALS

California Bearing Ratio

The CBR of an unbound material is the pressure required to penetrate a soil mass retained in a cylindrical model of standard dimensions with a standard circular piston with an area of 3 in^2, at the rate of 1.25 mm/min. to the standard penetration pressure for a crushed stone (ASTM D1883-16). The California Bearing Ratio (CBR) test is a penetration test developed by *California State Highway Department (U.S.A.)* for evaluating the bearing capacity of subgrade soil for design of flexible pavements. Tests are carried out on natural

or compacted soils in either saturated or un-soaked (as molded) conditions. The penetration pressure results, at given penetration depths, are compared to the results of a standard material. The CBR of the soil in question is the ratio (in percentage form) of the penetration pressure of the soil in question to that of the standard material, at constant penetration depths (0.1, 0.2, 0.3 etc.). The maximum ratio obtained is called the CBR of the soil. The CBR test is one of the most commonly used methods to evaluate the empirical strength of subgrade soils, subbases, and base course materials for the design of flexible (asphalt) pavements. The results obtained by these tests are used with the thickness-CBR curves to determine the required thickness of higher quality material required above the layer where CBR is used, to minimize shear displacements in this layer.

Vane Shear Test

The Vane Shear is moderately rapid and economical test used for determining the undrained shear strength of the soils. It can be used on either remolded (compacted) or undisturbed specimens. According to ASTM standard D2573, the apparatus has a four-bladed vane, which is inserted into a fine grained material and is rotated slowly until the necessary torque to rotate the vane remains constant. The Resisting torque is measured and used to predict the undrained shear strength of the soil (s_u), as follows:

$$s_u = T/K$$

Where: T is the Torque in N-m and K is the constant depending on the dimensions and shape of the vane.

Resilient Modulus

Pavement structures experience deformations under each load cycle. The total deformation is characterized as being comprised of recoverable (elastic or resilient) component as well

as a permanent (unrecoverable or plastic) component. This deformation can be related to the type and properties of the materials used in the pavement structure. The concept of Resilient Modulus (M_r) was initially conceived by Seed et al. (1962), after literature published by Hveem (1948) that showed the elastic component of the deformation as being directly related to the performance (life) of the pavement system. Thus, only recoverable strains are used to find the M_R of materials, a basic property of pavement materials being characterized (Hveem 1948). Seed et al. (1962) defined M_r as the ratio of applied dynamic deviatoric stress σ_d, to the resilient (recovered) strain component ε_r under a transient dynamic pulse load. Therefore, the resilient modulus is the elastic modulus based on the recoverable strain under repeated loads (repeated deviator stresses) and is defined as:

$$M_r = \frac{\sigma_d}{\varepsilon_r}$$

Where: M_r = resilient modulus, σ_d = repeated deviator stress, and ε_r = resilient strain.

Seed et al.'s initial pioneering work was done primarily with fine grained cohesive soils. For this class of materials, it was found that the M_r value was highly dependent upon the σ_d stress state magnitude. Thus, the M_r value must be recognized as a non-linear moduli response.

In the early 60's, Seed et al. (1962) introduced a test for M_r measurement. The simulation is accomplished by the repeated application of a deviator stress on a confined specimen mounted in a triaxial cell. Under the conditioning sequence, the specimen is subjected to a large number of deviator stress repetitions in order to obtain a stabilized resilient strain. Once the strain is measured, the procedure is repeated for different combinations of confining pressure and deviator stress to produce an array of different states of stress

expected to be encountered in the field. The data obtained from this test is then statistically analyzed to develop the specific M_r predictive model.

Under dynamic load, the stress state for unbound materials will vary according to certain parameters such as the wheel load magnitude, the location with respect to the wheel load, the material properties and the geometry of the pavement structure. Hence, stress invariants were used to represent the state of stress of a soil under dynamic loading for convenience to practice, due to the facts that the stress invariants are independent of coordinate transformation and are functions of the stress tensor. The most common way to express a stress invariant is by using the principal stresses. The state of stress in pavements, at a given point, can be described in terms of the following stress invariants: bulk stress (θ) or total volumetric component, and octahedral shear stress (τ_{oct}) or total deviator component. Under triaxial test conditions, the bulk stress is obtained from the following equation:

$$\theta = \sigma_1 + \sigma_2 + \sigma_3$$

Where: σ_1, σ_2 and σ_3 are the major, intermediate and minor principal stresses.

The octahedral shear stress can be obtained from:

$$\tau_{oct} = \frac{1}{3}\sqrt{(\sigma_1 - \sigma_2)^2 + (\sigma_1 - \sigma_3)^2 + (\sigma_2 - \sigma_3)^2}$$

The intermediate and the minor principal stresses have the same magnitude ($\sigma_2 = \sigma_3$) and hence, the expressions are reduced to:

$$\theta = \sigma_1 + 2\sigma_3$$

and

$$\tau_{oct} = \frac{\sqrt{2}}{3}(\sigma_1 - \sigma_3)^2$$

Different from unsaturated soils, the mechanical behavior of saturated soils can be expressed as a function of one stress state, conformed by two independent stress variables, called the effective stress:

$$\sigma' = \sigma - u_w$$

where: σ' = effective normal stress, σ = total normal stress, and u_w = pore-water pressure.

Stress conditions are generally regarded as the most important factor affecting the resilient behavior of granular and fine-grained materials. Over the last five decades, researchers have used different models to attempt to relate the stress state, represented by different variables, to the resilient modulus. Initially, the behavior of granular soils was found to vary primarily as a function of the bulk stress (first stress invariant), while the applied deviator stress was found to be more important for fine-grained soils. The stress-sensitive nature of the resilient modulus of granular materials has traditionally been characterized by the following equation:

$$M_r = K_1\theta^{K_2}$$

Where: θ is the bulk stress, and K_1 and K_2 are regression constants. Studies have clearly shown that the most typical ranges for K_2 are from 0.3 to 0.8, with an average value of 0.5 typical for most cohesionless materials.

On the other hand, the resilient modulus of fine-grained materials was found to be better characterized by the following equation:

$$M_r = k_1 \sigma_d^{-k_2}$$

Where, σ_d is the applied deviator stress, and k_1 and k_2 are regression constants. Note that the negative sign on the k_2 coefficient implies stress softening behavior, which is typical of fine–grained soils; whereas stress–hardening behavior is more often observed in granular materials. These two equations were combined in the current version of the stress dependent model called the Universal Model (Witczak and Uzan 1992):

$$M_r = k_1 . p_a . \left(\frac{\theta}{p_a}\right)^{k_2} . \left(\frac{\tau_{oct}}{p_a} + 1\right)^{k_3}$$

where, M_r= resilient modulus, p_a = atmospheric pressure, k_1, k_2, k_3 = regression constants, θ = bulk stress, and τ_{oct} = octahedral shear stress.

This model can be seen to be a single "universal" model used to characterize the non-linear M_r behavior of all soils. The use of the atmospheric pressure term (p_a) for the user to define dimensionless values of the three regression fitting coefficients (k_1, k_2 and k_3). Thus, regardless of which units are used during the M_r test (US system or metric system); only one set of k_i values will be obtained.

The complexity of the testing dynamics, test equipment and the implementation of these results in a practical design methodology required for the laboratory repeated load triaxial tests have led to the development of approximate methods for the estimation of M_r in design procedures. Simple empirical relationships between the CBR and M_r of materials were among the earliest attempts to incorporate M_r into pavement design approaches. One of the earliest such correlations introduced into the literature was the relationship developed by Henkelon and Foster (1960):

$$M_r(\text{psi}) = 1500\,\text{CBR}$$

This model was primarily developed from wave propagation theory related to the elastic modulus of the media the wave propagates through. While the relationship was initially used by many researches and organizations; it was eventually shown to be highly inaccurate for CBR value in excess of 10 to 12. Its use should not be applied in any current design or analysis methodologies.

The AASHTO MEPDG uses the following relationship developed by the Transport and Road Research Laboratory (TRRL) (Lister 1987) for estimating the modulus of unbound materials:

$$M_r(\text{psi}) = 2555.\ \text{CBR}^{0.64}$$

The correlation equations are non-stress dependent relationships, which is a limitation since it is clear that the M_r response is non-linear stress dependent. Hence, these relationships provide fair values. Some of the other direct correlations used in the MEPDG relate M_r with the resistance value of compacted soils (R) and the AASHTO layer coefficient (a_i). These relationships are expressed as follows and are currently used in the new AASHTO MEPDG approach:

$$M_r(\text{psi}) = 1155 + 555\,.\,R$$

$$M_r(\text{psi}) = 30000\,.\left(\frac{a_i}{0.14}\right)^3$$

where: R = Resistance value of compacted soils, and a_i = AASHTO layer coefficient.

Indirect relationships used in the MEPDG are based on expressions that relate CBR to index properties (percent passing #200 and Plasticity Index) or Dynamic Cone

Penetrometer index (DCP). There are two expressions available that relate CBR to index properties of the soils. The first one is a correlation between CBR and the weighted plasticity index of the soil termed wPI (NCHRP 1-37A, 2004). The wPI is the product of the percentage passing #200 sieve (used as a decimal) and the plastic index (PI) (ASTM D 4318-10) (in percentage form) obtained from Atterberg Limits tests. This correlation applies to soils that contains more than 12% fines and exhibit some plasticity for which wPI is greater than zero.

$$\mathrm{CBR} = \frac{75}{1 + 0.728\ (\mathrm{wPI})}$$

CBR for coarse, clean and typically non-plastic soils for which wPI is equal to 0, are correlated with the Diameter 60 (D_{60}) from the grain size distribution curves. The correlation is as follows:

$$\mathrm{CBR} = 28.09\ (D_{60})^{0.358}$$

In addition, the general relationship between CBR and the dynamic cone penetrometer index (ASTM D6951) is given by:

$$\mathrm{CBR} = \frac{292}{\mathrm{DCP}^{1.12}}$$

where: DCP = Dynamic Cone Penetrometer index (mm/blow).

In summary, while the empirical CBR-M_r relationships are generally satisfactory for use with typical highway loadings (i.e., 18 kips single axle load); it is important for the designer to understand that the implementation of this equation to predict layer moduli (M_r) based upon the CBR of the material, may be inaccurate when applied to airfield pavement design.

This is directly a consequence of the fact that the M_r is non-linear and stress state due to external loads, between highways and airfields, may be very significantly different. This fact should be evident throughout the research study described in this document.

ENVIRONMENTAL EFFECTS ON THE STIFFNESS/STRENGTH OF SUBGRADE MATERIALS

Thermal Effects on Unsaturated Soil Properties

Temperature and moisture play a major role in pavement performance. The effect of moisture on pavement performance is more significant on unbound materials than on bound materials, especially for asphalt pavement systems (Zapata et al. 2007). Furthermore, temperature affects both the bound (asphalt and cement) and unbound layers significantly.

Near the ground surface, unsaturated soil behaves as a dynamic system that interacts with the atmosphere and the deeper layers. Several phenomena take place, which affect the amount of water stored in the soil. These phenomena can be modeled using fundamental laws (e.g., conservation of momentum, mass and energy) and constitutive relationships for soils.

The flow of water in saturated/unsaturated soils and the soil-atmosphere fluxes have been studied by a variety of engineering and science disciplines. The different perspectives have led to different emphases related to driving potentials, soil phases, and gradients coupling. Two distinct mechanistic approaches to the analysis of moisture flow in soil can be found in the literature. The first approach considers that the flow of moisture occurs only in liquid form, while the second approach incorporates both liquid water and water vapor flows along with heat flow.

In the last three decades, the air phase of unsaturated soil systems has been incorporated into the multi-phase material analysis through the matric suction (the difference between the air and water pore pressures) as an independent stress state variable (Fredlund and Rahardjo 1993). As the soil moves from a saturated state to a drier condition, the distribution of soil, water, and air phases changes due to the stress state changes. The relationships between these phases take on different forms. For example, in some cases, the behavior may be primarily related to the volume of the separate phases (e.g., volumetric water content), or the continuity and tortuosity of the liquid phase (e.g., hydraulic conductivity, molecular diffusion) or the air phase (e.g., diffusion coefficient of vapor) (Barbour 1998). Hence, the complexity surrounding unsaturated soil systems (e.g., there is not a single effect, but a combination of conditions) explains the limited data available on the dependency of soil suction and conductivity on temperature changes.

Recent attempts to measure suction at different temperatures have shown a decrease in suction as temperature increases (Uchaipichat and Khalili 2009). Recent studies performed by Lu, 2015 for the two soils of County clay and Dupont clay contributes to the theory that as the temperature increases the suction decreases. Lu also performed a study on the unsaturated permeability of the soil and the effect of temperature on it. It showed that the permeability of unsaturated soil increases with temperature. However, the range of suction values and soil types investigated remain very limited. In addition, several investigators have provided theoretical and semi-empirical relationships to predict the variation of the hydraulic conductivity for unsaturated soil conditions (van Genuchten 1980; Toll 1990; Fredlund et al. 1994; Barbour 1998; Assouline and Tartakovsky 2001; Houston et al. 2001).

Most of these methods are used in design of soil covers, disposal barriers and other geotechnical structures (Lin and Benson 2000).

Effect of Moisture Content on Resilient Modulus and CBR

In general, most unbound pavement materials are generally compacted at optimum moisture conditions. However, once compacted the moisture content will change from the initial compaction moisture content to an equilibrium moisture content that will be heavily dependent upon the site environmental conditions, water table location as well as the properties of soil materials. Once the moisture content reaches equilibrium, the material moisture content will still deviate from equilibrium as long as seasonal environmental variations are present in the pavement layers.

Witczak et al. (2000) studied changes in moisture content from compaction to equilibrium and those due to seasonal variations and found that even low variations may cause a large effect in the resilient modulus of materials. A change in modulus over two orders of magnitude was observed for a clayey sand demonstrating that the effect of moisture content variation may be as significant as the effect of variations in the state of stress can cause. High moisture contents are deleterious for unbound materials in two ways: by affecting the stress of state through suction or pore water pressure or by affecting the structure of the soil through destruction of the cementation between soil particles.

The resilient modulus of any unbound material decreases as a consequence of an increase in the moisture content. Therefore, it is important to take into account the variations of moisture as one of the environmentally driven variables that can affect pavement layers and subgrade decreasing the capacity of the structure for carrying loads. The change of suction in the soil causes a change in the soil moisture content and the corresponding

modulus values. To reproduce field conditions more reliably, it would be desirable to induce the changes in moisture content in a given compacted specimen by controlling the matric suction.

A few research studies have been completed to incorporate the variations in moisture content directly on the prediction of resilient modulus for unbound pavement materials. The new MEPDG considers the changes in temperature and moisture content in the pavement structure and subgrade over the design life of a pavement through a climatic modeling tool known as Enhanced Integrated Climatic Model (EICM). The EICM analytically predicts changes in modulus due to changes in moisture by using a model that expresses modulus as a function of the degree of saturation introduced by Witczak et al. (2000). The model is described by:

$$\log_{10}\frac{M_r}{M_{ropt}} = a + \frac{b-a}{1+EXP\,(\beta + k_s\,.\,(S - S_{opt}))}$$

where: M_r = resilient modulus at a specified degree of saturation S (%); M_{ropt} = resilient modulus at optimum dry density and moisture content; a = minimum of $\log(M_r/M_{ropt})$; b = maximum of $\log(M_R/M_{Ropt})$; β = location parameter – obtained as a function of a and b. This parameter was defined through the imposed condition of a zero intercept so that (M_R/M_{Ropt} = 1 for $S = S_{opt}$); k_S = regression parameter; and ($S - S_{opt}$) = variation in degree of saturation expressed in decimal.

The β factor is defined as:

$$\beta = \ln_e\left(\frac{-b}{a}\right)$$

The degree of saturation was used as a predictive variable by the authors because it accommodates changes in both moisture content and density of the material. Also, the erroneous values corresponding to the degrees of saturation above 100% are easily detected and avoided. Regardless of the advantages of using degree of saturations as a predictive variable to obtain resilient modulus, in 2003, Andrei proposed the gravimetric moisture content as a predictive variable arguing that it is easiest to determine and more accurate since it is not a function of the specific gravity or the volume of the test specimen. The model proposed by Andrei is shown below

$$\mathrm{Log}\frac{\mathrm{M_r}}{\mathrm{M_{ropt}}} = \mathrm{Log\,a} + \frac{\mathrm{Log\,b} - \mathrm{Log\,a}}{1 + \mathrm{EXP}\,(\beta + \mathrm{k_w}\,.\,(\mathrm{w} - \mathrm{w_{opt}}))}$$

where: w = gravimetric moisture content expressed in decimal; w_{opt} = gravimetric optimum moisture content; M_{ropt} = resilient modulus at optimum moisture content and maximum dry density corresponding to standard compaction energy; a = the minimum value of the ratio M_r/M_{ropt}; and b = maximum value of the ratio M_r/M_{ropt}.

In this case, the equation for calculating the location parameter β changes to:

$$\beta = \ln(\frac{-Log\ b}{Log\ a})$$

As observed, numerous attempts to correlate the resilience response of unbound materials with moisture content have been completed by the use of a total stress approach. However, studies on modeling the variation of modulus within a soil due to moisture content changes

by using an equivalent effective stress approach for unsaturated soils, are not that numerous.

In order to express the mechanical behavior of unsaturated soils, one additional independent stress variable representing the air phase must be considered. In 1977, Fredlund and Morgenstern found that there are three possible stress variables that can be used to define the stress state in unsaturated soils: net normal stress, effective stress and matric suction. Two out of those mentioned stress state variables were proposed by Fredlund as commonly used in the formulation of unsaturated soil problems. Furthermore, he proposed that the resilient modulus could be expressed as a function of three state stress variables for the case of triaxial loading:

$$(\sigma_1 - \sigma_3), (\sigma_3 - u_a), \text{ and } (u_a - u_w)$$

where, $(\sigma_1 - \sigma_3)$ = deviator stress, $(\sigma_3 - u_a)$ = net normal stress, $(u_a - u_w)$ = matric suction, u_a = pore air pressure, and u_w = pore water pressure.

The use of total stresses, in addition to a parameter related to matric suction, like the water content or degree of saturation, could be a good approach in the definition of the stress state as used by Andrei in the development of a resilient modulus predictive equation in 2003. One of the objectives of Andrei's research was to find a predictive equation, based in the stress state variables proposed by Fredlund, which uses the matric suction as a predictor parameter. Therefore, in terms of stress invariants the three state parameters can be expressed in the following way:

$$\theta_{net} = \theta - 3u_a$$

$$\tau_{oct} = \frac{1}{3} \cdot \sqrt{(\sigma_1 - \sigma_2)^2 + (\sigma_1 - \sigma_3)^2 + (\sigma_2 - \sigma_3)^2}$$

$$(u_a - u_w)$$

Musharraf Zaman and Naji Khoury (2007) performed a study that focused on evaluating the effect of post-compaction moisture content on the resilient modulus of some selected soils in Oklahoma. The resilient modulus tests were performed on compacted specimens that were subjected to a wetting and drying process. After the completion of resilient modulus testing, the filter paper tests were performed in accordance with the ASTM standard D6836 The same technique was used to establish the soil-water characteristic curves. Results showed that the resilient modulus exhibited a hysteric loop with moisture variations. The M_r values due to wetting were found to be lower compared to the values after drying. It was also found that the initial compaction moisture content followed by drying or wetting affected the hysteritic loop of both SWCC and the M_r -moisture variation curve. It was also observed that the resilient modulus increased as the soil suction increased; however, such increase was found to vary from one soil to another.

Cary and Zapata (2010) studied the effects of the moisture content in the soil resilient modulus in terms of suction. The variation of the resilient modulus as a function of the stress state of unsaturated soil was measured. Based on the results obtained, the following model was proposed:

$$M_r = k_1 . p_a . \left(\frac{\theta_{net} - 3 . \Delta u_{w-sat}}{p_a}\right)^{k_2} . \left(\frac{\tau_{oct}}{p_a} + 1\right)^{k_3} . \left(\frac{\Psi_{m_0} - \Delta\Psi_m}{p_a} + 1\right)^{k_4}$$

where: M_r = resilient modulus; p_a = atmospheric pressure; k_1, k_2, k_3 and k_4 = regression constants; $\theta_{net} = \theta - 3u_a$, the net bulk stress; Δu_{w-sat} = buildup of pore water pressure under saturated conditions, in this case $\Delta \psi_m = 0$; τ_{oct} = octahedral shear stress; ψ_{m_0} = initial matric suction; and $\Delta \psi_m$ = relative change of matric suction with respect to the initial matric suction due to buildup of pore water pressure under unsaturated conditions, in this case $\Delta u_{w-sat} = 0$.

The strength of the soil, which is indirectly measured using the CBR value, is also significantly influenced by the moisture content. Kofi Ampadu (2007) analyzed the influence of moisture content on the CBR value at different dry densities. The study established a relationship between unsaturated CBR and soaked CBR as a function of the suction stress, as shown in the following equation:

$$CBR_u = CBR_s \times \left(\frac{u_a - u_w}{u_e}\right)^n$$

where, CBR_u =unsaturated CBR; CBR_s=soaked CBR; u_e = air-entry value; u_a = pore air pressure; u_w = pore water pressure; and n = constant which depends on the suction and the dry density. In this study, n was of the order of 1.4 and about 0.5 from the lowest to highest dry densities, respectively; and constant for suction values up to about 15,000 kPa.

Effect of Temperature Changes on the Unbound Materials Moduli

Temperature and moisture play a major role in pavement performance. The effect of moisture in pavement performance is more significant on unbound materials than on bound

materials. On the other hand, temperature affects both the bound (asphalt and cement) and unbound layers significantly (Zapata et al., 2007).

Hossain et al. (2000) performed a real time analysis of four pavement sections in regions of Kansas for a year in order to investigate the effect of moisture content and temperature on the moduli of the pavement. The study concluded that moisture content variation in the pavement was minimum and it had little effect on the variation in the moduli of the pavement. The study also concluded that the variation in the temperature induces a change in the horizontal and the vertical stress or deviator stress in the soil, which leads to a change in the moduli of the soil. On the other hand, Coccia (2013) showed that there was a change in the effective stress, and in turn, a change in the shear strength of the soil due to changes in suction induced by temperature gradients. The study succeeded in clearly explaining the consequences of the thermal gradient in the soil behavior. It explained that the thermal gradients in the soil influenced moisture flow, which was measured through the suction in the soil. The change in the hydraulic conductivity was related to the measurement of the suction in the soil. The study also showed that the initial moisture content might influence moisture flow. This can be due to the influence of moisture on the thermal properties of the soil, water and air phases. The paper also explained that the observed changes in the effective stress, shear strength and the volume change were attributed to the thermal gradients present in the soil.

Effect of Temperature on Soil Moisture Variability in Unbound Layers

Various research studies have been performed to validate the model with field data. Gurr et al. (1952) performed an experimental analysis to study the contribution of temperature gradients to liquid and vapor flows in the soil. The results showed that in all cases, there

was a transfer of water towards the cold end. Further analysis indicated that there was a vapor transfer, which occurred towards the low-temperature end while the liquid seemed to have moved in the direction of increasing temperature. The results obtained contradicted previous findings that liquid form of water always moves from higher to lower temperature.

Barbour (1995) performed a real time analysis of a pavement by measuring the matric suction and the moisture content of the railway embankment in Winnipeg, Manitoba. The real time data was compared with the data predicted using his model. The study concluded that suction decreased with a decrease in seasonal temperature. The data also showed the soil seemed to equilibrate slowly with the environmental temperature and moisture conditions, which validated his model. The field evidence along with the model further showed that subgrade beneath the highway attain equilibrium condition eventually and this equilibrium condition is controlled by the micro-climate and the material used for the shoulder. The infiltration resulted in the wetting of the pavement due to strong lateral flows under high flux rates. Evaporation tended to induce strong flow up across shoulders and ditches with little in the center of pavement.

Hossain (2000) performed an analysis to investigate the effect of temperature variation on the subgrade response. Though the research concluded the variation of moisture underneath the pavements is minimal, it showed there is an existence of moisture movement in the pavement through different seasons. Results showed that temperature has a direct effect on the moduli of the soil. A change in the temperature of the soil might cause a change in the properties of the asphalt layer. Thus, the load transferred through the asphalt layers to the subgrade material are affected by the changes in asphalt temperature. Hence, a change in

the deviator stress applied on the soil, caused by the variation in temperature, seemed to be responsible for the changes observed in the soil moduli.

PREDICTION OF FLUID FLOW DUE TO THERMAL GRADIENTS

Thermal moisture transport can be thought of as the moisture flux through soil that arises only due to a temperature gradient. In other words, thermal moisture transport is the phenomenon of water flowing in (or out) of a system due to a difference in soil temperatures. Cary (1966) specifically states "It is the flow of moisture which would occur even in the absence of all moisture content, osmotic, electrical, and pressure gradients". However, moisture transfer due to thermal gradients will produce changes in moisture contents and pressures. This, in turn, creates a hydraulic gradient that generates a coupled flow analysis that must be accounted for in analyzing net moisture flow (Cary, 1966). Research and observations tell us that moisture (both vapor and liquid) will tend to flow from areas of higher thermal energy to areas of lower thermal energy. Flow in the vapor phase is analyzed different than the flow in the liquid phase, and each will be discussed in the following paragraphs.

Vapor transport induced by a thermal gradient is a molecular diffusion process described by the following equation:

$$J_{vap} = -\beta \frac{DpH}{R^2 T^3} \frac{dT}{dz}$$

where: J_{vap}=thermally induced flow of vapor (moles $sec^{-1}cm^{-2}$); β = a factor accounting for pore geometry, cross sectional area of voids and microscopic temperature discontinuities; D = diffusion constant of water vapor in air (cm^2 sec^{-1}); p = vapor pressure

of water (cal/cm^3); H = heat of vaporization of water (cal/mole); R = gas constant (cal./°K/mole); T = temperature (°K); and z = soil depth (cm).

This equation can be derived from the theory of thermodynamics of irreversible processes. It may also be derived by combining the Clausius-Clapeyron equation with Fick's first law (Cary, 1966). Because the water vapor is not measure in the field, nor in the lab, this equation is included purely for reference to understand what causes the water to move thermally.

According to Cary, liquid moisture and liquid vapor, tends to flow from warm to cool regions. However, in-depth literature review shows that there are cases where moisture will flow from cool to warm regions. This anomaly is usually associated with organic type membranes. Because the flow of liquid moisture due to the influence of a thermal gradient is not well understood, there are four possibilities as to why liquid moisture will flow due to a thermal gradient (Cary, 1966):

1: Since the surface tension of water against air increases as the temperature decreases, moisture in unsaturated soil could flow from warm to cool regions under the influence of a surface tension gradient.

2: Another possibility is that soil moisture suction increases as the temperature decreases. This could contribute to the moisture flow. This theory is the basis of the thermally induced liquid flow equation developed by Philip and de Vries (1957).

3: Deryaguin and Melnikova (1956) studied liquid water flow through soil and hypothesized that water might flow from cool to warm regions due to the difference in specific heat content between the liquid layer adsorbed on the solid surface and the specific heat content of the bulk of the liquid in the pores. This led to a proposal

that liquid transport is a result of a net motion generated by random kinetic energy changes associated with the hydrogen bond distribution, which develops under a thermal gradient (Cary, 1965).

4: Finally, flow could result from thermally induced osmotic gradients. To explain, most dissolved salts spontaneously diffuse through a solution from warmer areas to cooler areas. This is known as the Soret effect.

Because of the uncertainties in the mechanism of thermally induced flow in the liquid phase, Cary (1966) states that a phenomenological equation must be used to describe this component of flow:

$$J_l = -\frac{KQ}{aT}\frac{dT}{dz}$$

where: J_l = thermally induced liquid phase of flow (mm hr^{-1}); K=capillary conductivity (mm hr^{-1}); Q = liquid phase heat of transport (ergs g^{-1}); a = acceleration due to gravity (cm sec^{-2}); T = temperature (°K); and z = soil depth (cm).

Taylor and Cary (1964) proved that the previous equations are essentially the same as those developed by Philip and de Vries (1957). This is an important validation because these equations are created from the theory of irreversible thermodynamics where the equation developed by Philip and de Vries (1957) do not.

When it comes to unsaturated soils, the magnitude of thermally induced flow increases dramatically as the moisture content drops. As Cary (1966) states, the decrease in moisture content brings about a decrease in the thermal liquid moisture flow and an increase in the thermal vapor moisture flow. No matter what moisture content the soil is at, the vapor flow due to thermal effects will increase faster with rising average temperatures than the liquid

flow. This is due to the exponential dependence of vapor pressure on temperature (Cary, 1966).

When modeling the heat movement, liquid, and vapor water flow in soil, the model developed by Philip and de Vries (1957) is generally the most widely accepted. The model they developed is a coupled analysis that presents two non-linear differential equations describing the simultaneous flow of liquid water, water vapor, and heat in soil (Arab, 2014). In order to model the moisture gradient, the following differential equation must be differentiated:

$$\frac{Q_m}{\rho_w} = -D_T \nabla T - D_\theta \nabla \theta - ki$$

where: Q_m = net mass water flux; ρ_w = density of liquid water; D_T = thermal moisture diffusivity; ∇T = thermal gradient; D_θ = isothermal moisture diffusivity; $\nabla \theta$ = moisture content gradient; k = unsaturated hydraulic conductivity; and I = unit vector in z direction (depth).

After differentiating the above equation and applying the necessary continuity requirements, the following general equation is found:

$$\frac{\partial \theta}{\partial t} = \nabla \cdot (D_T \nabla T) + \nabla \cdot (D_\theta \nabla \theta) + \frac{\partial k}{\partial z}$$

where: $\frac{\partial \theta}{\partial t}$ = change in volumetric water content with respect to time; and t = time.

From Mitchell and Soga (2005), in this equation, the vapor flow is driven by the moisture and temperature gradients, and the liquid flow is driven by the moisture and temperature flows.

Modeling Unsaturated Soil Moisture Flow in Non-Isothermal Conditions

Theoretically, it has been conclusively demonstrated that fluid flow might occur in soil systems under non-isothermal systems. For example, highway and airfield pavements (or any foundation system) built in an area where seasonal or daily temperature variation can cause temperature redistribution in soil systems. This results in a thermal gradient within the soil mass, which will result in fluid flow. Wilson (1990) accounted for water vapor flow due to diffusion and the advection process by adding one term into the water flow equation for one-dimensional consolidation. The one-dimensional fluid and vapor flow differential equation for water phase can be expressed as follows:

$$\frac{\partial u_w}{\partial t} = -C_w \frac{\partial u_a}{\partial t} + \frac{1}{g\rho_w m_2^w} \frac{\partial \left(k_w \frac{\partial u_w}{\partial y} \right)}{\partial y} + \frac{\overline{u_a} + \overline{u_v}}{\overline{u_a}} \frac{1}{\rho_w m_2^w} \frac{\partial \left(D_v \frac{\partial \overline{u_v}}{\partial y} \right)}{\partial y}$$

where: C_w is an interaction coefficient associated with the water phase partial differential equation; u_v is the partial pressure of water vapor in air; u_a is the gauge pore-air pressure; $\overline{u_a}$ is the absolute pore-air pressure; m_2^w is the coefficient of water volume change in respect to soil suction; D_v is coefficient of consolidation with respect to the water vapor through the soil.

D_v can be calculated as follows (Philip and de Vries, 1957; de Vries, 1975; Dakshanamurthy and Fredlund, 1981; Wilson, 1990) by:

$$D_v = \alpha\beta \left(D_{vm} \frac{\omega_v}{RT_k} \right)$$

where: α is the tortuosity factor for the soil; β is the cross-sectional area of the soil available for water vapor flow $[(1 - S)n]$; D_{vm} is the molecular diffusivity of the soil available for

water vapor in air; ω_v is the molecular mass of water vapor; T_k is the temperature in Kelvin; R is the universal gas constant; S is the degree of saturation; and n is the porosity.

Clearly, the diffusion coefficient is a function of soil properties (s, n) and temperature, and S (degree of saturation) is a function of matric suction.

If one neglects the variation of hydraulic conductivity (k_w) and coefficient of water vapor diffusion (D_v) with respect to space, Wilson (1990) proposed a differential equation for the combination of vapor and liquid flow, it is given by;

$$\frac{\partial u_w}{\partial t} = -C_w \frac{\partial u_a}{\partial t} + C_v^w \frac{\partial^2 u_w}{\partial y^2} + C_v^{wv} \frac{\partial^2 \overline{u_v}}{\partial y^2}$$

where: C_{vw} is the coefficient of consolidation with respect to water phase [i.e., $k_w / (\rho_w g m_2^w)$]; C_v^{wv} is the coefficient of consolidation with respect to water vapor phrase; and C_w is an interaction coefficient associated with the water phase partial differential equation.

Various researches (Wang et al., 2004; Wu et al., 2004; Dakshanamurthy and Fredlund, 1981) have performed numerical analyses on thermo-hydro-mechanical properties of unsaturated soil. Wu et al. (1981) created a thermo-hydro-mechanical model for unsaturated soils and implemented the solution within a finite element analysis code named LAGACOM to simulate experiments. The numerical modeling was compared with experiments results and found the model simulation reached satisfied results. The numerical modeling included creation of "thermal soften curve", "loading –collapse curve" and "thermal yield curve" to describe the relationship between temperature and soil consolidation and deformation when the soil is under loading. Experiments were performed

to compare the modeling result of two soil cubes varies with various dimensions and boundary conditions. The volumetric strain, vertical strain and water intake results of these experiments were compared to the modeling outcome and found to be satisfactory.

Dakshanamurthy and Fredlund (1981) presented a theoretical model to predict the moisture flow in unsaturated soil. The model consisted of two conditions: isothermal condition and non-isothermal condition. In the isothermal condition, water flow was a result of a hydraulic gradient. The non-isothermal condition involved moisture flow due to both temperature and hydraulic gradients. Solving the problems for non-isothermal conditions required both, a water phase and an air phase partial differential equations. The water flow partial differential gradient equation used Darcy's law and the air flow partial differential equation used Fick's law. Example problems solved involved the prediction of moisture flow under a thermal gradient in an unsaturated soil, which can simulate moisture flow in airfield and highway unbound material pavement foundation systems. The example used was initiated with an equilibrium condition, which was then subjected to various sudden environment changes such as evaporation, infiltration and temperature. The result of these modeling effort showed that all models reached new equilibrium conditions dictated by the initial and respective boundary conditions used in each example.

Several heat and moisture flow models can be found in the literature. Philip and de Vries (1957) presented a two-dimensional coupled heat and moisture flow model with two equations: the first for the moisture flow and the second equation for the heat flow.

Wilson (1990) proposed a set of differential equations to model liquid water, vapor and heat flow in the vadose zone based on differential equations derived by Dakshanamurthy and Fredlund (1981). The vapor partial pressure was added as a function of the soil relative

humidity, which was considered as the driving gradient for the vapor flow in the soil. A one-dimensional equation was proposed for the combined flow of the liquid water and water vapor, as follows:

$$\frac{\partial h}{\partial t} = C_w \frac{\partial}{\partial y}\left(k_w \frac{\partial h_w}{\partial y}\right) + C_v \frac{\partial}{\partial y}\left(D_v \frac{\partial P_v}{\partial y}\right)$$

where, the modulus of volume change with respect to the liquid phase, C_w, is a function of the coefficient of water volume change with respect to matric suction; C_v is a function of a correction factor for vapor diffusion and the partial pressure in the soil due to water vapor; and D_v is the diffusion coefficient of water vapor through the soil.

Wilson (1990) used the Jame and Norum (1980) equation for the heat flow. This equation neglects the convection term and accounts only for conduction and latent heat.

$$C_h \frac{\partial T}{\partial t} = \frac{\partial}{\partial y}\left(\lambda \frac{\partial T}{\partial t}\right) - L_v \left(\frac{p + p_v}{p}\right) \frac{\partial}{\partial y}\left(D_v \frac{\partial P_v}{\partial y}\right)$$

where, C_h is the volumetric specific heat; λ is thermal conductivity; and L_v is latent heat of water vaporization. The third term represents the phase change from vapor to liquid and vice versa.

The water and thermal energy balances are linked to the soil atmosphere interface through the evaporation, which is controlled by the climatic conditions and soil properties. Methods to estimate the evaporation are described by several authors: Thornthwaite and Mather (1955), Penman (1948), and Wilson et al. (1994).

The use of these equations requires the knowledge of four relationships to describe the properties of the soil in the system (Mitchell and Soga, 2005): 1) hydraulic conductivity as

a function of water content; 2) thermal conductivity as a function of water content; 3) volumetric heat capacity; and 4) suction head as a function of water content. This approach is only applicable to homogenous and isotropic porous media, and has several shortcomings: it assumes the soil volume will remain constant, it cannot account for flow due to the changes in total stress, and the water flow is in response to moisture content gradients (rather than gradients in head), which implies that the soil is homogeneous. Nevertheless, this modeling scheme is viewed as a very important piece of work as it opened the path for a better understanding of fluid flow in soils.

The models developed by Wilson et al. were expanded to two dimensions and presented by Gitirana et al. (2006). Limited verification of the model with sand column experiments demonstrated the importance of coupling between moisture and heat and the importance of the water vapor component during evaporation. The soil property functions needed to predict the soil moisture and heat flows in unsaturated soils are summarized and presented in Table 2.1 (modified after Gitirana et al. 2006).

Table 2.1. Soil Property Functions Required to Model Coupled Hydro-Thermal Flow

Type of Analysis	Soil Property Function
Moisture Flow	Soil water characteristic curve
	Unsaturated hydraulic conductivity
Vapor Flow	Diffusion coefficient of water vapor through the soil
	Water vapor partial pressure
Heat Flow	Thermal conductivity
	Volumetric specific heat

NUMERICAL MODELS AVAILABLE TO ESTIMATE UNSATURATED SOIL MOISTURE AND HEAT FLOW

Groundwater flow problems in geotechnical and geoenvironmental engineering involve the solution of partial differential equations (PDEs) presented above. The theory of groundwater flow embraces the physical behavior of material and the conservative laws of physics. The physical behavior of many materials, especially unsaturated soils, is nonlinear and therefore, the solution of nonlinear PDEs is a challenging task.

The software package chosen for this study is SVFux from SoilVision©. SVFlux is a finite element seepage analysis modeling software program which is part of the SVOffice analysis suite produced by SoilVision Systems, Inc. of Saskatoon, Saskatchewan, Canada. The software is designed to analyze both saturated and unsaturated flow in both steady-state and transient time conditions. The software is widely used in the field of civil engineering and hydrology to solve seepage problems. SVFlux solves the PDE using finite element analysis. Each finite element represents a discrete portion of the problem, for which the solution of the PDE must be obtained. The seepage algorithm in SVFLUX is based on Darcy's law, Fick's law and conservation of mass.

There are several numerical models available to estimate unsaturated soil moisture flow. All of them have the capability of modeling hydro-thermal processes but most of them have limitations associated with the numerical solution or with input requirements. Software packages that include water balance equations and are commonly used in design decision making processes are: 1) EPA Hydraulic Evaluation of Landfill Performance (HELP) model (Schroeder et. al., 1994); 2) Cornell University LEACHM model (Hutson and Wagenet, 1992); 3) UNSAT-H model (Fayer and Jones, 1990; Fayer, 2000); 4) U. of California Riverside HYDRUS-1D (University of California, 2005), HYDRUS-2D/3D

(University of California, 2007) ; 5) ERES Consultants and ASU EICM model (Dempsey et al., 1985; Guymon et al., 1986; Zapata et al., 2009); 6) ASU heat transfer ASU-NCE model (Gui et al., 2007); 7) SVFlux and SVHeat from Soil Vision Ltd. (2005), which includes the model presented by Wilson (1990) and Gitirana Jr. (2005); 8) Vadose/W from Geo-Slope Int. (2005); and 9) CODE_BRIGHT from the Barcelona group (Olivella et al., 1996).

Validation of some of the models described above has been attempted with limited soil types (Gitirana et al., 2006; Åkesson et al., 2009). Enhancements of the THM property functions of such models have further been suggested by authors such as Sakai et al., 2008 and Thomas et al., 2009. However, the studies have been limited to one property functions at a time, due to the complexity of the problem and the time associated with laboratory and field testing.

Chapter 3. HISTORICAL DATA COLLECTED FROM NAPTF

The main objective of this chapter is to present a summary of the engineering reports that have been developed at the National Airfield Pavement Test Facility (NAPTF). The review focused on three major areas directly relevant to the goals and objectives of this research study:

A) Test section layout/geometry

B) Historic unbound material properties

   1. Soil index properties/classification
   2. Strength-moduli parameters such as CBR
   3. Laboratory and field studies on the resilient moduli response of all unbound materials (lab M_r and/or field FWD test results)

C) Historic test section environmental/moisture information, including groundwater table depth changes with time.

TEST SECTION DATA

The physical layout and geometry of the test section site were obtained from NAPTF personnel and studied to aid in the placement of the sensors in the facility.

Test Section Layout/Geometry

The NAPTF test facility is 60 feet wide and 300 feet long. The depth of the test section is 144 inches. The plan view of the pavement is shown in Figure 3.1 and the section view is shown in Figure 3.2.

Materials Used for Construction

The subgrade material of the NAPTF has varied with time. For the Construction Cycle 1 (CC-1) completed in 1998, the entire subgrade was composed of County clay. When the Construction Cycle 5 began in 2007, some of the upper lifts of the clay subgrade were replaced with Dupont clay due to the fact that the County clay was no longer available and the subgrade had been contaminated with sub-base materials during experimentation. Therefore, after CC-5 the subgrade soil has been composed of two layers: County clay, which extend from 144 inches to 83 inches in depth; and above it, Dupont clay, which extends from 83 inches to 29 in depth. A cross section of the test section is presented in Figure 3.2.

Of especial interest but not collected yet is data about the construction of the on-site moisture barrier and the anticipated layouts of future load cart trafficking lanes.

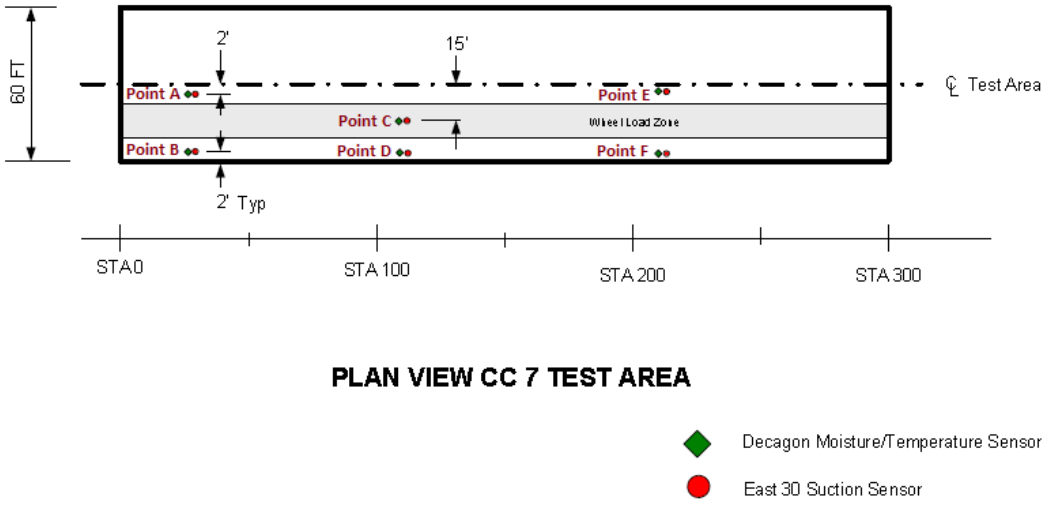

Figure 3.1. Plan View of NAPTF Test Section.

UNBOUND MATERIAL PROPERTIES

The data collected included information of all materials used for construction of the pavement section along with in-situ compaction material properties (moisture and dry density), CBR data and FWD data.

Index properties

The index properties provided by the NAPTF facility included grain size distribution, Atterberg limit and the classification of the soil. Two trials of results were given. The Atterberg limit test results for county clay was found to be missing. Table 1 shows the summary of index properties collected from the NAPTF.

Historic compaction data

Data of the CC-5 layer and CC-1 layer of the compacted soil in the NAPTF was obtained. The data available correspond to the dry density and the moisture content of the soil at the time of compaction. The dry density and moisture content was obtained using ASTM D2937. Table 2 shows the data obtained for the CC-1 airfield pavement and Table 3 show the data obtained for CC-5 airfield pavement. The Construction Cycle 1(CC-1) data correspond to the pavement laid in 1998, while the CC-5 is the data for the pavement layer laid in 2007. CC-7 corresponds to the Construction Cycle 7 data, which was collected during the 2013-2014 time period. NAPTF provided dry density and moisture content data for lifts 1 to 4 of CC-7, as shown in Table 4. Figure 3.3 presents the Modified compaction curve for the Dupont clay measured by FAA personnel. The maximum dry unit weight is about 115 pcf and the optimum water content is about 15%. The raw data was not available. Figure 3.4 shows the CBR values as a function of water content for the same clay.

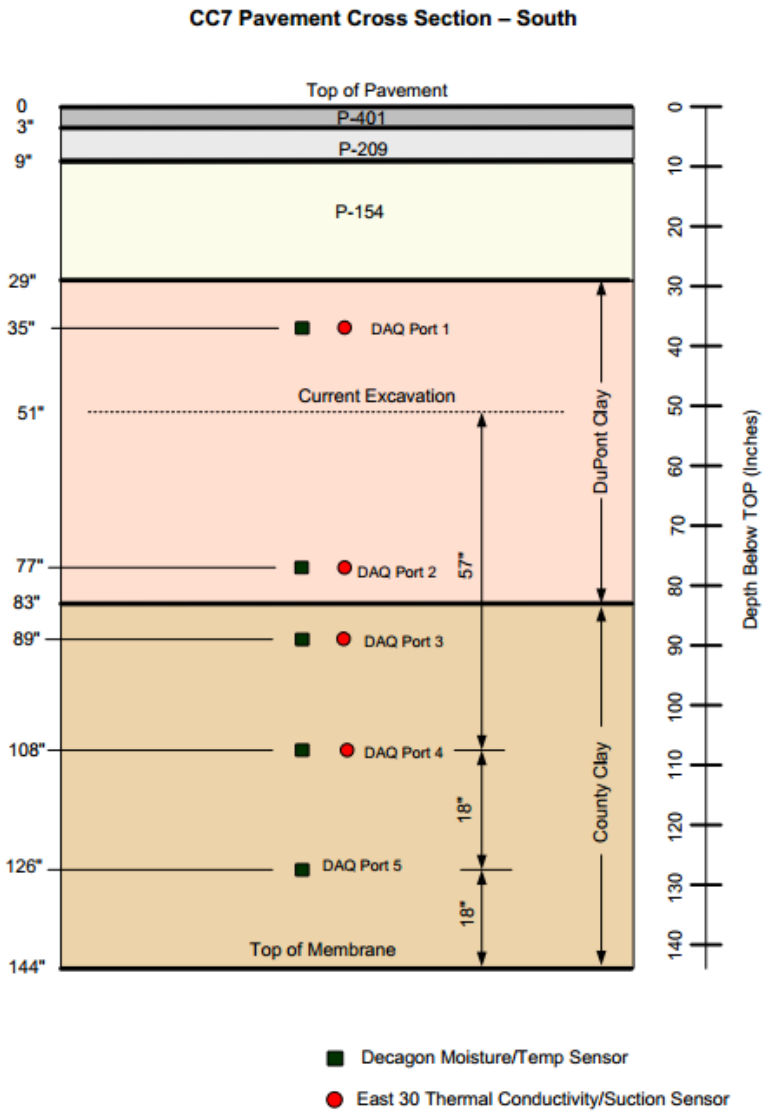

Figure 3.2. Section View of NAPTF Test Section

Table 3.1. Index Properties of Soil Used in NAPTF

Test		County		Dupont	
		Trial 1	Trial 2	Trial 1	Trial 2
Particle Size Distribution					
%Gravel	Coarse	0	0	0	0
	Fine	5.4	0.3	0.5	0
%Sand	Coarse	43.6	41.4	0.2	0
	Medium	31.4	36.4	2.5	0.4
%Fines	Fine	13.1	15.8	3.8	1.4
	Silt	6.5	6.1	23.5	26.9
	Clay			69.5	71.3
Atterberg Limits					
Liquid Limit		N/P	N/P	52	50
Plastic Limit		N/P	N/P	31	25
Plasticity Index		N/P	N/P	21	25
Classification					
USCS		SP-SM	SW-SM	CH	CH
AASHTO		A-1-b	A-1-b	A-7-6	A-7-6

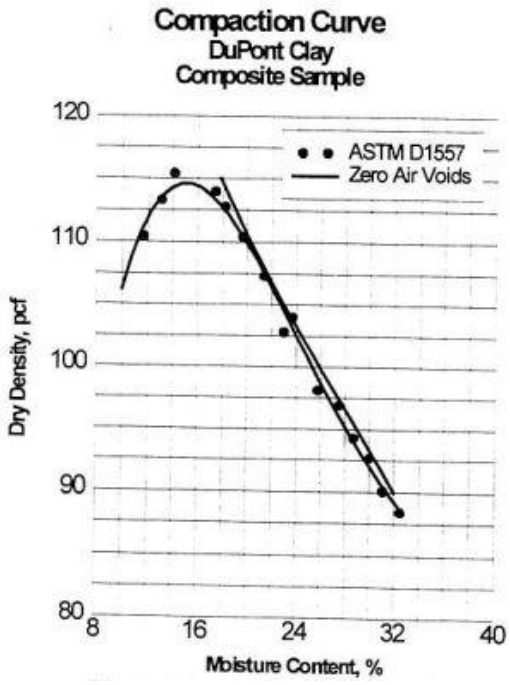

Figure 3.3. Modified Proctor Curve for Dupont Clay

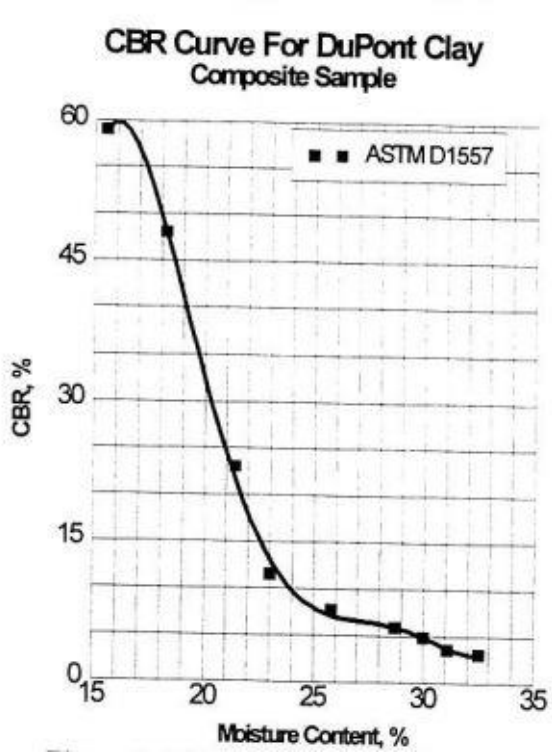

Figure 3.4. CBR Vs Moisture Content Curve for Dupont Clay

Table 3.2. Density, Moisture Content and CBR Data for CC-1 Pavement System

Date	Subgrade	Lift No.	Station	Offset from CL (ft.)	Point	CBR	MC (%)	Density (pcf)
6/24/1998	Low-Strength	1	0+52	5L	1	6.2		
6/24/1998	Low-Strength	1	0+52	5L	2	6.6	25.1	
6/24/1998	Low-Strength	1	0+52	5L	3	6.6		
6/24/1998	Low-Strength	1	1+18	2R	1	6.3		
6/24/1998	Low-Strength	1	1+18	2R	2	7.5	22.3	
6/24/1998	Low-Strength	1	1+18	2R	3	7.2		
6/24/1998	Low-Strength	1	1+90	23L	1	6.0		
6/24/1998	Low-Strength	1	1+90	23L	2	5.3	25.6	
6/24/1998	Low-Strength	1	1+90	23L	3	5.0		
6/24/1998	Low-Strength	1	2+40	15R	1	8.2		
6/24/1998	Low-Strength	1	2+40	15R	2	7.1	25.0	
7/1/1998	Low-Strength	2	0+62	22L	1	4.0		
7/1/1998	Low-Strength	2	0+62	22L	2	4.4	26.5	95.1
7/1/1998	Low-Strength	2	0+62	22L	3	4.4		
7/1/1998	Low-Strength	2	0+93	19R	1	3.8		
7/1/1998	Low-Strength	2	0+93	19R	2	4.0	26.0	95.9
7/1/1998	Low-Strength	2	0+93	19R	3	3.8		
7/1/1998	Low-Strength	2	1+86	7R	1	5.0		
7/1/1998	Low-Strength	2	1+86	7R	2	4.0	26.2	96.5
7/1/1998	Low-Strength	2	1+86	7R	3	4.9		
7/1/1998	Low-Strength	2	2+39	11L	1	4.5		
7/1/1998	Low-Strength	2	2+39	11L	2	4.9	26.7	96
7/1/1998	Low-Strength	2	2+39	11L	3	4.9		
7/11/1998	Low-Strength	3	0+13	1R	1	4.6		
7/11/1998	Low-Strength	3	0+13	1R	2	5.6	25.8	96.3
7/11/1998	Low-Strength	3	0+13	1R	3	5.6		
7/11/1998	Low-Strength	3	0+45	4L	1	4.4		
7/11/1998	Low-Strength	3	0+45	4L	2	5.7	25.5	97.4
7/11/1998	Low-Strength	3	0+45	4L	3	5.9		
7/11/1998	Low-Strength	3	1+93	19R	1	4.4		
7/11/1998	Low-Strength	3	1+93	19R	2	4.8	26.2	97.4
7/11/1998	Low-Strength	3	1+93	19R	3	4.0		
7/11/1998	Low-Strength	3	2+57	21L	1	4.5		
7/11/1998	Low-Strength	3	2+57	21L	2	4.6	26.3	97.4
7/11/1998	Low-Strength	3	2+57	21L	3	5.7		
7/14/1998	Low-Strength	4	1+09	19R	1	5.8		
7/14/1998	Low-Strength	4	1+09	19R	2	5.2	25.9	95.5
7/14/1998	Low-Strength	4	1+09	19R	3	5.8		

Table 3.3. Density, Moisture Content and CBR Data for CC-5 Pavement System

Table 3.3. Density, Moisture Content and CBR Data for CC-5 Pavement System

+	Lift No.	Station	Offset	CBR Value		Density Test		Subgrade Type	Specific Gravity	Degree of Saturation
				CBR	MC (%)	Dry Density(pcf)	MC %			
12/17/2007	0	30	15N	3.71	26.53	98.98	26.64	County Stone & Clay	2.83	96.1
12/17/2007	0	30	15S	3.78	26.36	97.69	27.11	County Stone & Clay	2.83	95.0
12/12/2007	0	135	15N	3.53	26.70	98.52	26.83	County Stone & Clay	2.83	95.8
12/12/2007	0	135	15S	3.70	26.60	98.06	27.05	County Stone & Clay	2.83	95.6
12/12/2007	0	200	15N	2.82	27.47	96.42	28.52	County Stone & Clay	2.83	97.1
12/12/2007	0	200	15S	2.87	27.41	96.49	28.89	County Stone & Clay	2.83	98.5
12/14/2007	0	260	15N	3.29	26.42	98.48	27.02	County Stone & Clay	2.83	96.4
12/12/2007	0	260	15S	2.89	26.49	97.03	27.34	County Stone & Clay	2.83	94.4
1/3/2008	1	60	15N	3.03	37.82	-	-	Dupont Clay	2.79	-
1/3/2008	1	60	15S	3.10	37.55	-	-	Dupont Clay	2.79	-
1/3/2008	1	130	15N	3.24	37.10	-	-	Dupont Clay	2.79	-
1/3/2008	1	130	15S	3.75	36.63	-	-	Dupont Clay	2.79	-
12/28/2007	1	165	15N	3.03	37.23	-	-	Dupont Clay	2.79	-
12/27/2007	1	165	15S	3.25	36.99	-	-	Dupont Clay	2.79	-
12/27/2007	1	235	15N	3.27	37.04	-	-	Dupont Clay	2.79	-
12/27/2007	1	235	15S	4.00	36.27	-	-	Dupont Clay	2.79	-
1/11/2008	2	55	15N	3.08	38.15	82.69	36.90	Dupont Clay	2.79	93.1
1/11/2008	2	55	15S	2.90	37.62	82.56	37.33	Dupont Clay	2.79	93.9
1/11/2008	2	85	15N	2.93	37.95	82.31	37.02	Dupont Clay	2.79	92.6
1/11/2008	2	85	15S	3.20	37.54	82.85	36.15	Dupont Clay	2.79	91.6
1/18/2008	2	165	15N	3.67	37.11	83.61	37.00	Dupont Clay	2.79	95.4
1/18/2008	2	165	15S	3.50	36.55	85.48	36.16	Dupont Clay	2.79	97.3
1/18/2008	2	235	15N	3.77	37.39	82.65	37.48	Dupont Clay	2.79	94.5
1/18/2008	2	235	15S	3.64	37.13	83.11	37.58	Dupont Clay	2.79	95.8
2/14/2008	3	15	15N	3.70	37.42	82.27	38.69	Dupont Clay	2.79	96.7
2/14/2008	3	15	15S	3.87	36.56	82.30	37.45	Dupont Clay	2.79	93.7
2/14/2008	3	85	15N	3.27	38.45	81.04	39.40	Dupont Clay	2.79	95.7
2/14/2008	3	85	15S	3.40	38.05	81.92	38.85	Dupont Clay	2.79	96.3
2/8/2008	3	170	15N	3.84	37.15	81.30	38.69	Dupont Clay	2.79	94.6

+	Lift No.	Station	Offset	CBR Value		Density Test		Subgrade Type	Specific Gravity	Degree of Saturation
				CBR	MC %	Dry Density, pcf	MC %			
2/8/2008	3	170	15S	3.23	38.72	80.78	38.86	Dupont Clay	2.79	93.9
2/8/2008	3	250	15N	3.50	37.34	81.03	38.66	Dupont Clay	2.79	93.9
2/8/2008	3	250	15S	3.00	38.15	80.93	39.10	Dupont Clay	2.79	94.8
3/20/2008	4	45	15N	3.20	38.09	81.40	37.93	Dupont Clay	2.79	92.9
3/20/2008	4	45	15S	3.13	38.96	79.73	38.75	Dupont Clay	2.79	91.3
3/20/2008	4	115	15N	3.17	38.18	81.79	38.21	Dupont Clay	2.79	94.5
3/20/2008	4	115	15S	3.50	37.10	82.41	37.68	Dupont Clay	2.79	94.5
3/10/2008	4	180	15N	3.17	37.29	80.35	38.84	Dupont Clay	2.79	92.9
3/10/2008	4	180	15S	2.83	39.38	79.60	38.58	Dupont Clay	2.79	90.7
3/10/2008	4	225	15N	3.98	36.74	81.90	37.46	Dupont Clay	2.79	92.8
3/10/2008	4	225	15S	3.00	39.21	79.92	39.60	Dupont Clay	2.79	93.8
3/26/2008	5	45	15N	2.96	37.72	82.74	36.89	Dupont Clay	2.79	93.2
3/26/2008	5	45	15S	2.83	38.49	81.16	37.25	Dupont Clay	2.79	90.8
3/14/2008	5	260	15N	2.97	38.05	82.95	37.48	Dupont Clay	2.79	95.2
3/14/2008	5	260	15S	3.27	37.63	82.00	37.16	Dupont Clay	2.79	92.3

Table 3.4. Field Moisture Content and Dry Density Obtained from NAPTF for CC-7

Lift	Station	Offset, feet	Moisture Content (%)	In-Situ Dry Density (pcf)	Degree of Saturation (%)
1	17	-6 (N)	34.7	87.6	98.0
1	115	-10(N)	32.4	89.2	95.0
1	220	-22(N)	33.6	87.4	94.5
1	30	13(S)	32.5	88.5	93.8
1	178	14(S)	33.9	86.5	93.4
1	285	13(S)	35.2	86.1	96.1
2	229	-14(N)	25.9	97.1	91.1
2	263	-14(N)	26.4	96.6	91.8
2	184	15(S)	27	96.2	93.0
2	252	12(S)	28.6	93.6	92.8
2	61	15(S)	27.9	95.3	94.1
2	116	17(S)	28.2	94.2	92.8
3	186	15(S)	27.5	94.1	90.3
3	257	18(S)	27.1	96	92.9
3	55	16(S)	26.4	97	92.7
3	110	17(S)	26.1	96.5	90.6
4	36	14(S)	26.4	95.9	90.3
4	68	16(S)	26.3	96	90.2
4	153	14(S)	26.9	96.3	92.9
4	253	16(S)	26.8	95.8	91.5

CBR records

The CBR data collected contained information from CC-5 and CC-1 construction cycles. Table 3.3 and Table 3.5 show samples of the CBR data for CC-1 and CC-5 airfield pavement systems, respectively.

The NAPTF provided CBR data related to the compaction tests performed in the field and also from in-field measured CBR data. To the best of our knowledge, the procedure followed during compaction and CBR testing in the field can be generalized as follows:

- A specific CBR target is fixed before the compaction is started. The moisture and the compaction are modified in order to achieve the target CBR.
- Moisture content is chosen from the modified compaction test and the soil is mixed for compaction.
- A Rubber tire roller is used to compact the soil at the field.
- The CBR for the particular moisture content and compaction is measured and is compared with the targeted CBR.
- If the CBR is not consistent, then water is added to the soil, retiled with a pulvomixer and the process is repeated.

Initially, a detailed map of the density, moisture content and the CBR for Lift 1 was collected. Then CBR data for the other four lifts were collected. Figure 3.5 shows the CBR values for Lift 1. The circled values represent the average of three tests performed at each location with MC representing the Moisture Content in %, DU is the dry unit weight of the soil in lb/ft^3 and DCMU is the Drive Cylinder Moisture Content in %. Table 3.3 provides the in-situ CBR measured in 2008, during the construction of the test facility, for various lifts in the construction sequence. Table 3.6 shows the CBR data obtained for the other four lifts.

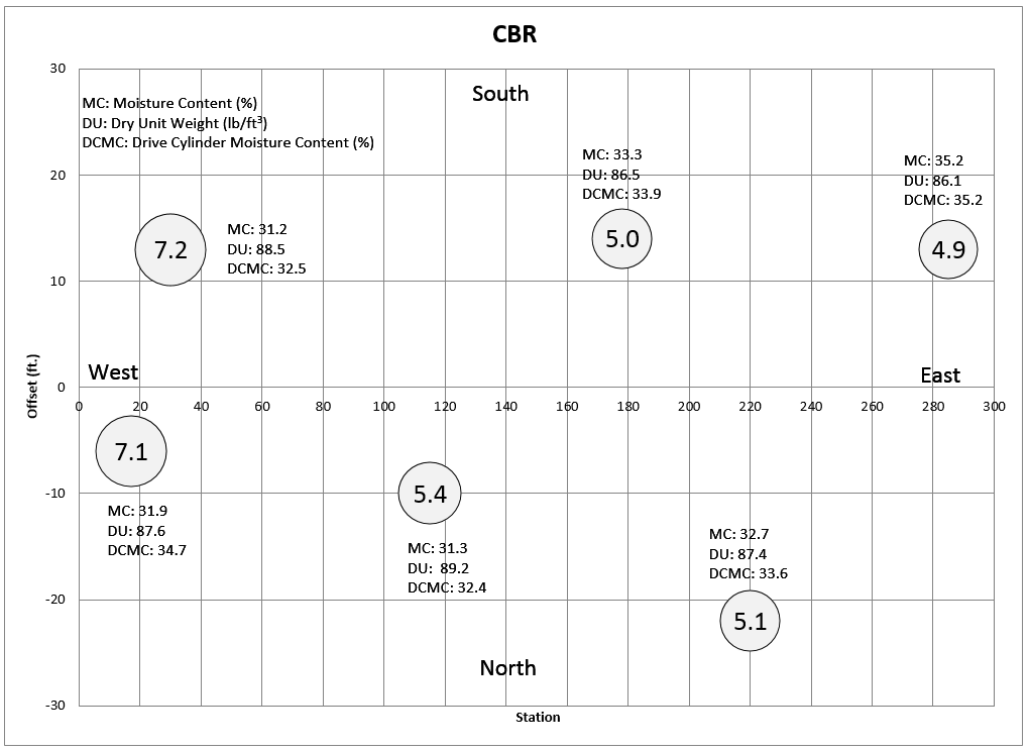

Figure 3.5. Subgrade CBR Values Measured in Field for Lift 1 (Data Received on 02/17/2014 – Unknown Testing Date)

Table 3.5. CBR Data for 4 Lifts of Test Section.

	CBR	
	(CC7 North)	(CC7 South)
Lift 1	5.20	5.00
	5.90	4.80
	5.30	4.80
	5.80	4.60
	5.20	4.80
	5.20	4.80
	6.00	4.80
	5.10	5.50
	4.90	5.00
Lift 2	6.20	5.70
	6.20	5.40
	5.30	5.50
	6.10	4.80

	5.30	4.90
	5.70	5.70
		5.40
		4.40
		5.30
		4.60
		5.20
		4.70
Lift 3		4.40
		5.40
		4.40
		4.70
		5.00
		4.80
		5.30
		5.20
		5.10
		4.60
		5.00
		4.80
Lift 4		5.60
		5.50
		4.70
		4.80
		4.90
		4.90
		4.40
		4.40
		4.80
		4.60
		4.80
		4.80
Number of CBR tests	15	45
Minimum CBR	4.9	4.4
Maximum CBR	6.2	5.7
Mean CBR	5.6	4.9
Standard Deviation	0.44	0.37
COV	7.95%	7.42%

TEST SECTION ENVIRONMENTAL AND MOISTURE INFORMATION

Environmental data collected included groundwater table depth, climate conditions near the site and moisture variation of subgrade materials.

Groundwater table depth

NAPTF facility provided a plot showing the variation of the groundwater table at the site for a period of 16 years in the county clay section. The data included records from July 1998 to October 2013. The groundwater depth variation with time is shown in Figure 3.6.

Pavement temperature

The temperature inside the pavement test facility has not been controlled in the past. The test pavement is enclosed by a pre-fabricated metal building without any provision for heating or cooling. The ambient temperature inside the facility usually lags outdoor temperature by about 8 hours and the peaks in temperature are lowered (Correspondence with Mr. Barbagallo). The variation of the ambient temperature was not provided by the FAA personnel.

Weather station data from Atlantic City airport

In order to collect climate data for the NAPTF facility, the National Oceanic and Atmospheric Administration (NOAA) was contacted. With the guidance from NOAA, hourly weather records from the Atlantic City airport were collected. The information included wind direction, wind speed, gust, cloud cover, sky cover, visibility, temperature, Dew point, relative humidity, maximum and minimum temperature, and precipitation.

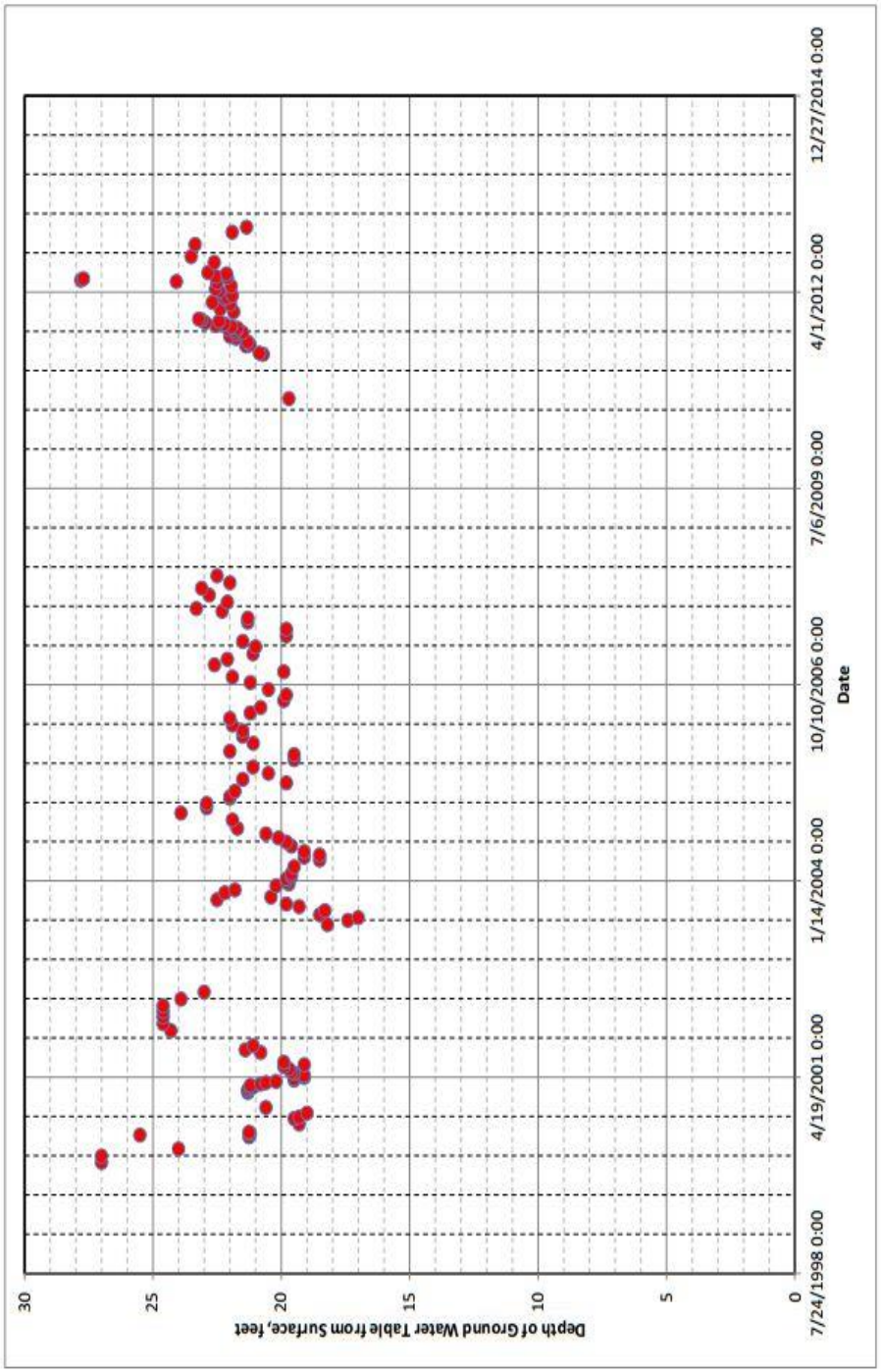

Figure 3.6. Plot of Depth of Ground Water Table Vs Time for a Period of 6 Years from 1998 to 2014

Historic water content records

NAPTF provided data of the variation of the subgrade water content, observed during two years from 1999 to 2001. The plot showed the variation of the water content at different depths for a period ranging from May 1999 to October 2001 measured using a moisture sensor. Figure 3.7 shows the plot of the water content variation with respect to time for various depths. The data was obtained with a gage that was not calibrated and hence, unprocessed data is shown. Nevertheless, this information is important to assess the fluctuations at different depths.

SUMMARY

This chapter is a collection of all the data collected from the FAA personnel in the NAPTF. The data collected includes the dry density, moisture content and CBR for the subgrade compacted in NAPTF. This data will be used in the further chapters for analysis.

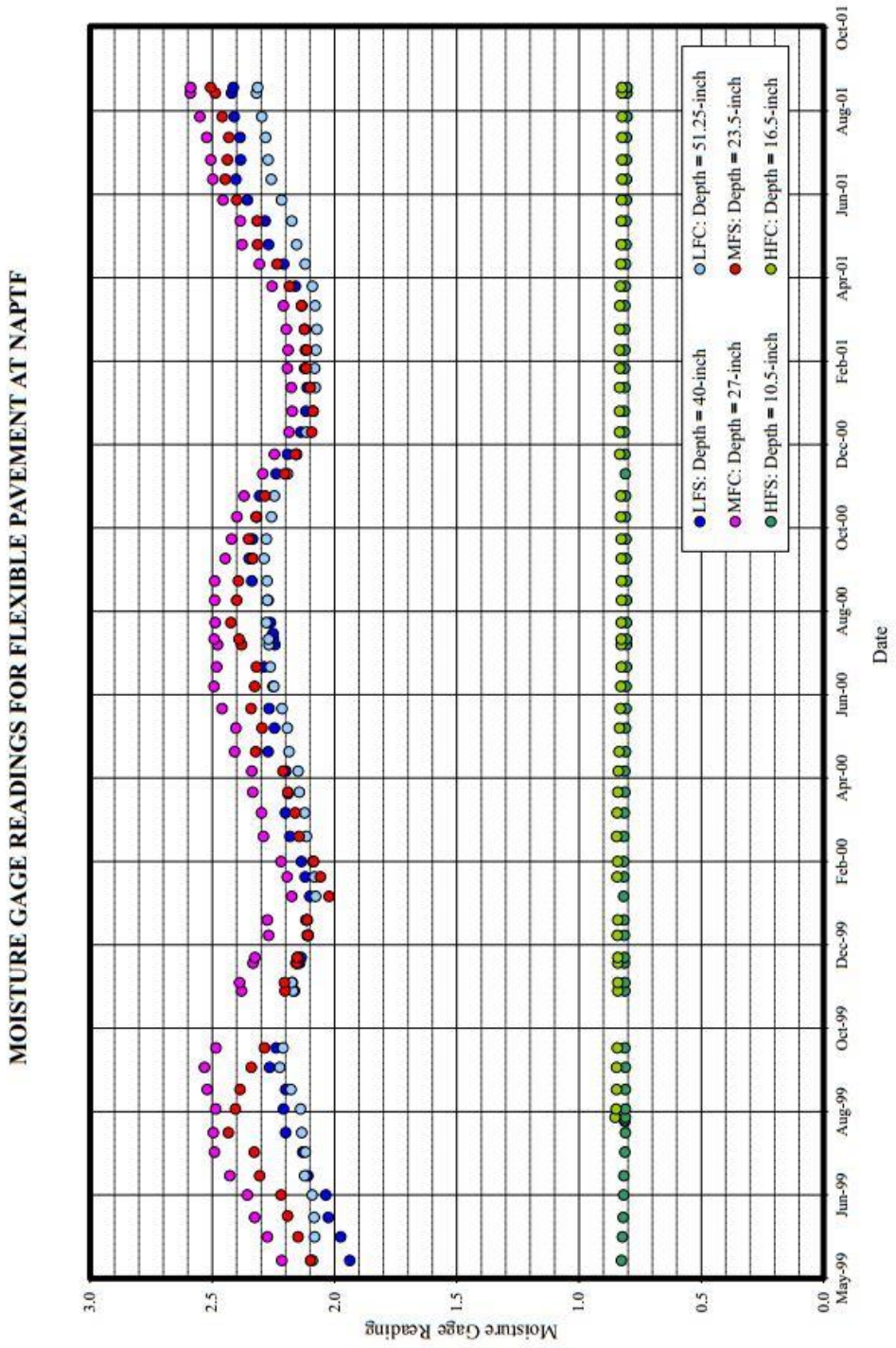

Figure 3.7. Plot of Variation of Water Content vs. Time for Different Depths of Airfield Pavement

Chapter 4. Laboratory Test Results for Index, Unsaturated and Thermal Properties of Soils.

This chapter presents the results of the laboratory testing program completed in order to characterized the soil materials used on this research study. The routine geotechnical tests performed on the material included: Grain size distribution, hydrometer analysis, Atterberg limits, specific gravity of solids, standard Proctor compaction, consolidation and response to wetting (swelling) test. In addition, a set of advance laboratory tests were completed, which include the unsaturated hydraulic soil properties (soil-water characteristic curves and unsaturated hydraulic conductivity) and thermal properties (thermal conductivity and heat capacity) of the soil.

The results presented in this chapter represents the effort done by the entire research group pursuing studies for the FAA grant No. 13-G-008 *Research Proposal for the Investigation of Subgrade Moisture Flow in an Airfield Pavement System*.

MATERIALS DELIVERED FROM NAPTF

A total of six 5-gallon buckets and 6 Shelby tubes containing soils of County clay and Dupont clay were obtained from the National Airfield Pavement Test Facility(NAPTF) in Atlantic City. The soils received are used as the main subgrade materials in the construction of the test pavement sessions in the NAPTF facility. The soil identified as County clay was denominated CC and the one identified as Dupont clay as DC. The disturbed soil material obtained from NAPTF consisted of wet clumps. That soil was broken down into small pieces after being dried for few days and then broken to pass through the No. 4 sieve. The passing material was passed through a pulverizer and broken down into particles that could pass through the No. 80 sieve. The soil that was retained in the No. 80 sieve was again

passed through the pulverizer. The soil was then mixed thoroughly in order to achieve a uniform gradation before the testing of the soil was initiated. Standard ASTM D1587 sampling procedures were followed when selecting material samples for the different tests to be performed.

PARTICLE SIZE ANALYSIS

The grain size distribution was the first test performed in order to classify the soil. ASTM Standard D 422-63 (2002) was followed to obtain the grain-size distribution of the material. A sieve analysis was initially performed to find the amount of coarse aggregates present in the soil. Both soils did not show any presence of rock particles or particles greater than 4.75 mm. There was a presence of fine sand in the soil which constituted about 42% for County clay and 20% for Dupont clay. The silt and the clay contents present in the soil were found by using the hydrometer analysis test. Based on the sieve and hydrometer analyses, the amount of silt content was found to be 33% for County clay and 50% for Dupont clay. The remaining soil was classified as clay material, which constituted about 25% in County clay and 30% in Dupont clay. Figure 4.1 and 4.2 shows the results of particle size distribution for the County and Dupont clays respectively. Table 4.1 shows the percentage of sand, silt and clay for both soils. From Figure 4.1, it can be seen that the County clay shows the attributes of a well graded soil.

Table 4.1. Results of Particle Size Analysis Test

	County Clay	Dupont Clay
Clay Content (%)	25	30
Silt Content (%)	33	50
Sand Content (%)	42	20

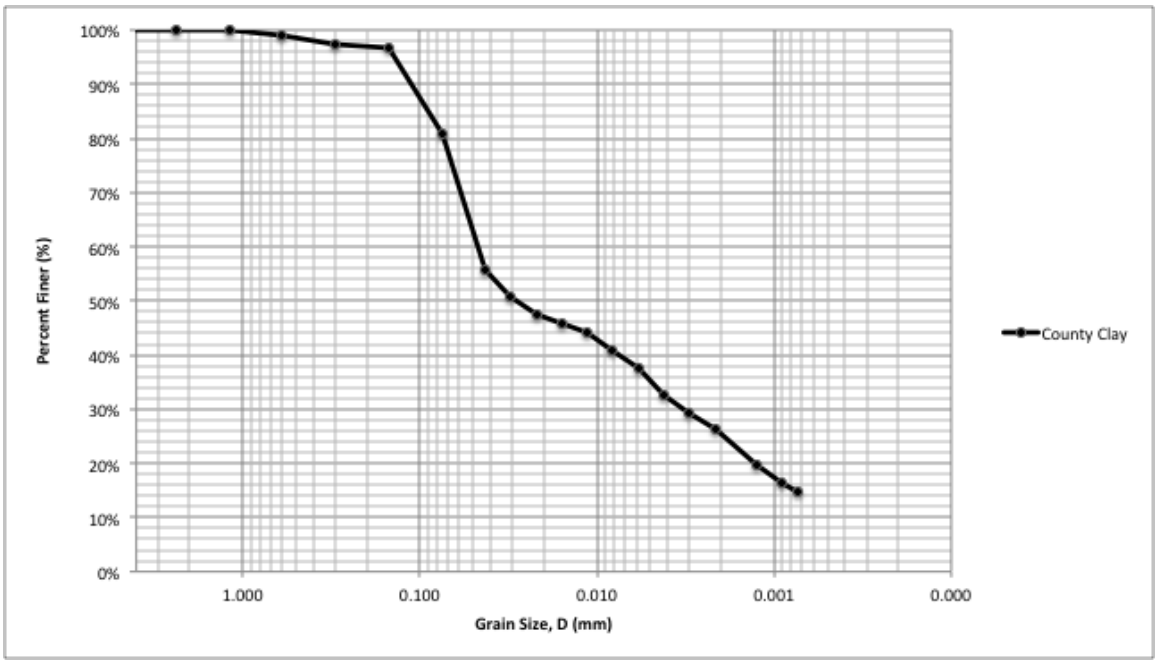

Figure 4.1. Particle Size Distribution Curve for County Clay

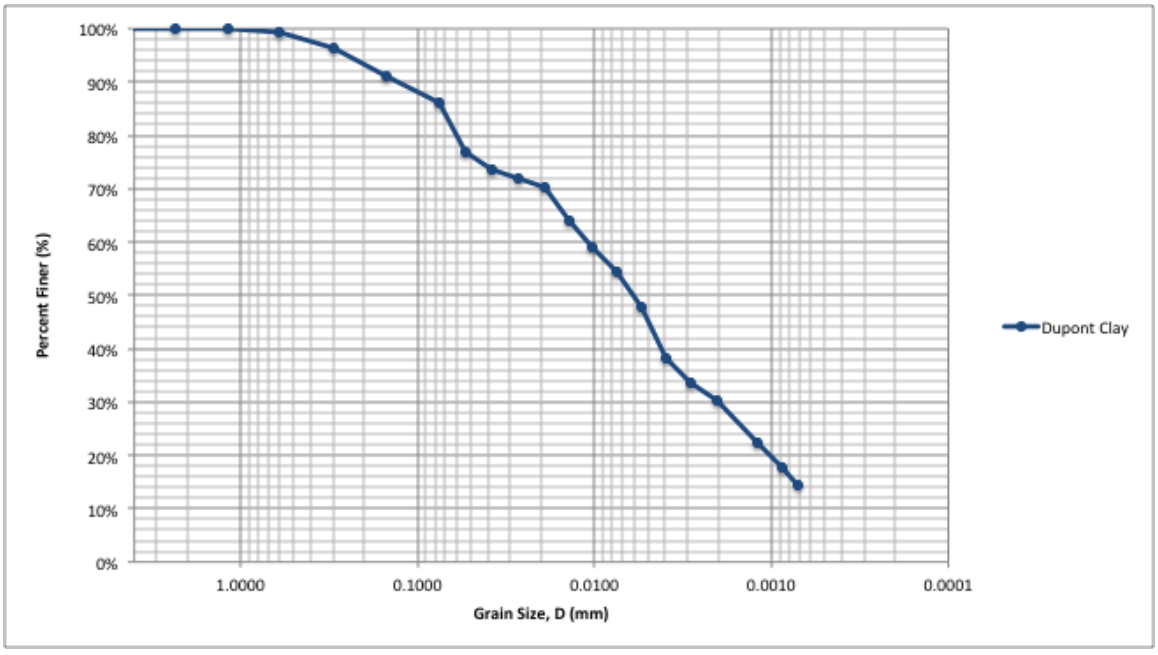

Figure 4.2. Particle Size Distribution Curve for Dupont Clay

ATTERBERG LIMIT TEST

Atterberg limit tests were performed in order to classify the soil according to USCS and AASHTO classification systems. The liquid limit and plastic limit tests were performed twice on each soil and then the data obtained was averaged. The liquid limit test was performed according to the ASTM standard D4318-10. Figure 4.3 and 4.4 shows the results of the Liquid Limit test performed on Dupont and County clay respectively.

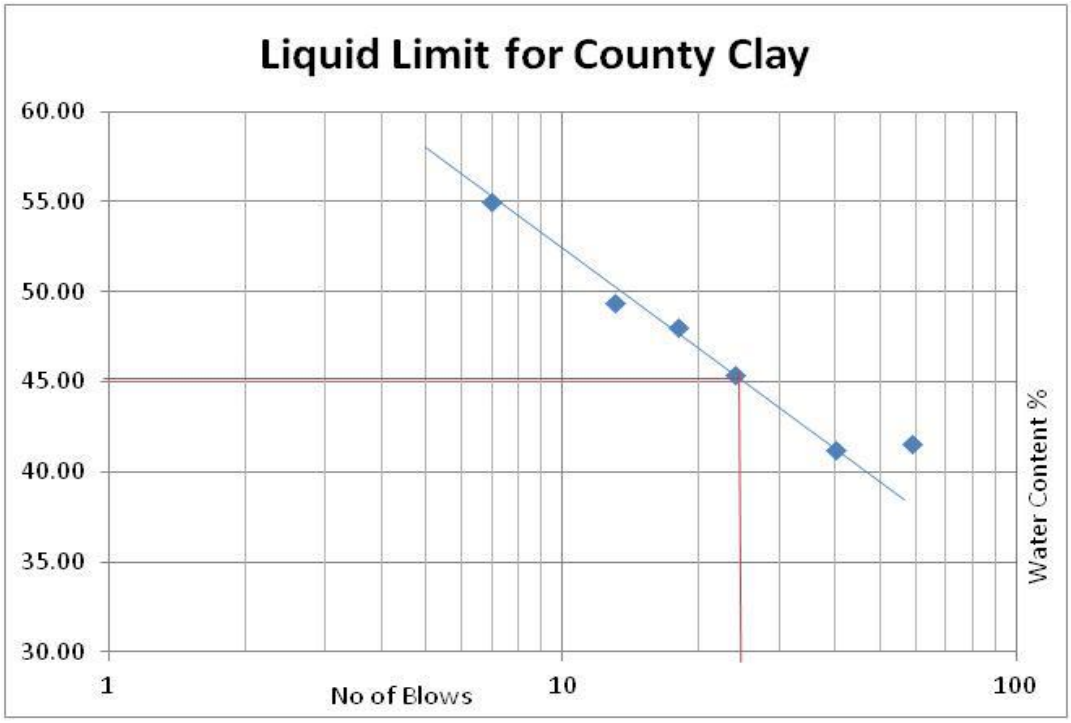

Figure 4.3. Results of Liquid Limit Test for County Clay

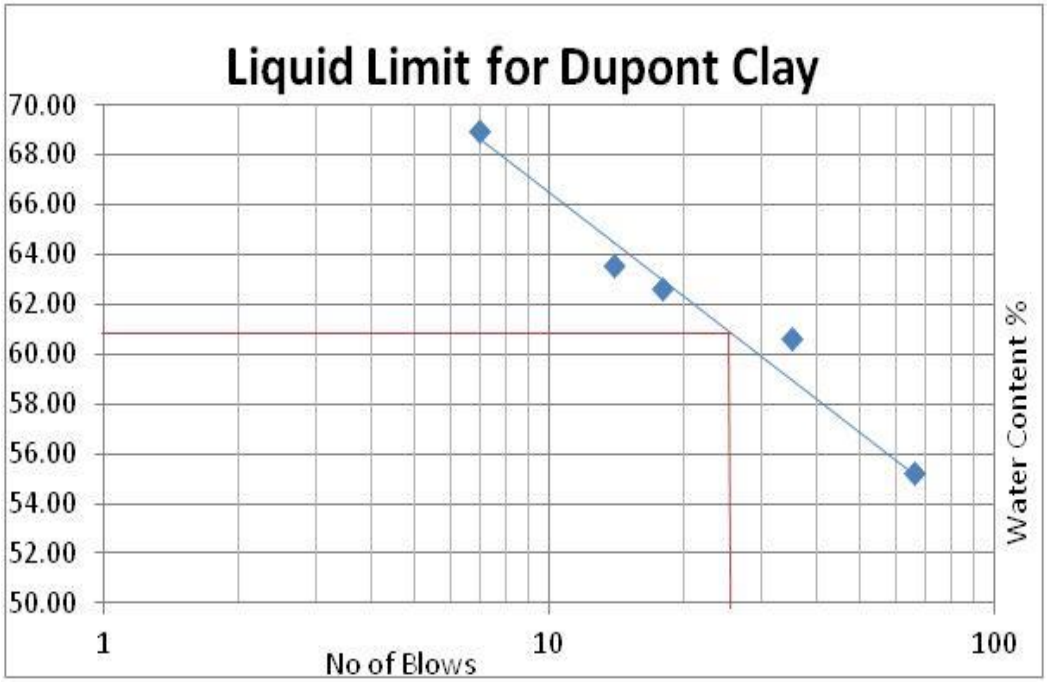

Figure 4.4. Results of Liquid Limit Test for Dupont Clay

Table 4.2. Results of Atterberg Limit Tests

Index Property	County Clay	Dupont Clay
Liquid Limit	45	61
Plastic Limit	28	32
Plasticity Index	17	29

SOIL CLASSIFICATION

The particle size analysis, the hydrometer test and Atterberg limits test were used to classify the soil. According to the USCS standard system, the so-called County clay was classified as low plasticity silt (ML) and Dupont clay was classified as High Plasticity silt (MH). According to AASHTO classification, the County clay was found to be A-7-6 (15) and Dupont clay an A-7-6 (29).

SPECIFIC GRAVITY TEST

Specific Gravity test was performed for both soils following the ASTM Standard C 128-04a. De-aired water was used to perform the tests. Among the methods to de air the soil and water mixture mentioned in the ASTM standard C 128-04a, the third method was used. The third method was the combined method of using both the hot plate and vacuum which both decreases the pressure and the increases the temperature to de air the soil-water mixture. Specific Gravity of the solids were found using the equation.

$$G_s = M_s / M_w$$

Where, G_s is the specific gravity of the solids, M_s is the mass of the solids and M_w is the mass of water displaced.

Three replicates were performed for Dupont Clay and two replicates were performed for County clay. The specific gravity of the two soil samples was calculated. The test was performed in the Arizona State University laboratory under a controlled temperature of 21 degrees Celsius. The specific gravity of County clay was found to be 2.83 and 2.79 for the Dupont clay. Table 4.3 shows the data obtained during the experiment.

Table 4.3. Specific Gravity of the two Clays

	County Clay		**Dupont Clay**		
	Trial 1	**Trial 2**	**Trial 1**	**Trial 2**	**Trial 3**
Calibration of the Volumetric Flask					
Ave. Dry Mass of Flask (g), M_p	165.26	165.26	165.26	165.26	165.26
Mass of Flask and De-Aired Water (g), $M_{pw,c}$	663.1	663.1	663.1	663.1	663.1
Mass Density H2O @ 23 °C (g/mL), ρ	0.997	0.997	0.997	0.997	0.997
Volume of Flask, (mL), $V = (M_{pw,c} - M_p)/\rho$	499.06	499.06	499.06	499.06	499.06
Experimental Data					
Temp. of the Test (°C), T	23	23	23	23	23
Mass of flask +water filled to mark (g), M_1	663.1	663.1	663.1	663.1	663.1
Mass of flask + soil + water filled to mark (g), M_2	695.37	694.37	695.42	694.32	691.6
Mass of Soil (g), $M_s = M_4 - M_3$	50	48.3	50.4	48.75	44.36
Mass of Equal Vol. of water (g), $M_w = (M_1 + M_s) - M_2$	17.73	17.03	18.08	17.53	15.86
Specific Gravity, $G_s = M_s / M_w$	2.82	2.84	2.79	2.78	2.80

COMPACTION CURVES

The Standard Proctor Compaction test was performed by applying two different compaction energy to determine the moisture-density relation for the materials investigated

in this study. The test followed the guidelines of the ASTM Standard D 698-00 method A for both soils. The first energy level used a 5.5 lb hammer with a drop height of 12 inches and using 3 layers and 25 blows per layer to yield an energy of 600 kN.m/m^3. The second energy level used a 10 lb. hammer with a drop height of 18 inches and using 5 layers and 25 blows per layer to yield an energy of 2700 kN.m/m^3. The first energy level is called as Standard energy level and the second energy level is referred as Modified energy level.

The compaction curve was found for two energy levels. Figure 5.5 and Figure 5.6 presents the compaction data obtained at ASU laboratory for both, the County and Dupont clays, respectively. The plots also show the standard and modified curves, the in-situ compaction data obtained and the moisture/density data obtained at ASU from Shelby tubes provided by FAA personnel is also shown in Figure. The specifications for the Proctor Compaction Tests are mentioned in Table 4.4.

Table 4.4. Specifications of the Proctor Compaction Test Performed

Method	**No. of Layer**	**No. of blows per layer**	**Hammer used**	**Height of Hammer Drop (in)**	**Force Applied (lb.)**	**Vol of Sample (ft^3)**	**Comp. Energy (kN.m/m^3)**
Standard Compaction	3	25	Standard Proctor Hammer	12	5.5	1/30	600
Modified Compaction	5	25	Modified Proctor Hammer	18	10	1/30	2700

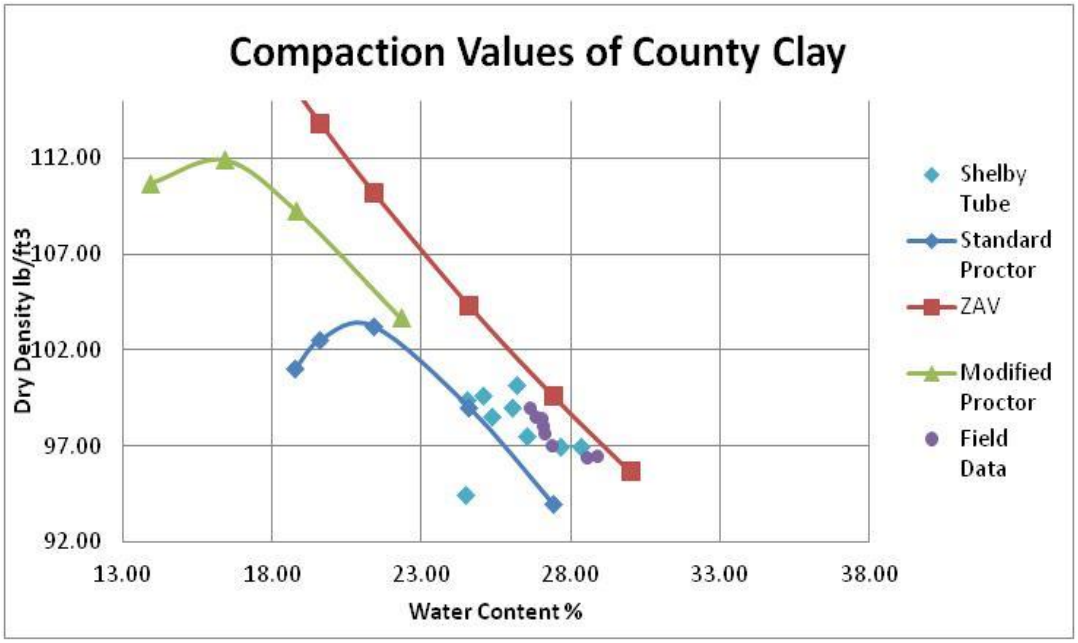

Figure 4.5. Compaction Test for County Clay performed in Lab

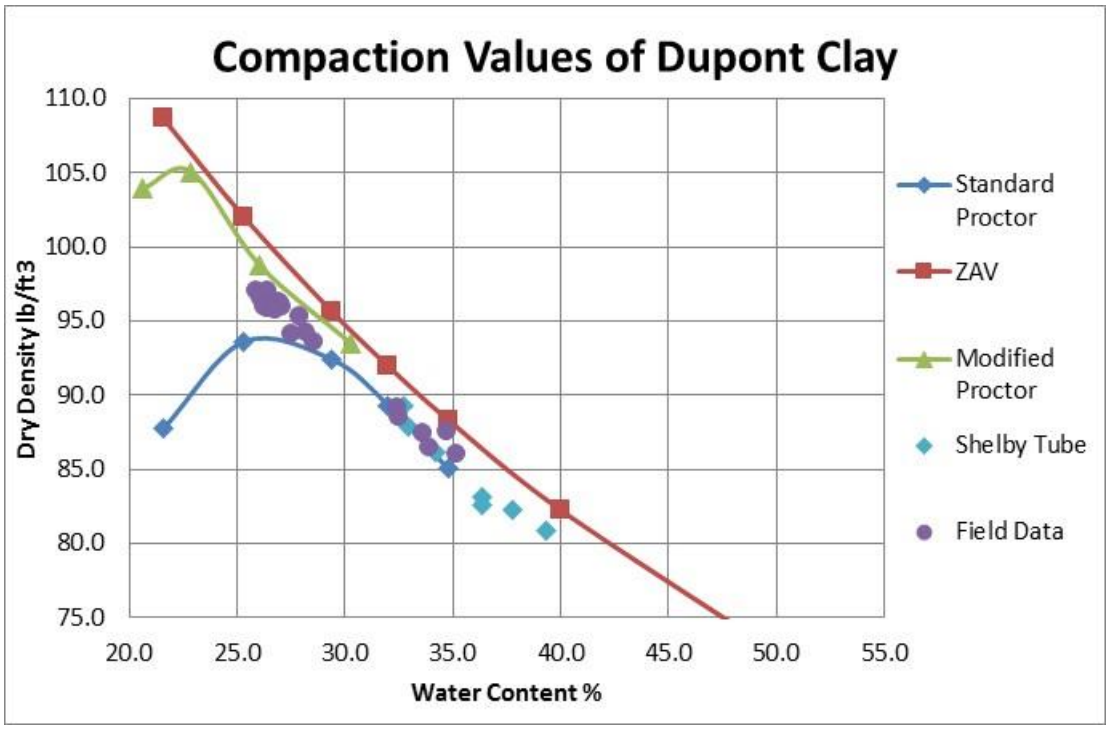

Figure 4.6. Compaction Test for Dupont Clay Performed in Lab

CONSOLIDATION TEST

According to the ASTM Standard D2435, consolidation tests were completed for both soils and the results are illustrated in Figure 4.7 and Figure 4.8 for County and Dupont soils, respectively. The preconsolidation pressure (P_c) was estimated using the Casagrande correction method. This parameter was found to be 120 kPa for County soil and 105 kPa for DuPont soil. The saturated hydraulic conductivity (k_{sat}) of the two soils at 25°C were also calculated based on the consolidation test. The k_{sat} for County soil was found to be 2.4×10^{-11} m/s and for DuPont soil was 8.0×10^{-11} m/s.

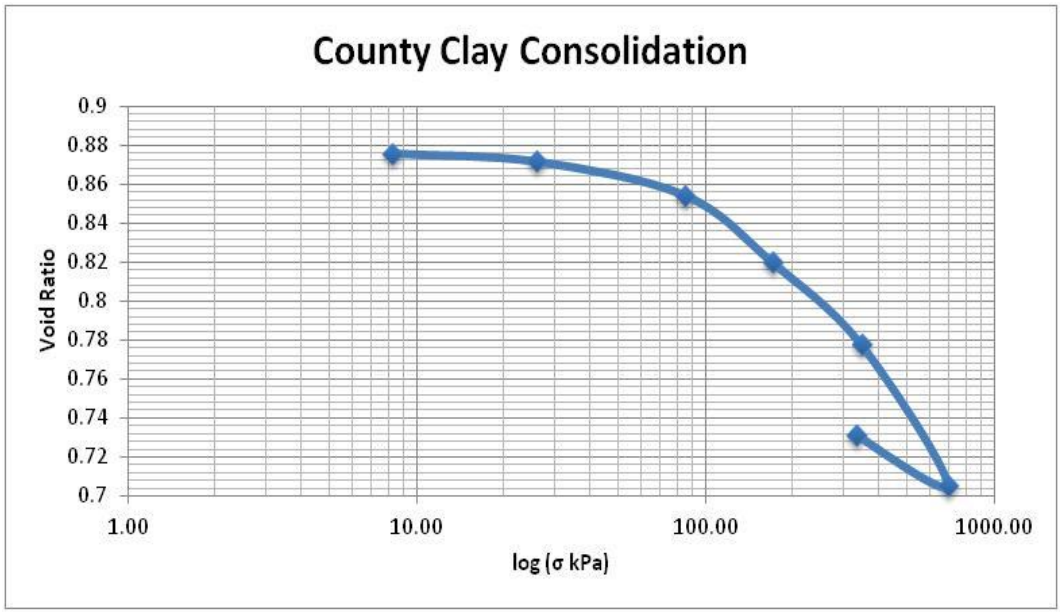

Figure 4.7. Results of Consolidation test for County Clay

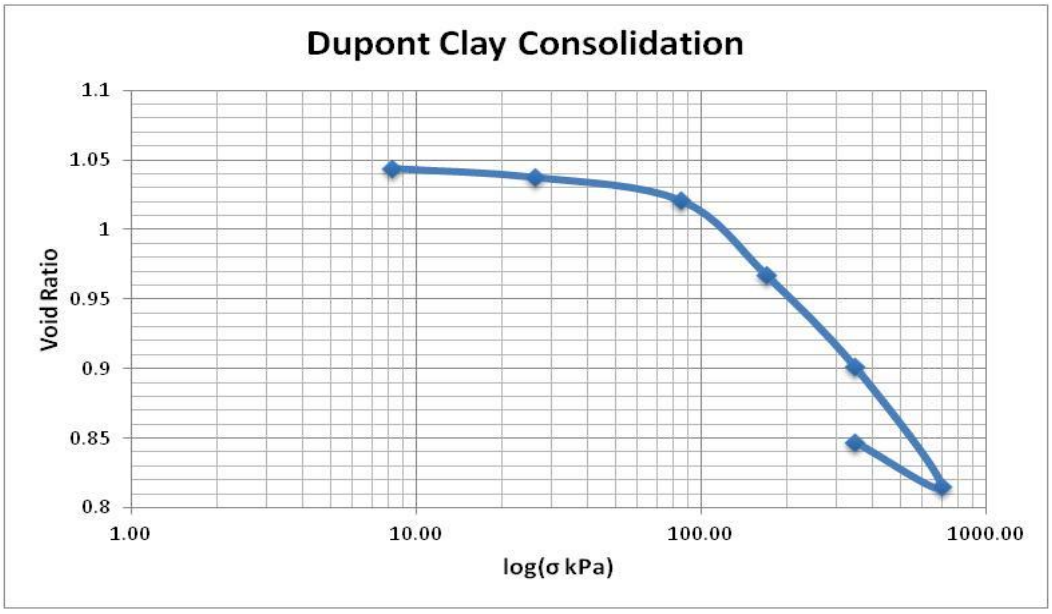

Figure 4.8. Results of Consolidation test for Dupont Clay

SWELL TEST

Response to wetting tests were performed on both clays according to the ASTM Standard D4546-08. The soil was compacted to 95% of the maximum dry density and at optimum moisture content. The swelling potential of the soil was then observed for different confining pressures. Figure 5.9 shows the Swell test results for both clays. The free swell was found to be 4% and 2.4% for County clay and Dupont clay, respectively, and the swelling pressure 7 and 5 kPa for County and Dupont clay, respectively. Based on the results obtained, the soils were considered of low swelling potential.

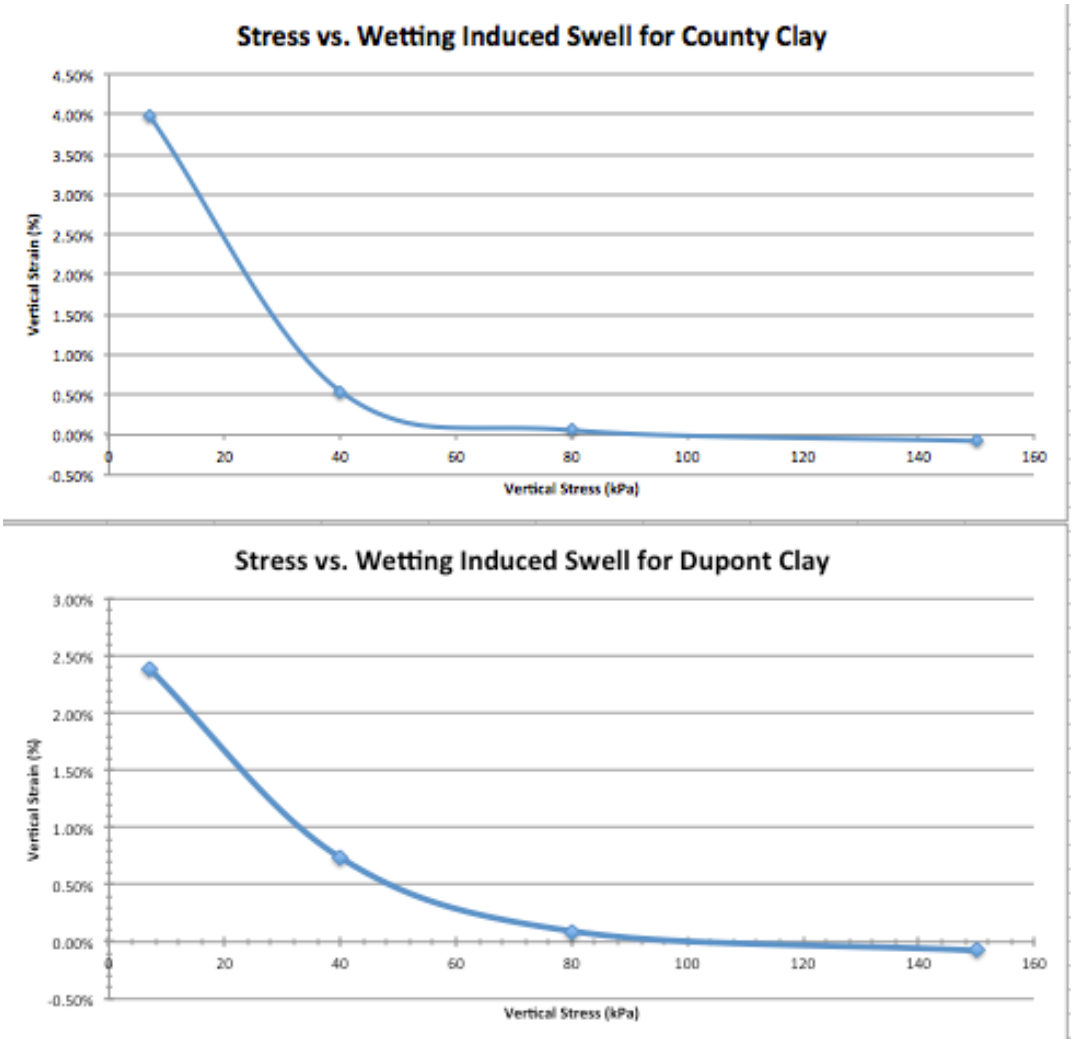

Figure 4.9. Results of Swell Test for County and Dupont Clays

SUMMARY:

The test results presented above are summarized in Table 4.5. As observed, the so-named clays were found to be silt materials. However, for the sake of consistency with the FAA studies, the names remained as they are for the rest of the research study.

Table 4.5. Summary of preliminary test results

Tests performed	Results	
	County Clay	Dupont Clay
Specific Gravity	2.84	2.79
Grain Size Distribution and Particle Size		
Clay Content (%)	25	30
Silt Content (%)	33	50
Sand Content (%)	42	20
Atterberg's Limit test		
Liquid Limit	45	61
Plastic Limit	28	32
Plasticity Index	17	29
Soil Classification USCS AASHTO	 Lean Silt (ML) A-7-6 (15)	 Elastic Silt (MH) A-7-6 (29)
Standard Compaction		
Optimum Moisture Content (%)	21	26.3
Maximum Dry Density (lb/ft^3)	103.5	94
Modified Compaction		
Optimum Moisture Content (%)	16.5	22.5
Maximum Dry Density (lb/ft^3)	112	105
Saturated Hydraulic Conductivity (m/s)	2.4×10^{-11}	8.0×10^{-11}

THERMAL PROPERTIES

An analysis on the thermal properties of the Dupont and County soils was performed by Rakshith Gowda and Joshua Contreras as a part of a FAA project 13G008 (Zapata et al, 2017) connected to this study. The results obtained from were used in this study for various purposes as discussed below. The KD2 Pro Thermal Properties Analyzer used to measure the thermal conductivity and specific heat capacity of both soils was acquired from Decagon Devices, Inc. Two sensors were used: the single needle TR-1 sensor of dimensions 10cm long and 2.1mm diameter for measuring the thermal conductivity and a dual needle SH-1 sensor for measuring the volumetric heat capacity. These sensors

collected the data by generating the heat pulse. The specific heat and thermal conductivity sensors from Decagon Devices, Inc. were embedded in the samples prepared in the laboratory. The data collected included the specific heat and thermal conductivity at three different temperatures and different moisture contents ranging from dry to saturated conditions.

Thermal Conductivity

A thermal conductivity study was performed as a part of this project. The variation of thermal conductivity of the Dupont clay with water content and temperature is depicted in Figure 4.10 and for County clay is shown in Figure 4.11. The thermal conductivity of Dupont clay was found to be susceptible to both temperature and water content changes; whereas the thermal conductivity of County clay was found to be more vulnerable to water content changes at the higher temperatures of 25^{o}C and 40^{o}C. Poly curve for three temperatures in the figures represents the curve formed using a 3rd degree polynomial equation.

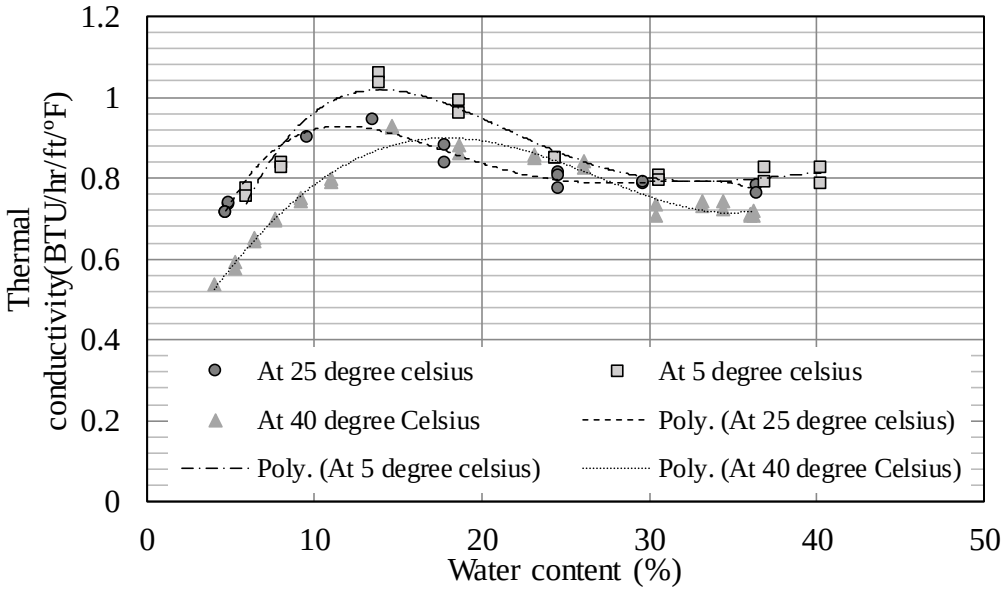

Figure 4.10. Thermal Conductivity Function of Dupont Clay

A model was developed to predict the change in the thermal conductivity of the soil as a function of changes in water content and temperature. The equation below represents the relation between the thermal conductivity, water content and temperature found for the two soils.

For Dupont clay:

$$k_{dupont} = 0.5878 + 0.07920w - 0.003354T + 0.000054w^3 - 0.004002w^2 + 0.000093wT$$

For County clay:

$$k_{county} = -3.27 + 0.616w + 0.0895T - 0.01806w^2 + 0.000111w^3 - 0.000235T^2 -$$

$$0.01457wT + 0.000101wT^2 + 0.000336Tw^2 - 0.000003T^3 - 0.000002w^2T^2$$

where k = Thermal Conductivity (BTU/hr/ft/°F), w = Water content (%), T = Temperature (°C). The R2 found were 0.92 for Dupont soil and 0.61 for County soil.

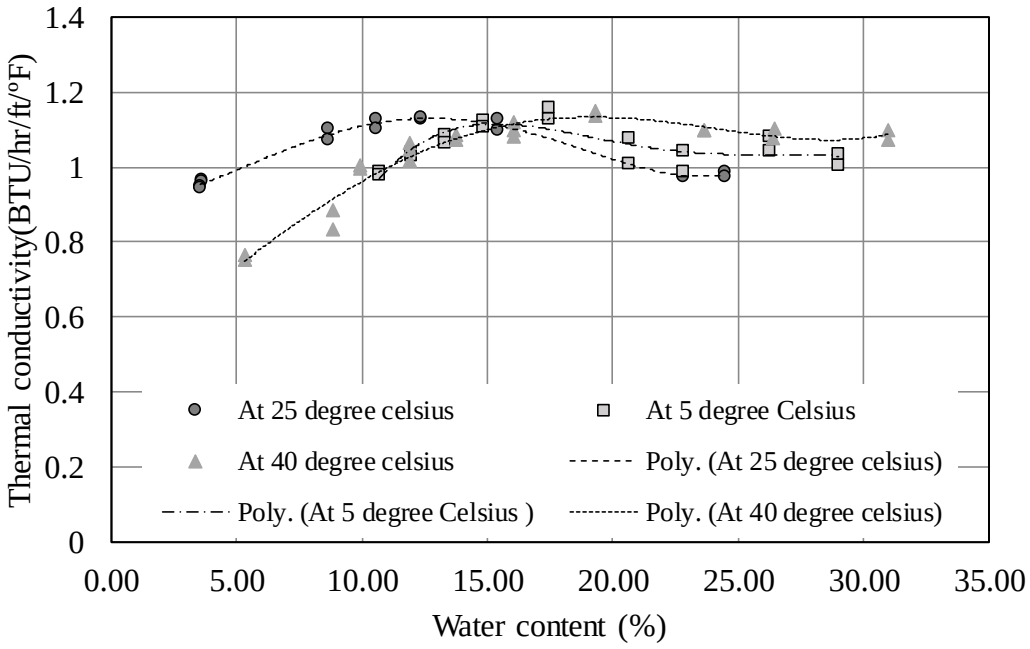

Figure 4.11. Thermal Conductivity Function of County Clay

Volumetric Heat Capacity

The test results of volumetric heat capacity as a function of water content for different temperatures are presented in Figure 4.12 for Dupont soil and Figure 4.13 for County soil. It is clear that the heat capacity increases as the water content increases. The equation below represents the relationship found between the volumetric heat capacity, water content and temperature.

For Dupont clay:

$$c_{V(dupont)} = -4.6 + 0.932T - 0.1202w^2 + 0.00504w^3 - 0.00580T^2 + 0.00580Tw^3 - 0.000047w^2T^2 + 0.000002w^3T^2$$

For County clay:

$$c_{V(county)} = 3.31 - 1.73w + 0.970T + 0.387w^2 - 0.01505w^3 - 0.007250T^2 + 0.000174w^4 - 0.001079Tw^2$$

where c_V = Volumetric heat capacity (BTU/ft/°F), w = Water content (%), T = Temperature (°C). The correlations yielded a coefficient of determination equal to 0.30 for Dupont soil and 0.70 for County soil.

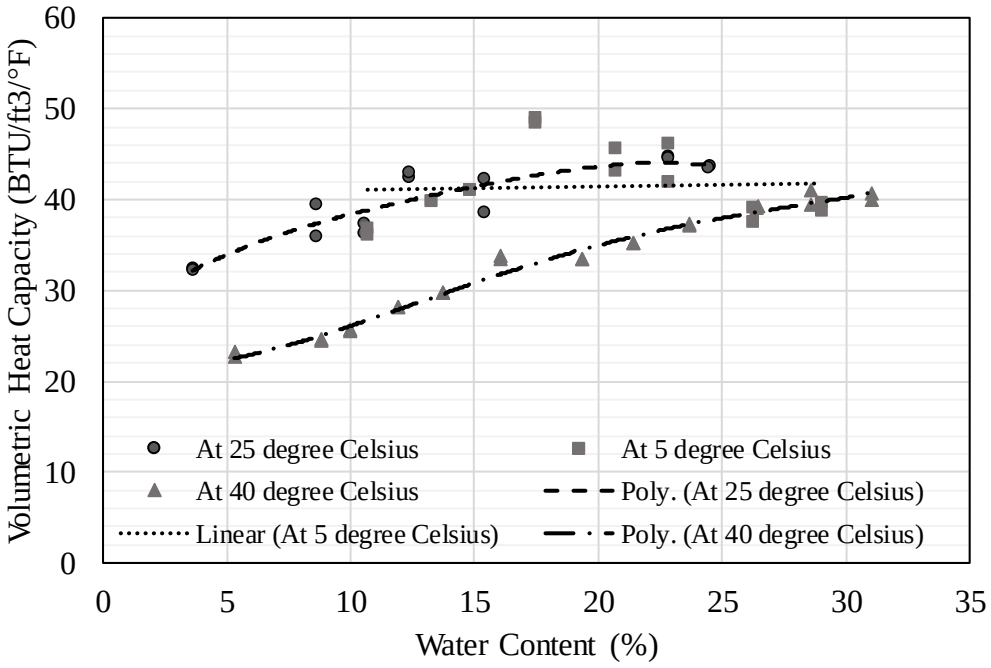

Figure 4.12. Variation of Volumetric Heat Capacity for Dupont Clay as a Function of Water Content at Different Temperatures

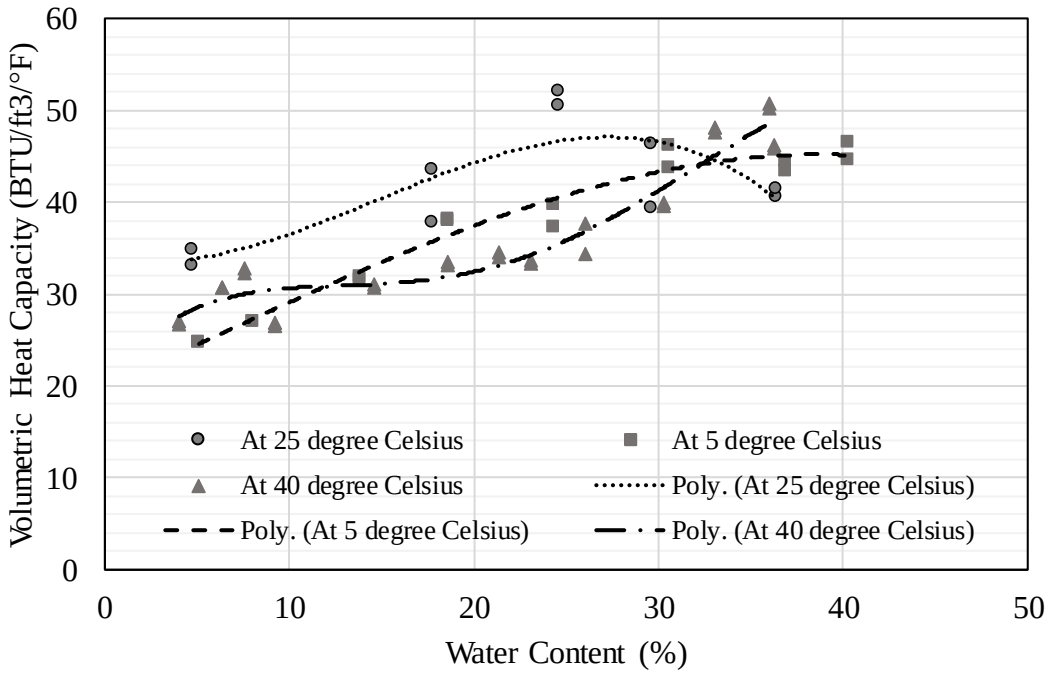

Figure 4.13. Variation of Volumetric Heat Capacity for County Clay as a Function of Water Content at Different Temperatures

UNSATURATED SOIL PROPERTIES

Lu (2015) performed Soil Water Characteristic Curve (SWCC) and unsaturated hydraulic conductivity. (k_{unsat}) tests to determine the unsaturated hydraulic functions on the two soils of this study at different temperatures. The following section shows the test results obtained from Lu's study. The analysis performed by Lu (2015) was revisited in order to find better regression parameters which would allow for more accurate prediction of the SWCC for the two soils. The k_{unsat} test results were also reanalyzed to find a more accurate relationship between matric suction and the unsaturated hydraulic conductivity. Further, a mathematical model was developed to predict changes in the SWCC and k_{unsat} functions with respect to changes in temperature.

Fundamental Aspects Relating SWCC to Temperature

Soil Water Characteristic Curve represents the prediction of the matric suction in the soil with respect to the amount of water present in the soil phase such as degree of saturation, gravimetric water content or volumetric water content. The matric suction of the soil is calculated as the difference of pore air pressure and pore water pressure. Theoretically, the matric suction of the soil developed can be attributed to the surface tension of water in the porous media due to the raise of the pore air pressure and the existing pore water pressure in the voids of a particular porous medium. The surface tension of water in the soil phase is mainly affected by the pore size, the viscosity of the water, and the pressures developed by the air and the liquid phases. Figure 4.14 shows the representation of the surface tension (T_s) developed in water, where R represents the radius of curvature, which is a function of the pores.

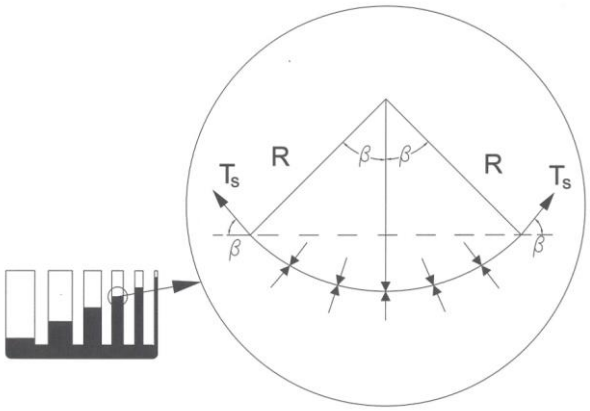

Figure 4.14. Surface Tension of Water in Porous Media

Milly, 1982 proved that the capillary pressure in a porous medium can be related with surface tension. Laplace's law shown below represents the relation between suction, surface tension and radius of curvature.

$$u_a - u_w = \frac{2\sigma_w}{r}$$

where u_a is the pore air pressure, u_w is the pore water pressure, σ_w is the surface tension of water and r is radius of curvature.

Tsuyoshi Miyazaki (2005) showed that the surface tension varies with temperature. He showed that as the temperature increases, surface tension decreases. A linear relationship was found to exist between surface tension and temperature as shown below.

$$\sigma_w = (75.6 - 0.154T)\times 10^{-3}$$

where σ_w is the surface tension of water (Nm^{-1}) and T is temperature in ^{0}C.

Pruess (1987) showed that capillary pressure or surface tension decreases with temperature. He developed two equations to predict the behavior of surface tension when there is a change in the temperature.

$\sigma_w = (1 - 0.625a)(0.2358a^{1.256})$ $\quad a = \frac{374.15-T}{647.3}$ For T<360^{0}C

$\sigma_w = 0.0019106exp(0.05(360 - T))$ For T>360^{0}C

Soil Water Characteristic Curve Results

Lu (2015) performed a series of 1-D oedometer and filter paper tests to obtain the equilibrium suction at different moisture contents. The tests were performed in a temperature controlled chamber. Three sets of data were obtained for three different temperatures: 5^{o}C, 25^{o}C and 40^{o}C. Using the test results obtained by Lu, the soil water characteristic curve was obtained using the Fredlund and Xing fitting equation as shown below (Fredlund and Rahardjo, 1994):

$$\theta = C(\psi)\theta_s \left[\frac{1}{ln\left[e + \left(\psi/a\right)^n\right]} \right]^m$$

where: θ is the volumetric water content; ψ (kPa) is the suction; a, n, and m are fitting parameters; and C(ψ) is a correction factor that forces the model through a prescribed suction value of 10^6 kPa at zero water content:

$$C(\psi) = \left[1 - \frac{\ln(1 + \psi/\psi_r)}{\ln(1 + 10^6/\psi_r)}\right]$$

Where: ψ (kPa) is the residual suction value.

Table 4.6 shows the Fredlund and Xing parameters obtained from the test results for three different temperatures for County and Dupont clay. Using the Fredlund and Xing paramters in the Fredlund and Xing fitting equation, the SWCC is obtained as shown in Figure 4.10 and Figure 4.11 for County Clay and Dupont Clay, respectively.

Table 4.6. Fredlund and Xing Parameters for County and Dupont Clays at Different Temperatures

Type of soil	County Clay			Dupont Clay		
Fredlund & Xing parameters	5 ^{0}C	25 ^{0}C	40 ^{0}C	5 ^{0}C	25 ^{0}C	40 ^{0}C
a	15186.27	15186.27	15186.27	3791.27	2091.28	791.28
n	0.39	0.39	0.46	0.81567	0.86	0.72
m	2.79	3.31	3.79	0.99103	1.09	0.89
h_r	83534.23	83534.23	83534.23	19026.24	19026.24	19026.24

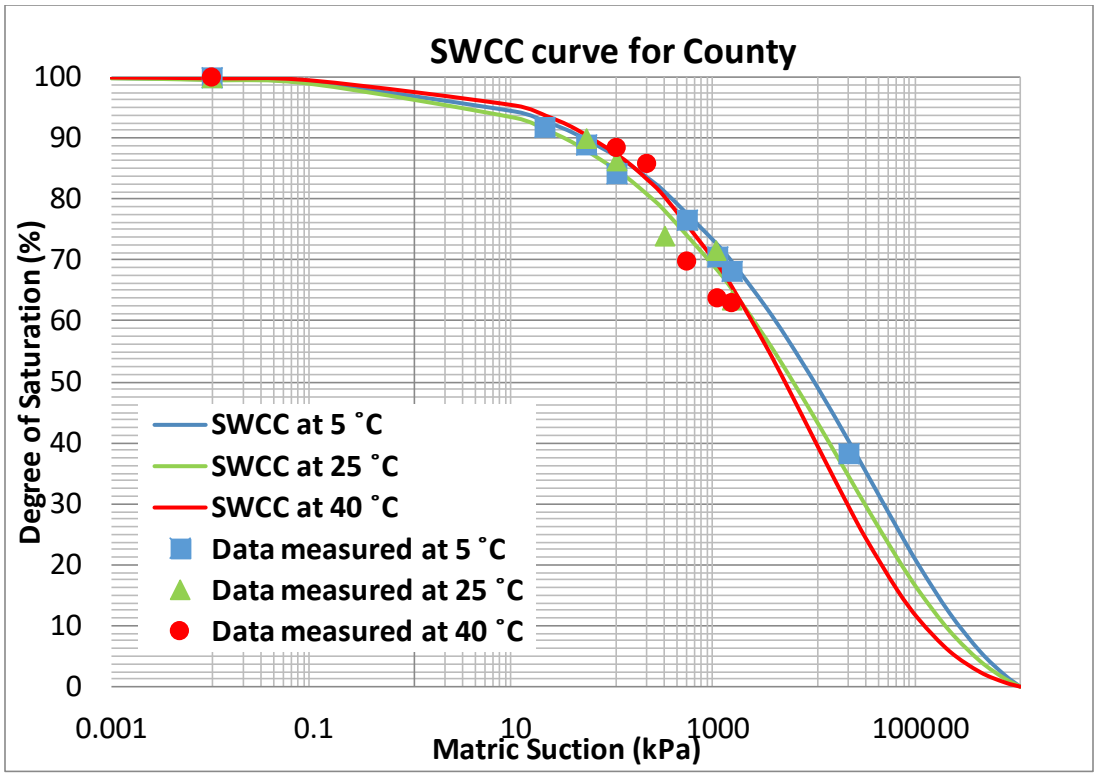

Figure 4.15. SWCC of County soil at Three Temperatures

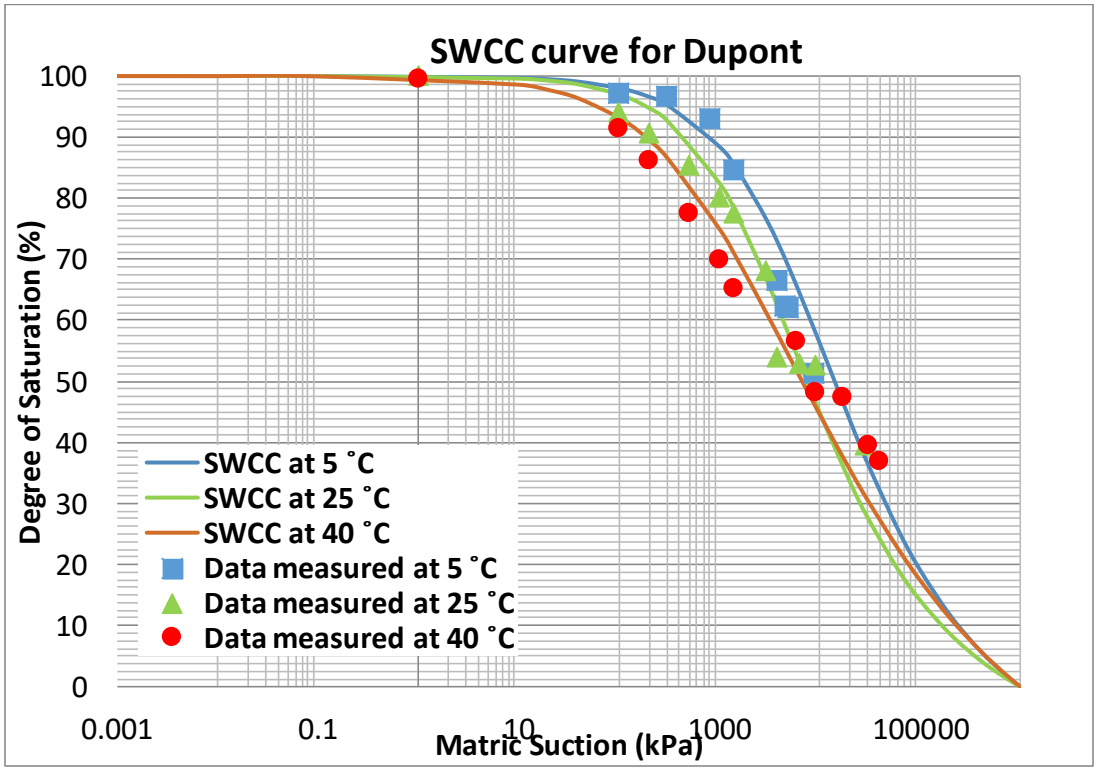

Figure 4.16. SWCC of DuPont soil at Three Temperatures

The analysis of the Fredlund and Xing parameters show that the variation of the parameters a, m, n and h_r are in a trend. Both clays exhibited a change in the air entry value and the shape of the curve when there is a change in the temperature. The parameter a is found to be a constant in County soil but it varies linearly with temperature in Dupont soil. The variation of m and n are related to the temperature as shown in Table 4.7. A mathematical model is created to relate the change of the parameters with temperature as shown in Table 4.7. The equations shown in Table 4.7 has been tested to be true and valid for temperature ranging from 0 ˚C to 40 ˚C.

Table 4.7. Model to predict the variation Fredlund and Xing parameter with Temperature

Fredlund & Xing parameters	County	Dupont	Applicable Ranges
a	15186.27	-85.676T + 4223.7	0 ˚C≤ T≤ 40 ˚C
m	$0.1474m^2$ - 0.8988m + 1.7481	$-0.0003T^2$ + 0.0102T + 0.7719	0 ˚C≤ T≤ 40 ˚C
n	$0.0002T^2$ + 0.0216T + 2.6734	$-0.0005T^2$ + 0.0207T + 0.9006	0 ˚C≤ T≤ 40 ˚C
ψ_r	83534.23	19026.24	

Figure 4.16 and Figure 4.17 shows the degree of saturation obtained from the Fredlund and Xing fitting curve equation using the individual regression parameters for 5, 25 and 40 degrees Celsius to the regression parameters found using the model developed.

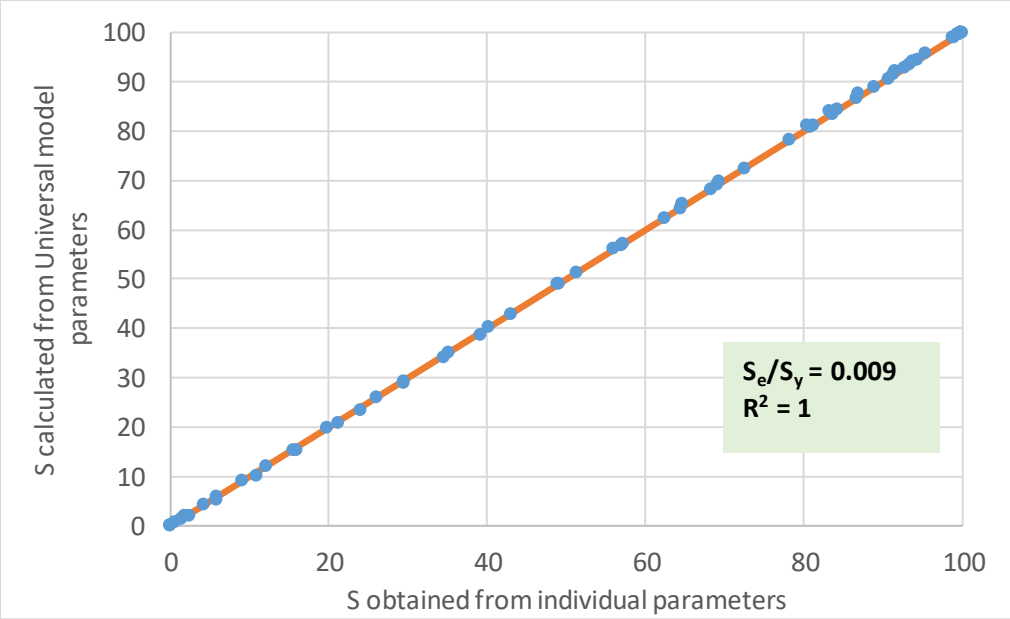

Figure 4.17. Comparison of Degree of Saturation Obtained from Individual Fredlund and Xing Parameters to Regression Parameters Obtained from Model (County Clay)

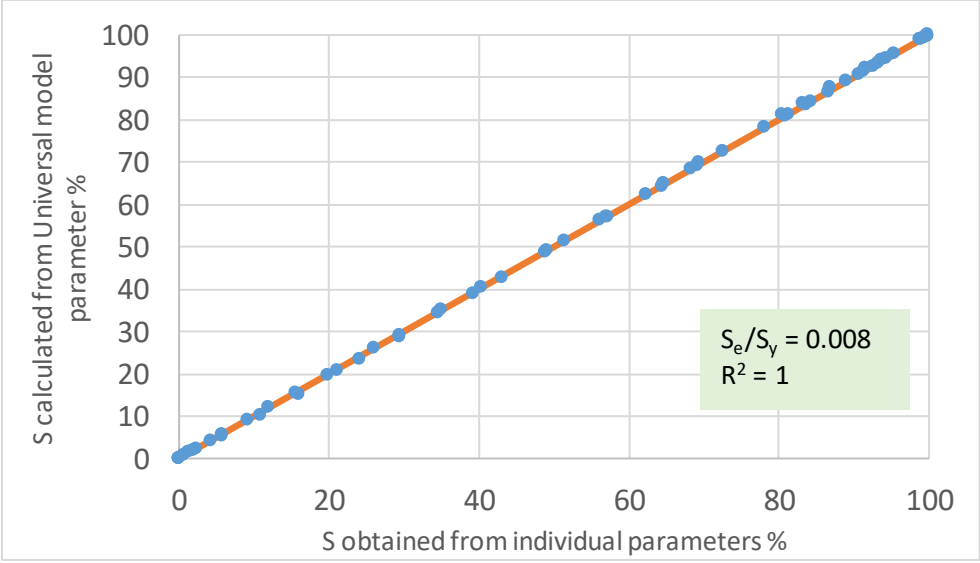

Figure 4.18. Comparison of Degree of Saturation Obtained from Individual Fredlund and Xing Parameters to Regression Parameters Obtained from Model (Dupont Clay)

S_e/S_y obtained from comparing the data predicted using the mathematical model developed for the regression parameters and the individual parameters developed for each temperature is 0.009 for County soil and 0.008. R- square value was found to be 1 both soils. This demonstrates that the correlations between the fitting parameters and temperature are excellent.

Figure 4.18 and Figure 4.19 shows a family of curves developed to show the change in SWCC for County and Dupont clay when there is a change in temperature. The curves clearly show the influence of the variation of temperature on the Fredlund and Xing parameters which leads to a change in the shape of the SWCC curve.

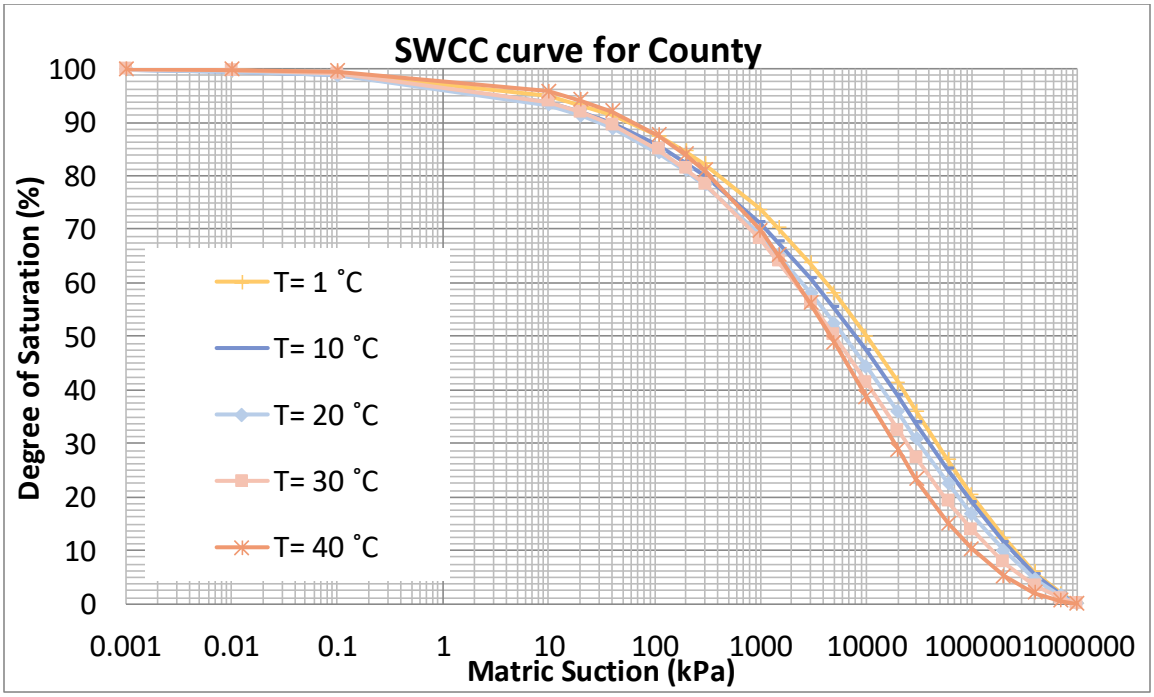

Figure 4.19. Prediction of Variation in SWCC with Temperature for County Soil

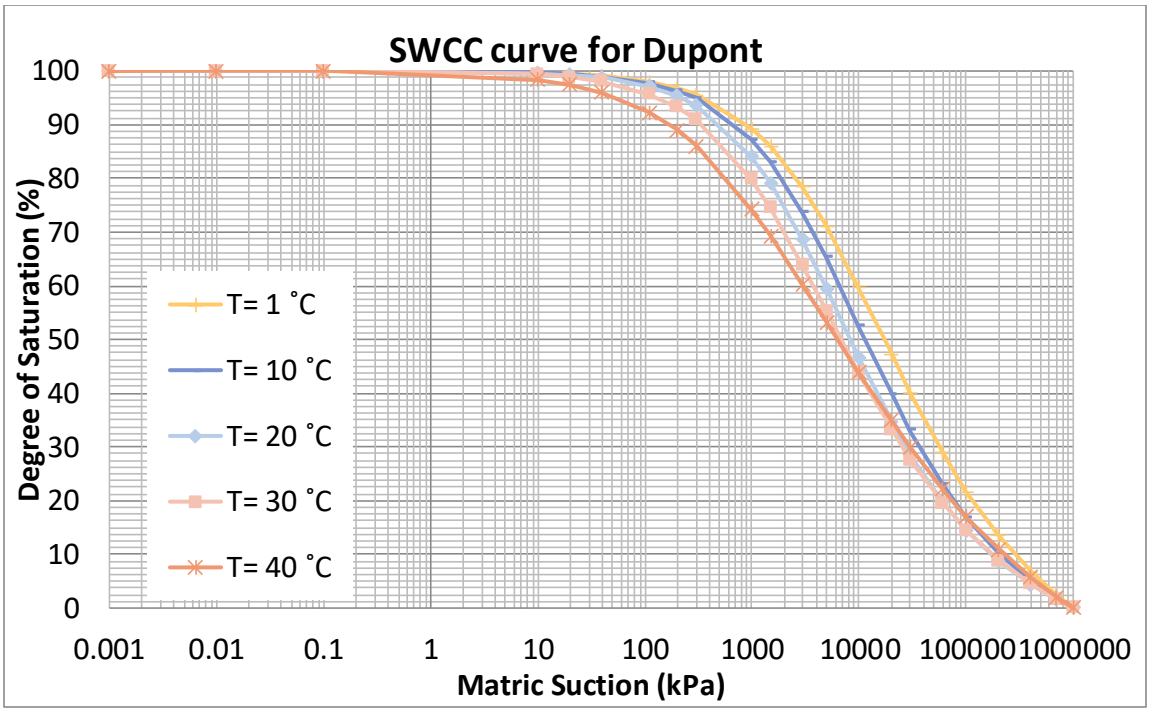

Figure 4.20. Prediction of Variation in SWCC with Temperature for Dupont Soil

Comparison of the Empirical SWCC-T Model to Published Models

Olivella (1996) put together the van Genuchten SWCC model to the Pruess model developed which associated surface tension with temperature. Van Genuchten model may be written as below:

$$S_l = S_{rl} + \frac{S_{ls} - S_{rl}}{\left(1 + \left(\frac{u_a - u_w}{P}\right)^{\frac{1}{1-\lambda}}\right)^{\lambda}}$$

Where, S_l is the degree of saturation for targeted water content, S_{rl} is the residual degree of saturation, S_{ls} is the maximum degree of saturation, u_a is the pore water pressure, u_w is the pore water pressure, P is the term related to the air entry value in kPa, and λ is related to slope of the curve. P and λ are the regression parameters of the van Genuchten SWCC.

Milly (1982) showed that the P parameter (air entry value) is associated with surface tension. The surface tension can be calculated using the equation shown below:

$\sigma_w = (1 - 0.625a)(0.2358a^{1.256})$ $\quad a = \frac{374.15-T}{647.3}$ For T<360°C

$\sigma_w = 0.0019106exp(0.05(360 - T))$ For T>360°C

The P value at any temperature can then be calculated using:

$$P = P_0 \frac{\sigma(T)}{\sigma(T_0)}$$

Where P_0 is the corresponding parameter at measured temperature T_0 and P is the parameter for the predicted temperature T. The substitution of the P parameter in the van Genuchten model yields the prediction of suction for a particular temperature. However, in this model, the slope of the SWCC (λ parameter) is independent of temperature. In the model developed as part of the current study, this was not the case.

A comparison of the two models for County and Dupont clay is shown in Figures 4.21 and 4.22, respectively. The van Genuchten parameters were found for 25°C and then the SWCC were developed for 5° and 40°C.The figures clearly shows that the change in suction due to temperature for the model developed by Olivella (2008) is not as marked as the changes found in our study, for both clayey soils.

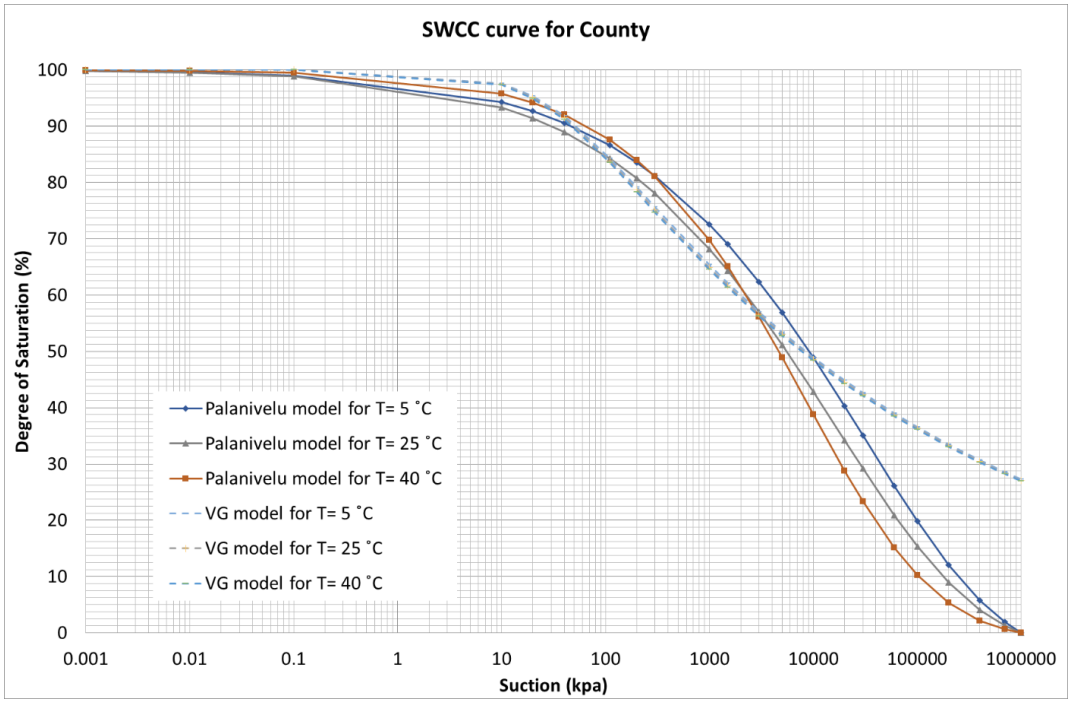

Figure 4.21. Comparison of Model Developed by Olivella to Model Developed in this Study for County Clay

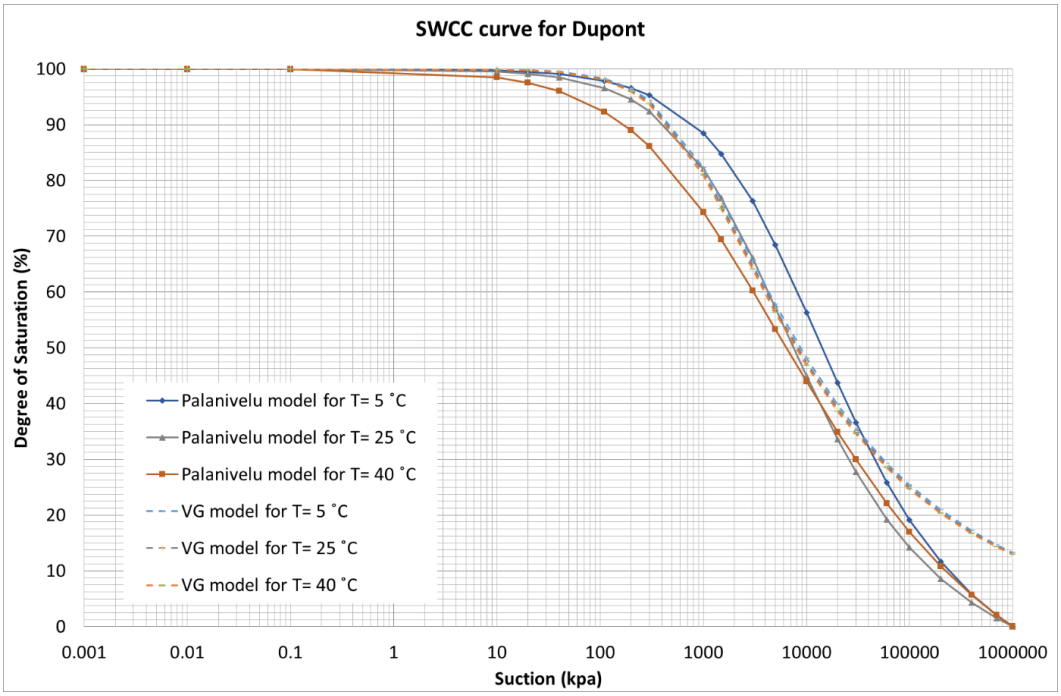

Figure 4.22. Comparison of Model Developed by Olivella to Model Developed in this Study for Dupont Clay

Fundamental Aspects Relating k_{unsat} to Temperature

Hydraulic conductivity is defined as the rate at which water is allowed to flow through its interconnected voids. It is generally assumed to be a constant value for saturated soil (Das, 2008). For unsaturated soil, however, it varies widely depending on the stress state (matric suction). Hydraulic conductivity of a porous media is directly proportional to liquid density, intrinsic hydraulic conductivity and the reciprocal of liquid viscosity.

$$k = \frac{\mathrm{K}\rho_l g}{\eta}$$

Where: k is the hydraulic conductivity, ρ_l is the liquid density, K is the intrinsic hydraulic conductivity of the porous matrix, g is the gravitational constant and η is the viscosity of liquid.

Temperature effects on hydraulic conductivity can be derived from viscosity and density changes. Research studies such as Kestin (1978) and IAPWS (2008) shows that the viscosity of liquid decreases as temperature increases due to the increase of the energy of liquid movement. Olivella (1996) shows an equation relating the variation of the viscosity (in Mpa.s) with temperature (°K).

$$\eta = 0.021\ exp\left[\frac{1808.5}{273.15 + T}\right]$$

Also, as temperature increases, the surface tension of the water decreases and a lower surface tension allows the liquid to more easily penetrate the soil pores.

The density changes can also change the hydraulic conductivity of the soil: An increase in density could increase the degree of saturation; therefore, increasing the hydraulic

conductivity. The liquid density variation with temperature was shown using the equation below (Sanchez et al., 2016).

$$\rho_l = 1002.6 \exp[4.5\times10^{-4}(P_l - 0.1) - 3.4\times10^{-4}T]$$

where ρ_l is the liquid density (g/cm^3), P_l is the fluid pressure (g/cm^3), and T is temperature in ^{0}C.

Figure 4.23 shows the variation of viscosity and liquid density with respect to temperature.

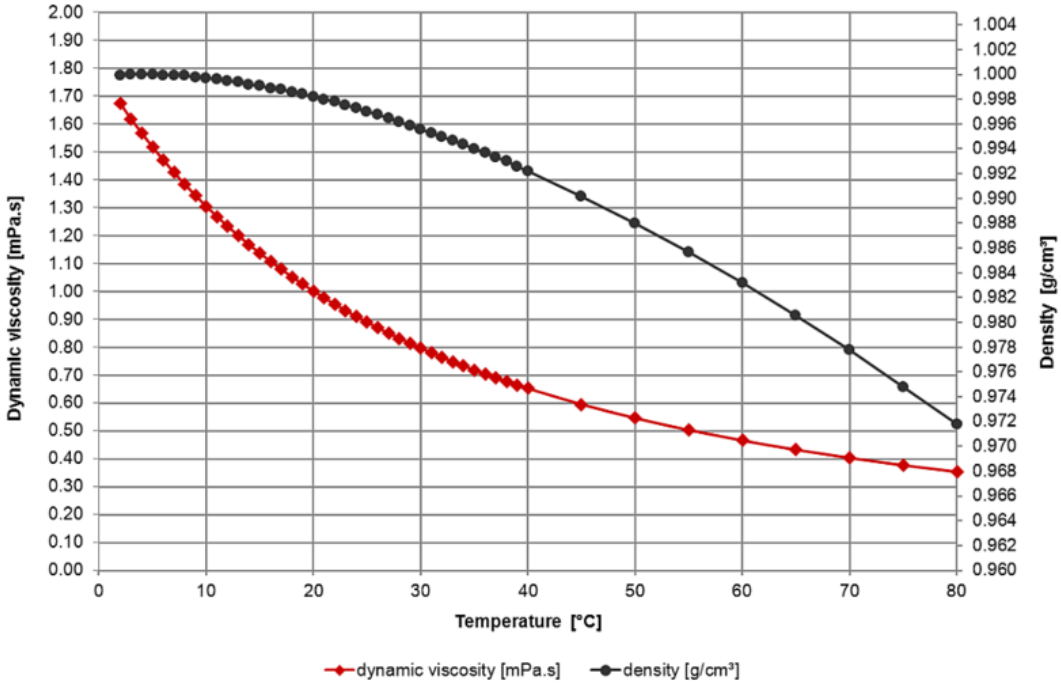

Figure 4.23. Variation of Dynamic Viscosity and Liquid Density with Temperature

Unsaturated Hydraulic Conductivity Function

The hydraulic conductivity of the soil at different suction values was obtained using the instantaneous profile method. Lu (2015) performed the method at three different temperatures. The result of this study is shown in Figure 4.20 and Figure 4.21 for County

and Dupont Clay, respectively. The fitting equations to predict the variation of the k_{unsat} with moisture content and temperature is also shown in Figure 4.20 and Figure 4.21.

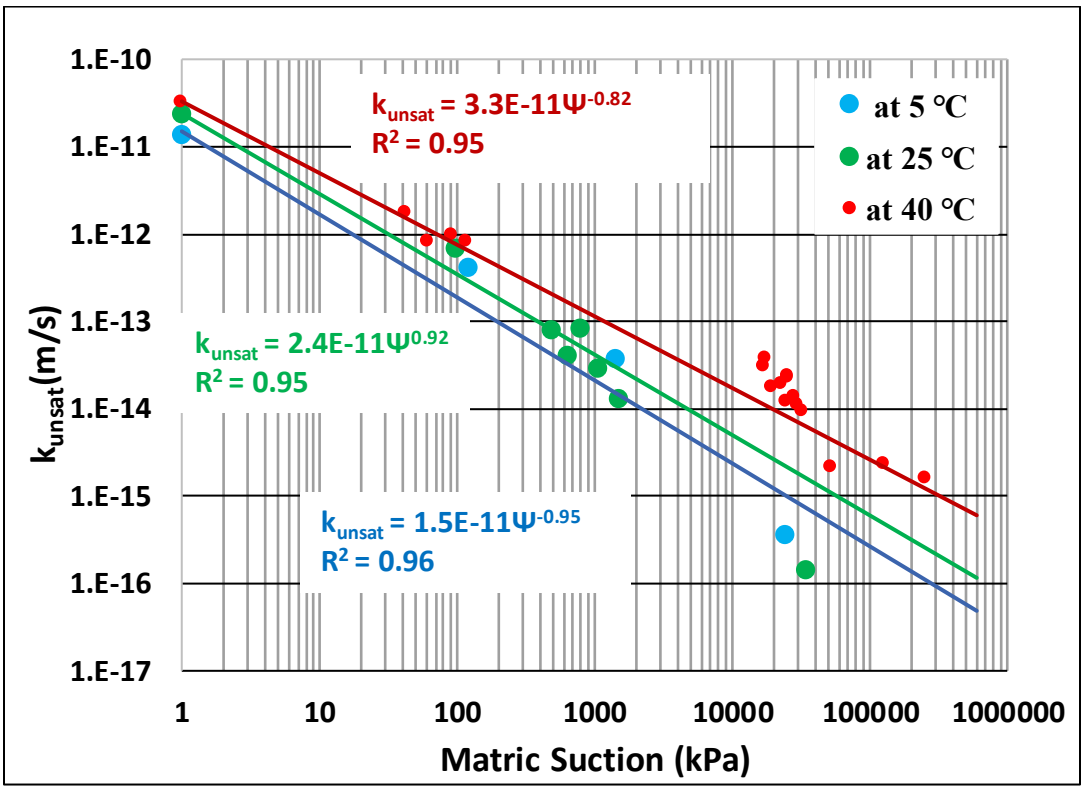

Figure 4.24. Unsaturated Hydraulic Conductivity Function of County Soil at Three Temperatures

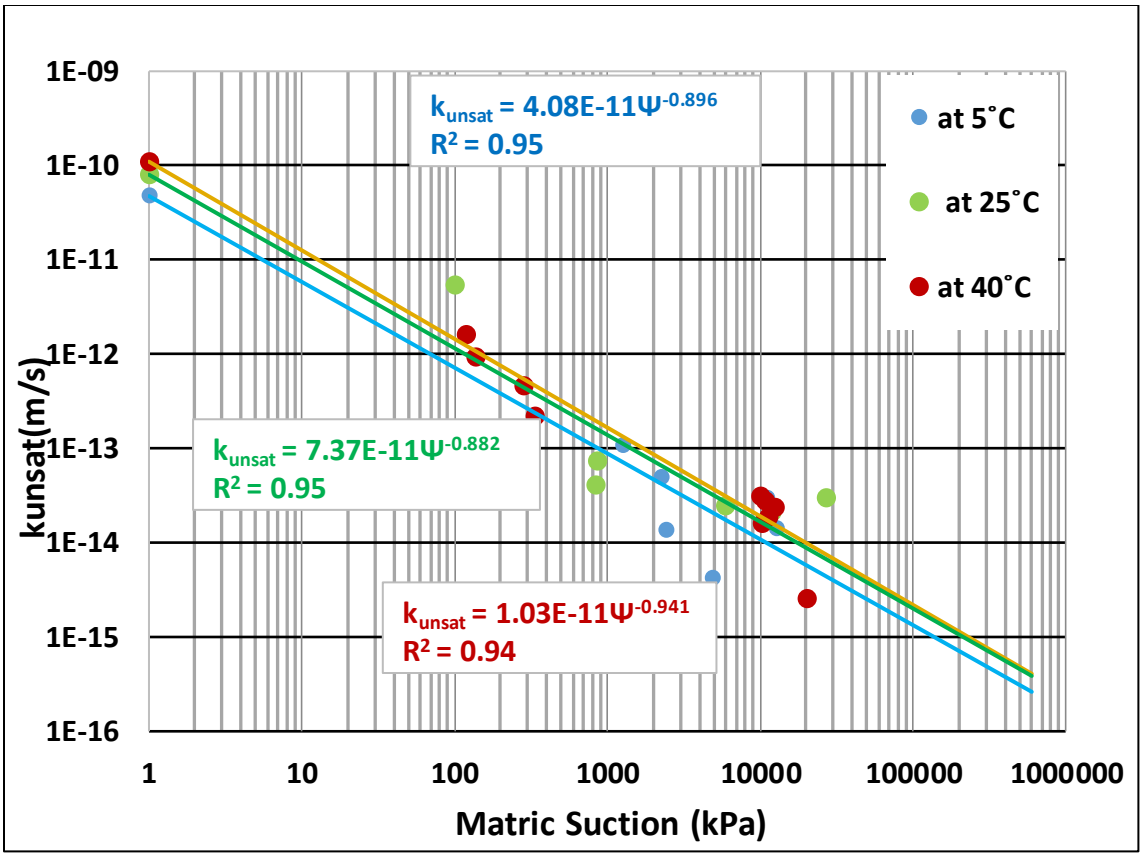

Figure 4.25. Unsaturated Hydraulic Conductivity Function of DuPont Soil at Three Temperatures

Using the data obtained from the instantaneous profile tests, a global fitting equation was developed for each soil type to predict the k_{unsat} at different temperatures. The equations below show the model developed:

For County Clay:

$$k_{unsat} = (5\times10^{-13}T + 1\times10^{-11})\psi^{-(-0.00015T^2+0.00293T+0.93905)}$$

For Dupont Clay:

$$k_{unsat} = (1.77\times10^{-12}T + 3.12\times10^{-11})\psi^{-(0.000132T^2-0.00467T+0.916)}$$

The parameters have been previously defined. The model works well with temperatures varying from 0°C to 40°C.

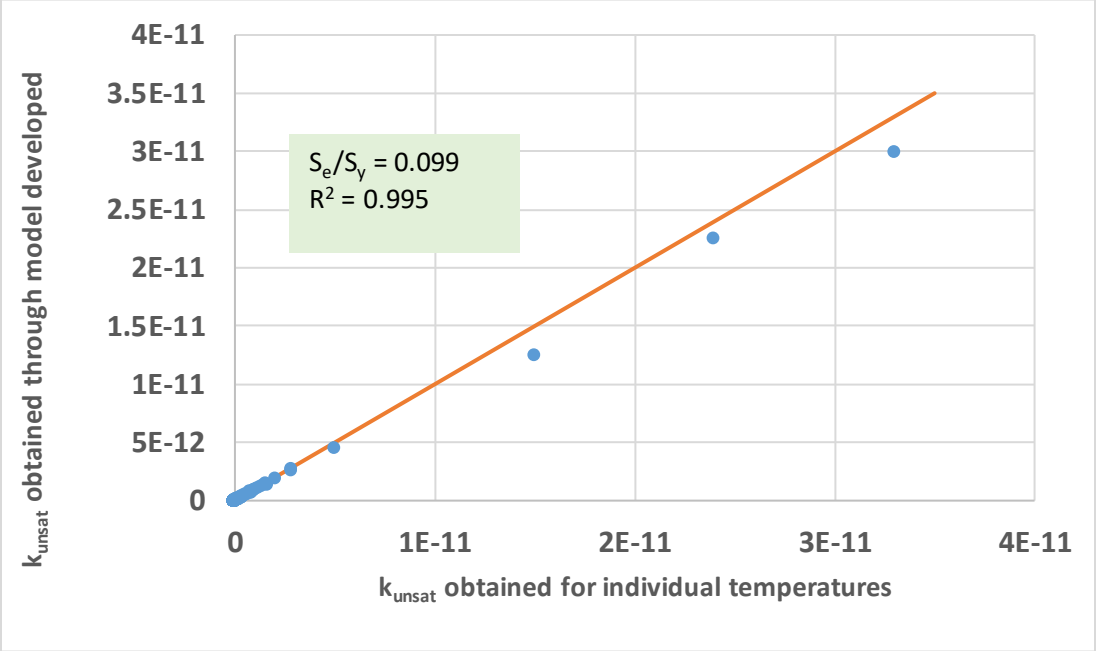

Figure 4.26. Comparison of k_{unsat} Obtained from Individual Temperatures to Model Developed for All Temperatures (County Clay)

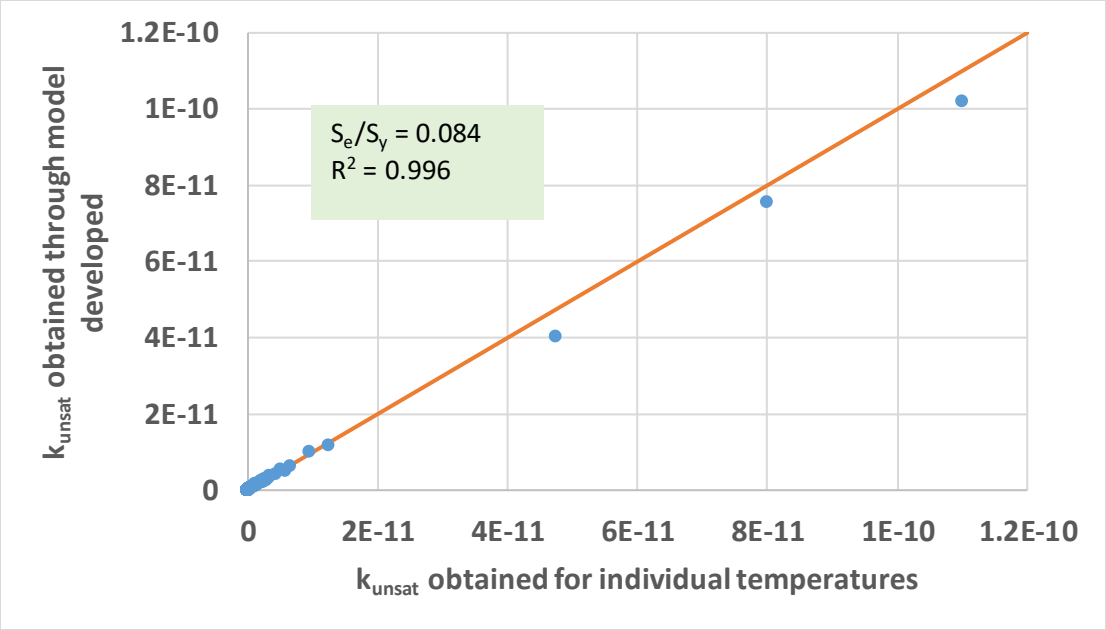

Figure 4.27. Comparison of k_{unsat} Obtained from Individual Temperatures to Model Developed for All Temperatures (Dupont Clay)

As shown in Figures 4.22 and 4.23, the statistical analysis of the k_{unsat} predicted using the global model and that obtained from the individual models at different temperatures yielded a S_e/S_y equal to 0.099 for County soil and 0.084 for Dupont soil. The R- square values were found to be 0.995 for County soil and 0.996 for Dupont soil. The goodness of fit results indicate that the overall model is excellent and can be used to represent the entire data set.

Using the model developed, a family of curves for different temperatures were developed for the two soils as shown in Figure 4.24 and Figure 4.25. The Figures show the variation of k_{unsat} with a change in temperatures ranging from 0°C to 40°C.

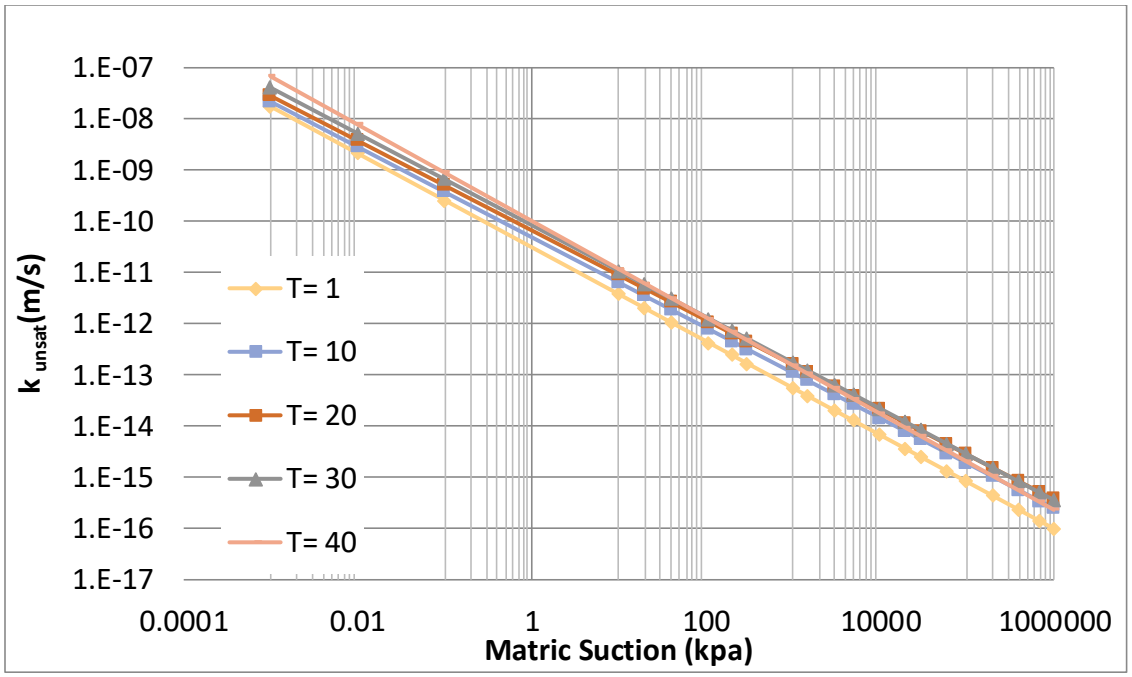

Figure 4.28. Prediction of Variation in k_{unsat} at Different Temperature for County Soil Using the Model Developed

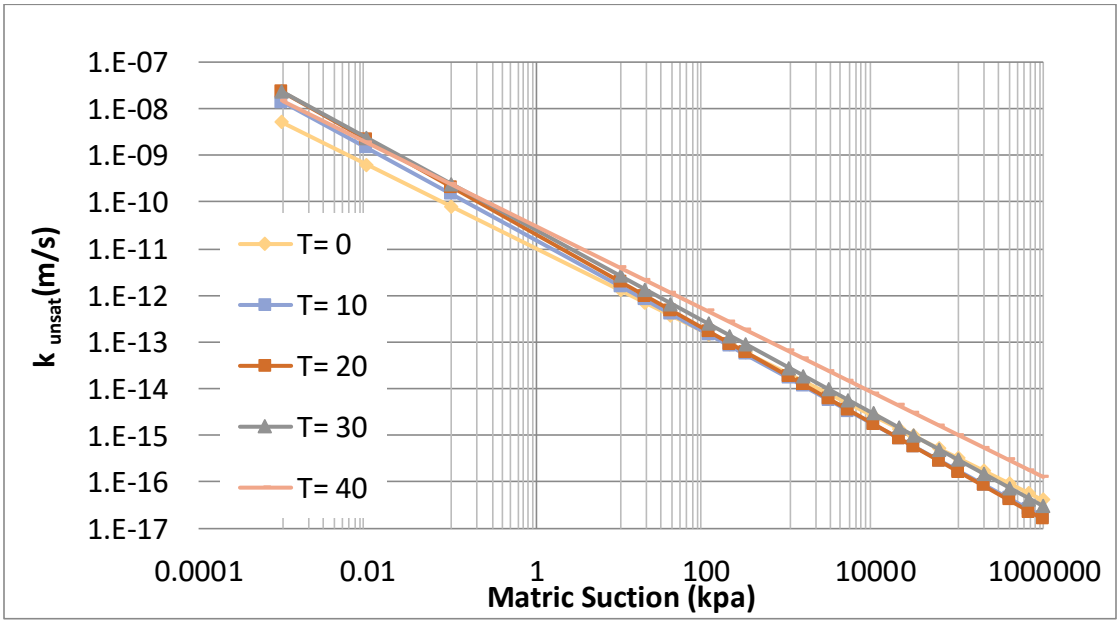

Figure 4.29. Prediction of Variation in k_{unsat} at Different Temperatures for Dupont Soil Using the Model Developed

Comparison of k_{unsat}-T Model to Previously Models Reported in Literature

In order to compare the model developed in this study with previously reported models, the relationship between the liquid viscosity and temperature reported in Olivella (2008) was substituted in Darcy's law to obtain a relationship between *T* and *k*:

$$k = \frac{\mathrm{K}\rho_l g}{0.021\, exp\left[\frac{1808.5}{273.15 + T}\right]}$$

This equation was then used with the model developed using Olivella (2008) equation to predict the k_{unsat} at any desired temperature:

$$k = k_0 \frac{\lambda(T_0)}{\lambda(T)}$$

Where k_0 is the corresponding k_{unsat} at measured temperature T_0 and *k* is the k_{unsat} for the temperature predicted T. The results are presented in Table 4.8.

Table 4.8. Comparison of k_{unsat}-T Model Developed with Olivella (2008) Model

Soil Type	County			Dupont		
Temperature (^{0}C)	25	5	40	25	5	40
Viscosity λ (mPa.s)	1.52	0.89	0.65	1.52	0.89	0.65
k_{unsat} using Model Developed (m/s)	1.46E-11	2.49E-11	3.25E-11	4.01E-11	7.55E-11	1.02E-10
k_{unsat} using Olivella (2008) study (m/s)	2.22E-11	2.49E-11	2.69E-11	6.73E-11	7.55E-11	8.18E-11

Figure 4.30 and Figure 4.31 shows the variation of k_{unsat} with viscosity for the model developed by Palanivelu in this study and by Olivella theory for County and Dupont clay respectively.

The difference in the prediction of k_{unsat} between the two models is primarily due to the use of different soils to develop the models. Also, the model developed in this study does not only incorporate the effect of viscosity on the hydraulic conductivity but also considers the change in the surface tension and hence, matric suction, due to temperature. In general, the results yield the same trend and agree with each other.

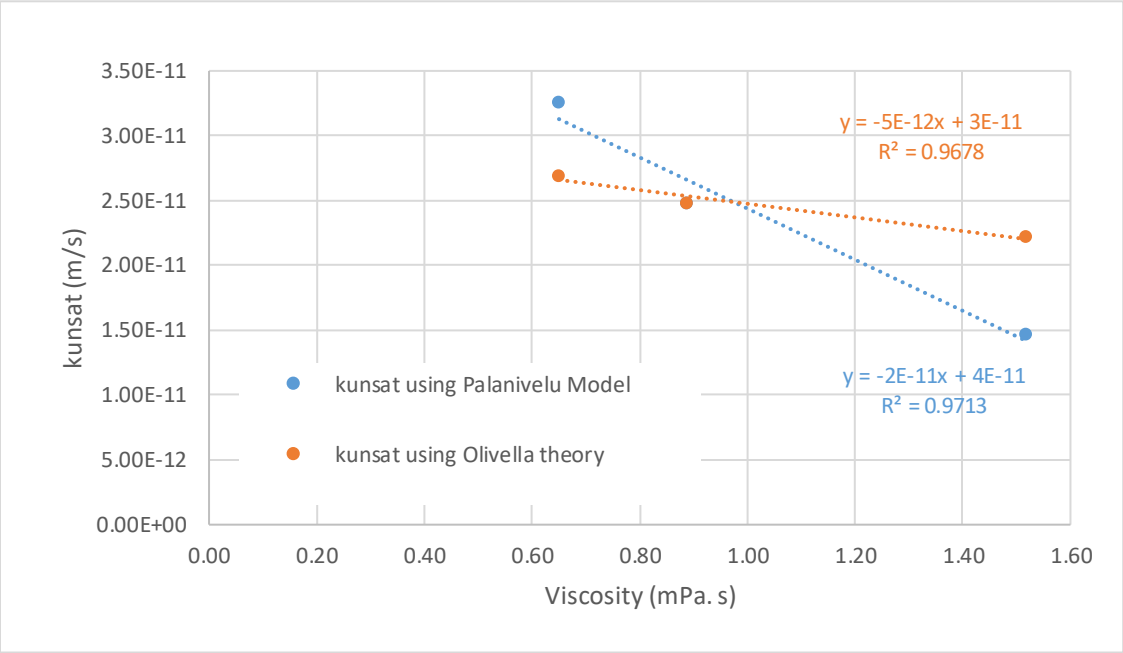

Figure 4.30. Prediction of k_{unsat} with Viscosity by Palanivelu Model and Olivella Theory for County Clay

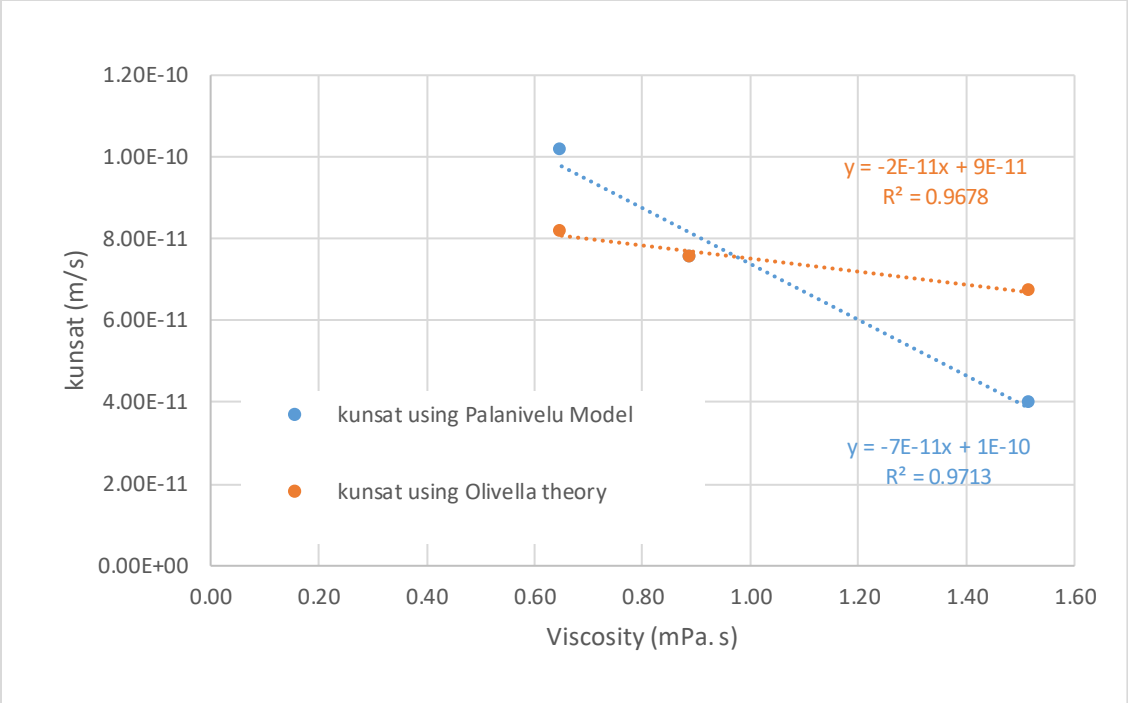

Figure 4.31. Prediction of k_{unsat} with Viscosity by Palanivelu Model and Olivella Theory for Dupont Clay

Chapter 5. CBR Testing and Results

This chapter explains in detail the California Bearing Ratio (CBR) and Vane Shear test performed for this study. The chapter details the general specifications, conditions and results of the tests performed. General information regarding the equipment involved in performing the CBR and the vane shear test are outlined. The preparation of the soil specimen for the test is also explained briefly in this section. CBR tests were performed on the subgrade clay materials for this study. Vane shear tests were also performed on the same CBR test specimen to develop correlations between these shear strength parameters, evaluated on both subgrade materials. The different factors affecting the CBR value of the soil are also analyzed in this section.

The California Bearing Ratio (CBR) test is usually performed in order to estimate the modulus of any unbound soils and aggregate materials. CBR is the **ratio of force per unit area** required to penetrate a soil mass with standard circular piston at the rate of 1.25 mm/min. to that required for the **corresponding penetration** of a standard material. The CBR test is a penetration test developed by *California State Highway Department (U.S.A.)* for evaluating the bearing capacity of subgrade soil for design of flexible pavement. Numerous studies have suggested that the CBR can be related to the Resilient Modulus of the specimen.

EQUIPMENT USED FOR CBR AND VANE SHEAR TESTS

The equipment used for the CBR test consisted of a 6-inch diameter Mold, Steel Cutting collar, Spacer Disc, Surcharge weight, Penetration Plunger and Loading Machine. A Universal Testing Machine (UTM) was used to apply the penetration at the rate of 1.25 mm/min. The system had a load cell capacity of 22.24 kN (5000 lb) and the load reaction

frame was capable of supporting up to 45 kN (10,000 lb) in tension or compression. The UTM was adjusted to move the penetration piston at a rate of penetration approximately equal to 0.05 in. (1.27 mm/min) until it reached a penetration of 0.5 in. (12.7 mm). The equipment used to prepare the CBR samples is shown in Figure 5.1.

An E-285 pocket vane shear tester from Gibson was also used to measure the shear strength of the soil. The equipment consists of a dial and three types of blades. The medium type of blade was used in this study. The vane blades are immersed in the soil and rotated. The dial rotates along with the vane during the shearing process. At failure, the dial shows the shear strength of the soil in terms of tsf. Figure 5.2 shows a typical E-285 pocket vane shear tester.

Figure 5.1. CBR Equipment Used to Prepare Samples

Figure 5.2. Pocket Vane Shear Tester

PREPARATION OF SOIL

The specimens was prepared for a specified moisture content and compacted to three different compaction energies: 12486 (Standard), 20810 (Intermediate), 56756 (Modified) lbs.ft/ft^3. The energy levels chosen corresponded to the same levels of energy use to obtain the Proctor compaction test results. The standard and the modified compaction conditions were performed according to ASTM D698 and D1557 for a 6-inch mold. Table 5.1 shows the specifications of the tests performed at each energy level.

Table 5.1. Specifications of the Tests Performed

Energy Level	No. of Layers	No. of blows per layer	Hammer used	Height of Hammer Drop (in)	Force Applied (lbs)	Vol. of Sample (ft^3)	Comp. Energy ($lbs.ft/ft^3$)
Standard	3	56	Standard Proctor Hammer	12	5.5	0.074	12486
Intermediate	5	56	Standard Proctor Hammer	12	5.5	0.074	20810
Modified	5	56	Modified Proctor Hammer	18	10	0.074	56756

All the tests were performed under as-molded conditions. A range of water contents were chosen for the two types of soil based upon the Proctor compaction test results obtained previously and also based on the range of water contents found in NAPTF facility. The water contents ranged from dry to wet of optimum. The soil obtained from the test facility was pulverized to pass through #80 sieve and mixed to a targeted moisture content. The mixed soil was kept in an airtight container and the soil was allowed to equilibrate. The soil was compacted to the three different compaction energies mentioned before and the dry densities of the soil were obtained. Table 5.2 presents a list of the CBR tests performed, including the targeted water contents and test condtions.

TESTING PROCEDURE

CBR test

The CBR test performed was conducted according to ASTM Standard D1883-07. A step by step test procedure followed for each water content is as follows:

1. The dimensions of the mold used for the test were taken and the volume of the mold was calculated.
2. The empty weight of the mold was taken without the collar.
3. The soil, which was mixed to the particular water content, was compacted inside the mold according to one of the specifications mentioned in Table 5.2.
4. After compaction, the collar was removed and the soil projecting out of the mold was scrapped off.
5. The weight of the mold with the compacted soil was taken.

Table 5.2. CBR Tests Performed

Clay	Targeted Water Content	No of Layers	No of blows	Type of Hammer	Test Condition	File Name
County Clay	15	3	56	Standard	Unsoaked	CCS315USO
		5	56	Standard	Unsoaked	CCI515USO
		5	56	Modified	Unsoaked	CCM515USO
	20	3	56	Standard	Unsoaked	CCS320USO
		5	56	Standard	Unsoaked	CCI520USO
		5	56	Modified	Unsoaked	CCM520USO
	25	3	56	Standard	Unsoaked	CCS325USO
		5	56	Standard	Unsoaked	CCI525USO
		5	56	Modified	Unsoaked	CCM525USO
	27	3	56	Standard	Unsoaked	CCS327USO
		5	56	Standard	Unsoaked	CCI527USO
		5	56	Modified	Unsoaked	CCM527USO
	30	3	56	Standard	Unsoaked	CCS330USO
		5	56	Standard	Unsoaked	CCI530USO
		5	56	Modified	Unsoaked	CCM530USO
	35	3	56	Standard	Unsoaked	CCS335USO
		5	56	Standard	Unsoaked	CCI535USO
		5	56	Modified	Unsoaked	CCM535USO
Dupont Clay	13	3	56	Standard	Unsoaked	DCS313USO
		5	56	Standard	Unsoaked	DCI513USO
		5	56	Modified	Unsoaked	DCM513USO

	18	3	56	Standard	Unsoaked	DCS318USO
		5	56	Standard	Unsoaked	DCI518USO
		5	56	Modified	Unsoaked	DCM518USO
	22	3	56	Standard	Unsoaked	DCS322USO
		5	56	Standard	Unsoaked	DCI522USO
		5	56	Modified	Unsoaked	DCM522USO
	27	3	56	Standard	Unsoaked	DCS327USO
		5	56	Standard	Unsoaked	DCI527USO
		5	56	Modified	Unsoaked	DCM527USO
	37	3	56	Standard	Unsoaked	DCS337USO
		5	56	Standard	Unsoaked	DCI537USO
		5	56	Modified	Unsoaked	DCM537USO
	42	5	56	Standard	Unsoaked	DCI542USO
		5	56	Modified	Unsoaked	DCM542USO

6. After the mold was inverted, a surcharge load of 10lbs was placed on the soil specimen.
7. The specimen was placed on the UTM and the piston was moved at a penetration rate of 1.25 mm/min and the load corresponding to the penetration values were noted.
8. A plot was drawn between the penetration of the piston (in) and penetration load (psi). The plot was corrected according to the ASTM standards for the irregularities.
9. CBR value was calculated by taking a ratio of the stress at 0.1 in, 0.2 in and 0.3 in penetration with the standard stresses of 1000 psi, 1500 psi and 1900 psi (10.3 MPa) respectively, and multiplying by 100.
10. For the large majority (90%) of all CBR tests completed; the maximum CBR was found to occur with the 0.1 in penetration. As a result, all CBR values reported in this document are those at 0.1-inch penetration.

11. After the CBR test was completed, the vane shear test was performed. The procedure for the vane shear test is mentioned in the next section.
12. The soil was then extracted from the mold and the moisture content was measured.
13. The whole process was repeated for different compaction conditions along with different water contents.

Vane Shear test

After the CBR test was completed, a vane shear test was performed to find the shear strength using a pocket vane shear test. The procedure by which the vane shear test was done is as follows:

1. The pointer in the pocket vane shear test was brought to zero.
2. The blades of the equipment were completely immersed into the soil and the dial was turned along with the pointer until the soil failed.
3. The pointer in the dial showed the shear strength of the soil being tested.

CBR AND VANE SHEAR TEST RESULTS

The results of the CBR tests were used to develop a plot between the penetration and the load. A typical plot between penetration and load for a water content is shown in Figure 5.3. These plots were used to obtain the CBR value as mentioned in the testing procedure. As previously noted, CBR values were calculated at penetration values of: 0.1", 0.2", 0.3", 0.4" and 0.5". Penetration resistance values for the standard material used in computing the CBR, are: For δ= 0.1", p_s = 1000 psi; for δ= 0.2", p_s = 1500 psi; for δ= 0.3", p_s = 1900 psi; for δ= 0.4", p_s = 2300 psi; for δ= 0.5", p_s = 2600 psi. As noted, the maximum CBR

value were typically found at the 0.1" penetration for most of the specimen. Because of this, all CBR test results shown are the CBR value at 0.1" penetration.

The plot in Figure 5.3 shows the penetration vs load for a modified compaction energy specimen at a water content of 20% for the County clay. The CBR values, for the different energy levels and water contents were tabulated. Table 5.3 shows the results of the CBR test and the vane shear test for County clay and Table 5.4 shows the test results for Dupont clay.

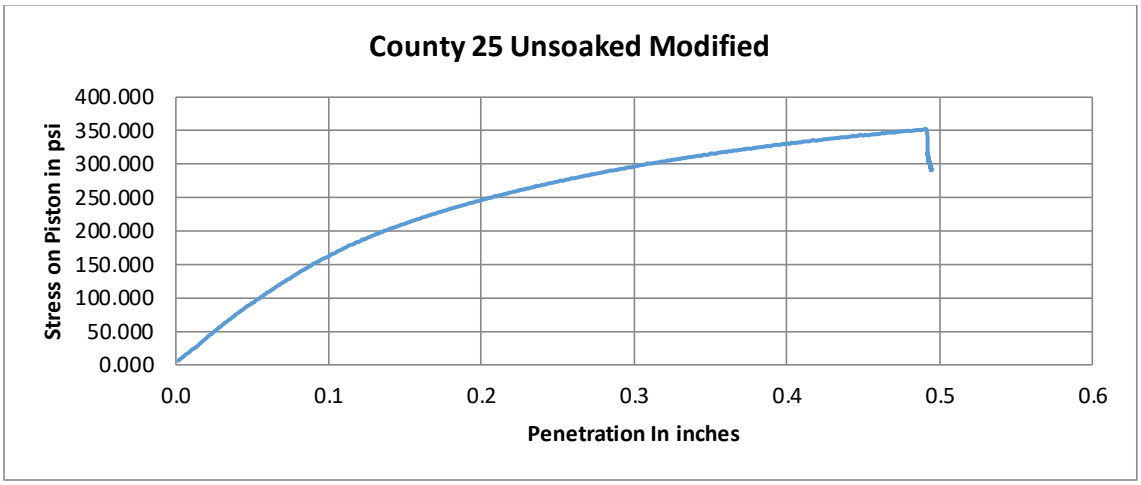

Figure 5.3. Typical Plot of the Penetration and Stress in Piston for CBR Test in Three Different Energy Levels

Table 5.3 and 5.4 shows the vane shear value performed along with the CBR values for County soil and Dupont soil, respectively. It is to be noted that the vane shear values depend on both, the energy level and the moisture content of the soil. The vane shear value increased with an increase in the density of the soil and it decreased with an increase in the water content of the soil.

Table 5.3. CBR and Vane Shear Test Results for County Clay

Compaction Energy level	Sample Name	Dry Density (pcf)	Moisture Content (%)	CBR (%)	Vane Shear (tsf)
Standard	CCS315Uso	96.9	17.0	14.6	10.6
	CCS320Uso	100.2	20.6	12.5	7.3
	CCS325Uso	100.8	22.2	3.0	6.0
	CCS326 new	94.9	26.7	2.17	
	CCS327Uso	93.8	26.1	0.4	0.9
	CCS330Uso	85.0	31.8	0.2	0.5
	CCS335Uso	83.7	34.5	0.1	0.2
Intermediate	CCI514	97.5	14.5	29.0	
	CCI515Uso	99.7	16.0	20.8	12.3
	CCI520Uso	104.4	18.9	9.5	7.0
	CCI525Uso	102.0	22.5	1.6	10.6
	CCI527Uso	96.2	26.2	0.5	3.5
	CCI535Uso	84.8	34.5	0.1	0.2
	CCM508	106.9	9.6	65.0	
Modified	CCM510Uso	108.7	11.4	38.0	23.2
	CCM515Uso	113.3	16.5	48.0	21.6
	CCM517	111.9	17.0	12.5	
	CCM525Uso	105.5	22.4	15.6	20.4
	CCM527Uso	98.1	26.5	0.7	4.2
	CCM535Uso	85.6	34.6	0.2	0.5

Table 5.4. CBR and Vane Shear Test Results for Dupont Clay

Compaction Energy level	Sample Name	Dry Density (pcf)	Moisture Content (%)	CBR (%)	Vane Shear (tsf)
Standard	DCS313Uso	89.2	14.1	12.5	13.50
	DCS318Uso	91.8	17.4	8.0	10.70
	DCS322Uso	92.3	25.8	13.5	6.10
	DCS330	87.8	31.0	3.1	
	DCS327Uso	88.6	29.6	3.2	6.37
	DCS337	81.70	36.50	0.84	
	DCS339Uso	77.9	39.9	0.2	1.54
	DCS342Uso	75.7	43.3	0.5	
Intermediate	DCI513Uso	93.9	14.1	13.5	15.00
	DCI518Uso	97.8	18.3	13.0	13.75
	DCI522Uso	95.8	25.4	13.5	13.79
	DCI532	90.7	29.0	3.6	
	DCI527Uso	90.2	29.9	1.5	5.75
	DCI537	83.20	35.40	1.12	
	DCI539Uso	78.0	39.6	0.5	2.07
	DCI542Uso	76.7	40.8	0.5	1.50
Modified	DCM508	96.9	8.6	68.0	
	DCM511	106.7	12.5	82.0	
	DCM513	103.2	13.6	27.0	
	DCM518Uso	107.2	17.5	21.0	20.25
	DCM522Uso	100.8	23.7	21.0	21.18
	DCM525	97.8	25.2	5.8	
	DCM527	96.31	27.31	7.90	
	DCM530	93.1	28.4	4.8	
	DCM527Uso	93.2	28.7	3.1	8.84
	DCM537	82.20	36.50	1.06	
	DCM539Uso	79.2	39.2	0.6	3.33
	DCM542Uso	77.5	40.5	0.4	3.58

ANALYSIS OF CBR FROM COMPACTION CURVES

The ultimate goal of this analysis was to develop a global predictive model between the dry density (γ_d) and the as-molded moisture content (w), for any specified level of compaction energy (E_c); and a model between CBR and as-molded moisture content (w) and compaction energy that would allow prediction of the in-situ CBR based on test results from the in-situ compaction (w- γ_d) process.

This was accomplished in the following manner: For a given clay type, the individual plots of the actual compaction tests were initially developed. These plots were then used to develop a smooth compaction curve for each specific compaction energy. These "smoothed" curves allowed for the establishment of a new database of compaction results, generally defined at moisture intervals of 2% for each level of compactive energy and clay type

This database was subsequently used for the statistical regression analysis to determine the best fit model for a given compaction energy. It was found that the best fitting model for this compaction analysis was a third order polynomial. Further statistical studies of the polynomial constants (c_1, c_2, c_3 and c_4) were highly correlated to the level of compaction energy used in the compaction study. Relationships were then determined to build models relating each constant (c_i) to the compaction energy (E_c).

Once this was established, it was then possible to develop a single predictive model of dry density that was a function of the moisture content and compaction energy. This global model was ultimately compared to the actual compaction test results to evaluate whether any bias existed in the model needing further calibration. Estimates of the S_e (standard error of estimate) and the S_e/S_y value of the final model were obtained to evaluate the accuracy of the model developed.

Specific details of this process, for each clay type investigated, are presented in the following sections of this report.

Dupont Clay

Figure 5.4 illustrates the actual compaction data for the Dupont clay. As shown, the data points are indicated by each specific compaction energy used (standard: 12,486 ft-lb/cf; intermediate: 20,811 ft-lb/cf and modified: 56,757 ft-lb/cf). From these data points, smooth curves were manually developed and a new database, using the smooth curve compaction data, was then developed.

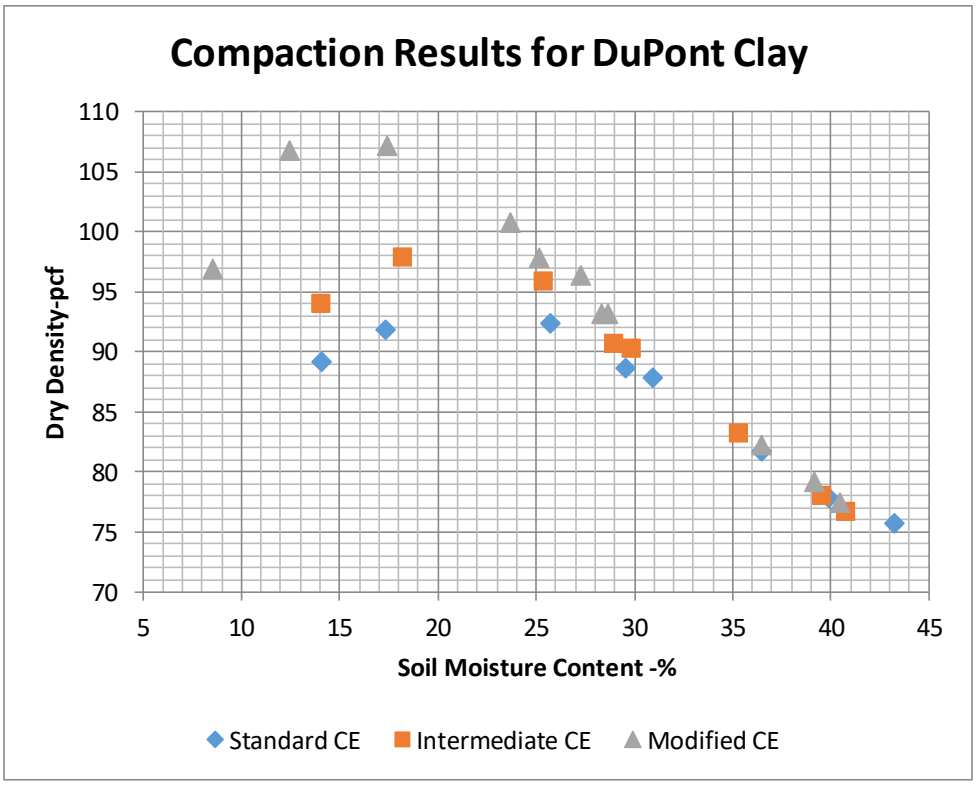

Figure 5.4. Actual Compaction Data for Dupont Clay

This data was then regressed to establish models for each individual compaction energy. This was accomplished through the statistical programs in Excel®. The analysis showed that the most accurate model form to predict dry density from the as-molded moisture content was a third order polynomial of the form:

$$\gamma_d = f_i w^3 + g_i w^2 + j_i w + k_i$$

The results of the individual Compaction Energy (E_c) regression models are shown in Figure 5.5. Further analysis of the regression constants (f_i, g_i, j_i and k_i) indicated that each of them were highly related to the compaction energy (E_c) used to establish each polynomial. Thus, each constant was related by the form:

$$(f_i, g_i, j_i, k) = c_1 E_c + c_2$$

Table 5.5 is a final summary of the statistical analysis. The individual values of each constant (f, g, j and k), by compaction energy, are shown in the upper portion of the table. In addition, for each polynomial constant, the relationship (denoted by the c_i constants) to the compaction energy (E_c) is also shown. Finally, the bottom portion of the table shows the comparison of the predicted constants using the slope-intercept parameters developed.

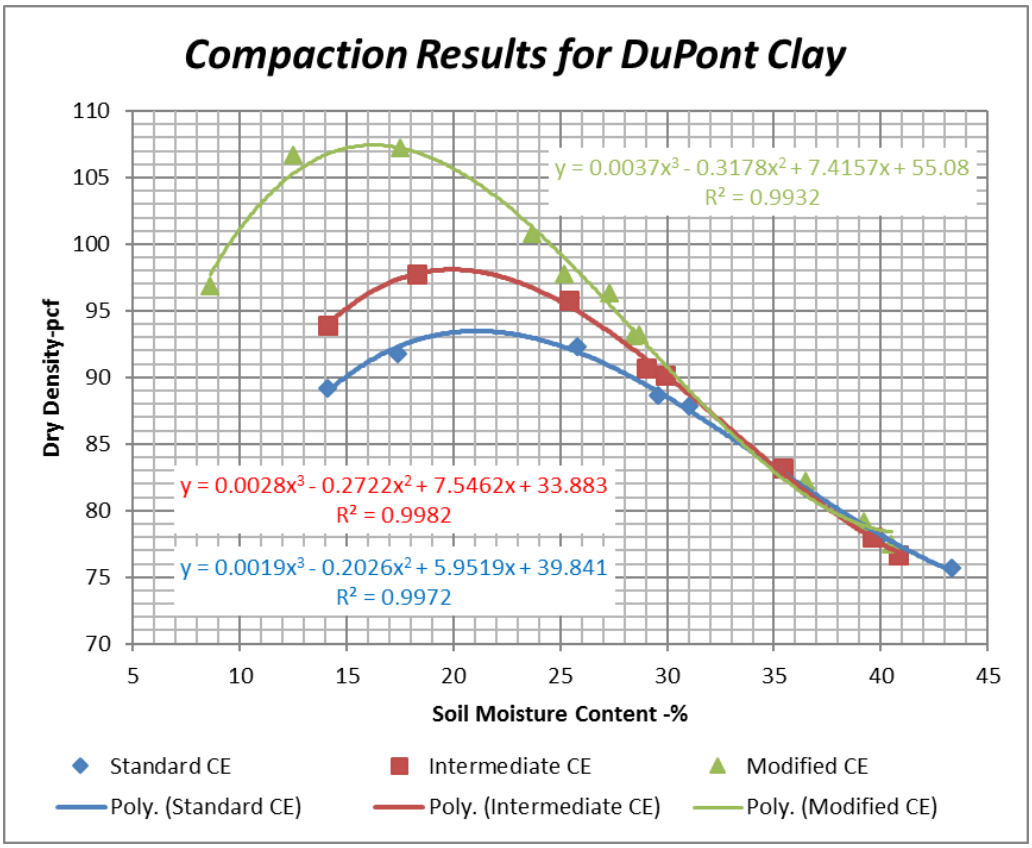

Figure 5.5. Results of the Individual CE Regression Models for The Dupont Clay

Table 5.5. Summary of the Predicted Constants for Dupont Clay

	$\Upsilon_d=f_i*(w^3)+g_i*(w^2)+j_i*(w)+k_i$			
E_c (ft-lb/cf)	f	g	j	k
12,486	0.0019	-0.2026	5.9519	39.8410
20,811	0.0028	-0.2722	7.5462	33.8830
56,757	0.0037	-0.3178	7.4157	55.0800
Individual Reg. Constants	$C_i=c_1*E_c+c_2$			
	f	g	j	k
Constant 1	3.60E-08	-2.20E-06	2.21E-05	4.18E-04
Constant 2	1.72E-03	-1.98E-01	6.31E+00	3.04E+01
	Global Regression Predicted Coefficients			
	f	g	j	k
12,486	0.0022	-0.2256	6.5839	35.6133
20,811	0.0025	-0.2439	6.7678	39.0898
56,757	0.0038	-0.3231	7.5621	54.1009

Based upon this analysis, the final combined model, developed to predict the dry density of the Dupont clay, as a function of the as-molded moisture content and the compaction energy, is defined by:

$$\gamma_d = (f_1 E_c + f_2)w^3 + (g_1 E_c + g_2)w^2$$

$$+(j_1 E_c + j_2)w + (k_1 E_c + k_2)$$

Or an alternate form of the equation is:

$$\gamma_d = (f_1 w^3 + g_1 w^2 + j_1 w + k_1)E_c + (f_2 w^3 + g_2 w^2 + j_2 w + k_2)$$

Where, γ_d is the dry density (pcf); w is moisture content (%), and E_c is compaction energy (ft-lb/cf).

Table 5.6 is the final summary of all regression constants used in the Dupont clay model for the dry density.

Table 5.6. Regression Constants for Dry Density Relationship for Dupont Clay

Constant No	f	g	j	k
1	3.60E-08	-2.20E-06	2.21E-05	4.18E-04
2	1.72E-03	-1.98E-01	6.31E+00	3.04E+01

Table 5.7 is a summary comparing the individual E_c dry density values from the individual sets of the enhanced visual data set (at $\Delta w = 2\%$) to those predicted from each separate E_c regression equation. Figure 5.6 shows the plot of this tabular summary. It is obvious that the individual regression models precisely simulate this enhanced data set. The solid red line in the figure represents the 45 degree line.

Table 5.8 is the final overall comparison of the combined predictive equation for the global data to the dry density that was actually determined in the laboratory. This data illustrates this comparison for each compaction energy used in the lab study. The comparative results of the full regression model predicted dry density to the actual lab results are shown in Figure 5.7. . The solid red line in the figure represents the 45 degree line. As noted, the $S_e/S_y = 0.195$, is indicative of an excellent predictive equation for the Dupont Clay dry density.

Table 5.7. Comparison of Individual Regression Models to Set of Enhanced Data (Dupont Clay)

Individual CE Regression Equations						
Moisture Content (%)	Dry Density (pcf)					
	Actual	Predicted	Actual	Predicted	Actual	Predicted
	Standard		Intermediate		Modified	
15	90.0	89.9	95.0	95.3	108.2	107.3
17	91.8	91.8	97.0	97.3	107.2	107.5
19	92.8	92.8	98.6	98.2	105.6	106.6
21	93.0	93.1	99.0	98.2	103.0	104.9
23	93.2	92.7	98.0	97.5	100.5	102.5
25	92.8	91.7	96.3	96.2	98.0	99.7
27	91.6	90.2	94.0	94.3	95.0	96.5
29	89.7	88.4	91.1	92.1	92.2	93.1
31	87.8	86.3	88.8	89.6	89.8	89.8
33	86.0	83.9	86.2	87.1	87.0	86.7
35	83.8	81.4	83.8	84.6	84.3	84.0
37	81.2	78.9	81.3	82.3	82.0	81.8
39	78.8	76.5	79.0	80.3	79.2	80.4
41	76.5	74.2	76.3	78.7	77.0	79.9

Table 5.8. Summary of Combined Prediction Model to Actual Lab Compaction Test Results

Moisture Content (%)	Pred.	Actual	Pred.	Actual	Pred.	Actual
	Standard		Intermediate		Modified	
14.10	89.7	89.20				
17.40	93.3	91.80				
25.80	92.6	92.30				
31.00	87.6	87.80				
29.60	89.1	88.60				
36.50	80.9	81.70				
39.90	77.0	77.90				
43.30	73.9	75.70				
14.10			92.9	93.90		
18.30			96.4	97.80		
25.40			94.1	95.80		
29.00			90.4	90.70		
29.90			89.4	90.20		
35.40			82.5	83.20		
39.60			77.9	78.00		
40.80			76.9	76.70		
8.60					97.6	96.90
12.50					105.5	106.70
17.50					107.6	107.20
23.70					101.9	100.80
25.20					99.7	97.80
28.40					94.4	93.10
27.31					96.3	96.31
28.70					93.9	93.20
36.50					82.6	82.20
39.20					80.6	79.20
40.50					80.3	77.50

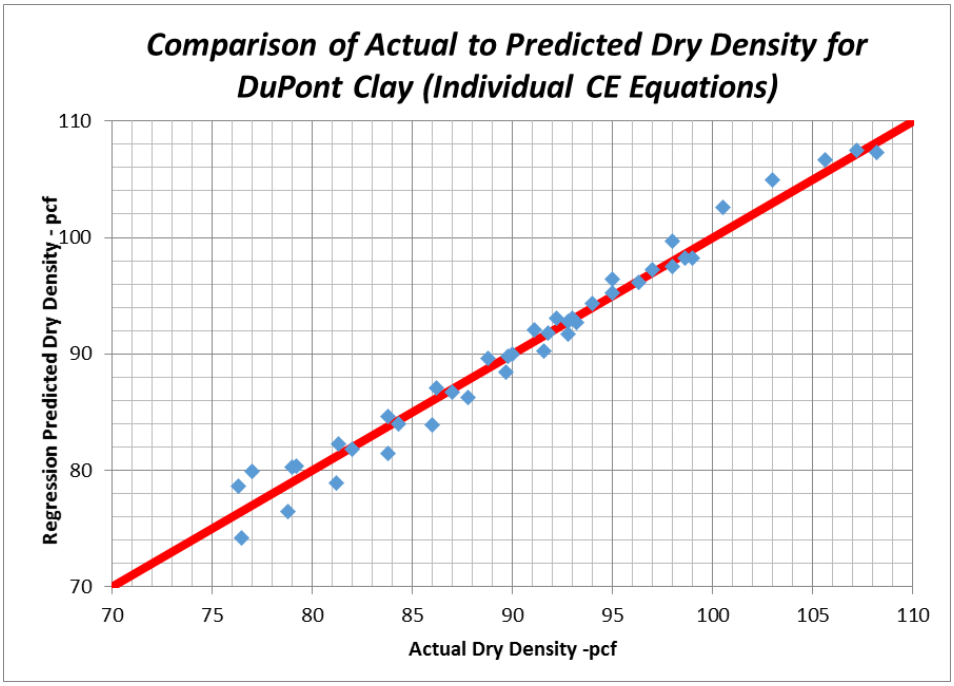

Figure 5.6. Comparison of Actual Enhanced Dry Density to Individual E_c Regression Predicted Models (Dupont Clay)

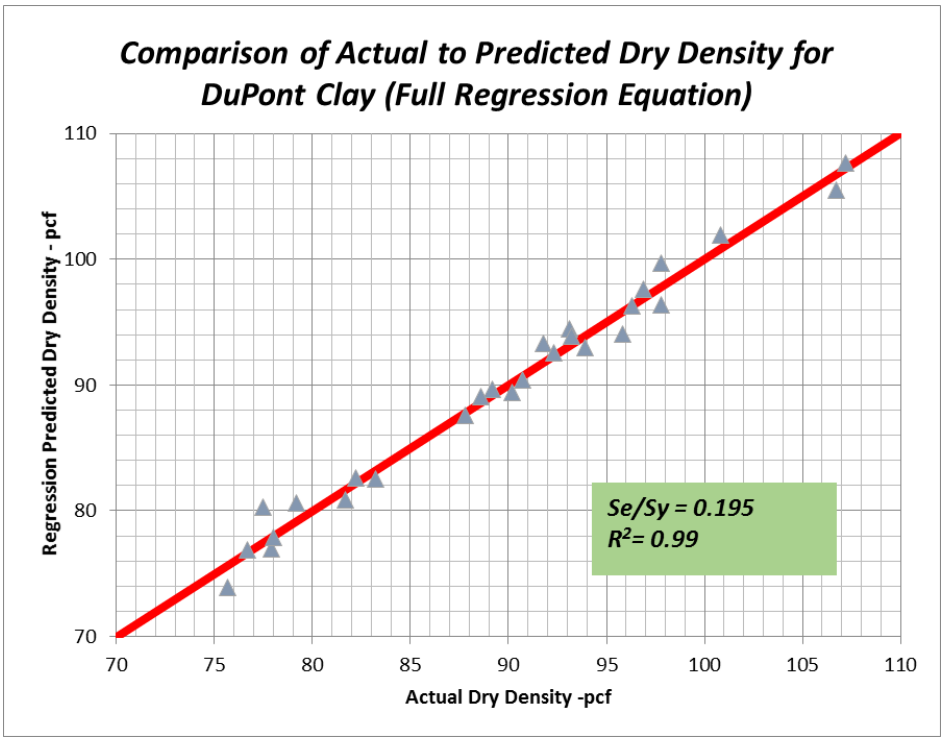

Figure 5.7. Comparison of Actual Lab Results to Full Regression Predicted Model (Dupont Clay)

County Clay

The analysis of the County Clay compaction data was conducted in a similar statistical manner as the Dupont clay analysis previously discussed. Figure 5.8 illustrates the actual compaction data for the County clay, while a new enhanced database was established from visually developed "smooth" compaction curves developed from the data shown in Figure 5.8. This data was then regressed to establish models for each individual compaction energy with the Excel statistical programs. Again, a third order polynomial of the form:

$$\gamma_d = f_i w^3 + g_i w^2 + j_i w + k_i$$

was found to be the most accurate predictive model to be used for the County Clay.

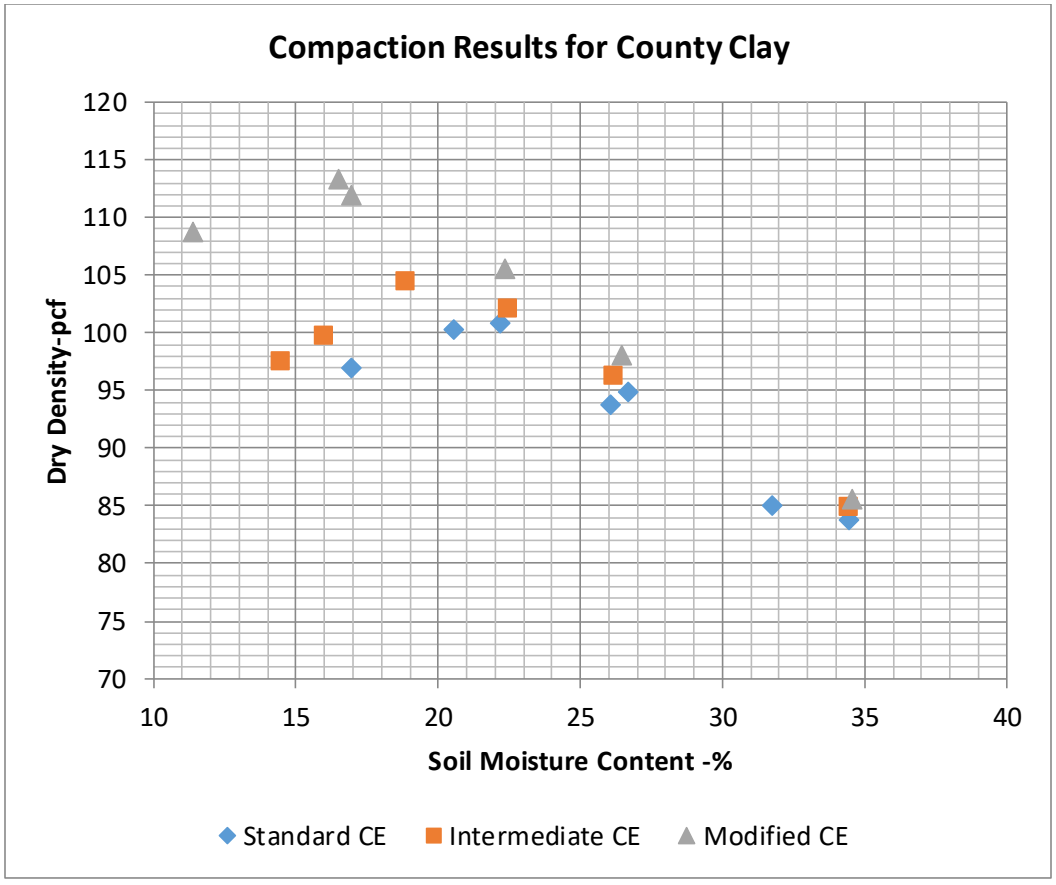

Figure 5.8. Actual Compaction Data for the County Clay

The results of the individual E_c regression models are shown in Figure 5.9. Like the Dupont clay, each constant in the compaction energy (E_c) relationship was then found to be related to a second order polynomial of the form.

$$(f_i, g_i, j_i, k) = c_1 E_c + c_2$$

Table 5.9 is the final summary of the statistical analysis for the County clay. Again, the individual values of each constant (f, g, j, and k), by compaction energy, are shown in the upper portion of the table. The central portion of the table indicates the regressed coefficient of the linear equation, for each dry density predictive equation. Finally, the lower portion of the table shows the comparison of the predicted constants using the second order polynomial expressions developed.

Thus, for the County clay analysis, the final combined model developed to predict the dry density of the County clay as a function of the as-molded moisture content and the compaction energy, is identical to the combined model found for the Dupont clay. This equation is:

$$\gamma_d = (f_1 E_c + f_2)w^3 + (g_1 E_c + g_2)w^2 + (j_1 E_c + j_2)w + (k_1 E_c + k_2)$$

Or an alternate form of the equation is:

$$\gamma_d = (f_1 w^3 + g_1 w^2 + j_1 w + k_1)E_c + (f_2 w^3 + g_2 w^2 + j_2 w + k_2)$$

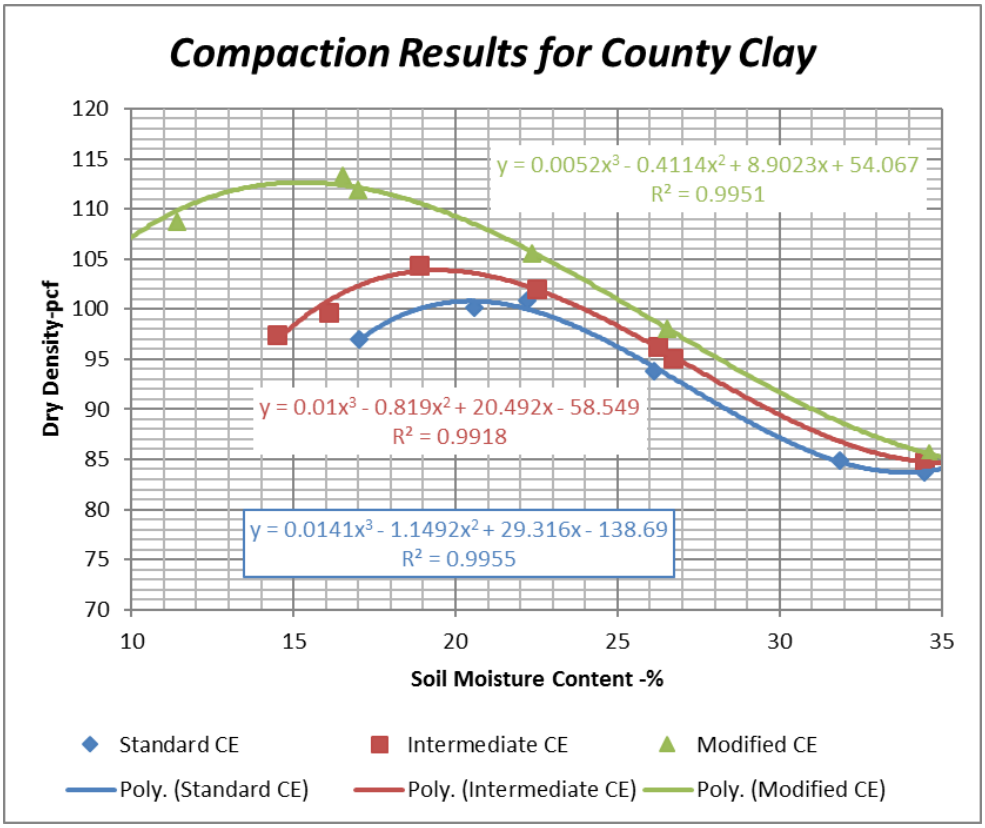

Figure 5.9. 5.1 **Results of the Individual CE Regression Models for the County Clay**

Table 5.9. Final Summary of the Predicted Constants for County Clay

	$\Upsilon_d=f_i*(\omega^3)+g_i*(\omega^2)+j_i*(\omega)+k_i$			
E_c	f	g	j	k
12,486	0.0141	-1.1492	29.3160	-138.6900
20,811	0.0100	-0.8190	20.4920	-58.5490
56,757	0.0052	-0.4114	8.9023	54.0670
Individual Reg. Constants	$C_i=c_1*E_c+c_2$			
Constant 1	-1.809E-07	1.507E-05	-4.196E-04	3.989E-03
Constant 2	1.520E-02	-1.246E+00	3.217E+01	-1.675E+02
	Global Regression Predicted Coefficients			
12,486	0.0129	-1.0575	26.9274	-117.6590
20,811	0.0114	-0.9320	23.4338	-84.4507
56,757	0.0049	-0.3902	8.3491	58.9377

Table 5.10 is the final set of regression constants to be used for the combined dry density regression model for County clay.

Table 5.10. Regression Constants for Dry Density and Moisture Content Relationship for County Clay

Constant No	f	g	j	k
1	-1.809E-07	1.507E-05	-4.196E-04	3.989E-03
2	1.520E-02	-1.246E+00	3.217E+01	-1.675E+02

Table 5.11 presents a comparison between the individual E_c regression models to the enhanced lab test data results, for all three levels of compaction energy measured in the study. Figure 5.10 illustrates the excellent correlation for these two dry density values.

Table 5.11. Comparison of Individual Regression Models to Set of Enhanced Data (County Clay)

Individual CE Regression Equations						
Moisture Content (%)	Dry Density (pcf)					
	Actual	Predicted	Actual	Predicted	Actual	Predicted
	Standard		Intermediate		Modified	
14	90.0	85.2	96.0	95.3	113.0	112.3
16	94.2	93.9	100.8	100.6	113.3	112.5
18	98.6	98.9	103.8	103.3	111.4	111.3
20	100.4	100.8	104.8	103.7	108.8	109.2
22	100.3	100.2	103.0	102.4	105.8	106.2
24	98.0	97.9	100.0	99.8	102.0	102.6
26	94.8	94.5	96.7	96.4	98.4	98.8
28	91.8	90.7	93.3	92.7	95.0	94.9
30	89.0	87.2	90.6	89.1	92.0	91.3
32	86.2	84.7	87.6	86.2	88.8	88.1
34	83.6	83.8	84.8	84.5	85.7	85.5
36	80.8	85.2	82.0	84.3	83.0	84.0

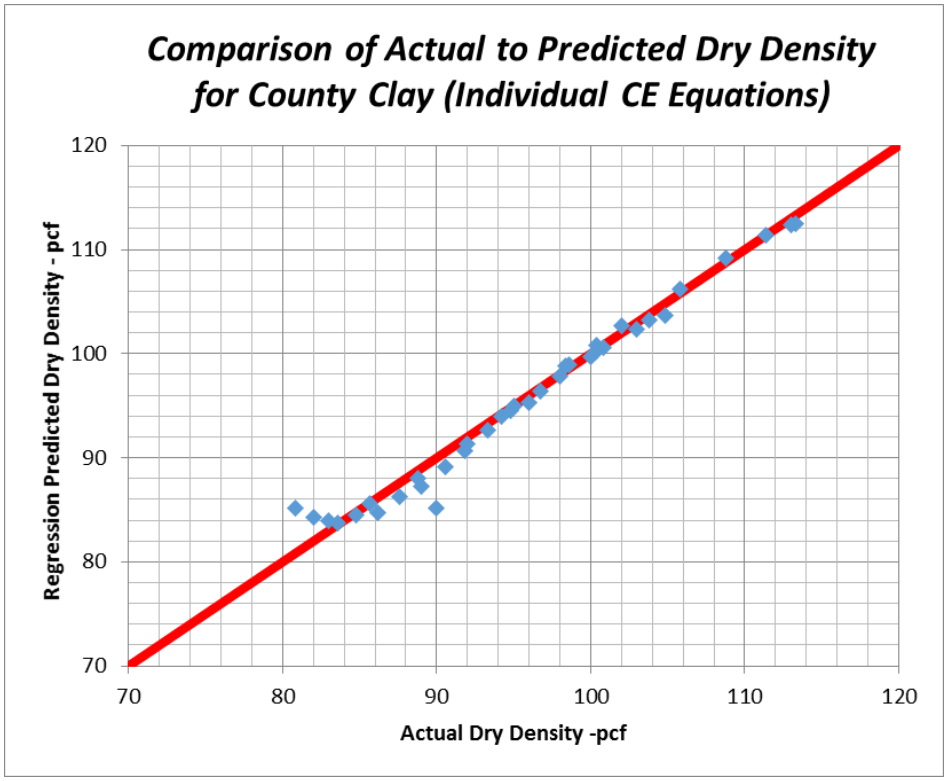

Figure 5.10. Comparison of Actual Enhanced Dry Density to Individual E_c Regression Predicted Model (County Clay)

Table 5.12 is the final comparison of the combined regression equation for the global data to the dry density that was actually determined in the laboratory compaction study. Figure 5.11 illustrates the final comparison of these results. An analysis of the data presented in Table 5.12 and Figure 5.11 resulted in the final model having a S_e/S_y = 0.308. These statistics clearly show that the final global model is an excellent predictive equation for estimating the dry density of the County clay. The model can be used to predict dry density for moisture content of positive compaction energy and for a maximum degree of saturation of 100%.

Table 5.12. Summary of Comparison of Combined Prediction Models to Actual Lab Compaction Tests (County Clay)

Full Regression Predictions						
Moisture Content (%)	Pred.	Actual	Pred.	Actual	Pred.	Actual
	Standard		Intermediate		Modified	
17.0	98.1	96.9				
20.6	101.4	100.2				
22.2	100.5	100.8				
26.1	93.7	94.9				
31.8	94.8	93.8				
34.5	85.3	85				
14.5	83.9	83.7				
16.1			94.2	97.5		
18.9			98.7	99.7		
22.5			102.7	104.4		
26.7			101.2	102		
26.2			95.4	96.2		
34.5			84.2	84.8		
9.6					107.5	106.9
11.4					110.7	108.7
16.5					112.6	113.3
17.0					112.3	111.9
22.4					105.6	105.5
26.5					97.9	98.1
34.6					85.0	85.6

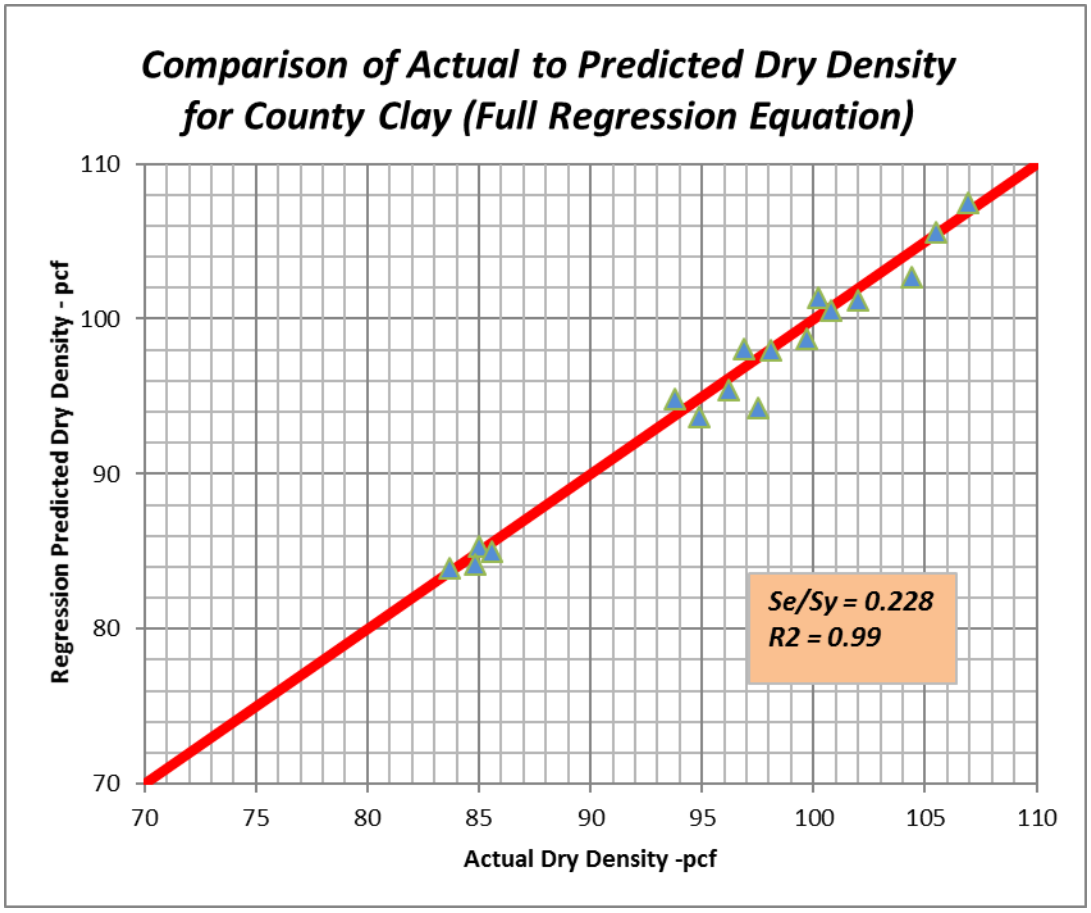

Figure 5.11. Comparison of Actual Lab Test Results to Full Regression Predicted Model (County Clay)

CBR Analysis

General Approach

The approach used to establish the global regression models to predict the CBR of both clay types studied, as a function of the moisture content (ω) and compaction energy (CE), closely followed the mathematical methodology used to establish the soil compaction (dry density) models. This process relied upon the development of a larger database of test results, generated from smooth curves visually established from the actual test results. This expanded database was then used to develop a stepwise regression procedure that was used to establish the final model for each clay soil.

Dupont Clay

Figure 5.12 presents the actual results of the CBR moisture relationship, by compaction energy, for the Dupont clay. All the data obtained from the CBR tests showed that the relationship between CBR and water content can be achieved through the following sigmoidal equation.

$$Log\ CBR = (q) + \frac{(p-q)}{\left[1 + EXP\ (\frac{w-r}{s}\right]}$$

Hence, a Solver analysis using the coefficients p, q, r and s was performed to obtain a smooth curve, which would best fit all the test results for that particular energy. Table 5.13 shows the actual and the predicted data obtained for each compaction energy through the sigmoidal curve. The final models developed were eventually built upon the log transformed variable of the CBR (log CBR). Thus, this final transformed dependent variable used in the ensuing statistical analysis is also shown in Table 5.13. This was accomplished to eventually develop a more accurate and simplified model for the final analysis within the real in-situ ranges of water content values occurring at NAPTF.

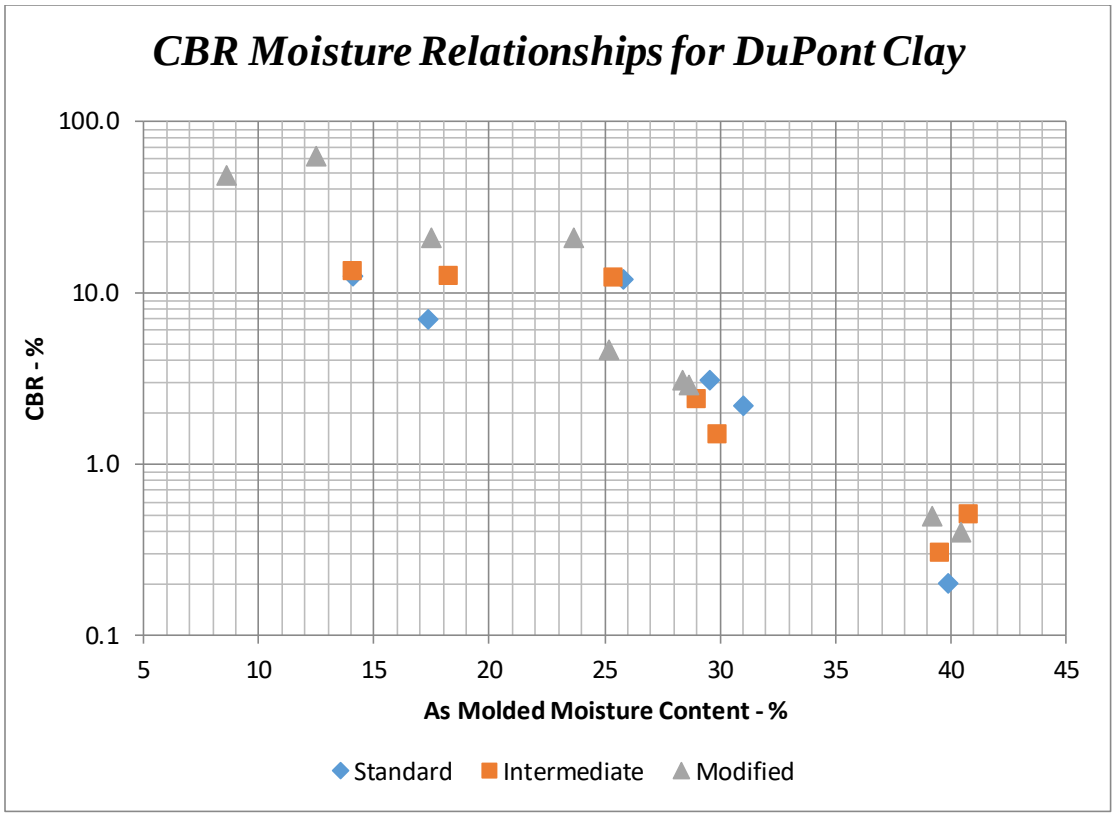

Figure 5.12. Actual Laboratory CBR Test Results for Dupont Clay

Table 5.13. Summary of CBR Data versus Moisture Content for Actual and Predicted using Individual Regression Models and Final Regression Predicted CBR Values for Dupont Clay

CBR Predicted from Individual Regression Models						
Moisture Content (%)	Pred.	Actual	Pred.	Actual	Pred.	Actual
	Standard		Intermediate		Modified	
14.10	11.33	12.50				
17.40	10.93	8.00				
25.80	7.21	13.50				
31.00	2.90	3.10				
27.03	6.21	5.90				
29.60	3.99	3.20				
36.50	0.57	0.84				
39.90	0.24	0.20				
43.30	0.13	0.05				
14.10			17.42	13.50		
18.30			14.45	13.00		
25.40			7.54	13.50		
29.00			4.34	3.60		
28.07			5.08	10.20		
29.90			3.69	1.50		
35.40			1.19	1.12		
39.60			0.50	0.50		
40.80			0.40	0.50		
8.60					65.98	68.00
12.50					56.49	82.00
13.60					53.20	27.00
17.50					39.71	21.00
23.70					17.59	21.00
25.20					13.37	5.80
27.31					8.64	7.90
28.70					6.31	3.10
28.40					6.76	4.80
36.50					0.94	1.06
39.20					0.53	0.60
40.50					0.41	0.40

CBR Predicted from Final Regression Model						
Moisture	Pred.	Actual	Pred.	Actual	Pred.	Actual
Content (%)	Standard		Intermediate		Modified	
14.10	12.26	12.50				
17.40	11.45	8.00				
25.80	6.66	13.50				
31.00	2.77	3.10				
27.03	5.67	5.90				
29.60	3.70	3.20				
36.50	0.71	0.84				
39.90	0.32	0.20				
43.30	0.18	0.05				
14.10			16.62	13.50		
18.30			14.53	13.00		
25.40			8.09	13.50		
29.00			4.49	3.60		
28.07			5.35	10.20		
29.90			3.74	1.50		
35.40			1.00	1.12		
39.60			0.37	0.50		
40.80			0.29	0.50		
8.60			66.41		65.98	68.00
12.50			56.39		56.49	82.00
13.60					52.97	27.00
17.50					39.23	21.00
23.70					17.35	21.00
25.20					13.24	5.80
27.31					6.80	7.90
28.70					8.63	3.10
28.40					6.35	4.80
36.50					0.99	1.06
39.20					0.56	0.60
40.50					0.44	0.40

Figure 5.13 is the plot of the enhanced data set used for each E_c compaction energy level. The linear nature of the model for the log transformed CBR value is obvious.

The results of the individual constants (p_i, q_i, r_i, and s_i) were also found to be a function of each separate compaction energy (E_c). Each constant was then analyzed as a function of E_c and was found to be a linear relationship.

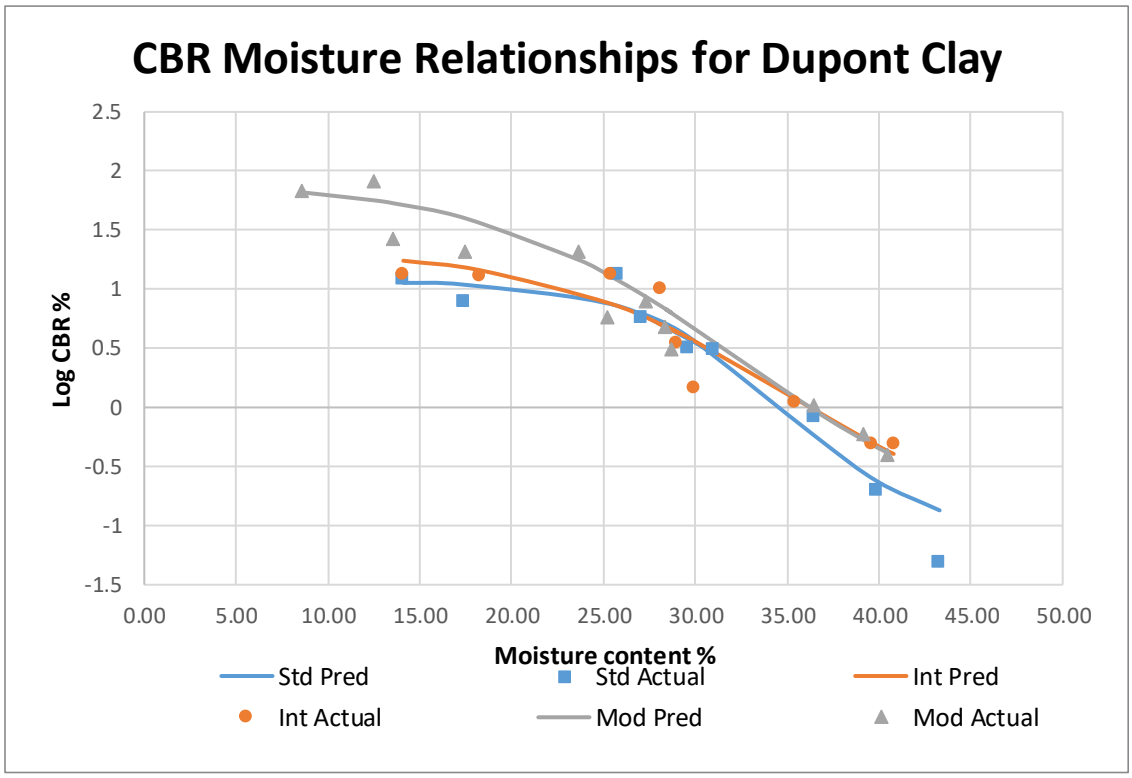

Figure 5.13. Results of Individual E_c Regression Models for CBR (Dupont Clay)

Table 5.14 is the final summary of the model regression constants found in the analysis for the Dupont clay. The upper portion of the table summarizes the individual constants for each compaction energy variable. The middle portion of the table illustrates the computed slope-intercept constants for each of the (p_i,q_i,r_i and s_i) constants obtained. Finally, the lower portion of the table presents the predicted values of the regression constants shown in the upper portion of the table.

Table 5.14. Final Summary of the Predicted Constants for Dupont Clay

CE	p	q	r	s
Individual Regression Coefficients				
12,486	1.0670	-1.1100	34.8529	4.0378
20,811	1.3390	-1.1091	34.9906	6.5734
56,757	1.9140	-1.1053	32.4271	6.9435
	$Ci=c_1*E_c+c_3$			
Constant 1	1.820E-05	1.062E-07	-5.973E-05	4.909E-05
Constant 2	8.938E-01	-1.111E+00	3.588E+01	4.378E+00
Global Regression Predicted Coefficients				
12,486	1.1210	-1.1100	35.1374	4.9909
20,811	1.2725	-1.1091	34.6402	5.3996
56,757	1.9265	-1.1053	32.4930	7.1643

Table 5.15 is the final summary of the CBR Model constants used in the global model for the Dupont clay.

Table 5.15. Regression Constants for CBR Relationship (Dupont Clay)

	p	q	r	s
Constant 1	1.820E-05	1.062E-07	-5.973E-05	4.909E-05
Constant 2	8.938E-01	-1.111E+00	3.588E+01	4.378E+00

The overall predictive model for the Dupont clay CBR results is given by:

$$Log\ CBR = (q_1 E_c + q_2) + \frac{((p_1 \times (E_c) + p_2) - (q_1 E_c + q_2))}{\left[1 + EXP\ (\frac{w - (r_1 \times (E_c) + r_2)}{(s_1 \times (E_c) + s_2)}\right]}$$

The coefficients shown in Table 5.15 along with the equation presented was used to predict the individual CBR results, shown in the lower portion of Table 5.13, for a specific w% and E_c level of the enhanced data set.

The comparison of the enhanced data to those predicted by the individual E_c regression models, for the Dupont clay, is shown in Figure 5.14. It is readily apparent that the individual prediction models yield an excellent prediction capability.

The final analysis portion dealt with a direct comparison of the global model to the actual CBR tests that were obtained in the laboratory. The results of this study are shown in Figure 5.15. The S_e/S_y value found in this study was 0.305, which yielded a R^2 value of 0.95.

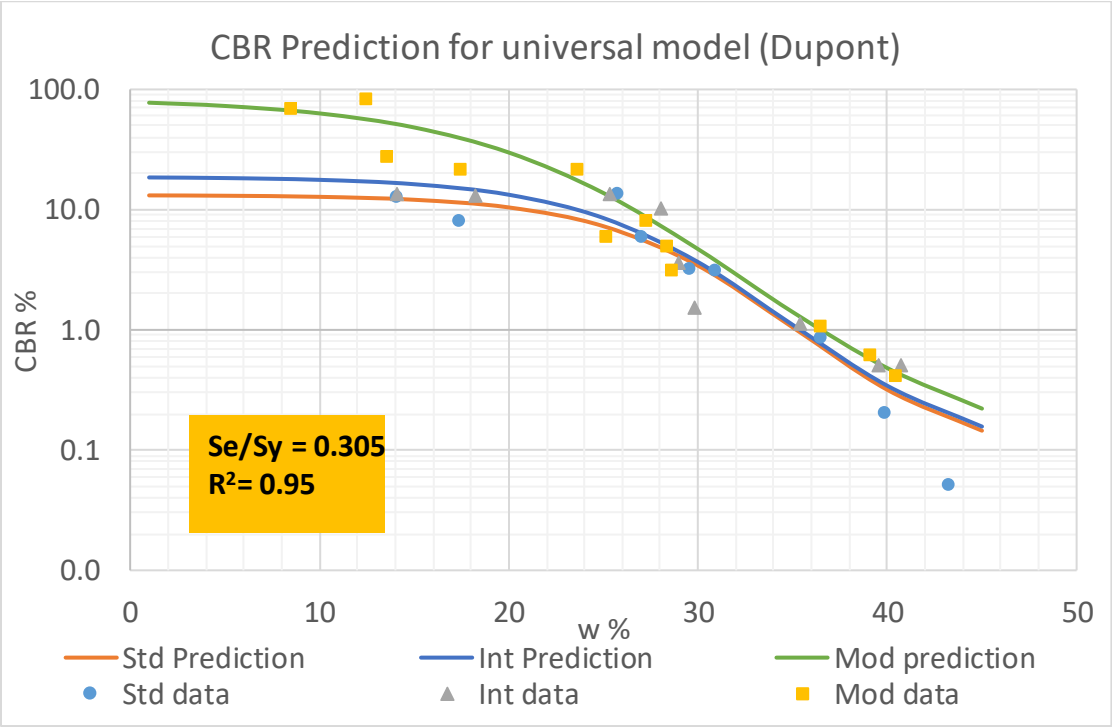

Figure 5.14. Comparison of Actual Enhanced CBR Test Results to Individual E_c Regression Predicted Models (Dupont Clay)

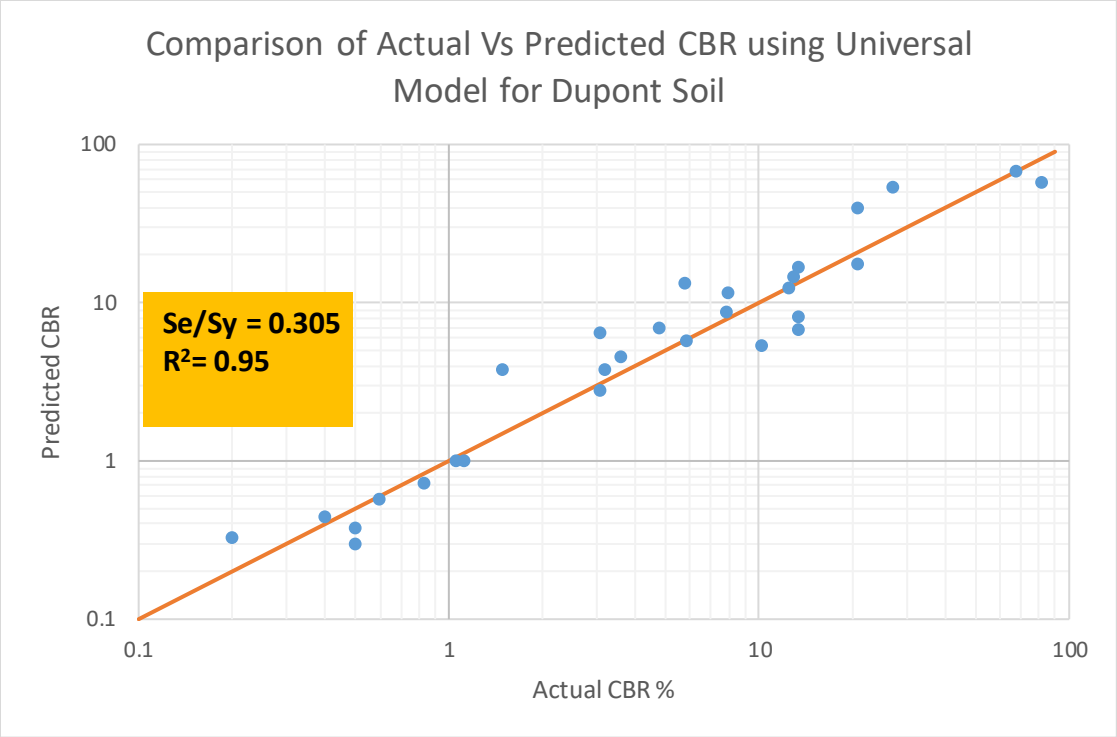

Figure 5.15. Comparison of Actual CBR Test Results to Final Regression Models (Dupont Clay)

County Clay

The analysis of the County Clay CBR analysis was identical to that already presented for the Dupont Clay. Figure 5.16 presents the actual CBR test results for the County clay. All the data obtained from the CBR tests showed that the relationship between CBR and water content can be achieved through a sigmoidal curve equation. Hence, a sigmoidal equation was used with coefficients p, q, r and s. A Solver analysis was performed based upon the test results to obtain a smooth curve, which would best fit all the test results for a particular energy. Table 5.16 shows the actual and predicted CBR results. The initial model form determined to be the most accurate for the data was identical to the form found for the Dupont clay. The model coefficients are shown in Table 5.17. Like the Dupont clay analysis, the table also shows the values for each regression constant (p_i, q_i, r_i and s_i) as a

function of the Compaction Energy (E_c) variable. Figure 5.17 shows the individual plots and models for the County clay CBR, for each Compaction Energy (E_c), determined from the visually enhanced database set developed from the test points.

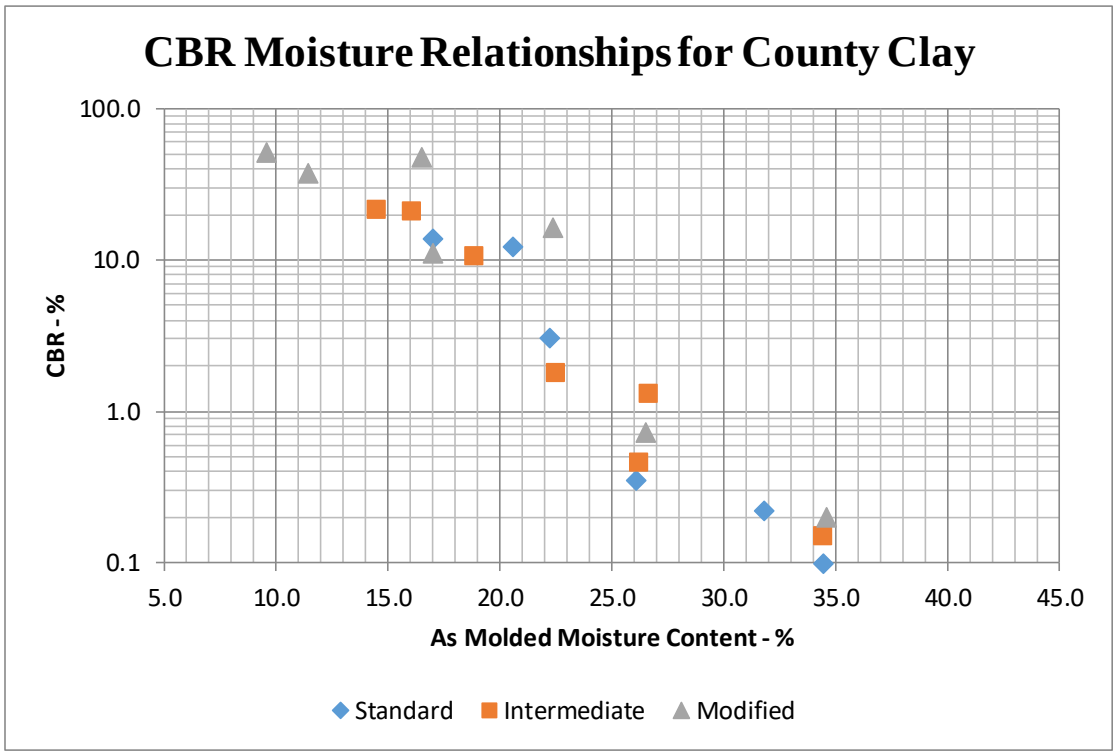

Figure 5.16. Actual Laboratory CBR Test Results for County Clay

Table 5.16. Summary of Enhanced CBR Data versus Moisture Content and Final Regression Predicted CBR Value for County Clay

CBR Predicted with Individual Regression Models						
Moisture Content (%)	Pred.	Actual	Pred.	Actual	Pred.	Actual
	Standard		Intermediate		Modified	
17.00	17.35	14.60				
20.60	7.29	12.50				
22.20	3.77	3.00				
26.70	0.41	2.17				
26.10	0.54	0.40				
31.80	0.11	0.20				
34.50	0.09	0.10				
14.50			21.95	29.00		
16.08			17.28	20.80		
18.88			9.28	9.50		
22.50			2.82	1.60		
26.70			0.59	1.30		
26.24			0.70	0.50		
34.46			0.11	0.10		
9.60					54.37	65.00
11.40					49.82	38.00
16.50					29.00	48.00
17.00					26.55	12.50
22.40					6.01	15.60
26.50					1.31	0.70
34.60					0.20	0.20
CBR Predicted with Final Regression Model						
Moisture	Pred.	Actual	Pred.	Actual	Pred.	Actual
Content (%)	Standard		Intermediate		Modified	
17.00	11.86	14.60				
20.60	4.45	12.50				
22.20	2.49	3.00				
26.70	0.46	2.17				
26.10	0.56	0.40				
31.80	0.14	0.20				
34.50	0.09	0.10				
14.50			20.56	29.00		
16.08			16.60	20.80		
18.88			8.85	9.50		

22.50			2.67	1.60		
26.70			0.65	1.30		
26.24			0.12	0.50		
34.46			0.11	0.10		
9.60					55.42	65.00
11.40					50.68	38.00
16.50					29.30	48.00
17.00					26.81	12.50
22.40					6.07	15.60
26.50					1.32	0.70
34.60					0.20	0.20

Table 5.17. Summary of the Predicted Constants for County Clay

CE	p	q	r	s
Individual Regression Coefficients				
12,486	1.4252	-1.1038	23.4617	3.6491
20,811	1.5955	-1.1280	23.8152	4.0963
56,757	1.8075	-0.9136	24.4549	4.1235
	$Ci=c_1*E_c+c_2$			
Constant 1	7.818E-06	4.794E-06	2.105E-05	7.739E-06
Constant 2	1.375E+00	-1.192E+00	2.328E+01	3.724E+00
Global Regression Predicted Coefficients				
12,486	1.4723	-1.1325	23.5416	3.8206
20,811	1.5374	-1.0926	23.7168	3.8850
56,757	1.8184	-0.9203	24.4734	4.1632

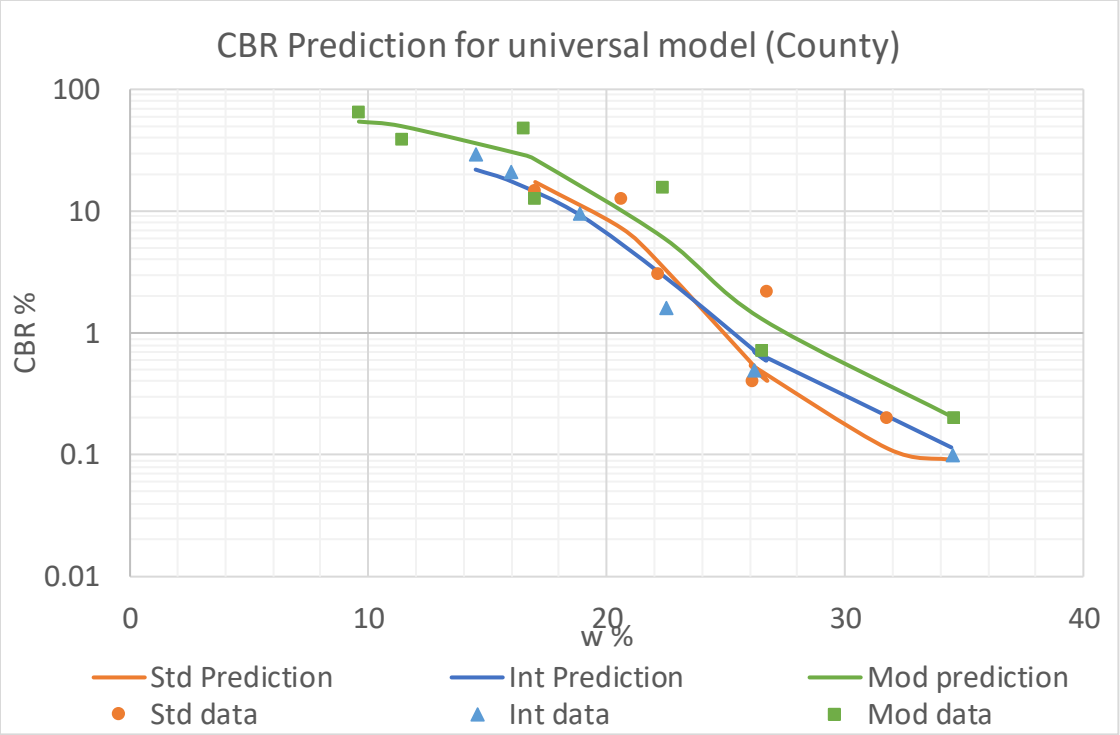

Figure 5.17. CBR Results of Individual E_c Regression Models (County Clay)

Based upon the analysis conducted, the global CBR model, for the County Clay, was found to be:

$$Log\ CBR = (q_1 E_c + q_2) + \frac{((p_1 \times (E_c) + p_2) - (q_1 E_c + q_2))}{\left[1 + EXP\ (\frac{w - (r_1 \times (E_c) + r_2)}{(s_1 \times (E_c) + s_2)}\right]}$$

The coefficients shown in Table 5.18 along with the equation presented were used to predict the individual CBR results, shown in the lower portion of Table 5.16, for a specific w% and E_c level of the enhanced data set.

Table 5.18 is the final summary of the CBR model constants used in the global model for the County clay.

Table 5.18. Regression Constants for CBR Relationship (County Clay)

	p	q	r	s
Constant 1	7.818E-06	4.794E-06	2.105E-05	7.739E-06
Constant 2	1.375E+00	-1.192E+00	2.328E+01	3.724E+00

The comparison of the enhanced data to that predicted by the individual E_c regression models, for the Dupont clay, is shown in Figure 5.18. It is readily apparent that the individual prediction models yield an excellent estimation of the CBR results.

The final analysis portion dealt with a direct comparison of the global model to the actual CBR tests that were obtained in the laboratory. The results of this study are shown in the Figure 5.19. the S_e/S_y value found in this study was found to 0.275 which was a better fit which yielded a R^2 value of 0.96.

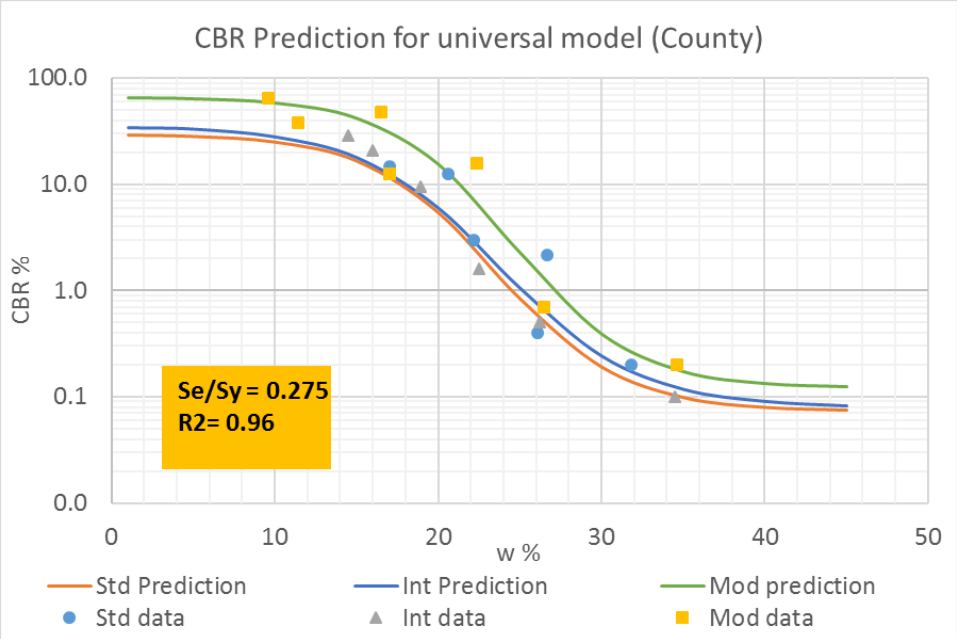

Figure 5.18. Comparison of Actual Enhanced CBR Test Results to Individual E_c Regression Models (County Clay)

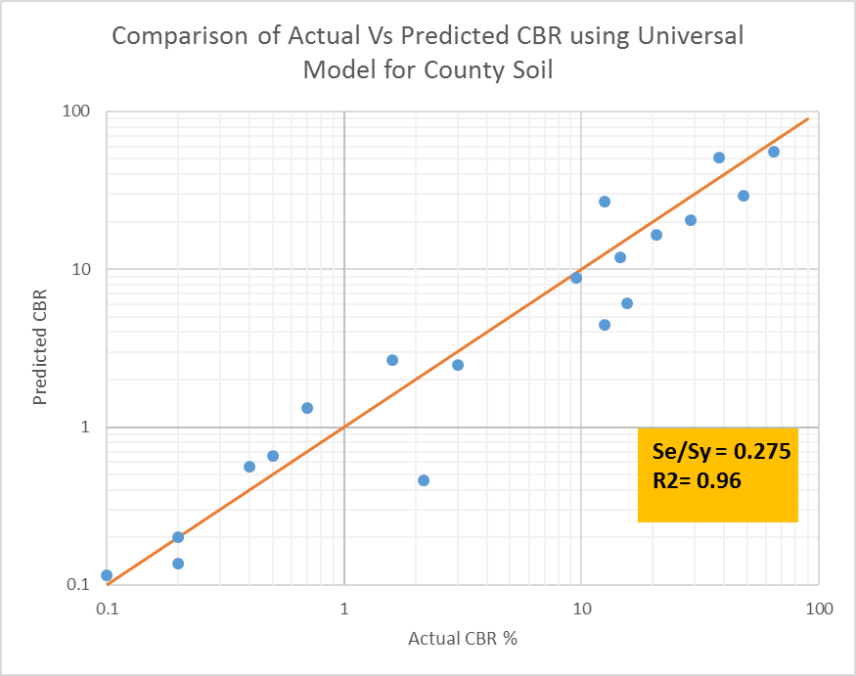

Figure 5.19. Comparison of Actual CBR Lab Test Results to Full Regression Model (County Clay)

CBR VANE SHEAR RELATIONSHIPS

Vane shear strength (see Figure 5.2) was measured on each clay specimen that was used to evaluate the CBR in the laboratory. The main purpose of this study was to investigate if accurate relationships existed and, if so, could be established between the hand held vane shear device and the more tedious, time consuming CBR test protocol.

It should be recognized that, for cohesive type soils, the vane shear is a direct measure of the "cohesion" or shear strength of the soil. In fact, it is a reasonable estimate of the UU shear strength of the clay soil. In contrast, the CBR is an empirical estimate of the shearing strength of a material. For cohesive soils ($\varphi = 0$ soils), this empirical measurement is a direct indicator of the cohesion or shear strength of the material as well. Consequently, this study was conducted to ascertain if any correlation could be found between these two devices. Table 5.3, previously presented in this chapter, summarizes the individual

moisture content (w), dry density (γ_d), compaction energy (E_c), CBR and vane shear (V_s) test results determined in the study, for both clays. It should be noted that not all of the 42 Dupont and County clay specimens were used to measure the vane shear strength. However, CBR and vane shear measurements were performed on 32 specimens. An initial plot of these data points showed that there were four data points that appeared to be significant outliers. Table 5.19 presents the complete data set of the remaining 28 pairs of CBR- V_s results that were statistically analyzed. These results are also plotted in Figure 5.20. It is apparent that a statistically relationship exists between the two variables. The form of the regression model found was:

$$CBR = p_1 V_s^{\,2} + p_2 V_s + p_3$$

Where, V_s = Vane shear strength (tsf); p_1= 0.06252; p_2= 0.05551; p_3= 0.05866

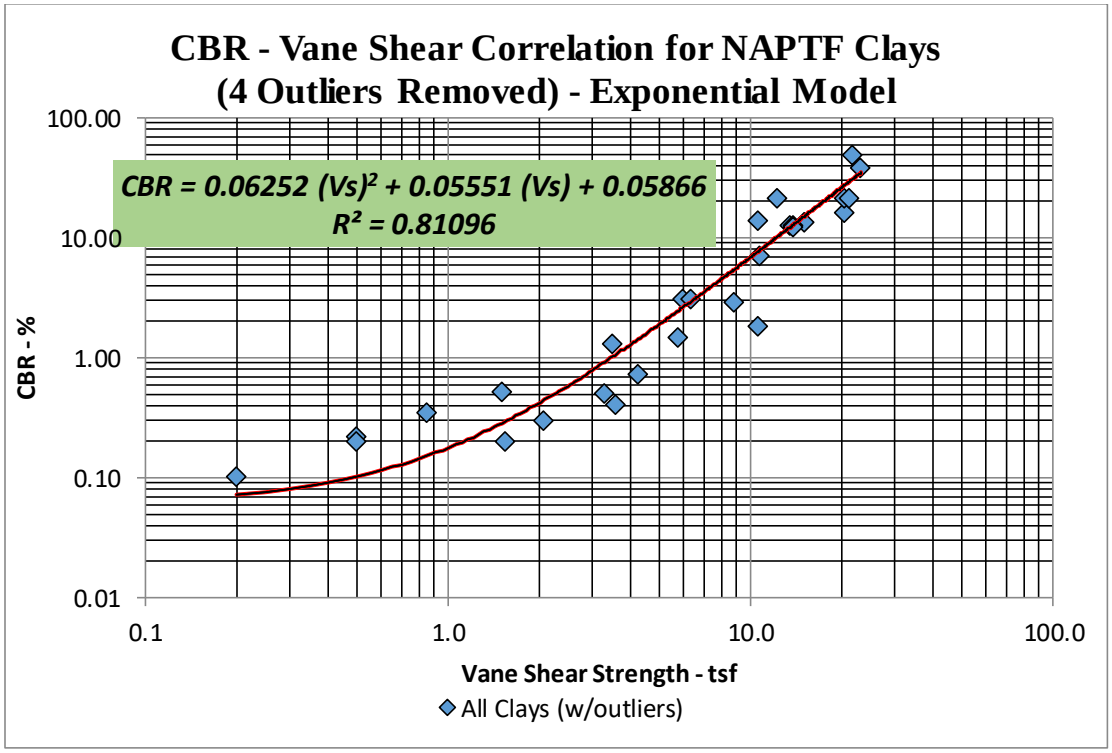

Figure 5.20. Relationship between Vane Shear Strength and CBR Test Results for Both NAPTF Clays

Table 5.19. Summary of CBR- Vane Shear Strength Data Points used in Final Regression Model (Combined Data for DuPont and County Clays)

Clay Type	Compaction	Sample	Dry Density (pcf)	Moisture Content (%)	CBR (%)	Vane Shear (tsf)
County Clay	Standard	CCS315	96.9	17.0	14.0	10.6
		CCS325	100.8	22.2	3.1	6.0
		CCS327	93.8	26.1	0.4	0.9
		CCS330	84.9	31.8	0.2	0.5
		CCS335	83.7	34.5	0.1	0.2
	Intermediate	CCI515	99.7	16.1	21.0	12.3
		CCI525	102.0	22.5	1.8	10.6
		CCI526	95.1	26.7	1.3	3.5
	Modified	CCM510	108.7	11.4	38.0	23.2
		CCM515	113.3	16.5	48.0	21.6
		CCM525	105.5	22.4	16.3	20.4
		CCM527	98.1	26.5	0.7	4.2
		CCM535	85.6	34.6	0.2	0.5
Dupont Clay	Standard	DCS313	89.2	14.1	12.5	13.5
		DCS318	91.8	17.4	7.0	10.7
		DCS327	88.6	29.6	3.1	6.4
		DCS337	77.9	39.9	0.2	1.5
	Intermediate	DCI513	93.9	14.1	13.4	15.0
		DCI518	97.8	18.3	12.5	13.8
		DCI522	95.8	25.4	12.2	13.8
		DCI527	90.2	29.9	1.5	5.8
		DCI537	78.0	39.6	0.3	2.1
		DCI542	76.7	40.8	0.5	1.5
	Modified	DCM518	107.2	17.5	21.0	20.3
		DCM522	100.8	23.7	21.0	21.2
		DCM527	93.2	28.7	2.9	8.80
		DCM537	79.2	39.2	0.5	3.30
		DCM542	77.5	40.5	0.4	3.60

As noted, the R^2=0.81 and the S_e/S_y= 0.258 are both indicators of a good statistical model.

The significance of this relationship should not be overlooked by the NAPTF team as it opens a promising methodology that can be quickly and easily used to estimate the CBR

of either in-situ compaction (during initial construction/compaction operations of test sections) or from in-situ specimens obtained from driven Shelby tubes throughout the performance of testing. The use of hand held vane shear devices has the capability to accurately estimate the CBR, in minutes, using a single hand held device This should be contrasted to the more significant use of labor, time of test and complexity of manufacturing specimens for CBR testing, as well as completing/ analyzing the CBR test results.

In summary, it is recommended that an enhancement of this database be continued with future testing at NAPTF on both clay types. This testing should be used to refine and enhance these initial regression relationships found from this study.

SUMMARY AND CONCLUSIONS

The main objective of this study was to predict the change in CBR and shear strength of the soil with a given moisture content and dry density. The CBR test was performed along with the vane shear test using a pocket vane shear apparatus on the two soils for three different compaction levels. A model was initially developed to obtain the relationship between the dry density and water content for the three compaction curves. The model used in the relationship of moisture content and dry density is as follows:

$$\gamma_d = (f_1 E_c + f_2) w^3 + (g_1 E_c + g_2) w^2 + (j_1 E_c + j_2) w + (k_1 E_c + k_2)$$

f_i, g_i, j_i and k_i denotes the constants used in the equation which varies according to the type of soil. The values for the two types of soil is given in Table 5.20.

Table 5.20. Regression Constants for Dry Density and Moisture Content Relationship for County and Dupont Soils

	f	g	j	k
	County soil			
Constant 1	-1.809E-07	1.507E-05	-4.196E-04	3.989E-03
Constant 2	1.520E-02	-1.246E+00	3.217E+01	-1.675E+02
	Dupont soil			
Constant 1	3.60E-08	-2.20E-06	2.21E-05	4.18E-04
Constant 2	1.72E-03	-1.98E-01	6.31E+00	3.04E+01

Further, a model was developed to obtain the relationship between the CBR and the moisture content for each soil. The form of equation is as follows:

$$Log\ CBR = (q_1 E_c + q_2) + \frac{((p_1 \times (E_c) + p_2) - (q_1 E_c + q_2))}{\left[1 + EXP\ (\frac{w - (r_1 \times (E_c) + r_2)}{(s_1 \times (E_c) + s_2)}\right]}$$

Where p_i, q_i, r_i and s_i are constants depending upon the type of soil. The constants are summarized in Table 5.21.

Table 5.21. Regression Constants for CBR and Moisture Content Relationship for County and Dupont Soils

	p	q	r	s
	County soil			
Constant 1	1.820E-05	1.062E-07	-5.973E-05	4.909E-05
Constant 2	8.938E-01	-1.111E+00	3.588E+01	4.378E+00
	Dupont soil			
Constant 1	7.818E-06	4.794E-06	2.105E-05	7.739E-06
Constant 2	1.375E+00	-1.192E+00	2.328E+01	3.724E+00

Finally, a model was developed to obtain the relationship between the CBR and the vane shear strength. The equation obtained reads as follows:

$$CBR = p_1 V_s^{\,2} + p_2 V_s + p_3$$

Where, V_s- Vane shear strength (tsf); p_1= 0.06252; p_2= 0.05551; p_3= 0.05866

The models developed in this chapter will be used in subsequent chapters to predict the change in the CBR and vane shear strength of the soil when there is a change in the moisture content.

Figure 5.21 to Figure 5.28 shows the prediction of CBR using the final models for the estimation of dry density as a function of moisture content and compaction energy; along with the final model for the estimation of CBR as a function of moisture content and compaction energy. Figure 5.21 and Figure 5.22 shows the CBR change with water content for various compaction energies of Dupont and County clay, respectively. Figure 5.23 and Figure 5.24 shows the CBR changes with water content for different dry densities for Dupont and County clays, respectively. Figure 5.25 and Figure 5.26 shows the CBR versus dry density for different moisture content for Dupont and County clay, respectively. Figure 5.27 and Figure 5.28 shows contour lines of CBR values for different combinations of dry densities and moisture contents for Dupont and County clays, respectively. It is to be noted that the prediction of the CBR using the final equations are subjected to two practical constraints: 1) the compaction energy must be positive; and 2) the dry density and moisture contents used cannot yield a degree of saturation value greater than 100%.

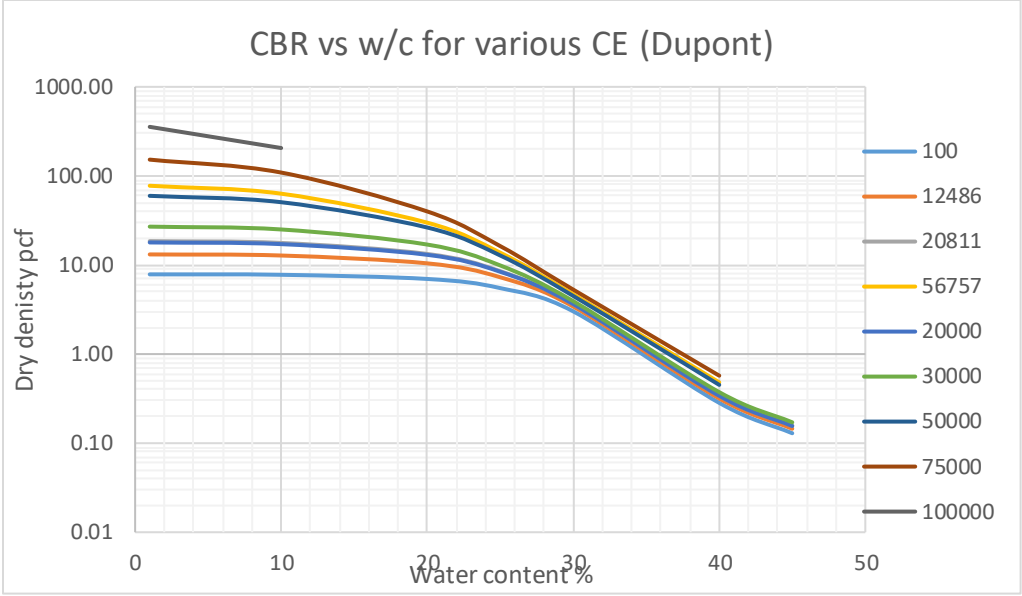

Figure 5.21. CBR versus Moisture Content for Different Compaction Energies ((ft-lb/cf). Predicted Using the Global Model for Dupont Clay

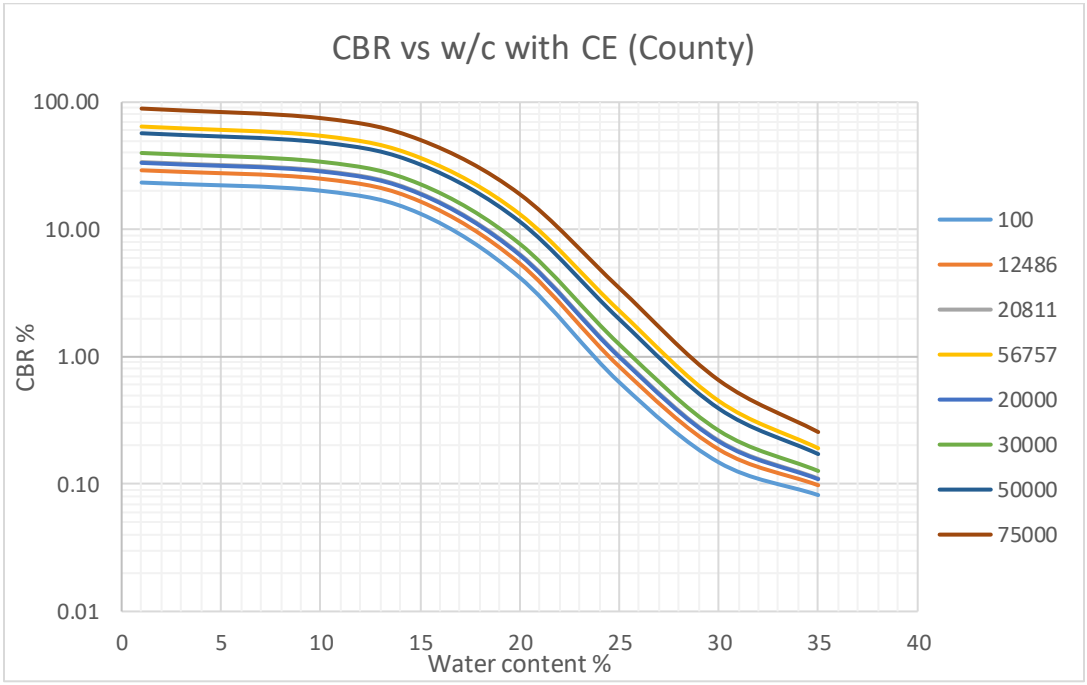

Figure 5.22. CBR Versus Moisture Content for Different Compaction Energy (ft-lb/cf). Predicted Using Global Model for County Clay

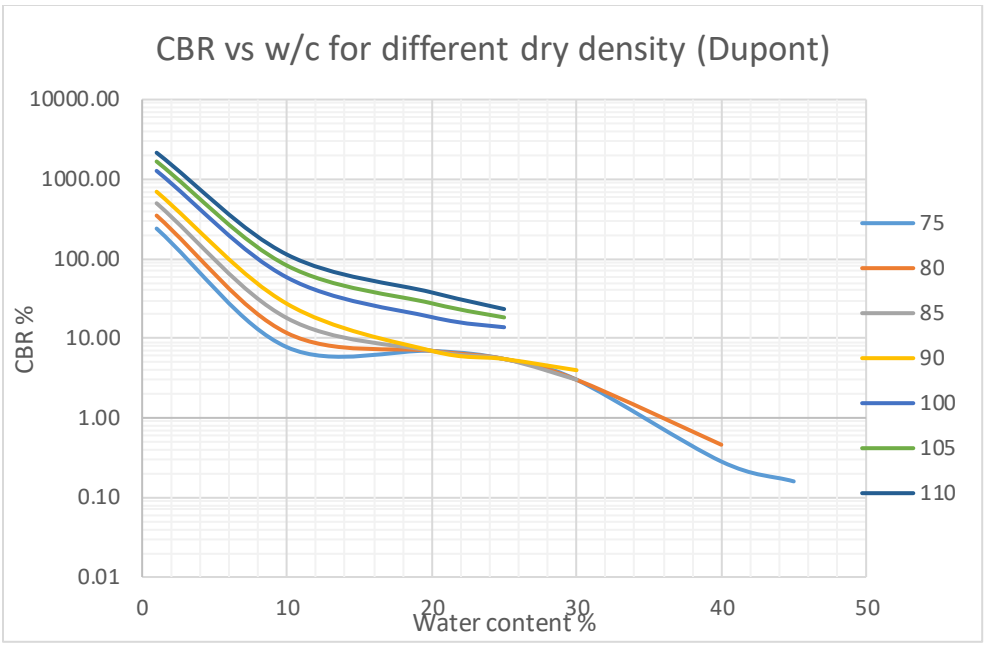

Figure 5.23. CBR versus Moisture Content for Different Dry Densities (pcf) Predicted Using the Global Model for Dupont Clay

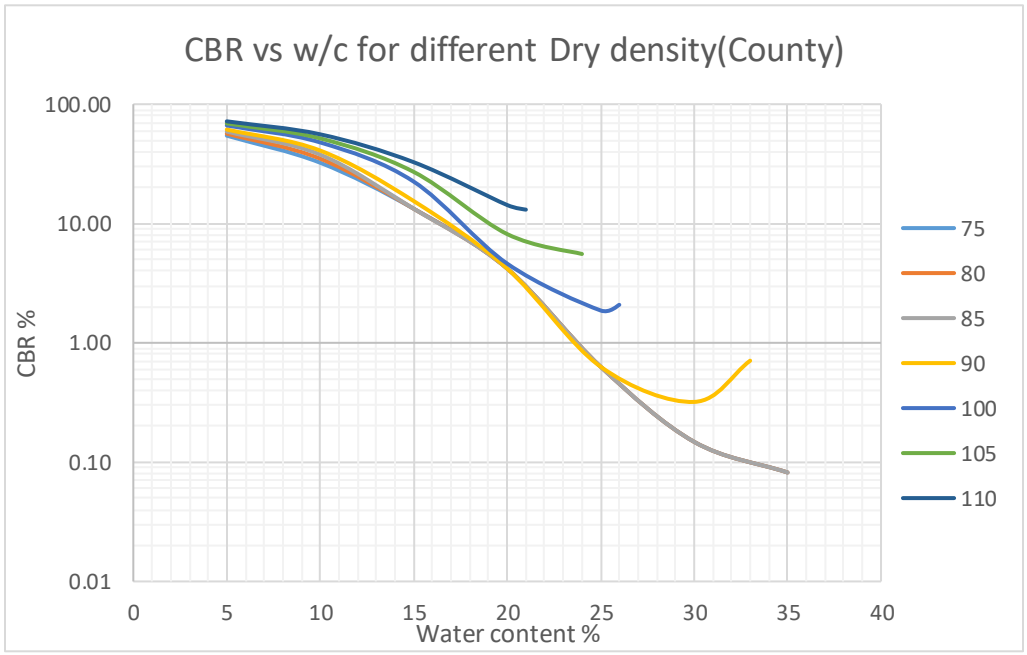

Figure 5.24. CBR versus Moisture Content for Different Dry Densities (pcf) Predicted Using the Global Model for County Clay

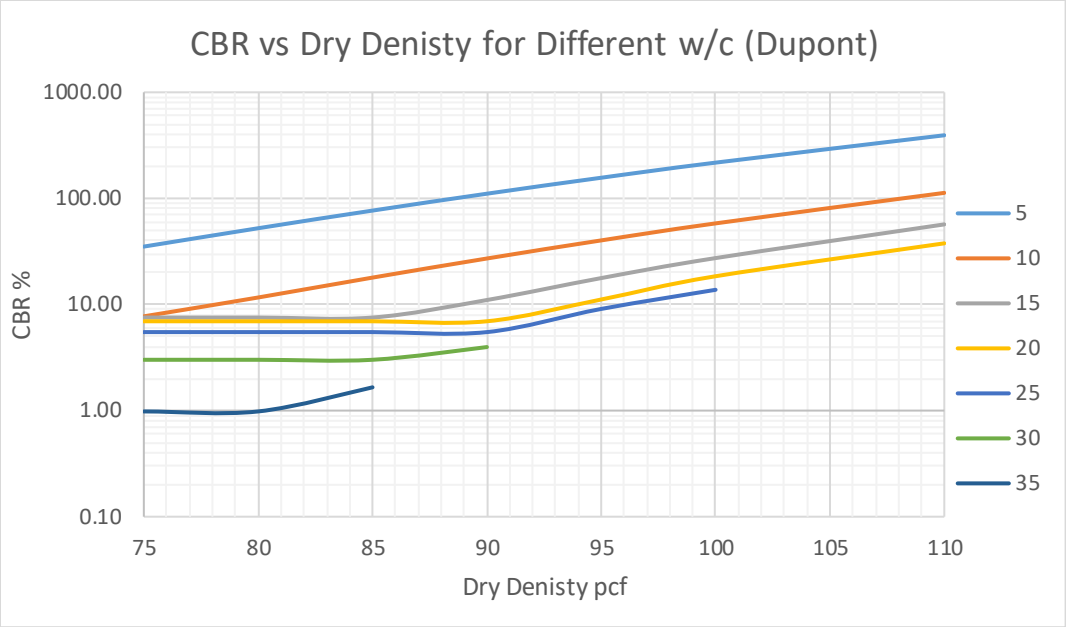

Figure 5.25. CBR versus Dry Density for Different Moisture Contents (%) Predicted Using the Global Model for Dupont Clay

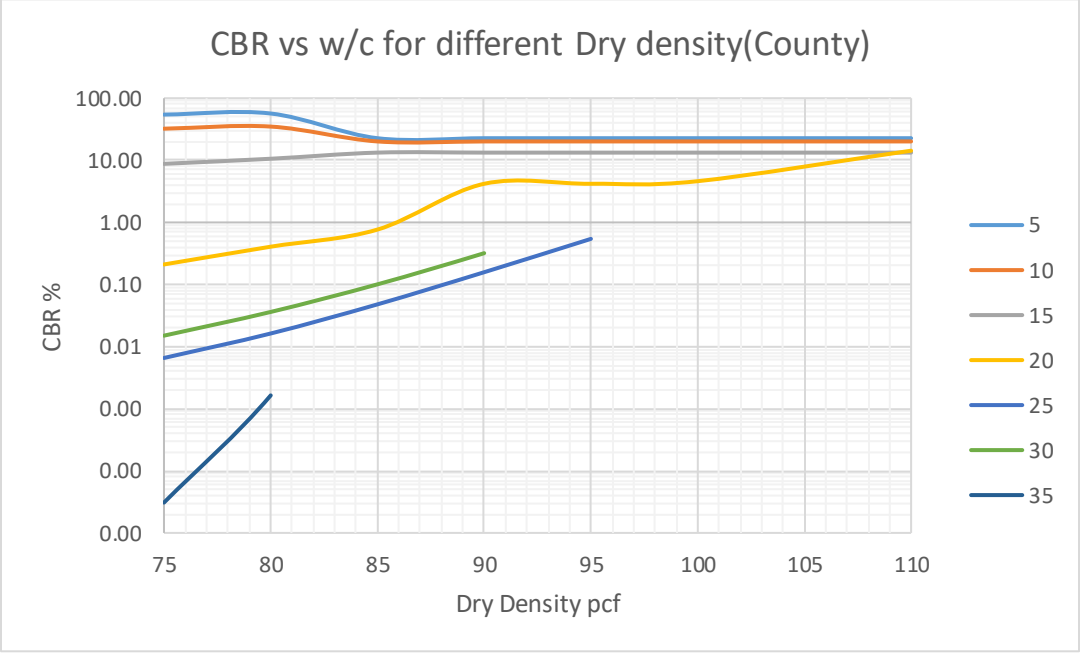

Figure 5.26. CBR versus Dry Density for Different Moisture Contents (%) Predicted Using the Global Model for County Clay

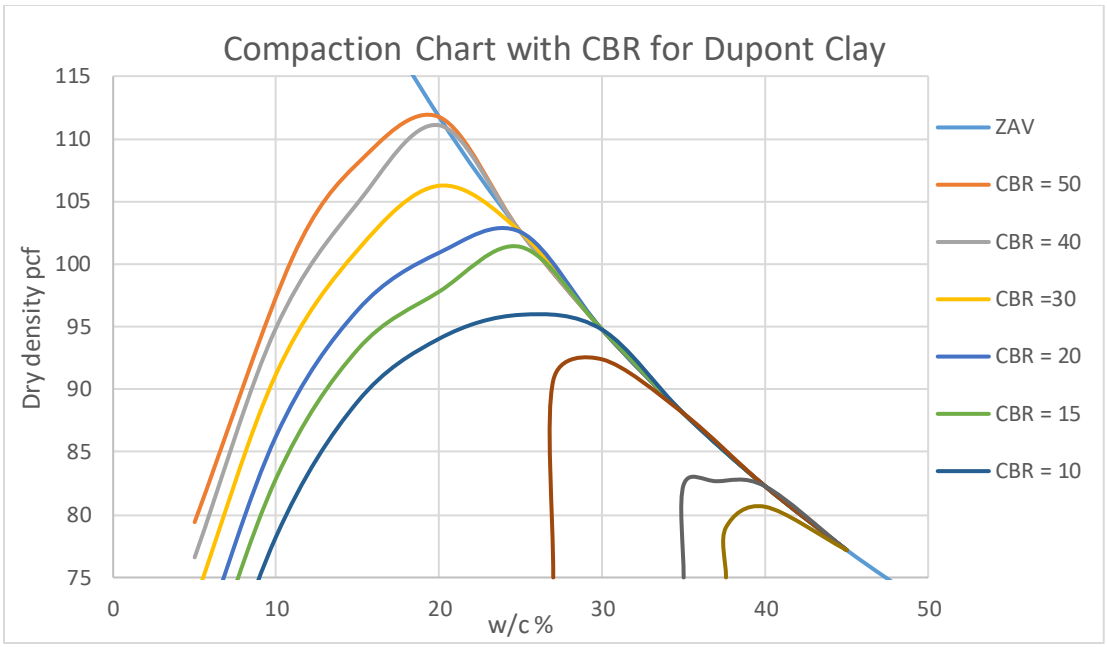

Figure 5.27. CBR Contour Lines for Different Dry Densities and Moisture Contents for Dupont Clay

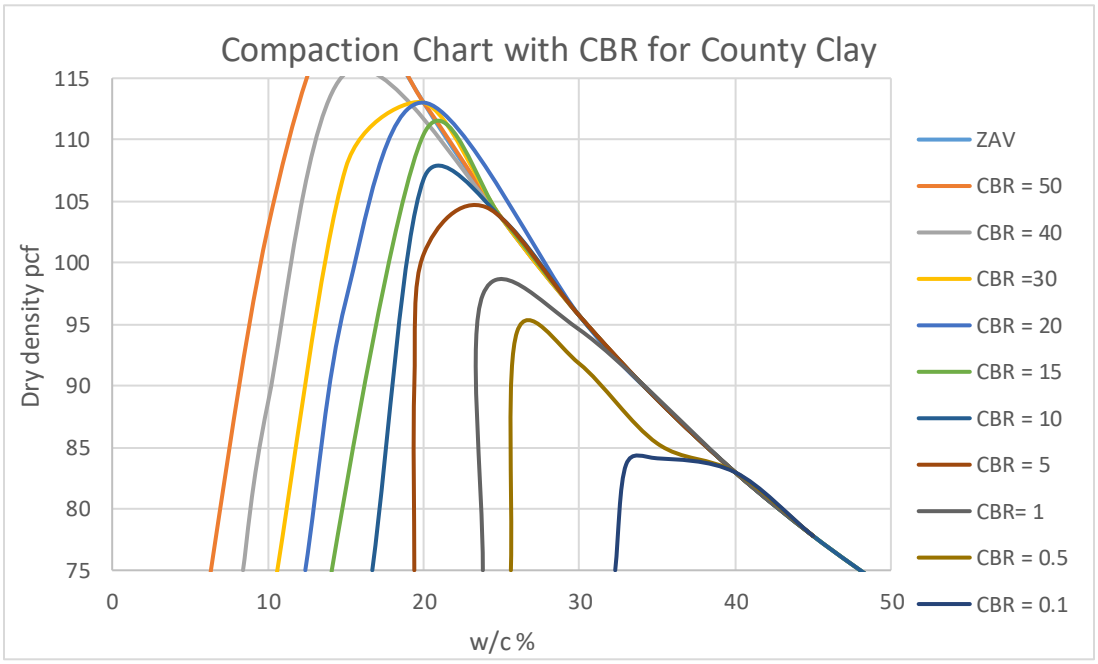

Figure 5.28. CBR Contour Lines for Different Dry Densities and Moisture Contents for County Clay

Chapter 6. Pavement Response Analysis of NAPTF Pavement Sections Using a Multilayer Elastic Theory

GENERAL OVERVIEW

The major objective of this chapter is to evaluate the potential critical stress states, caused by any given load cart, on the unbound (base, subbase and subgrade) layers of the NAPTF pavement cross sections. Of major importance to the overall research project is an in depth study of the stress state in the subgrade Dupont and County clay layers.

The primary focus of this effort was to assess the probable in-situ layer moduli of these unbound layers to study their non-linear moduli response. The efforts of this chapter examines these two critical stress components: the bulk stress (θ) and the octahedral shear stress in the subgrade layers (τ_{oct}).

NAPTF PAVEMENT CROSS SECTION

For purposes of the multilayer elastic theory (MLET) analysis presented in this chapter, the NAPTF pavement cross section used in all subsequent stress studies is shown in Figure 6.1. This pavement section is a classical "flexible pavement" composed of an HMA (asphalt concrete) surface layer (P401), having a layer of crushed stone (CS) base material (P209); a granular subbase (P154) layer overlaying a 54"-thick layer of Dupont clay, in turn, overlaying a 61"-thick layer of County clay that rests on a membrane encapsulating the test section.

LOAD CART PROPERTIES

Gear Geometry/Configurations

According to information obtained from correspondence with NAPTF, the recently constructed test section has predominantly been loaded with a test gear composed of: a)

dual gear (D), b) twin (dual) tandem gear (DT), and c) triple tandem (TT) gear. For all test cart gears, the dual tire spacing has been set at $S_d = 54"$, while the tandem distance between both the dual tandem and triple tandem spacing has been set at $S_t = 57"$.

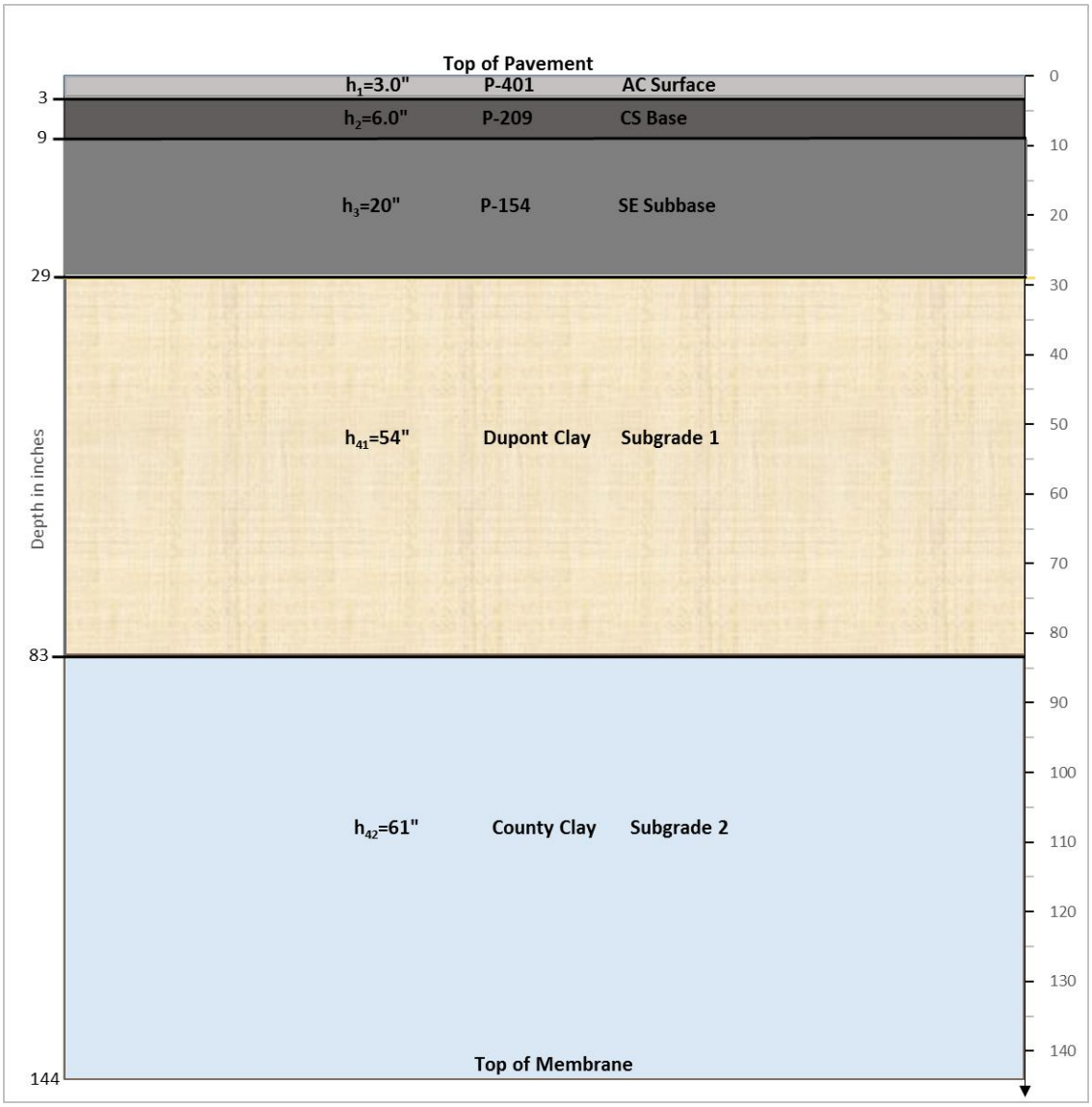

Figure 6.1. NAPTF Pavement Test Section

Tire Load/Contact Pressure

Based upon information received from NAPTF, tires on all load carts were radial aircraft tire size 52 x 21 OR 22. These tires have a constant contact pressure (p_c) of 243 psi. Wheel

(tire) loads are variable, depending upon the construction cycle being tested. Wheel loads on a single tire were noted to range from 55,000 lb (55 kips) to 65,000 lb (65 kips). For the purposes of the MLET presented in this chapter, loads ranging from 50-kips to 70-kips were used. This matrix resulted in the design input properties for each tire load shown in Table 6.1.

Cart Speed

Information provided by NAPTF stated that a given load cart pass on a pavement section was conducted at a nominal cart velocity of v =2.5 mph (3.67 ft/sec).

COMPUTATIONAL POINTS

It has been previously noted that the primary stress computational points were developed to ascertain the distribution of critical stresses within the base and subbase layers, as well as the two subgrade clay layers. Figure 6.2 shows the horizontal x-y computational locations used in the MLET stress analysis for each specific gear type investigated: D, DT and TT. As can be noted, the (x-y) computational points were selected to insure that the maximum critical stress value, at any given depth (z), could be found underneath the entire tire assembly for each gear.

The depth (z) used for each x-y computational location are identified in Table 6.2. A total of 11 specific computation depths (z) were evaluated at each x-y location. The master summary of the tire and computational location points are identified in Table 6.3. Table 6.2 and Table 6.3 identifies the coordinates of the: (a) tire location by gear type, (b) x-y computational points by gear type and (c) the individual computational depths (z) used in the MLET study.

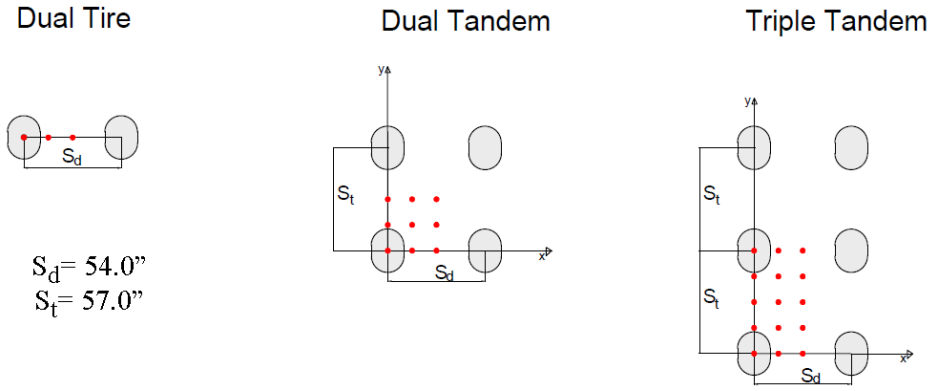

Figure 6.2. Tire and Computational Coordinates for Individual Gear Types Analyzed

Table 6.1. Contact Pressure, Contact Area and Radius of Contact of Tire for Different Loads

P- Load (lb)	p_c- pressure (psi)	A_c- Contact Area (in^2)	a_c- Radius of Contact (in)
50000	243	205.761	8.093
60000	243	246.914	8.865
70000	243	288.066	9.576

Table 6.2. Summary of Depth (z) Computational Locations

Point No	Depth z (in)	Location Description
1	3.00	Bottom of AC Layer
2	6.00	Midpoint of P209 Base
3	14.00	Midpoint of P154 Subbase Layer 1
4	24.00	Midpoint of P154 Subbase Layer 2
5	29.00	Top of Dupont Clay
6	42.50	Midpoint of Dupont Clay Subgrade Sublayer 1
7	69.50	Midpoint of Dupont Clay Subgrade Sublayer 2
8	83.00	Top of County Clay Subgrade
9	98.25	Midpoint of County Clay Subgrade Sublayer 1
10	128.75	Midpoint of County Clay Subgrade Sublayer 2
11	144.00	Bottom of County Clay/ Top of Membrane

Note: All dual (twin) tire spacing, S_d = 54.0 in; all tandem spacing, S_t = 57.0 in; z computational points identical for all runs

Table 6.3. Summary of Tire and (x,y) Computational Points Location

`	Tire Locations			x.y Computational Locations		
Gear Type	Tire No	x (in)	y (in)	Point No	x (in)	y (in)
D (Dual)	1	0.0	0.0	1	0.0	0.00
	2	54.0	0.0	2	13.5	0.00
				3	27.0	0.00
DT (Dual Tandem)	1	0.0	0.0	1	0.0	0.00
	2	54.0	0.0	2	13.5	0.00
	3	0.0	57.0	3	27.0	0.00
	4	54.0	57.0	4	0.0	14.25
				5	13.5	14.25
				6	27.0	14.25
				7	0.0	28.50
				8	13.5	28.50
				9	27.0	28.50
TT (Triple Tandem)	1	0.0	0.0	1	0.0	0.00
	2	54.0	0.0	2	13.5	0.00
	3	0.0	57.0	3	27.0	0.00
	4	54.0	57.0	4	0.0	14.25
	5	0.0	114.0	5	13.5	14.25
	6	54.0	114.0	6	27.0	14.25
				7	0.0	28.50
				8	13.5	28.50
				9	27.0	28.50
				10	0.0	42.75
				11	13.5	42.75
				12	27.0	42.75
				13	0.0	57.00
				14	13.5	57.00
				15	27.0	57.00

PAVEMENT LAYER MODULI

The computation of critical pavement response variables (stress/strain) by the MLET solution requires that two elastic properties of each pavement layer/sublayer be determined.

The following section describes the details that were used to select the dynamic resilient modulus of each pavement layer comprising the NAPTF test sections and the values of the Poisson's Ratio that were assumed for the analysis.

AC P401 E* – Temperature Relationship

Objective

The major objective of this study phase involved the selection of a typical Master Curve of the P401 AC mix that could be used to determine the relationship of the dynamic complex modulus (E*) of the AC mix for the ranges of pavement temperatures expected to be encountered at the test facility.

For a given AC mix, the E* is a function of the specific mix properties (M_p), test specimen temperature (T) and the load frequency (f). Thus:

$$E^* = f(M_p, T, f)$$

In laboratory complex modulus testing, the test frequency (f) is related to the time of loading (t_l) for a given cycle by:

$$t_l = \frac{1}{f}$$

Because of this effect, the E* will also be a function of the type of gear arrangement used as this will control the load stress pulse in the AC layer, for a given velocity (v) of the load cart repetition.

Selection of Typical AC E* Master Curve

It is important to understand that in the FAA AC 150/5320-6E manual and the FAARFIELD computer program, the elastic moduli of the AC are conveniently assumed

to always be a simplified value of 200,000 psi for all temperatures and gear arrangements. This is obviously an extreme simplification that does not come near modeling the annual site environmental conditions, actual pavement cross section and specific gear arrangements of the multitude of aircraft operational, at a given airport facility, upon the E* of an asphalt mix. It is significant to realize that the E* of an AC mix may typically range between the moduli of a PCC layer (3-5×10^6 psi) to that of a dense graded crushed stone layer (30-60 ksi), throughout a given year due to seasonal environmental changes. It is therefore critical to accurately predict the actual in-situ E* behavior of the P401 mix at NAPTF.

It is a widely accepted fact in current day asphalt mix modeling and characterization studies, to characterize the E* as a function of the temperature and time of load, by a Master Curve of the mix. The most widely used relationship to model the master curve is by a sigmoidal function of the form (Witczak, 1996):

$$\log E = \delta + \frac{\alpha}{(1 + e^{\beta + \gamma \log t_r})}$$

In this equation; t_r is the reduced time of the Master curve function and is defined by:

$$\alpha_T = \frac{t_l}{t_r}$$

with α_T being the "shift factor", t_l being the actual time of load for the stress pulse caused by the load-pavement combination in question and t_r is the reduced time.

In pure linear visco-elasticity, the shift function is theoretically a linear function of the test temperature. However, Witczak has conclusively demonstrated that the most accurate

model of the α_T – T (temperature) relationship, for over 350 separate AC mixtures he evaluated, takes on a non-linear form and may be modeled by:

$$\log \alpha_T = AT^2 + BT + C$$

Thus, the complete moduli-time-temperature relationship of any specific AC mixture can be characterized by a series of seven coefficients that are dependent upon the specific properties of the mix. These coefficients are: δ, α, β, γ, A, B, and C.

As this research study did not encompass the measurement of the dynamic complex moduli, E*, in the 3-inch layer constructed in the test section; a typical set of coefficients, representative of a common P401 mix specification, used by FAA, was selected from an extensive database of E* mix test results. This database was developed by Witczak from the early 1970's and has been used as the basis for characterizing the E* behavior of asphalt mixtures in several (Witczak et al, 1996). The Asphalt Institute Manual Series publications (MS-1 and MS-11) as well as the recent MEPDG developed by AASHTO. The specific coefficients used in this study are: δ = 0.4368606, α = 1.936506, β = -0.297275, γ = 0.87176, A = 0.000065, B = -0.072016, and C = 4.725074.

Estimating the Time of Load Pulse (t_l) in AC Layer

In order to predict the AC E* at any given temperature; it is necessary to determine the t_l for the pavement- gear combination in question. For this solution, it is necessary to utilize "transformed section" theory to establish the t_l of the gear load pulse within the AC layer. In this study, the stress pulse was derived at a depth equal to the total thickness of the AC layer, in order to provide the most conservative estimate for the load pulse.

Figure 6.3 illustrates the principles of the transformed section concept. This approach is based upon equating the layer stiffness, D, of the actual AC layer in the test section (having a thickness of h_1 and moduli of E_1) to the transformed section of an equivalent thickness of AC (h_{1e}) and having a modulus, equivalent to the lowest (subgrade) layer of the pavement system.

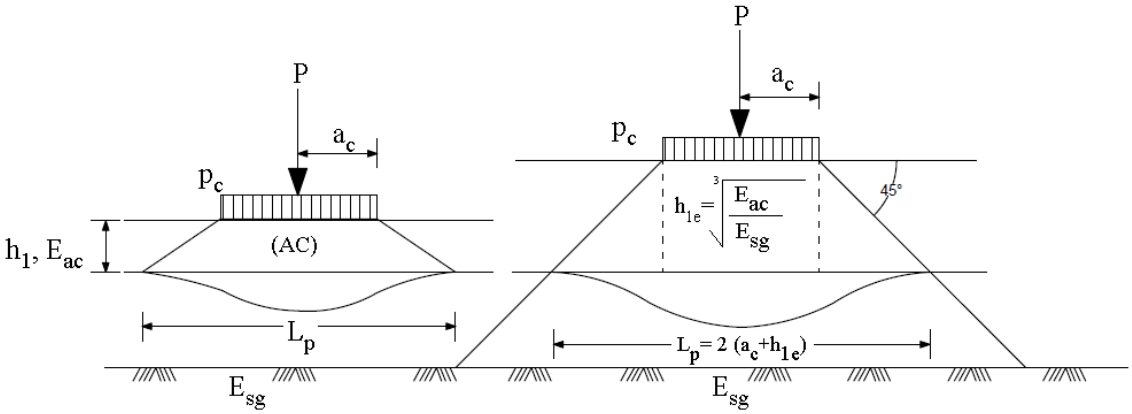

Figure 6.3. Principle of Transformed Section

This is accomplished so that the transformed section is now a "Boussinesq" one-layer elastic system. The equivalent thickness is equated to:

$$h_{1e} = h_1 \sqrt[3]{\frac{E_{ac}(1-\mu_{sg}{}^2)}{E_{sg}(1-\mu_{ac}{}^2)}}$$

While the actual pulse length (L_p) is desired for the actual AC layer, the L_p can be established from:

$$L_p = 2h_{1e} + 2a_c$$

for the transformed section, because the stress distribution in a Boussinesq solid, (E_i/E_{i+1} =1) is typically near 45°. As a_c is the radius of contact of a tire, it is computed from:

$$a_c = \sqrt{\frac{P}{p_c \pi}}$$

With P being the tire load and p_c being the contact pressure.

At NAPTF, the nominal cart load velocity (v) has been previously noted to be 2.5 mph (3.67 ft/s) Using the fact that $v = \frac{X}{t} = \frac{L_p}{t_l}$, the specific load time (under a single tire stress pulse) can be obtained to be (assuming $\mu_{ac} = \mu_{sg}$):

$$t_l = \frac{2(a_c + h_1)\sqrt[3]{\frac{E_{ac}}{E_{sg}}}}{6v}$$

With v in units of ft/s, a_c and h_1 in inches, and E_{ac} and E_{sg} in psi.

Because, the L_p value, and hence load time, is directly related to the E_{sg} value; a range of E_{sg} values was selected for the parametric sensitivity studies conducted with the MLET stress analysis presented in this chapter. Three levels of E_{sg} were used for the clay subgrade layers. They were: 4,000 psi, 6,000 psi, and 10,000 psi.

Example Solution of Time of Load

In order to illustrate the computational sequence for an example set of inputs; the following inputs are assumed: E_{ac} = 500,000 psi, E_{sg} = 4,000 psi, and h_{ac} = 3 inches.

The h_{1e} (equivalent transformed AC thickness) would be:

$$h_{1e} = 3.0\sqrt[3]{\frac{500000}{4000}} = 15\ inches$$

If it were assumed that the t_l was to be determined for a dual tandem gear, with a 54" dual x 57" tandem spacing, and each tire was characterized by P= 60,000 lb and p_c = 243 psi; the $a_c = \sqrt{\frac{P}{p_c \pi}} = \sqrt{\frac{60000}{243\ \pi}} = 8.865\ inches$.

For this analysis, the expected load pulse (at the bottom of the 3.0 in AC layer) would be:

$L_p = 2(h_{1e} + a_c)$ = $2(15.0 + 8.865) = 47.73"\ or\ 3.9775\ ft$

Finally, if the load cart was travelling at a velocity of v= 3.6663 ft/sec, the time of the stress pulse in the ac would be estimated by $t_l = \frac{L_p}{v} = \frac{3.9775}{3.6663} = 1.085\ sec$.

For this example, Figure 6.4, illustrates an important fact for the dual tandem gear. In this figure, the distance y represents the distance between the end of the load pulse from the first dual to the beginning of the second dual. It can be observed that if $L_p \leq S_t$ (tandem spacing); there will be no stress pulse occurring in the distance y. For this example:

$y = S_t - 2(h_{1e} + a_c)$ = 57.0 – 47.73 = 9.27 inches.

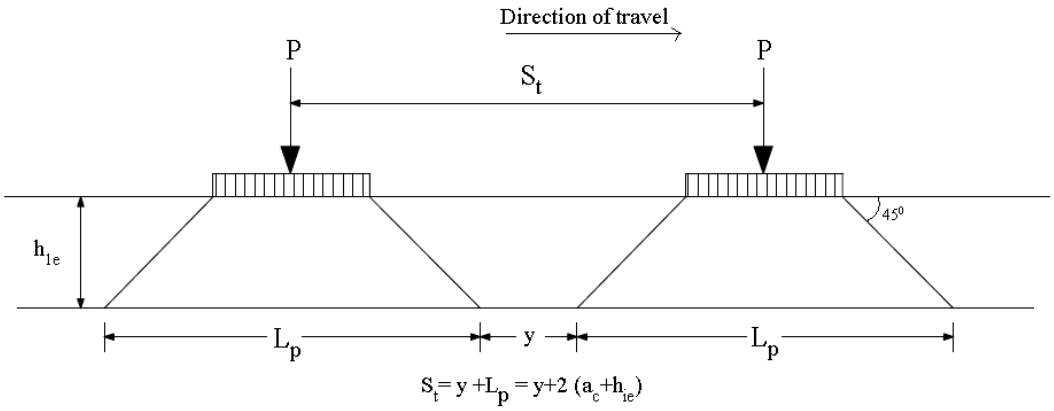

Figure 6.4. Assessment of Presence of No Stress Pulse Zone (y)

Of considerable importance, for this example, is the fact that it can be observed that each tire will provide an individual stress pulse or repetition (at the bottom of the AC layer) that is completely independent of any adjacent dual tire set in a multiple tandem gear. Thus, one pass of a triple tandem gear should really be treated as six separate load (stress) repetitions in the AC layer. Therefore, it would be totally incorrect to utilize the historic USACE/FAA Pass/Coverage analysis methodology to assess the number of stress repetitions within the AC layer given by:

$$P/C = \frac{T(12)}{\alpha\ 2\ a_c n_t}$$

For taxiway wander, (T= 7.5' and $\alpha = 0.75$), this analysis would result in an unconservative estimate of 0.9 stress repetitions per pass, compared to the more accurate estimate of 6 repetitions per pass, which actually occurs.

Development of Final E*- Reduced Time Relationship

Based upon the principals presented to this point, it is to be recognized that there are two equations with the unknown t_l and E* that need to be solved simultaneously. One of the

most direct solutions is to use a trial and error process until the error (difference between the assumed and predicted E value) is within a pre-specified error range. The specific computational sequence is as follows:

1. Compute a_c for a given single tire wheel load (use p_c= 243 psi)
2. For a specified load cart velocity, change the units to v (ft/sec)
3. For a given AC pavement temperature T, compute the shift factor α_T by: $\alpha_T = AT^2+BT+C$
4. Assume an initial E_{ac} value (E_a)
5. Compute the L_p for this assumed E_{ac} value
6. Compute the t_l (stress pulse time) from: $t_l = \frac{L_p}{v}$
7. Knowing t_l and the α_T values, compute the reduced time t_r value: $t_r = \frac{t_l}{\alpha_t}$
8. With this t_r value, compute the E_{ac} value (E_p) from the Master Curve sigmoidal function
9. Compare E_p to E_a and check if the error percentage (specified by user) is met. If the error exceeds this limit, select a new initial seed value, noted in step 4 and repeat the iteration until error is less than specified criteria.

Results of Computer Spreadsheet Solution

The computational scheme previously described was solved in Excel. Tables 6.4 to 6.9 illustrate the results of this effort. As noted, each table is the solution for a given E_{sg} value (4, 6, 10 ksi). The seven Master Curve coefficients for the sigmoidal function and shift factor are identified at the top of each table. Also noted is the load cart properties, relative to the tire load (P), contact pressure (p_c), cart speed during the load test (v) and the tandem

spacing (S_t). It should be noted that the results shown are fully applicable to any type of tandem multiple gear (dual, dual tandem, triple tandem, etc.); because, there is no stress overlap of any adjacent tires for the majority of pavement temperatures investigated.

Table 6.4. Analysis of FAA NAPF AC E* for Esg = 4000 psi

Typical Assumed Sigmoidal and Shift Function Properties

Master Curve Sigmoid		*Shift Factor*		*Load Cart*	
Delta =	4.368606	**A =**	0.000065	**P Load (lb) =**	**60000.0**
Alpha =	1.936506	**B =**	-0.072016	**p_c pressure (psi) =**	**243.0**
Beta =	-0.297275	**C =**	4.725074	**a_{c-} radius (in)=**	**8.865**
Gamma =	0.87176			**v-speed (mph)=**	**2.5**
				v-speed (ft/sec)=	**3.667**
AC Layer Properties		*Subgrade Properties*		**S_t Tand Sp (in)**	**57.0**
h_1 (in) =	3.0	**E_{sg} (psi) =**	4000		

T(°F)	Log (α(T))	α(T)	Assumed E_1 (psi) =	L_p (in)	L_p (ft)	t_i (sec)	t_r (sec)	E_1 (pred)	Δ Err (%)	E_1 (avg)
10	4.0114	10266.3012	1800000	63.700	5.308	1.448	1.410E-04	1804076	0.2%	1802038
20	3.3108	2045.2858	1650000	62.386	5.199	1.418	6.932E-04	1650647	0.0%	1650323
30	2.6231	419.8498	1420000	60.206	5.017	1.368	3.259E-03	1423723	0.3%	1421862
40	1.9484	88.8043	1120000	56.976	4.748	1.295	1.458E-02	1129059	0.8%	1124529
50	1.2868	19.3541	800000	52.812	4.401	1.200	6.202E-02	806150	0.8%	803075
60	0.6381	4.3462	515000	48.023	4.002	1.091	2.511E-01	516628	0.3%	515814
70	0.0025	1.0057	304000	43.142	3.595	0.980	9.750E-01	304978	0.3%	304489
80	-0.6202	0.2398	175000	38.870	3.239	0.883	3.684E+00	174603	-0.2%	174802
90	-1.2299	0.0589	103000	35.446	2.954	0.806	1.368E+01	103314	0.3%	103157
100	-1.8265	0.0149	66500	33.042	2.754	0.751	5.037E+01	66297	-0.3%	66399
110	-2.4102	0.0039	47000	31.370	2.614	0.713	1.833E+02	47197	0.4%	47099
120	-2.9808	0.0010	37000	30.325	2.527	0.689	6.595E+02	37049	0.1%	37024

Table 6.5. Analysis of FAA NAPTF AC E* for Esg = 6000 psi

Typical Assumed Sigmoidal and Shift Function Properties

Master Curve Sigmoid		*Shift Factor*		*Load Cart*	
Delta =	4.368606	**A =**	0.000065	**P Load (lbs) =**	60000.0
Alpha =	1.936506	**B =**	-0.072016	**p_c pressure (psi) =**	243.0
Beta =	-0.297275	**C =**	4.725074	**a_c- radius (in)=**	8.865
Gamma =	0.87176			**v-speed (mph)=**	2.5
				v-speed (ft/sec)=	3.667
AC Layer Properties		*Subgrade Properties*		**S_t Tand S_p (in)=**	57.0
h_1 (in) =	3.0	**E_{sg} (psi)=**	6000		

(^{0}F)	Log (α(T))	α(T)	Assumed E_1 (psi) =	L_p (in)	L_p (ft)	t_t (sec)	t_r (sec)	E_1 (pred)	Δ Err (%)	E_1 (avg)
10	4.0114	10266.3012	1811000	57.970	4.831	1.318	1.283E-04	1811030	0.0%	1811015
20	3.3108	2045.2858	1660000	56.820	4.735	1.291	6.314E-04	1661735	0.1%	1660867
30	2.6231	419.8498	1440000	55.010	4.584	1.250	2.978E-03	1439244	-0.1%	1439622
40	1.9484	88.8043	1145000	52.268	4.356	1.188	1.338E-02	1147618	0.2%	1146309
50	1.2868	19.3541	825000	48.694	4.058	1.107	5.718E-02	824254	-0.1%	824627
60	0.6381	4.3462	530000	44.448	3.704	1.010	2.324E-01	531063	0.2%	530531
70	0.0025	1.0057	315000	40.194	3.350	0.914	9.084E-01	313988	-0.3%	314494
80	-0.6202	0.2398	180000	36.372	3.031	0.827	3.448E+00	179525	-0.3%	179763
90	-1.2299	0.0589	105500	33.331	2.778	0.758	1.286E+01	105736	0.2%	105618
100	-1.8265	0.0149	67500	31.174	2.598	0.708	4.752E+01	67482	0.0%	67491
110	-2.4102	0.0039	47500	29.688	2.474	0.675	1.735E+02	47788	0.6%	47644
120	-2.9808	0.0010	37500	28.782	2.398	0.654	6.259E+02	37355	-0.4%	37428

Table 6.6. Analysis of FAA NAPTF AC E* for Esg = 10000 psi

Typical Assumed Sigmoidal and Shift Function Properties

Master Curve Sigmoid		*Shift Factor*		*Load Cart*	
Delta =	4.368606	**A =**	0.000065	**P Load (lb) =**	60000.0
Alpha =	1.936506	**B =**	-0.072016	**p_c pressure (psi)=**	243.0
Beta =	-0.297275	**C =**	4.725074	**a_c radius (in)=**	8.865
Gamma =	0.87176			**v-speed (mph)=**	2.5
				v-speed (ft/sec)=	3.667
AC Layer Properties		***Subgrade Properties***		**S_t Tand Sp (in)=**	57.0
h_1 (in) =	3.0	**E_{sg} (psi)=**	10000		

T(°F)	Log (α(T))	α(T)	Assumed E_1 (psi) =	L_p (in)	L_p (ft)	t_l (sec)	t_r (sec)	E_1 (pred)	Δ Err (%)	E_1 (avg)
10	4.0114	10266.3012	1820000	51.727	4.311	1.176	1.145E-04	1819163	0.0%	1819581
20	3.3108	2045.2858	1675000	50.799	4.233	1.155	5.645E-04	1674653	0.0%	1674827
30	2.6231	419.8498	1460000	49.319	4.110	1.121	2.670E-03	1457649	-0.2%	1458824
40	1.9484	88.8043	1170000	47.072	3.923	1.070	1.205E-02	1169946	0.0%	1169973
50	1.2868	19.3541	848000	44.087	3.674	1.002	5.177E-02	846502	-0.2%	847251
60	0.6381	4.3462	550000	40.545	3.379	0.921	2.120E-01	548507	-0.3%	549253
70	0.0025	1.0057	326000	36.895	3.075	0.839	8.338E-01	325191	-0.2%	325595
80	-0.6202	0.2398	186000	33.626	2.802	0.764	3.187E+00	185534	-0.3%	185767
90	-1.2299	0.0589	109000	31.033	2.586	0.705	1.197E+01	108643	-0.3%	108822
100	-1.8265	0.0149	69000	29.152	2.429	0.663	4.444E+01	68890	-0.2%	68945
110	-2.4102	0.0039	48500	27.886	2.324	0.634	1.630E+02	48479	0.0%	48490
120	-2.9808	0.0010	37600	27.060	2.255	0.615	5.885E+02	37727	0.3%	37663

Table 6.7. Analysis of FAA NAPTF AC E* for Esg = 20000 psi

Typical Assumed Sigmoidal and Shift Function Properties

Master Curve Sigmoid		*Shift Factor*		*Load Cart*		
Delta =	4.368606	**A =**	0.000065	**P Load (#) =**	60000.0	
Alpha =	1.936506	**B =**	-0.072016	**pc pressure =**	243.0	
Beta =	-0.297275	**C =**	4.725074		**ac- radius (in)**	8.865
Gamma =	0.87176			**v-speed (mph)**	2.5	
					v-speed (ft/sec)	3.667
				St Tand Sp (in)	57.0	

AC Layer Properties		**Subgrade Properties**	
h1 (in) =	3.0	**Esg =**	20000

T(deg F)	Log (α(T))	α(T)	E1 (psi) =	Lp (in)	Lp (ft)	tl (sec)	tr (sec)	E1 (pred)	Δ Err (%)	E1 (avg)
10	4.0114	10266.3012	1829283	44.76	3.73	1.017	9.91E-05	1829066	0.00	1829174
20	3.3108	2045.2858	1691026	44.06	3.67	1.001	4.90E-04	1690494	0.00	1690760
30	2.6231	419.8498	1480441	42.92	3.58	0.975	2.32E-03	1480470	0.00	1480456
40	1.9484	88.8043	1197897	41.20	3.43	0.936	1.05E-02	1197987	0.00	1197942
50	1.2868	19.3541	874640	38.87	3.24	0.883	4.56E-02	874816	0.00	874728
60	0.6381	4.3462	570966	36.07	3.01	0.82	1.89E-01	571175	0.00	571071
70	0.0025	1.0057	339506	33.15	2.76	0.753	7.49E-01	339662	0.00	339584
80	-0.6202	0.2398	193212	30.51	2.54	0.693	2.89E+00	193282	0.00	193247
90	-1.2299	0.0589	112379	28.40	2.37	0.645	1.10E+01	112403	0.00	112391
100	-1.8265	0.0149	70664	26.87	2.24	0.611	4.10E+01	70669	0.00	70667
110	-2.4102	0.0039	49348	25.84	2.15	0.587	1.51E+02	49350	0.00	49349
120	-2.9808	0.0010	38175	25.17	2.10	0.572	5.47E+02	38175	0.00	38175

Table 6.8. Analysis of FAA NAPTF AC E* for Esg = 30000 psi

Typical Assumed Sigmoidal and Shift Function Properties

Master Curve Sigmoid		*Shift Factor*		*Load Cart*	
Delta =	4.368606	**A =**	0.000065	**P Load (lb) =**	**60000.0**
Alpha =	1.936506	**B =**	-0.072016	**p_c pressure (psi) =**	**243.0**
Beta =	-0.297275	**C =**	4.725074	**a_c- radius (in)=**	**8.865**
Gamma =	0.87176			**v-speed (mph)=**	**2.5**
				v-speed (ft/sec)=	**3.667**
				S_t Tand Sp (in)	**57.0**

AC Layer Properties			*Subgrade Properties*							
T(deg F)	Log (α(T))	α(T)	E1 (psi) =	Lp (in)	Lp (ft)	tl (sec)	tr (sec)	E1 (pred)	Δ Err (%)	E1 (avg)
10	4.0114	10266.3012	1834432	41.365	3.447	0.940	9.16E-05	1834272	0.00	1834352
20	3.3108	2045.2858	1699339	40.770	3.398	0.927	4.53E-04	1698869	0.00	1699104
30	2.6231	419.8498	1492575	39.795	3.316	0.904	2.15E-03	1492596	0.00	1492585
40	1.9484	88.8043	1213008	38.322	3.193	0.871	9.81E-03	1213075	0.00	1213041
50	1.2868	19.3541	890053	36.303	3.025	0.825	4.26E-02	890183	0.00	890118
60	0.6381	4.3462	583405	33.864	2.822	0.770	1.77E-01	583575	0.00	583490
70	0.0025	1.0057	347491	31.305	2.609	0.711	7.08E-01	347612	0.00	347552
80	-0.6202	0.2398	197469	28.974	2.415	0.659	2.75E+00	197526	0.00	197498
90	-1.2299	0.0589	114424	27.105	2.259	0.616	1.05E+01	114443	0.00	114433
100	-1.8265	0.0149	71622	25.749	2.146	0.585	3.93E+01	71627	0.00	71624
110	-2.4102	0.0039	49813	24.835	2.070	0.564	1.45E+02	49815	0.00	49814
120	-2.9808	0.0010	38428	24.247	2.021	0.551	5.27E+02	38414	0.00	38421

Table 6.9. Analysis of FAA NAPTF AC E* for Esg = 40000 psi

Typical Assumed Sigmoidal and Shift Function Properties

Master Curve Sigmoid		*Shift Factor*		*Load Cart*		
Delta =	4.368606	**A =**	0.000065	**P Load (#) =**	60000.0	
Alpha =	1.936506	**B =**	-0.072016	**pc pressure =**	243.0	
Beta =	-0.297275	**C =**	4.725074		**ac- radius (in)**	8.865
Gamma =	0.87176			**v-speed (mph)**	2.5	
					v-speed (ft/sec)	3.667
				St Tand Sp (in)	57.0	

AC Layer Properties		**Subgrade Properties**	
h1 (in) =	3.0	**Esg =**	40000

T(deg F)	Log (α(T))	α(T)	E1 (psi) =	Lp (in)	Lp (ft)	tl (sec)	tr (sec)	E1 (pred)	Δ Err (%)	E1 (avg)
10	4.0114	10266.3012	1837830	39.22	3.27	0.891	0.00	1837716	0.00	1837773
20	3.3108	2045.2858	1704761	38.69	3.22	0.879	0.00	1704427	0.00	1704594
30	2.6231	419.8498	1500661	37.81	3.15	0.859	0.00	1500676	0.00	1500668
40	1.9484	88.8043	1223142	36.49	3.04	0.829	0.01	1223188	0.00	1223165
50	1.2868	19.3541	900460	34.67	2.89	0.788	0.04	900553	0.00	900506
60	0.6381	4.3462	591871	32.46	2.71	0.738	0.17	591988	0.00	591929
70	0.0025	1.0057	352929	30.13	2.51	0.685	0.68	353018	0.00	352974
80	-0.6202	0.2398	200365	28.00	2.33	0.636	2.65	200406	0.00	200385
90	-1.2299	0.0589	115807	26.28	2.19	0.597	10.14	115820	0.00	115813
100	-1.8265	0.0149	72265	25.04	2.09	0.569	38.17	72269	0.00	72267
110	-2.4102	0.0039	50123	24.20	2.02	0.550	141.40	50124	0.00	50124
120	-2.9808	0.0010	38587	23.66	1.97	0.538	514.50	38573	0.00	38580

The solution was developed for a range of temperatures (AC) within the pavement test section facility. This range (for the MLET analysis) was taken from 10° F to 120° F. However, the actual range of in-situ temperature at NAPTF appears to be closer to the 30° F to 90° F range.

The reader should scrutinize the L_p column results for all 6 subgrades moduli values evaluated and recognize that the y distance (no stress overlap) will be a positive integer when the L_p shown is less than the S_t (tandem spacing). This only occurs for the E_{sg} = 4000 psi subgrade when the temperature is approximately 30° F or less.

For a specific temperature row, the computational column for α_T were determined. Then, using an assumed E_1 value (E_a), the L_p, t_l, and t_r values were computed. The computed t_r value is then used in the sigmoidal E* Master Curve equation to find the predicted E_1 value (E_p). An error term (%) was then computed between the E_a and E_p values. If the error was larger than 1% (error limit assumed in this study), an average E_1 of the E_a and E_p is then used again as the initial assumed E_1 (E_a) value for the next iteration. This process is continued until an error less than specified for the solution is obtained.

Figure 6.5 represents the final E* dynamic modulus pavement temperature for any type of tandem load cart travelling at a nominal speed of 2.5 mph. Fortunately, it can be observed that the influence of the subgrade E_{sg} range used in this study, resulted in only a minor influence upon the final E* for the P401 layer (3.0 inches thick) used at NAPTF. It should also be noted the solutions shown are uniquely related to the test load cart velocity of 2.5 mph.

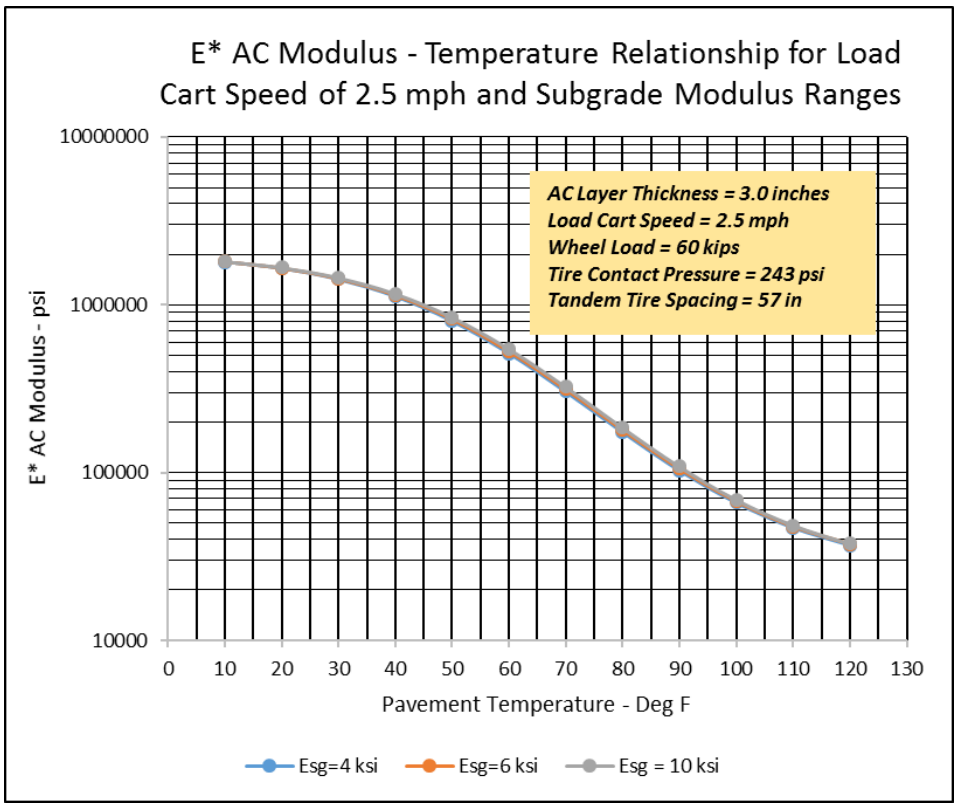

Figure 6.5. E* AC Modulus- Temperature Relationship for Load Cart Speed 2.5 mph and Subgrade Modulus Ranges

Resilient Modulus of Unbound Base (P209) and Subbase (P154) Layers

FAA/US Military UFC Modulus Approach

The assessment of the critical pavement response predictions in the pavement test section requires that moduli of the unbound base (P209) and unbound subbase (P154) layers are estimated for the MLET analysis. While direct non-linear M_r testing was not conducted on these materials; the initial values used in the ensuing MLET analysis were based upon current FAA methodology, which in turn, was based upon the modulus procedure developed in the 1970's by the U.S. Army Corps of Engineers Waterways Experiment Station (USACE-WES). This approach is also the procedure used in the UFC (United

Facilities Command) (UFC-3-260-02, 2007) and is the current reference stated in FAA AC 150/5320-6E.

A series of equations were developed by Dr. Walter Barker of the USACE-WES in 1974 (UFC-3-260-02, 2007). The graphical solution of these equations is shown in Figure 6.6. The equation noted in the UFC document (and also in the FAA FAARFIELD computer program) are:

Base Course

$$E_n = E_{n+1}(1 + 10.52 \log t - 2.10 \log E_{n+1} \log t)$$

Subbase Course

$$E_n = E_{n+1}(1 + 7.18 \log t - 1.56 \log E_{n+1} \log t)$$

In these equations, E (*n* and *n+1*) are in psi while the sublayer (base or subbase) thickness, t, is in inches.

This approach was used to estimate E for the base/subbase layers of the NAPTF test section. For enhanced accuracy, the 20-inch thick P154 subbase layer was subdivided into 2-10.0-inch thick sublayers. In addition, as the subbase/base layer moduli are functions of the subgrade (initial E_{n+1} layer), solutions were developed for E_{sg} values of 4, 6, 10, 20, 30 and 40 ksi. The results of this analysis are shown in Table 6.10.

Table 6.10. Results of Granular Base and Subbase Estimated Moduli

Sublayer	*h(in)*	*Granular layer moduli (psi)*					
		E_{sg} *4 ksi*	E_{sg} *6 ksi*	E_{sg} *10 ksi*	E_{sg} *20 ksi*	E_{sg} *30 ksi*	E_{sg} *40 ksi*
Base- E_b	6.0	42800	48250	55000	62207	65225	66674
Subbase (1) – E_{sb1}	10.0	19700	23700	29000	35560	38547	40042
Subbase (2) – E_{sb2}	10.0	10250	13700	19400	29408	35871	40031

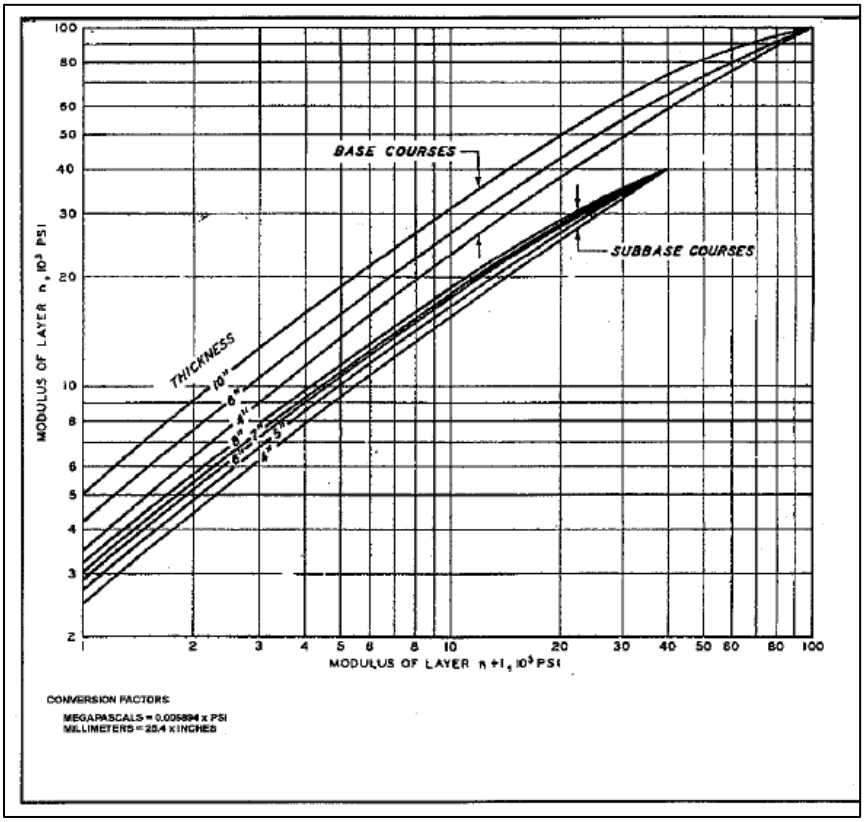

Figure 6.6. Relationships between Modulus of Layer *n* and Modulus of Layer *n+1* for Various Thicknesses of Unbound Base Course and Subbase Course

Even though Barker's model was adopted by the Federal Aviation Administration (FAA) and the United States Army Corps of Engineers (USACE) (UFC-3-260-02, 2007), to the best of the author's knowledge, Barker never published his work. The model was put forward in 1970's by Barker for discussion. From direct communication with one of the

consultants hired by the USACE, Dr. Matthew Witczak, I was able to provide the details of the study performed by Barker, which were explained in the discussion.

Barker used 80-kip single wheel load for his study. He used k1-k2-k3 models which was being developed during that time by Townsend (Townsend et al, 1976) for his study. FE models were used in the analysis. The model suggested by Barker were criticized largely by the consultants, but nevertheless, it was adopted in the design procedures. Some of the major disadvantages of this model are as follows:

- The modulus of the AC layer was never used as a consideration to predict the modulus of the layers below. The procedure is a bottom-up design approach. That means that you need the modulus of the lower layer to find out the modulus of the layer immediately up.
- An 80-kip single wheel load was used, which is overly conservative.
- The influence of tire load combinations for Dual, Dual tandem and Triple tandem was not considered in his model.

Since UFC, USACE and FAA use this model, this model was also adopted in this study for the prediction of E of base and subbase layers. To my knowledge, there is no other model to account for granular base and subbase moduli for airfield pavement systems. And unless we measured the moduli (material was not available), that was the best choice for this study.

Limitations of FAA/UFC Modulus Approach

While these results follow the current FAA and U.S. Military UFC procedures; it is important to note that a significant exception in using this approach was made by the USACE Consultant Board assigned to provide a technical review of the entire new layered

elastic approach that was being developed in the early 1970's. While the Board's recommendations were not followed by the USACE-WES Pavement group, the following limitations still exist and should be noted in subsequent future revisions by the FAA to AC 150/5320.

These limitations, noting that the solution may be inappropriate and inaccurate for continued use, are:

1. The solution was developed by analyzing the results of a FEM (Finite Element Model) pavement response analysis for only an 80-kip single wheel load. This tire load clearly exceeds, even with today's aircraft, the heaviest single tire wheel load existing. It should be recognized that the use of this wheel load magnitude will lead to predicted granular layer moduli that are more unconservative (higher E) than those stressed by today's lower wheel load aircraft gears. In addition, the stress overlap influence caused by additional tires in a multi tire gear (dual, dual tandem, triple tandem etc.) will seriously alter the moduli in the lower, thicker subbase layers.
2. A major error is caused by the fact that the original analysis was only based upon a pavement structure that had a very thin, low modulus AC layer. In reality, in most heavy load airfield pavements, thicker layers of a stabilized AC or CTB base/subbase layer will be used. The reality of the presence of thick, stiff (high modulus) upper layers in the surface and base layer will cause a dramatic difference

in stress state of the subbase layers. For granular base/subbase materials, a decrease in in-situ stress, caused by the external wheel load, will significantly decrease the layer moduli of these layers.

3. Because the Modulus solution presented in the FAA/UFC approach starts at the very lowest subgrade layer, it should be obvious from Figure 6.6 that as the total pavement thickness is continually increased, the upper base/subbase layers will also increase. This is in direct contrast to the reality of non-linear behavior of unbound granular materials. As a general rule, the moduli of a base layer (directly under an aircraft tire) will be subjected to the same relative stress magnitude regardless of the pavement thickness.

In summary, it is highly probable that the current FAA/UFC procedure for determining the layer moduli of base/subbase granular materials will lead to highly inaccurate moduli (E) estimate that do not reflect the true principles of unbound material nonlinear stress dependent behavior.

While this is a qualifying statement of the research team, it is again noted that this approach was used in the MLET computer analysis presented in this report to provide an analysis that conforms with present day FAA methodology.

MLET (JULEA) ANALYSIS

Critical Stress Analysis Objective

The objective in this study phase was to investigate the typical range of moduli for all unbound pavement layers (i.e., base, subbase and subgrade). This was accomplished through the use of the USACE developed WINJULEA program, after JULEA (Jacob Uzan Layered Elastic Analysis) computer program. The study entailed the development of the

stress-depth relationships in the NAPTF test section previously described. These relationships allowed for the assessment of layer moduli based upon fundamental nonlinear material behavior of all unbound layer materials.

Input Matrix Summary

A comprehensive matrix of computer runs was generated in this study with JULEA. The pavement cross sections investigated were comprised of three AC temperatures levels and three subgrade moduli which led to nine differing combinations for the AC E* values. In addition, for each subgrade modulus value, there were three separate combinations of the base layer moduli, subbase layer No 1 and subbase layer No 2. The full summary matrix of pavement layer inputs for the MLET computer runs are shown in Tables 6.11 and 6.12 for different subgrade moduli. Finally, as previously noted, the study also considered three specific levels of the single tire load occurring with three differing gear combinations.

This combination of input variables led to the initial development of 81 separate JULEA computer runs. Recalling the number of computational points previously shown in Table 6.1, a total of 8,019 computational (x-y-z) points under each gear type were initially planned to be investigated in this study. Finally, as the output of each JULEA solution yields 48 separate specific pavement response variables of stress/strain/displacement, the initially planned study yielded 384,912 pavement response variables to be generated.

In order to minimize the total number of JULEA runs that were necessary with the original planned matrix of runs, the first steps of this initial study focused only upon the detailed analysis of all combinations associated with the use of a 60-kip single tire wheel load. After this was completed, a special single wheel load stress study of 48 JULEA runs was then conducted to see if a simplified, but accurate, estimate of the 50-kip and 70-kip wheel loads

could be made by determining a relationship for stress states of the 50-kip and 70-kip wheel loads to the 60-kip wheel load results already determined from the initial detailed JULEA runs. This special study was found to be an accurate tool for the stress prediction of the 50-kip and 70-kip wheel load; that eliminated the need for 54 separate full matrix JULEA runs. The details of this approach are presented in later portions of this chapter.

A special ID was developed to clearly identify each specific computer run conducted with JULEA. This number ID designation was based upon: (a) load magnitude, (b) gear type, (c) subgrade modulus and d) AC Temperature. Thus, a computer run ID of 60K-DT-6-90F, implied a computer run for 60,000-lb wheel load in a dual tandem gear configuration on a subgrade modulus of 6 ksi at an AC temperature of 90^{o} F. Table 6.13 presents the summary of the initially planned computer run ID description, along with the total number (x-y-z) of computational points to be evaluated under the various gear configurations at the 11 computational depths identified in Table 6.2.

Table 6.11. Summary of Pavement Layer MLET Inputs for E_{sg} = 4, 6 and 10 ksi

Layer	Parameter	AC Temperature: 30 ^{0}F			AC Temperature: 60 ^{0}F			AC Temperature: 90 ^{0}F		
Subgrade	E_4 (psi)	4000	6000	10000	4000	6000	10000	4000	6000	10000
	ν_4	0.5	0.5	0.5	0.5	0.5	0.5	0.5	0.5	0.5
	h_4 (in)	∞	∞	∞	∞	∞	∞	∞	∞	∞
P401 AC Layer	E_1 (psi)	1422000	1440000	1460000	516000	530000	549000	103000	106000	109000
	ν_1	0.2	0.2	0.2	0.3	0.3	0.3	0.45	0.45	0.45
	h_1 (in)	3.0	3.0	3.0	3.0	3.0	3.0	3.0	3.0	3.0
P209 CS Base	E_2 (psi)	42800	48250	55000	42800	48250	55000	42800	48250	55000
	ν_2	0.35	0.35	0.35	0.35	0.35	0.35	0.35	0.35	0.35
	h_2 (in)	6.0	6.0	6.0	6.0	6.0	6.0	6.0	6.0	6.0
P154 Subbase Sublayer 1	E_{31} (psi)	19700	23700	29000	19700	23700	29000	19700	23700	29000
	ν_{31}	0.40	0.40	0.40	0.40	0.40	0.40	0.40	0.40	0.40
	h_{31} (in)	10.0	10.0	10.0	10.0	10.0	10.0	10.0	10.0	10.0
P154 Subbase Sublayer 2	E_{32} (psi)	10250	13700	19400	10250	13700	19400	10250	13700	19400
	ν_{32}	0.40	0.40	0.40	0.40	0.40	0.40	0.40	0.40	0.40
	h_{32} (in)	10.0	10.0	10.0	10.0	10.0	10.0	10.0	10.0	10.0

Table 6.12. Summary of Pavement Layer MLET Inputs for E_{sg} = 20, 30, 40 ksi

Layer	Parameter	AC Temperature: 30 °F			AC Temperature: 60 °F			AC Temperature: 90 °F		
Subgrade	E_4 (psi)	20000	30000	40000	20000	30000	40000	20000	30000	40000
	ν_4	0.5	0.5	0.5	0.5	0.5	0.5	0.5	0.5	0.5
	h_4 (in)	inf	inf	inf	inf	inf	inf	inf	inf	inf
P401 AC Layer	E_1 (psi)	1480441	1492585	1500688	570966	583490	591929	112379	114433	115813
	ν_1	0.2	0.2	0.2	0.3	0.3	0.3	0.5	0.5	0.5
	h_1 (in)	3	3	3	3	3	3	3	3	3
P209 CS Base	E_2 (psi)	62207	65225	66674	62207	65225	66674	62207	65225	66674
	ν_2	0.4	0.4	0.4	0.4	0.4	0.4	0.4	0.4	0.4
	h_2 (in)	6	6	6	6	6	6	6	6	6
P154 Subbase Sublayer 1	E_{31} (psi)	35560	38547	40042	35560	38547	40042	35560	38547	40042
	ν_{31}	0.4	0.4	0.4	0.4	0.4	0.4	0.4	0.4	0.4
	h_{31} (in)	10	10	10	10	10	10	10	10	10
P154 Subbase Sublayer 2	E_{32} (psi)	29408	35871	40031	29408	35871	40031	29408	35871	40031
	ν_{32}	0.4	0.4	0.4	0.4	0.4	0.4	0.4	0.4	0.4
	h_{32} (in)	10	10	10	10	10	10	10	10	10

Table 6.13. Summary of Computer Run ID Description

Run No	Run ID Designation	Tire Load (kips)	Type Gear	E_{sg} Modulus (ksi)	AC Temp (deg F)	No of Computational Points		
						(x,y)	(z)	Total
1	50K-D-4-30F	50K	D	4	30F	3	11	33
2	50K-D-4-60F	50K	D	4	60F	3	11	33
3	50K-D-4-90F	50K	D	4	90F	3	11	33
4	50K-D-6-30F	50K	D	6	30F	3	11	33
5	50K-D-6-60F	50K	D	6	60F	3	11	33
6	50K-D-6-90F	50K	D	6	90F	3	11	33
7	50K-D-10-30F	50K	D	10	30F	3	11	33
8	50K-D-10-60F	50K	D	10	60F	3	11	33
9	50K-D-10-90F	50K	D	10	90F	3	11	33
10	60K-D-4-30F	60K	D	4	30F	3	11	33
11	60K-D-4-60F	60K	D	4	60F	3	11	33
12	60K-D-4-90F	60K	D	4	90F	3	11	33
13	60K-D-6-30F	60K	D	6	30F	3	11	33
14	60K-D-6-60F	60K	D	6	60F	3	11	33
15	60K-D-6-90F	60K	D	6	90F	3	11	33
16	60K-D-10-30F	60K	D	10	30F	3	11	33
17	60K-D-10-60F	60K	D	10	60F	3	11	33
18	60K-D-10-90F	60K	D	10	90F	3	11	33
19	70K-D-4-30F	70K	D	4	30F	3	11	33
20	70K-D-4-60F	70K	D	4	60F	3	11	33
21	70K-D-4-90F	70K	D	4	90F	3	11	33
22	70K-D-6-30F	70K	D	6	30F	3	11	33
23	70K-D-6-60F	70K	D	6	60F	3	11	33
24	70K-D-6-90F	70K	D	6	90F	3	11	33

Run No	Run ID Designation	Tire Load (kips)	Type Gear	E_{sg} Modulus (ksi)	AC Temp (deg F)	No of Computational Points		
						(x,y)	(z)	Total
25	70K-D-10-30F	70K	D	10	30F	3	11	33
26	70K-D-10-60F	70K	D	10	60F	3	11	33
27	70K-D-10-90F	70K	D	10	90F	3	11	33
28	50K-DT-4-30F	50K	DT	4	30F	9	11	99
29	50K-DT-4-60F	50K	DT	4	60F	9	11	99
30	50K-DT-4-90F	50K	DT	4	90F	9	11	99
31	50K-DT-6-30F	50K	DT	6	30F	9	11	99
32	50K-DT-6-60F	50K	DT	6	60F	9	11	99
33	50K-DT-6-90F	50K	DT	6	90F	9	11	99
34	50K-DT-10-30F	50K	DT	10	30F	9	11	99
35	50K-DT-10-60F	50K	DT	10	60F	9	11	99
36	50K-DT-10-90F	50K	DT	10	90F	9	11	99
37	60K-DT-4-30F	60K	DT	4	30F	9	11	99
38	60K-DT-4-60F	60K	DT	4	60F	9	11	99
39	60K-DT-4-90F	60K	DT	4	90F	9	11	99
40	60K-DT-6-30F	60K	DT	6	30F	9	11	99
41	60K-DT-6-60F	60K	DT	6	60F	9	11	99
42	60K-DT-6-90F	60K	DT	6	90F	9	11	99
43	60K-DT-10-30F	60K	DT	10	30F	9	11	99
44	60K-DT-10-60F	60K	DT	10	60F	9	11	99
45	60K-DT-10-90F	60K	DT	10	90F	9	11	99
46	70K-DT-4-30F	70K	DT	4	30F	9	11	99
47	70K-DT-4-60F	70K	DT	4	60F	9	11	99
48	70K-DT-4-90F	70K	DT	4	90F	9	11	99
49	70K-DT-6-30F	70K	DT	6	30F	9	11	99
50	70K-DT-6-60F	70K	DT	6	60F	9	11	99

Run No	Run ID Designation	Tire Load (kips)	Type Gear	E_{sg} Modulus (ksi)	AC Temp (deg F)	No of Computational Points		
						(x,y)	(z)	Total
51	70K-DT-6-90F	70K	DT	6	90F	9	11	99
52	70K-DT-10-30F	70K	DT	10	30F	9	11	99
53	70K-DT-10-60F	70K	DT	10	60F	9	11	99
54	70K-DT-10-90F	70K	DT	10	90F	9	11	99
55	50K-TT-4-30F	50K	TT	4	30F	9	11	99
56	50K-TT-4-60F	50K	TT	4	60F	9	11	99
57	50K-TT-4-90F	50K	TT	4	90F	9	11	99
58	50K-TT-6-30F	50K	TT	6	30F	9	11	99
59	50K-TT-6-60F	50K	TT	6	60F	9	11	99
60	50K-TT-6-90F	50K	TT	6	90F	9	11	99
61	50K-TT-10-30F	50K	TT	10	30F	9	11	99
62	50K-TT-10-60F	50K	TT	10	60F	9	11	99
63	50K-TT-10-90F	50K	TT	10	90F	9	11	99
64	60K-TT-4-30F	60K	TT	4	30F	9	11	99
65	60K-TT-4-60F	60K	TT	4	60F	9	11	99
66	60K-TT-4-90F	60K	TT	4	90F	9	11	99
67	60K-TT-6-30F	60K	TT	6	30F	9	11	99
68	60K-TT-6-60F	60K	TT	6	60F	9	11	99
69	60K-TT-6-90F	60K	TT	6	90F	9	11	99
70	60K-TT-10-30F	60K	TT	10	30F	9	11	99
71	60K-TT-10-60F	60K	TT	10	60F	9	11	99
72	60K-TT-10-90F	60K	TT	10	90F	9	11	99
73	70K-TT-4-30F	70K	TT	4	30F	9	11	99
74	70K-TT-4-60F	70K	TT	4	60F	9	11	99
75	70K-TT-4-90F	70K	TT	4	90F	9	11	99

Run No	Run ID Designation	Tire Load (kips)	Type Gear	E_{sg} Modulus (ksi)	AC Temp (deg F)	No of Computational Points		
						(x,y)	(z)	Total
76	70K-TT-6-30F	70K	TT	6	30F	9	11	99
77	70K-TT-6-60F	70K	TT	6	60F	9	11	99
78	70K-TT-6-90F	70K	TT	6	90F	9	11	99
79	70K-TT-10-30F	70K	TT	10	30F	9	11	99
80	70K-TT-10-60F	70K	TT	10	60F	9	11	99
81	70K-TT-10-90F	70K	TT	10	90F	9	11	99

Run No	Run ID	Tire Load	Type Gear	Esg Modulus	AC Temp	No of Computational Points		
	Designation	(kips)		(ksi)	(deg F)	(x,y)	(z)	Total
V10	60K-D-20-30F	60K	D	20	30F	3	11	33
V11	60K-D-20-60F	60K	D	20	60F	3	11	33
V12	60K-D-20-90F	60K	D	20	90F	3	11	33
V13	60K-D-30-30F	60K	D	30	30F	3	11	33
V14	60K-D-30-60F	60K	D	30	60F	3	11	33
V15	60K-D-30-90F	60K	D	30	90F	3	11	33
V16	60K-D-40-30F	60K	D	40	30F	3	11	33
V17	60K-D-40-60F	60K	D	40	60F	3	11	33
V18	60K-D-40-90F	60K	D	40	90F	3	11	33
V37	60K-DT-20-30F	60K	DT	20	30F	9	11	99
V38	60K-DT-20-60F	60K	DT	20	60F	9	11	99
V39	60K-DT-20-90F	60K	DT	20	90F	9	11	99
V40	60K-DT-30-30F	60K	DT	30	30F	9	11	99
V41	60K-DT-30-60F	60K	DT	30	60F	9	11	99

Run No	Run ID	Tire Load	Type Gear	Esg Modulus	AC Temp	No of Computational Points		
	Designation	(kips)		(ksi)	(deg F)	(x,y)	(z)	Total
V42	60K-DT-30-90F	60K	DT	30	90F	9	11	99
V43	60K-DT-40-30F	60K	DT	40	30F	9	11	99
V44	60K-DT-40-60F	60K	DT	40	60F	9	11	99
V45	60K-DT-40-90F	60K	DT	40	90F	9	11	99
V64	60K-TT-20-30F	60K	TT	20	30F	9	11	99
V65	60K-TT-20-60F	60K	TT	20	60F	9	11	99
V66	60K-TT-20-90F	60K	TT	20	90F	9	11	99
V67	60K-TT-30-30F	60K	TT	30	30F	9	11	99
V68	60K-TT-30-60F	60K	TT	30	60F	9	11	99
V69	60K-TT-30-90F	60K	TT	30	90F	9	11	99
V70	60K-TT-40-30F	60K	TT	40	30F	9	11	99
V71	60K-TT-40-60F	60K	TT	40	60F	9	11	99
V72	60K-TT-40-90F	60K	TT	40	90F	9	11	99

As previously noted, the most significant stress states, along with their computational depths are shown in Table 6.14.

Table 6.14. Stress Critical Variables and Computational Depths used in JULEA Runs

Layer	Stress variable	Z computational depths
Base	σ_x, σ_y, σ_z (θ)	6.0”
Subbase No 1	σ_x, σ_y, σ_z (θ)	14.0”
Subbase No 2	σ_x, σ_y, σ_z (θ)	24.0”
Dupont clay	τ_{oct}	29.0”, 42.5”, 69.5”, 83.0”
County clay		98.25”, 128.75”, 144.0”

Assumptions Made for JULEA Analysis

It is important to understand that the calculations presented in this study are for a special case, where the pavement is enclosed in a hangar and therefore, the temperature and climatic conditions do not directly affect the asphalt layer in the pavement system. Considering the special case situation, the following were the assumptions made in the MLET analysis:

1) The pavement layers were assumed to be homogenous and isotropic for the given depth.
2) The modulus of the pavement layers was considered to be the same for both horizontal and vertical direction for a given depth.
3) The deformation occurring due to the tire load applied was not considered during the calculation of the stresses.

4) The Poisson's ratio of the base, subbase and subgrade layer was assumed to be constant for all temperatures, whereas the Poisson's ratio for the AC layer varied with temperature.
5) The stresses were calculated at the 3 inches for AC layer and the mid depth of each layer.

Limitation and Concerns of the Assumptions Made in the MLET Analysis.

Since the research objective deals with a special case study, the assumptions made are related to this special conditions. There are a few concerns or limitations which are discussed in this section.

The analysis of MLET considers the pavement layers to be homogenous and isotropic. In order to analyze heterogeneous layers (modulus varying radially and vertically); a finite element (FE) analysis needs to be performed. Though using FEM could provide a more accurate prediction of results, the FEM analysis will require a substantial amount of time for the 164 runs that were initially planned. Hence, a pseudo nonlinear elastic (MLET) analysis was considered, as it provided the results regarding the relative effect of temperature on the stress state needed, in a reasonable amount of time. In addition, only the vertical stress effect was of interest in this study, and therefore the MLET advantages outweigh the disadvantages.

The Poisson's ratio for different materials varies with temperature, and the magnitude of the variation differs from material to material. The estimated Poisson's ratio ranges for different pavement materials due to seasonal changes in temperature is shown in Table 6.15 (Maher et al, 2008). As it can be seen, the maximum variation of the Poisson's ratio occurs in the AC layer.

Table 6.15. Range of Poisson Ratio for Pavement Layers

Layer	Range of Poisson's ratio
AC layer	0.2-0.5
Granular base	0.3-0.4
Subbase	0.35-0.45
Subgrade	0.4-0.5

In addition, the stiffness of the layers depends largely on the modulus and thickness of the layer: and hence, the variation of Poisson's ratio causes a minimum effect on the variation of base and subbase layers's stiffness. The stiffness of the layer is found using the following equation.

$$Stiffness = \sqrt[3]{\frac{Eh^3}{12(1-\mu^2)}}$$

Where, E is the modulus of the layer, h is the thickness and μ is the Poisson's ratio. The equation shows the influence of Poisson's ratio on the calculation of the stiffness of the layer.

As the AC layer thickness was just three inches thick, the consideration of the modulus at 1.5 inches or 3 inches does not make a big difference. It is to be noted that the thickness of the AC layer for the NAPTF study is much smaller than that of an actual airfield pavement system. As the thickness of the AC layer is small, the temperature variation between the mid and the bottom of the AC layer is not considerably large. Also, since the range in temperatures experienced inside the hangar is smaller than the range experience by a

pavement under normal environmental conditions, the assumption that the modulus of the AC layer is constant through the 3 inches is reasonable.

The time period considered for this study also contributes to the validity of the assumption made. The time period considered for this study was just 2.5 years. With no solar radiation or any other climatic condition affecting the pavement structure, the aging effect of the AC layer was also considered to be negligible.

STATISTICAL MODELING OF STRESS RESULTS

Octahedral Shear Stress Analysis (60-kip wheel load)

The summary analysis of the octahedral shear stress occurring within the chosen computational depths within the two subgrade clay soils (Dupont clay and County clay) are shown in Table 6.16 for dual wheel, Table 6.17 for dual tandem, and Table 6.18 for triple tandem. As can be observed, the specific τ_{oct} stress values, at a given depth (z) and at the (x-y) computational locations under the gear type are identified. The extreme right hand column identifies the maximum octahedral shear stress occurring, at a given depth (z) under the gear, in x-y space. These tables present the summary of the maximum τ_{oct} values used in the next section of this chapter to develop τ_{oct}-z (depth) models that are eventually used in the non-linear M_r evaluation for the clay subgrade materials.

Table 6.19 presents a summary of the maximum octahedral shear stress, under a given gear type, as function of each depth (z), evaluated for all of the computer runs solutions for the 60-kip wheel load.

Table 6.16. Octahedral Shear Stress Analysis for Dual Wheel Gear Load

Gear Type	Temp AC (deg F)	Esr (ksi)	Run No	z (depth) (in)	Octahedral Shear Stress (ksi) for x,r Computational Points: (0,0)	(13.5,0)	(27,0)	(0,14.25)	(13.5,14.25)	(27,14.25)	(0,28.5)	(13.5,28.5)	(27,28.5)	(0,42.75)	(13.5,42.75)	(27,42.75)	(0,57)	(13.5,57)	(27,57)	Max Oct Shear (ksi)
D	30	4	10	29.00	4.13	4.45	3.81													4.45
	30	4		42.50	3.48	3.41	3.30													3.48
	30	4		69.50	2.16	2.24	2.26													2.26
	30	4		83.00	1.79	1.85	1.88													1.88
	30	4		98.25	1.47	1.52	1.54													1.54
	30	4		128.75	1.04	1.07	1.08													1.08
	30	4		144.00	0.89	0.91	0.92													0.92
	30	6	11	29.00	5.77	4.90	4.08													5.77
	30	6		42.50	3.85	3.75	3.58													3.85
	30	6		69.50	2.33	2.41	2.44													2.44
	30	6		83.00	1.91	1.98	2.01													2.01
	30	6		98.25	1.56	1.62	1.64													1.64
	30	6		128.75	1.09	1.12	1.13													1.13
	30	6		144.00	0.93	0.95	0.96													0.96
	30	10	12	29.00	6.69	5.54	4.44													6.69
	30	10		42.50	4.37	4.17	3.96													4.37
	30	10		69.50	2.56	2.66	2.69													2.69
	30	10		83.00	2.08	2.17	2.19													2.19
	30	10		98.25	1.68	1.75	1.77													1.77
	30	10		128.75	1.16	1.19	1.20													1.2
	30	10		144.00	0.98	1.00	1.01													1.01
	60	4	13	29.00	5.60	4.70	3.88													5.6
	60	4		42.50	3.70	3.58	3.43													3.7
	60	4		69.50	2.27	2.35	1.37													2.35
	60	4		83.00	1.87	1.94	1.97													1.97
	60	4		98.25	1.54	1.59	1.61													1.61
	60	4		128.75	1.08	1.11	1.12													1.12
	60	4		144.00	0.92	0.95	0.95													0.95
	60	6	14	29.00	6.27	5.16	4.14													6.27
	60	6		42.50	4.08	3.91	3.71													4.08
	60	6		69.50	2.44	2.53	2.56													2.56
	60	6		83.00	2.00	2.08	2.10													2.1
	60	6		98.25	1.63	1.69	1.71													1.71
	60	6		128.75	1.13	1.16	1.17													1.17
	60	6		144.00	0.96	0.98	0.99													0.99
	60	10	15	29.00	7.25	5.82	4.47													7.25
	60	10		42.50	4.62	4.35	4.08													4.62
	60	10		69.50	2.68	2.77	2.80													2.8
	60	10		83.00	2.17	2.26	2.29													2.29
	60	10		98.25	1.75	1.82	1.84													1.84
	60	10		128.75	1.20	1.23	1.24													1.24
	60	10		144.00	1.01	1.04	1.04													1.04
	90	4	16	29.00	6.38	5.15	4.05													6.38
	90	4		42.50	4.17	3.98	3.76													4.17
	90	4		69.50	2.55	2.64	2.67													2.67
	90	4		83.00	2.10	2.18	2.21													2.21
	90	4		98.25	1.71	1.78	1.80													1.8
	90	4		128.75	1.19	1.22	1.23													1.23
	90	4		144.00	1.01	1.03	1.04													1.04
	90	6	17	29.00	7.13	5.64	4.28													7.13
	90	6		42.50	4.58	4.32	4.04													4.58
	90	6		69.50	2.72	2.82	2.85													2.85
	90	6		83.00	2.23	2.32	2.35													2.35
	90	6		98.25	1.80	1.87	1.90													1.9
	90	6		128.75	1.24	1.28	1.29													1.29
	90	6		144.00	1.05	1.07	1.08													1.08
	90	10	18	29.00	8.21	6.35	4.59													8.21
	90	10		42.50	5.16	4.77	4.39													5.16
	90	10		69.50	2.96	3.07	3.10													3.1
	90	10		83.00	2.39	2.49	2.53													2.53
	90	10		98.25	1.92	2.00	2.02													2.02
	90	10		128.75	1.30	1.34	1.35													1.35
	90	10		144.00	1.09	1.12	1.13													1.13

Table 6.17. Octahedral Shear Stress Analysis for Dual Tandem Wheel Gear Load

Gear Type	Temp AC (deg F)	Esg (ksi)	Run No	z (depth) (in)	Octahedral Shear Stress (psi) for x,y Computational Points									Max Oct Shear (psi)
					(0,0)	(13.5,0)	(27,0)	(0,14.25)	(13.5,14.25)	(27,14.25)	(0,28.5)	(13.5,28.5)	(27,28.5)	
DT	30	4	37	29.00	5.27	4.82	4.17	4.71	4.11	3.66	3.95	3.58	3.34	5.27
	30	4		42.50	4.34	4.26	4.15	4.21	4.13	4.06	4.07	4.02	3.96	4.34
	30	4		69.50	3.23	3.34	3.37	3.34	3.44	3.48	3.37	3.47	3.50	3.5
	30	4		83.00	2.83	2.92	2.95	2.93	3.03	3.06	2.96	3.06	3.09	3.09
	30	4		98.25	2.44	2.51	2.54	2.52	2.60	2.62	2.55	2.63	2.65	2.65
	30	4		128.75	1.83	1.88	1.89	1.88	1.92	1.93	1.89	1.94	1.96	1.96
	30	4		144.00	1.60	1.63	1.64	1.63	1.67	1.68	1.65	1.68	1.69	1.69
	30	6	38	29.00	6.10	5.15	4.31	5.01	4.24	3.65	4.09	3.53	3.24	6.1
	30	6		42.50	4.62	4.52	4.37	4.46	4.34	4.21	4.26	4.17	4.07	4.62
	30	6		69.50	3.42	3.53	3.56	3.52	3.64	3.67	3.55	3.67	3.70	3.7
	30	6		83.00	2.98	3.08	3.11	3.08	3.19	3.23	3.12	3.23	3.26	3.26
	30	6		98.25	2.56	2.64	2.67	2.65	2.73	2.76	2.67	2.76	2.79	2.79
	30	6		128.75	1.90	1.95	1.97	1.96	2.00	2.02	1.97	2.02	2.04	2.04
	30	6		144.00	1.62	1.69	1.70	1.69	1.73	1.74	1.71	1.74	1.76	1.76
	30	10	39	29.00	6.87	5.29	4.42	5.44	4.39	3.56	4.18	3.43	2.99	6.87
	30	10		42.50	5.09	4.85	4.63	4.78	4.56	4.37	4.49	4.31	4.15	5.09
	30	10		69.50	3.66	3.78	3.81	3.77	3.89	3.93	3.80	3.92	3.95	3.95
	30	10		83.00	3.18	3.29	3.33	3.29	3.41	3.45	3.33	3.45	3.49	3.49
	30	10		98.25	2.71	2.81	2.84	2.81	2.91	2.94	2.84	2.94	2.98	2.98
	30	10		128.75	2.00	2.05	2.07	2.06	2.11	2.13	2.08	2.13	2.15	2.15
	30	10		144.00	1.73	1.77	1.78	1.77	1.81	1.83	1.79	1.83	1.84	1.84
	60	4	40	29.00	5.95	4.96	4.13	4.84	4.08	3.52	3.92	3.43	3.15	5.95
	60	4		42.50	4.52	4.38	4.23	4.33	4.22	4.10	4.14	4.06	3.98	4.52
	60	4		69.50	3.35	3.46	3.50	3.46	3.57	3.60	3.49	3.60	3.63	3.63
	60	4		83.00	2.94	3.04	3.07	3.04	3.14	3.18	3.08	3.18	3.21	3.21
	60	4		98.25	2.53	2.61	2.64	2.62	2.70	2.73	2.65	2.73	2.76	2.76
	60	4		128.75	1.90	1.94	1.96	1.95	1.99	2.01	1.96	2.01	2.03	2.03
	60	4		144.00	1.65	1.69	1.70	1.69	1.73	1.74	1.70	1.74	1.75	1.75
	60	6	41	29.00	6.51	5.29	4.24	5.15	4.19	3.47	4.00	3.37	3.01	6.51
	60	6		42.50	4.83	4.63	4.43	4.57	4.39	4.23	4.31	4.18	4.07	4.83
	60	6		69.50	3.54	3.65	3.69	3.65	3.76	3.79	3.68	3.79	3.82	3.82
	60	6		83.00	3.09	3.20	3.23	3.20	3.31	3.35	3.23	3.35	3.38	3.38
	60	6		98.25	2.65	2.74	2.77	2.74	2.83	2.87	2.78	2.87	2.90	2.9
	60	6		128.75	1.97	2.02	2.04	2.03	2.08	2.10	2.04	2.10	2.11	2.11
	60	6		144.00	1.71	1.75	1.76	1.75	1.79	1.80	1.77	1.81	1.82	1.82
	60	10	42	29.00	7.33	5.74	4.52	5.58	4.33	3.33	4.06	3.21	2.69	7.33
	60	10		42.50	5.27	4.95	4.67	4.87	4.59	4.36	4.52	4.29	4.12	5.27
	60	10		69.50	3.78	3.90	3.93	3.89	4.01	4.04	3.92	4.03	4.06	4.06
	60	10		83.00	3.29	3.40	3.44	3.40	3.53	3.57	3.44	3.57	3.61	3.61
	60	10		98.25	2.91	2.91	2.94	2.91	3.01	3.04	2.94	3.04	3.08	3.08
	60	10		128.75	2.07	2.12	2.14	2.13	2.18	2.20	2.15	2.20	2.22	2.22
	60	10		144.00	1.78	1.83	1.84	1.83	1.87	1.89	1.84	1.89	1.90	1.9
	90	4	43	29.00	6.23	5.17	4.03	5.03	4.01	3.25	3.80	3.13	2.75	6.23
	90	4		42.50	4.88	4.65	4.43	4.58	4.39	4.22	4.31	4.17	4.06	4.88
	90	4		69.50	3.67	3.78	3.82	3.78	3.89	3.93	3.81	3.92	3.96	3.96
	90	4		83.00	3.21	3.33	3.36	3.33	3.43	3.49	3.37	3.49	3.52	3.52
	90	4		98.25	2.77	2.86	2.89	2.86	2.96	2.99	2.90	3.00	3.03	3.03
	90	4		128.75	2.06	2.11	2.13	2.12	2.17	2.19	2.14	2.19	2.21	2.21
	90	4		144.00	1.78	1.83	1.84	1.83	1.87	1.89	1.84	1.89	1.90	1.9
	90	6	44	29.00	7.15	5.52	4.11	5.36	4.11	3.13	3.84	3.01	2.52	7.15
	90	6		42.50	5.21	4.89	4.60	4.81	4.54	4.31	4.48	4.23	4.09	5.21
	90	6		69.50	3.85	3.97	4.00	3.96	4.08	4.11	3.99	4.10	4.13	4.13
	90	6		83.00	3.36	3.48	3.52	3.48	3.61	3.65	3.52	3.63	3.69	3.69
	90	6		98.25	2.88	2.98	3.01	2.99	3.09	3.13	3.02	3.13	3.17	3.17
	90	6		128.75	2.13	2.19	2.20	2.19	2.23	2.27	2.21	2.27	2.29	2.29
	90	6		144.00	1.84	1.88	1.90	1.89	1.93	1.95	1.90	1.95	1.96	1.96
	90	10	45	29.00	8.08	6.04	4.18	5.86	4.27	2.94	3.87	2.79	2.08	8.08
	90	10		42.50	5.66	5.20	4.80	5.10	4.69	4.37	4.61	4.29	4.06	5.66
	90	10		69.50	4.07	4.19	4.23	4.18	4.30	4.33	4.20	4.32	4.34	4.34
	90	10		83.00	3.54	3.67	3.71	3.67	3.80	3.85	3.71	3.83	3.89	3.89
	90	10		98.25	3.02	3.13	3.17	3.14	3.25	3.29	3.17	3.29	3.33	3.33
	90	10		128.75	2.21	2.27	2.29	2.28	2.35	2.37	2.30	2.37	2.39	2.39
	90	10		144.00	1.90	1.95	1.97	1.96	2.00	2.02	1.97	2.02	2.04	2.04

Table 6.18. Octahedral Shear Stress Analysis for Triple Tandem Wheel Gear Load

Gear Type	Temp AC (deg F)	Esg (ksi)	Run No	z (depth) (in)	Octahedral Shear Stress (psi) for x,z Computational Points																Max Oct Shear (psi)
					(0,0)	(13.5,0)	(27,0)	(0,14.25)	(13.5,14.25)	(27,14.25)	(0,28.5)	(13.5,28.5)	(27,28.5)	(0,42.75)	(13.5,42.75)	(27,42.75)	(0,57)	(13.5,57)	(27,57)	
TT	30	4	64	29.00	3.53	4.75	4.10	4.62	3.99	3.54	4.10	3.62	3.35	4.99	4.28	3.75	5.70	4.79	4.06	5.70
	30	4		42.50	4.46	4.56	4.26	4.34	4.25	4.16	4.30	4.21	4.14	4.56	4.45	4.34	4.75	4.69	4.47	4.75
	30	4		69.50	3.56	3.67	3.70	3.72	3.82	3.85	3.82	3.93	3.96	3.90	4.01	4.04	3.93	4.03	4.07	4.07
	30	4		83.00	3.22	3.31	3.34	3.37	3.47	3.51	3.48	3.58	3.62	3.54	3.65	3.68	3.57	3.67	3.70	3.70
	30	4		98.25	2.86	2.94	2.97	3.00	3.08	3.11	3.09	3.18	3.21	3.15	3.24	3.27	3.17	3.26	3.29	3.29
	30	4		128.75	2.26	2.31	2.23	2.35	2.41	2.42	2.43	2.48	2.50	2.47	2.52	2.54	2.49	2.54	2.56	2.56
	30	4		144.00	2.01	2.05	2.06	2.09	2.13	2.14	2.15	2.19	2.21	2.19	2.23	2.24	2.20	2.24	2.26	2.26
	30	6	65	29.00	6.03	5.04	4.20	4.89	4.08	3.47	4.18	3.58	3.22	4.18	3.58	3.22	6.15	5.01	4.06	6.15
	30	6		42.50	4.74	4.59	4.43	4.54	4.40	4.27	4.45	4.32	4.21	4.45	4.32	4.21	5.01	4.79	4.60	5.01
	30	6		69.50	3.75	3.84	3.87	3.88	3.99	4.03	3.99	4.10	4.13	3.99	4.10	4.13	4.10	4.21	4.24	4.24
	30	6		83.00	3.36	3.46	3.49	3.52	3.63	3.66	3.63	3.74	3.77	3.63	3.74	3.77	3.71	3.82	3.86	3.86
	30	6		98.25	2.97	3.06	3.09	3.12	3.21	3.33	3.22	3.31	3.34	3.22	3.31	3.34	3.30	3.39	3.42	3.42
	30	6		128.75	2.24	2.38	2.40	2.43	2.49	2.51	2.51	2.57	2.59	2.51	2.57	2.59	2.57	2.63	2.65	2.65
	30	6		144.00	2.07	2.11	2.12	2.15	2.20	2.21	2.22	2.26	2.27	2.22	2.26	2.28	2.27	2.32	2.33	2.33
	30	10	66	29.00	6.77	5.45	4.30	5.27	4.16	3.50	4.26	3.64	2.93	5.68	4.49	3.55	6.81	5.31	4.02	6.81
	30	10		42.50	5.13	4.87	4.65	4.80	4.56	4.36	4.63	4.40	4.23	5.04	4.75	4.52	5.35	5.01	4.73	5.35
	30	10		69.50	3.95	4.06	4.09	4.10	4.21	4.25	4.20	4.32	4.34	4.28	4.39	4.42	4.31	4.42	4.44	4.44
	30	10		83.00	3.54	3.65	3.69	3.70	3.82	3.86	3.81	3.93	3.97	3.88	4.00	4.03	3.90	4.02	4.06	4.06
	30	10		98.25	3.12	3.21	3.24	3.27	3.37	3.40	3.37	3.48	3.51	3.44	3.54	3.58	3.46	3.56	3.60	3.60
	30	10		128.75	2.42	2.48	2.50	2.53	2.60	2.62	2.61	2.68	2.70	2.67	2.73	2.75	2.68	2.75	2.77	2.77
	30	10		144.00	2.14	2.19	2.20	2.24	2.28	2.30	2.30	2.35	2.37	2.35	2.40	2.41	2.36	2.41	2.43	2.43
	60	4	67	29.00	5.88	4.86	4.02	4.71	3.92	3.34	4.02	3.46	3.13	5.12	4.23	3.57	6.03	4.85	3.91	6.03
	60	4		42.50	4.60	4.45	4.30	4.41	4.28	4.16	4.33	4.22	4.13	4.65	4.48	4.34	4.89	4.67	4.48	4.89
	60	4		69.50	3.67	3.77	3.81	3.82	3.93	3.96	3.93	4.04	4.07	4.01	4.12	4.15	4.04	4.15	4.18	4.18
	60	4		83.00	3.31	3.42	3.45	3.48	3.58	3.62	3.59	3.69	3.73	3.65	3.76	3.80	3.68	3.78	3.82	3.82
	60	4		98.25	2.95	3.03	3.06	3.09	3.18	3.21	3.19	3.28	3.32	3.25	3.35	3.38	3.27	3.37	3.40	3.40
	60	4		128.75	2.32	2.38	2.39	2.43	2.48	2.50	2.50	2.56	2.58	2.55	2.61	2.63	2.56	2.26	2.64	2.64
	60	4		144.00	2.07	2.11	2.12	2.15	2.20	2.21	2.21	2.26	2.28	2.25	2.30	2.32	2.27	2.31	2.33	2.33
	60	6	68	29.00	6.41	5.16	4.09	4.99	3.98	3.23	4.08	3.37	2.95	5.41	4.31	3.47	6.50	5.07	3.88	6.50
	60	6		42.50	4.89	4.67	4.46	4.61	4.41	4.24	4.47	4.30	4.17	4.85	4.61	4.41	5.14	4.84	4.59	5.14
	60	6		69.50	3.83	3.94	3.98	3.99	4.10	4.13	4.10	4.20	4.23	4.18	4.28	4.31	4.21	4.32	4.35	4.35
	60	6		83.00	3.45	3.56	3.60	3.62	3.73	3.77	3.73	3.85	3.88	3.80	3.91	3.95	3.82	3.94	3.97	3.97
	60	6		98.25	3.06	3.15	3.18	3.21	3.31	3.34	3.32	3.41	3.45	3.38	3.48	3.51	3.40	3.50	3.53	3.53
	60	6		128.75	2.40	2.45	2.47	2.51	2.56	2.59	2.58	2.65	2.67	2.63	2.70	2.72	2.65	2.71	2.73	2.73
	60	6		144.00	2.13	2.17	2.19	2.22	2.26	2.28	2.28	2.33	2.35	2.32	2.37	2.39	2.34	2.39	2.40	2.40
	60	10	69	29.00	7.20	5.58	4.16	5.39	4.08	3.03	4.14	3.20	2.61	5.82	4.42	3.29	7.20	5.37	3.79	7.20
	60	10		42.50	5.28	4.94	4.65	4.86	4.54	4.30	4.63	4.35	4.16	5.11	4.75	4.46	5.49	5.04	4.69	5.49
	60	10		69.50	4.05	4.16	4.19	4.20	4.31	4.34	4.30	4.41	4.44	4.38	4.49	4.51	4.42	4.52	4.55	4.55
	60	10		83.00	3.64	3.75	3.79	3.81	3.93	3.97	3.92	4.04	4.08	3.98	4.10	4.14	4.01	4.13	4.16	4.16
	60	10		98.25	3.21	3.31	3.34	3.36	3.47	3.50	3.47	3.58	3.62	3.54	3.64	3.68	3.56	3.66	3.70	3.70
	60	10		128.75	2.49	2.55	2.57	2.61	2.67	2.69	2.69	2.76	2.78	2.74	2.81	2.84	2.76	2.83	2.85	2.85
	60	10		144.00	2.20	2.25	2.27	2.30	2.35	2.37	2.37	2.42	2.44	2.41	2.47	2.48	2.43	2.48	2.50	2.50
	90	4	70	29.00	6.40	5.01	3.86	4.85	3.77	2.98	3.85	3.12	2.66	5.25	4.08	3.20	6.45	4.87	3.58	6.45
	90	4		42.50	4.90	4.66	4.43	4.59	4.37	4.19	4.43	4.24	4.11	4.83	4.57	4.36	5.14	4.80	4.53	5.14
	90	4		69.50	3.94	4.05	4.08	4.09	4.20	4.24	4.21	4.31	4.34	4.29	4.40	4.43	4.33	4.44	4.47	4.47
	90	4		83.00	3.56	3.68	3.72	3.74	3.86	3.90	3.86	3.98	4.01	3.93	4.05	4.09	3.95	4.07	4.11	4.11
	90	4		98.25	3.17	3.27	3.30	3.33	3.43	3.46	3.44	3.54	3.58	3.51	3.61	3.65	3.53	3.63	3.67	3.67
	90	4		128.75	2.49	2.55	2.57	2.60	2.67	2.69	2.69	2.75	2.78	2.74	2.81	2.83	2.76	2.82	2.85	2.85
	90	4		144.00	2.21	2.26	2.27	2.30	2.35	2.37	2.37	2.42	2.44	2.42	2.47	2.49	2.43	2.48	2.50	2.50
	90	6	71	29.00	7.01	5.34	3.91	5.16	3.85	2.82	3.89	2.98	2.40	5.56	4.16	3.04	6.99	5.11	3.51	7.01
	90	6		42.50	5.20	4.86	4.57	4.77	4.46	4.23	4.54	4.28	4.09	5.02	4.66	4.39	5.39	4.95	4.60	5.39
	90	6		69.50	4.10	4.21	4.24	4.25	4.36	4.39	4.35	4.46	4.49	4.44	4.55	4.58	4.48	4.59	4.62	4.62
	90	6		83.00	3.70	3.82	3.86	3.87	4.00	4.04	3.99	4.12	4.16	4.06	4.19	4.23	4.09	4.21	4.25	4.25
	90	6		98.25	3.28	3.38	3.41	3.44	3.55	3.58	3.55	3.66	3.70	3.62	3.73	3.77	3.64	3.76	3.79	3.79
	90	6		128.75	2.56	2.62	2.64	2.68	2.74	2.77	2.76	2.83	2.86	2.82	2.89	2.91	2.84	2.91	2.93	2.93
	90	6		144.00	2.26	2.31	2.33	2.36	2.41	2.43	2.44	2.49	2.51	2.48	2.54	2.56	2.50	2.55	2.57	2.57
	90	10	72	29.00	7.93	5.83	3.94	5.65	3.99	2.57	3.94	2.78	1.97	6.04	4.30	2.82	7.81	5.49	3.37	7.93
	90	10		42.50	5.62	5.13	4.72	5.01	4.56	4.23	4.66	4.27	4.01	5.26	4.75	4.38	5.74	5.12	4.64	5.74
	90	10		69.50	4.29	4.40	4.44	4.43	4.54	4.56	4.53	4.60	4.66	4.62	4.72	4.74	4.67	4.76	4.79	4.79
	90	10		83.00	3.86	3.98	4.03	4.04	4.17	4.21	4.15	4.29	4.32	4.22	4.35	4.39	4.25	4.37	4.41	4.41
	90	10		98.25	3.41	3.52	3.55	3.58	3.69	3.73	3.69	3.81	3.85	3.76	3.88	3.92	3.78	3.90	3.94	3.94
	90	10		128.75	2.64	2.71	2.73	2.76	2.84	2.86	2.86	2.93	2.96	2.91	2.99	3.02	2.93	3.01	3.03	3.03
	90	10		144.00	2.33	2.38	2.40	2.43	2.49	2.51	2.51	2.57	2.59	2.56	2.62	2.64	2.57	2.63	2.65	2.65

Table 6.19. Summary of Maximum Octahedral Shear Stress Under Gear for 60 kips Tire Load

Tire Load (kips)	Gear Type	Temp AC (deg F)	E_{sg} (ksi)	Run No	Maximum Octahedral Shear Stress at Depth (z-in) Shown						
					29	42.5	69.5	83	98.25	128.75	144
60	D	30	4	10	4.45	3.48	2.26	1.88	1.54	1.08	0.92
			6	11	5.77	3.85	2.44	2.01	1.64	1.13	0.96
			10	12	6.69	4.37	2.69	2.19	1.77	1.2	1.01
		60	4	13	5.6	3.7	2.35	1.97	1.61	1.12	0.95
			6	14	6.27	4.08	2.56	2.1	1.71	1.17	0.99
			10	15	7.25	4.62	2.8	2.29	1.84	1.24	1.04
		90	4	16	6.38	4.17	2.67	2.21	1.8	1.23	1.04
			6	17	7.13	4.58	2.85	2.35	1.9	1.29	1.08
			10	18	8.21	5.16	3.1	2.53	2.02	1.35	1.13
60	DT	30	4	37	5.57	4.34	3.5	3.09	2.65	1.96	1.69
			6	38	6.1	4.65	3.7	3.26	2.79	2.04	1.76
			10	39	6.87	5.09	3.95	3.49	2.98	2.15	1.84
		60	4	40	5.95	4.52	3.63	3.21	2.76	2.03	1.75
			6	41	6.51	4.83	3.82	3.38	2.9	2.11	1.82
			10	42	7.33	5.27	4.06	3.61	3.08	2.22	1.9
		90	4	43	6.53	4.88	3.96	3.52	3.03	2.21	1.9
			6	44	7.15	5.21	4.13	3.69	3.17	2.29	1.96
			10	45	8.08	5.66	4.34	3.89	3.33	2.39	2.04
60	TT	30	4	64	5.7	4.75	4.07	3.7	3.29	2.56	2.26
			6	65	6.15	5.01	4.24	3.86	3.42	2.65	2.33
			10	66	6.81	5.35	4.44	4.06	3.6	2.77	2.43
		60	4	67	6.03	4.89	4.18	3.82	3.4	2.64	2.33
			6	68	6.5	5.14	4.35	3.97	3.53	2.73	2.4
			10	69	7.2	5.49	4.55	4.16	3.7	2.85	2.5
		90	4	70	6.45	5.14	4.47	4.11	3.67	2.85	2.5
			6	71	7.01	5.39	4.62	4.21	3.79	2.93	2.57
			10	72	7.93	5.74	4.79	4.41	3.94	3.03	2.65
60	D	30	20	V10	9.17	5.86	3.24	2.57	2.03	1.35	1.12
			30	V11	10.3	6.5	3.5	2.76	2.16	1.41	1.17

			40	V12	11.1	6.97	3.7	2.89	2.25	1.46	1.2
		60	20	V13	9.87	6.16	3.36	2.67	2.1	1.39	1.16
			30	V14	11.1	6.81	3.62	2.84	2.22	1.45	1.2
			40	V15	8.09	5.17	2.95	2.38	1.91	1.29	1.09
		90	20	V16	11.1	6.8	3.66	2.89	2.27	1.48	1.23
			30	V17	12.4	7.45	3.88	3.03	2.36	1.53	1.26
			40	V18	13.4	7.93	4.04	3.13	2.42	1.55	1.28
60	DT	30	20	V37	8.81	6.19	4.58	4.07	3.45	2.45	2.08
			30	V38	9.73	6.66	4.79	4.26	3.62	2.55	2.16
			40	V39	10.4	7	4.92	4.39	3.74	2.62	2.21
		60	20	V40	9.42	6.41	4.68	4.18	3.55	2.52	2.14
			30	V41	10.4	6.89	4.86	4.35	3.71	2.61	2.21
			40	V42	11.2	7.24	4.99	4.47	3.81	2.68	2.26
		90	20	V43	10.4	6.86	4.91	4.42	3.78	2.67	2.26
			30	V44	11.6	7.35	5.05	4.54	3.89	2.74	2.31
			40	V45	12.5	7.72	5.13	4.62	3.96	2.78	2.34
60	TT	30	20	V64	8.88	6.7	5.31	4.84	4.26	3.22	2.79
			30	V65	9.68	7.08	5.51	5.02	4.42	3.34	2.88
			40	V66	10.3	7.34	5.63	5.14	4.53	3.41	2.95
		60	20	V67	9.41	6.86	5.41	4.94	4.36	3.3	2.86
			30	V68	10.3	7.24	5.58	5.1	4.51	3.41	2.94
			40	V69	11.1	7.53	5.69	5.21	4.6	3.47	3
		90	20	V70	10.3	7.19	5.63	5.17	4.58	3.46	3
			30	V71	11.5	7.6	5.75	5.29	4.69	3.54	3.06
			40	V72	12.4	7.91	5.83	5.36	4.75	3.58	3.09

Dual Gear Analysis

The individual τ_{oct}- z plots for each combination of AC Temperature (or E*) and E_{sg} subgrade modulus are illustrated in Figure 6.7 for the dual gear results. For this gear type, it can be seen that the relationship of τ_{oct}- z is a power model, with excellent statistical fitting properties of the form:

$$\boldsymbol{\tau_{oct} = a\, z^{-b}}$$

Table 6.20 is the summary of the individual regression constants (*a* and *b*), along with R^2 correlation found. This is shown on the left hand side of the table. Further mathematical analysis of these results, as well as for all other gear type results, showed that the E_{sg} influence could be normalized by developing a new coefficient, β_i, such that:

$$\beta_i = \frac{X\,(T)}{X\,(T = 60^o F)}$$

Furthermore, this approach was found to be valid for both the *a* and *b* regression constant values shown in Table 6.20. This analysis is shown in the right hand side of this table. For all practical purposes, the individual β_i factors (β_a and β_b), along with the overall average of β_a and β_b parameters for each temperature are shown in the table.

Figure 6.8 represents the individual regression plots of a-E_{sg} and b-E_{sg} at T= 60°F along with the normalized plots of the β_a and β_b – T regressions.

The final summary of the regression models developed for the 60-kip dual gear are as follows:

$a_{60} = 62.031\ E_{sg}^{0.8682}$ $\qquad\qquad$ $R^2 = 0.998$

$b_{60} = 0.9044\ E_{sg}^{0.1243}$ $R^2 = 1.0000$

$\beta_a = 0.6978\ e^{0.0063T}$ $R^2 = 0.9973$

$\beta_b = -7.10e\text{-}6T^2 + 1.82e\text{-}3T + 0.961$ $R^2 = 1.0000$

Recognizing that $A' = a_{60}\beta_a$ and $B' = b_{60}\beta_b$ and $\tau_{oct} = A' z^{-B'}$, the statistical coefficient can be summarized as follows:

$$A' = c_1 {E_{sg}}^{c_2} c_5 e^{c_6 T}$$

$$B' = (c_3 {E_{sg}}^{c_4})\,(c_7 T^2 + c_8 T + c_9)$$

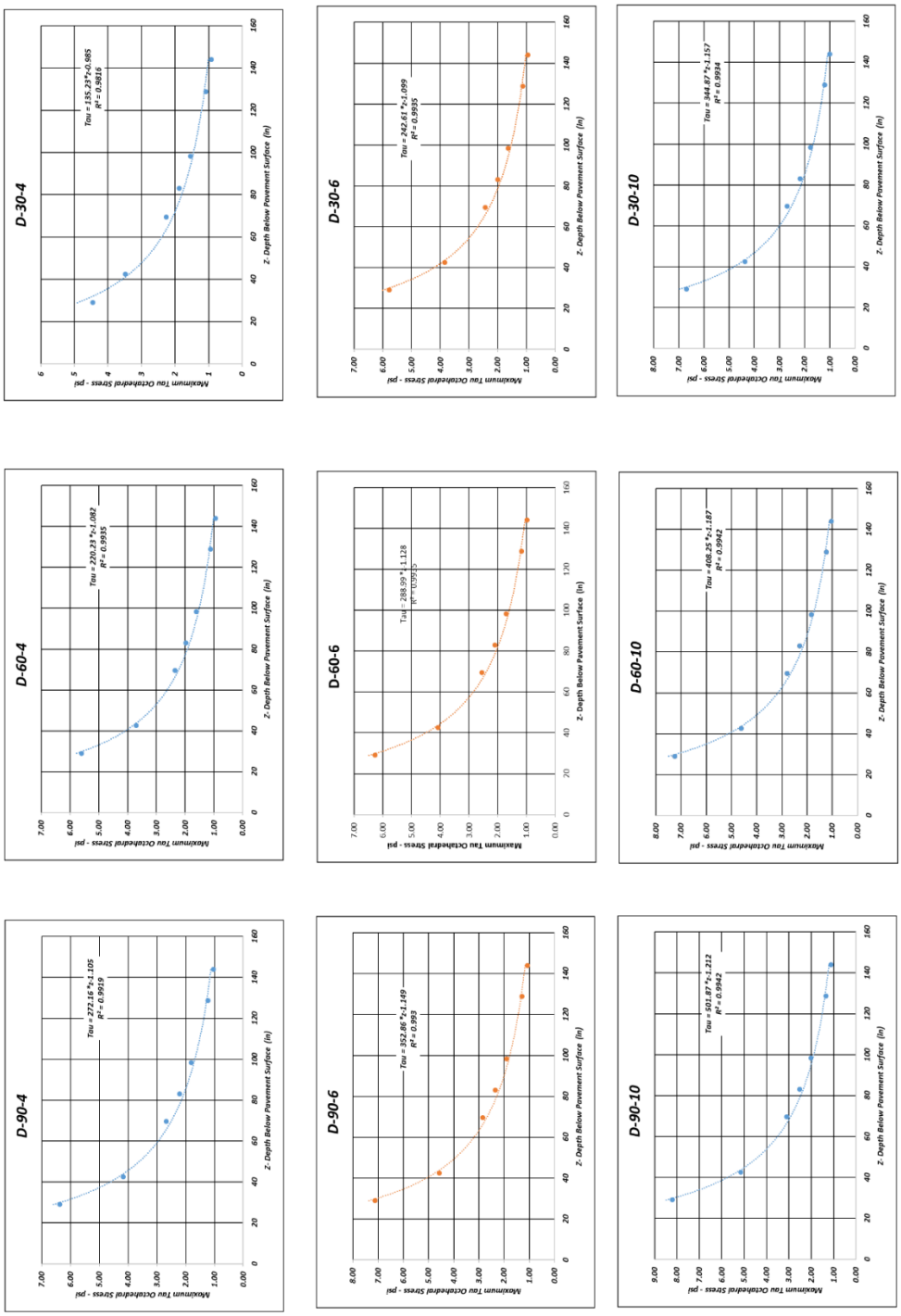

Figure 6.7. Octahedral Shear Stress Versus Depth as Function of E_{sg} and AC Temperature - Dual Tire 60 Kip Wheel Load

Table 6.20. Dual Tire Regression Analysis - 60 kip Tire Load

Model Form:(Power) $\tau = a*z^{-b}$						Normalized Coefficients to T=60 deg F			
Gear Type	T (^oF)	E_{sg} (ksi)	a	b	R^2	β_a	β_b	Avg β_a	Avg β_b
D	30	4	135.23	0.985	0.9816	0.6140	0.9104	0.8508	0.9645
	30	6	242.61	1.099	0.9935	0.8395	0.9743		
	30	10	344.87	1.159	0.9934	0.8448	0.9764		
	30	20	770.68	1.302	0.9963	0.8656	0.9819		
	30	30	1019.5	1.35	0.9963	0.8531	0.9797		
	30	40	1223.1	1.38	0.9980	2.2564	1.1138		
	60	4	220.23	1.082	0.9935	1.0000	1.0000	1.0000	1.0000
	60	6	288.99	1.128	0.9935	1.0000	1.0000		
	60	10	408.25	1.187	0.9942	1.0000	1.0000		
	60	20	890.33	1.326	0.9972	1.0000	1.0000		
	60	30	1195	1.378	0.9973	1.0000	1.0000		
	60	40	542.05	1.239	0.9970	1.0000	1.0000		
	90	4	272.16	1.105	0.9919	1.2358	1.0213	1.2417	1.0227
	90	6	352.86	1.149	0.9930	1.2210	1.0186		
	90	10	501.87	1.212	0.9942	1.2293	1.0211		
	90	20	1123.6	1.36	0.9972	1.2620	1.0256		
	90	30	1506	1.415	0.9978	1.2603	1.0269		
	90	40	1868.8	1.456	0.9980	3.4477	1.1751		

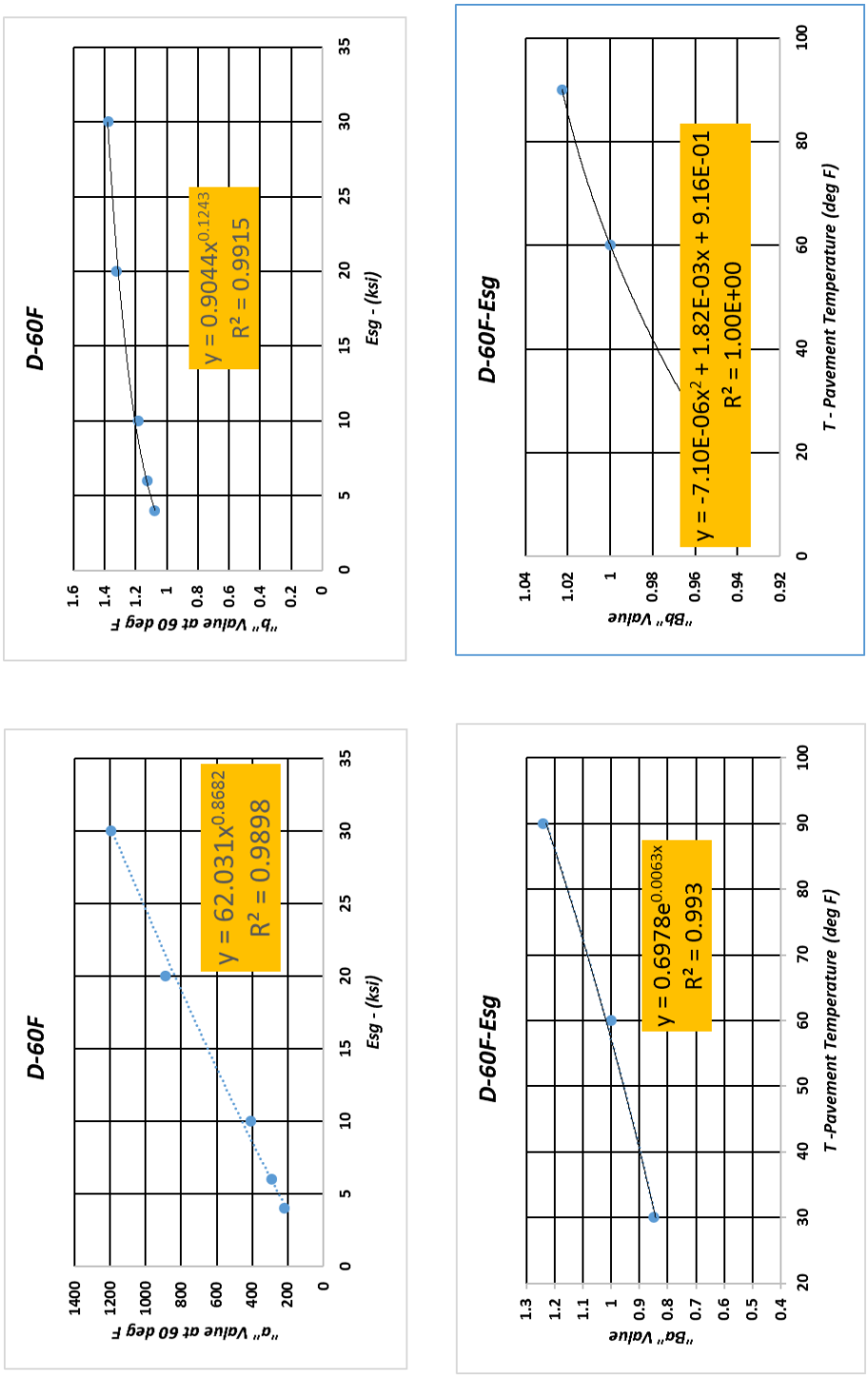

Figure 6.8. Octahedral Shear Regression Constants as Function of E_{sg} and AC Temperature - Dual Tire 60 Kip Wheel Load

And the final regression for the τ_{oct}- z model for the 60-kip wheel load- dual gear is:

$$\tau_{oct} = c_1 {E_{sg}}^{c_2} c_5 e^{c_6 T} \, z^{-(c_3 {E_{sg}}^{c_4})\,(c_7 T^2 + c_8 T + c_9)}$$

The final coefficients are: c_1 = 62.031, c_2 = 0.8682, c_3 = 0.9044, c_4 = 0.1243, c_5 = 0.6978, c_6 = 0.0063, c_7 = -7.10E-0.6, c_8 = 1.82E-03, and c_9= 0.9161.

Figure 6.9 shows the final regression results for the 60-k wheel load - dual gear scenario for the τ_{oct}- z depth model developed. It also contains the error term (predicted-actual JULEA). The goodness of the test yielded an average error = 0.285 psi, S_e = 0.534 psi, S_e/S_y = 0.180, and R^2 = 0.98.

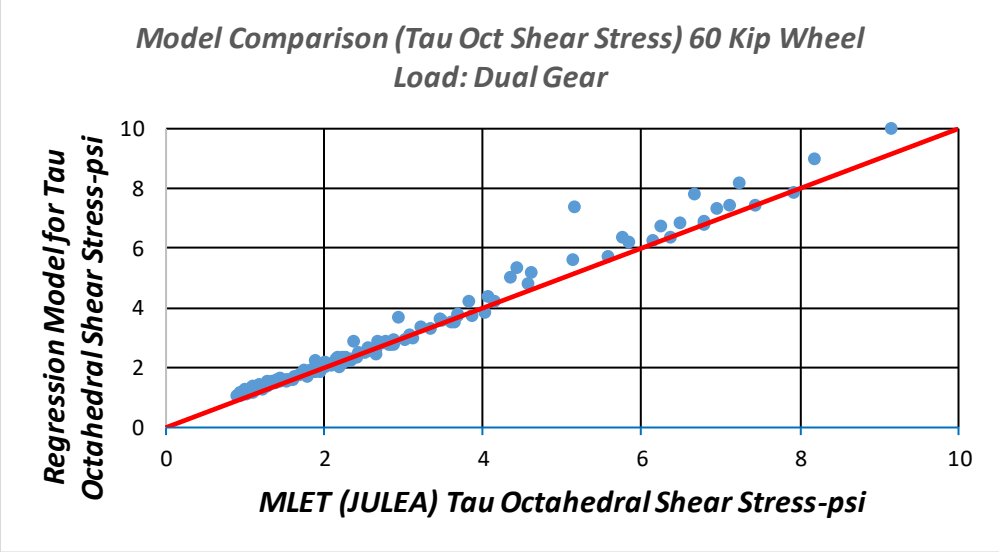

Figure 6.9. Model Comparison (τ_{oct} Shear Stress) 60 kip Wheel Load - Dual Gear

Dual Tandem Gear Analysis

The individual τ_{oct}- z plots for the dual tandem gear are shown in Figure 6.10. The ideal regression model for the dual tandem gear was found to be a log model of the form:

$$\boldsymbol{\tau_{oct} = a\, z^{-b}}$$

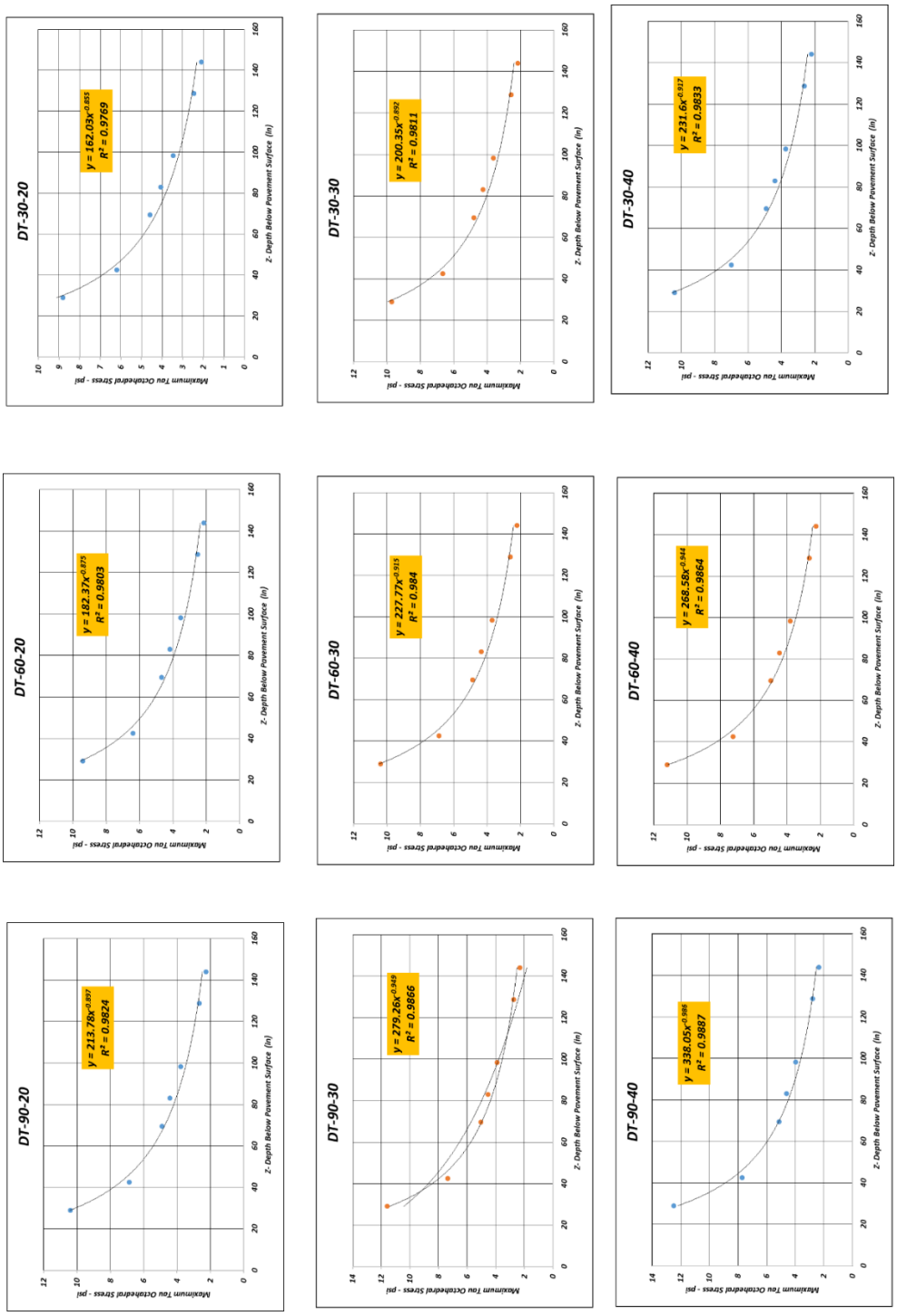

Figure 6.10. Octahedral Shear Stress Versus Depth as Function of E_{sg} and AC Temperature: Dual Tandem Gear- 60 Kip Load

The individual *a-b* regression constants are summarized in Table 6.21, along with the R^2 values. An identical approach with the β_i parameter which normalizes both the *a* and *b* parameters to the results at T= 60° F is shown in Table 6.21. The final models for *a* and *b* as functions of E_{sg} at 60°F, along with the β_a and β_b functions for T (temperature) are shown in Figure 6.11.

Table 6.21. Octahedral Shear Stress Analysis: Dual Tandem Regression Analysis - 60-Kip Tire Load

Model Form: τ = - a*(z^b)						Normalized Coefficients to T=60 deg F			
Type Gear	T (deg F)	E_{sg} (ksi)	a	b	R^2	β_a	β_b	Avg β_a	Avg β_b
DT	30	4	64.78	0.71	0.992	0.82	0.98	0.88	0.98
	30	6	78.02	0.74	0.991	0.90	0.98		
	30	10	100.46	0.78	0.988	0.90	0.98		
	30	20	162.04	0.86	0.978	0.89	0.98		
	30	30	200.35	0.89	0.9720	0.88	0.97		
	30	40	231.60	0.92	0.9669	0.86	0.97		
	60	4	79.09	0.73	0.9901	1.00	1.00	1.00	1.00
	60	6	86.59	0.76	0.9874	1.00	1.00		
	60	10	111.49	0.80	0.9825	1.00	1.00		
	60	20	182.37	0.88	0.9700	1.00	1.00		
	60	30	227.77	0.92	0.9619	1.00	1.00		
	60	40	268.58	0.94	0.9540	1.00	1.00		
	90	4	78.95	0.73	0.9804	1.00	1.00	1.15	1.02
	90	6	96.10	0.76	0.9654	1.11	1.01		
	90	10	125.79	0.81	0.9761	1.13	1.01		
	90	20	213.78	0.90	0.9602	1.17	1.03		
	90	30	279.26	0.95	0.9469	1.23	1.04		
	90	40	338.05	0.99	0.9370	1.26	1.04		

The summary of the regression models developed for the 60-kip dual gear is as follows:

$a_{60} = 33.3374\ E_{sg}^{0.5606}$ $R^2 = 0.9866$

$b_{60} = 0.6149\ E_{sg}^{0.1164}$ $R^2 = 0.998$

$\beta_a = 1.3412E\text{-}5\ T^2 + 2.9507E\text{-}7T + 0.77467$ $R^2 = 1.000$

$\beta_b = -1.0329E\text{-}06\ T^2 + 8.549E\text{-}4\ T + 0.95242$ $R^2 = 1.000$

recognizing that $A' = a_{60}\beta_a$ and $B' = b_{60}\beta_b$ and $\tau_{oct} = - A' \ln z + B$, the equations for A' and B' are:

$$A' = (c_1 {E_{sg}}^{c_2})(c_3 T^2 + c_4 T + c_5)$$

$$B' = (c_6 {E_{sg}}^{c_7})(c_8 T^2 + c_9 T + c_{10})$$

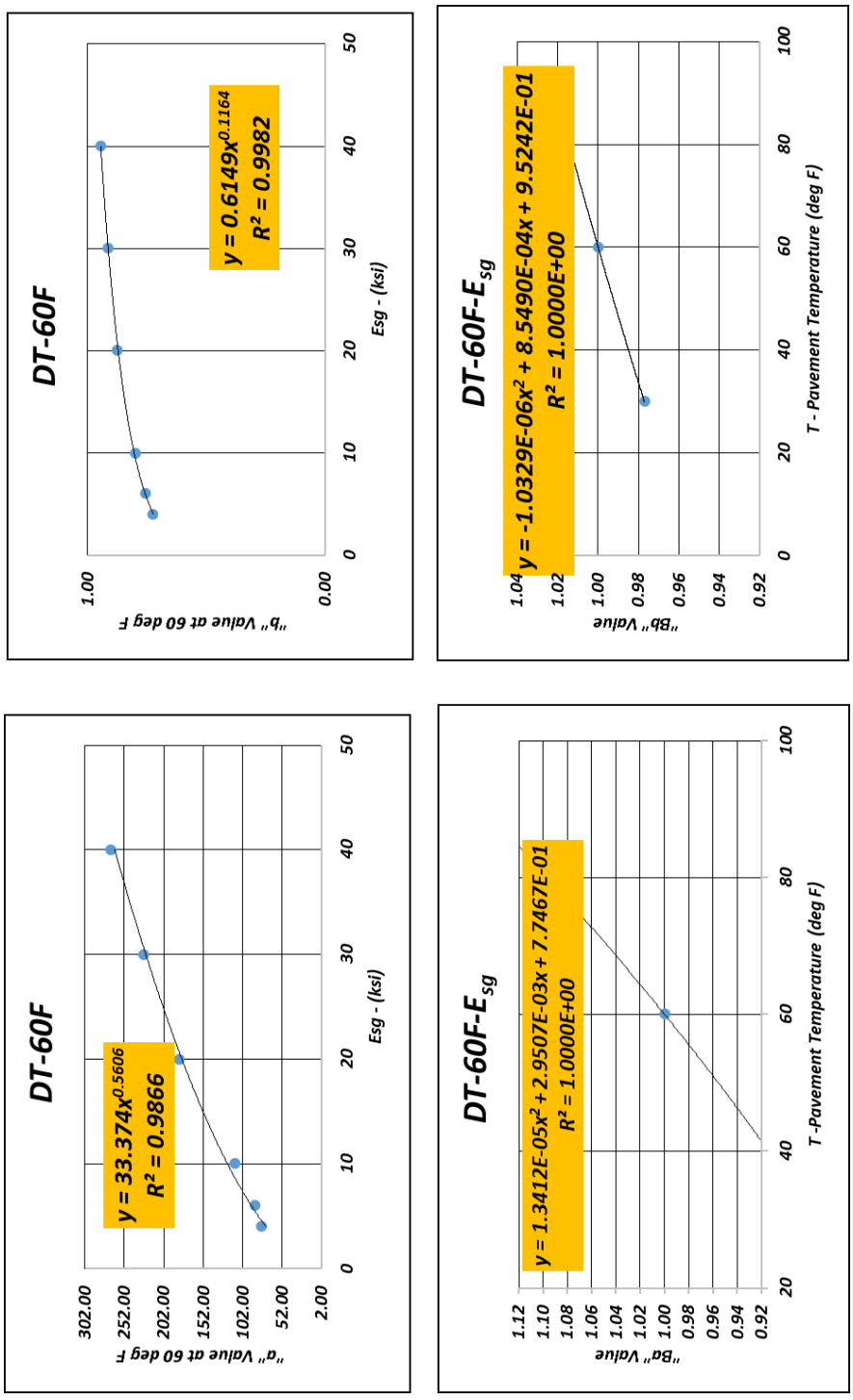

Figure 6.11. Octahedral Shear Regression Constants as Function of E_{sg} and AC Temperature: Dual Tandem Gear-60 Kip Wheel Load

And the final regression for the τ_{oct}- z model for the 60-kip wheel load- dual tandem gear is:

$$\tau_{oct} = (c_1 {E_{sg}}^{c_2})\,(c_3 T^2 + c_4 T + c_5) z^{({c_6 {E_{sg}}^{c_7}})\,(c_8 T^2 + c_9 T + c_{10})}$$

The final coefficients are: c_1 = 33.374, c_2 = 0.5606, c_3 = 1.3412E-5, c_4 = 2.9507E-3, c_5 = 0.77467, c_6 = 0.6149, c_7 = 0.1164, c_8 = -1.0329 E-6, c_9 = 8.549E-4, and c_{10}= 0.95242.

The final comparison plot between the model predicted τ_{oct} values and those actually computed from JULEA are shown in Figure 6.12. Figure 6.12 shows the final regression results for the 60-kip wheel load – dual tandem gear scenario for the τ_{oct}- z depth model developed. As noted, the final model has excellent statistical properties with an average relative error = -0.024 psi, S_e = 0.38 psi, S_e/S_y = 0.162, and R^2 = 0.99.

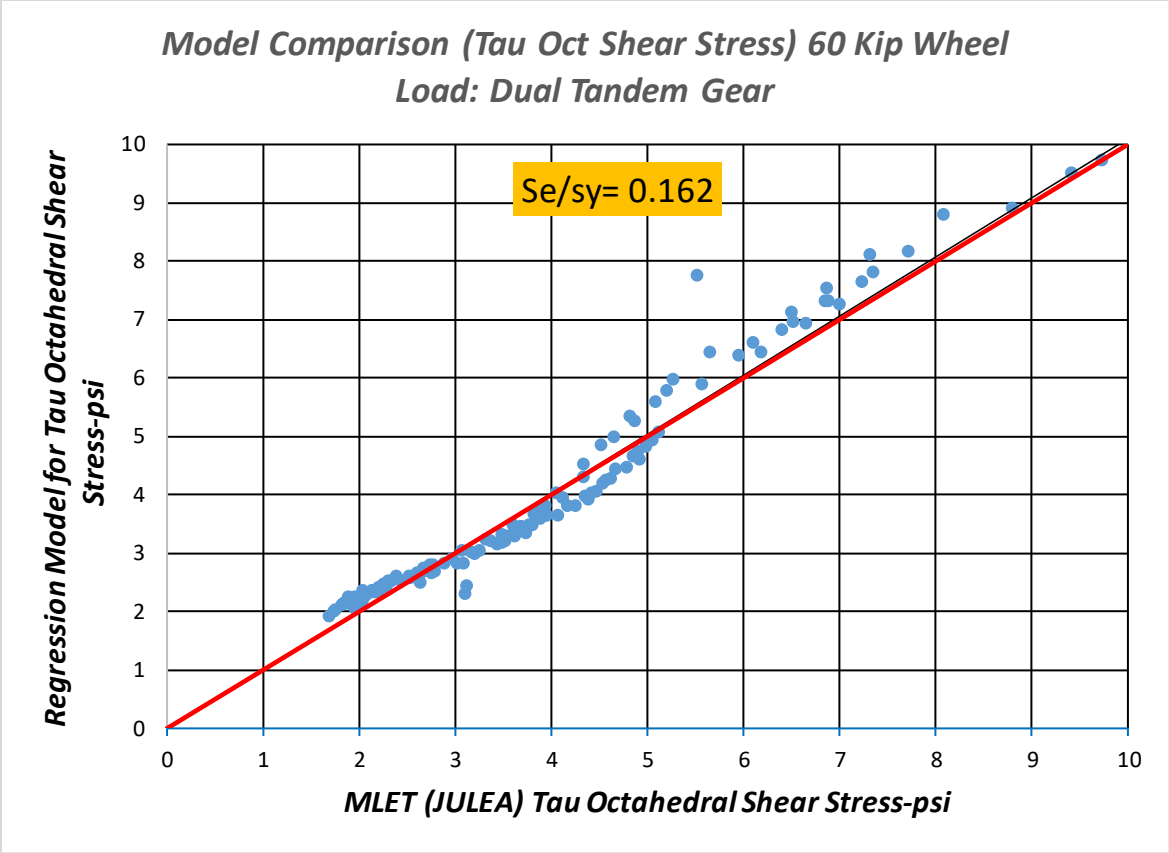

Figure 6.12. Model Comparison (τ_{oct} Shear Stress) 60 Kip Wheel Load- Dual Tandem Gear

Triple Tandem Gear Analysis

The individual τ_{oct}- z plots for the triple tandem gear are shown in Figure 6.13. All of the regression models found were of the same mathematical form as those previously found for the dual tandem gear. The overall model form was:

$$\tau_{oct} = a\, z^{-b}$$

The individual regression constants for *a* and *b* are shown in Table 6.22, along with the R^2 values. This table shows the value for the *a* and *b* coefficients at 60° F as well as the β_a and β_b models. The β_a and β_b functions for T (temperature) are shown in Figure 6.14.

The summary of the regression models developed for the analysis were:

$a_{60} = 17.968\ E_{sg}^{0.557}$ $R^2 = 0.9882$

$b_{60} = 0.4562\ E_{sg}^{0.1384}$ $R^2 = 0.9939$

$\beta_a = 2.50E\text{-}5\ T^2 + 8.59E\text{-}04\ T + 0.858$ $R^2 = 1.0000$

$\beta_b = -1.37E\text{-}6\ T^2 + 9.27E\text{-}04\ T + 0.949$ $R^2 = 1.0000$

Recognizing that $A' = a_{60}\beta_a$ and $B' = b_{60}\beta_b$ and $\tau_{oct} = -A'\ z^{B'}$, the equations for A′ and B′ are:

$$A' = (c_1 {E_{sg}}^{c_2})\ (c_3 T^2 + c_4 T + c_5)$$

$$B' = (c_6 {E_{sg}}^{c_7})\ (c_8 T^2 + c_9 T + c_{10})$$

And the final regression for the τ_{oct}- z model for the 60-kip wheel load- triple tandem gear is:

$$\tau_{oct} = (c_1 {E_{sg}}^{c_2})\ (c_3 T^2 + c_4 T + c_5) z^{(c_6 {E_{sg}}^{c_7})\ (c_8 T^2 + c_9 T + c_{10})}$$

The final coefficients are: $c_1 = 17.968$, $c_2 = 0.557$, $c_3 = 1.3412E\text{-}5$, $c_4 = 2.950E\text{-}03$, $c_5 = 0.858$, $c_6 = 0.4562$, $c_7 = 0.1384$, $c_8 = -1.37\ E\text{-}06$, $c_9 = 9.27E\text{-}04$, and $c_{10} = 0.949$.

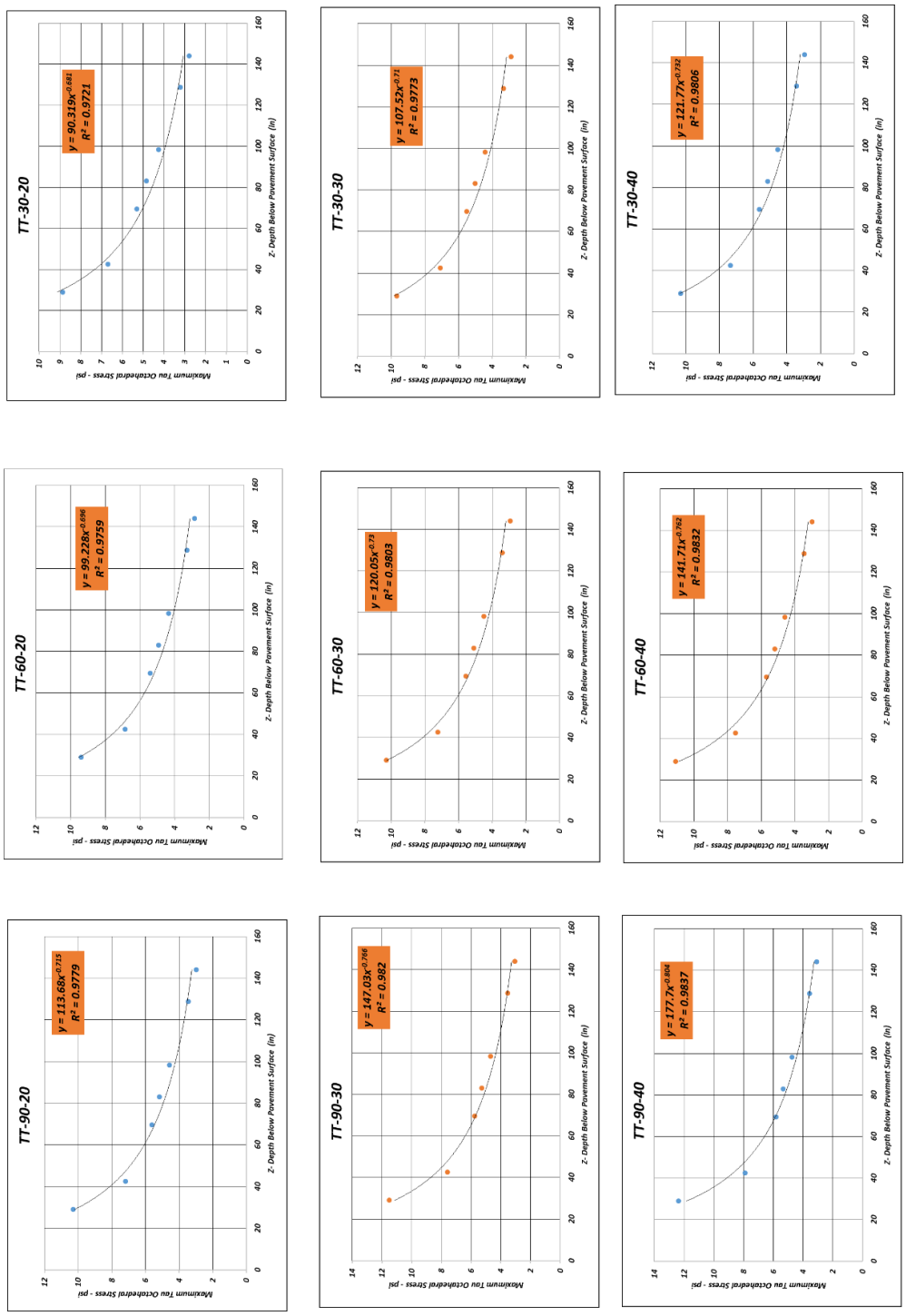

Figure 6.13. Octahedral Shear Stress Versus Depth as Function of E_{sg} and AC Temperature - Triple Tandem Gear - 60 Kip Wheel Load

Table 6.22. Octahedral Shear Stress Analysis Triple Tandem Regression Analysis - 60 kip Tire Load

Model Form: τ = - a*(z^b)						Normalized Coefficients to T=60°F			
Type Gear	T (deg F)	Esg (ksi)	a	b	R^2	βa	βb	Avg βa	Avg βb
TT	30	4	38.265	0.548	0.9886	0.925	0.980	0.907	0.976
	30	6	44.394	0.572	0.9889	0.927	0.983		
	30	10	54.191	0.605	0.9886	0.923	0.981		
	30	20	90.319	0.681	0.9721	0.910	0.978		
	30	30	107.52	0.71	0.9773	0.896	0.973		
	30	40	121.77	0.732	0.9806	0.859	0.961		
	60	4	41.357	0.559	0.9864	1	1	1	1
	60	6	47.897	0.582	0.9866	1	1		
	60	10	58.695	0.617	0.9836	1	`1		
	60	20	99.228	0.696	0.9759				
	60	30	120.05	0.73	0.9803				
	60	40	141.71	0.762	0.9832				
	90	4	42.524	0.549	0.9659	1.028	0.982	1.138	1.022
	90	6	50.541	0.58	0.9485	1.055	0.997		
	90	10	65.832	0.629	0.936	1.122	1.019		
	90	20	113.68	0.715	0.9779	1.146	1.027		
	90	30	147.03	0.766	0.982	1.225	1.049		
	90	40	177.7	0.804	0.9837	1.254	1.055		

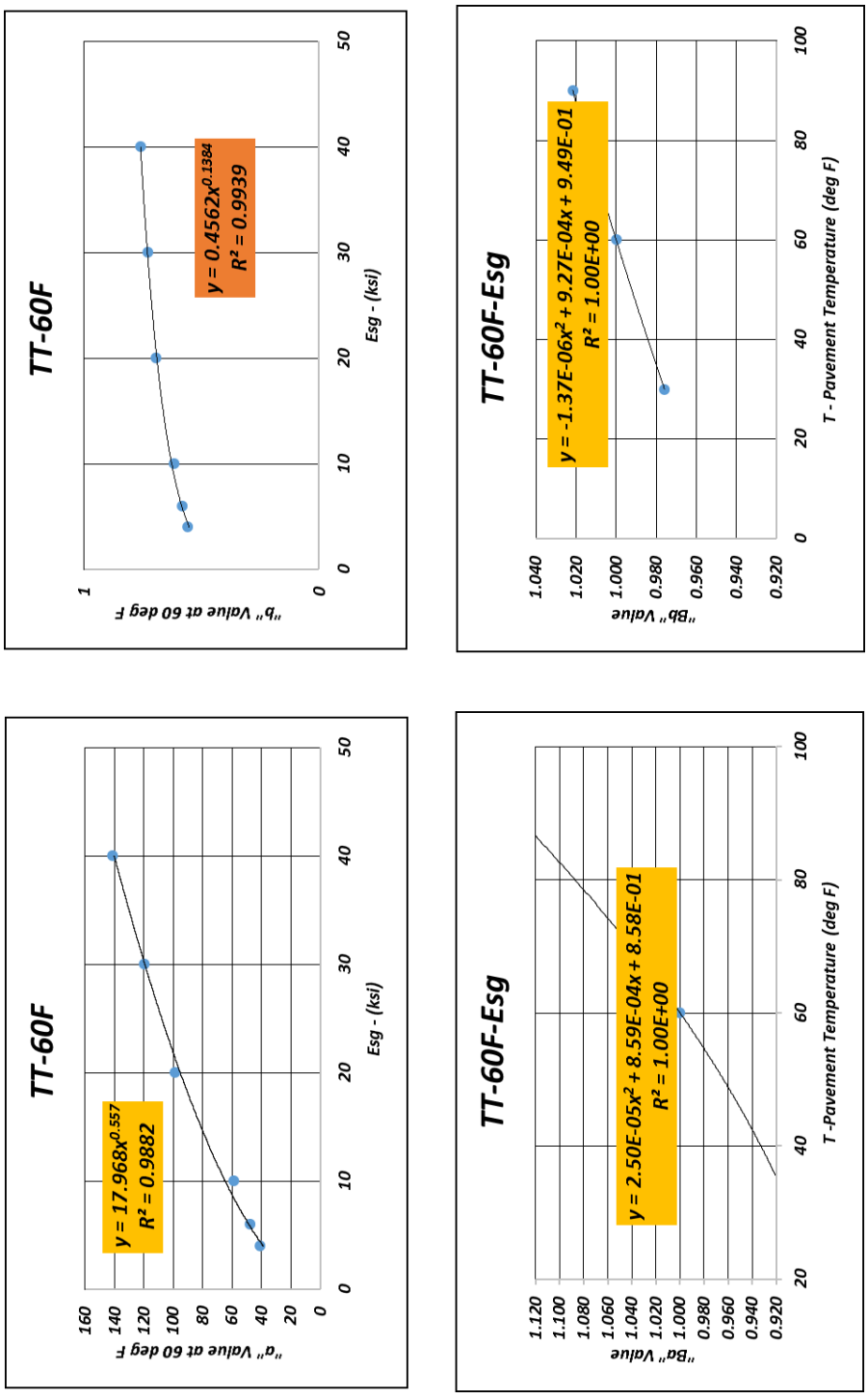

Figure 6.14. Octahedral Shear Regression Constant as Function of E_{sg} and AC Temperature for Triple Tandem Gear - 60 Kip Wheel Load

The final comparison plot between the model predicted τ_{oct} values and those computed from JULEA are shown in Figure 6.15. As can be observed, this model also has very excellent statistical properties with an average error = 0.057 psi, S_e = 0.323 psi, S_e/S_y = 0.152, and R^2 = 0.988.

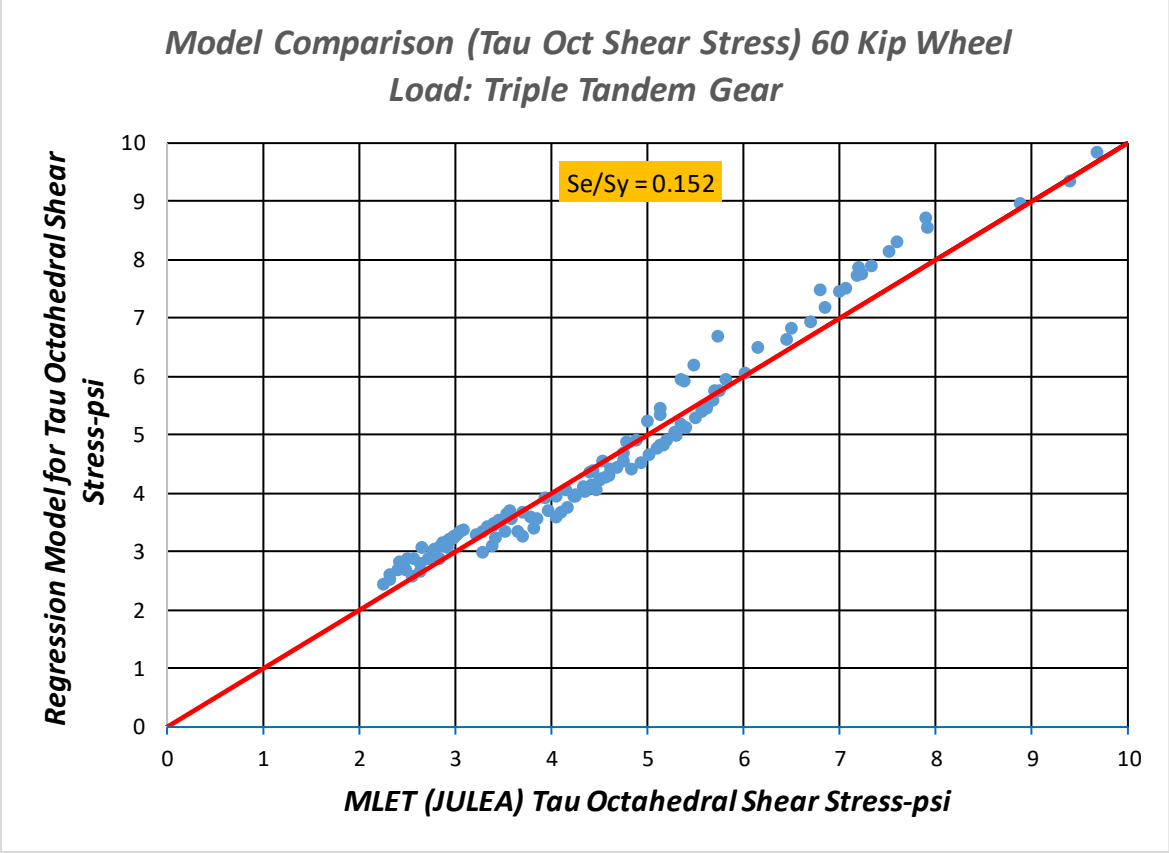

Figure 6.15. Model Comparison (τ_{oct} Shear Stress) 60 Kip Wheel Load- Triple Tandem Gear

Bulk Stress Analysis (60-kip Wheel Load)

Similar to the octahedral analysis of the subgrade layers, the overall approach was utilized to establish θ relationships for the subgrade layer for the detailed results of the 60-kip wheel

load study. The same procedure was used to find the maximum octahedral stress values for each location.

Dual Gear Analysis

The individual θ- z plots for each combination of AC Temperature (or E*) and E_{sg} subgrade modulus are illustrated in Table 6.23 and Figure 6.16 for the dual gear results. For this gear type, it can be seen that the relationship of θ - z is a power model, with excellent statistical fitting properties of the form:

$$\boldsymbol{\theta = a\, z^{-b}}$$

Table 6.24 is the summary of these individual regression constants (*a* and *b*), along with R^2 correlation found. Figure 6.17 represents the individual regression plots of a-E_{sg} and b-E_{sg} at T= 60°F along with the normalized plots of the β_a and β_b – T regressions. The summary of the regression models developed for the 60-kip dual gear are as follows:

$a_{60} = 410.56\ E_{sg}^{0.8066}$ R^2= 0.998

$b_{60} = 1.0836\ E_{sg}^{0.1079}$ R^2= 0.9998

β_a=0.0003T^2-0.0171T +1.1016 R^2 = 1

β_b=-2E-5T^2-0.0013T +0.9944 R^2 = 1.0000

Recognizing that $A' = a_{60}\beta_a$ and $B' = b_{60}\beta_b$ and $\theta = A' z^{-B'}$, the statistical coefficient can be summarized as follows:

$$A' = \left(c_1 {E_{sg}}^{c_2}\right)\left(c_3 T^2 + c_4 T + c_5\right)$$

$$B' = \left(c_6 {E_{sg}}^{c_7}\right)\left(c_8 T^2 + c_9 T + c_{10}\right)$$

Table 6.23. Summary of Maximum Bulk Stress Under Gear for Different Depths

Tire Load (kips)	Gear Type	Temp AC (°F)	Esg (ksi)	Run No	Maximum Octahedral Shear Stress at Depth z (in) Shown						
					29	42.5	69.5	83	98.25	128.75	144
60	D	30	4	10	15.86	10.75	6.20	4.94	3.93	2.63	2.20
			6	11	17.56	11.75	6.59	5.20	4.09	2.71	2.25
			10	12	20.60	13.29	7.12	5.55	4.33	2.82	2.34
		60	4	13	17.15	11.62	6.59	5.23	4.12	2.73	2.28
			6	14	19.36	12.72	6.99	5.50	4.31	2.82	2.34
			10	15	22.69	14.34	7.55	5.86	4.54	2.94	2.43
		90	4	16	22.69	14.34	7.55	5.86	4.54	2.94	2.43
			6	17	23.90	15.17	8.00	6.19	4.78	3.08	2.53
			10	18	27.63	16.87	8.53	6.54	5.00	3.17	2.61
60	DT	30	4	37	23.72	18.84	11.86	9.60	7.70	5.20	4.36
			6	38	25.24	19.97	12.48	10.06	8.01	5.36	4.48
			10	39	27.59	21.62	13.32	10.68	8.44	5.58	4.64
		60	4	40	25.35	20.04	12.55	10.11	8.07	5.40	4.53
			6	41	27.00	21.25	13.22	10.60	8.40	5.58	4.65
			10	42	29.42	22.97	14.06	11.24	8.85	5.80	4.81
		90	4	43	29.63	23.30	14.33	11.39	8.98	5.90	4.89
			6	44	31.50	24.56	14.92	11.86	9.31	6.05	5.01
			10	45	33.88	25.97	15.76	12.43	9.69	6.24	5.15
60	TT	30	4	64	29.28	23.47	15.51	12.80	10.46	7.26	6.15
			6	65	31.03	24.69	16.11	13.30	10.83	7.46	6.31
			10	66	33.56	26.29	17.03	14.00	11.31	7.73	6.50
		60	4	67	31.15	24.87	16.27	13.41	10.92	7.53	6.37

			6	68	33.11	26.16	17.02	13.90	11.30	7.74	6.52
			10	69	35.69	27.82	17.95	14.59	11.80	8.01	6.73
		90	4	70	36.00	28.29	18.28	14.94	12.02	8.16	6.85
			6	71	37.94	29.51	18.92	15.05	12.37	8.35	6.99
			10	72	40.31	31.00	19.72	15.95	12.80	8.57	7.17
60	D	30	20	V10	25.95	15.77	7.97	6.12	4.69	3.00	2.46
			30	V11	29.74	17.41	8.52	6.46	4.92	3.09	2.53
			40	V12	32.58	18.68	8.92	6.71	5.07	3.18	2.59
		60	20	V13	28.28	16.83	8.39	6.40	4.89	3.10	2.54
			30	V14	32.11	18.53	8.89	6.73	5.10	3.19	2.61
			40	V15	22.69	14.34	7.55	5.86	4.54	2.94	2.43
		90	20	V16	33.57	19.24	9.25	6.98	5.28	3.29	2.69
			30	V17	37.32	20.71	9.64	7.22	5.42	3.36	2.73
			40	V18	40.10	21.80	9.90	7.37	5.51	3.39	2.75
60	DT	30	20	V37	31.73	23.98	14.72	11.62	9.09	5.90	4.87
			30	V38	35.11	25.34	15.50	12.19	9.49	6.10	5.01
			40	V39	37.73	26.43	16.11	12.59	9.78	6.23	5.11
		60	20	V40	34.15	25.13	15.35	12.13	9.47	6.10	5.03
			30	V41	37.52	26.41	16.11	12.66	9.83	6.28	5.16
			40	V42	40.13	27.26	16.59	13.05	10.07	6.39	5.24
		90	20	V43	39.20	27.63	16.78	13.11	10.18	6.47	5.31
			30	V44	42.61	28.42	17.25	13.48	10.41	6.58	5.38
			40	V45	45.06	29.06	17.57	13.72	10.56	6.65	5.43
60	TT	30	20	V64	37.47	28.73	18.43	14.99	12.03	8.11	6.79
			30	V65	40.49	30.17	19.26	15.59	12.47	8.36	6.98

			40	V66	42.85	31.15	19.80	16.03	12.77	8.52	7.10
		60	20	V67	39.91	30.03	19.15	15.57	12.49	8.38	7.00
			30	V68	42.99	31.29	19.94	16.14	12.87	8.59	7.16
			40	V69	45.30	32.26	20.44	16.46	13.13	8.72	7.26
		90	20	V70	44.95	32.62	20.70	16.65	13.27	8.84	7.36
			30	V71	47.88	33.58	21.17	17.05	13.51	8.96	7.45
			40	V72	49.96	34.21	21.37	17.20	13.73	9.03	7.50

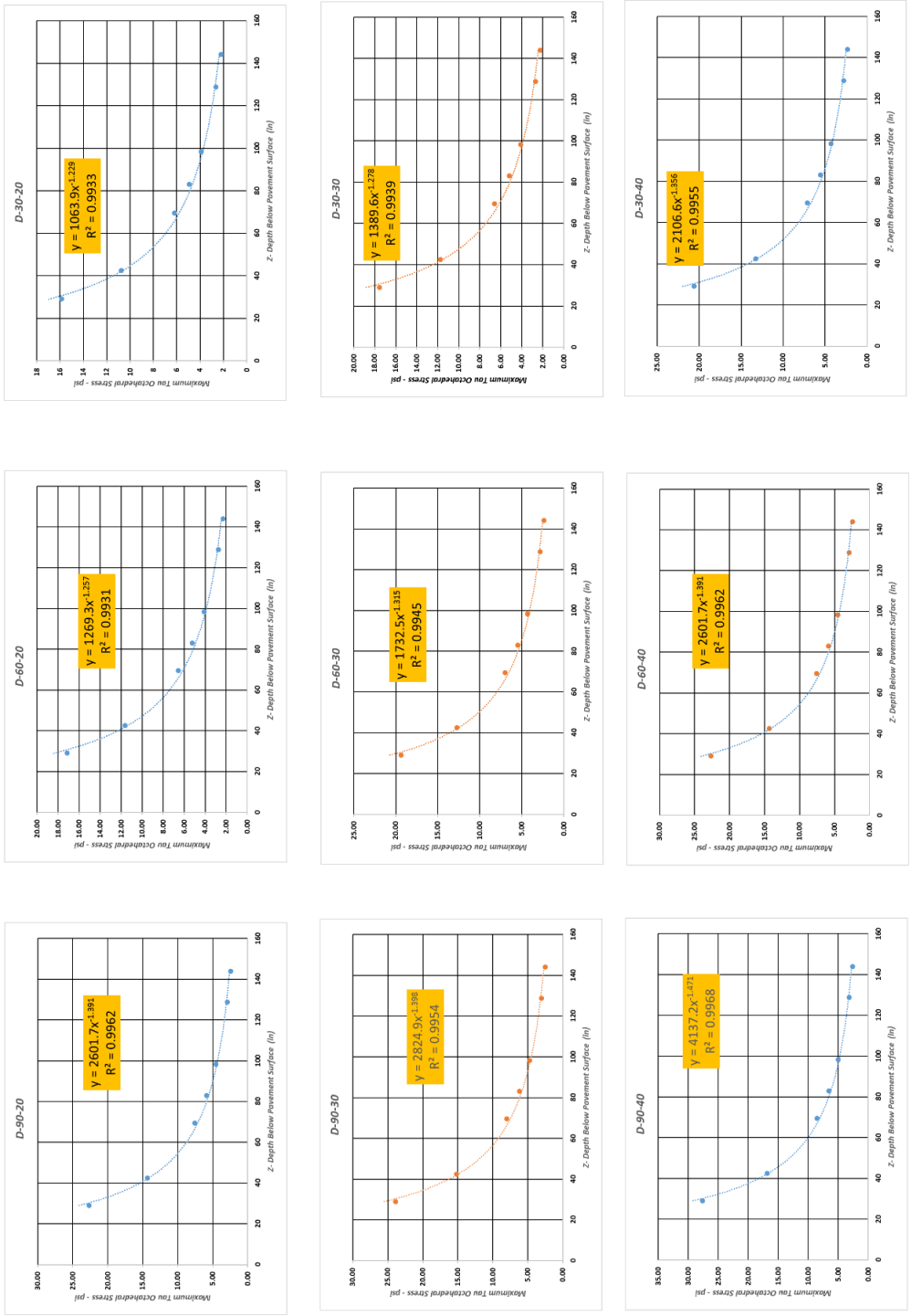

Figure 6.16. Bulk Stress Versus Depth as Function of E_{sg} and AC Temperature: Dual Tire 60 Kip Wheel Load

Table 6.24. Dual Tire Regression Analysis-60 Kip Tire Load

Model Form:(Power) $\tau = a*z^{-b}$						Normalized Coefficients to T=60°F			
Gear Type	T (deg F)	E_{sg} (ksi)	a	"-b"	R^2	β_a	β_b	Avg β_a	Avg β_b
D	30	4	1063.9	1.229	0.9816	0.838	0.978	0.820	0.977
	30	6	1389.6	1.278	0.9935	0.802	0.972		
	30	10	2106.6	1.358	0.9934	0.810	0.976		
	30	20	3804	1.466	0.9963	0.828	0.979		
	30	30	5406.4	1.532	0.9963	0.842	0.981		
	30	40	6841.4	1.576	0.9980				
	60	4	1269.3	1.257	0.9935	1.0000	1.0000	1.0000	1.0000
	60	6	1732.5	1.315	0.9935	1.0000	1.0000		
	60	10	2601.7	1.391	0.9942	1.0000	1.0000		
	60	20	4595.7	1.498	0.9972	1.0000	1.0000		
	60	30	6424.3	1.562	0.9973	1.0000	1.0000		
	90	4	2601.7	1.391	0.9919	2.050	1.107	1.641	1.063
	90	6	2824.9	1.398	0.9930	1.631	1.063		
	90	10	4137.2	1.471	0.9942	1.590	1.058		
	90	20	6905.3	1.57	0.9972	1.503	1.048		
	90	30	9194.6	1.626	0.9978	1.431	1.041		
	90	40	11280	1.667	0.9980				

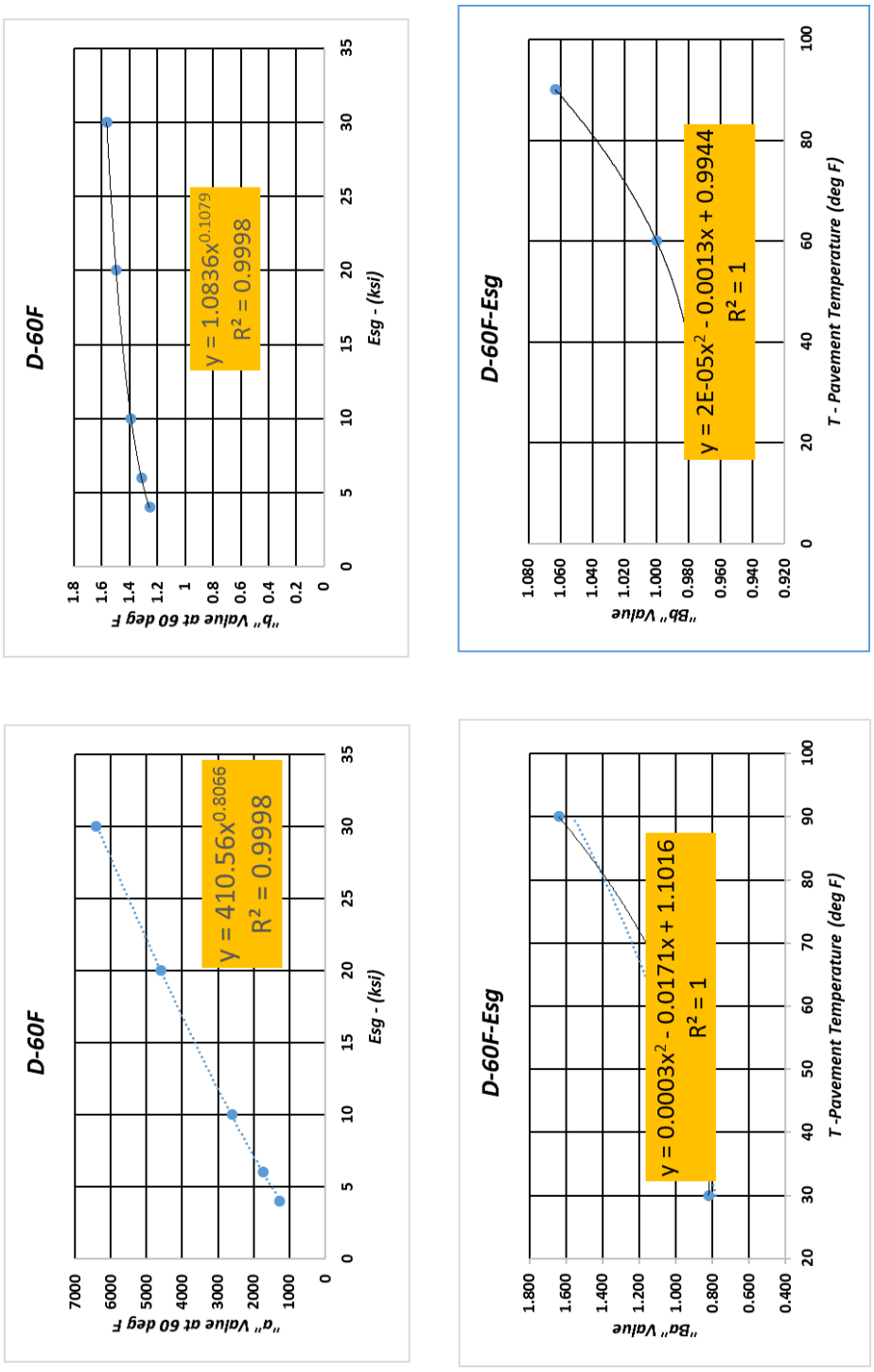

Figure 6.17. Bulk Stress Regression Constants as Function of E_{sg} and AC Temperature: Dual Tire 60 Kip Wheel Load

And the final regression for the θ- z model for the 60-kip wheel load- dual gear is:

$$\theta = (c_1 {E_{sg}}^{c_2})\,(c_3 T^2 + c_4 T + c_5)\, z^{-(c_6 {E_{sg}}^{c_7})\,(c_8 T^2 + c_9 T + c_{10})}$$

The final coefficients are: c_1 = 410.56, c_2 = 0.8066, c_3= 0.0002, c_4 = -0.0123, c_5= 1.012, c_6 = 1.0836, c_7 = 0.1079, c_8 = 2.24E-05, c_9 = -1.251E-03, and c_{10} = 0.9944.

Figure 6.18 shows the final regression results for the 60 k wheel load- dual gear scenario for the τ_{oct}- z depth model developed. It also contains the error term (predicted-actual JULEA). The final equation has excellent fitness qualities: S_e/S_y = 0.258 and R^2 = 0.99.

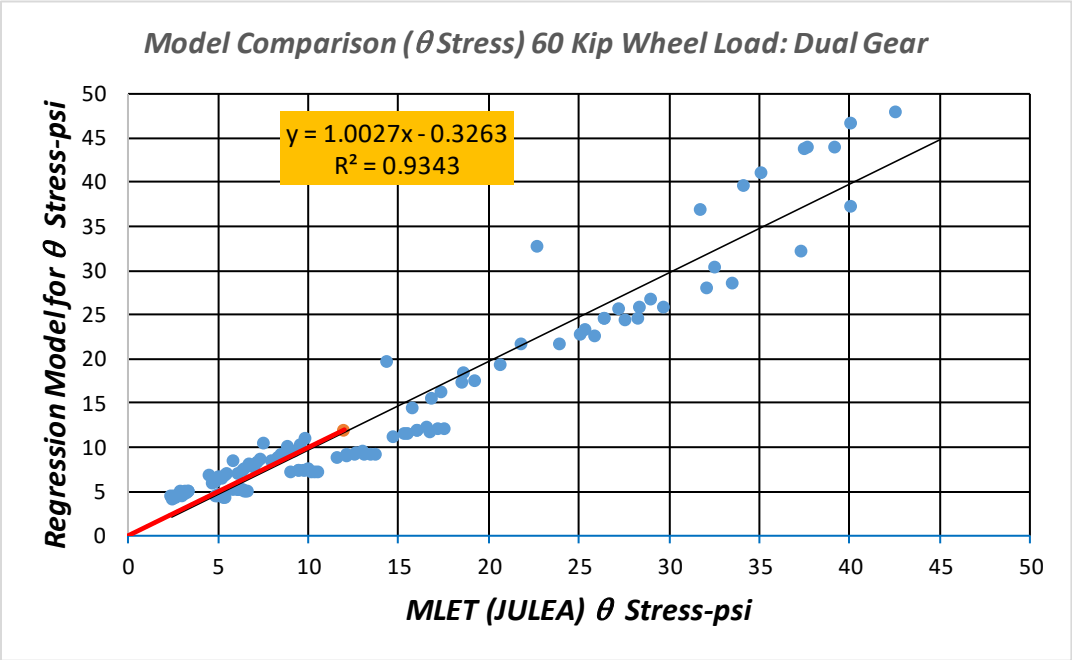

Figure 6.18. Model Comparison (θ Stress) 60 Kip Wheel Load - Dual Gear

Dual Tandem Gear Analysis

The individual θ- z plots for the dual tandem gear are shown in Figure 6.19. The ideal regression model for the dual tandem gear was found to be a log model of the form:

$$\theta = -a \ln z + b$$

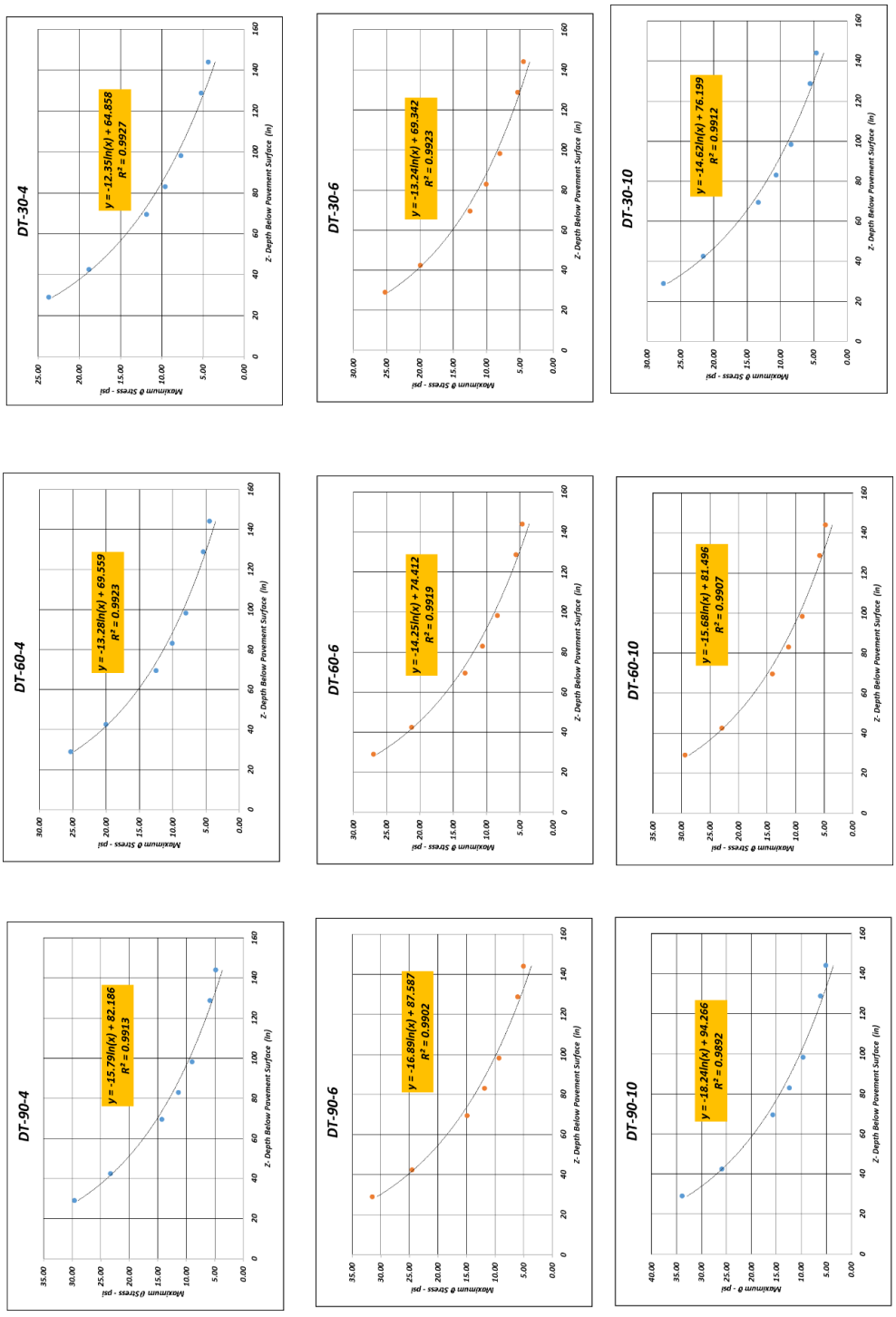

Figure 6.19. θ Stress Versus Depth as Function of E_{sg} and AC Temperature: Dual Tandem Gear- 60 Kip Load

It is apparent that the log model provides a slightly better fit for the θ- z power model found for the dual gear. This is attributed to the deeper depth stress overlap from the tandem set of wheels which causes increased θ values as the depth (z) is increased.

The individual *a-b* regression constants are summarized in Table 6.25, along with the R^2 values. An identical approach with the β_i parameter which normalizes both the *a* and *b* parameters to T = 60° F results is shown in Table 6.24. The final models for *a* and *b* as functions of E_{sg} at 60° F., along with the β_a and β_b functions for T (temperature) are shown in Figure 6.20.

Table 6.25. Octahedral Shear Stress Analysis - Dual Tandem Regression Analysis-60-Kip Tire Load

Model Form: θ = -a* ln Z+b						Normalized Coefficients to T=60 deg F			
Type Gear	T (°F)	E_{sg} (ksi)	a	b	R^2	β_a	β_b	Avg β_a	Avg β_b
DT	30	4	12.35	64.86	0.9928	0.930	0.932	0.931	0.933
	30	6	13.24	69.34	0.9915	0.929	0.932		
	30	10	14.62	76.20	0.9885	0.932	0.935		
	60	4	13.28	69.56	0.9901	1.00	1.00	1.00	1.00
	60	6	14.25	74.41	0.9874	1.00	1.00		
	60	10	15.68	81.50	0.9825	1.00	1.00		
	90	4	15.49	82.19	0.9804	1.166	1.182	1.172	1.172
	90	6	16.89	87.59	0.9654	1.185	1.177		
	90	10	18.24	94.27	0.9761	1.163	1.157		

The summary of the regression models developed for the 60-kip dual gear is as follows:

$a_{60} = 10.314\ E_{sg}^{01816}$ $R^2 = 0.9996$

$b_{60} = 54.668\ E_{sg}^{0.1731}$ $R^2 = 0.9996$

$\beta_a = 5.6894E\text{-}5\ T^2\text{-}2.8124E\text{-}03T + 0.96393$ $R^2 = 1.0000$

β_b=5.8253E-05 T^2-3.0126E-03 T +0.97105 R^2 = 1.0000

Recognizing that A′ =$a_{60}\beta_a$ and B′ = $b_{60}\beta_b$ and θ = - A′ ln z +B′, the equations for A′ and B′ are:

$$A' = (c_1 {E_{sg}}^{c_2})(c_3 T^2 + c_4 T + c_5)$$

$$B' = (c_6 {E_{sg}}^{c_7})(c_8 T^2 + c_9 T + c_{10})$$

And the final regression for the θ model for the 60-kip wheel load- dual tandem gear is:

$$\theta = -(c_1 {E_{sg}}^{c_2})(c_3 T^2 + c_4 T + c_5) \ln z + (c_6 {E_{sg}}^{c_7})(c_8 T^2 + c_9 T + c_{10})$$

The final coefficients are: c_1= 10.314, c_2 =0.1816, c_3= 5.6894E-05, c_4= -2.8124E-3, c_5= 0.96393, c_6 =54.668, c_7 = 0.1731, c_8 = 5.8253 E-05, c_9 = -3.0126E-03, and c_{10} = 0.97105.

The final comparison plot between the model predicted θ values and those actually computed from JULEA are shown in Figure 6.21. Figure 6.21 shows the final regression results for the 60-kip wheel load – dual tandem gear scenario for the θ - z depth model developed. As noted the final model has very excellent statistical properties with an average error = -0.153 psi, S_e = 0.827 psi, S_e/S_y = 0.101, and R^2 = 0.99.

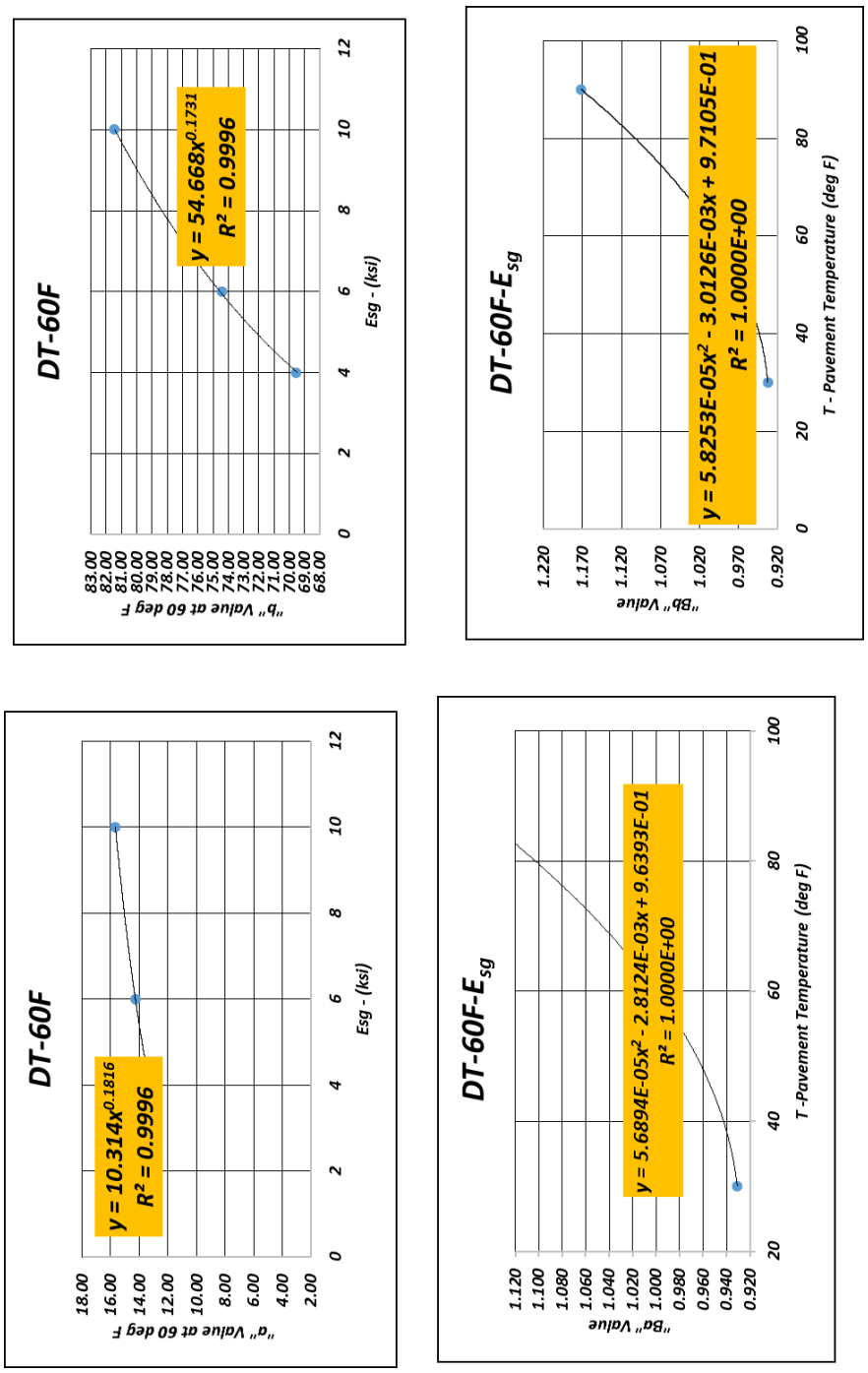

Figure 6.20. θ Regression Constants as Function of E_{sg} and AC Temperature: Dual Tandem Gear-60 Kip Wheel Load

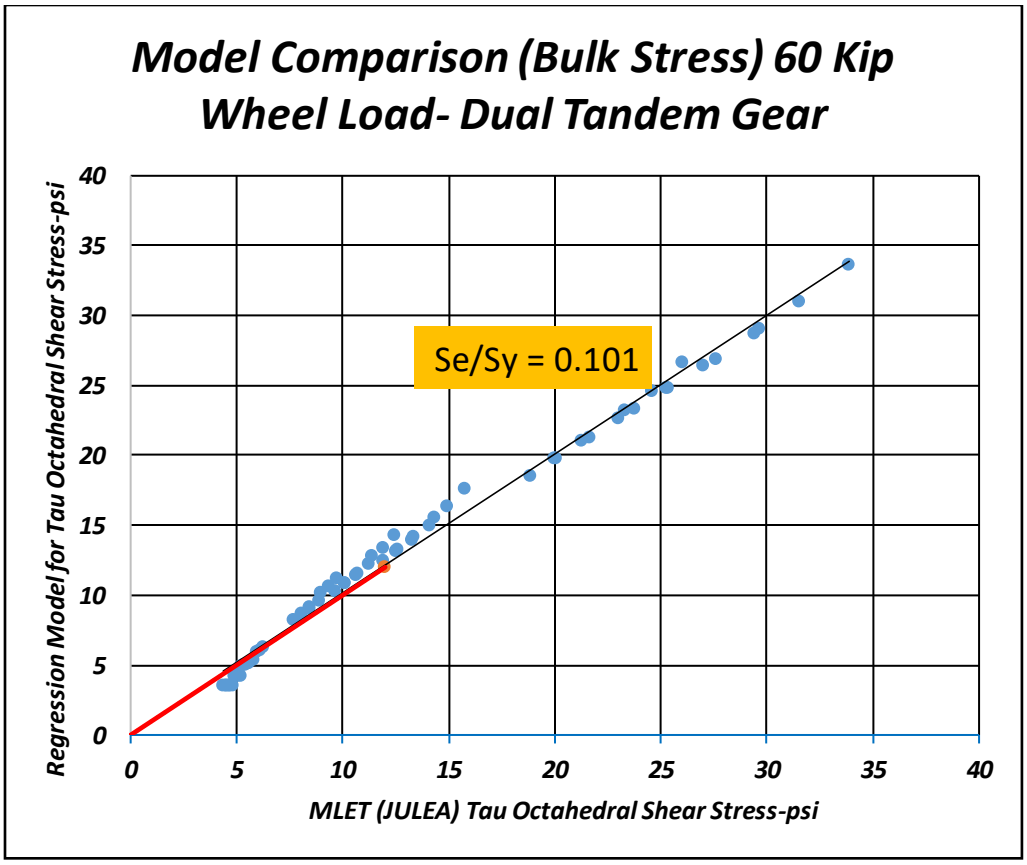

Figure 6.21. Model Comparison (τ_{oct} Shear Stress) 60 Kip Wheel Load- Dual Tandem Gear

Triple Tandem Gear Analysis

The individual θ z plots for the triple tandem gear are shown in Figure 6.22. All of the regression models were found to be of the same mathematical form as those previously found for the dual tandem gear. The overall model form was:

$$\theta = -a \ln z + b$$

The individual regression constants for a and b are shown in Table 6.26, along with the R^2 values. This table shows the value for the a and b coefficients at 60° F as well as the β_a and β_b models. The β_a and β_b functions for T (temperature) are shown in Figure 6.23.

The summary of the regression models developed for the analysis were:

$a_{60} = 17.968\ E_{sg}^{0.557}$ $R^2 = 0.9882$

$b_{60} = 0.4562\ E_{sg}^{0.1384}$ $R^2 = 0.9939$

$\beta_a = 2.50E\text{-}5\ T^2 + 8.59E\text{-}04\ T + 0.858$ $R^2 = 1.0000$

$\beta_b = -1.37E\text{-}6\ T^2 + 9.27E\text{-}04\ T + 0.949$ $R^2 = 1.0000$

Recognizing that $A' = a_{60}\beta_a$ and $B' = b_{60}\beta_b$ and $\tau_{oct} = -A' \ln z + B'$, the equations for A′ and B′ are:

$$A' = (c_1 {E_{sg}}^{c_2})(c_3 T^2 + c_4 T + c_5)$$

$$B' = (c_6 {E_{sg}}^{c_7})(c_8 T^2 + c_9 T + c_{10})$$

And the final regression for the θ- z model for the 60-kip wheel load- triple tandem gear is:

$$\theta = (c_1 {E_{sg}}^{c_2})(c_3 T^2 + c_4 T + c_5) z^{(c_6 {E_{sg}}^{c_7})(c_8 T^2 + c_9 T + c_{10})}$$

The final coefficients are: $c_1 = 17.968$, $c_2 = 0.557$, $c_3 = 1.3412E\text{-}5$, $c_4 = 2.950E\text{-}03$, $c_5 = 0.858$, $c_6 = 0.4562$, $c_7 = 0.1384$, $c_8 = -1.37\ E\text{-}06$, $c_9 = 9.27E\text{-}04$, and $c_{10} = 0.949$.

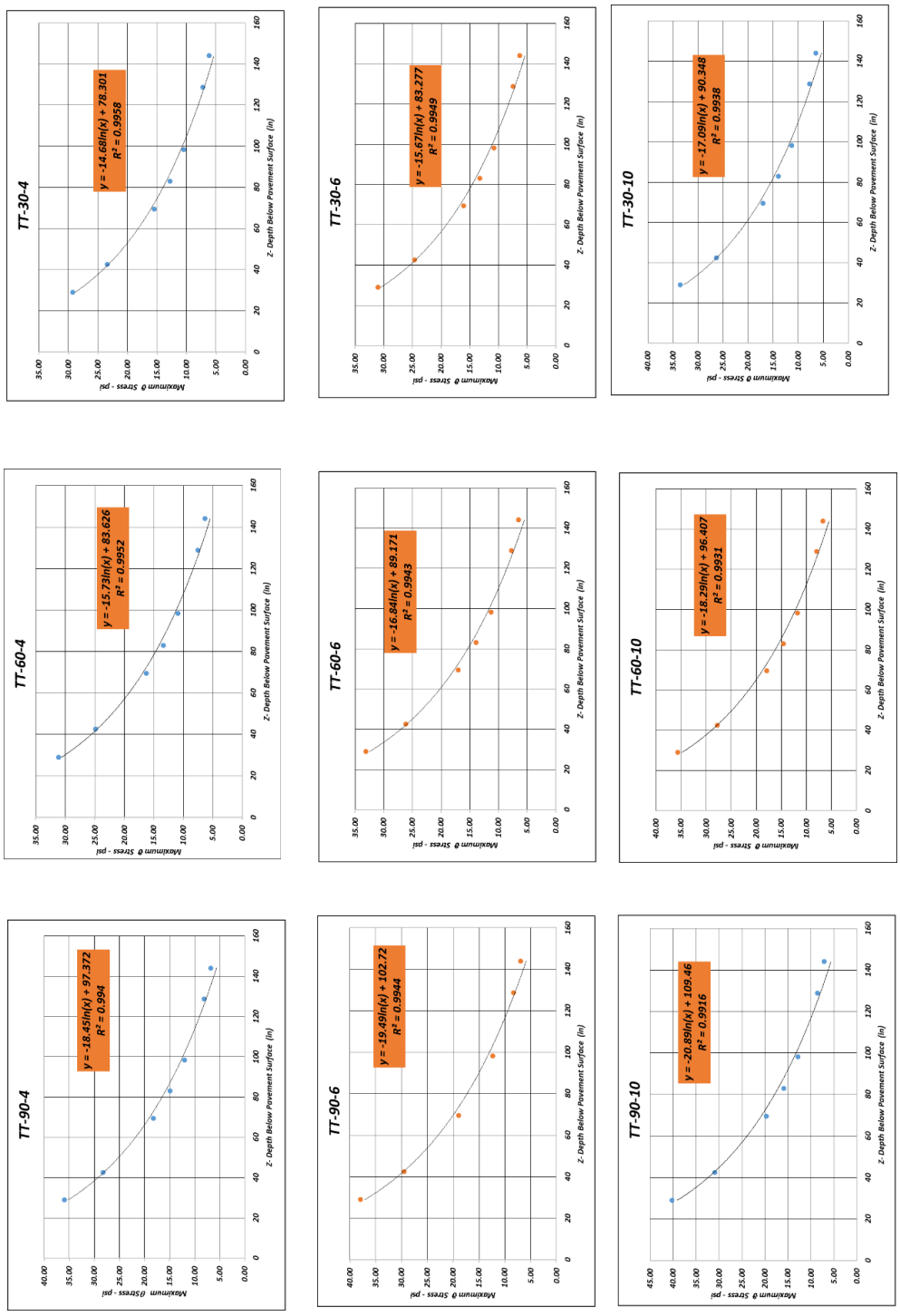

Figure 6.22. θ Stress Versus Depth as Function of E_{sg} and AC Temperature - Triple Tandem Gear - 60 Kip Wheel Load

Table 6.26. Octahedral Shear Stress Analysis Tandem Regression Analysis - 60 Kip Tire Load

Model Form: θ = - a*ln z+b						Normalized Coefficients to T=60°F			
Type Gear	T (deg F)	Esg (ksi)	a	b	R^2	βa	βb	Avg βa	Avg βb
TT	30	4	14.68	78.301	0.9886	0.933	0.936	0.937	0.940
	30	6	15.67	83.277	0.9889	0.931	0.934		
	30	10	17.09	90.348	0.9886	0.934	0.937		
	30	20	19.29	101.29	0.9721	0.937	0.940		
	30	30	20.91	109.23	0.9773	0.942	0.945		
	30	40	22.15	115.3	0.9806	0.945	0.948		
	60	4	15.73	83.626	0.9864	1	1	1	1
	60	6	16.84	89.171	0.9866	1	1		
	60	10	18.29	96.407	0.9836	1	`1		
	60	20	20.58	107.7	0.9759	1	1		
	60	30	22.2	115.62	0.9803	1	1		
	60	40	23.45	121.64	0.9832	1	`1		
	90	4	18.45	97.372	0.9659	1.173	1.164	1.137	1.131
	90	6	19.49	102.72	0.9485	1.157	1.152		
	90	10	20.89	109.46	0.936	1.142	1.135		
	90	20	23.3	121.12	0.9779	1.132	1.125		
	90	30	24.73	128.31	0.982	1.114	1.110		
	90	40	25.91	133.61	0.9837	1.105	1.098		

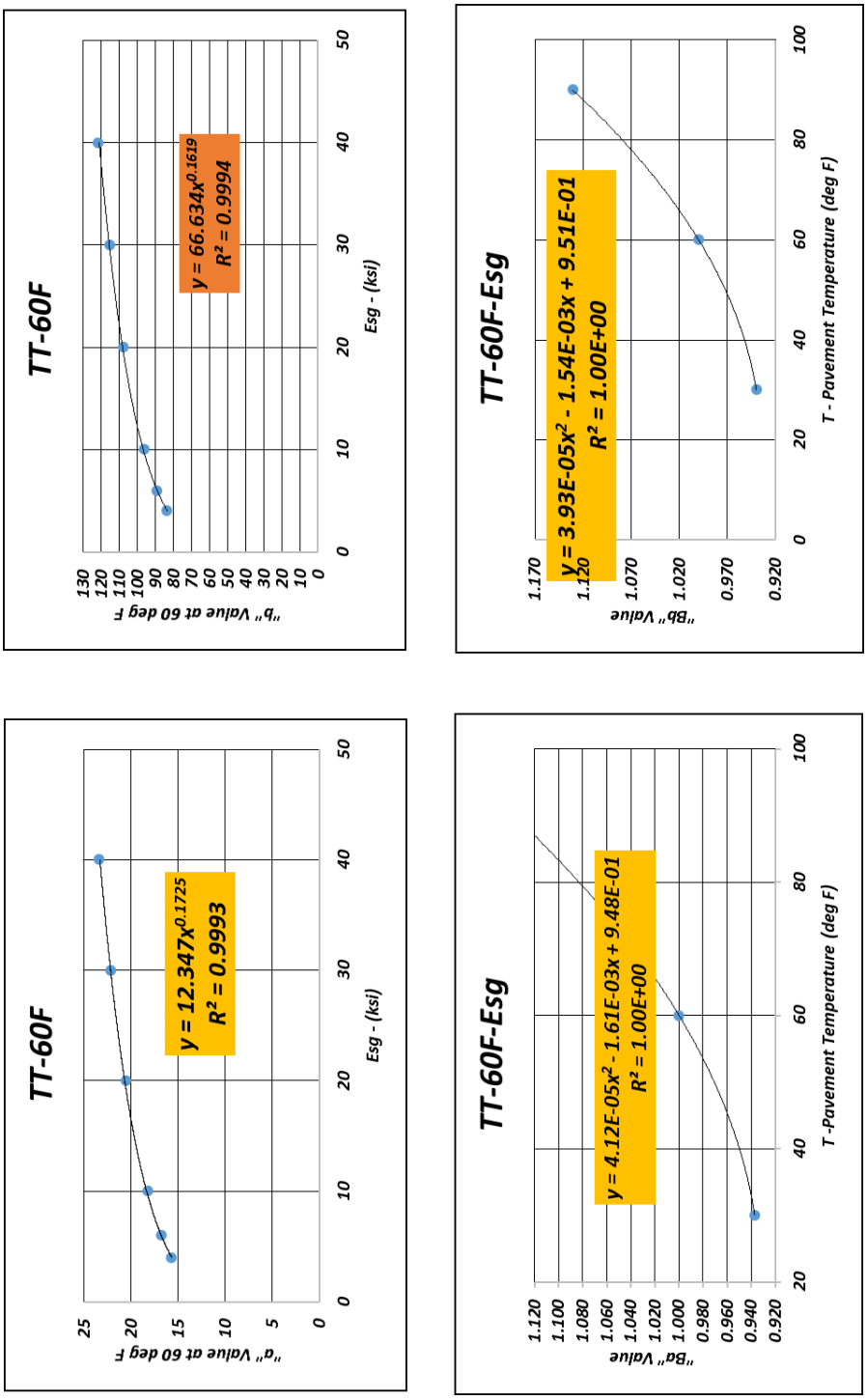

Figure 6.23. θ Regression Constant as Function of E_{sg} and AC Temperature – Triple Tandem Gear - 60 kip Wheel Load

The final comparison plot between the model predicted θ values and those actually computed from JULEA are shown in Figure 6.24. As can be observed, this model also has excellent statistical properties with an average error = 0.065 psi, S_e = 0.787 psi, S_e/S_y = 0.083, and R^2 = 0.99.

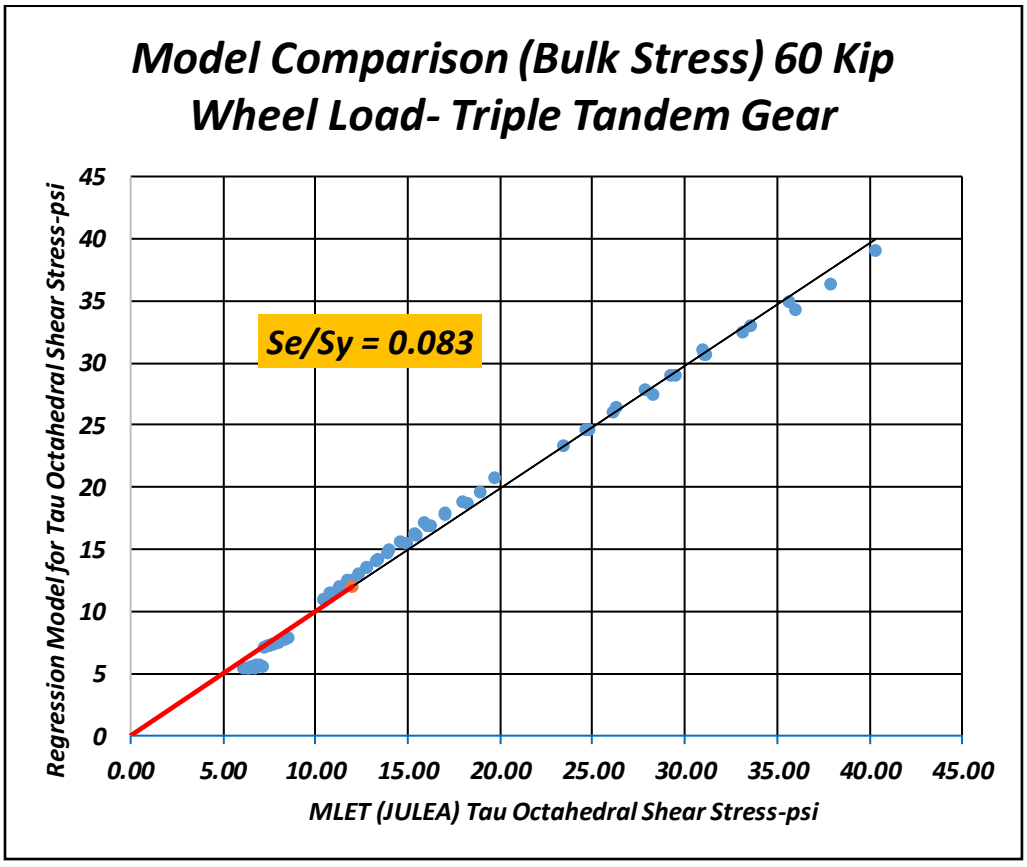

Figure 6.24. Model Comparison (θ Stress) 60 Kip Wheel Load- Triple Tandem Gear

SPECIAL SINGLE WHEEL LOAD STUDY

General Overview

All of the models presented to this point, represent stress solutions (θ or τ_{oct}) as a function of the subgrade modulus (E_{sg}), AC temperature (T), and type of gear (Dual, Dual Tandem and Triple Tandem). Quite importantly, all of these stress solutions have been achieved using a 60-kip load on one of the tires in the gear in question.

The major objective of this study phase was to assess if simplified relationships of the various stress state (θ or τ_{oct}) could be related to wheel loads differing from the 60-kip load used to establish the detailed stress models. If such an approach could be formulated, it would eliminate the need to perform two thirds of the initial planned JULEA computer runs (i.e., eliminate the 50-kip and 70-kip wheel load analysis).

The pursuit of this relationship does have some theoretical basis as the states of stress, in layered systems, are typically directly proportional, to the contact pressure/contact radius (p_c/a_c) ratio. If the contact area (A_c), and hence a_c is constant, the change in the stress magnitude should be directly proportional to the tire (plate) load magnitude. However, the reader should recall that according to NAPTF information; all gear type-load combination used a contact tire pressure of p_c= 243 psi. Thus as the tire (plate) load would change, the A_c (and hence a_c) value of the tire would also change. However, it was the initial hope that this difference would be minor in developing accurate simplified stress analysis

In order to investigate the feasibility of developing such a simplified approach to predict stress state for loads other than the 60-kip load; a special JULEA study was initiated to see if accurate tire load adjustment factors could be determined for the θ or τ_{oct} stress parameters.

Table 6.27 is a summary of the 27 special JULEA MLET runs conducted, with single wheel loads of 50, 60 and 70-kip, on the same matrix of input parameters used in the main 60-kip stress study (E_{sg} and T values). The table also shows the summary of all stress results found from this study. The locations were the θ stress at the midpoints of the base layer, subbase no 1 and subbase no 2 layers, as well as the τ_{oct} values, as a function of the same seven depths (z) previously investigated for the Dupont and County clay subgrade layers.

Table 6.27. Summary of Bulk and Octahedral Shear Stresses for Single Wheel Study

				Comp Pt 2				Comp Pt 3				Comp Pt 4				5	6	7	8	9	10	11
Run ID	P- Wbl	Esg	AC Temp	Base Layer Bulk Stress				Subbase No 1 Layer Bulk Stress				Subbase No 2 Layer Bulk Stress				tau octahedral Stress at Depth (z)						
No	Load (kips)	(ksi)	(deg F)	sig x	sig y	sig z	Θ (I1)	sig x	sig y	sig z	Θ (I1)	sig x	sig y	sig z	Θ (I1)	z=29.5	z=42.5	z=69.5	z=83	z=98.25	z=128.8	z=144
SW 1	50	4	30	-18.4	-18.4	88	51.2	-13.8	-13.8	33	5.4	-8.5	-8.5	12.2	-4.8	3.95	2.35	1.2	0.94	0.74	0.49	0.41
SW 10	60	4	30	-20.9	-20.9	97.8	56	-16.1	-16.1	38.2	6	-10	-10	14.5	-5.5	4.59	2.81	1.44	1.12	0.88	0.59	0.49
SW 19	70	4	30	-22.7	-22.7	106.4	61	-18.3	-18.3	43.1	6.5	-11.6	-11.6	16.7	-6.5	5.41	3.26	1.67	1.31	1.03	0.69	0.58
SW 2	50	4	60	-14.7	-14.7	94.1	64.7	-11.4	-11.4	36.6	13.8	-8	-8	14.1	-1.9	4.54	2.67	1.32	1.02	0.79	0.52	0.43
SW 11	60	4	60	-15.9	-15.9	104.4	72.6	-13.2	-13.2	42.4	16	-9.4	-9.4	16.7	-2.1	5.38	3.19	1.58	1.22	0.95	0.62	0.52
SW 20	70	4	60	-16.9	-16.9	113.3	79.5	-14.9	-14.9	47.8	18	-10.8	-10.8	17.8	-3.8	6.2	3.69	1.84	1.42	1.1	0.72	0.6
SW 3	50	4	90	-9.9	-9.9	101.2	81.4	-7.9	-7.9	41.3	25.5	-6.9	-6.9	16.8	3	5.4	3.14	1.49	1.13	0.86	0.55	0.46
SW 12	60	4	90	-10.2	-10.2	112.1	91.7	-9.1	-9.1	47.9	29.7	-8.2	-8.2	19.9	3.5	6.4	3.74	1.79	1.36	1.04	0.66	0.55
SW 21	70	4	90	-10.3	-10.3	121.4	100.8	-10.1	-10.1	53.9	33.7	-9.4	-9.4	22.9	4.1	7.36	4.33	2.08	1.58	1.21	0.77	0.64
SW 4	50	6	30	-18.3	-18.3	118	81.4	-15	-15	41	11	-9.2	-9.2	14.1	-4.3	4.4	2.55	1.28	0.99	0.77	0.51	0.43
SW 13	60	6	30	-19.2	-19.2	128.1	89.7	-17.3	-17.3	47.2	12.6	-10.9	-10.9	16.6	-5.2	5.22	3.05	1.53	1.19	0.93	0.61	0.51
SW 22	70	6	30	-19.9	-19.9	136.6	96.8	-19.5	-19.5	52.7	13.7	-12.5	-12.5	19.1	-5.9	6.01	3.53	1.78	1.38	1.08	0.72	0.6
SW 5	50	6	60	-13.1	-13.1	123.7	97.5	-12.2	-12.2	44.8	20.4	-8.6	-8.6	16.1	-1.1	5.03	2.88	1.4	1.08	0.83	0.54	0.45
SW 14	60	6	60	-13.2	-13.2	134.1	107.7	-14	-14	51.5	23.5	-10.1	-10.1	19	-1.2	5.95	3.44	1.68	1.29	1	0.65	0.54
SW 23	70	6	60	-13	-13	142.7	116.7	-15.5	-15.5	57.5	26.5	-11.6	-11.6	21.8	-1.4	6.84	3.98	1.96	1.5	1.16	0.75	0.63
SW 6	50	6	90	-7.6	-7.6	130	114.8	-8.4	-8.4	49.8	33	-7.4	-7.4	19	4.2	5.94	3.37	1.58	1.19	0.91	0.58	0.47
SW 15	60	6	90	-6.7	-6.7	140.7	127.3	-9.4	-9.4	57.1	38.3	-8.7	-8.7	22.4	5	7.02	4.02	1.89	1.43	1.09	0.69	0.57
SW 24	70	6	90	-5.6	-5.6	149.5	138.3	-10.3	-10.3	63.8	43.2	-9.9	-9.9	25.7	5.9	8.07	4.65	2.2	1.66	1.27	0.8	0.66
SW 7	50	10	30	6.2	6.2	154.9	167.3	-13.1	-13.1	53.4	27.2	-9.9	-9.9	17.5	-2.3	5.17	2.98	1.47	1.13	0.88	0.57	0.47
SW 16	60	10	30	10.1	10.1	163.2	183.4	-14.7	-14.7	60.7	31.3	-11.6	-11.6	20.6	-2.6	6.11	3.55	1.76	1.36	1.05	0.68	0.57
SW 25	70	10	30	13.8	13.8	169.6	197.2	-16.2	-16.2	67.3	34.9	-13.3	-13.3	23.5	-3.1	7.02	4.11	2.05	1.58	1.23	0.8	0.66
SW 8	50	10	60	11.4	11.4	159.8	182.6	-9.9	-9.9	57.7	37.9	-9	-9	19.8	1.8	5.86	3.35	1.61	1.22	0.93	0.6	0.49
SW 17	60	10	60	15.8	15.8	168.2	199.8	-11	-11	65.6	43.6	-10.6	-10.6	23.3	2.1	6.93	3.99	1.93	1.47	1.12	0.71	0.59
SW 26	70	10	60	20.2	20.2	174.7	215.1	-11.9	-11.9	72.7	48.9	-12.1	-12.1	26.6	2.4	7.95	4.62	2.24	1.71	1.31	0.83	0.69
SW 9	50	10	90	16.2	16.2	165.5	197.9	-5.8	-5.8	63.2	51.6	-7.6	-7.6	23.1	7.9	6.88	3.88	1.79	1.34	1.01	0.63	0.51
SW 18	60	10	90	21.3	21.3	174	216.6	-6.1	-6.1	71.8	59.6	-8.9	-8.9	27.2	9.4	8.12	4.62	2.15	1.61	1.21	0.75	0.62
SW 27	70	10	90	26.1	26.1	180.6	232.8	-6.2	-6.2	79.6	67.2	-10.1	-10.1	31.1	10.9	9.31	5.34	2.5	1.87	1.41	0.88	0.72

Bulk Stress Results

The results of this study for all JULEA predictions of the θ stress are plotted in Figure 6.25. Figure 6.25 (a) shows the comparison of all θ values for the 50-kip wheel load to those found for the 60-kip wheel load. Figure 6.25 (b) shows this same comparison between the 70-kip and 60-kip wheel loads.

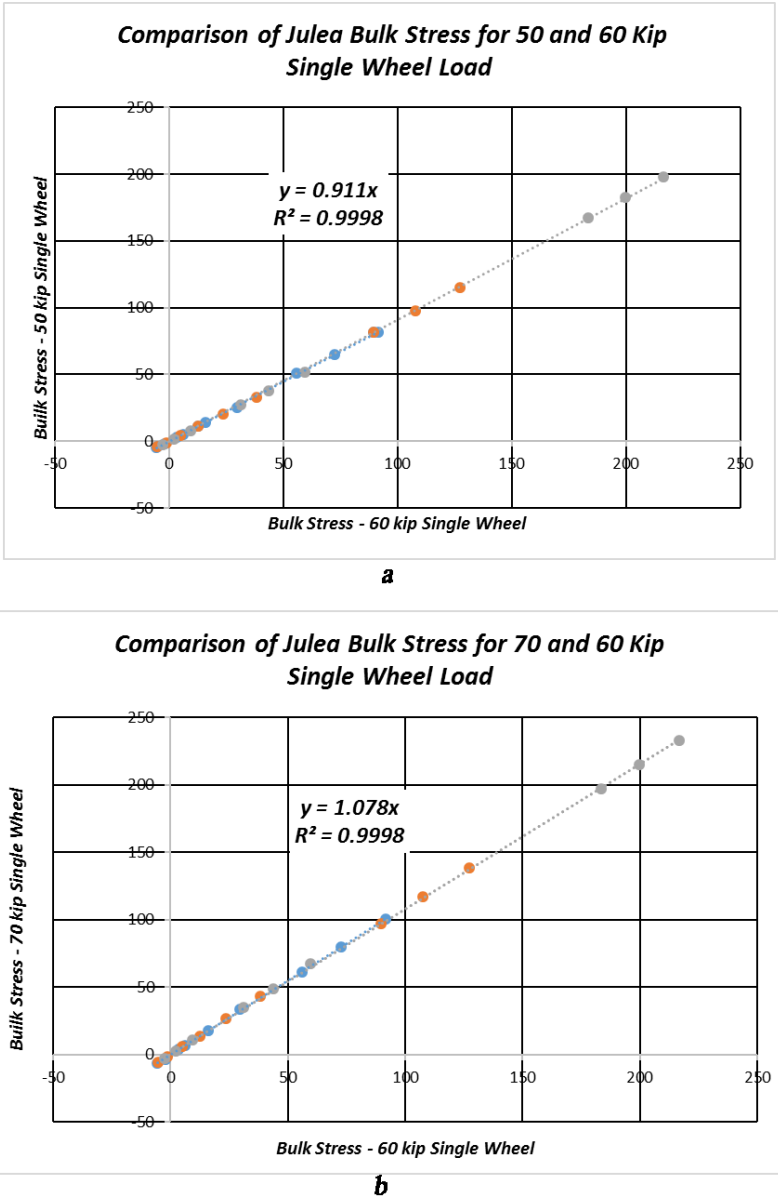

Figure 6.25. Bulk Stress Comparison for 50, 60 and 70 kip Single Wheel Loads

It can be observed that there is almost a near perfect relationship for each wheel load to the 60-kip single wheel. The relationship of the bulk stress ratio for the 50 to 60-kip and the 70 to 60-kip loads are shown in Table 6.28.

Table 6.28. Relationship of Bulk Stress Ratio to Different Wheel Loads

Load- Pi	θ ratio
50 k	0.911
60 k	1.00
70 k	1.078

Octahedral Shear Stress Results

Figure 6.26 illustrates a similar result for all of the JULEA comparisons for the τ_{oct} shear stress results within the clay subgrades. The τ_{oct} stress ratio found for the 50 to 60-kip and the 70 to 60-kip loads are shown Table 6.29.

Table 6.29. Relationship of τoct Stress Ratio to Different Wheel Loads

Load- Pi	τ_{oct} ratio
50 k	0.844
60 k	1.00
70 k	1.151

Both the θ and τ_{oct} relationships are, for all practical purposes, a perfect correlation with $R^2 \sim 1.00$ for 27 data points (θ analysis) and 63 points (τ_{oct} analysis).

Final Tire Load Stress Adjustment Factors

Figure 6.27 summarizes the simple models that were developed to adjust the θ and τ_{oct} stress models, from the 60-kip wheel load equations previously presented. The adjustment factor (λ_i) allows the stress state to be adjusted by using the actual wheel load magnitude in question (P_i) and the results for the 60-kip wheel load. The final models developed were:

Bulk stress:

$$\theta_i = \lambda_i \theta_{60}$$

with θ_i= bulk stress at a given single wheel load P_i, θ_{60} = bulk stress for the 60-kip wheel load, and λ_i= bulk stress load adjustment factor.

with:

$$\lambda_i = 0.4961 \ln(P_i) - 1.0301$$

Octahedral shear stress:

$$\tau_i = \lambda_i \tau_{60}$$

with τ_i = octahedral shear stress at a given single wheel load P_i, τ_{60} = octahedral shear stress for the 60-kip wheel load, and λ_i= octahedral shear stress load adjustment factor.

with

$$\lambda_i = 0.9131 \ln(P_i) - 2.7361$$

With P_i in both adjustment factors models in kips.

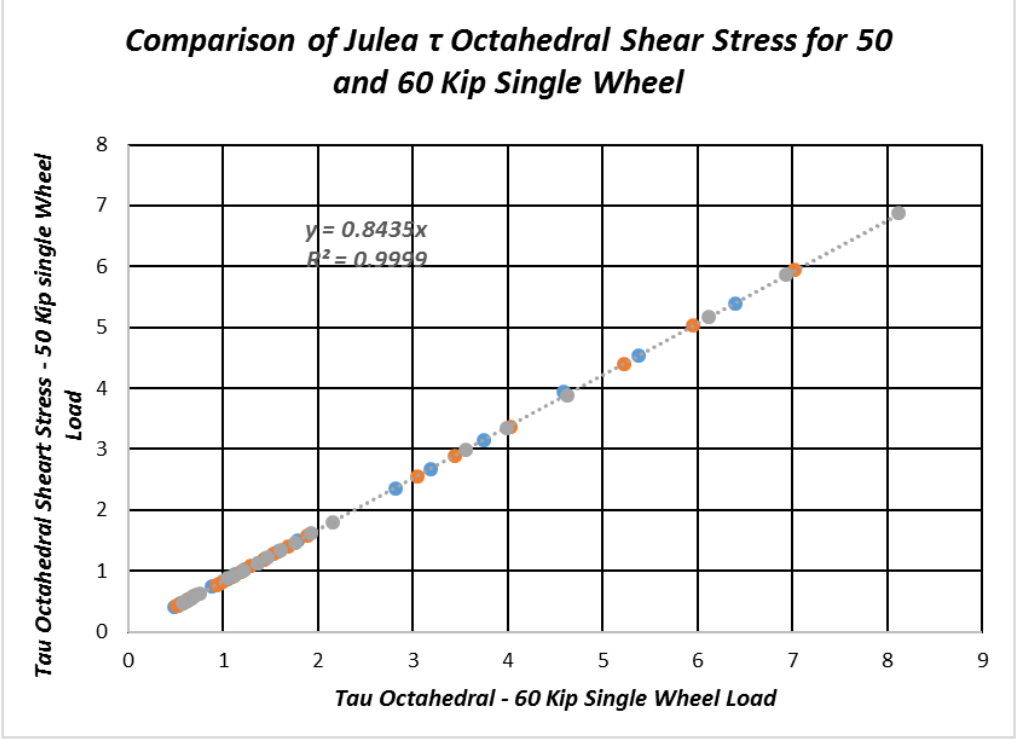

a

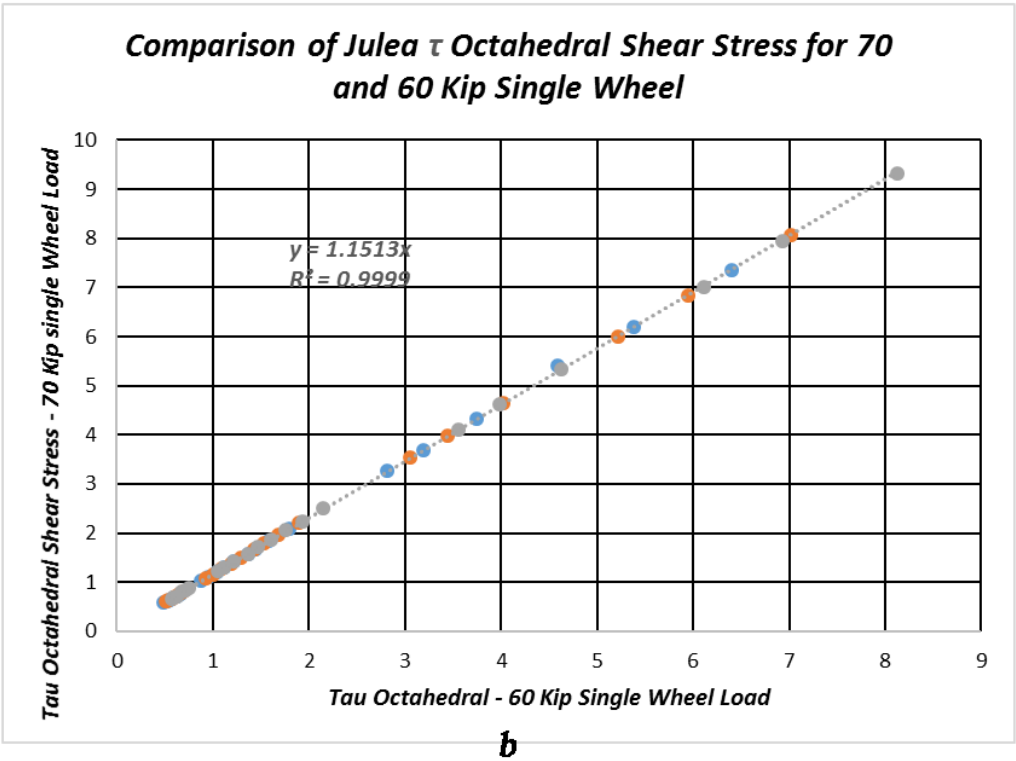

b

Figure 6.26. Octahedral Shear Stress Comparison for 50, 60 and 70 kip Single Wheel Loads

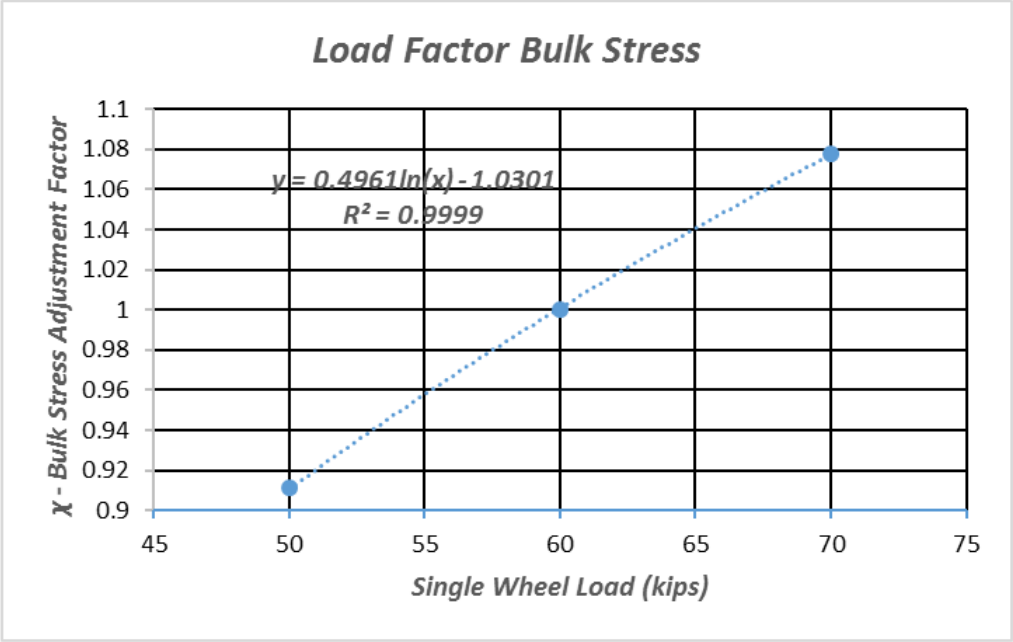

a

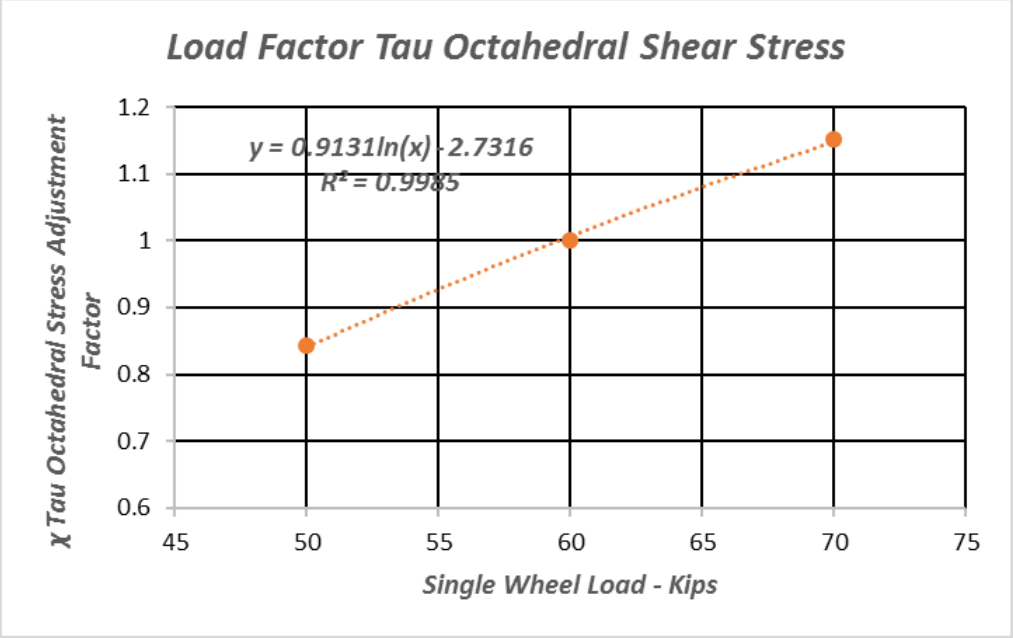

b

Figure 6.27. Bulk and Octahedral Shear Load Factors versus Wheel Load

SUMMARY OF JULEA STRESS MODELS

General

The following sections provide a final summary of all models developed/presented in this chapter. This is done for user convenience so that predictions of both the θ and τ_{oct} values can be easily simulated for the critical stress states within the NAPTF test sections.

Bulk Stress Results

Table 6.30 is the summary of all bulk stress (θ) models to be used to predict mid layer θ stress states within the subgrade. These equations allow for the prediction of θ as a function of:

- Layer type: Base, Subbase No 1 layer, Subbase No 2 layer
- Gear type: Dual, Dual Tandem, Triple Tandem.
- Subgrade Modulus: E_{sg} (ksi)
- AC Temperature: T (°F)
- Single wheel loads: P_i (kips)

Octahedral Shear Stress

Table 6.31 is the summary of all models developed in this chapter that can be used to accurately predict the τ_{oct} shear stress values within any depth of the Dupont and County clay subgrade materials. These equations allow for the prediction of τ_{oct} as a function of:

- Gear type: Dual, Dual Tandem, Triple Tandem.
- Depth within subgrade: z inches from pavement surface
- Subgrade Modulus: E_{sg} (ksi)
- AC Temperature: T (°F)
- Single wheel loads: P_i (kips)

Table 6.30. Summary of Bulk Stress Models - 60 Kip Single Tire Load

General Models for A' and B' Stress Coefficients				
Layer	Gear Type	Tau 60 Eqn	A'60	B'60
Dupont/County Clay Subgrade	Dual Tire	=A'*z^(-B')	=(c1*Esg^c2)(c3*T^2+c4*T+c5)	=(c6*Esg^c7)(c8*T^2+c9*T+c10)
	Dual Tandem	=-A'*ln(z)+B'	=(c1*Esg^c2)(c3*T^2+c4*T+c5)	=(c6*Esg^c7)(c8*T^2+c9*T+c10)
	Triple Tandem	=-A'*ln(z)+B'	=(c1*Esg^c2)(c3*T^2+c4*T+c5)	=(c6*Esg^c7)(c8*T^2+c9*T+c10)

Summary of A' and B' Regression Constants (ci)										
Gear Type	c1	c2	c3	c4	c5	c6	c7	c8	c9	c10
Dual Tire	410.56	0.8066	0.0002	-0.0123	1.012	1.0836	0.1079	2.24E-05	-1.251E-03	0.9944
Dual Tandem	10.314	0.1816	5.6894E-05	-2.8124E-03	9.6393 E-01	54.668	0.1731	5.8253E-05	-3.0126E-03	0.9710 5
Triple Tandem	12.347	0.1725	4.12E-05	-1.61E-03	0.948	66.63	0.1619	3.39E-05	-1.54E-03	0.951

Stress Equation for Single Tire Loads (Pi) Other than 60 Kip
Ti = χi *T(60)
χi = 0.9131*ln(Pi)-2.7316

Units for Variables Used in Models	
Pi: (Tire Load)	kips
Esg: (Subgrade Modulus)	ksi
T: (AC Layer Pavement Temperature)	deg F
z: (Depth into Subgrade-From Pvt Surface)	inches

Table 6.31. Summary of Octahedral Shear Stress Models - 60 Kip Single Tire Load

General Models for A' and B' Stress Coefficients				
Layer	Gear Type	Tau 60 Eqn	A'60	B'60
Dupont/County Clay Subgrade	Dual Tire	=-A'*z^(-B')	=(c1*Esg^c2)(c5*e^(c6*T))	=(c3*Esg^c4)(c7*T^2+c8*T+c9)
	Dual Tandem	=-A'*z^(-B)'	=(c1*Esg^c2)(c3*T^2+c4*T+c5)	=(c6*Esg^c7)(c8*T^2+c9*T+c10)
	Triple Tandem	=-A'*(z^(-B')	=(c1*Esg^c2)(c3*T^2+c4*T+c5)	=(c6*Esg^c7)(c8*T^2+c9*T+c10)

Summary of A' and B' Regression Constants (ci)										
Gear Type	c1	c2	c3	c4	c5	c6	c7	c8	c9	c10
Dual Tire	62.031	0.8682	0.9044	0.1243	0.6978	0.0063	-7.10E-06	1.82E-03	9.16E-01	
Dual Tandem	33.374	0.5606	1.3412E-05	2.9507E-03	7.7467 E-01	0.6149	0.1164	-1.0329E-06	8.549E-04	0.9524 2
Triple Tandem	17.968	0.557	2.50E-05	8.59E-04	8.58E-01	0.4562	0.1384	-1.37E-06	9.27E-04	0.949

Stress Equation for Single Tire Loads (Pi) Other than 60 Kip
Ti = χi *T(60)
χi = 0.9131*ln(Pi)-2.7316

Units for Variables Used in Models	
Pi: (Tire Load)	kips
Esg: (Subgrade Modulus)	ksi
T: (AC Layer Pavement Temperature)	deg F
z: (Depth into Subgrade-From Pvt Surface)	inches

Chapter 7. : Non-Linear Soil Resilient Modulus Testing and Results

This chapter provides a description of the resilient modulus testing, evaluation and analysis of the two clay subgrades at NAPTF. A comprehensive procedure for measuring resilient modulus in unsaturated soil specimens has been explained in this chapter. The procedure used in the testing of the resilient modulus of the clay subgrade was based upon the new protocol offered in NCHRP 1-28A. This protocol was modified to control and measure the suction of the soil during the testing of resilient modulus. The method used by Cary and Zapata (2010) to perform unsaturated resilient modulus testing of soil was used for this particular study. This chapter also details the procedure used to perform the preconditioning of the specimens, and to test a specimen for resilient modulus of soil under a matric suction measuring mode.

The nonlinear test results obtained were then analyzed to conform to the model developed by Cary and Zapata (CZ) which was modified to simplify the prediction of the M_r without any loss in accuracy. Typical non-linear coefficients (ki) were statistically obtained through regression analysis.

RESILIENT MODULUS EQUIPMENT SET UP AND TESTING DETAILS

The equipment involved in the preparation of the sample and the testing of the resilient modulus of the soil is presented in this section.

Resilient Modulus Testing

The triaxial system used for this testing is a custom built system, capable of applying repeated cyclic loads of a haversine-shaped load pulse to perform the resilient modulus testing of both clay types at NAPTF. This system is capable to perform all functions needed for an unsaturated resilient modulus testing except for the preparation of the specimen and

the pressure cell assembly. The unsaturated soil testing system is an electro-hydraulic system with a closed-loop digital servo control. Direct measurement and control of the pore water pressure (u_w) and pore air pressure(u_a) can be achieved in this system. The system has a load cell capacity of 22.24 kN (5000 lbs) and the load reaction frame is capable of supporting up to 45 kN (10,000 lbs) in tension or compression. The primary advantages of this system are the highly precise Pressure/Volume controller and the soil suction measuring/controlling device. The arrangement consists of top and bottom load platens. The pore air pressure(u_a) is applied through the top platen, which also consists of a porous stone. The bottom plate consists of a High Air Entry Value (HAEV) disc similar to the one used for a SWCC device. The pore water pressure (u_w) is applied through the bottom platen. The HAEV disc restricts the air and allows only the water to pass through the disc. All the components mentioned above can be seen in Figure 7.1. GCTS CATS v1.6 is the software available for the operation of the testing systems used in this study. It is a user-friendly Windows 98, XP™ compatible software for automated test control. For this study, a user defined testing sequence, according to the NCHRP 1-28 A protocol and further modified according to recommendations made by Cary and Zapata (2010) were utilized. A double layered glass chamber was used for confinement and air was used as the confining material for this study. The vertical deformations on the test specimen were measured using two Linear Variable Differential Transformers (LVDTs). The LVDTs are mounted directly onto the studs which were buried into the soil specimen during preparation.

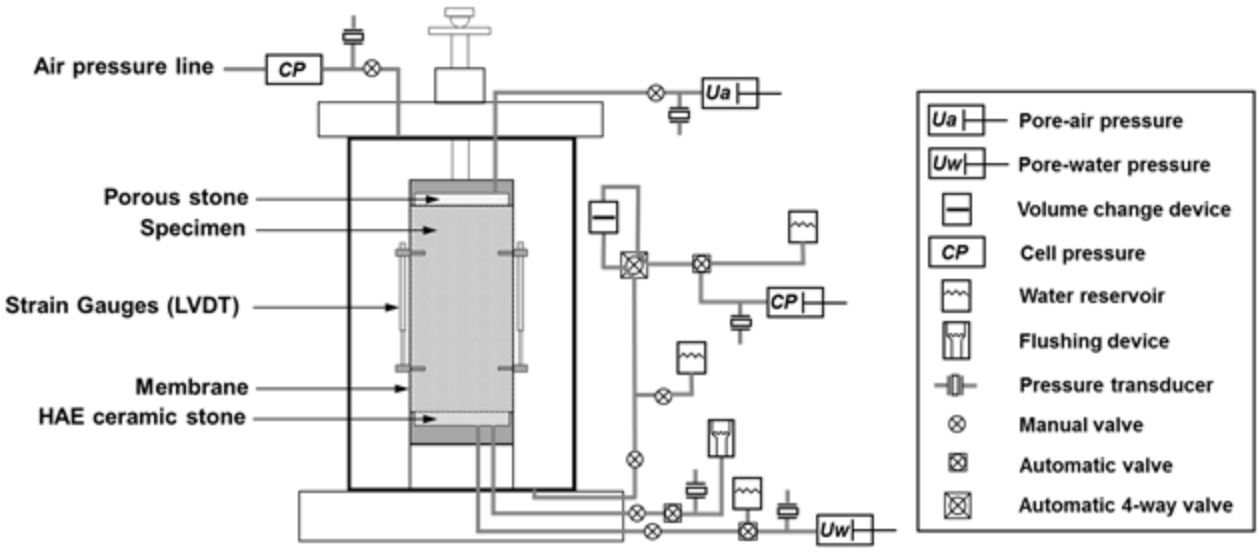

Figure 7.1 Layout of Unsaturated Soil Testing System (Source: Farhad, 2015)

Preparation of Test Specimens

The equipment used to prepare the specimen were in accordance to the NCHRP 1-28A protocol which are a 4-inch mold, 0.025 inch rubber membrane, vacuum pump, a base platten and a top platen with porous stones. Since the soil was panned to be compacted at three different energy levels, two different hammers were used in the test. They are 5.5 lb hammer and a 10 lb hammer. Three levels of compaction energy were selected to approximate standard and modified energies along with one intermediate compaction energy.

The specimens used to test the resilient modulus of the soil followed the harmonized protocol developed in NCHRP 1-28 A. The following steps were involved in the preparation of the specimen.

1. According to NCHRP 1-28 A, the test specimen size is determined based on the sieve analysis test results. For the clay subgrades used in the research, the test specimen was prepared with a height of 9.5 in and diameter of 4 inch.
2. The soil was mixed to a targeted water content. An additional small percentage of water content (~0.5%) was considered in the mixture to compensate for any loss of material moisture due to evaporation during the test specimen preparation.
3. The moist soil was placed in a plastic bag for at least 96 hours to ensure a uniform distribution of water throughout the soil sample.
4. The soil was compacted in the molds, which had rubber membranes on the inner circumference of the mold, to produce 4-inch specimen according to the compaction method and the required compaction energy as shown in Table 7.1.
5. Excess amount of soil was trimmed from the top of the mold.
6. Once the soil was compacted, the weight of the soil sample was noted and the wet(mass) and dry density of the soil specimen was calculated.
7. Since the pre-conditioned method adopted in this study is "as prepared moisture content", no extra steps were taken for pre-conditioning.
8. Internal studs were placed in the sample at equal distance from the center after cutting the rubber membrane surrounding the soil and the distance between the studs being 10 cms.
9. Once the studs are inserted, the holes in the rubber membrane were closed with 2-part epoxy. A 12-hour time duration was selected to ensure that the epoxy had completely set.

10. After the epoxy dried, clamps were installed on the studs inserted and LVDTs were then installed on the clamps.
11. The soil sample was then placed on the bottom platen of the triaxial system which consists of a HAEV disk.

Table 7.1. Compaction Energy at which M_r Tests were Performed

Name	Energy Level	No.of Layers	No. of blows per layer	Hammer used	Hammer Drop Height (in)	Load (lbs)	Volume of Sample (ft^3)	Comp. Energy ($lbs.ft/ft^3$)
3S	Standard	3	56	Standard	12	5.5	0.0706	13087.8
5I	Intermediate	5	56	Standard	12	5.5	0.0706	21813
5M	Modified	5	56	Modified	18	10	0.0706	59490

Disk Saturation and De-Airing of System

Air bubbles must be completely removed from the HAEV ceramic disk in order to ensure a continuous flow of water through the disk. The following steps were adopted as a procedure for the HAEV disk saturation in this study:

1. Place the bottom platen, with the ceramic disk already glued, inside the triaxial cell.
2. Assemble the cell and fill it with water up to a height of 2 inches above the top of the bottom platen.
3. Leave the pore water pressure port opened to allow the flow of the water passing through the ceramic disk.
4. Close the valves and apply cell pressure to push the water through the ceramic disk for about 24 hours.

5. Once water is flowing out of the cell through the pore water pressure port, it can be assumed that the saturation process has been completed.
6. Reduce slowly the cell pressure applied and drain the water out of the chamber.
7. Take the cell apart and wipe the exceeding water to get the chamber ready for placing the specimen.

The system should be flushed or de-aired before and during the pre-conditioning of test specimens, and before the resilient modulus test in order to insure accurate measurements of water volume change and pressure changes. The following steps were adopted as a procedure for de-airing of the system:

1. Open the valve of the flushing device reservoir to allow the flow of water through the system.

2. Push de-aired water out of the pore pressure PVC cylinder to flush the line connected to the pore water port in the cell, the spiral compartment below the ceramic disk in the bottom platen and the line connecting the cell with the flushing device.

3. The water should be flushed back and forth until no more air bubbles are observed coming out of the flushing device reservoir.

RESILIENT MODULUS TEST PROCEDURE

Testing Protocol

The procedure for M_r testing followed the guidelines of the latest "harmonized" protocol NCHRP 1-28A. As mentioned, the modifications by Cary and Zapata (2010), in the loading procedures and additional steps that are introduced in order to implement the control and measuring of matric suction during the test were adopted in this study. The test measuring matric suction can be identified as a constant water content test. The following procedure

is an attempt to summarize the basic steps to perform this new type of M_r test under the "effective stress" approach for unsaturated soils. The following are the steps to perform the resilient modulus test in unsaturated soil specimens:

1. Once the specimen has been pre-conditioned, flush the system following the procedure explained in previous sections, to remove all air bubbles and then make sure to close the valve of the flushing device.
2. Recall that the confining pressure corresponding to the first sequence of the loading procedures and target matric suction was already applied on the specimen for pre-conditioning purposes.
3. Input all the information required by the controlling software regarding the specimen dimensions and axial gauge.
4. Keep the pore water pressure valve closed if matric suction is to be measured when running the test (constant water test).
5. The appropriate loading procedure for each test specimen is selected from the stress-load repetition sequence suggested by NCHRP 1-28A and Cary and Zapata (2010) according to the material to be tested. Table 7.2 shows the loading sequence adopted for fine grained soils.
6. Once the test starts, it is important to monitor that the vertical permanent strain does not reach 5% or that the vertical displacement ratio R_v between the maximum and minimum vertical displacements are within a reasonable range. While the NCHRP 1-28A specifies a maximum R_v of 1.1; any vertical displacement ratio smaller than 2 was considered acceptable for this study, due to the extreme testing difficulty with high moisture, plastic clays (such as found at NAPTF)

7. If the first requirement of the previous step is not satisfied, the test should be terminated and no further testing of this material is warranted. If the second requirement in the previous step fails, the test should be discontinued and any specimen alignment difficulties corrected before continuing the test to completion.
8. Once the test has been completed, the air pressure is first reduced to zero and then the confining pressure is then eliminated from the chamber. Open the cell valves to release the cell pressure.
9. Remove the specimen from the triaxial chamber.
10. Remove the membrane from the specimen and determine the moisture content of the specimen.
11. Export the data to be analyzed
12. As all tests were run under suction measurement (undrained); the water volume of the specimen was not allowed to vary and changes in pore water pressure during the test were monitored. While the air pressure is intended to be held constant (at a fixed desired value) some variation in the air pressure will occur. This change should always be made to as small as practical during the testing operation.

As a general observation, it is noted that the M_r testing of the clay subgrades, especially at moisture contents in excess of optimum and requiring the mounting of LVDT system on unconfined specimens was a very, very difficult and complex operation.

Physical Properties of Test Specimen

As mentioned in the previous section, the M_r test was performed on the two clay subgrade soils at various water contents and compaction efforts. The M_r tests were initially planned to be performed on all water contents that the CBR test was performed at as shown in

Chapter 5. However, the maximum confining pressure that was produced by the triaxial system in the ASU laboratory, was 150 kPa. Since the confining pressure that needs to be applied to the soil is based upon the pore air pressure of the soil, the soil suction cannot exceed 130 kPa. Though a translation technique was used to translate the change in suction and translate it into the actual suction; water contents less than 20% for the County Clay and less than 25 % for Dupont clay could not be performed. This was not considered a limitation as the in-situ compaction properties for both clays exceeded these moisture levels. The tests performed were found to be insufficient to correlate and understand the influence of the moisture content and suction on the resilient modulus of the soil. Hence a 18 more samples were prepared. The samples were prepared to three moisture contents and three dry densities. Then the sample was allowed to dry out to attain the target moisture content. The samples were then wrapped in plastic wraps and were kept in air tight containers for 30-day period in order for the water to equilibrate throughout the soil sample. While testing these 18 samples, the suction (u_a and u_w) was set to zero and the change in suction throughout the test was measured.

The list of M_r tests performed on the County clay is shown in Table 7.4 and for Dupont clay is shown in Table 7.5. Each specimen was initially prepared at a targeted water content. After the water content in the soil was equilibrated, the soil was then compacted into a mold to obtain a specimen of the dimension as shown in Table 7.3. The mass of the soil for that volume of the specimen was then measured to obtain the dry density of the material. The degree of saturation for each soil was calculated based upon the equation:

$$S\% = \frac{w\ \%}{\frac{\rho_w}{\rho_d} - \frac{1}{G_s}}$$

The matric suction of the soil was measured from the SWCC curves obtained in Chapter 4.

Table 7.2. Modified Test Sequence for Unsaturated Mr Testing

Air Pressure u_a (kPa) =					
Sequence	**Confining Pressure (kPa)**	**Contact Stress (kPa)**	**Cyclic Stress (kPa)**	**Maximum Stress (kPa)**	**Nrep**
0	27.6 + u_a	5.5	48.3	53.8	1000
1	55.2 + u_a	11.0	27.6	38.6	100
2	41.4 + u_a	8.3	27.6	35.9	100
3	27.6 + u_a	5.5	27.6	33.1	100
4	13.8 + u_a	2.8	27.6	30.4	100
5	55.2 + u_a	11.0	48.3	59.3	100
6	41.4 + u_a	8.3	48.3	56.6	100
7	27.6 + u_a	5.5	48.3	53.8	100
8	13.8 + u_a	2.8	48.3	51.1	100
9	55.2 + u_a	11.0	69.0	80.0	100
10	41.4 + u_a	8.3	69.0	77.3	100
11	27.6 + u_a	5.5	69.0	74.5	100
12	13.8 + u_a	2.8	69.0	71.8	100
13	55.2 + u_a	11.0	96.6	107.6	100
14	41.4 + u_a	8.3	96.6	104.9	100
15	27.6 + u_a	5.5	96.6	102.1	100
16	13.8 + u_a	2.8	96.6	99.4	100

Table 7.3. Dimensions of the M_r specimens

Dimensions	**Values**
Diameter (inch)	4.0
Height (inch)	9.5
Volume (ft^3)	0.0706

Table 7.4. M_r tests performed for County Clay

ID	w%	γ_d (pcf)	S %	Ψ (psi)
CC223S	21.4	96.9	73.3	101.5
CC225I	22.9	98.0	80.3	29.0
CC225M	22.5	100.5	83.7	18.9
CC253S	25.3	93.7	80.7	29.0
CC255I	25.4	94.8	83.0	26.1
CC255M	25.2	95.3	83.3	16.0
CC265I	26.5	94.0	85.0	10.2
CC265M	25.5	94.3	82.2	5.8
C 19 1	18.7	106.9	83.0	45.0
C 19 2	17.2	105.8	74.4	137.8
C 19 3	15.4	106.9	68.2	275.5
C 22 1	22.3	100.4	84.6	27.6
C 22 2	18.3	99.2	67.8	304.5
C 22 3	19.8	101.1	76.4	108.8
C 25 1	24.0	99.2	88.5	12.3
C 25 2	22.0	97.3	77.9	87.0
C 25 3	20.8	97.7	74.4	137.8

Table 7.5. M_r tests performed for Dupont Clay

ID	w%	γ_d (pcf)	S %	Ψ (psi)
DC263S	25.7	90.6	77.6	72.5
DC265I	26	92.8	82.3	43.5
DC265M	26.3	94.3	86.9	29
DC303S	31.1	86.1	84.7	39.15
DC305I	32	86.2	87.6	23.2
DC305M	29.5	88.1	84.2	40.6
DC343S	32.4	85.2	86.5	29
DC345I	32	86.3	87.7	24.65
DC345M	32.6	87.1	91	15.95
D 23 1	25.0	95.1	84.1	37.7
D 23 2	20.1	97.2	70.9	116.0
D 23 3	19.8	95.0	66.3	137.8
D 27 1	29.1	91.1	89.0	21.8
D 27 2	24.1	93.1	77.4	72.5
D 27 3	23.1	96.7	80.6	58.0

D 30 1	29.9	88.5	86.2	29.0
D 30 2	26.2	86.0	71.4	103.0
D 30 3	27.3	88.7	79.1	59.5

Test Data Response Collected

The M_r tests were performed on the soil specimen after the specimen was allowed to be equilibrated for two days in the triaxial system before the M_r test was performed. The M_r tests are performed on the sample as mentioned in the previous section and the data is extracted from the system. The data extracted include the Force applied on the system in 16 different cycles along with the contact force, max force applied in the cycle, confining cell pressure, pore air pressure, cell pressure and the two LVDT displacement measurements. Using the data obtained, the values of the stress applied in each cycle, maximum deviator stress obtained, cyclic stress on the sample, the recoverable deformation, resilient strain and finally the resilient modulus of the soil is calculated. The Resilient modulus of the soil is calculated using the equation

$$M_r = \frac{\sigma_d}{\varepsilon_r}$$

Where, Mr = resilient modulus, σ_d = repeated deviator stress, ε_r = resilient strain

Table 7.6 shows a typical set of data extracted for the soil sample DC263S. The test data for the other samples are shown in the Appendix C. From the deviator stress, cell pressure, pore air and pore water pressure obtained from the test data; the bulk stress and octahedral stress applied on the sample is calculated and tabulated. This information was then subsequently used in the statistical regression analysis that followed.

Table 7.6. Test data for DC263S

Sequence	Nominal Cell Pressure	Actual Cell Pressure	Nominal Max Deviator Stress	Actual Max Load	Actual Cyclic Load	Actual Contact Load	Actual Max Deviator Stress	Cyclic Stress	Recoverable Deformation 1	Recoverable Deformation 2	Recoverable Deformation Average	Vertical Displacement Ratio	Resilient Strain Average	Resilient Modulus Avg
	NCP	ACP	$S_{d\,max}$	P_{max}	P_{cyclic}	$P_{contact}$	$S_{d\,Max}$	$S_{d\,cyclic}$	ΔH_1	ΔH_2	H_{avg}	H2/H1	$\epsilon_{r\,avg}$	M_r
	(kPa)	(kPa)	(kPa)	(N)	(N)	(N)	(kPa)	(kPa)	(mm)	(mm)	(mm)		(%)	(psi)
0	28	155	54	519	396	122	56	50.00	0.0093	0.0052	0.0093	1.7713	0.0073	
1	55	176	39	415	238	177	41	30.00	0.0049	0.0028	0.0049	1.7332	0.0039	612429
2	41	171	36	385	232	152	38	30.00	0.0046	0.0028	0.0046	1.6271	0.0037	652370
3	28	157	33	356	232	123	35	30.00	0.0047	0.0023	0.0047	2.0238	0.0035	638489
4	14	142	30	324	230	94	32	29.00	0.0043	0.0023	0.0043	1.8516	0.0033	674621
5	55	177	59	572	395	176	61	50.00	0.0092	0.0056	0.0092	1.6567	0.0074	543641
6	41	168	57	553	402	151	60	51.00	0.0092	0.0052	0.0092	1.7522	0.0072	554514
7	28	154	54	520	399	121	56	51.00	0.0089	0.0048	0.0089	1.8363	0.0069	573206
8	14	142	51	493	398	94	54	51.00	0.0090	0.0049	0.0090	1.8191	0.0070	566837
9	55	177	80	736	560	177	82	71.00	0.0153	0.0093	0.0153	1.6471	0.0123	464192
10	41	170	77	709	558	151	79	71.00	0.0148	0.0089	0.0148	1.6657	0.0118	479874
11	28	153	75	685	563	121	77	72.00	0.0150	0.0085	0.0150	1.7686	0.0117	480144
12	14	139	72	658	565	93	75	72.00	0.0149	0.0084	0.0149	1.7779	0.0116	483366
13	55	177	108	959	782	177	110	99.00	0.0237	0.0160	0.0237	1.4762	0.0199	417847
14	41	167	105	931	778	152	107	99.00	0.0244	0.0157	0.0244	1.5491	0.0201	405859
15	28	153	102	900	779	121	104	99.00	0.0242	0.0154	0.0242	1.5665	0.0198	409214
16	14	138	99	866	774	92	101	98.00	0.0239	0.0147	0.0239	1.6213	0.0193	410165

Table 7.7. Stress state data for different test sequences in sample DC263S

Cycle	S_d	CP+u_a	u_w	u_a	ψ	Bulk Stress	τ_{oct}	Net bulk Stress	Resilient Modulus Measured
	(kPa)	(kPa)	(kPa)	(kPa)		psi	psi	psi	psi
1	30	176.00	-10.86	184.08	513.84	94.83	2.05	14.75	112624
2	30	171.00	-9.66	183.69	512.25	92.66	2.05	12.75	117173
3	30	157.00	-8.71	169.58	497.19	86.57	2.05	12.80	123928
4	29	142.00	-8.16	154.25	481.31	79.90	1.98	12.80	127033
5	50	177.00	-7.72	186.71	513.33	98.17	3.42	16.95	98312
6	51	168.00	-7.42	181.09	507.41	94.40	3.49	15.62	102380
7	51	154.00	-6.99	167.03	492.92	88.31	3.49	15.65	107623
8	51	142.00	-6.85	154.18	479.92	83.09	3.49	16.02	106072
9	71	177.00	-6.73	187.51	513.14	101.21	4.85	19.64	83761
10	71	170.00	-6.55	182.59	508.05	98.17	4.85	18.74	86957
11	72	153.00	-6.31	165.42	490.64	90.92	4.92	18.96	88948
12	72	139.00	-6.36	151.09	476.36	84.83	4.92	19.10	89716
13	99	177.00	-6.45	187.91	513.26	105.27	6.77	23.53	72240
14	99	167.00	-6.35	179.32	504.57	100.92	6.77	22.92	71526
15	99	153.00	-6.31	165.14	490.35	94.83	6.77	22.99	72433
16	98	138.00	-6.27	150.05	475.22	88.16	6.70	22.89	73570

MODELS FOR DEVELOPMENT OF NON-LINEAR M_r RELATIONSHIPS

Witczak-Uzan Universal Model Analysis

Over the last five decades, researchers have used different models to attempt to relate the stress state (represented by different variable) (Townsend et, 1976) (Witczak et al, 1995) (Witczak et al, 2000) to the resilient modulus. Stress conditions are generally regarded as the most important influence on resilient behavior of granular and fine-grained materials. Initially, the behavior of granular soils was found to vary primarily as a function of the bulk stress (first stress invariant), while the applied deviator stress was found to be more important for fine-grained soils. The initial historic research efforts concluded that the stress dependent M_r of granular materials could be characterized by below.

$$M_r = K_1 \theta^{K_2} \text{ (cohesionless)}$$

where θ is the bulk stress (i.e., the sum of the normal stresses), and K_1 and K_2 are regression constants.

On the other hand, the resilient modulus of fine-grained materials was found to be characterized by below

$$M_r = k_1 \sigma_d^{-k_2} \text{ (cohesive)}$$

where σ_d is the applied deviator stress, and k_1 and k_2 are regression constants. Note that the negative sign on the k_2 coefficient implies stress softening behavior (which is typical of fine grained soils), whereas stress hardening behavior is more often observed in granular materials. The current version of the stress dependent Universal Model is a combination of both the models presented above (Witczak and Uzan, 1992) as shown in below

$$M_r = k_1 . p_a . \left(\frac{\theta}{p_a}\right)^{k_2} . \left(\frac{\tau_{oct}}{p_a} + 1\right)^{k_3}$$

where, M_r= resilient modulus, p_a = atmospheric pressure, k_1, k_2, k_3 = regression constants, θ = bulk stress $= \sigma_1 + \sigma_2 + \sigma_3$, and τ_{oct} = octahedral shear stress = $\frac{1}{3}\sqrt{(\sigma_1 - \sigma_2)^2 + (\sigma_1 - \sigma_3)^2 + (\sigma_2 - \sigma_3)^2}$. This model can be seen to be a single "universal" model that can be used to characterize the non-linear M_r behavior of all soils. The use of the atmospheric pressure term (p_a) for the user to define dimensionless values of the three regression fitting coefficients (k_1, k_2 and k_3). The model developed by Witczak and Uzan (1992) clearly explain the influence of the externally applied stress parameters on the resilient modulus, but it does not directly account for the influence of the environmental factors into the stress sate conditions.

Cary and Zapata Model Analysis

Cary and Zapata (2010) proposed a model that incorporates the influence of seasonal environmental variations by including the matric suction as stress state variable into the model developed by Witczak and Uzan. They studied the effects of the moisture content in the soil in terms of suction and obtained sets of regression constants from triaxial experiments on granular base and subgrade materials. The proposed model is shown in below.

$$M_r = c_1.p_a.\left(\frac{\theta_{net} - 3\,.\,\Delta u_{w-sat}}{p_a}\right)^{c_2}.\left(\frac{\tau_{oct}}{p_a}+1\right)^{c_3}.\left(\frac{\Psi_{m_0} - \Delta\Psi_m}{p_a}+1\right)^{c_4}$$

where $\theta_{net} = \theta - 3u_a$ = the net bulk stress and $u_a =$ pore-air pressure; Δu_{w-sat} = pore-water pressure build up under saturated condition; ψ_{m_0} = initial matric soil suction; $\Delta\psi_m$ = relative change in soil matric suction with respect to ψ_{m_0} due to pore-water pressure build up under unsaturated condition ; $k_1 \geq 0$, $k_2 \geq 0$, $k_3 \leq 0$ and $k_4 \geq 0$ are regression constants.

Modified Cary and Zapata Model Analysis

The incorporation of the change in suction parameter($\Delta\Psi$) in the Cary and Zapata model leads to a complicated test and study of the analysis of the influence of suction on the resilient modulus of the soil. The model incorporates the change in suction during the loading process along with the initial suction of the soil as one of the fundamental predictors. The measurement of the change in the suction during the loading process involves expensive assembly of triaxial machine. The measurement of the change in suction means that the values of pore air pressure and pore water pressure has to be monitored separately. The reliability of these measurements depends on the apparatus and the sensors used in the study.

In this study, it was found that the influence of the $\Delta\Psi$ parameter on the two fine grained was very little to none. Hence a modified version of the Cary and Zapata model was used for this study. As mentioned before the model uses the change in the matric suction as one the parameters involved in the prediction of the M_r. The measurement of the change in the matric suction parameter is difficult due to two major reasons: (1) It is a difficult parameter to measure when the triaxial machine with suction control/measured set up is not available. (2) In fine grained soils, the pore pressure responses are much lower than our capability to actually measure it. Hence the regression was performed using CZ model without $\Delta\Psi$ parameter as shown in Eqn.

$$M_r = z_1 . p_a . \left(\frac{\theta_{net}}{p_a}\right)^{z_2} . \left(\frac{\tau_{oct}}{p_a} + 1\right)^{z_3} . \left(\frac{\Psi_{m_0}}{p_a} + 1\right)^{z_4}$$

The regression was performed in logarithmic space and used the classical least square error analysis. In this approach,

$$Error = (\log M_{r-predicted} - \log M_{r-actual})^2$$

This sum of the squares of the errors between the measured and the predicted resilient modulus is minimized for the regression.

ANALYSIS OF TEST RESULTS

The resilient modulus tests were performed according to the NCHRP 1-28A test pro-tocol. The deviator stress and the resilient strain measured during the test were used to calculate the actual resilient modulus of the test. The test results showed that the variation of the resilient modulus of the soil was not only due to the bulk stress and the octahedral stress applied on the soil but was also found to vary with the moisture content of the specimen.

The subgrade materials generally exhibited a softening behavior with respect to increase in the deviator stress. For a constant confinement stress, an increase in the deviator stress resulted in decrease in the resilient modulus. However, the softening behavior of the materials diminished as the moisture content was increased. The data extracted from the test results includes the deviator stress, confining pressure, pore water pressure and pore air pressure applied to the sample. The stress variables were then used bulk stress, net bulk stress octahedral stress, matric suction and the change in the matric suction due to the loading sequences. Using the stress state predictors, the parameters used for various models were found using regression. The test results were analyzed for the three models.

Witczak- Uzan Universal Model

The universal model as described in Eqn (3) is the model which combines both eqn (1) and (2) to be used in all types of unbound materials. It has been found in various studies that bulk stress influences the M_r value for a granular soil and the octahedral stress for fine grained soil. Since the soils used for this study is fine grained soil with County clay being MH and Dupont clay being CH with high value of PI. The k_2 parameter in the model is should be considered to be zero for County and Dupont clay. An analysis was performed in order to understand the role of k_2 in the two soils and whether it should be included in the analysis. A regression was performed for the Universal model in two cases and were compared: (1) Universal model with a constraint k_2=0 and (2) Universal model without k_2=0 constraint. Table 7.8 shows the regression parameters k_1, k_2 and k_3 for Universal model. One of the phase of the analysis was to re-analyze the data with the modified Witczak-Uzan model through the use of linear regression techniques of log M_r (y axis) versus log $\left(\frac{\tau_{oct}}{p_a}+1\right)$ for the (x axis). Figure 7.2 shows the individual test results for

specimen DC 27 1. The specific regression model is shown on each figure. For the model form used, the equation slope term is equal to the k_3 parameter while the k_1 intercept term of the Witczak- Uzan model is derived from

$$k_3 = \frac{10^b}{p_a}$$

Where "b" is the intercept term from the regression model shown in the figure. Table 7.8 is the final statistical summary of the Witczak- Uzan Universal model with k_2=0 and removal of a few obvious test outliers. It can be seen from the left figure in Figure 7.2 that the relationship between the log of octahedral stress parameter with the log of Mr has an involvement of another stress state parameter. The plot on right side of Figure 7.2 was plotted with the Octahedral stress parameter deduced from the M_r and the log bulk stress. It can be seen that there is slight relationship between the bulk stress and the M_r value. Thus, the slope of the equation gives the k_2 parameter and the b intercept can be equated to the k_1 regression parameter. Thus, it can be understood that the bulk stress plays a role in equating the M_r value with the stress parameter. Hence the k_2 value is not recommended to be zero for more accurate prediction of the M_r values. Table 6.8 shows the results of the analysis performed on various tests for regression parameters with k_2 value not equal to zero.

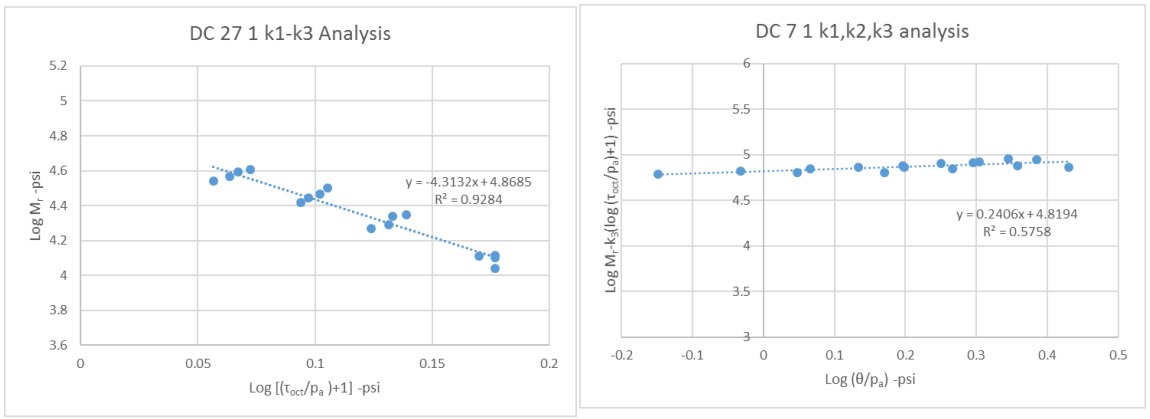

Figure 7.2. Regression Parameters of Universal Model Using Graphical Method

Table 7.8 shows that inclusion of the value of k_2 typically affects the value of k_1 and k_3. This directly increases the accuracy in the prediction of the M_r as seen in Table 7.8. The R square value of the M_r prediction for Universal Model with k_2 value seems to be much higher than the Universal model without k_2. Considering on an average of all samples, the R square value of Universal model with k_2=0 is 0.91 while the model with non-zero k_2 value is 0.98. It can also be seen in Figure 7.3 that the M_r values predicted with k_2=0 seems to be more dispersed than the M_r values predicted with k_2. Thus, it can be seen that the accuracy in the prediction of the M_r increases.

Table 7.8. Regression Parameters for Universal Model for two cases

Type of soil	Moisture content	Dry density	k_2=0				$k_2 \neq 0$			
			k_1	k_2	k_3	R^2	k_1	k_2	k_3	R^2
County	18.70	106.9	3743.3	0	-0.789	0.10	4063.4	0.460	-1.973	0.69
	17.22	105.8	8174.8	0	-2.300	0.94	7769.2	0.110	-2.300	0.97
	15.37	106.9	6120.4	0	-2.051	0.90	5840.9	0.101	-2.051	0.92
	22.28	100.4	480.5	0	-1.009	0.56	127.9	0.757	-1.009	0.75
	18.33	99.2	6044.9	0	-1.031	0.24	6417.6	0.489	-2.135	0.93
	19.79	101.1	13049.0	0	-2.434	0.72	10346.1	0.409	-2.434	0.92
	23.96	99.2	2267.1	0	-1.930	0.63	2072.4	0.194	-1.930	0.68
	22.05	97.3	8262.9	0	-1.494	0.29	8930.9	0.627	-2.929	0.97
	20.83	97.7	9760.6	0	-4.272	0.83	8417.4	0.316	-4.272	0.95
Dupont	25.03	95.1	8244.1	0	-1.651	0.73	8572.9	0.273	-2.282	0.98
	20.10	97.2	3415.2	0	-1.238	0.08	3186.4	1.009	-2.893	0.91
	19.81	95.0	2652.0	0	-0.283	0.01	2890.4	0.815	-2.188	0.90
	29.05	91.1	5029.0	0	-4.313	0.89	4491.4	0.241	-4.313	0.97
	24.12	93.1	4132.3	0	-0.201	0.03	5653.1	0.428	-2.055	0.91
	23.14	96.7	8439.9	0	-1.198	0.73	8662.9	0.197	-1.641	0.96
	29.87	88.5	8266.4	0	-6.527	0.89	8944.6	0.300	-7.387	0.92
	26.19	86.0	5832.5	0	-1.515	0.43	6203.1	0.466	-2.589	0.93
	27.33	88.7	6823.1	0	-2.108	0.91	7018.7	0.173	-2.518	0.99

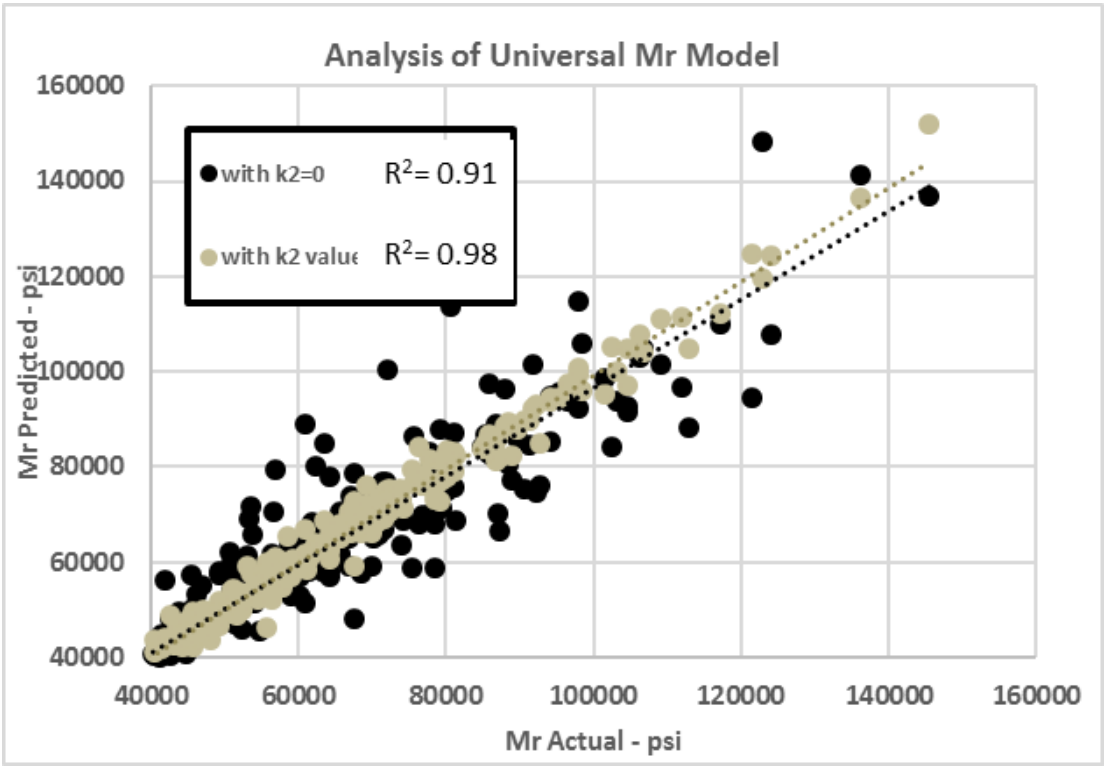

Figure 7.3. Comparison of the Prediction of Universal Model with k2 value as zero and non-zero value for both soils.

Table 7.8 shows the regression parameters k_1, k_2 and k_3 for the different tests. It can be seen that there is a variation of k_1, k_2 and k_3 for different moisture contents or degree of saturation. Hence different tests needs to be performed for different moisture contents for accurate prediction of M_r in Universal model. This can be overcome by using CZ model. CZ model includes the suction parameter in the model which makes the prediction of the M_r more accurate with less effort.

Cary and Zapata Model

Table 7.9 shows the CZ regression parameters considered as a whole for the two types of the soil. Then, the CZ model prediction parameters were compared with the normalized Universal Model.

Table 7.9. Regression Parameters for CZ model and Universal Model for the two soils.

Type of soil	CZ model				Universal model		
	c_1	c_2	c_3	c4	k_1	k_2	k_3
County	1131.41	0.334	-2.720	0.392	5998.42	0.385	-2.337
Dupont	3805.52	0.429	-2.781	0.105	6180.38	0.433	-3.096

Figure 7.4 and Figure 7.5 shows the M_r values predicted using the two models along with the actual M_r obtained from the test. It can be seen from the figure that the CZ model gives a more accurate prediction of M_r when compared to the universal model. The R square value of the model prediction was also calculated to analyze the prediction of the Mr using the two models. The universal model yielded a R square value of 0.60 and 0.45 whereas the CZ model yielded values of 0.87 and 0.58. In conclusion, the CZ parameters shows to predict the M_r more accurately than the universal model.

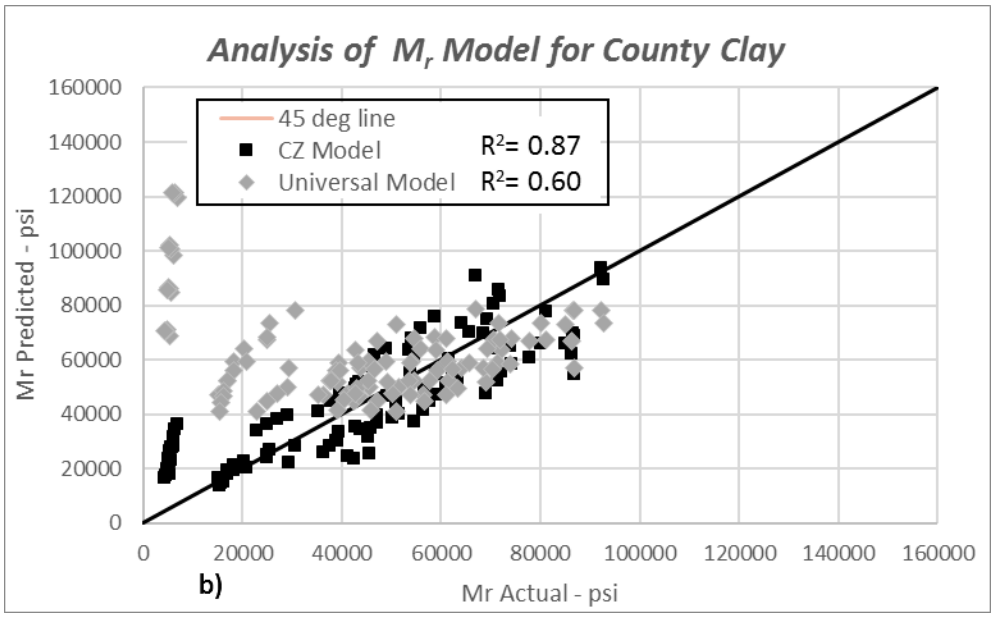

Figure 7.4. Comparison of the Prediction of CZ model with Universal Model for County Clay

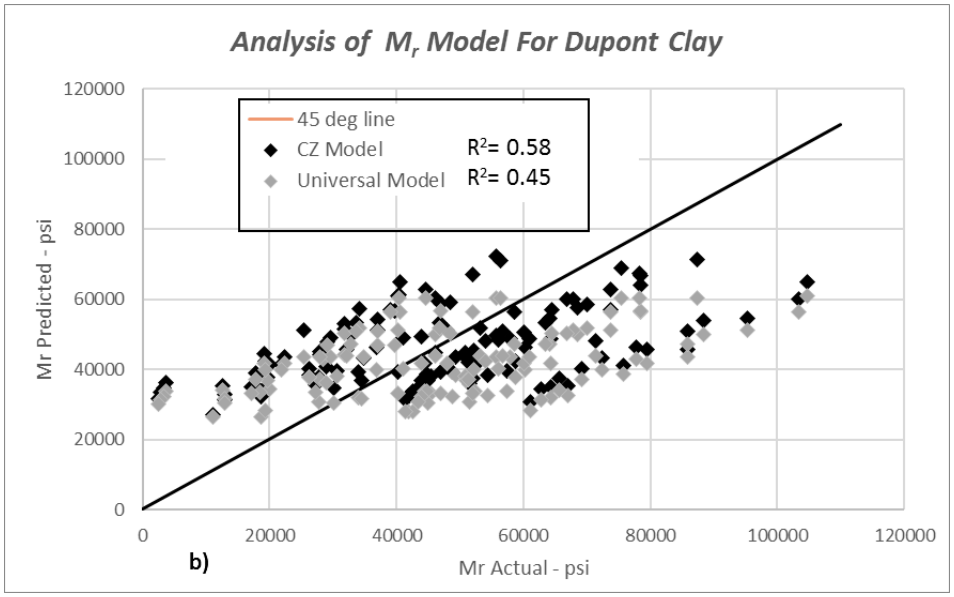

Figure 7.5. Comparison of the Prediction of CZ model with Universal Model for Dupont clay

Modified Cary and Zapata Model

Table 7.9 shows the CZ regression parameters considered as a whole for the two types of the soil. The CZ model using matric suction as stress parameter is evaluated to find c_1, c_2, c_3 and c_4. As mentioned before the model uses the change in the matric suction as one the parameters involved in the prediction of the M_r. The measurement of the change in the matric suction parameter is difficult as discussed previously. Hence the regression was performed in cases: (1) CZ model with $\Delta\Psi$ parameter and (2) CZ model without $\Delta\Psi$ parameter as shown.

$$M_r = z_1 . p_a . \left(\frac{\theta_{net}}{p_a}\right)^{z_2} . \left(\frac{\tau_{oct}}{p_a} + 1\right)^{z_3} . \left(\frac{\Psi_{m_0}}{p_a} + 1\right)^{z_4}$$

Table 7.10 shows the CZ model with the regression parameters c_1, c_2, c_3 and c_4 along with the modified CZ model regression parameters z_1, z_2, z_3 and z_4.

Table 7.10. Regression Parameters for CZ model and Universal Model for the two soils.

Type of soil	CZ model				Modified CZ model			
	c_1	c_2	c_3	c4	z_1	z_2	z_3	z_4
County	1131.41	0.334	-2.720	0.392	1084.37	0.334	-2.742	0.401
Dupont	3805.52	0.429	-2.781	0.105	2198.67	0.520	-3.025	0.240

Figure 7.6 and Figure 7.7 shows the M_r values predicted using the two models along with the actual M_r obtained from the test. It can be seen from the figure that the Modified CZ model gives almost the same or a little more accurate prediction of M_r when compared to the CZ model. The R square value of the model prediction was also calculated to analyze the prediction of the M_r using the two models. The Modified CZ model yielded a R square

value of 0.89 and 0.60 whereas the CZ model yielded values of 0.87 and 0.58. In conclusion, the Modified CZ parameters shows to predict the M_r a little more accurately than the CZ model.

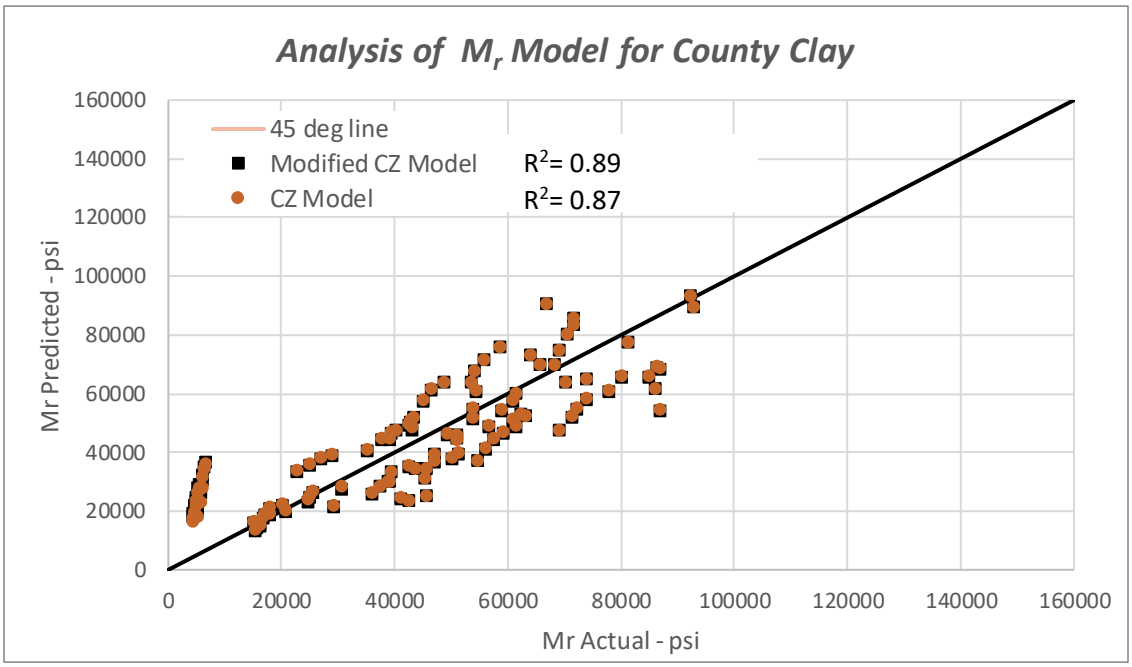

Figure 7.6. Comparison of the Prediction of CZ model with Modified CZ Model for County Clay

Hence the Modified CZ model is chosen to be used for the further analysis of the prediction of variation of the Resilient Modulus in NAPTF.

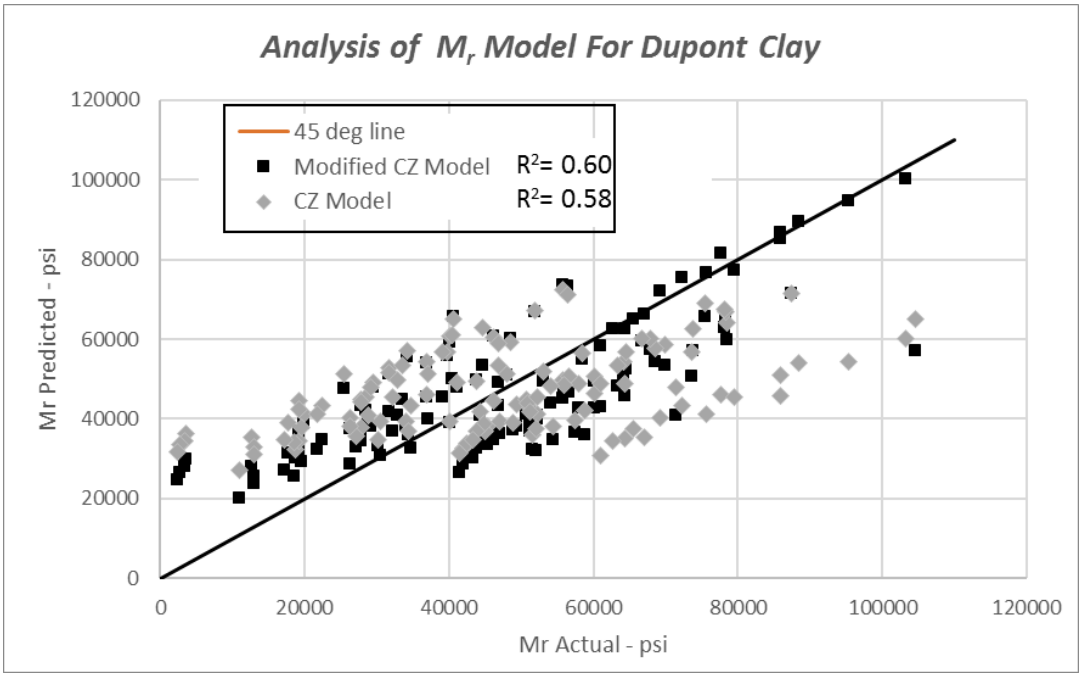

Figure 7.7. Comparison of the Prediction of CZ model with Modified CZ Model for Dupont Clay

SUMMARY

An analysis of the resilient modulus of county and dupont clay was performed from 18 tests that were performed in the ASU lab according to the modified NCHRP protocol. The test results were analyzed for three models of Universal model, CZ model and modified CZ model. Initially the impact of assuming k2 value to be zero was analyzed for the two type of the soil. An analysis of the influence of the octahedral stress parameter and the bulk stress parameters separately showed that the inclusion of the k2 parameter yielded a much more accurate prediction of the Mr. Then an analysis was performed on the CZ model with the inclusion of $\Delta\psi$ value and modified CZ without the inclusion of $\Delta\psi$ value. The results yielded that modified CZ model leads to a more accurate prediction of Mr with the three

stress parameters of bulk, octahedral and suction. Hence, it was decided that modified CZ model will be used in the analysis of the prediction of Mr in the NAPTF.

Chapter 8. Collection and Analysis of Sensor Data from NAPTF Facility

The National Airfield Pavement Test Facility (NAPTF) in Atlantic City, New Jersey was used as the construction site to monitor and analyze the changes in the moisture content and temperature with real time changes atmospheric changes. This chapter aims in providing the information regarding the installation of the sensors to measure volumetric moisture content (VMC) and temperature in the NAPTF. The chapter also explains the compaction data obtained from the test facility and the manner in which the compaction condition of the soil near the sensor that is matched with VMC in order to calculate gravimetric moisture content (w%) and the degree of saturation (S_r%)of the soil. The analyses of the atmospheric temperature data and the relationship between the atmospheric temperature data to the pavement temperature is also shown. The data collected from the sensors were obtained for a three-year period.

INSTALLATION LAYOUT OF MOISTURE/TEMPERATURE SENSOR IN TEST SECTION OF NAPTF

NAPTF is a large airfield pavement test facility located near the airport of Atlantic City, New Jersey. The facility spans 300 feet in length, 60 feet in width and 144 inches deep. Figure 8.1 and Figure 8.2 show the plan and section view of the test facility. The test facility consists of two types of soil as subgrade as shown in Figure 8.2 and Figure 8.3a. The two soils that were used for this particular study are called County Clay and Dupont Clay. Figure 8.3a shows the two soils. The County clay layer occurs at an 83" to 144" depth below the pavement surface and is grey in color. Dupont clay, which is brown in color, occurs at a depth of 29" to 83" below the pavement surface and is also shown in Figure 8.3 a. The test section is enclosed on all four sides below the surface of the pavement using a membrane. Since the facility is basically a hangar, the top of the facility is also a closed

area. This condition helps in preventing the infiltration of any atmospheric precipitation into the soil and also helps mitigate the extreme cold and warm ambient air environment at the site.

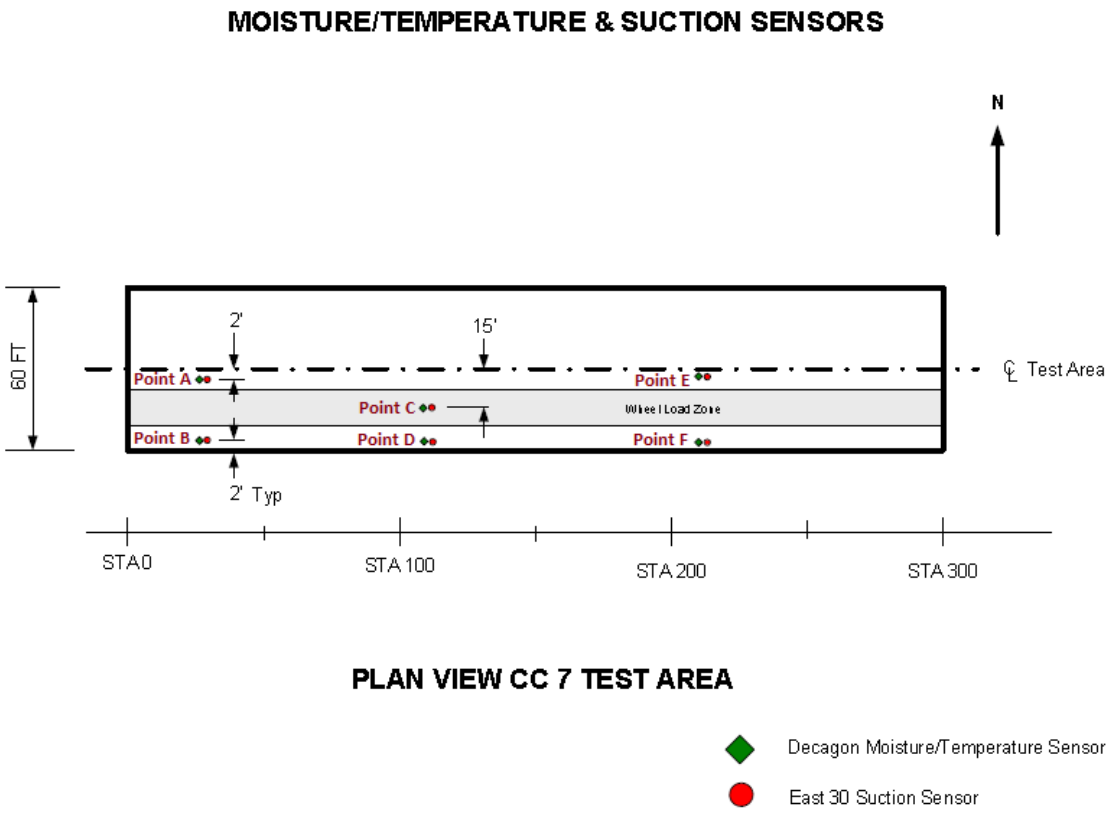

Figure 8.1. Plan View of NAPTF Test Section.

A total of 30 sensors were installed at various locations and depths throughout the test facility. The test section was divided into two identical sections of 30 feet. Six (6) locations were chosen, of which 3 sensors were installed at 2' from the edge of the pavement (Sensor locations B, D and F), 2 sensors were installed 2' from the centerline of the test section

(Sensor locations A and E) and 1 sensor was installed at 15' from the centerline of the test section (Sensor location C). In each location, sensors were installed at five different depths underneath the pavement. In each location, 2 sensors were installed in the Dupont clay at 35" and 77" below the pavement surface and 3 sensors were installed in County clay layers at depths of 89", 106" and 129" below the pavement surface. The sensors at deeper locations were installed on forensic trenches that FAA had previously dug, which saved them some time in excavation and compaction. That resulted in the sensors being placed around stations 25, 110, and 210. While not exactly symmetrical, they have approximately the same spread needed for the study. For shallower depths, after the soil layer was compacted, a borehole was dug in the specified spots. After the sensor was placed, the hole was filled back with the soil cuttings, making sure the wet density was as close as the in-place compaction density. The sensors were installed horizontally, but the prongs were vertically aligned to avoid standing water on top of the them. This was necessary to prevent erroneous measurements of water content.

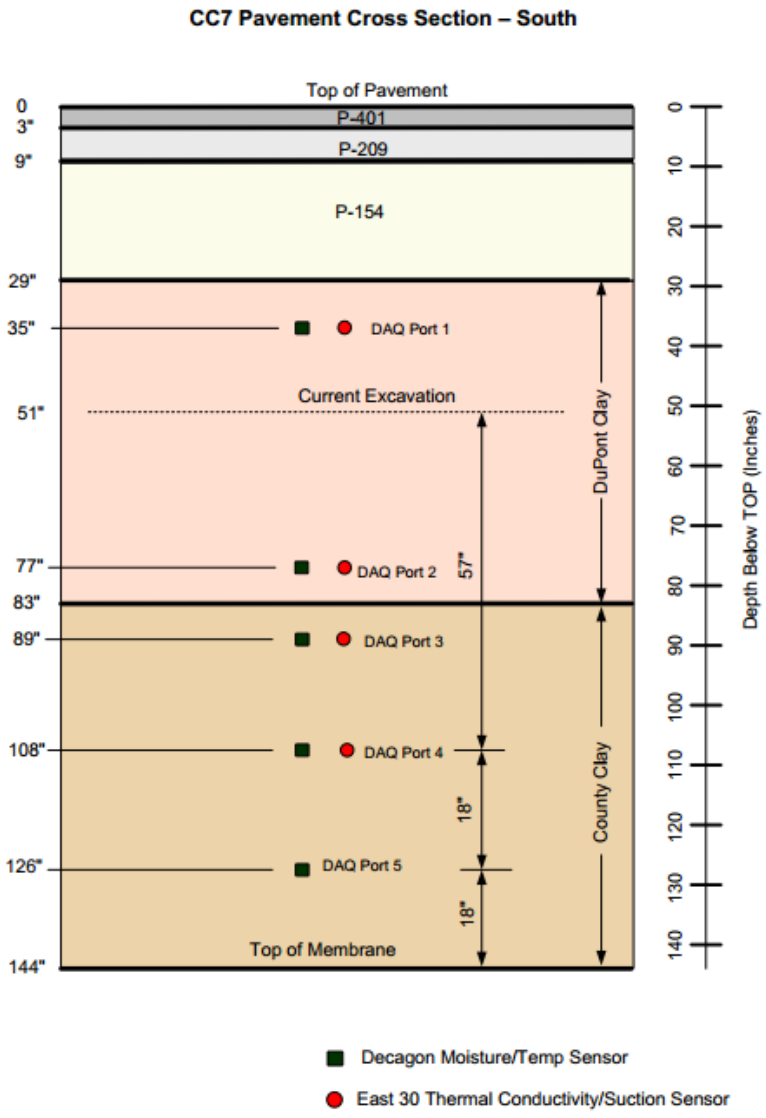

Figure 8.2. Section View of NAPTF Test Section.

A borehole was dug in the specified spots. After the sensor was placed, the hole was filled with the soil. The installation of the sensor was made in such a way that the no water was deposited on the sensor. This was accomplished to eliminate erroneous values of the water content. The sensor was installed in such a way that all three pongs of the sensor were perpendicular to the horizontal axis. The installation of the sensor in a vertical axis also avoids water to be retained on the sensor.

a) Soil layers in NAPTF

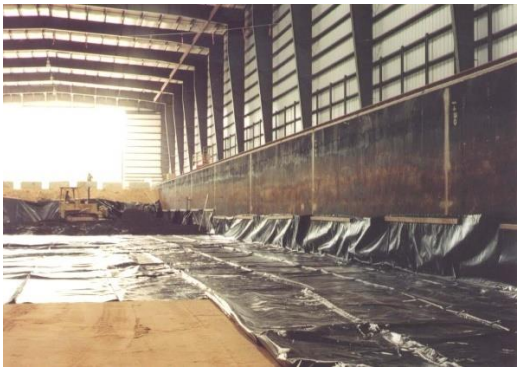

b) Inside View of NAPTF.

Figure 8.3. View of Soil and Hangar in NAPTF

INFORMATION AND CALIBRATION OF MOISTURE/ TEMPERATURE SENSOR

Basic Information of 5TM sensor

5TM water content and temperatures sensors were used in NAPTF in order to measure the volumetric water content and temperature at the same time. The configuration of these sensors is shown in Figure 8.4. The sensor contains three prongs. Two prongs are dielectric volumetric water content sensors. These two sensors use an oscillator running at 70 MHz to measure the dielectric permittivity of the soil used to determine the volumetric water content. A thermistor in thermal contact with the sensor prongs provides the temperature reading of the soil (Decagon Devices, Inc.2015). The specifications for the 5TM sensor is shown in Table 8.1.

Sensor Measurement of Volumetric Water Content

The 5TM sensors measure the volumetric water content of soil by measuring the dielectric permittivity of the soil. Topp's et al. (1980) performed a series of experiments on dielectric permittivity on varies materials and verified that the dielectric permittivity is a function of

the volumetric water content of the tested material. In Topp's research, four mineral soils with a range of texture from sandy loam to clay were tested to find out what soil properties determined the dielectric permittivity of soil. Topp's et al. used time domain reflectometry (TDR) to measure the dielectric constant of materials that were tested. He found that the results varied with texture, bulk density, volumetric water content, temperature and soluble salt content. All soil specimens were placed in a coaxial transmission line and the water or salt solution placed in the material were continuously changed through a porous disk around the soil sample. From the test results, Topp et al. concluded that the dielectric constant and volumetric water content were highly related to each other. Figure 8.5 shows the measured relationship between dielectric constant and volumetric water content of materials that Topps used in his research.

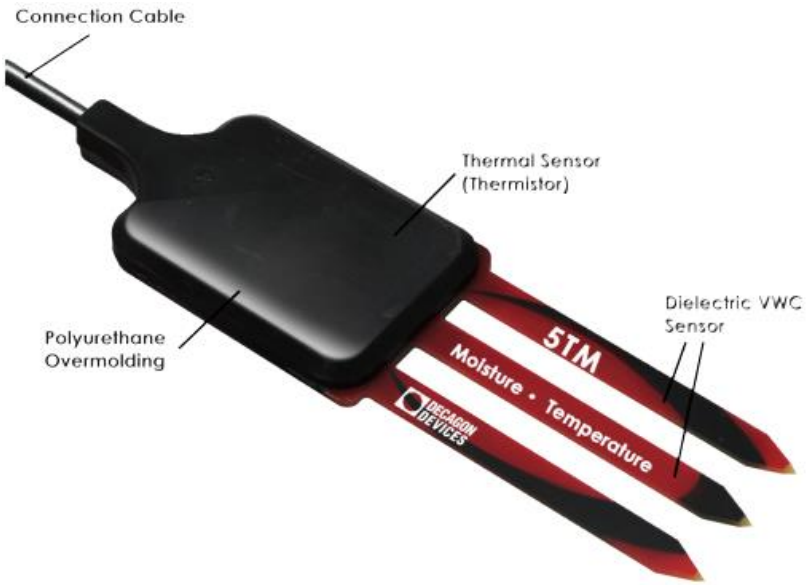

Figure 8.4. Configuration of 5TM Sensors

Table 8.1. Specifications of 5TM Sensors (Decagon Devices, Inc., 2015)

Dimension	10 cm (1) x 3.2 cm (w) x 0.7 cm (d)
Prong length	5.2 cm
Dielectric Measurement Frequency	70 MHZ
Dielectric permittivity range	Apparent dielectric permittivity (ε_a): 1 (air) to 80 (water)
Dielectric permittivity resolution	0.1 ε_a (unitless) from 1 to 20, < 0.75 ε_a (unitless) from 20 to 80 Volumetric Water Content: 0.0008 m^3/m^3 (0.08% VWC) from 0 to 50% Volumetric Water Content
Dielectric permittivity accuracy	ε_a: ±1 ε_a (unitless) from 1 to 40 (soil range), ±15% from 40 to 80 (VWC)
Temperature range	−40 to 60 ◦C
Temperature resolution	0.1 ◦C
Temperature accuracy	±1 ◦C

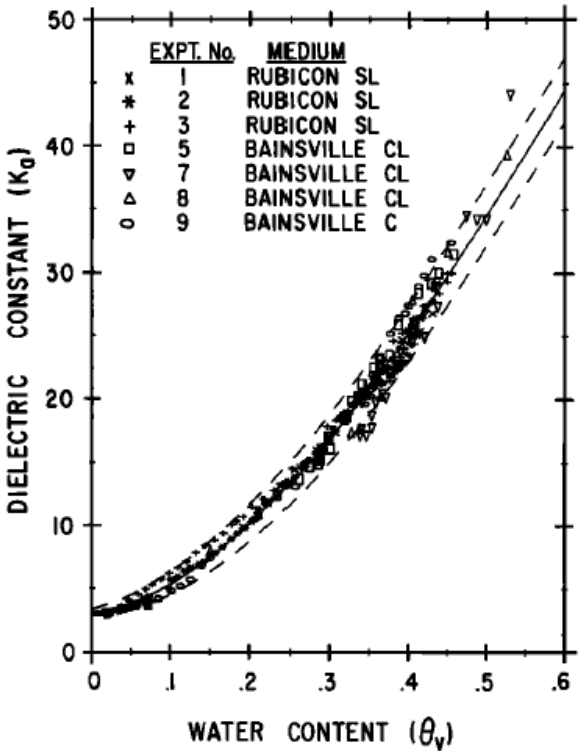

Figure 8.5. Measured Relationship Between Dielectric Constant and Volumetric Water Content

In each 5TM sensor, an electromagnetic field is used to determine the dielectric permittivity of the surrounding material. A 70 MHZ oscillating wave to the sensor prongs directly affects in the determination of the dielectric properties of soil. The sensor's microprocessor measures the charges and outputs the dielectric permittivity of the surrounding soil material.

The raw data output of the sensor is valid in a range of 0 to 4094. This correlates to a dielectric permittivity value from 0 to 81.88. The raw data output is converted to dielectric permittivity of the testing material with the use of following equation:

Dielectric permittivity: $\varepsilon_a = \varepsilon_{raw}/50$

Topp et al. (1980) developed the following equation to determine the volumetric moisture content(VMC or θ) of the testing material:

$$\theta = -5.3 \times 10^{-2} + 2.92 \times 10^{-2} R - 5.5 \times 10^{-4} R^2 + 4.3 \times 10^{-6} R^3$$

Where θ is the volumetric water content of testing material and R is the raw data of the output of the sensor.

Calibration of Topp's Equation

During the field and laboratory testing of the sensors, it appeared that the raw data (dielectric output of sensor) was not just a function of the dielectric permittivity but also the temperature of the soil. Because of this, a laboratory experiment to calibrate the 5TM moisture/temperature sensor was performed at the ASU laboratory. The experiment involved the measurement of the raw data from the 5TM sensor and the actual volumetric moisture content of the soil sample with a change in temperature.

The apparatus used in the test relied upon Shelby tubes of 15 cm in length and a diameter of 6.5 cm. The pulverized soil was prepared at three gravimetric water contents of 15 %, 25 % and 31 % which were then sealed in a zip lock bag for 7 days. The soil was then compacted into the tubes in order to obtain an average dry density existing in the field. The soil was compacted in three layers in the tubes. A 5TM moisture-temperature sensor was inserted into the soil after compaction of the second layer was finished. Care was taken to ensure that the installation would not damage sensors. The three probes were inserted into the second layer of soil, pointing in the long direction of the section. 18 tubes were prepared with 9 tubes consisting of Dupont clay and 9 tubes consisting of County clay. Three tubes were prepared at the same water content for each of the three water contents used for each soil.

The installation of the sensor interrupted the compaction of the third layer so a small compactor was used to make the final compaction easier. After compaction, sections were dried out to its target volumetric moisture content and sealed with duck tapes and plastic caps as shown in Figure 8.6

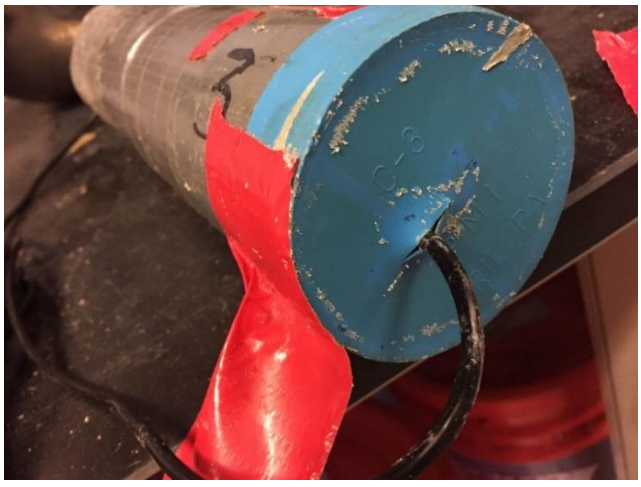

Figure 8.6. Prepared Soil Specimen Tube

Tapes and Shelby tube caps were used on both ends of each section to avoid any loss of moisture. Each sample was sealed and allowed to equilibrate for at least 24 hours. The tubes containing the soil were then transferred to an environmental chamber in which the temperature could be adjusted and set to a target level.

After a review of the temperature data from the field, all of the calibration tests were conducted at 5, 25 and 40 degrees Celsius. After the reading of the raw data and temperature was taken, the soil was then removed to measure the volumetric water content by drying in an oven.

After reviewing the general trends in the data that has been collected, it was observed that when the volumetric water content was constant, the raw data increased as the temperature increased. Thus, the volumetric water content was found to be a function of the ratio between the raw measurement data and temperature. Based upon these experimental findings, Topp's equation was then recalibrated to the soil conditions of this study. The equations obtained after the calibration procedure and used in this study are:

For DuPont soil:

$$VMC = 0.698144 \times \left[0.818814 - 0.992436^{\left(\frac{R}{T^{0.5}+2}\right)} + 0.0145732 \right]$$

For County soil:

$$VMC = 0.796544 \times \left[0.372384 - 0.99673^{\left(\frac{R}{T^{0.6}+2}\right)} + 0.422945 \right]$$

Where VMC is the volumetric water content of the tested material, R is the raw data from the output of the sensor and T is the temperature in Celsius.

Statistical analysis of the test results show that both of the proposed calibration models are very reasonable indication of the volumetric water content. The R^2 of the Dupont Clay calibration model and County Clay calibration model is 0.89 and 0.98 respectively. The standard error of the Dupont Clay calibration model is 0.0467 and County Clay calibration model is 0.0180. These statistics are indicators of good to excellent predictive models.

Figure 8.7 and Figure 8.8 show the comparison of the calibrated VMC (θ) versus the measured data for the County Clay and Dupont Clay separately.

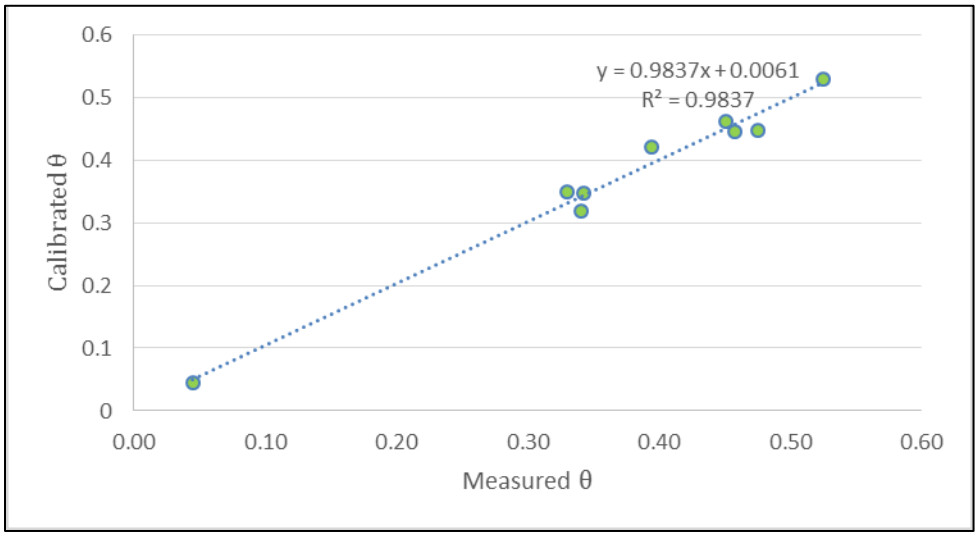

Figure 8.7. Calibrated VMC Data Versus Measured VMC Data for County Clay

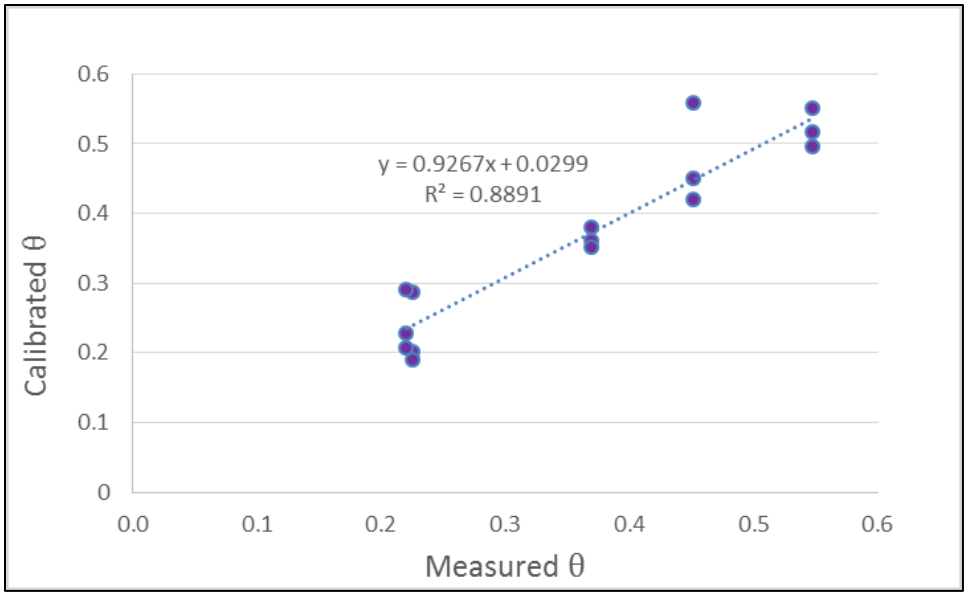

Figure 8.8. Calibrated VMC Data Versus Measured VMC Data for Dupont Clay

To further justify the rationality of the calibration models, the model has been plotted in a temperature range from 0 to 40 degree Celsius. These results are then compared with the measured data to check the range of volumetric water content from the calibration model. The results are shown in Figures 8.9 and 8.10.

In Figure 8.9, the measured data is mostly distributed within each test temperature group of the calibration model curves. The range of volumetric water content out of calibration is -0.08 to 0.72. As for Figure 8.10, the measured data is distributed within the group of calibration curves and the range of volumetric water content is -0.1 to 0.6. For both models, the volumetric water content may become negative when the raw data and temperature are extremely low, which are rarely encountered in the field.

The volumetric moisture content calculated with the original Topp's equation, along with the calibrated equation for the Dupont clay and County clay at different temperatures, is shown in Figure 8.11. Figure 8.11 shows that Topp's equation must be restricted to the

maximum volumetric water content that can be achieved by the soil. While this was achieved by the calibrated equation, this is not the case for the original (non calibrated) Topp's equation. The calibrated equation also shows the influence of temperature in the two types of soil which was not included in Topp's equation.

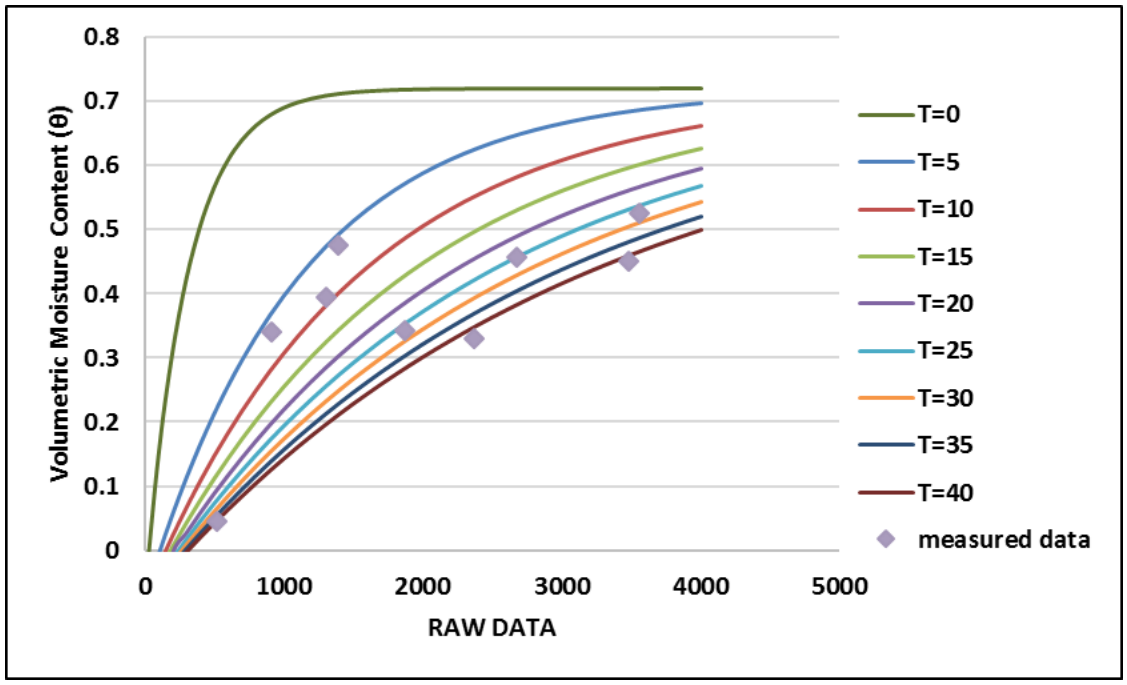

Figure 8.9. Calibration Curve (County Clay)

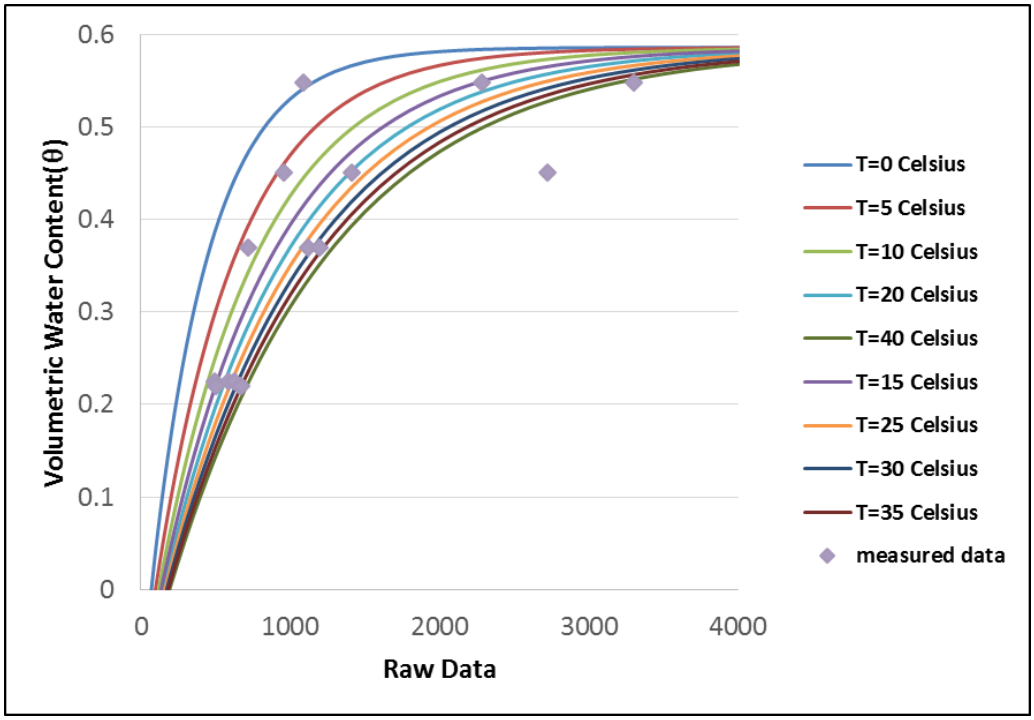

Figure 8.10. Calibration Curve (Dupont Clay)

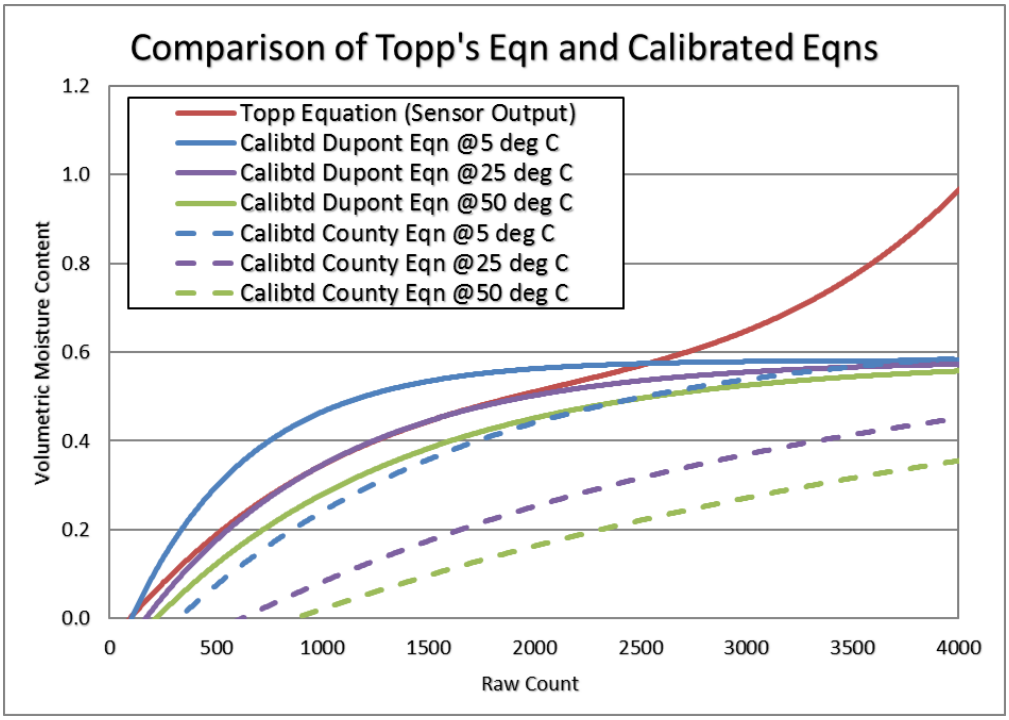

Figure 8.11. Comparison of Topp's Equation with Calibrated Equation of Dupont Clay and County Clay

SOIL MOISTURE CONTENT AND DRY DENSITY FROM THE NAPTF

As explained in the previous section, the 5TM decagon sensor measures the water content in terms of volumetric water content. In order to measure the initial compacted condition of the field, the measurement of the VWC from the field is required. Based on the data obtained from NAPTF, dry density and moisture content of the soil, in the field, at different locations were used to calculate the initial volumetric water content in the site at (near) the time of the initial sensor readings. The dry density and moisture content were obtained through three ways as follows:

Moisture content and density data obtained while performing the in-situ CBR tests: The data was obtained from FAA personnel during the initial phase of the project in August 2013 which shows the CBR, dry density and moisture content of the soil. The data obtained is shown in Chapter 3 in Table 3.3 and Table 3.4.

Dry density and moisture content data obtained through drive cylinder testing which were collected by the officials in NAPTF: During mid-2014, ASU requested dry density and moisture content data from FAA personnel as the data provided during the initial phase of the project was was not felt to be sufficient to accurately establish the in-situ moisture and density of both soils. FAA personnel delivered the data shown in Table 8.2. It was also reported that the data of dry density and moisture content was obtained from Drive cylinder tests performed in various points of time from 2011 to 2013.

Table 8.2. Dry Density and Moisture Content Data Obtained from NAPTF Facility

Lift No.	St. (ft.)	Offset (ft.)	Depth (in) (CC5)	Depth (in) (CC7)	Source	Layer	Date	Moisture Content (%)	Dry Density (pcf)	VMC (%)
LFC1	32	21	77	83	CC5 Post Traffic Density Summary	County Clay	11-Nov	25.3	98.3	39.9
LFC1	30	21	71	77	CC5 Post Traffic Density Summary	Dupont Clay	11-Nov	37.4	84.0	50.4
LFC1	30	21	65	71	CC5 Post Traffic Density Summary	Dupont Clay	11-Nov	36.7	84.6	49.8
LFC1	31	22	59	65	CC5 Post Traffic Density Summary	Dupont Clay	11-Oct	37.8	82.9	50.2
LFC1	42	22	59	65	CC5 Post Traffic Density Summary	Dupont Clay	11-Oct	38.0	82.2	50.1
LFC1	31	21	53	59	CC5 Post Traffic Density Summary	Dupont Clay	11-Oct	37.3	82.5	49.4
LFC1	42	22	53	59	CC5 Post Traffic Density Summary	Dupont Clay	11-Oct	37.2	83.1	49.5
LFC1	30	22	47	53	CC5 Post Traffic Density Summary	Dupont Clay	11-Oct	38.6	82.0	50.8
LFC1	42	22	47	53	CC5 Post Traffic Density Summary	Dupont Clay	11-Oct	37.3	83.8	50.1
LFC1	30	13		50	CC7 Dupont SG Acceptance Lift 1	Dupont Clay	13-Jul	32.5	88.5	46.1
LFC1	36	14		32	CC7 Dupont SG Acceptance Lift 4	Dupont Clay	13-Aug	26.4	95.9	40.6
LFC2	55	21	71	77	CC5 Post Traffic Density Summary	Dupont Clay	11-Nov	36.8	83.6	49.4
LFC2	63	17	71	77	CC5 Post Traffic Density Summary	Dupont Clay	11-Nov	36.3	84.2	49.0
LFC2	63	5	71	77	CC5 Post Traffic Density Summary	Dupont Clay	11-Nov	37.9	82.5	50.1
LFC2	55	21	65	71	CC5 Post Traffic Density Summary	Dupont Clay	11-Oct	37.7	83.2	50.2
LFC2	63	17	65	71	CC5 Post Traffic Density Summary	Dupont Clay	11-Oct	37.5	82.2	49.3
LFC2	63	5	65	71	CC5 Post Traffic Density Summary	Dupont Clay	11-Oct	37.4	82.1	49.2
LFC2	55	22	59	65	CC5 Post Traffic Density Summary	Dupont Clay	11-Oct	37.9	82.3	50.0
LFC2	63	24	59	65	CC5 Post Traffic Density Summary	Dupont Clay	11-Oct	37.0	82.4	48.9

LFC2	63	17	59	65	CC5 Post Traffic Density Summary	Dupont Clay	11-Oct	37.6	83.4	50.2
LFC2	63	8	59	65	CC5 Post Traffic Density Summary	Dupont Clay	11-Oct	38.4	82.8	50.9
LFC2	63	2	59	65	CC5 Post Traffic Density Summary	Dupont Clay	11-Oct	38.0	83.5	50.9
LFC2	55	21	53	59	CC5 Post Traffic Density Summary	Dupont Clay	11-Oct	38.5	83.1	51.2
LFC2	63	24	53	59	CC5 Post Traffic Density Summary	Dupont Clay	11-Oct	39.0	81.8	51.1
LFC2	63	16	53	59	CC5 Post Traffic Density Summary	Dupont Clay	11-Oct	38.5	81.7	50.4
LFC2	63	9	53	59	CC5 Post Traffic Density Summary	Dupont Clay	11-Oct	37.9	83.3	50.6
LFC2	63	2	53	59	CC5 Post Traffic Density Summary	Dupont Clay	11-Oct	37.8	82.6	50.0
LFC2	53	22	47	53	CC5 Post Traffic Density Summary	Dupont Clay	11-Oct	38.0	82.6	50.3
LFC2	63	24	47	53	CC5 Post Traffic Density Summary	Dupont Clay	11-Oct	37.0	82.8	49.1
LFC2	63	16	47	53	CC5 Post Traffic Density Summary	Dupont Clay	11-Oct	37.2	83.4	49.7
LFC2	63	8	47	53	CC5 Post Traffic Density Summary	Dupont Clay	11-Oct	37.8	82.9	50.3
LFC2	63	2	47	53	CC5 Post Traffic Density Summary	Dupont Clay	11-Oct	38.0	83.5	50.9
LFC2	61	15		44	CC7 Dupont SG Acceptance Lift 2	Dupont Clay	13-Aug	28.2	94.2	42.6
LFC2	55	16		38	CC7 Dupont SG Acceptance Lift 3	Dupont Clay	13-Aug	26.4	97.0	41.0
LFC2	68	16		32	CC7 Dupont SG Acceptance Lift 4	Dupont Clay	13-Aug	26.4	95.9	40.6
LFC3	115	18	77	83	CC5 Post Traffic Density Summary	County Clay	13-Mar	25.5	98.8	40.5
LFC3	115	23	71	77	CC5 Post Traffic Density Summary	Dupont Clay	13-Mar	37.7	82.6	50.0
LFC3	115	16	71	77	CC5 Post Traffic Density Summary	Dupont Clay	13-Mar	37.4	82.8	49.6
LFC3	115	23	59	65	CC5 Post Traffic Density Summary	Dupont Clay	13-Mar	37.7	83.1	50.3
LFC3	115	16	59	65	CC5 Post Traffic Density Summary	Dupont Clay	13-Mar	37.3	82.9	49.6
LFC3	115	23	51	57	CC5 Post Traffic Density Summary	Dupont Clay	13-Mar	38.0	83.1	50.6

LFC3	115	16	51	57	CC5 Post Traffic Density Summary	Dupont Clay	13-Mar	37.1	83.7	49.8
LFC3	116	17		44	CC7 Dupont SG Acceptance Lift 2	Dupont Clay	13-Aug	28.2	94.2	42.6
LFC3	110	17		38	CC7 Dupont SG Acceptance Lift 3	Dupont Clay	13-Aug	26.1	96.5	40.4
LFC4	160	18	77	83	CC5 Post Traffic Density Summary	County Clay	13-Mar	24.2	101.2	39.3
LFC4	160	23	71	77	CC5 Post Traffic Density Summary	Dupont Clay	13-Mar	36.0	84.9	49.0
LFC4	160	16	71	77	CC5 Post Traffic Density Summary	Dupont Clay	13-Mar	36.8	83.4	49.2
LFC4	160	9	71	77	CC5 Post Traffic Density Summary	Dupont Clay	13-Mar	36.4	84.2	49.2
LFC4	160	23	59	65	CC5 Post Traffic Density Summary	Dupont Clay	13-Mar	36.7	83.3	49.0
LFC4	160	16	59	65	CC5 Post Traffic Density Summary	Dupont Clay	13-Mar	36.1	83.7	48.5
LFC4	160	9	59	65	CC5 Post Traffic Density Summary	Dupont Clay	13-Mar	36.8	83.4	49.2
LFC4	160	23	51	57	CC5 Post Traffic Density Summary	Dupont Clay	13-Mar	38.7	83.1	51.6
LFC4	160	16	51	57	CC5 Post Traffic Density Summary	Dupont Clay	13-Mar	38.7	82.5	51.1
LFC4	160	9	51	57	CC5 Post Traffic Density Summary	Dupont Clay	13-Mar	38.2	82.2	50.4
LFC4	178	14		50	CC7 Dupont SG Acceptance Lift 1	Dupont Clay	13-Jul	33.9	86.5	47.0
LFC4	184	15		44	CC7 Dupont SG Acceptance Lift 2	Dupont Clay	13-Aug	27.0	96.2	41.7
LFC4	186	15		38	CC7 Dupont SG Acceptance Lift 3	Dupont Clay	13-Aug	27.5	94.1	41.5
LFC4	153	14		32	CC7 Dupont SG Acceptance Lift 4	Dupont Clay	13-Aug	26.9	96.3	41.5
LFC5	210	23	77	83	CC5 Post Traffic Density Summary	County Clay	13-Feb	26.4	98.0	41.6
LFC5	210	18	77	83	CC5 Post Traffic Density Summary	County Clay	13-Feb	24.9	98.6	39.3
LFC5	210	23	71	77	CC5 Post Traffic Density Summary	Dupont Clay	13-Feb	35.7	83.8	48.0
LFC5	210	16	71	77	CC5 Post Traffic Density Summary	Dupont Clay	13-Feb	36.1	84.0	48.6
LFC5	210	9	71	77	CC5 Post Traffic Density Summary	Dupont Clay	13-Feb	36.5	83.6	48.9

LFC5	210	23	59	65	CC5 Post Traffic Density Summary	Dupont Clay	13-Feb	36.5	83.2	48.7
LFC5	210	16	59	65	CC5 Post Traffic Density Summary	Dupont Clay	13-Feb	36.9	82.6	48.9
LFC5	210	9	59	65	CC5 Post Traffic Density Summary	Dupont Clay	13-Feb	37.8	82.5	50.0
LFC5	210	23	51	57	CC5 Post Traffic Density Summary	Dupont Clay	13-Feb	37.7	82.8	50.1
LFC5	210	16	51	57	CC5 Post Traffic Density Summary	Dupont Clay	13-Feb	39.0	82.6	51.6
LFC5	210	9	51	57	CC5 Post Traffic Density Summary	Dupont Clay	13-Feb	37.7	82.8	50.0
LFC6	260	18	77	83	CC5 Post Traffic Density Summary	County Clay	13-Feb	25.3	98.9	40.2
LFC6	260	23	71	77	CC5 Post Traffic Density Summary	Dupont Clay	13-Feb	36.3	84.9	49.4
LFC6	260	16	71	77	CC5 Post Traffic Density Summary	Dupont Clay	13-Feb	36.5	84.3	49.3
LFC6	260	9	71	77	CC5 Post Traffic Density Summary	Dupont Clay	13-Feb	36.9	84.3	49.9
LFC6	260	23	59	65	CC5 Post Traffic Density Summary	Dupont Clay	13-Feb	37.4	83.0	49.8
LFC6	260	16	59	65	CC5 Post Traffic Density Summary	Dupont Clay	13-Feb	37.3	83.5	49.9
LFC6	260	9	59	65	CC5 Post Traffic Density Summary	Dupont Clay	13-Feb	37.3	84.2	50.3
LFC6	260	23	47	53	CC5 Post Traffic Density Summary	Dupont Clay	13-Feb	36.7	83.9	49.4
LFC6	260	16	47	53	CC5 Post Traffic Density Summary	Dupont Clay	13-Feb	37.6	83.3	50.2
LFC6	260	9	47	53	CC5 Post Traffic Density Summary	Dupont Clay	13-Feb	38.0	83.0	50.6
LFC6	285	13		50	CC7 Dupont SG Acceptance Lift 1	Dupont Clay	13-Jul	35.2	86.1	48.6
LFC6	252	12		44	CC7 Dupont SG Acceptance Lift 2	Dupont Clay	13-Aug	28.6	93.6	43.0
LFC6	257	18		38	CC7 Dupont SG Acceptance Lift 3	Dupont Clay	13-Aug	27.1	96.0	41.8
LFC6	253	16		32	CC7 Dupont SG Acceptance Lift 4	Dupont Clay	13-Aug	26.8	95.8	41.2

1) Dry density and moisture content were obtained through drive cylinder testing which were collected by officials at NAPTF, 2) Shelby tubes which were extracted from the facility and sent to ASU, and 3) Moisture content and density data obtained while performing the in-situ CBR tests. Table 8.2 shows the data obtained from the NAPTF. Table 8.2 shows the locations and the soil type for each row data entry in the table. Table 8.2 also shows the Lift no, station, offset and the depth in the field from which the sample was obtained. The moisture content and density was measured in the appropriate locations and the volumetric moisture content was calculated. Table 8.3 shows the dry density and moisture content measured in the ASU laboratory from the Shelby tubes sent from NAPTF. Table 3.3 and Table 3.4 shown in Chapter 3 was also used in the analysis of the density and moisture content in the field.

Shelby Tube data obtained at ASU: During the initial phase of the project, Six Shelby tubes (3 feet length) were obtained from the NAPTF to analyze the dry density and moisture content of the soil. Figure 8.12 shows the depths at which the Shelby tube sample were extracted. Tube 1 and Tube 2 consisted entirely of County Clay and were extracted from Location E and Location F of Figure 8.1. Tubes 3- 6 consisted partly of County clay and partly of Dupont clay as shown in Figure 8.12 and were extracted from Location A, B, C and D respectively. Table 8.3 shows the results of the soil data extracted from the Shelby tube.

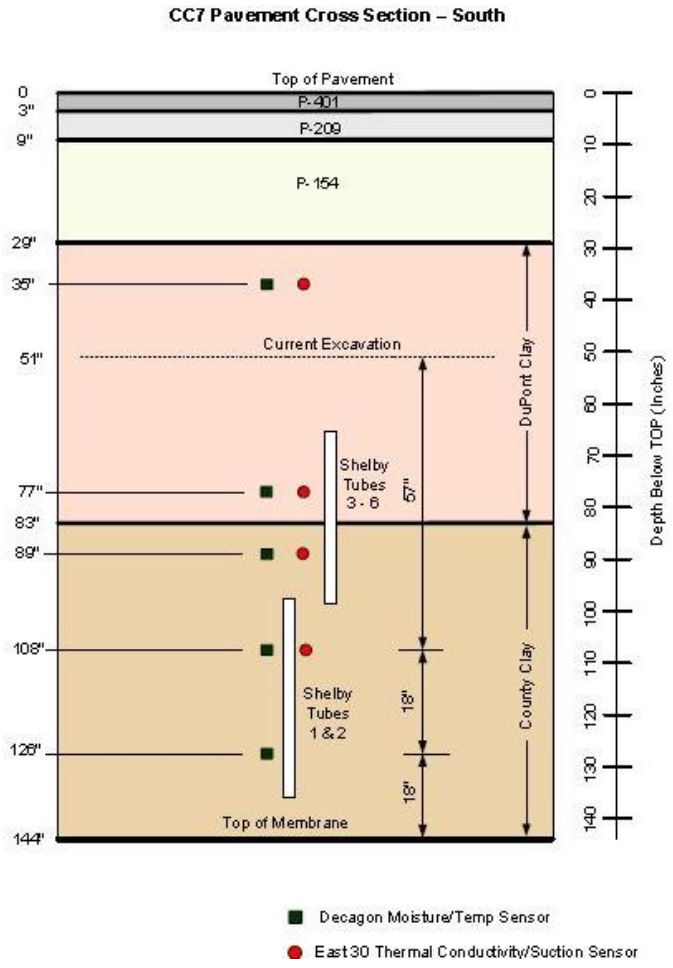

Figure 8.12. Details of Soil Sample Extracted Using Shelby Tubes

It was observed from Table 8.2, Table 3.3 and Table 3.4 that the soil was obtained from two Construction Cycles denoted as CC. NAPTF labels the different projects performed in the facility as Construction Cycles (CC). CC-5 denotes the project that was performed in the duration of 2008-2013. And CC-7 denotes the current project which was started in 2013. It is also important to note that the entire subgrade soil was not replaced for CC-7 and only a partial soil layer was replaced. The soil beneath the depth of 51" consists of the same soil that was used for CC-5. However, the CC-7 soil was laid over the CC-5 soil which was from a depth of 29" to 51" below the pavement surface after which the flexible/asphalt pavement was constructed. (See Figure 8.2 for further clarification).

Table 8.3. Shelby Tube Data Measured in ASU Lab

Tube no.	Clay Layer	Depth	Station	Dry Density	Wet Density	Gravimetric Water Content (%)
		Inches		lb/ft^3	lb/ft^3	
1T	County	103	209	99.0	124.8	26.0
1B	County	134	209	89.6	113.9	27.0
2T	County	103	208	97.0	123.8	27.7
2B	County	133	208	97.0	124.5	28.4
3B	County	98	110	100.2	126.5	26.2
4B	County	98	110	94.5	117.6	24.5
5B	County	97	23	99.4	123.8	24.5
6B	County	97	23	97.5	123.4	26.5
4M2	County	86	110	98.5	123.5	25.3
5M2	County	86	23	85.0	115.7	36.2
6M2	County	86	23	99.6	124.6	25.1
3T	Dupont	71	110	85.5	118.4	38.4
4T	Dupont	67	110	80.8	112.6	39.3
5T	Dupont	72	23	82.2	113.3	37.8
6T	Dupont	66	23	89.3	118.5	32.7
3M1	Dupont	76	110	83.1	113.3	36.3
4M1	Dupont	76	110	82.6	112.7	36.4
5M1	Dupont	76	23	90.4	124.3	37.4
6M1	Dupont	76	23	87.9	116.8	33.0
3M2	Dupont	86	110	86.2	115.7	34.2

Initial Compaction State of Soil Near Sensor

The data from Table 8.2 and Table 8.3 was analyzed and categorized according to station, offset and depth. The analysis showed that there was no dry density and moisture content data that was obtained very close to the location of each sensor. Since there was no actual measurement of dry density and moisture content near the sensor, it was initially decided to examine the values of the data available closest to the sensor and assume they would be

the same as the soil surrounding the sensor. It was important to find the initial compaction condition of the soil near the sensor for various purposes. Since the main aim of this work phase was to monitor/analyze the variation in moisture content and temperature of soil through the sensor measurements, it was necessary to understand the initial state of the soil in order to quantify the order of change in moisture, if present at the site.

Table 8.4 shows the dry density and moisture content data near Station 30. Using the data obtained from Table 8.4, Figure 8.13 was developed to show the location of the data points obtained along with the location of the sensor in the section of the profile at station 30. As shown in Figure 8.13, it can be seen that there is no (to little) actual data obtained in the immediate vicinity of most sensors.

Table 8.4. Moisture Content and Dry Density Data Near Station 30

Source	Station. (ft.)	Offset (ft.)	Depth (in) (CC7)	Layer	Date	Moisture Content (%)	Dry Density (pcf)	VMC (%)	Data near to Sensor
1	17	-6	53	Dupont Clay	Aug-17	34.7	87.6	48.7	
2	23	2	66	Dupont Clay	Aug-17	32.7	89.3	46.8	
2	23	2	76	Dupont Clay	Aug-17	33.0	87.9	46.5	A2
2	23	26	72	Dupont Clay	Aug-17	37.8	82.2	49.9	B2
2	23	26	76	Dupont Clay	Aug-17	37.4	90.4	54.3	
4	30	13	50	Dupont Clay	Jul-17	32.5	88.5	46.1	
4	30	22	53	Dupont Clay	Oct-17	38.6	82.0	50.8	
4	30	21	71	Dupont Clay	Nov-17	36.7	84.6	49.8	
4	30	21	77	Dupont Clay	Nov-17	37.4	84.0	50.4	
4	31	21	59	Dupont Clay	Oct-17	37.3	82.5	49.4	
4	31	22	65	Dupont Clay	Oct-17	37.8	82.9	50.2	
4	36	14	32	Dupont Clay	Aug-17	26.4	95.9	40.6	A1
4	42	22	53	Dupont Clay	Oct-17	37.3	83.8	50.1	
4	42	22	59	Dupont Clay	Oct-17	37.2	83.1	49.5	
4	42	22	65	Dupont Clay	Oct-17	38.0	82.2	50.1	
4	53	22	53	Dupont Clay	Oct-17	38.0	82.6	50.3	
4	55	16	38	Dupont Clay	Aug-17	26.4	97.0	41.0	B1
4	55	21	59	Dupont Clay	Oct-17	38.5	83.1	51.2	
4	55	22	65	Dupont Clay	Oct-17	37.9	82.3	50.0	
4	55	21	71	Dupont Clay	Oct-17	37.7	83.2	50.2	
4	55	21	77	Dupont Clay	Nov-17	36.8	83.6	49.4	
4	61	15	44	Dupont Clay	Aug-17	28.2	94.2	42.6	
1	61	15	47	Dupont Clay	Aug-17	27.9	95.3	42.6	
4	63	2	53	Dupont Clay	Oct-17	38.0	83.5	50.9	
4	63	2	59	Dupont Clay	Oct-17	37.8	82.6	50.0	
4	63	2	65	Dupont Clay	Oct-17	38.0	83.5	50.9	
4	63	5	71	Dupont Clay	Oct-17	37.4	82.1	49.2	
4	63	5	77	Dupont Clay	Nov-17	37.9	82.5	50.1	
4	63	8	53	Dupont Clay	Oct-17	37.8	82.9	50.3	
4	63	8	65	Dupont Clay	Oct-17	38.4	82.8	50.9	
4	63	9	59	Dupont Clay	Oct-17	37.9	83.2	50.6	
4	63	16	53	Dupont Clay	Oct-17	37.2	83.4	49.7	

Table 8.4. Moisture Content and Dry Density Data Near Station 30 (Cont'd)

4	63	16	59	Dupont Clay	Oct-17	38.5	81.7	50.4	
4	68	16	32	Dupont Clay	Aug-17	26.4	95.9	40.6	
4	63	17	65	Dupont Clay	Oct-17	37.6	83.4	50.2	
4	63	17	71	Dupont Clay	Oct-17	37.5	82.2	49.3	
4	63	17	77	Dupont Clay	Nov-17	36.3	84.2	49.0	
4	63	24	53	Dupont Clay	Oct-17	37.0	82.7	49.1	
4	63	24	59	Dupont Clay	Oct-17	39.0	81.8	51.1	
4	63	24	65	Dupont Clay	Oct-17	37.0	82.4	48.9	
1	68	16	35	Dupont Clay	Aug-17	26.3	96.0	40.5	
2	23	2	86	County Clay	Aug-17	25.1	99.6	40.0	A3
2	23	2	97	County Clay	Aug-17	26.5	97.5	41.5	A4, A5
2	23	26	86	County Clay	Aug-17	36.2	85.0	49.4	B3
2	23	26	97	County Clay	Aug-17	24.5	99.4	39.1	B4, B5
3	30	15	142	County Clay	Dec-17	26.6	99.0	42.3	
3	30	15	142	County Clay	Jan-17	27.1	97.7	42.5	
4	32	21	83	County Clay	Nov-17	25.3	98.3	39.9	

Notes:
Source 1 = CC-7 Data obtained directly from NAPTF in Aug 2013, during the initial phase of the project (Table 3.4)
Source 2 = Shelby Tube data obtained at ASU (Table 4.3)
Source 3 = CC-5 Data obtained directly from NAPTF in Aug 2013 from previous project (Table 3.3)
Source 4 = Data sent by Dr. Cary (Table 8.2)

Note:
The offset denotes the distance from the center line of the pavement.
Negative offset denotes north side of the center line
Positive offset denotes south side of the center line

The points A1 to A5 and B1 to B5 shown in black represents the 10 sensors located in this section at station 30. The colored points of A1 to A5 and B1 to B5 shows the data point nearest to the sensor. It can be clearly seen in Figure 8.13 that no compaction data was obtained near the placement of the sensor.

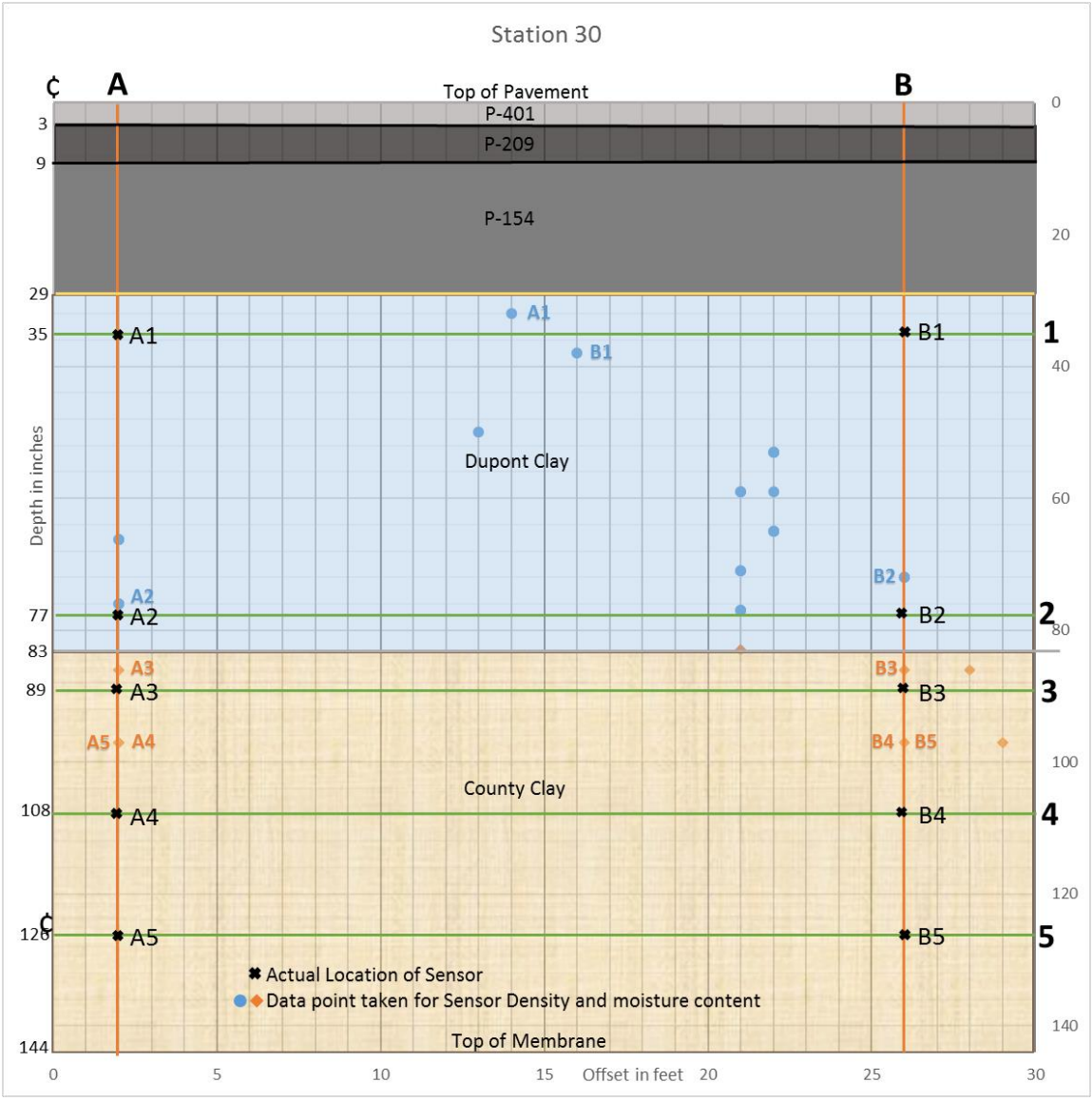

Figure 8.13. Moisture Content and Dry Density Data Near Station 30

The dry density and moisture content data near Station 110 is shown in Table 8.5. Figure 8.14 was created using the data from Table 8.5. C1 to C5 and D1 to D5 shown in black represents the 10 sensors located in this section at station 110. The colored points of C1 to C5 and D1 to D5 shows the data point nearest to the corresponding sensor. Again it can be

observed that actual field measurements may be significantly away from the sensor location as shown in Figure 8.14.

Table 8.5. Moisture Content and Dry Density Data Near Station 110

Source	Station. (ft.)	Offset (ft.)	Depth (in) (CC7)	Layer	Date	Moisture Content (%)	Dry Density (pcf)	VMC (%)	Data near to Sensor
1	17	-6	53	Dupont Clay	Aug-17	34.7	87.6	48.7	
2	23	2	66	Dupont Clay	Aug-17	32.7	89.3	46.8	
2	23	2	76	Dupont Clay	Aug-17	33.0	87.9	46.5	A2
2	23	26	72	Dupont Clay	Aug-17	37.8	82.2	49.9	B2
2	23	26	76	Dupont Clay	Aug-17	37.4	90.4	54.3	
4	30	13	50	Dupont Clay	Jul-17	32.5	88.5	46.1	
4	30	22	53	Dupont Clay	Oct-17	38.6	82.0	50.8	
4	30	21	71	Dupont Clay	Nov-17	36.7	84.6	49.8	
4	30	21	77	Dupont Clay	Nov-17	37.4	84.0	50.4	
4	31	21	59	Dupont Clay	Oct-17	37.3	82.5	49.4	
4	31	22	65	Dupont Clay	Oct-17	37.8	82.9	50.2	
4	36	14	32	Dupont Clay	Aug-17	26.4	95.9	40.6	A1
4	42	22	53	Dupont Clay	Oct-17	37.3	83.8	50.1	
4	42	22	59	Dupont Clay	Oct-17	37.2	83.1	49.5	
4	42	22	65	Dupont Clay	Oct-17	38.0	82.2	50.1	
4	53	22	53	Dupont Clay	Oct-17	38.0	82.6	50.3	
4	55	16	38	Dupont Clay	Aug-17	26.4	97.0	41.0	B1
4	55	21	59	Dupont Clay	Oct-17	38.5	83.1	51.2	
4	55	22	65	Dupont Clay	Oct-17	37.9	82.3	50.0	
4	55	21	71	Dupont Clay	Oct-17	37.7	83.2	50.2	
4	55	21	77	Dupont Clay	Nov-17	36.8	83.6	49.4	
4	61	15	44	Dupont Clay	Aug-17	28.2	94.2	42.6	
1	61	15	47	Dupont Clay	Aug-17	27.9	95.3	42.6	
4	63	2	53	Dupont Clay	Oct-17	38.0	83.5	50.9	
4	63	2	59	Dupont Clay	Oct-17	37.8	82.6	50.0	
4	63	2	65	Dupont Clay	Oct-17	38.0	83.5	50.9	
4	63	5	71	Dupont Clay	Oct-17	37.4	82.1	49.2	
4	63	5	77	Dupont Clay	Nov-17	37.9	82.5	50.1	

Table 8.5. Moisture Content and Dry Density Data Near Station 110 (Cont'd)

4	63	8	53	Dupont Clay	Oct-17	37.8	82.9	50.3	
4	63	8	65	Dupont Clay	Oct-17	38.4	82.8	50.9	
4	63	9	59	Dupont Clay	Oct-17	37.9	83.2	50.6	
4	63	16	53	Dupont Clay	Oct-17	37.2	83.4	49.7	
4	63	16	59	Dupont Clay	Oct-17	38.5	81.7	50.4	
4	68	16	32	Dupont Clay	Aug-17	26.4	95.9	40.6	
4	63	17	65	Dupont Clay	Oct-17	37.6	83.4	50.2	
4	63	17	71	Dupont Clay	Oct-17	37.5	82.2	49.3	
4	63	17	77	Dupont Clay	Nov-17	36.3	84.2	49.0	
4	63	24	53	Dupont Clay	Oct-17	37.0	82.7	49.1	
4	63	24	59	Dupont Clay	Oct-17	39.0	81.8	51.1	
4	63	24	65	Dupont Clay	Oct-17	37.0	82.4	48.9	
1	68	16	35	Dupont Clay	Aug-17	26.3	96.0	40.5	
2	23	2	86	County Clay	Aug-17	25.1	99.6	40.0	A3
2	23	2	97	County Clay	Aug-17	26.5	97.5	41.5	A4, A5
2	23	26	86	County Clay	Aug-17	36.2	85.0	49.4	B3
2	23	26	97	County Clay	Aug-17	24.5	99.4	39.1	B4, B5
3	30	15	142	County Clay	Dec-17	26.6	99.0	42.3	
3	30	15	142	County Clay	Jan-17	27.1	97.7	42.5	
4	32	21	83	County Clay	Nov-17	25.3	98.3	39.9	

Notes:

Source 1 = CC-7 Data obtained directly from NAPTF in Aug 2013, during the initial phase of the project (Table 3.4)

Source 2 = Shelby Tube data obtained at ASU (Table 4.3)

Source 3 = CC-5 Data obtained directly from NAPTF in Aug 2013 from previous project (Table 3.3)

Source 4 = Data sent by Dr. Cary (Table 8.2)

Note:

The offset denotes the distance from the center line of the pavement.

Negative offset denotes north side of the center line

Positive offset denotes south side of the center line

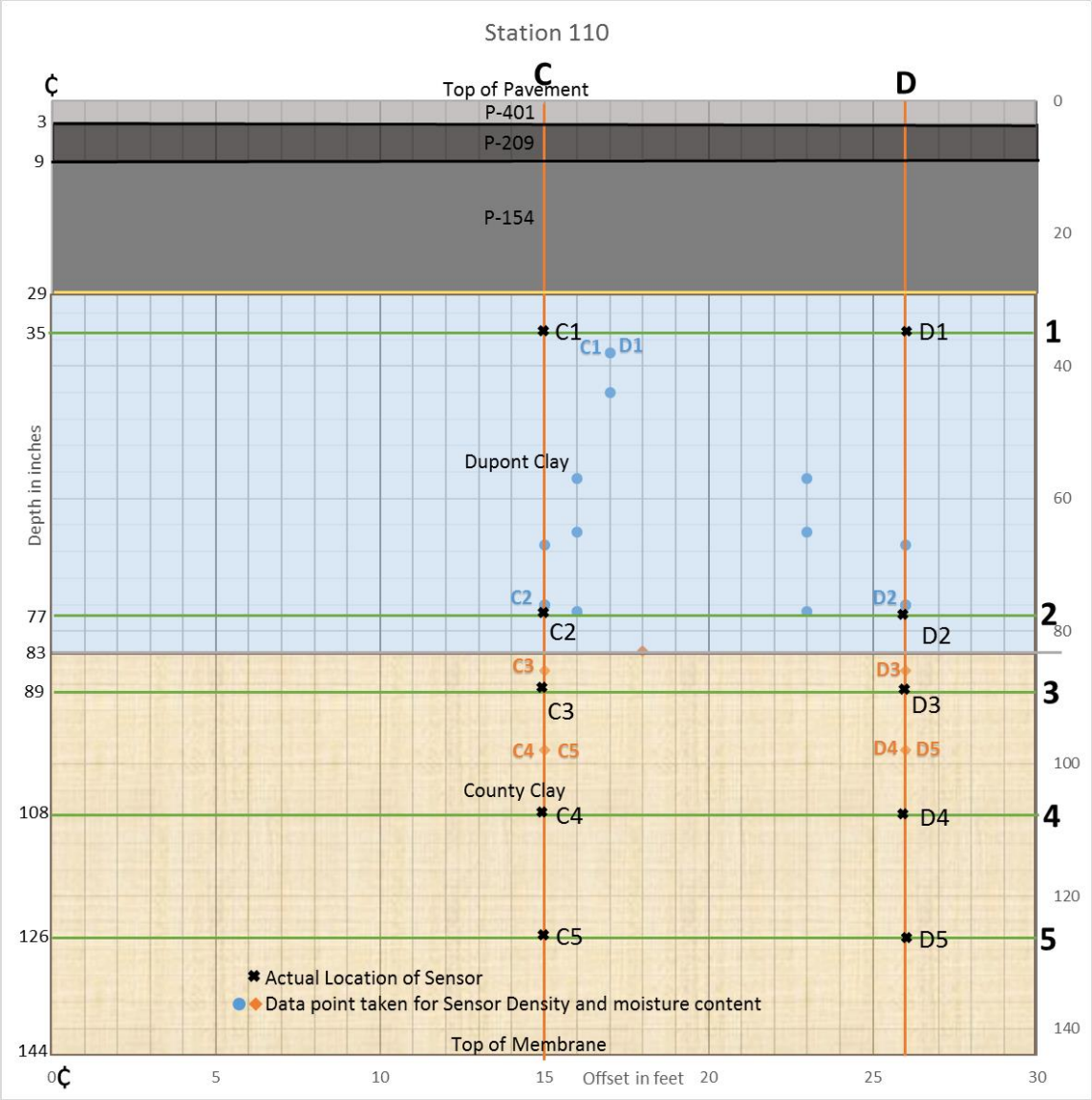

Figure 8.14. Moisture Content and Dry Density Data Near Station 110

Table 8.6 and Figure 8.15 shows the dry density and moisture content data near Station 210. It can be observed from Table 8.6 that there are, again, little to no actual data points obtained near the sensor. Table 8.6 shows which data values were initially assumed to which sensor. Figure 8.15 shows the actual location of the sensor along with location of the data point in which the values were assumed to be. The points E1 to E5 and F1 to F5

shown in black represents the 10 sensors located in this section at station 210. The colored points of E1 to E5 and F1 to F5 shows the data point nearest to the corresponding sensor.

Table 8.6. Moisture Content and Dry Density Data Near Station 210

Source	Station. (ft.)	Offset (ft.)	Depth (in) (CC7)	Layer	Date	Moisture Content (%)	Dry Density (pcf)	VMC (%)	Data near sensor
1	178	14	53	Dupont Clay	Aug-17	33.9	86.5	47.0	
4	184	15	44	Dupont Clay	Aug-17	27.0	96.2	41.7	
4	186	15	38	Dupont Clay	Aug-17	27.5	94.1	41.5	E1, F1
4	210	9	57	Dupont Clay	Feb-17	37.7	82.8	50.0	
4	210	9	65	Dupont Clay	Feb-17	37.8	82.5	50.0	
4	210	9	77	Dupont Clay	Feb-17	36.5	83.6	48.9	E2
4	210	16	57	Dupont Clay	Feb-17	39.0	82.6	51.6	
4	210	16	65	Dupont Clay	Feb-17	36.9	82.6	48.9	
4	210	16	77	Dupont Clay	Feb-17	36.1	84.0	48.6	
4	210	23	57	Dupont Clay	Feb-17	37.7	82.8	50.1	
4	210	23	65	Dupont Clay	Feb-17	36.5	83.2	48.7	
4	210	23	77	Dupont Clay	Feb-17	35.7	83.8	48.0	F2
1	220	-22	53	Dupont Clay	Aug-17	33.6	87.4	47.1	
1	229	-14	47	Dupont Clay	Aug-17	25.9	97.1	40.3	
4	252	12	44	Dupont Clay	Aug-17	28.6	93.6	43.0	
4	253	16	32	Dupont Clay	Aug-17	26.8	95.8	41.2	
4	257	18	38	Dupont Clay	Aug-17	27.1	96.0	41.8	
4	260	9	53	Dupont Clay	Feb-17	38.0	83.0	50.6	
4	260	9	65	Dupont Clay	Feb-17	37.3	84.2	50.3	
4	260	9	77	Dupont Clay	Feb-17	36.9	84.3	49.9	
4	260	16	53	Dupont Clay	Feb-17	37.6	83.3	50.2	
4	260	16	65	Dupont Clay	Feb-17	37.3	83.5	49.9	
4	260	16	77	Dupont Clay	Feb-17	36.5	84.3	49.3	
Table 8.6 Moisture Content and Dry Density Data Near Station 210									
4	260	23	53	Dupont Clay	Feb-17	36.7	83.9	49.4	
4	260	23	65	Dupont Clay	Feb-17	37.4	83.0	49.8	
4	260	23	77	Dupont Clay	Feb-17	36.3	84.9	49.4	

1	263	-14	47	Dupont Clay	Aug-17	26.4	96.6	40.9	
4	285	13	50	Dupont Clay	Jul-17	35.2	86.1	48.6	
3	200	15	142	County Clay	Apr-17	28.5	96.4	44.1	
3	200	15	142	County Clay	May-17	28.9	96.5	44.7	
2	208	2	134	County Clay	Aug-17	28.4	97.0	44.1	E5
2	208	2	103	County Clay	Aug-17	27.7	97.0	43.0	E4
2	209	26	134	County Clay	Aug-17	27.0	89.6	38.9	F5
2	209	26	103	County Clay	Aug-17	26.0	99.0	41.3	
4	210	18	83	County Clay	Feb-17	24.9	98.6	39.3	
4	210	23	83	County Clay	Feb-17	26.4	98.0	41.6	F3
3	260	15	142	County Clay	Jun-17	27.0	98.5	42.7	
3	260	15	142	County Clay	Jul-17	27.3	97.0	42.5	
4	260	18	83	County Clay	Feb-17	25.3	98.9	40.2	E3

Notes:
Source 1 = CC-7 Data obtained directly from NAPTF in Aug 2013, during the initial phase of the project (Table 3.4)
Source 2 = Shelby Tube data obtained at ASU
(Table 4.3)
Source 3 = CC-5 Data obtained directly from NAPTF in Aug 2013 from
previous project (Table 3.3)
Source 4 = Data sent by Dr. Cary
(Table 8.2)
The offset denotes the distance from the center line of the
pavement.
Negative offset denotes north side of the center
line
Positive offset denotes south side of the center line

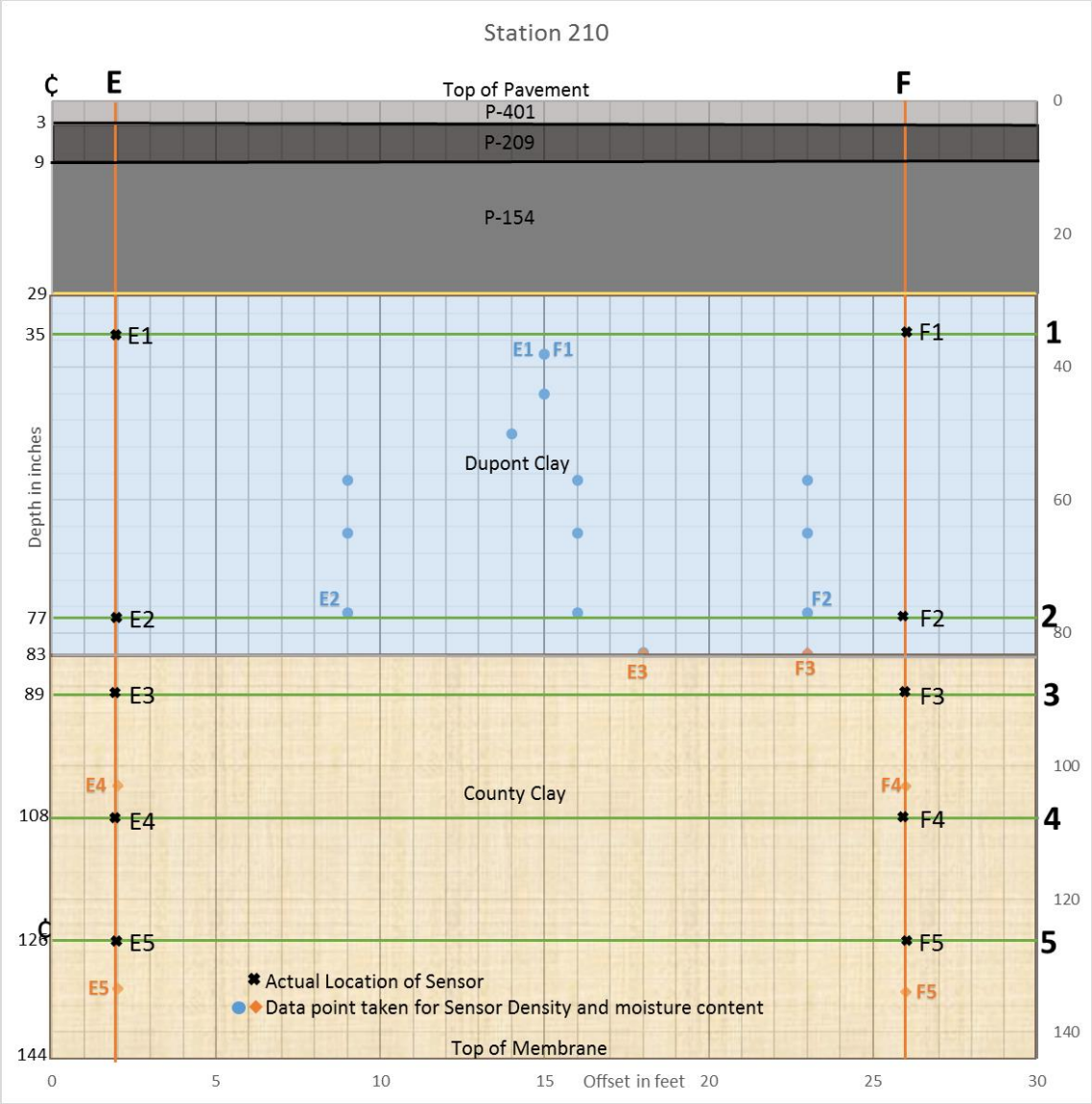

Figure 8.15. Moisture Content and Dry Density Data Near Station 210

Based on the intial analysis performed to relate a specific dry density and moisture content for each of the 30 sensors, it became apparent that the continued use of this approach into the analysis would result in highly variable results and information. The initial assumption that was performed was to consider the data point closest to the sensor location as the initial compaction data for that particular sensor. As it is seen from Table 8.4, 8.5 and 8.6, the compaction data obtained from the data is not uniform for all locations of same depth and

there is a variability involved. Hence it was then decided to perform a statistical analysis of all data and use the average layer properties from this analysis to predict typical VMC changes due to the thermal-hydraulic gradients occurring at the site before assuming the initial dry density and moisture content. The statistical study of the compaction data is performed in the next section.

ANALYSIS OF IN-SITU COMPACTION PROPERTIES

General Background

A wide range of data, relating to the in-situ moisture, density and CBR strength test results have been historically kept in the NAPTF databases. The following study focuses upon three (3) key compaction properties:

a. w%- gravimetric moisture content
b. γ_d – dry density
c. θ= VMC – Volumetric water content

   Note: $\theta = \left(\frac{w\gamma_d}{\gamma_w}\right)$

In addition, a limited amount of historic CBR strength test results were available for further analysis.

Data Sources

The information for the ensuing statistical analysis was derived from a variety of sources. In the following tables, each of these references are denoted by numerals (1) to (5), and are identified as follows:

(1) CC-7 Dupont clay data obtained directly from NAPTF in August 2013, representing the initial phase of the project.

(2) CC-7 Shelby tube data (tested at ASU representing both Dupont and County clay layers.

(3) CC-5 data obtained directly from NAPTF at the project (ASU study) beginning; information in both County and Dupont clay post traffic forensic analysis of CC-5 and results of CC-7 Dupont clay subgrade compaction acceptance tests.

(4) Data sent by Dr. Carlos Cary relating to Dupont and County clay test results from both CC-5 and CC-7

(5) CC-5 data obtained directly from NAPTF on initial construction records during December 2007 and January to March 2008 period.

Data Organization into Cells

All of this historic information was then further processed by organizing all of the data into "cells" that were categorized by the following considerations of

1. Clay type
    a. Dupont (depth z= 29"-83")
    b. County (depth z= 83"-144")
2. Clay sublayer
    a. Dupont No 1 (depth z= 29"-51")
    b. Dupont No 2 (depth z= 51"-83")
    c. County No 1 (depth z= 83"-110")
    d. County No 2 (depth z= 110"-144")
3. Station
    - 0'-100'
    - 100'-200'

- 200’-300’

4. Radial offset (from centerline) any offsets north of centerline were treated as -r (offset) while all points south of centerline were treated as + r(offsets)
    - r< 0’
    - r= 0’-10’
    - r= 10’-20’
    - r=20’-30’

There was an important reason as to why sublayers, within each major clay type, were selected. For the upper “Dupont clay”; the depth z= 51” used to distinguish sublayer No 1 from No 2 is critical as it represents the limit of where the older CC-5 Dupont sublayer was removed, reprocessed and the recompacted as the “new” Dupont clay sublayer No. 1 for the CC-7 tests in the 2013 period. The sub-layering for the lower County clay layer was merely done to subdivide it into 2 roughly equal subgrade sublayers to assess if true significant differences in properties were present between the top and bottom portions of the County clay layer.

Table 8.7 and 8.8 represents the complete data summary of the w, γ_d and VMC (θ) values for the County clay and Dupont clay, respectively. As noted each table identifies the: data source, station, offset, depth, data and in-situ compaction results. It should also be observed that within each table, the data is sorted by station numbers.

Table 8.7. Summary of County Clay Compaction Input Properties used in Statistical Analysis

Source	Station. (ft.)	Offset (ft.)	Depth (in)	Layer	Date	Gravimetric Moisture Content (%)	Dry Density (pcf)	VMC (%)
2	23	2	86	County Clay	Aug-17	25.1	99.6	40.0
2	23	2	97	County Clay	Aug-17	26.5	97.5	41.5
2	23	26	86	County Clay	Aug-17	36.2	85.0	49.4
2	23	26	97	County Clay	Aug-17	24.5	99.4	39.1
3	30	15	142	County Clay	Dec-17	26.6	99.0	42.3
3	30	15	142	County Clay	Jan-17	27.1	97.7	42.5
4	32	21	83	County Clay	Nov-17	25.3	98.3	39.9
2	110	15	86	County Clay	Aug-17	34.2	86.2	47.3
2	110	15	98	County Clay	Aug-17	26.2	100.2	42.1
2	110	26	86	County Clay	Aug-17	25.3	98.5	40.0
2	110	26	98	County Clay	Aug-17	24.5	94.5	37.1
4	115	18	83	County Clay	Mar-17	25.5	98.8	40.5
3	135	15	142	County Clay	Feb-17	26.8	98.5	42.4
3	135	15	142	County Clay	Mar-17	27.1	98.1	42.5
1	153	14	35	County Clay	Aug-17	26.9	96.3	41.5
4	160	18	83	County Clay	Mar-17	24.2	101.2	39.3
3	200	15	142	County Clay	Apr-17	28.5	96.4	44.1
3	200	15	142	County Clay	May-17	28.9	96.5	44.7
2	208	2	134	County Clay	Aug-17	28.4	97.0	44.1
2	208	2	103	County Clay	Aug-17	27.7	97.0	43.0
2	209	26	134	County Clay	Aug-17	27.0	89.6	38.9
2	209	26	103	County Clay	Aug-17	26.0	99.0	41.3
4	210	18	83	County Clay	Feb-17	24.9	98.6	39.3
4	210	23	83	County Clay	Feb-17	26.4	98.0	41.6
3	260	15	142	County Clay	Jun-17	27.0	98.5	42.7
3	260	15	142	County Clay	Jul-17	27.3	97.0	42.5
4	260	18	83	County Clay	Feb-17	25.3	98.9	40.2

Table 8.8. Summary of Dupont Clay Compaction Input Properties used in Statistical Analysis

Source	Station. (ft.)	Offset (ft.)	Depth (in)	Layer	Date	Gravimetric Moisture Content (%)	Dry Density (pcf)	VMC (%)
1	17	-6	53	Dupont Clay	Aug-17	34.7	87.6	48.7
2	23	2	66	Dupont Clay	Aug-17	32.7	89.3	46.8
2	23	2	76	Dupont Clay	Aug-17	33.0	87.9	46.5
2	23	26	72	Dupont Clay	Aug-17	37.8	82.2	49.9
2	23	26	76	Dupont Clay	Aug-17	37.4	90.4	54.3
4	30	13	50	Dupont Clay	Jul-17	32.5	88.5	46.1
4	30	22	53	Dupont Clay	Oct-17	38.6	82.0	50.8
4	30	21	71	Dupont Clay	Nov-17	36.7	84.6	49.8
4	30	21	77	Dupont Clay	Nov-17	37.4	84.0	50.4
4	31	21	59	Dupont Clay	Oct-17	37.3	82.5	49.4
4	31	22	65	Dupont Clay	Oct-17	37.8	82.9	50.2
4	36	14	32	Dupont Clay	Aug-17	26.4	95.9	40.6
4	42	22	53	Dupont Clay	Oct-17	37.3	83.8	50.1
4	42	22	59	Dupont Clay	Oct-17	37.2	83.1	49.5
4	42	22	65	Dupont Clay	Oct-17	38.0	82.2	50.1
4	53	22	53	Dupont Clay	Oct-17	38.0	82.6	50.3
4	55	16	38	Dupont Clay	Aug-17	26.4	97.0	41.0
4	55	21	59	Dupont Clay	Oct-17	38.5	83.1	51.2
4	55	22	65	Dupont Clay	Oct-17	37.9	82.3	50.0
4	55	21	71	Dupont Clay	Oct-17	37.7	83.2	50.2
4	55	21	77	Dupont Clay	Nov-17	36.8	83.6	49.4
4	61	15	44	Dupont Clay	Aug-17	28.2	94.2	42.6
1	61	15	47	Dupont Clay	Aug-17	27.9	95.3	42.6
4	63	2	53	Dupont Clay	Oct-17	38.0	83.5	50.9
4	63	2	59	Dupont Clay	Oct-17	37.8	82.6	50.0
4	63	2	65	Dupont Clay	Oct-17	38.0	83.5	50.9
4	63	5	71	Dupont Clay	Oct-17	37.4	82.1	49.2
4	63	5	77	Dupont Clay	Nov-17	37.9	82.5	50.1
4	63	8	53	Dupont Clay	Oct-17	37.8	82.9	50.3
4	63	8	65	Dupont Clay	Oct-17	38.4	82.8	50.9

Table 8.8. Summary of Dupont Clay Compaction Input Properties used in Statistical Analysis (Cont'd)								
Source	**Station. (ft.)**	**Offset (ft.)**	**Depth (in)**	**Layer**	**Date**	**Gravimetric Moisture Content (%)**	**Dry Density (pcf)**	**VMC (%)**
4	63	9	59	Dupont Clay	Oct-17	37.9	83.2	50.6
4	63	16	53	Dupont Clay	Oct-17	37.2	83.4	49.7
4	63	16	59	Dupont Clay	Oct-17	38.5	81.7	50.4
4	68	16	32	Dupont Clay	Aug-17	26.4	95.9	40.6
4	63	17	65	Dupont Clay	Oct-17	37.6	83.4	50.2
4	63	17	71	Dupont Clay	Oct-17	37.5	82.2	49.3
4	63	17	77	Dupont Clay	Nov-17	36.3	84.2	49.0
4	63	24	53	Dupont Clay	Oct-17	37.0	82.7	49.1
4	63	24	59	Dupont Clay	Oct-17	39.0	81.8	51.1
4	63	24	65	Dupont Clay	Oct-17	37.0	82.4	48.9
1	68	16	35	Dupont Clay	Aug-17	26.3	96.0	40.5
2	110	15	76	Dupont Clay	Aug-17	36.3	83.1	48.4
2	110	15	70	Dupont Clay	Aug-17	38.4	85.5	52.7
4	110	17	38	Dupont Clay	Aug-17	26.1	96.5	40.4
2	110	26	67	Dupont Clay	Aug-17	39.3	80.8	50.9
2	110	26	76	Dupont Clay	Aug-17	36.4	82.6	48.2
1	115	-10	53	Dupont Clay	Aug-17	32.4	89.2	46.3
4	115	16	57	Dupont Clay	Mar-17	37.1	83.7	49.8
4	115	16	65	Dupont Clay	Mar-17	37.3	82.9	49.6
4	115	16	77	Dupont Clay	Mar-17	37.4	82.8	49.6
4	115	23	57	Dupont Clay	Mar-17	38.0	83.1	50.6
4	115	23	65	Dupont Clay	Mar-17	37.7	83.1	50.3
4	115	23	77	Dupont Clay	Mar-17	37.7	82.6	50.0
4	116	17	44	Dupont Clay	Aug-17	28.2	94.2	42.6
4	153	14	32	Dupont Clay	Aug-17	26.9	96.3	41.5
4	160	9	57	Dupont Clay	Mar-17	38.2	82.2	50.4
4	160	9	65	Dupont Clay	Mar-17	36.8	83.4	49.2
4	160	9	77	Dupont Clay	Mar-17	36.4	84.2	49.2
4	160	16	57	Dupont Clay	Mar-17	38.7	82.5	51.1
4	160	16	65	Dupont Clay	Mar-17	36.1	83.7	48.5

Table 8.8. Summary of Dupont Clay Compaction Input Properties used in Statistical Analysis (Cont'd)								
Source	**Station. (ft.)**	**Offset (ft.)**	**Depth (in)**	**Layer**	**Date**	**Gravimetric Moisture Content (%)**	**Dry Density (pcf)**	**VMC (%)**
4	160	16	77	Dupont Clay	Mar-17	36.8	83.3	49.2
4	160	23	57	Dupont Clay	Mar-17	38.7	83.0	51.6
4	160	23	65	Dupont Clay	Mar-17	36.7	83.3	49.0
4	160	23	77	Dupont Clay	Mar-17	36.0	84.9	49.0
1	178	14	53	Dupont Clay	Aug-17	33.9	86.5	47.0
4	184	15	44	Dupont Clay	Aug-17	27.0	96.2	41.7
4	186	15	38	Dupont Clay	Aug-17	27.5	94.1	41.5
4	210	9	57	Dupont Clay	Feb-17	37.7	82.8	50.0
4	210	9	65	Dupont Clay	Feb-17	37.8	82.5	50.0
4	210	9	77	Dupont Clay	Feb-17	36.5	83.6	48.9
4	210	16	57	Dupont Clay	Feb-17	39.0	82.6	51.6
4	210	16	65	Dupont Clay	Feb-17	36.9	82.6	48.9
4	210	16	77	Dupont Clay	Feb-17	36.1	84.0	48.6
4	210	23	57	Dupont Clay	Feb-17	37.7	82.8	50.1
4	210	23	65	Dupont Clay	Feb-17	36.5	83.2	48.7
4	210	23	77	Dupont Clay	Feb-17	35.7	83.8	48.0
1	220	-22	53	Dupont Clay	Aug-17	33.6	87.4	47.1
1	229	-14	47	Dupont Clay	Aug-17	25.9	97.1	40.3
4	252	12	44	Dupont Clay	Aug-17	28.6	93.6	43.0
4	253	16	32	Dupont Clay	Aug-17	26.8	95.8	41.2
4	257	18	38	Dupont Clay	Aug-17	27.1	96.0	41.8
4	260	9	53	Dupont Clay	Feb-17	38.0	83.0	50.6
4	260	9	65	Dupont Clay	Feb-17	37.3	84.2	50.3
4	260	9	77	Dupont Clay	Feb-17	36.9	84.3	49.9
4	260	16	53	Dupont Clay	Feb-17	37.6	83.3	50.2
4	260	16	65	Dupont Clay	Feb-17	37.3	83.5	49.9
4	260	16	77	Dupont Clay	Feb-17	36.5	84.3	49.3
4	260	23	53	Dupont Clay	Feb-17	36.7	83.9	49.4
4	260	23	65	Dupont Clay	Feb-17	37.4	83.0	49.8
4	260	23	77	Dupont Clay	Feb-17	36.3	84.9	49.4
1	263	-14	47	Dupont Clay	Aug-17	26.4	96.6	40.9
4	285	13	50	Dupont Clay	Jul-17	35.2	86.1	48.6

Breakdown of input cells.

Table 8.9 is the master summary of the number of historic cell entries (of w, γ_d and VMC) for each cell combination for both clay subgrade layers. There are several relevant conclusions that are obvious from this table. It can be initially observed that the results provided by NAPTF show the greatest frequency, by far, of results to be in the bottom (original) Dupont clay layer. In contrast to the 104 results shown in this sublayer, the number of cell entries within the other three sublayers ranged from 10 to 16.

Table 8.9. Number of Cell Entries for Both Clays

Clay type	Depth (z) (in)	Station (feet)	r<0’	r= 0'-10'	r= 10'-20'	r= 20'-30'	Total
Dupont	29-51	0-100	0	0	6	0	16
		100-200	0	0	5	0	
		200-300	2	0	3	0	
	51-83	0-100	7	10	11	18	104
		100-200	5	3	14	8	
		200-300	6	6	9	7	
County	83-110	0-100	0	2	0	2	14
		100-200	0	0	3	2	
		200-300	0	1	2	2	
	110-144	0-100	0	0	2	0	10
		100-200	0	0	2	0	
		200-300	0	1	4	1	

It is also obvious that there does not appear to have been any early (initial) attempt to subdivide these historic in-situ compaction properties into any future formal statistical analysis (e.g.. ANOVA) to examine if significant difference in subgrade properties may have existed in the entire NAPTF test sections (subgrade volume of 172,500 ft^3)

Recognizing that statistical hypothesis testing for differing populations requires the computation of an appropriate population standard deviation; any cells showing a cell entry

of n=0 and n=1 values, provide no ability for computing the standard deviation, variance or coefficient of variation for a given cell.

Analysis Results

A statistical analysis was performed to study the variation of the dry density, gravimetric moisture content and volumetric moisture content data in the NAPTF. After careful consideration, an average value was fixed for the different sublayers of the subgrade. The subgrade was split into four different layers for the analysis. Two Dupont clay layers and two County clay layer were considered as a part of the analysis. Table 8.10 shows the results of the statistical analysis.

The following are the conclusions after analyzing the compaction data obtained.

1. The two Dupont sublayers (z = 29”-51”) and (z= 51”-83”) depths; have different populations of w, γ_d and VMC. Each sublayer must be treated separately in any analysis.
2. Within each sublayer of the Dupont clay; there appears to be no statistically significant differences in w, γ_d and VMC populations due to any station effect and radial offset effect of the test section.
3. Within each sublayer of the County clay, there was no significant, practical, difference found in the w, γ_d and VMC parameters due to an effect of either station or radial offset in the CC-7 test section.
4. A very slight, but statistically significant difference in w, γ_d and VMC populations was found between the top sublayer (z =83”-110”) and bottom sublayer (z =111”-140”).

Based upon the analysis performed, the compaction properties of each sublayers are considered as shown in Table 8.11.

Table 8.10. Statistical Summary for Various Subgrade Sublayers

Statistical Summary for Dupont Clay (z=29"-51")			
	w(%)	**Density (pcf)**	**Theta (Vol %)**
n(count)	16	16	16
Avg	27	95.5	0.413
Std Dev	0.81	1.268	0.01
Var	0.6568	1.6071	0.0001
CV(%)	3.00%	1.33%	2.39%
Statistical Summary for Dupont Clay (z=52"-83")			
	w(%)	**Density (pcf)**	**Theta (Vol %)**
n(count)	104	104	104
Avg	37.2	83.4	0.497
Std Dev	1.424	2.142	0.013
Var	2.0278	4.5889	0.0002
CV(%)	3.82%	2.57%	2.65%
Statistical Summary for County Clay (z=83"-110")			
	w(%)	**Density (pcf)**	**Theta (Vol %)**
n(count)	14	14	14
Avg	25.7	99	0.407
Std Dev	0.964	1.207	0.012
Var	0.9291	1.458	0.00014
CV(%)	3.75%	1.22%	2.94%
Statistical Summary for County Clay (z=111"-140")			
	w(%)	**Density (pcf)**	**Theta (Vol %)**
n(count)	10	10	10
Avg	27.5	96.8	0.426
Std Dev	0.769	2.555	0.015
Var	0.5921	6.5281	0.0002
CV(%)	2.80%	2.64%	3.62%

Table 8.11. Final Water Content, Dry Density and Volumetric Moisture Content for Sublayers of Pavement Subgrade

Clay Layer	Depth	w%	$\gamma_{d\ (pcf)}$	VMC (%)
Dupont	z_1 (29”-51”)	27.0	95.5	41.3
	z_2 (51”-83”)	37.2	83.4	49.7
County	z_1 (83”-110”)	25.7	99.0	0.407
	z_2 (111”-140”)	27.5	96.8	0.426

Hydraulic thermal moisture movement analysis

The objective of this work phase was to evaluate the data obtained from the 5TM moisture/temperature sensor data and to analyze the variation of moisture/temperature in the NAPTF hangar facility. It should be recalled that evaporation of water from subgrade is restricted due to being bounded by the asphalt pavement and a membrane on top and bottom and with membranes and metal plates on sides of the subgrade. Hence the main reason that there would be any observed increase or decrease in water content would have to be due to the variation of temperature and its subsequent thermal hydraulic flow of moisture within the encapsulated subgrade system.

Compilation of sensor data:

As mentioned in the previous section, the 5TM Decagon Sensors were installed at 30 different locations in the two subgrade materials of the NAPTF. As reported by NAPTF personnel, the sensors were installed in the facility around May 2013 and the construction of the subgrade was completed. The sensor data obtained from the NAPTF personnel contained data starting from July 29, 2013, 4 p.m. to March 22, 2016, 7 am. Each sensor provided 21388 data points. For 30 sensors, the total amount of data points that were compiled and analyzed mounted to 641,640 data points. The number of data points

obtained for each month is shown in Table 8.11. The table shows that the sensors did not obtain data all throughout the year, as several of the sensors malfunctioned collecting the data at certain points of time.

Table 8.12. Number of Data Points Obtained during the Time Duration

Month	Number of data points			
	2013	2014	2015	2016
January		744	502	744
February		648	672	697
March		694	744	510
April		720	719	
May		793	744	
June		720	720	
July	60	744	744	
August	744	744	221	
September	384	720	33	
October	744	744	744	
November	720	720	744	
December	744	744	474	

It was also noted that a few of the sensors recorded voltage levels that were out of proportion and not acceptable. Any reading that was considered suspect was subsequently eliminated in the final analysis.

Correction of the data

The sensor data obtained from the NAPTF facility consisted of Raw voltage points along with the temperature and volumetric water content calculated using Topp's equation. As explained in the previous section, a calibration equation was developed in the ASU laboratory to calculate the VMC from the sensor Raw voltage data and temperature. The equation used are:

For DuPont soil:

$$VMC = 0.698144 \times \left[0.818814 - 0.992436^{\left(\frac{R}{T^{0.5}+2}\right)} + 0.0145732 \right]$$

For County soil:

$$VMC = 0.796544 \times \left[0.372384 - 0.99673^{\left(\frac{R}{T^{0.6}+2}\right)} + 0.422945 \right]$$

The data obtained from the sensors consisted of Raw data in terms of voltage. Using the raw data and the temperature, the VMC was calculated for that particular time. This procedure was repeated for all sensors for the data collected during the 2.5 years duration. After the VMC was calculated using the calibration equation, the VMC measured by the sensor during the first few days were evaluated to see if it yielded the same VMC as calculated from the initial analysis field compacted moisture content and dry density. However, the comparison showed that there were differences between the initial VMC measured by the sensor and the VMC calculated from the previously noted approach to select an initial field compacted moisture and dry density values. The difference is shown in Table 8.12. This table shows the compacted dry density, moisture content and the initially selected VMC along with the VMC measured by the sensor for the first two days. The difference between the sensor measured VMC and the "compaction" data VMC is shown in the last column of Table 8.12. It was assumed that the VMC calculated using the calibration data had to be further modified in order to match the VMC of the compaction data.

As a result, the VMC measured by the sensor was ultimately decided to match the VMC obtained from the field compaction data as shown in Table 8.13. In order to illustrate the process used to adjust the initial sensor readings; Table 8.13 shows the data obtained from the sensors for a period of 20 consecutive hours over two days, from sensors installed in Location A at the depths of 77" (A2, Dupont clay layer) and 89"(A3, County clay layer). The table shows the calculation of VMC from the calibration equation. Using the difference of the initial compaction measurement obtained from Table 8.12.; a translation of all the data obtained from sensors A2 and A3 were performed. The difference between sensor measured and field compaction VMC was found to be -0.094 for A2 and -0.019 for A3. The values was subtracted to the VMC calculated from the calibration equation and are shown under the column corrected to Field VMC. This process was then repeated for all 30 sensors, for every reading recorded in the 2.5 year data collection period.

Table 8.13. Difference in VMC between Calibration VMC and Initial Sensor VMC Assumption

Type of soil	Depth (inches)	Station (feet)	Offset(feet)	Sensor Title	Field Compaction Data			Sensor measured data	ΔVMC Correction (Comp VMC-Initial Sensor VMC)
					Initial Gravimetric Moisture Content (%)	Initial Dry density (pcf)	Initial Assumed Compacted VMC (%)	Initial Sensor measured VMC (%)	
Dupont Clay	35	30	2	A1	27	95.5	0.410	0.440	0.031
			26	B1	27	95.5	0.410	0.480	0.067
		110	15	C1	27	95.5	0.410	0.480	0.064
			26	D1	27	95.5	0.410	0.450	0.035
		210	2	E1	27	95.5	0.410	0.410	-0.001
			26	F1	27	95.5	0.410	0.460	0.047
	77	30	2	A2	37.2	83.4	0.500	0.400	-0.094
			26	B2	37.2	83.4	0.500	0.550	0.049
		110	15	C2	37.2	83.4	0.500	0.520	0.02
			26	D2	37.2	83.4	0.500	0.540	0.041
		210	2	E2	37.2	83.4	0.500	0.370	-0.123
			26	F2	37.2	83.4	0.500	0.520	0.023
County Clay	89	30	2	A3	25.7	99	0.410	0.390	-0.019
			26	B3	25.7	99	0.410	0.590	0.183
		110	15	C3	25.7	99	0.410	0.370	-0.036
			26	D3	25.7	99	0.410	0.360	-0.048
		210	2	E3	25.7	99	0.410	0.380	-0.028
			26	F3	25.7	99	0.410	0.370	-0.037
	108	30	2	A4	25.7	99	0.410	0.340	-0.069
			26	B4	25.7	99	0.410	0.490	0.083
		110	15	C4	25.7	99	0.410	0.320	-0.091
			26	D4	25.7	99	0.410	0.220	-0.192
		210	2	E4	25.7	99	0.410	0.370	-0.034
			26	F4	25.7	99	0.410	0.440	0.028
	126	30	2	A5	27.5	96.8	0.430	0.310	-0.121
			26	B5	27.5	96.8	0.430	0.380	-0.048
		110	15	C5	27.5	96.8	0.430	0.260	-0.165
			26	D5	27.5	96.8	0.430	0.310	-0.119
		210	2	E5	27.5	96.8	0.430	0.280	-0.143
			26	F5	27.5	96.8	0.430	0.330	-0.093

Table 8.14. Calibration and Correction of VMC for Sensor Data

EM50(1)	Port 2 (A2)					Port 3 (A3)				
	Raw data	Temperature	Topp eqn	Calibrated	Corrected to Field VWC	Raw data	Temperature	Topp eqn	Calibrated	Corrected to Field VWC
	VWC		VWC	VWC	VWC	VWC		VWC	VWC	VWC
7/29/13 4:00 PM	1189	22.4	0.388	0.404	0.497	1979	21.9	0.508	0.389	0.407
7/29/13 5:00 PM	1189	22.4	0.388	0.404	0.497	1978	21.9	0.508	0.389	0.407
7/29/13 6:00 PM	1189	22.4	0.388	0.404	0.497	1978	21.9	0.508	0.389	0.407
7/29/13 7:00 PM	1189	22.4	0.388	0.404	0.497	1978	21.9	0.508	0.389	0.407
7/29/13 8:00 PM	1189	22.4	0.388	0.404	0.497	1978	21.9	0.508	0.389	0.407
7/29/13 9:00 PM	1189	22.4	0.388	0.404	0.497	1978	21.9	0.508	0.389	0.407
7/29/13 10:00 PM	1189	22.4	0.388	0.404	0.497	1978	21.9	0.508	0.389	0.407
7/29/13 11:00 PM	1189	22.4	0.388	0.404	0.497	1978	21.9	0.508	0.389	0.407
7/30/13 12:00 AM	1189	22.4	0.388	0.404	0.497	1979	21.9	0.508	0.389	0.407
7/30/13 1:00 AM	1189	22.4	0.388	0.404	0.497	1978	21.9	0.508	0.389	0.407
7/30/13 2:00 AM	1189	22.4	0.388	0.404	0.497	1977	21.9	0.508	0.389	0.407
7/30/13 3:00 AM	1189	22.4	0.388	0.404	0.497	1977	21.9	0.508	0.389	0.407
7/30/13 4:00 AM	1189	22.4	0.388	0.404	0.497	1977	21.9	0.508	0.389	0.407
7/30/13 5:00 AM	1189	22.4	0.388	0.404	0.497	1978	21.9	0.508	0.389	0.407
7/30/13 6:00 AM	1189	22.4	0.388	0.404	0.497	1977	21.9	0.508	0.389	0.407
7/30/13 7:00 AM	1189	22.4	0.388	0.404	0.497	1977	21.8	0.508	0.389	0.407
7/30/13 8:00 AM	1189	22.4	0.388	0.404	0.497	1977	21.8	0.508	0.389	0.407
7/30/13 9:00 AM	1189	22.4	0.388	0.404	0.497	1978	21.8	0.508	0.389	0.407
7/30/13 10:00 AM	1189	22.4	0.388	0.404	0.497	1977	21.8	0.508	0.389	0.407
7/30/13 11:00 AM	1189	22.4	0.388	0.404	0.497	1977	21.8	0.508	0.389	0.407

Analysis of the data

As previously noted, the main objective of this study was to analyze if variation of moisture content could be observed in the two subgrade soils with the use of the 5TM Moisture/Temperature Sensors. The moisture/temperature data obtained from the sensors were analyzed after the calibration and correction. Two plots of VMC and Temperature with time were created in order to study the variation of VMC and temperature during the

2.5-years duration. Figures 8.16 to 8.27 shows the plot of VMC and temperature for each of the five different depths and for six locations(A, B, C, D, E and F).

The next set of figures were developed to visually show the time influence of the change in the VMC and (temperature) for each of the five sensor depth and six sensor locations. This ΔVMC value represents the difference betwenn the VMC at any specific time, to the initial VMC values from which the field compaction moisture and density. Thus a +ΔVMC is indication of an increase in moisture (at a given depth- location), while a -ΔVMC would imply a moisture loss, at any specific time, from its original (intial) moisture Figure 8.28 to Figure 8.39.

Finally, the last set of figures developed are plots that show the temperature and VMC values, with time, averaged at a given depth (average of all sensor location (A to F). This series of plots are contained in Figure 8.40 and Figure 8.41.

The information from the plots shown in Figures 8.16 to Figure 8.41, were then summarized in tabular form and are shown in Tables 8.14 (Temperature), Table 8.15 (Volumetric Moisture Content- VMC) and Table 8.16 (Gravimetric Moisture Content- w %). In each table, a column identified by: Δ (Max-Min) is shown. This value represents the maximum range in the specific parameter (temperature, VMC and GMC- w%) that occurred over time. Information is also identified for a column heading identified by "Same Offset Location Average". For a particular depth, it can be observed that there are "3"boxes of data. Sensor location "A and E" were placed at an approximate offset of 2 feet south of the centerline; sensor "C" corresponded to tan offset of 15 feet while sensor "B, D and F" had an offset of approximately 28 feet. Thus this set of entries examines if there was any

noticeable impact of the radial distance from the test section centerline. Finally, the last column is the grand average of each variable(temperature, VMC and GMC – w %) across sensor location, at a specific depth.

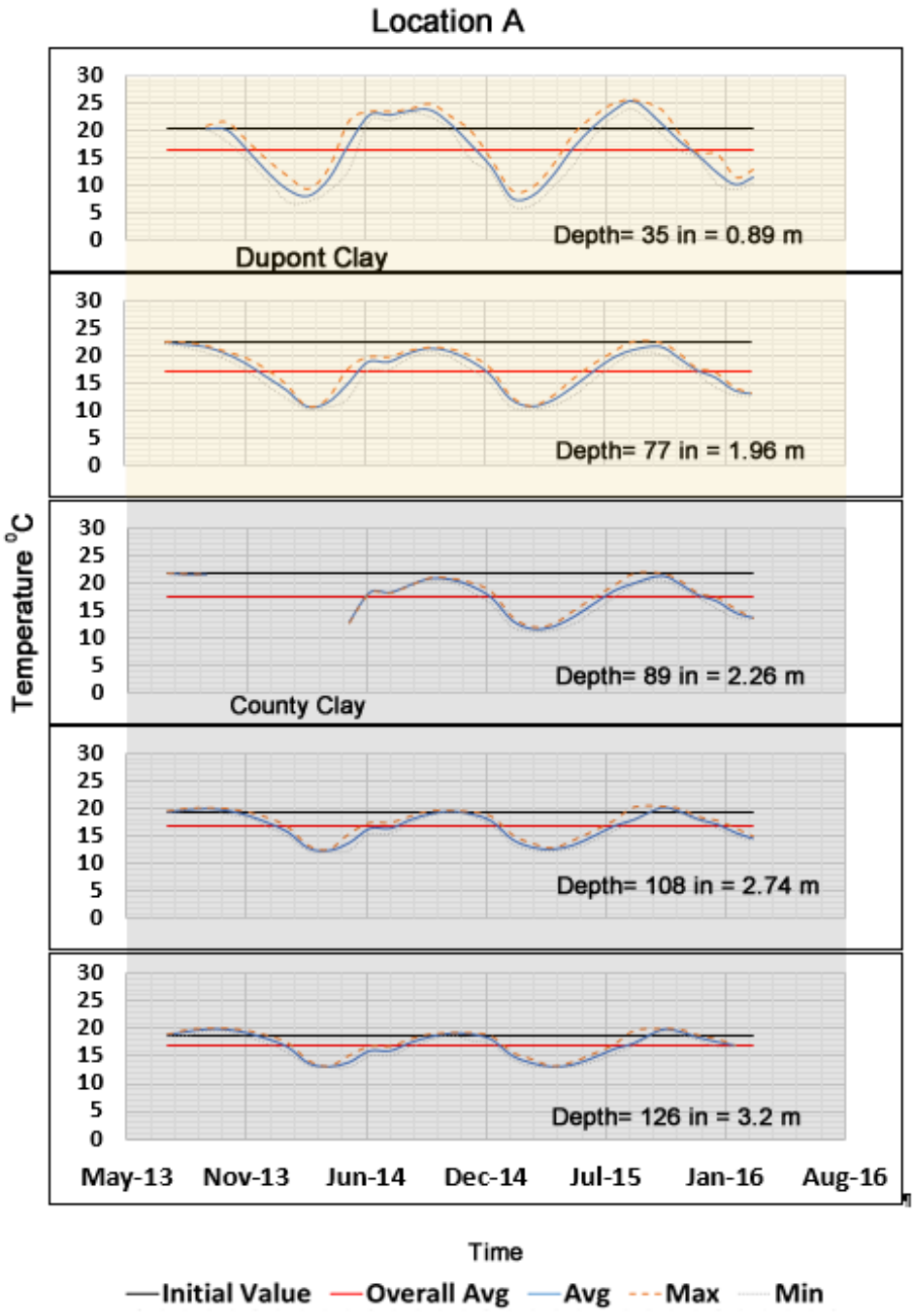

Figure 8.16. Temperature Distribution from Sensor Data in Location A

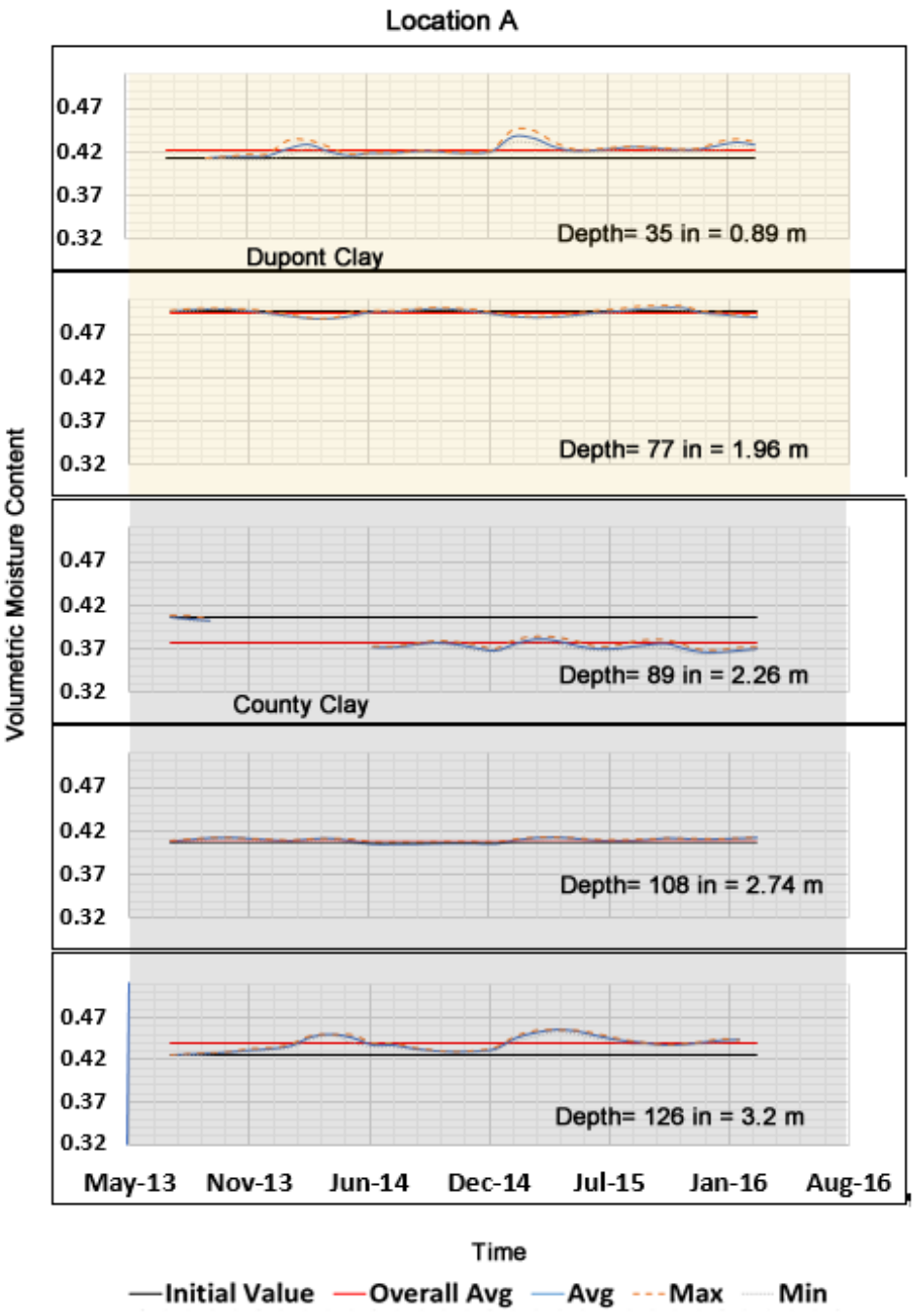

Figure 8.17. VMC Distribution from Sensor Data in Location A

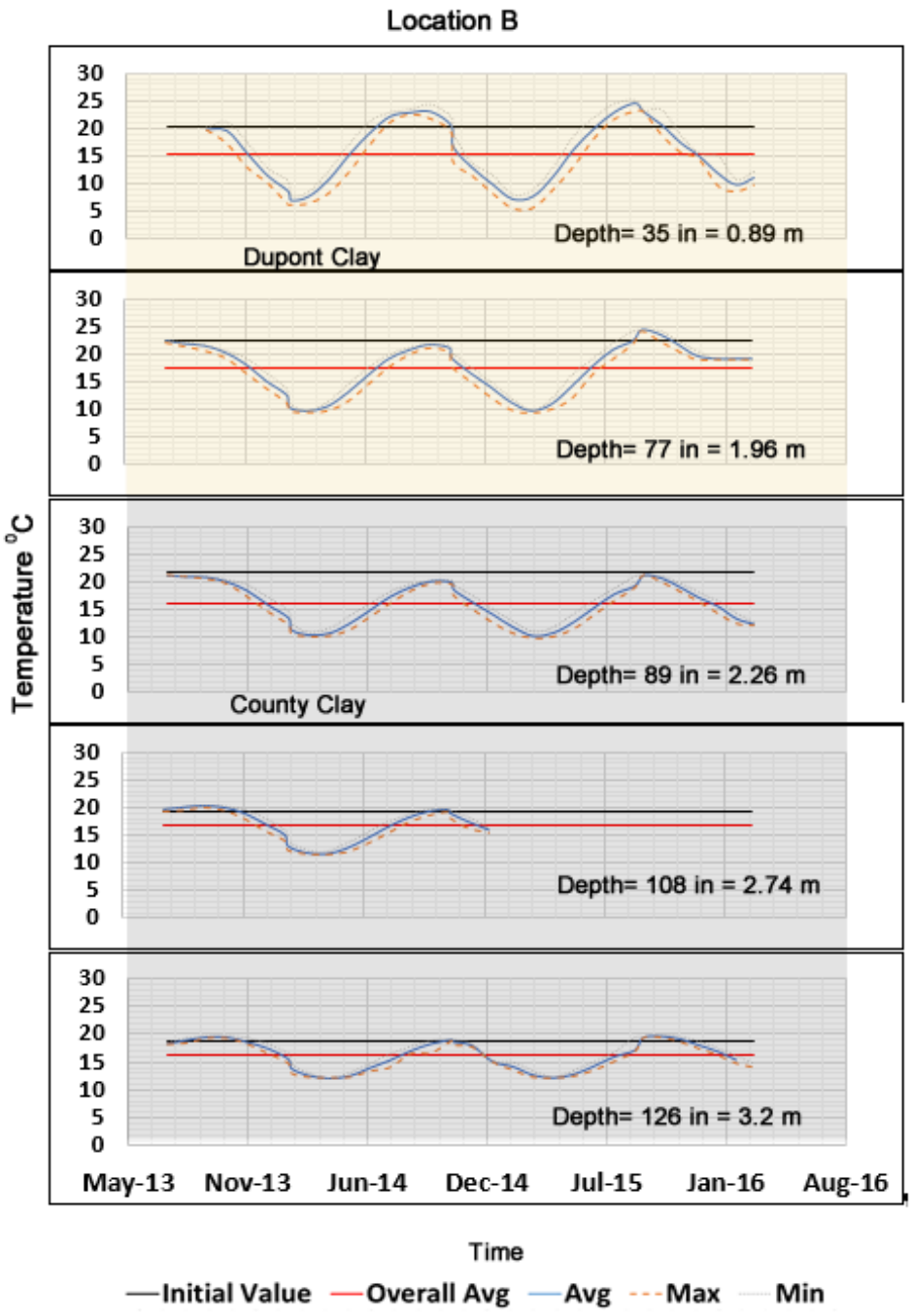

Figure 8.18. Temperature Distribution from Sensor Data in Location B

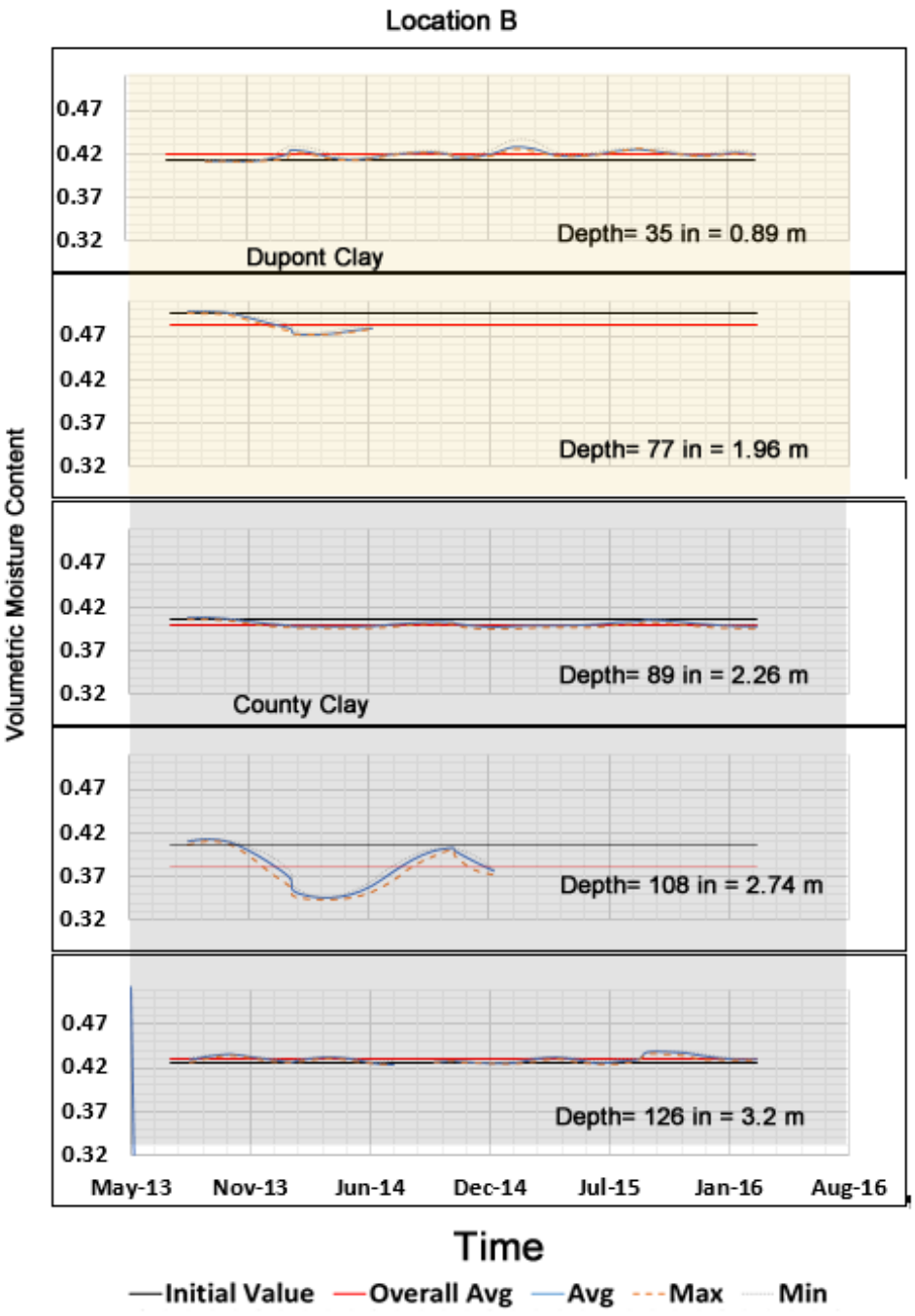

Figure 8.19. VMC Distribution from Sensor Data in Location B

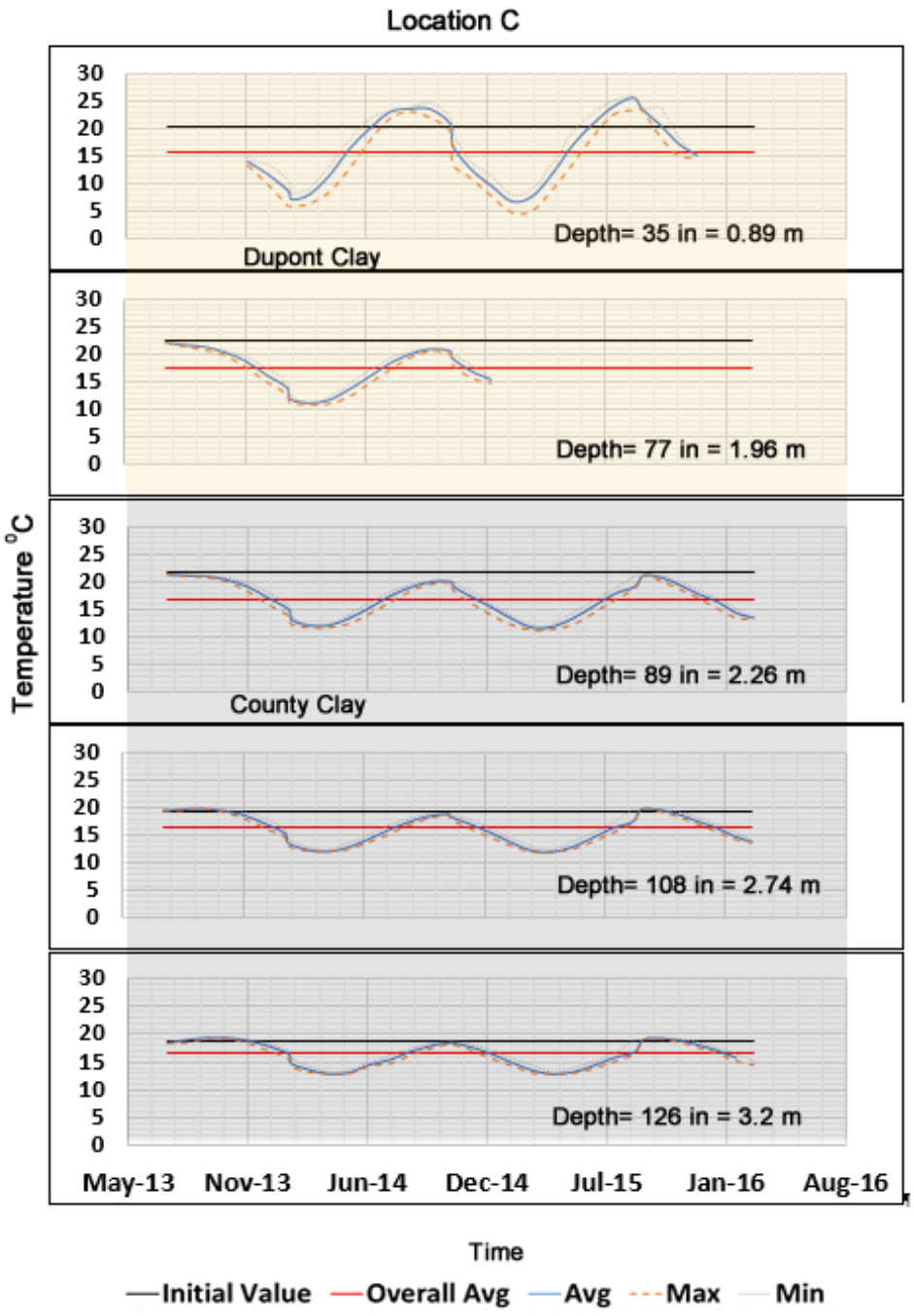

Figure 8.20. Temperature Distribution from Sensor Data in Location C

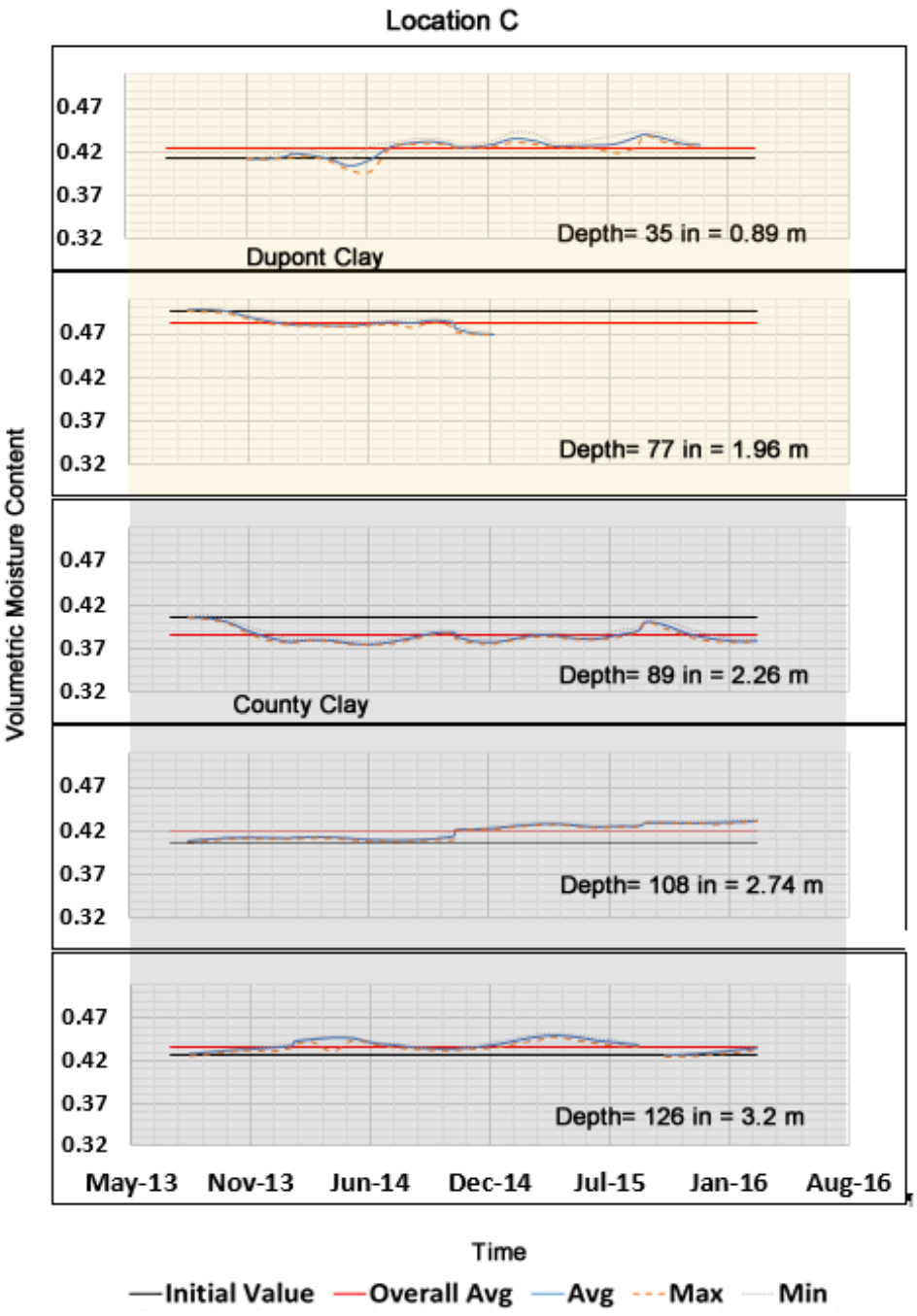

Figure 8.21. VMC Distribution from Sensor Data in Location C

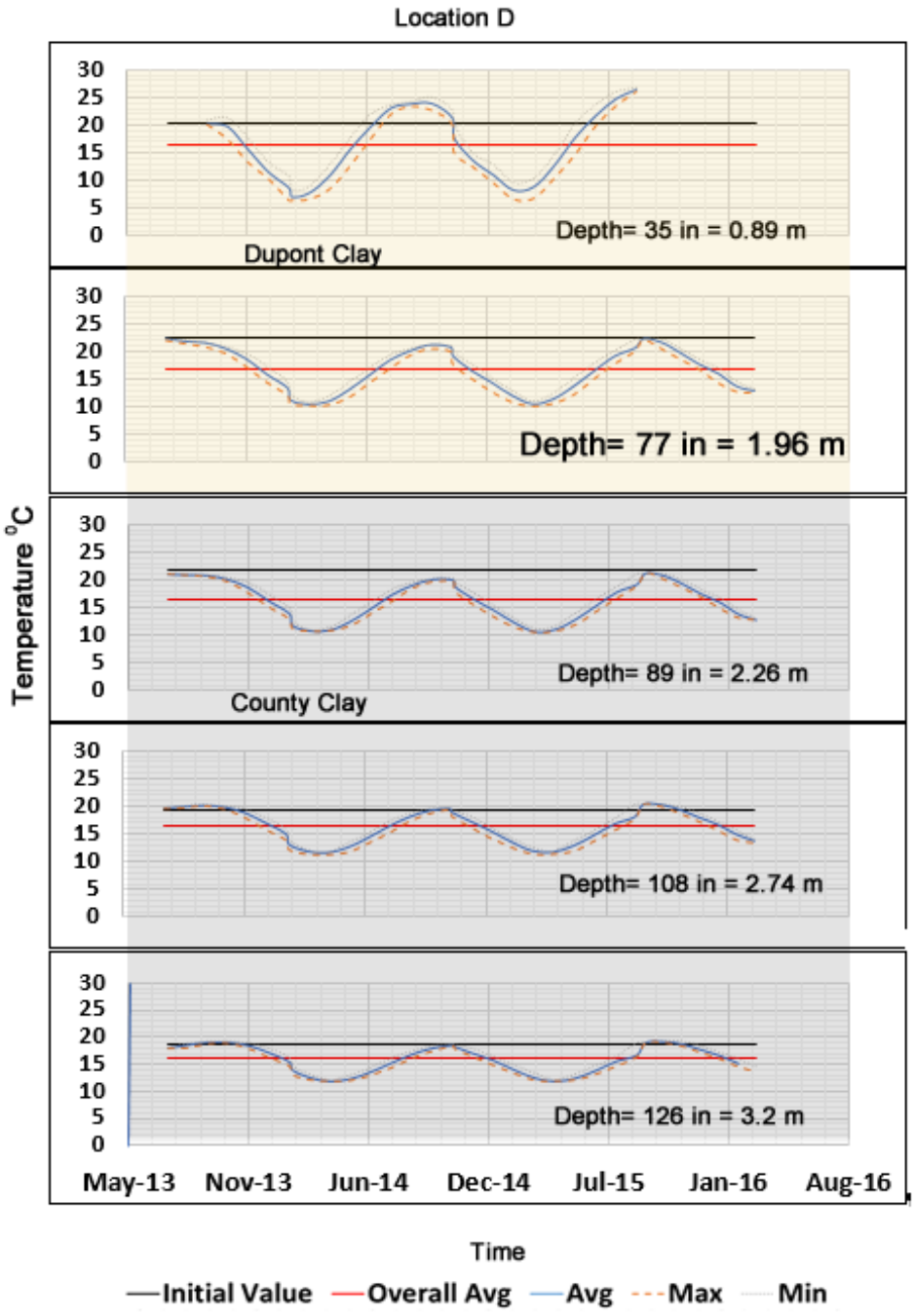

Figure 8.22. Temperature Distribution from Sensor Data in Location D

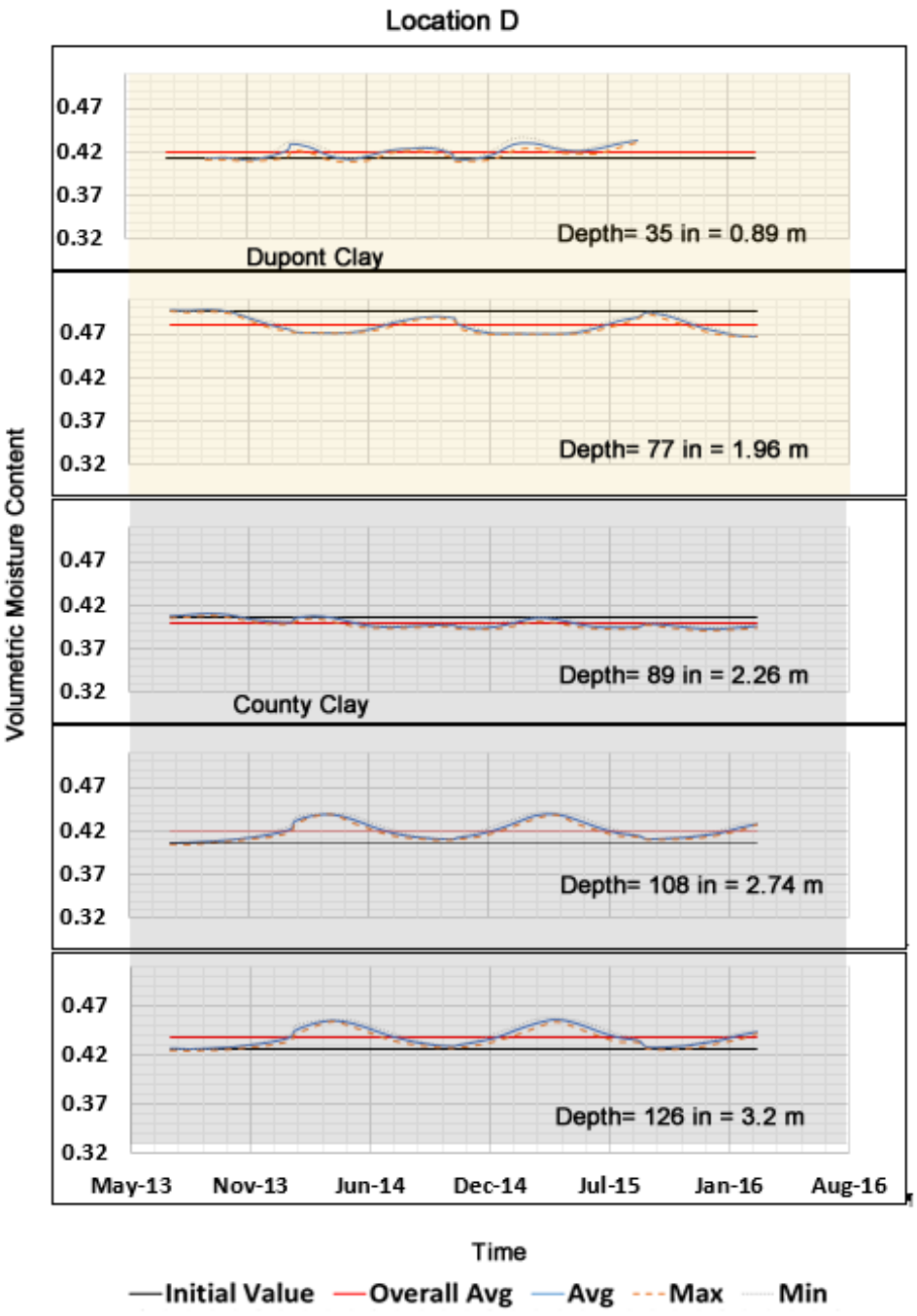

Figure 8.23. VMC Distribution from Sensor Data in Location D

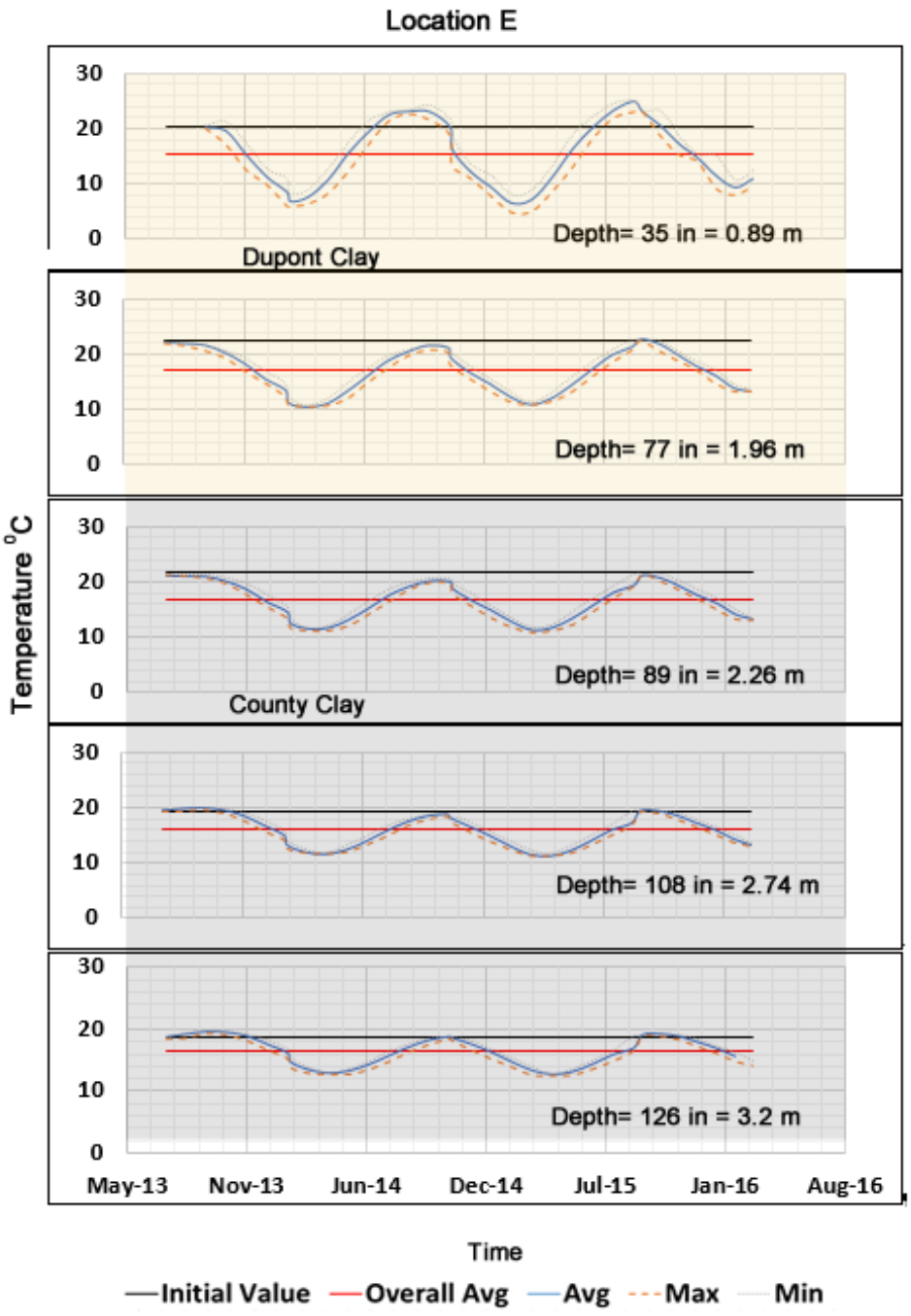

Figure 8.24. Temperature Distribution from Sensor Data in Location E

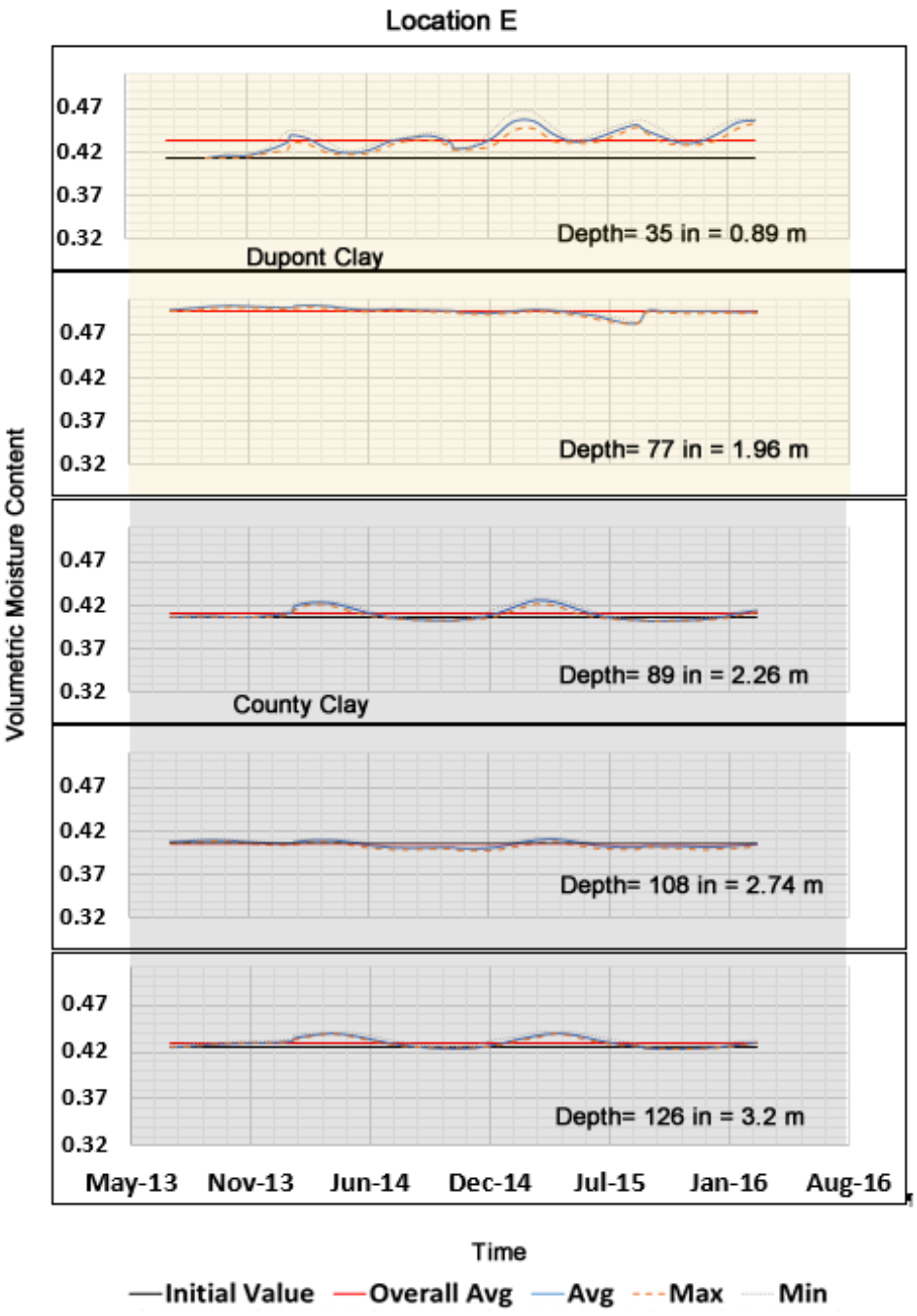

Figure 8.25. VMC Distribution from Sensor Data in Location E

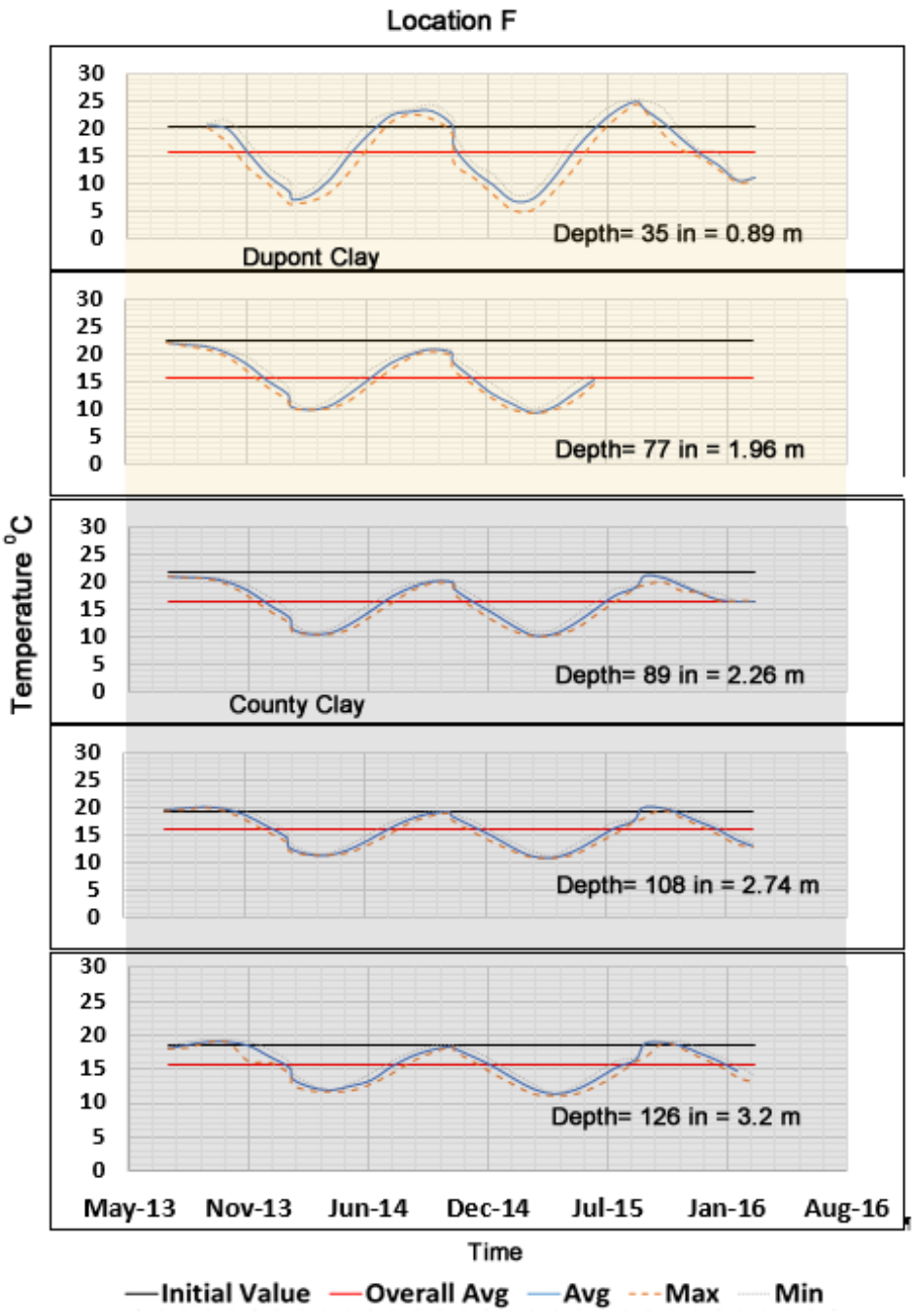

Figure 8.26. Temperature Distribution from Sensor Data in Location F

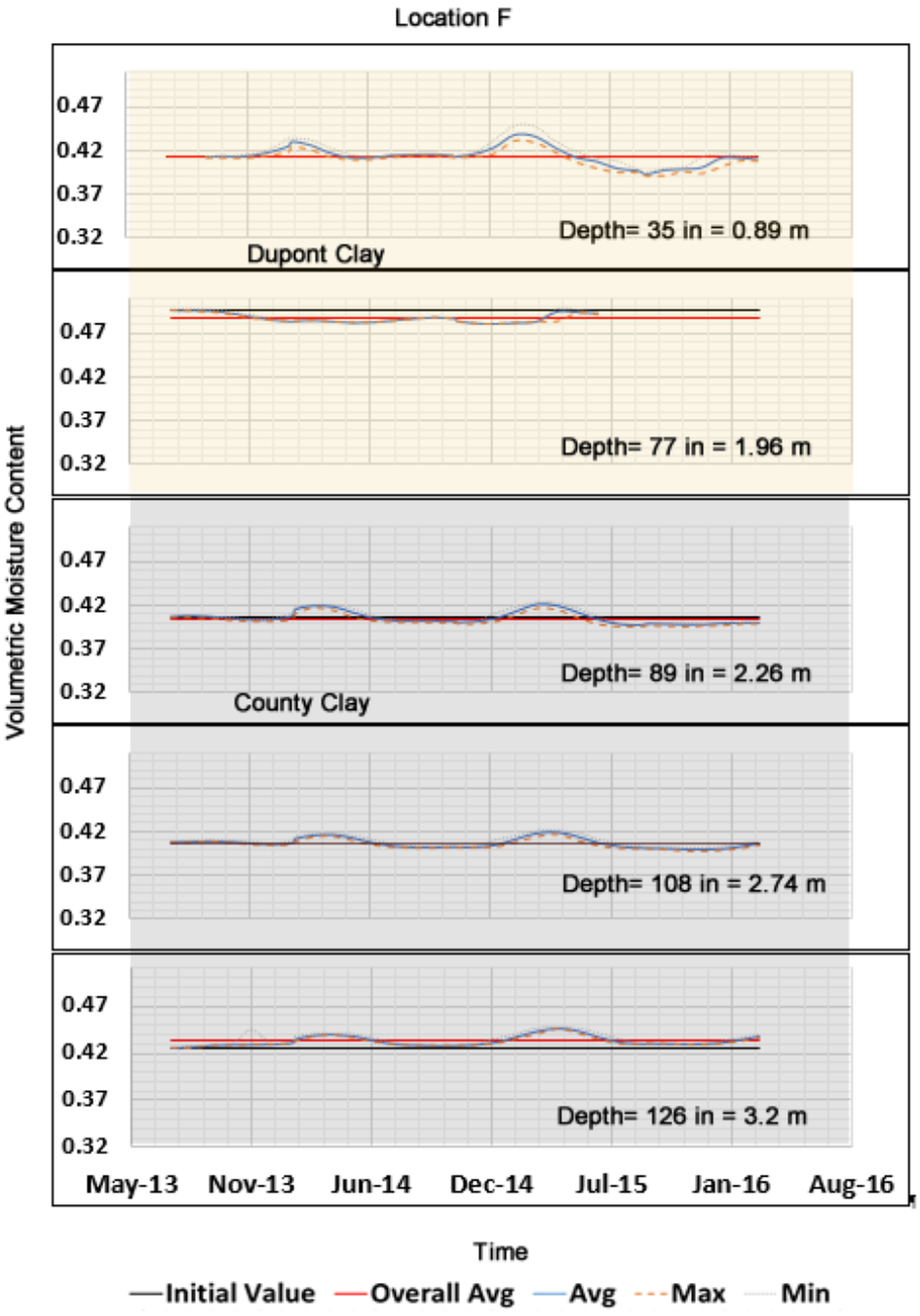

Figure 8.27. VMC Distribution from Sensor Data in Location F

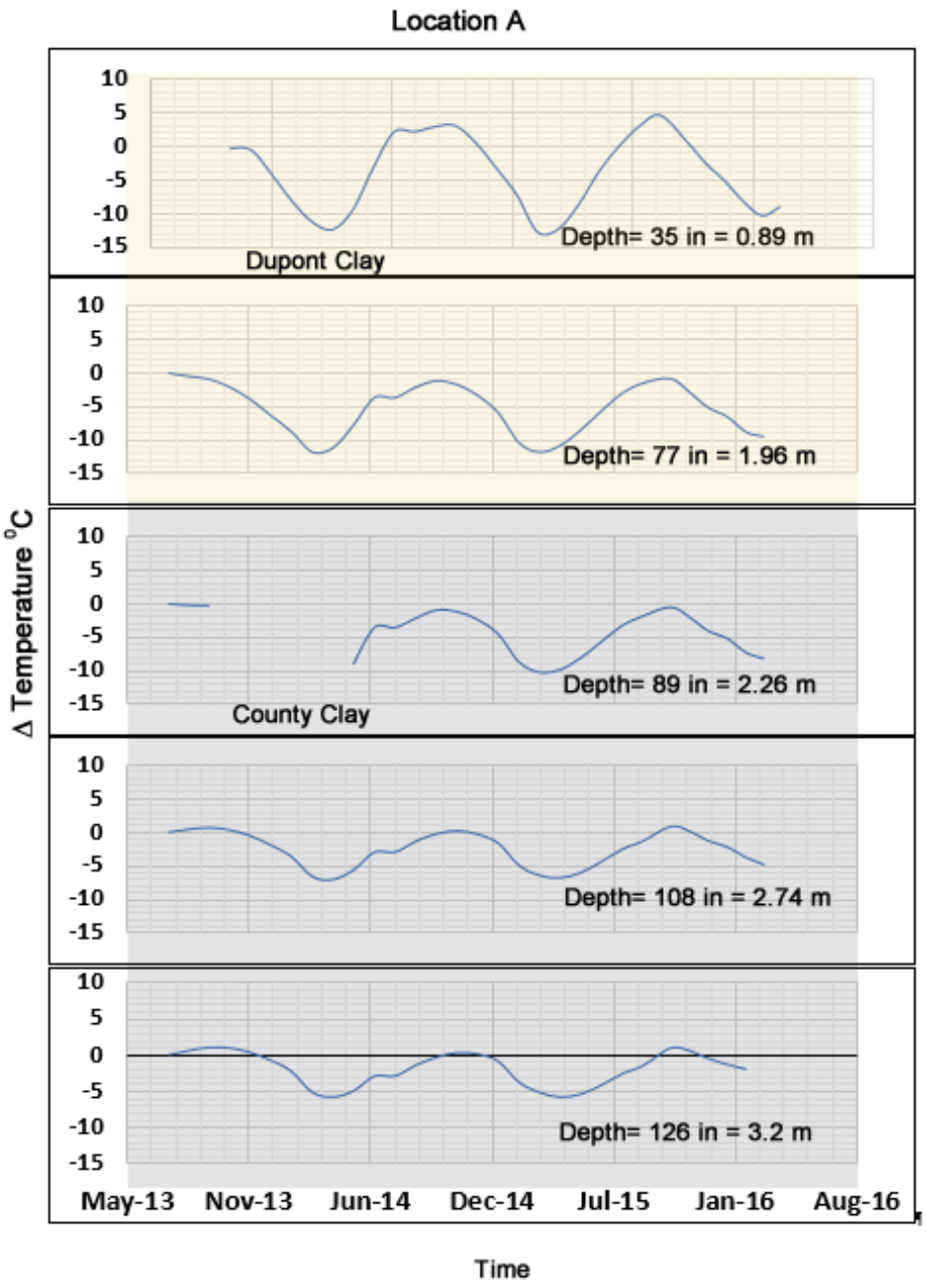

Figure 8.28. Change in Temperature from Initial Compacted State in Sensor Data in Location A

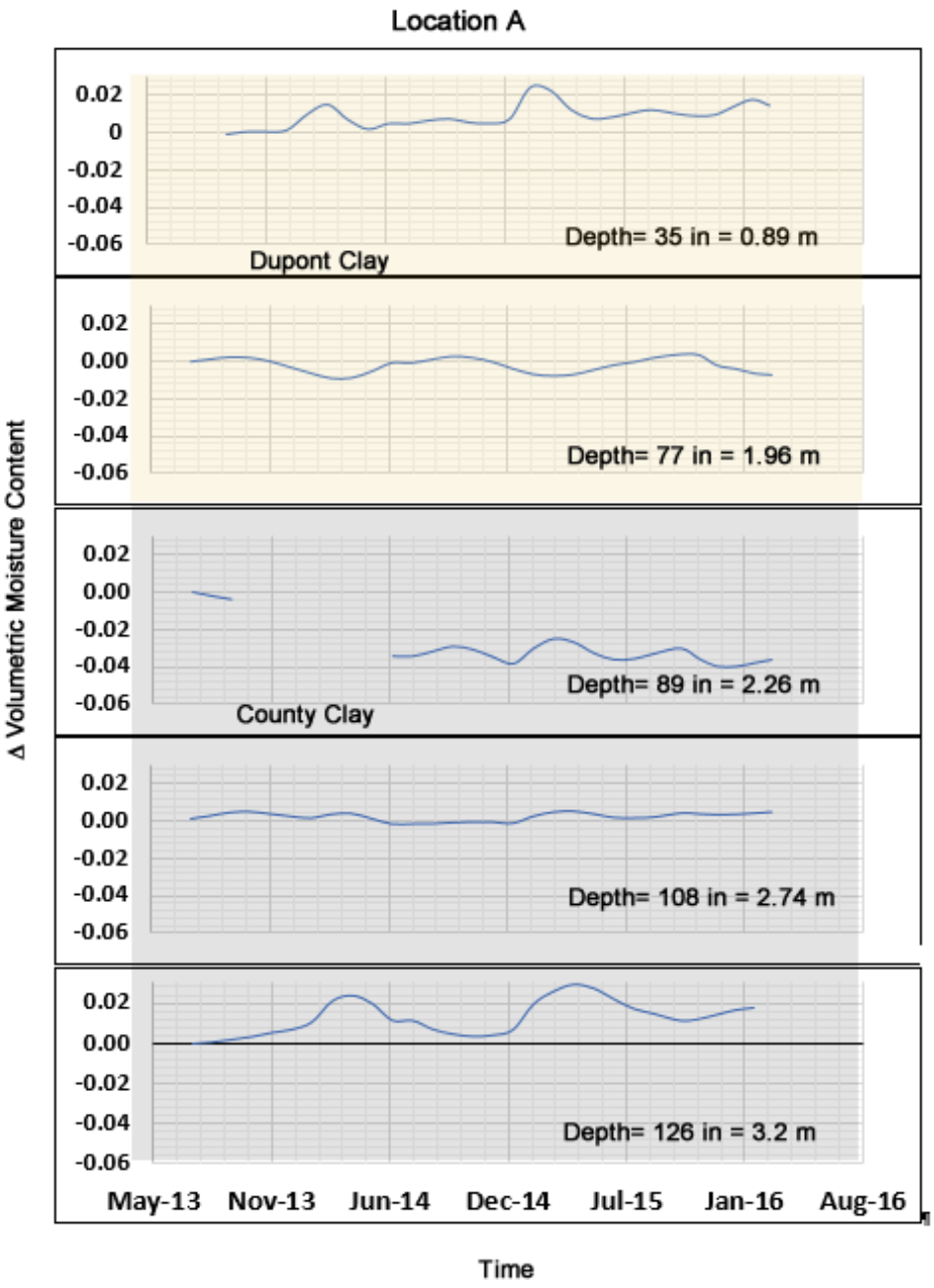

Figure 8.29. Change in VMC from Initial Compacted State in Sensor Data in Location A

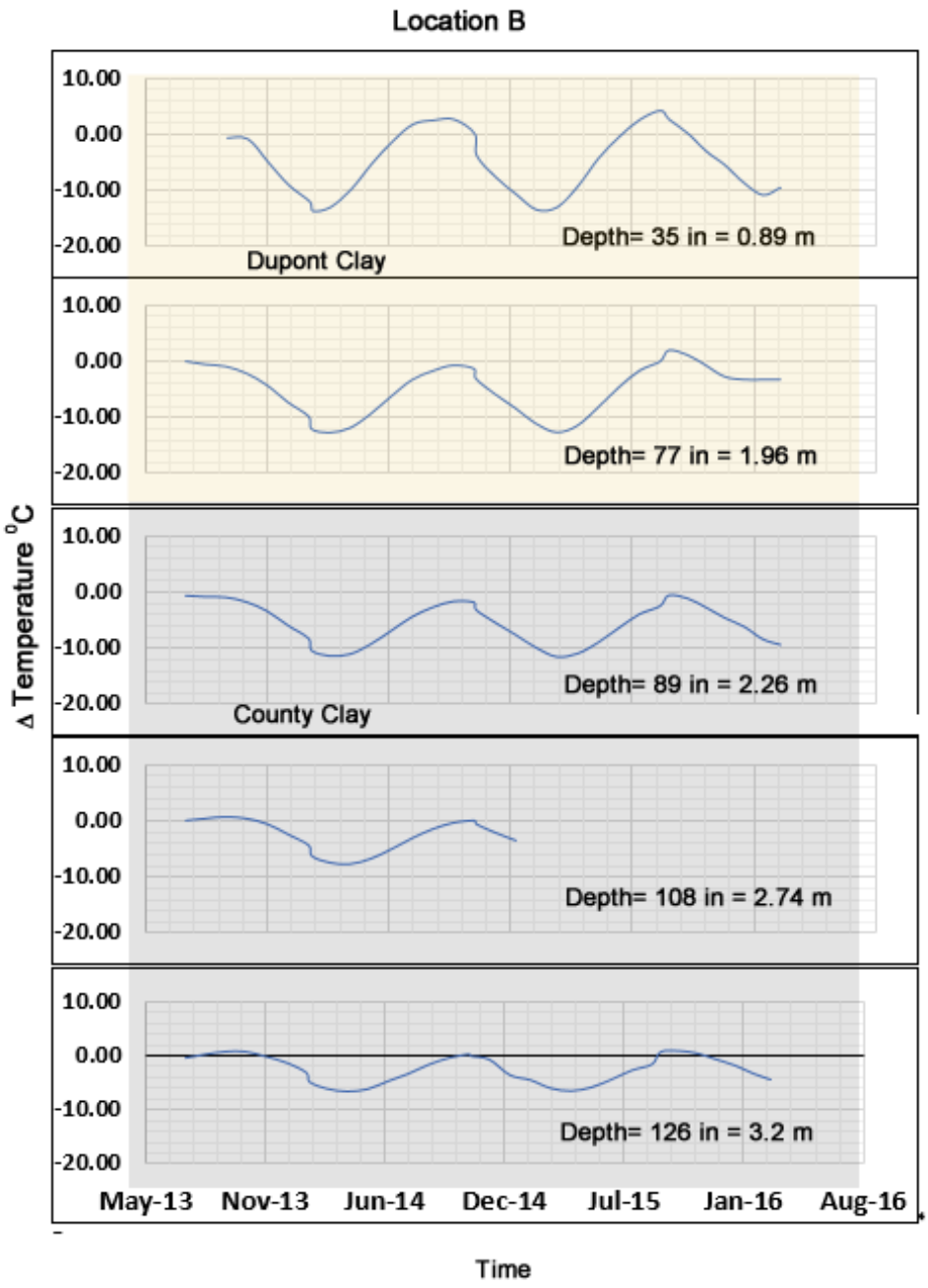

Figure 8.30. Change in Temperature from Initial Compacted State in Sensor Data in Location B

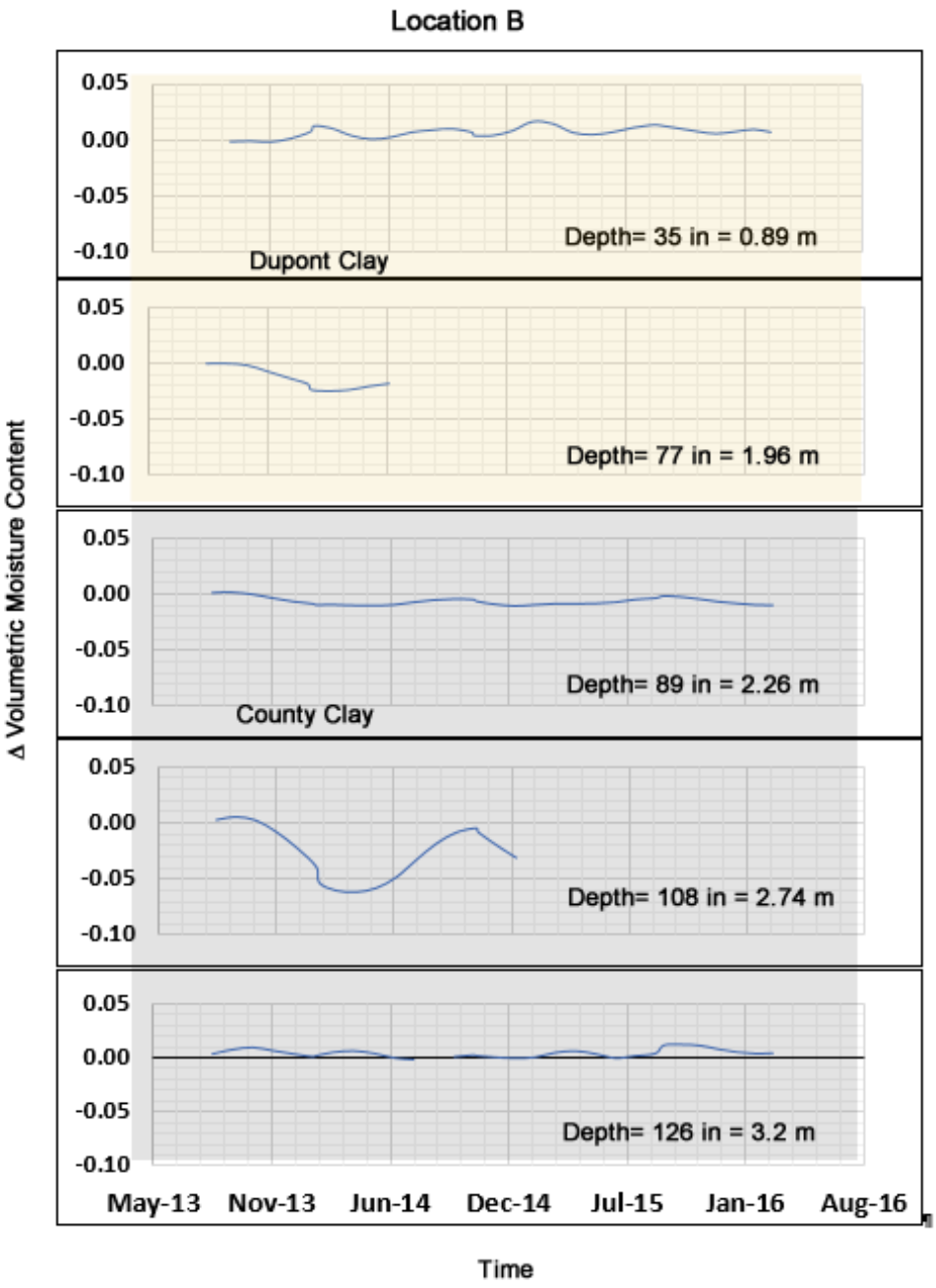

Figure 8.31. Change in VMC from Initial Compacted State in Sensor Data in Location B

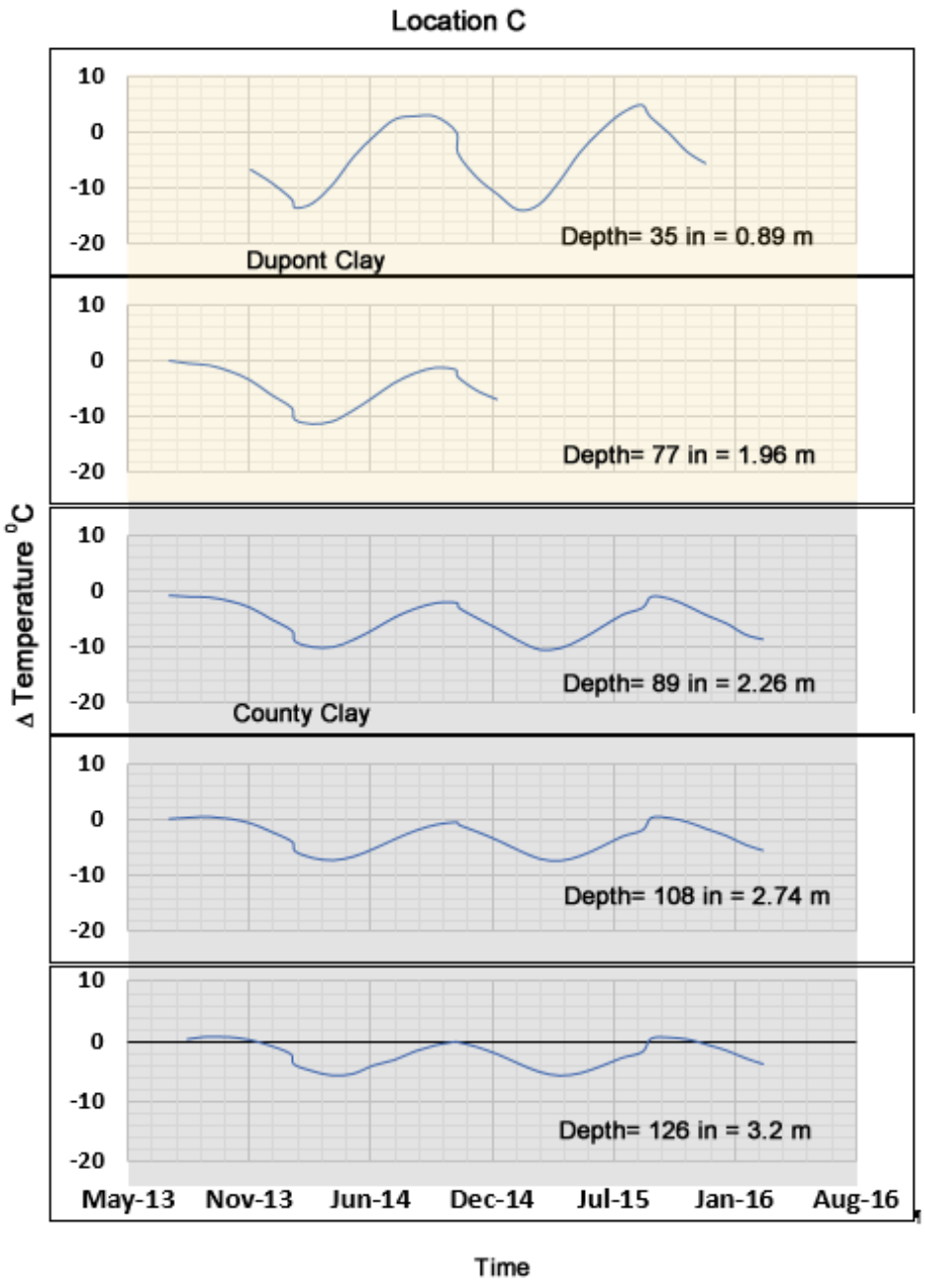

Figure 8.32. Change in Temperature from Initial Compacted State in Sensor Data in Location C

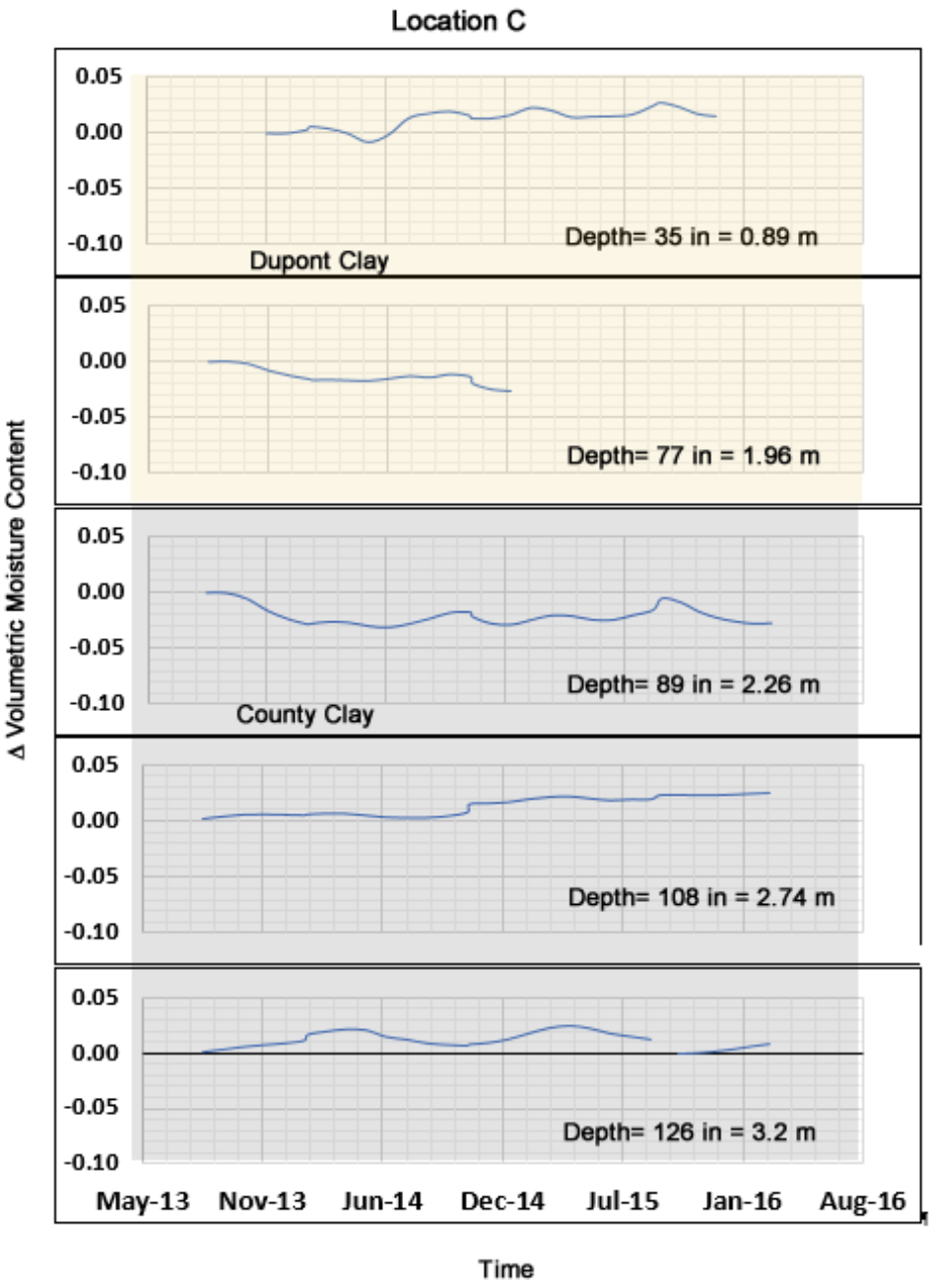

Figure 8.33. Change in VMC from Initial Compacted State in Sensor Data in Location C

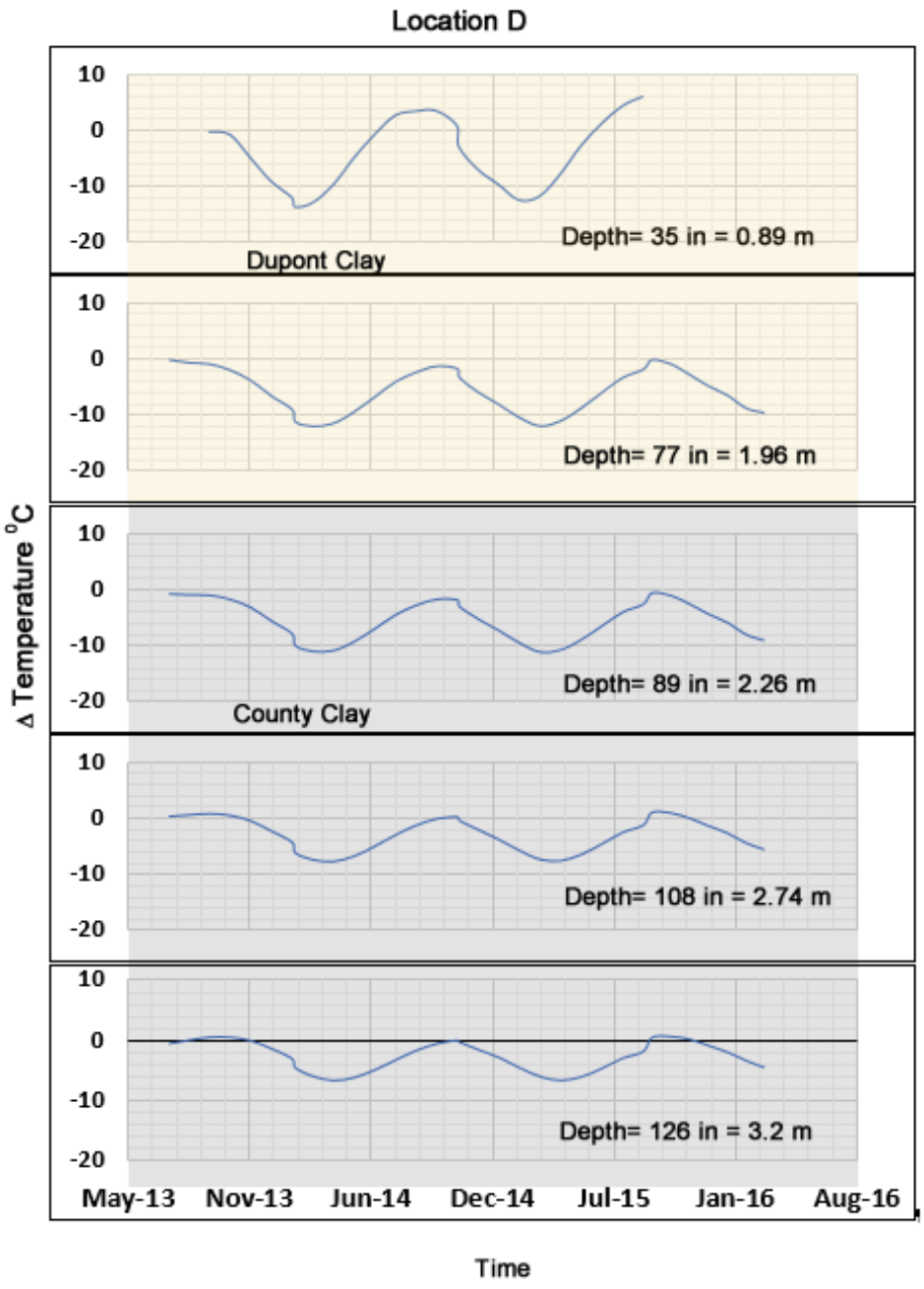

Figure 8.34. Change in Temperature from Initial Compacted State in Sensor Data in Location D

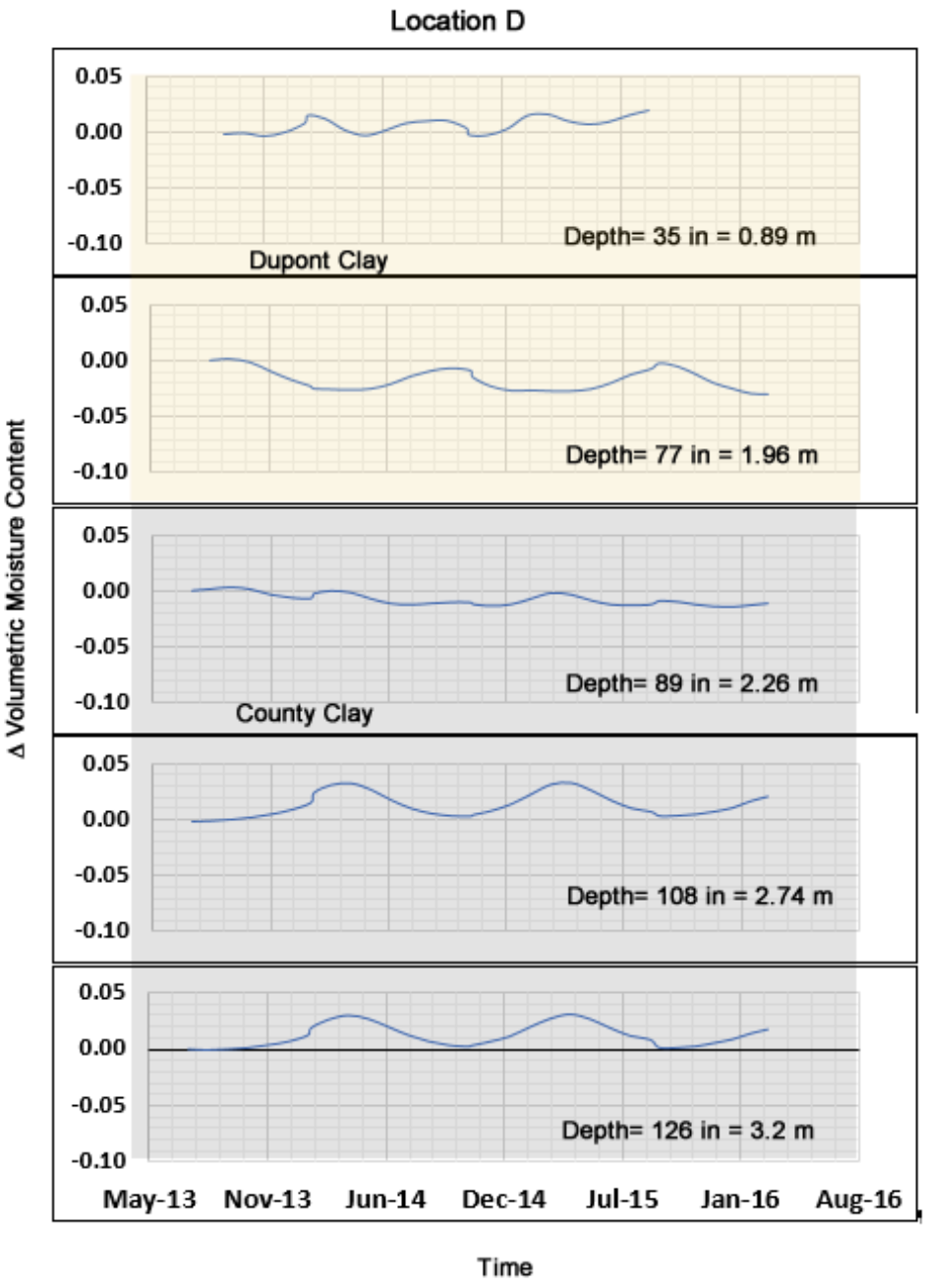

Figure 8.35. Change in VMC from Initial Compacted State in Sensor Data in Location D

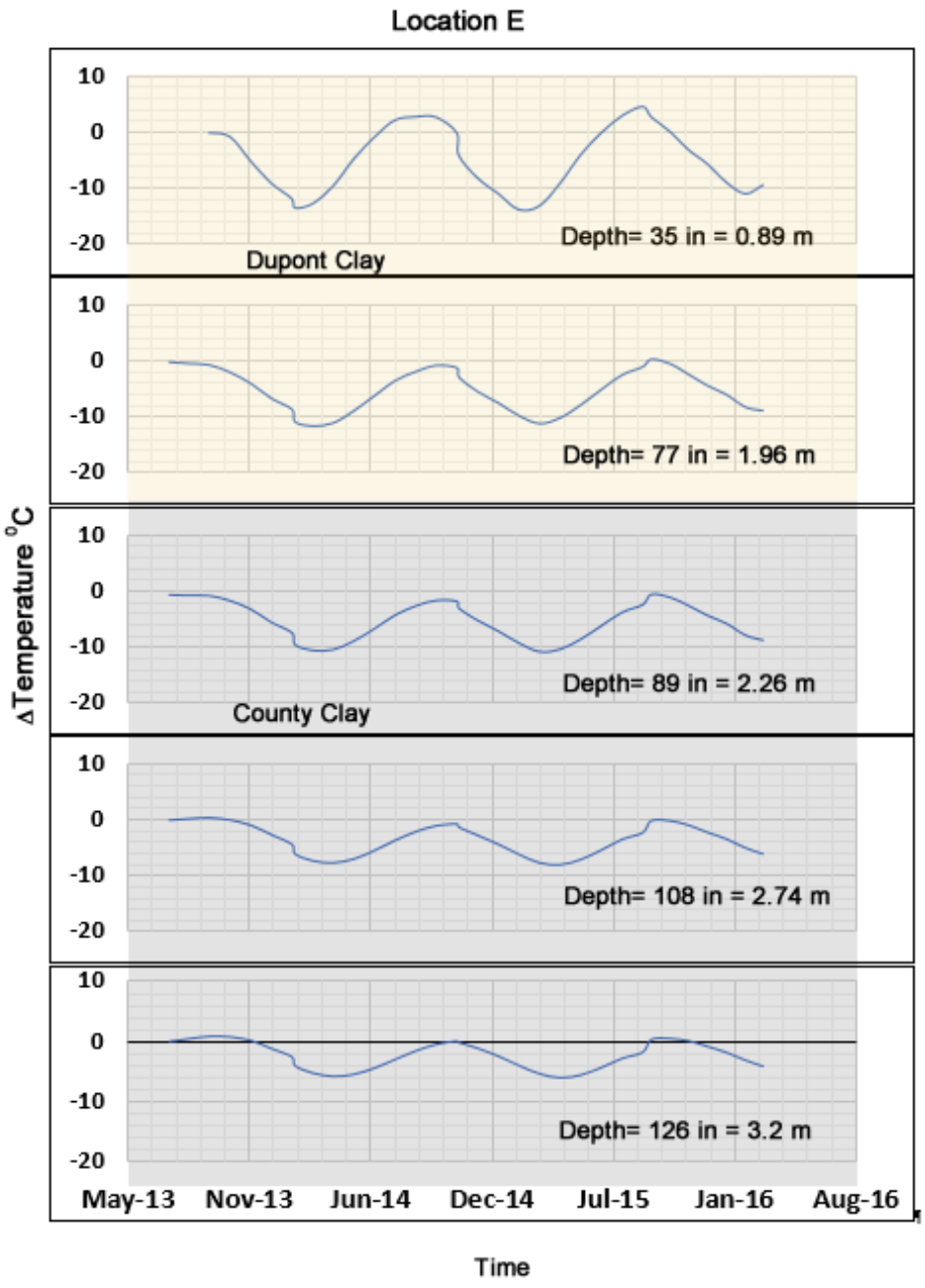

Figure 8.36. Change in Temperature from Initial Compacted State in Sensor Data in Location E

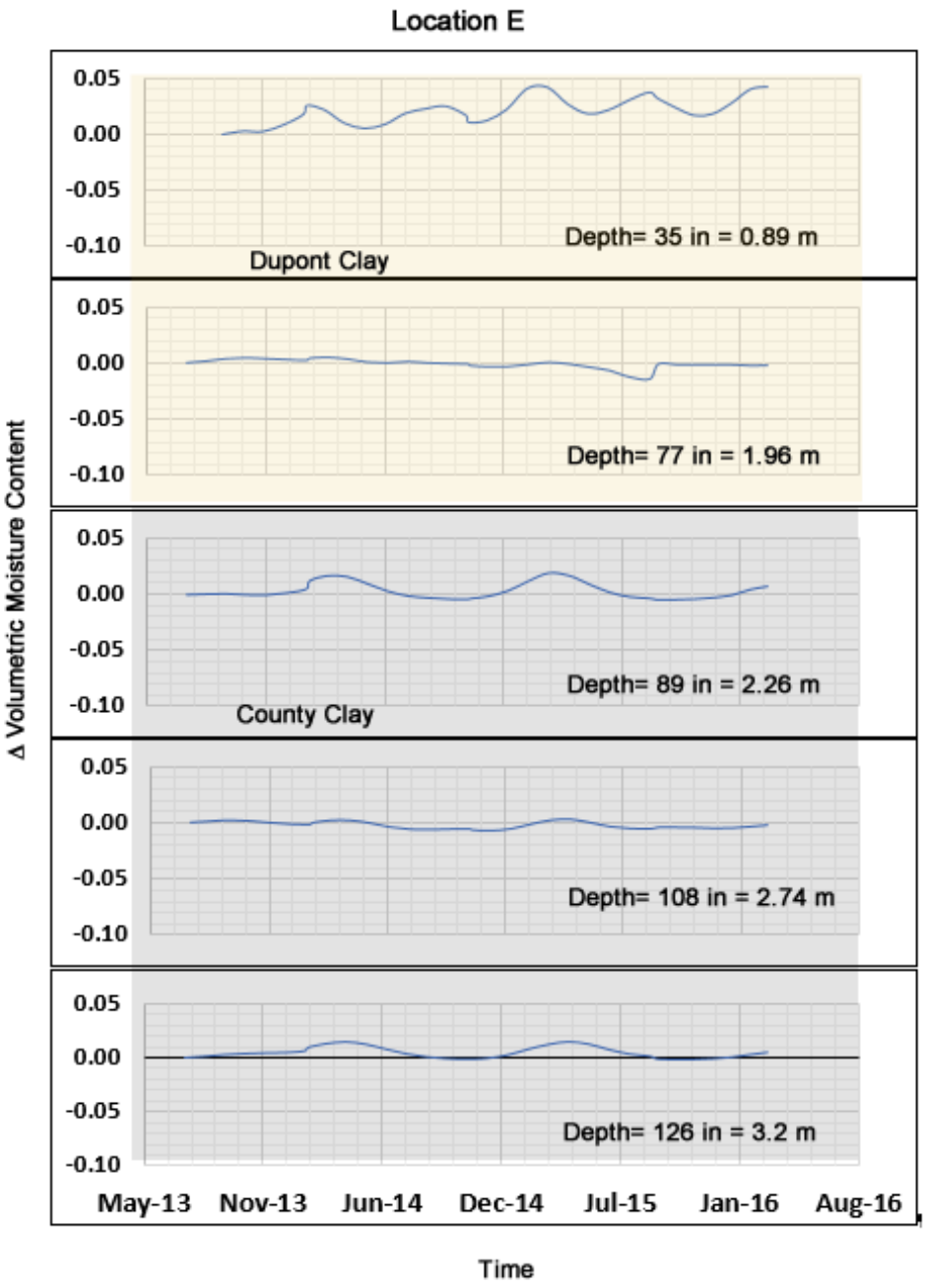

Figure 8.37. Change in VMC from Initial Compacted State in Sensor Data in Location E

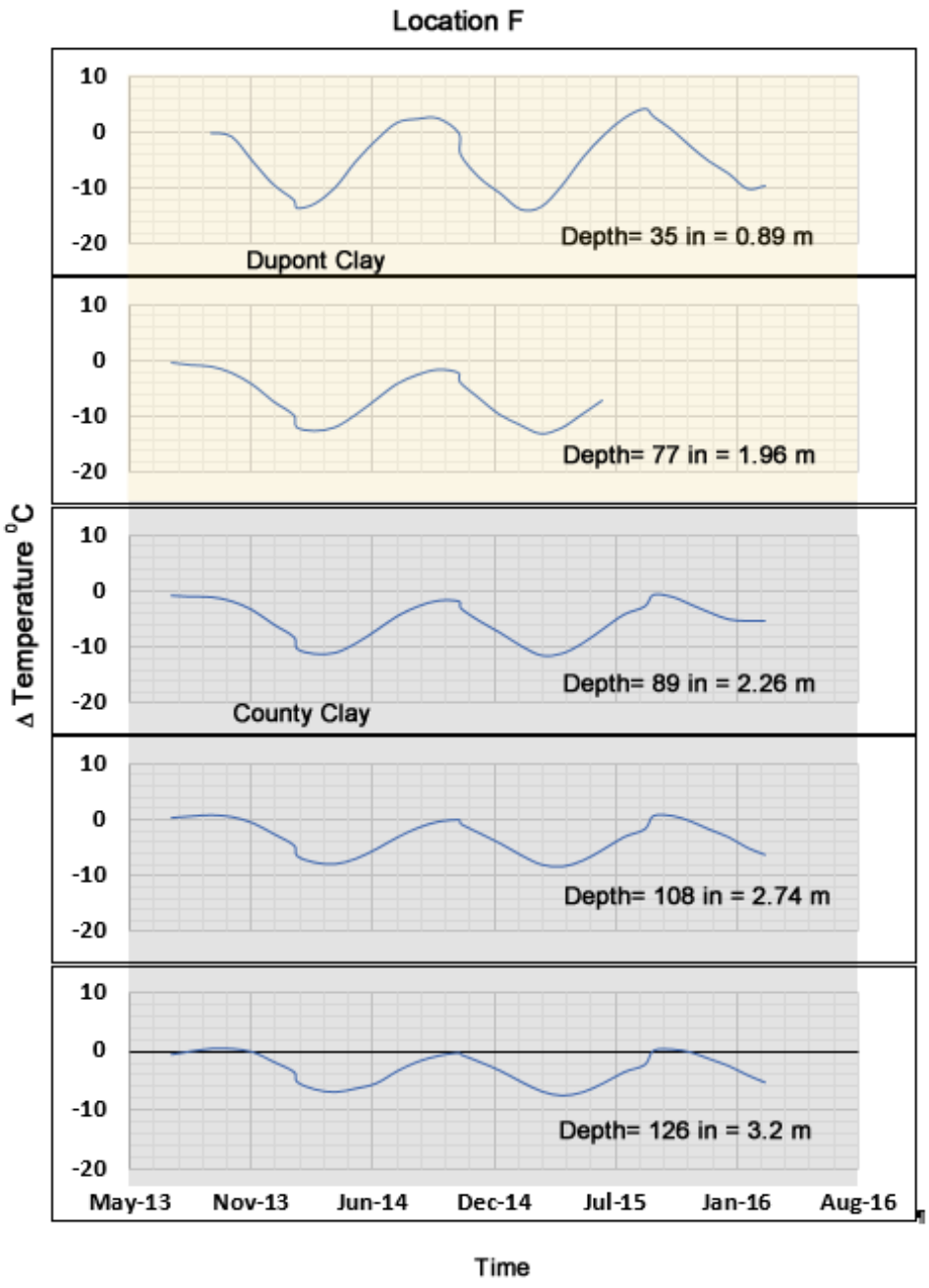

Figure 8.38. Change in Temperature from Initial Compacted State in Sensor Data in Location F

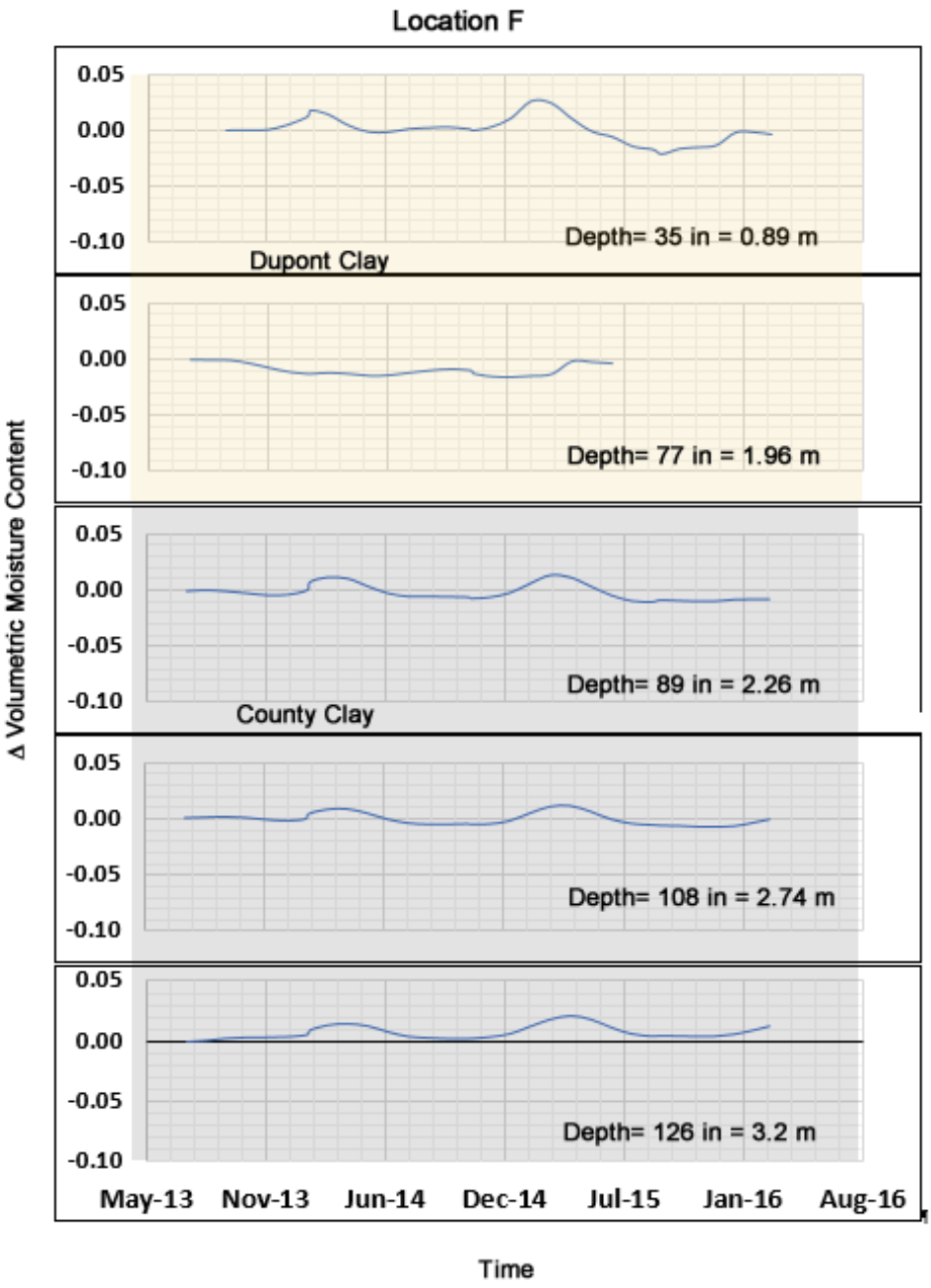

Figure 8.39. Change in VMC from Initial Compacted State in Sensor Data in Location F

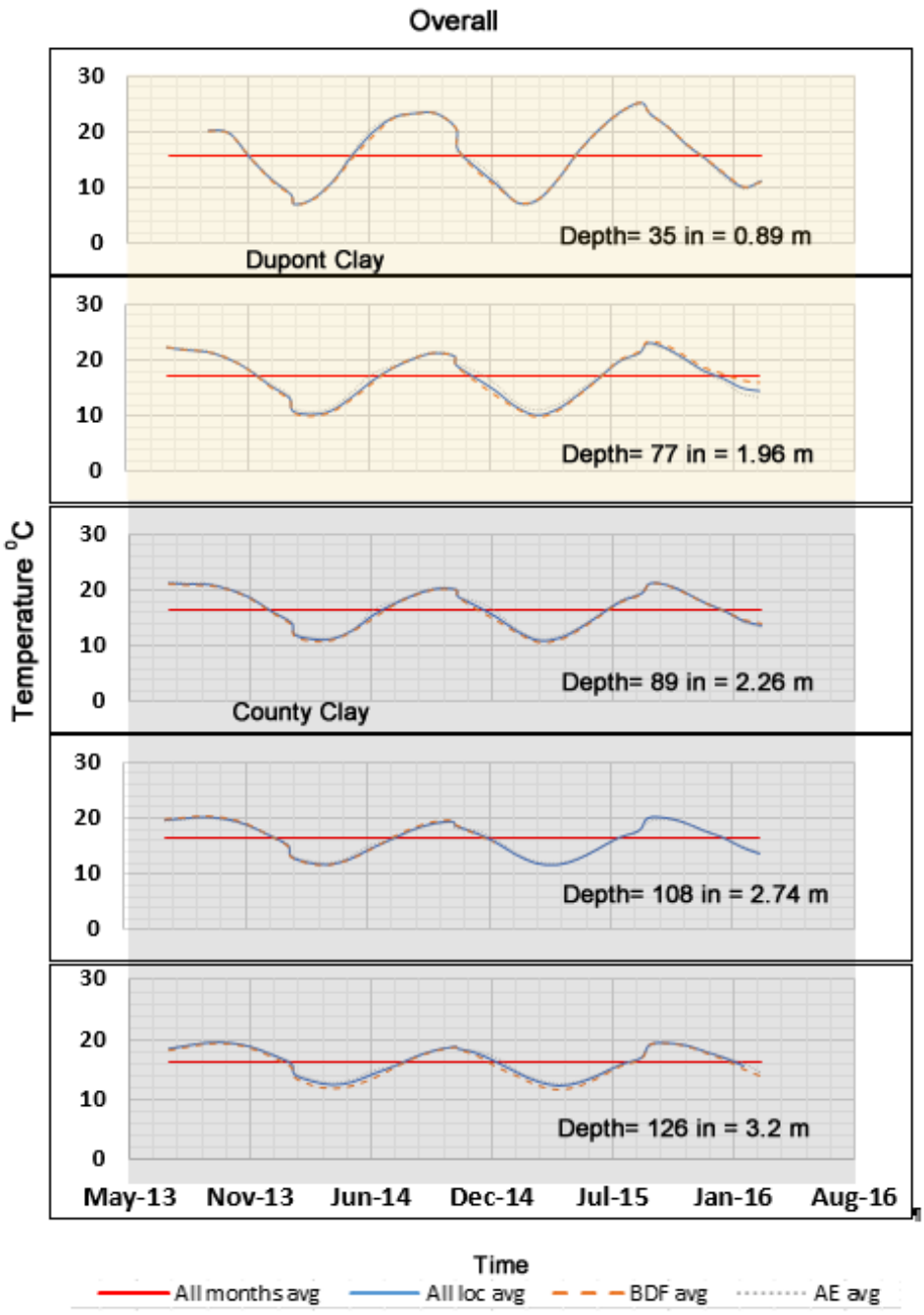

Figure 8.40. Temperature Variation Measured through Sensor with Average of all Locations

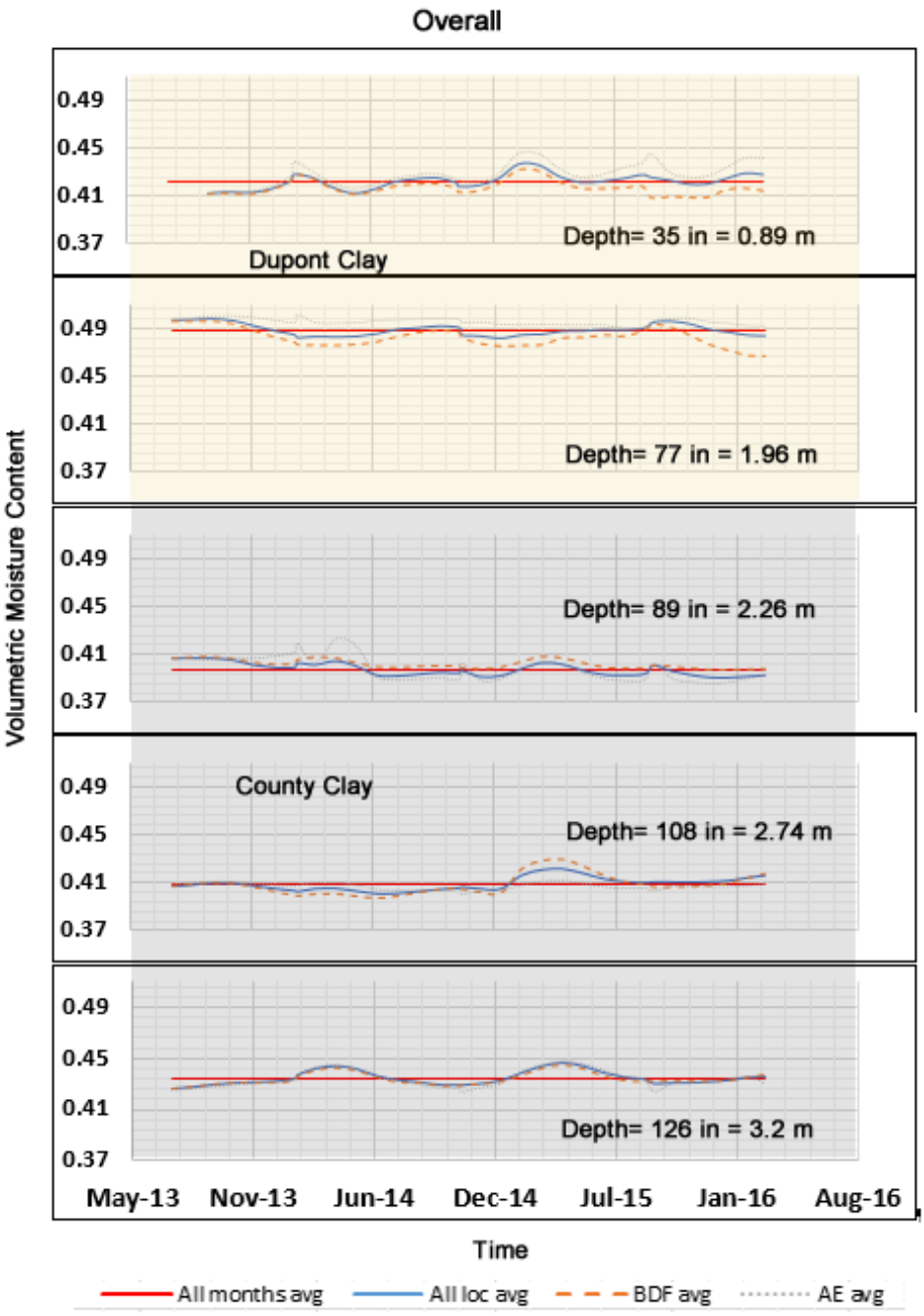

Figure 8.41. VMC Variation Measured through Sensor with Average of all Locations

Table 8.15. Summary of Temperature Data Obtained from Sensor in NAPTF

Depth	Sensor Title	Initial MC	Initial Dry density	Initial VMC	Individual Port Temperature (°C)			Same Offset Location Average (°C)			All Location Average (°C)		
in		%	pcf		Average	Std. Dev	Δ(Max-Min)	Average	Std. Dev	Δ(Max-Min)	Average	Std. Dev	Δ(Max-Min)
35	A1	27.0	95.5	0.413	16.50	5.37	17.30	15.96	5.59	18.10	15.86	5.65	18.30
	E1	27.0	95.5	0.413	15.52	5.72	18.40						
	C1	27.0	95.5	0.413	15.93	5.96	18.80	15.93	5.96	18.80			
	B1	27.0	95.5	0.413	15.57	5.61	17.90	15.83	5.66	18.40			
	D1	27.0	95.5	0.413	16.34	6.06	19.50						
	F1	27.0	95.5	0.413	15.70	5.64	18.00						
77	A2	37.2	83.4	0.498	17.10	3.67	11.60	17.11	3.78	12.00	17.02	3.91	12.80
	E2	37.2	83.4	0.498	17.05	3.81	12.00						
	C2	37.2	83.4	0.498	17.37	3.61	11.20	17.37	3.61	11.20			
	B2	37.2	83.4	0.498	17.47	4.39	14.60	16.99	4.08	13.40			
	D2	37.2	83.4	0.498	16.71	3.87	11.80						
	F2	37.2	83.4	0.498	15.73	4.16	12.50						
89	A3	25.7	99	0.407	17.35	3.40	10.20	16.95	3.37	10.20	16.63	3.40	10.30
	E3	25.7	99	0.407	16.68	3.37	10.20						
	C3	25.7	99	0.407	16.76	3.16	9.70	16.76	3.16	9.70			
	B3	25.7	99	0.407	16.24	3.62	11.00	16.38	3.51	10.80			
	D3	25.7	99	0.407	16.34	3.48	10.50						
	F3	25.7	99	0.407	16.56	3.49	10.80						
108	A4	25.7	99	0.407	16.82	2.52	7.90	16.39	2.59	7.90	16.33	2.77	8.30
	E4	25.7	99	0.407	15.95	2.70	8.40						
	C4	25.7	99	0.407	16.34	2.62	7.90	16.34	2.62	7.90			
	B4	25.7	99	0.407	16.80	2.87	8.60	16.72	2.89	8.70			
	D4	25.7	99	0.407	16.40	2.93	8.90						
	F4	25.7	99	0.407	16.11	3.03	9.20						
126	A5	27.5	96.8	0.427	16.91	2.22	6.70	16.65	2.20	6.80	16.32	2.33	7.10
	E5	27.5	96.8	0.427	16.43	2.21	6.90						
	C5	27.5	96.8	0.427	16.54	2.13	6.50	16.54	2.13	6.50			
	B5	27.5	96.8	0.427	16.26	2.48	7.50	16.03	2.48	7.50			
	D5	27.5	96.8	0.427	16.04	2.42	7.30						
	F5	27.5	96.8	0.427	15.79	2.56	7.90						

Table 8.16. Summary of VMC Data Obtained from Sensor in NAPTF

Depth	Sensor Title	Initial VMC	Individual Port			Same Offset Location Averaged			All Location Average		
in			Average	Std. Dev	Δ(Max-Min)	Average	Std. Dev	Δ(Max-Min)	Average	Std. Dev	Δ(Max-Min)
35	A1	0.413	0.422	0.0059	0.0245	0.429	0.0091	0.0328	0.423	0.0061	0.0247
	E1	0.413	0.434	0.0118	0.0426						
	C1	0.413	0.425	0.0090	0.0352	0.425	0.0090	0.0352			
	B1	0.413	0.419	0.0045	0.0179	0.418	0.0058	0.0228			
	D1	0.413	0.42	0.0067	0.0222						
	F1	0.413	0.414	0.0109	0.0459						
77	A2	0.498	0.495	0.0040	0.0131	0.496	0.0027	0.0103	0.489	0.0049	0.0165
	E2	0.498	0.496	0.0040	0.0187						
	C2	0.498	0.483	0.0073	0.0274	0.483	0.0073	0.0274			
	B2	0.498	0.484	0.0094	0.0247	0.483	0.0080	0.0302			
	D2	0.498	0.48	0.0097	0.031						
	F2	0.498	0.487	0.0052	0.0157						
89	A3	0.407	0.378	0.0112	0.0401	0.398	0.0102	0.037	0.398	0.0051	0.0162
	E3	0.407	0.41	0.0069	0.0236						
	C3	0.407	0.386	0.0085	0.0313	0.386	0.0085	0.0313			
	B3	0.407	0.401	0.0030	0.0107	0.402	0.0038	0.0113			
	D3	0.407	0.399	0.0050	0.0169						
	F3	0.407	0.405	0.0070	0.0243						
108	A4	0.407	0.409	0.0022	0.007	0.406	0.0028	0.0113	0.409	0.0053	0.0206
	E4	0.407	0.405	0.0034	0.0113						
	C4	0.407	0.42	0.0083	0.0232	0.42	0.0083	0.0232			
	B4	0.407	0.381	0.0227	0.0675	0.408	0.0083	0.0326			
	D4	0.407	0.42	0.0102	0.0338						
	F4	0.407	0.407	0.0053	0.0187						
126	A5	0.427	0.439	0.0082	0.029	0.434	0.0065	0.0236	0.434	0.0055	0.0212
	E5	0.427	0.43	0.0053	0.0169						
	C5	0.427	0.437	0.0067	0.0237	0.437	0.0067	0.0237			
	B5	0.427	0.43	0.0036	0.0138	0.434	0.0050	0.0196			
	D5	0.427	0.438	0.0097	0.0316						
	F5	0.427	0.433	0.0055	0.0216						

Table 8.17. Summary of Gravimetric Moisture Content Data Obtained from Sensor in NAPTF

Depth	Sensor Title	Initial GMC	Individual Port		Same Offset Location Averaged		All Location Average	
in		%	Average (w%)	Δ(Max-Min)	Average (w%)	Δ(Max-Min)	Average (w%)	Δ(Max-Min)
35	A1	27	27.6	1.6	28.0	2.1	27.6	1.6
	E1	27	28.4	2.8				
	C1	27	27.8	2.3	27.8	2.3		
	B1	27	27.4	1.2	0.6	1.5		
	D1	27	27.4	1.5				
	F1	27	27.1	3.0				
77	A2	37.2	37.0	1.0	37.1	0.8	36.6	1.2
	E2	37.2	37.1	1.4				
	C2	37.2	36.1	2.1	36.1	2.1		
	B2	37.2	36.2	1.8	36.1	2.3		
	D2	37.2	35.9	2.3				
	F2	37.2	36.4	1.2				
89	A3	25.7	23.8	2.5	25.1	2.3	25.1	1.0
	E3	25.7	25.8	1.5				
	C3	25.7	24.3	2.0	24.3	2.0		
	B3	25.7	25.3	0.7	25.3	0.7		
	D3	25.7	25.1	1.1				
	F3	25.7	25.5	1.5				
108	A4	25.7	25.8	0.4	25.6	0.7	25.8	1.3
	E4	25.7	25.5	0.7				
	C4	25.7	26.5	1.5	26.5	1.5		
	B4	25.7	24.0	4.3	25.7	2.1		
	D4	25.7	26.5	2.1				
	F4	25.7	25.7	1.2				
126	A5	27.5	28.3	1.9	28.0	1.5	28.0	1.4
	E5	27.5	27.7	1.1				
	C5	27.5	28.2	1.5	28.2	1.5		
	B5	27.5	27.7	0.9	28.0	1.3		
	D5	27.5	28.2	2.0				
	F5	27.5	27.9	1.4				

Discussion of Results Observed:

Temperature

Table 8.14 shows that while three is no significant difference in the average sensor (location) temperature, with depth; there was a noticeable trend in the variation of the temperature difference (between the maximum and minimum temperature) with depth. Also, as would be expected from this conclusion, there was also a significant trend with the standard deviation of the temperature data. For both of these parameters, it was observed that the variation (and standard deviation) of the temperature population decreased with increasing depth. In other words, the upper portion of the Dupont clay were subjected to a much greater degrees of temperature change than the lower level of the County clay. Figure 8.42 illustrates both these depths trend found for the temperature data.

Because of the lack of a statistically significant database, it is difficult to conclude any significant effect in the mean population temperature, aa a function of the radial offset. The average change in the average temperature with depth, was found to be only about 0.2^0C different. From the data summarized, it is concluded that if there are any radial offset effects in the sensor temperature; they are very insignificant.

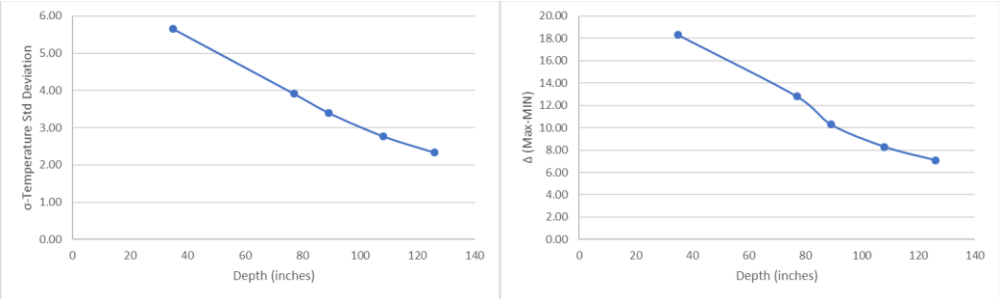

Figure 8.42. Influence of Subgrade Clay Layer Depth upon Range of Temperature Observed

Temperature where peak VMC occurs

Visual observation was made to assess the general temperature condition (minimum or maximum) at which the maximum (peak) VMC (w%) occurred. Figure 8.28 to 8.39 were examined to see if this condition of the maximum VMC was present during the minimum or maximum temperature condition.

While the majority of trends were obvious (easy to detect); they were found to be quite difficult to reach any final decision. Examples to illustrate where the maximum VMC (w%) occurred may be found in:

High Temperature Sensor A (z=77")

Low Temperature Sensor D (z=108")

Unable to distiguish Sensor B (z=126")

Table 8.17 is a summary distribution of the observed frequency categories found by the sensor location (A to F) while Table 8.18 is a summary distribution sorted by depth within the clay sublayers. It is observed that the majority of sensors (17 to 30) measured the peak on temperature near/at the lowest temperature occurring at the sensor locations.

Table 8.18.Summary of Temperature Occurrences where Maximum VMC Occurs (By Sensor Location)

Sensor Location	Low Temp	High Temp	Unable To Distinguish
A	3	2	0
B	1	3	1
C	1	2	2
D	4	1	0
E	4	0	1
F	4	0	1
Total	17	8	5

Table 8.19. Summary Of Temperature Occurrences Where Maximum VMC Occurs (By Sensor Depth)

Sensor Location	Low Temp	High Temp	Unable To Distinguish
35"	5	0	1
77"	0	4	2
89"	4	2	0
108"	3	2	1
126"	5	0	1
Total	17	8	5

In contrast, 8 of 30 sensors appeared to have a maximum moisture content at the warmest portion of the seasonal temperature distribution at any particular depth. While it was not possible to genralize any conceptual conclusions realtion to the influence of any sensor stationing; Table 8.18 does appear to suggest that the presence of maximum VMC with the lowest temperature were definitely found throughout all of the depths investigated (z=77" being the only exception).

Finally, while this section has addressed some genral observations visulayy associated with the hydraulic- thermal moisture movements; it must be strongly emphasized that the ability to accurately define and predict the moisture flow is a highly theoratical methodology and process, that can only be eventually modelled by 2, or even 3, dimensional finite element coupled hydraulic and thermal gradients.

Long term trends in VMC

A visual assessment of the plots shown in Figures 8.28 to 8.39 were also made to see what, if any , long term trends in the VMC (w%) could be made over the 2.5 year study interval.

Three categories were selected to note whether the VMC: a)increase b)decreased or c) no change. Example sensor location for each of these categories may be found in:

Increasing VMC Sensor A (z=35")

Decreasing VMC Sensor D (z=89")

No change VMC Sensor E (z=126")

Table 8.19 is a summary distribution of the observed frequency categories by sensor location; while Table 8.20 presents the frequency distribution of the categories by sensor depth. These tables indicate that it is quite difficult to truly observed consistent trends in moisture movement with time.

While the greatest majority of the trends appeared to indicate little to no change over the 2.5 year period; it is also interesting to note that the number of sensors showing an increasing trend (9) was nearly equivalent to the sensors that showed a decreasing trend (7) of the VMC with time.

Table 8.20. Summary of Sensors Showing Long Term Trends in VMC (By Sensor Location)

Sensor Location	Increased VMC	Decreased VMC	No change
A	2	1	2
B	1	0	4
C	4	1	0
D	1	2	2
E	1	1	3
F	0	2	3
Total	9	7	14

Table 8.21. Summary of Sensors Showing Long Term Trends in VMC (By Sensor Depth)

Sensor Location	Increased VMC	Decreased VMC	No change
35"	5	1	0
77"	0	3	3
89"	1	2	3
108"	1	0	5
126"	2	1	3
Total	9	7	14

Like the prior discussion, it is apparent that precise conclusions regrading long term changes in the moisture content (VMC and w%) will only be accomplished through an extensive modelling effort using a coupled hydraulic thermal methodology that can analyse a 2 (or preferably 3) dimensioned half space.

Nonetheless a significant conclusion (observation) is presented in the ensuing section of this chapter regarding a generalized estimate of the total net change of moisture predicted from an analysis of the entire sensor system in the NAPTF clay subgrade.

Presence of Moisture movement in the NAPTF subgrade

It has been previously noted that the principal goal of this study effort concurring the analysis of moisture- temperature sensor data obtained at 30 locations within the NAPTF subgrade has been to determine, if moisture movements have been occurring throughout these clay layers throughout the last 2 to 2.5 years during the pavement performance testing.

In order to accomplish this effect, a series of tabular summaries have been developed from the comprehensive database that has been collected, analyzed and plotted in the previous

sequence of figures presented. These tables have been presented in Table 8.14, 8.15 and 8.16.

All of this salient information shown in the previous figures and tables has been summarized into one final comprehensive table to present the critical findings of this important aspect of the overall research project. These summary findings are presented in Table 8.21.

In this table, the summary is organized by the specific depth (z) of the family of sensor locations A through F. Thus the properties shown under a given depth are the average (typical) values of all0 sensors within the clay sublayer populations previously determined. In fact, the γ_d and VMC initial are the specified values of the in-situ compaction properties from the statistical hypothesis analysis previously presented in this chapter. The next tabular row entry: VMC (avg 2.5year) represents the calibrated- corrected VMC found from the sensor readings shown in Figures 8.10 to 8.15. the difference between this row entry and the previous entry yields the estimate of the ΔVMC (long term) change. The next row entry is the ΔVMC (max-min) and corresponds to the last column entry in Table 8.16. This value defines the average seasonal change in the VMC that is a result of the hydraulic-thermal moisture movements occurring (on the average) at a given (typical) sensor depth.

Knowledge of the annual range (or change) in the VMC value at a given sensor depth, allows one to estimate the typical maximum and minimum VMC values occurring at a given depth. These parameters: VMC (max) and VMC (min) are shown in the next two row entries. Finally, these volumetric moisture content maximum and minimum values are translated into the gravimateric moisture content (w%). The last three row entries show the

maximum w%, minimum w% and the typical average annual change in w% (Δw%) expected at each sensor depth.

Table 8.22. Summary of Final Hydraulic-Thermal Moisture Change at NAPTF Clay Subgrade

	z=35"	**z=77"**	**z=89"**	**z=108"**	**z=126"**
Clay type	Dupont	Dupont	County	County	County
ɣd (pcf)	95.5	83.4	99.0	99.0	96.8
VMC_0 (initial)	0.413	0.498	0.407	0.407	0.427
VMC (Avg 2.5 yr)	0.423	0.489	0.398	0.409	0.434
ΔVMC (long term)	+0.010	-0.009	-0.009	+0.002	+0.007
ΔVMC (max-min)	0.025	0.017	0.016	0.021	0.021
VMC (max)	0.436	0.498	0.406	0.420	0.445
VMC (min)	0.411	0.481	0.390	0.399	0.424
w% (max)	28.5	37.3	25.6	26.5	28.7
w% (min)	26.9	36.0	24.6	25.1	27.3
Δw% (max-min)	1.6	1.3	1.0	1.4	1.4

Avg Δw% (all depths) = 1.34%

Based upon the key information contained in Table 4.35; the following conclusions can be summarized.

1. The analysis of the moisture sensor data, obtained over a 2.5 year period clearly indicate that moisture flow is occurring throughout both subgrade layer.
2. These moisture movements must be a direct result of internal hydraulic and thermal gradients that occur due to variations in intial volumetric moisture caused by the normal construction/ compaction process and y seasonal thermal changes that occur with depth within an annual temperature cycle within the hangar facility at NAPTF.
3. It is noteworthy to point out that the overall net balance of the moisture changes, for all sensor depths, (ΣΔVMC) is approximately 0.0 (actually +0.001 or 0.1% change in the average VMC at the facility. This average VMC at the facility. This

finding lends credulence to the hypothesis that any changes in the moisture regime of the clay subgrade is not caused by any new additional moisture within the subgrade zone. This supports the theory that both moisture grains and/or moisture losses may occur due to moisture migration in the subgrade.

4. On a more positive condition, it is concluded that the average ΔVMC (max-min), at a given depth, that was found to occur at the test facility over a 2.5 year period was only 0.020 (2.0% change in VMC). This moisture change is equivalent to a gravimetric moisture content (w%) change of only 1.3% during an annual cycle.
5. In summary, while moisture moment has been conclusively shown to exist within the Dupont and County clay subgrade layers; the estimated change in the quantity of moisture movement is considered to be quite small. (ΔVMC=2.0% or Δw%= 1.3%)
6. As will be demonstrated in later chapter of this report; the impact of this seasonal moisture change is not expected to lead to significant changes in the in-situ CBR (strength) or M_r (resilient modulus) of the subgrade.

Temperature data in the NAPTF

Goal

The basic purpose of this work phase was to collect, synthesize and analyze the distribution of temperature, primarily within the test section 3.0-inch asphalt layer, used in the various test sections. While temperatures, at several depths in the unbound base and subbase, were also collected from sensors; the most salient temperatures investigated were that of the AC

layer throughout the cycles of performance testing for use in defining the E* of the asphalt layers in the MLET (Multilayer Elastic Theory) analysis shown in Chapter 10.

The AC temperature range in the pavement is critical to determining the AC layer dynamic modulus (E*) during the test process. The impact of this parameter is clearly explained, in more specific detail, in Chapter 10 of this report. In general, the range of AC temperatures at the facility will result in large changes of the AC E* value. This, in turn, will result in changes in stress state throughout the base, subbase and subgrade layers. These changes in stress state will also result in differing dynamic moduli of the underlying nonlinear base, subbase and subgrade layers.

Because of this, this work phase focused upon the development of statistical relationships between the air temperature (T_a) inside the NAPTF hangar facility and AC pavement temperature (T_p) of the AC surface layer of the pavement test sections. Emphasis was also placed on developing a model to predict the dispersion (standard deviation) of these temperature so that a simplified statistical procedure could be developed to estimate the frequency of occurrence within a given period of time, that would be predicted for any specified temperature interval.

Data files used

Temperature information was obtained from temperature sensors installed at the NAPTF facility. Because of the relatively "thin" AC layer used (3.0 inches); sensor temperatures of the AC layer were only analyzed for the z=2.5" depth sensor. The temperature sensor data was supplied by the FAA personnel to the project term in three separate files.

Each file typically contained 24 hourly temperature readings per day. However, in the subsequent analysis, the statistical analysis was always conducted only with hourly temperature results between 8:00 a.m. and 5:00 p.m. for a period of 10 hourly results/day.

The details of each of the 3 separate files analyzed are as follows:

File No 1

T5b Data

June, July, August 2014

Days of Temperature Readings:83

No. of Temperature Readings: 830.

File No. 2

T5b Data

Sept, Oct, December 2014; January, February, December 2015; January, February, March, April, May 2106

Days of Temperature Readings: 247

No. Temperature Readings: 2470

File No. 3

T2b; T3b; T4b; T5b; T6b; T7b

2 Air Temperature (Hourly) At Each T_p

March April, May June, July, August, September, October, November 2015; June, July, August 2016

Day of Temperature Readings: 367

No. of Temperature Readings: 3670

For File No 3, it can be observed that temperature reading were recorded at 6 separate sensors at a depth z= 2.5". For simplicity, the average hourly temperature was used, as there was very little, if any, difference in the T_p recorded value between all 6 site locations at a given moment in time.

In summary, it can be observed that nearly 700 days, each with 10 hourly readings between 8:00 am- 5:00 pm, were used in the subsequent analysis.

Analysis of results

A typical portion of the spreadsheet temperature file, developed for the analysis is shown in Table 8.22. This table represents the T2B through T7B pavement temperature results for 2 days of measurements (3/1/2015 and 3/2/2015). It can be observed that 10 separate hourly readings are shown in Table 8.22 for each day. The right hand portion of the table presents the summary of the daily statistics of the z=2.5" AC pavement temperature, for each day.

The results shown in Table 8.22 were then completed for the nearly 700 days of temperature readings. This information was then summarized into a temperature format shown in Table 8.23. The table represents the summary of each day within a typical month (March 2015). The right hand portion of this table represents the monthly statistical information for the March 2015 period (average, standard deviation, variance and count).

Similar tables were developed for each of the 26 separate months (June 2014 to August 2016) that were evaluated in this study.

Table 8.24 is the final statistical distribution summary compilation of the AC temperature study for the time period investigated. This table shows the monthly statistical distribution parameter for the AC pavement temperature at a depth of z=2.5" in the asphalt layer.

Table 8.23. Temperature of Air and Pavement Recorded in 2 Days

TOA5											
TIMESTAMP	T2B	T3B	T4B	T5B	T6B	T7B	Avg Pvt		8 am to 5 pm		
TS	Deg F	Deg F	Deg F	Deg F	Deg F	Deg F	Temp (2.5")		Avg Daily Temp	Std Dev	Variance
	Smp	Smp	Smp	Smp	Smp	Smp	(deg F)	Date			
3/1/2015 8:00	35.21	34.4	35.05	34.99	33.63	34.34	34.60				
3/1/2015 9:00	35.04	34.38	35.08	35.08	33.78	34.55	34.65				
3/1/2015 10:00	35.29	34.73	35.37	35.38	34.21	34.89	34.98				
3/1/2015 11:00	35.65	35.16	35.68	35.68	34.63	35.22	35.34				
3/1/2015 12:00	36.01	35.58	35.98	35.98	35.1	35.54	35.70				
3/1/2015 13:00	36.33	35.93	36.21	36.21	35.51	35.82	36.00				
3/1/2015 14:00	36.59	36.24	36.56	36.54	35.82	36.16	36.32				
3/1/2015 15:00	36.82	36.46	36.85	36.8	36.06	36.45	36.57				
3/1/2015 16:00	37.07	36.74	37.17	37.11	36.31	36.76	36.86				
3/1/2015 17:00	37.17	36.82	37.37	37.3	36.37	36.91	36.99	3/1/15	35.80	0.84	0.710
3/2/2015 8:00	37.42	37.12	37.88	37.76	36.75	37.49	37.40				
3/2/2015 9:00	37.44	37.19	37.82	37.73	36.85	37.56	37.43				
3/2/2015 10:00	37.11	36.97	37.36	37.4	36.94	37.5	37.21				
3/2/2015 11:00	36.29	36.44	36.54	36.89	37.24	37.71	36.85				
3/2/2015 12:00	37.96	38.28	39.25	39.41	39.51	40.51	39.15				
3/2/2015 13:00	38.61	39.11	38.84	39.13	40.76	40.7	39.53				
3/2/2015 14:00	39.43	40.03	39.62	39.8	41.91	41.55	40.39				
3/2/2015 15:00	40.59	41.23	40.94	41.02	43.27	42.92	41.66				
3/2/2015 16:00	41.59	42.1	42.04	41.94	43.81	43.51	42.50				
3/2/2015 17:00	42.16	42.47	42.8	42.59	43.6	43.66	42.88	3/2/15	39.50	2.17	4.692

Table 8.24. Mean Daily Temperature Calculated

	8 am to 5 pm Data Only			8 am to 5 pm Data Only			
Date of	Avg Daily			Avg Monthly			
Temperature	Temp	Std Dev	Variance	Temp	Std Dev	Variance	No of Days
3/1/15	35.80	0.84	0.71				
3/2/15	39.50	2.17	4.69				
3/3/15	39.25	1.93	3.74				
3/4/15	41.36	1.02	1.05				
3/6/15	38.13	2.20	4.83				
3/7/15	37.30	2.78	7.71				
3/8/15	41.46	2.41	5.79				
3/9/15	43.81	3.16	9.96				
3/10/15	44.84	2.29	5.25				
3/11/15	48.12	2.10	4.42				
3/12/15	49.02	2.64	6.98				
3/13/15	46.67	2.11	4.45				
3/14/15	46.92	0.43	0.19				
3/15/15	47.27	0.36	0.13				
3/16/15	47.87	3.01	9.03				
3/17/15	51.17	2.86	8.18				
3/18/15	49.09	2.48	6.18				
3/19/15	47.27	2.44	5.96				
3/20/15	45.15	0.12	0.01				
3/21/15	45.94	2.10	4.42				
3/22/15	48.68	2.27	5.14				
3/23/15	47.61	2.77	7.65				
3/24/15	46.19	0.97	0.94				
3/25/15	45.41	2.26	5.10				
3/26/15	48.86	1.05	1.11				
3/27/15	48.38	0.19	0.04				
3/28/15	48.83	1.51	2.27				
3/29/15	47.63	2.56	6.55				
3/30/15	47.03	1.73	2.99				
3/31/15	49.30	1.87	3.50	45.46	3.98	15.809	31

Table 8.25. Historic NAPTF Statistical Distribution Paramters for Monthly Pavement Temperature (z=2.5")

	2014			2015			2016		
Month	Avg	Std Dev	No of Days	Avg	Std Dev	No of Days	Avg	Std Dev	No of Days
January				43	2.57	30	46.26	3.593	31
February				45.3	3.898	28	46.18	3.688	29
March				45.46	3.98	31	53.31	3.686	30
April				55.76	3.21	30	57.33	3.297	30
May				67.69	3.64	31	59.49	2.451	15
June	74.89	2.084	21	73.95	4.23	30	74.44	1.83	30
July	77.74	1.234	31	79.38	1.94	31	81.19	2.66	31
August	77.36	1.163	31	80.53	1.52	31	83.26	2.04	31
September	73.17	1.762	9	77.44	2.92	30			
October	71.88	0.476	2	65.44	3.22	31			
November				59.5	3.3	30			
December	49.69	1.7	12	56.59	2.558	31			

Prediction models

From a pure thermodynamics viewpoint, the transfer of temperature from one body (i.e., external air boundary) to a layered pavement surface is typically a function of the thermal conductivity values of the materials; latent heat (moisture); solar radiation (cloud cover) and wind velocity. There exists, in the literature, several very precise thermal models to predict layered system (materials) temperature, given an external air temperature environment (regime).

However, inside the NAPTF hangar facility; these models are of little value for predicting pavement temperatures as the "internal" hanger environment is significantly different from an external climatic regime due to vast difference in the enclosed air (conduction

temperature boundary) and the lack of any direct solar radiation or wind speed influence upon the transfer of thermal energy.

Figure 8.43 is a statistically developed model of the daily T_p (pavement temperature) readings versus the daily T_a (air temperature). It can be observed that, for all practical purpose, there is a nearly one to one relationship between the two temperatures. Upon reflection, this relationship is quite rational and logical; as one would (should) expect that the daily pavement temperatures (at a near surface depth of z=2.5") should approximate the ambient air temperature within the NAPTF facility.

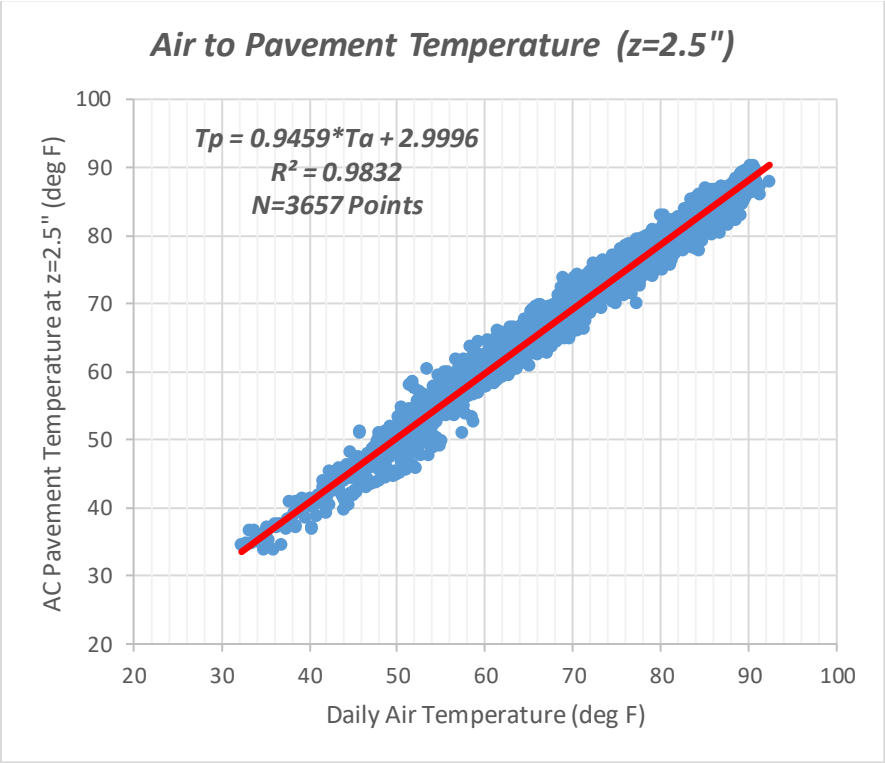

Figure 8.43. Correlation of Air And Pavement Temperature

Table 8.25 is a statistical summary of both the monthly air and monthly pavement temperatures for 9 months were such data was available from the FAA records. In some cases, a particular month may have had multiple year (2 or 3) readings. When this occurred,

"pooled" variances were computed and the square root of the pooled variance is used as the standard deviation value is shown in the table.

Table 8.26. Statistical Summary of Monthly Air and Pavement Temperature

	Air Temp (^{0}F)		Pvt Temp (z=2.5") (^{0}F)	
Month	Avg	Std Dev	Avg	Std Dev
3/15	46.04	5.13	45.46	4.48
4/15	56.28	4.30	55.77	3.76
5/15	68.91	4.66	67.69	4.26
6/15	75.08	5.50	73.95	4.35
7/15	80.76	3.30	79.38	2.76
8/15	81.39	3.21	80.53	2.64
9/15	78.32	4.31	77.44	3.61
10/15	65.17	4.22	65.44	3.65
11/15	58.88	4.11	59.50	3.60
6/16	76.09	3.23	74.44	2.77
7/16	82.85	3.62	81.17	3.34
8/16	84.49	3.15	83.26	2.90

The left hand side portion of Figure 8.44 shows the almost perfect correlation of the mean monthly pavement and air temperature (T_p vs T_a). As noted previously, for the daily temperatures, the mean monthly pavement temperature (MMPT) is 98.7 % of the mean monthly air temperature (MMAT). It is very important to note that the MMAT represents

the distribution statistics for ambient temperature readings within the NAPTF facility and not outside the building. The right hand side portion of Figure 8.44 shows that there is also a very excellent correlation between the standard deviation of the monthly pavement temperature (at z= 2.5") and the standard deviation of the air temperature within the hangar facility. As noted, the standard deviation of the pavement temperature is 86.2% of the ambient hangar air temperature monthly standard deviation.

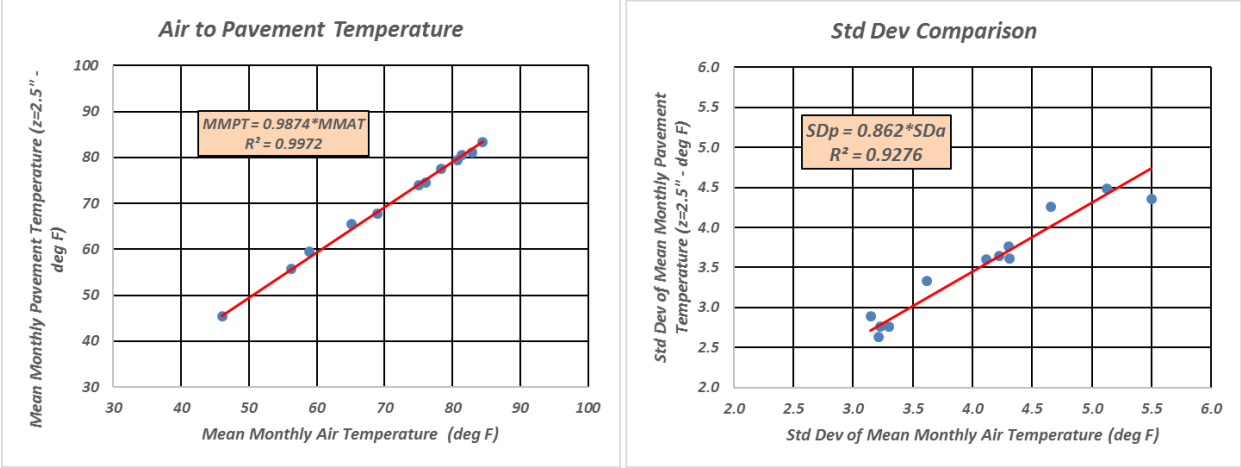

Figure 8.44. Correlation and Statistical Analysis of Mean Monthly Air Temperature

Finally Figure 8.45 illustrates a fair to good statistical model that can be used to estimate the approximate standard deviation of the mean monthly pavement temperature (SD_P) from the mean monthly pavement temperature (MMPT). It can be observed that the SD_P value will vary from a high level of near 4.5 (at MMPT= 40^0F) to a value near 2.5 to 3.0 for higher temperature near 80-90^0 F.

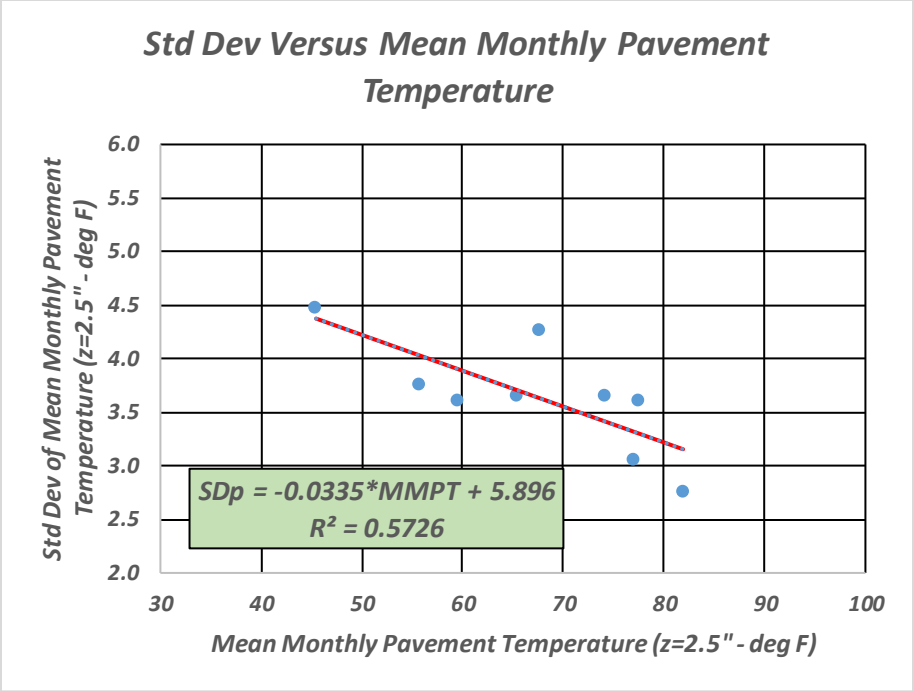

Figure 8.45. Statistical Analysis of Mean Monthly Pavement Temperature at Depth 2.5”

Implementation formats

The analyses of the temperature sensor data within the NAPTF facility (for 26 months between 2014 and 2016) results in a simple method to establish the expected frequency of occurrence for the pavement temperature, at a depth of z= 2.5” within the AC layer, to be within a specified temperature interval.

An approximate solution would be to simply rely upon the measurement of the monthly (daily) air temperature within the facility (hangar). If the MMAT is known, the relationship shown in Figure 8.23.

$$MMPT = 0.9874 \times MMAT$$

can be used to directly estimate the mean monthly pavement temperature. Figure 8.18 can then be used to estimate the probable standard deviation of the mean monthly pavement temperature by

$$SD_p = -0.0035 \times MMPT + 5.896$$

Knowledge of the mean and standard deviation (MMPT, SD_p) allows simple normal probability theory to determine the probability (α) that the pavement temperature will be between a specified temperature interval (T_{p1}; T_{p2}) by:

$$P_R\{T_{p1} < \bar{X} < T_{p2}\} = \alpha$$

with

$$K_{\alpha 2} = \frac{(T_{p_2} - MMPT)}{SD_p}$$

and

$$K_{\alpha 1} = \frac{(T_{p_1} - MMPT)}{SD_p}$$

However, it is recommended that if frequency if occurrences are desirable for research use at NAPTF; the exact approach used should definitely rely upon the actual distribution statistics of the measured sensor air and pavement temperature to precisely define the actual MMPT and SD_p value directly. These values can then be directly used with probability theory to compute any desired frequency. Development of an interactive computer software program that would yield theoretical frequency distributions within certain specified periods of time could be easily developed for future use by NAPTF staff.

Chapter 9. : Assessment of the Effect of Subgrade Thermo-Hydraulic Moisture Changes upon Soil Strength/Stiffness Properties

GENERAL OVERVIEW

One of the major goals of this research study was to investigate what effect, if any, changes in in-situ subgrade layer moisture content could be observed due to thermal-hydraulic gradients and their subsequent effect on strength/stiffness properties. Chapter 8 provided details and demonstrated that seasonal temperature variations within the entire pavement system resulted in moisture flows, and subsequently, changes in the seasonal moisture content within the Dupont and County clay subgrade layers.

This chapter presents a summary of the key moisture and temperature changes found in Chapter 8 and how it affects soil properties such as the moisture retention (suction stress state) and the hydraulic conductivity (k_{unsat}). Then, the strength models presented in Chapter 5, the stress state parameters predicted in Chapter 6 and subgrade M_r results presented in Chapter 7, are used to provide overall estimates of the probable changes in CBR, Vss and M_r subgrade responses expected due to the seasonal thermo-hydraulic gradients that occurs at the NAPTF.

SUMMARY OF CRITICAL MOISTURE CONTENT AND TEMPERATURE CHANGES AT THE NAPTF

The detailed research approach and findings dealing with the analysis of the TDR temperature and moisture seasons embedded at the NAPTF facility have been presented in Chapter 8. Based upon an analysis of the temperature-moisture data collected; it was concluded that annual changes (fluctuations) in both temperature (within the pavement depths) as well as the moisture content decreased with depth into the clay subgrades. While the maximum differences in moisture content (Δw), at a given depth, were not overly

excessive (Δw varied from 4.5% to 1.5%), it is considered important to assure what impact these changes in moisture content had upon the shear strength (CBR and vane shear strength) and resilient modulus (M_r) of each specific clay type sublayer at the NAPTF.

A brief summary of the key sensor readings determined over an approximate 2.5-year period is shown in Table 9.1. As previously noted, the letters A…F indicate the six general horizontal locations where a specific sensor group was buried into the NAPTF test sites; while the numbers 1…5 are indicative of the five specific depths that sensor readings were obtained at as shown in Figure 8.2. The table shows the average moisture and dry density, for each sublayer (depth) found and reported in Chapter 8, along with the maximum and minimum temperature (at specific depth (z) noted); minimum and maximum moisture contents, and the minimum and maximum degrees of saturation. It should be noted that these minimum/maximum values are those found over the 2.5-year monitoring period. It should also be noted that few degree of saturation values were estimated to be slightly over 100% and therefore, a value of 100% was assumed. The notation defining the average sensor readings is explained in Table 9.2.

Table 9.1. Variation of Temperature, Moisture Content and Degree of Saturation in NAPTF

.	Depth	Sensor Name	Compacted			Sensor Measured						Calculated		
			Initial Moisture Content	Initial Dry density	Sr	Temp ^{0}C			w (%)			S (%)		
	in		%	pcf	%	Initial	Max	Min	Initial	Max	Min	Initial	Max	Min
Dupont	35	A1	27.0	95.5	91.5	20.5	6.3	25.4	27.0	29.1	26.9	92.5	99.5	92.1
		B1	27.0	95.5	91.5	20.2	5.5	25.0	27.0	28.5	26.9	94.9	100.2	94.4
		C1	27.0	95.5	91.5	14.6	5.0	25.8	27.0	28.9	25.9	93.8	100.0	89.9
		D1	27.0	95.5	91.5	20.9	6.3	26.8	27.0	28.5	26.8	93.8	99.1	92.9
		E1	27.0	95.5	91.5	20.5	5.0	25.2	27.0	30.0	27.0	88.7	98.6	88.5
		F1	27.0	95.5	91.5	20.8	5.2	25.1	27.0	29.4	25.7	88.7	96.3	84.3
		Mean	27.0	95.5	91.5	19.6	5.6	25.6	27.0	29.1	26.5	92.1	99.0	90.3
		Std. Dev	0.0	0.0	0.0	2.2	0.6	0.6	0.0	0.5	0.5	2.5	1.4	3.3
	77	A2	37.2	83.4	95.4	22.4	10.4	22.4	37.3	37.7	36.6	100	100	100
		B2	37.2	83.4	95.4	21.9	9.4	24.3	37.3	37.3	35.4	93.0	93.1	88.3
		C2	37.2	83.4	95.4	21.9	10.9	22.3	37.3	37.3	35.2	94.9	95.1	89.6
		D2	37.2	83.4	95.4	22.3	10.2	22.3	37.3	37.4	34.9	93.8	94.1	87.9
		E2	37.2	83.4	95.4	22.2	10.5	22.7	37.3	37.7	36.2	96.1	97.2	93.3
		F2	37.2	83.4	95.4	22.1	9.3	22.1	37.3	37.3	36.0	96.4	96.7	93.1
		Mean	37.2	83.4	95.4	22.1	10.1	22.7	37.3	37.5	35.7	96.7	97.2	92.7
		Std. Dev	0.0	0.0	0.0	0.2	0.6	0.7	0.0	0.2	0.6	4.3	4.7	5.5
		Mean	32.1	89.4	93.5	20.9	7.8	24.1	32.1	33.3	31.1	94.4	98.1	91.5
		Std. Dev	5.1	6.1	2.0	2.0	2.4	1.6	5.1	4.2	4.6	4.2	3.6	4.7

County	89	A3	25.7	99.0	92.2	21.9	11.4	21.9	25.7	25.7	23.0	93.6	93.8	83.9
		B3	25.7	99.0	92.2	21.1	10.0	21.3	25.7	25.8	25.0	67.2	67.4	65.4
		C3	25.7	99.0	92.2	21.2	11.3	21.3	25.7	25.7	23.6	69.1	69.2	63.6
		D3	25.7	99.0	92.2	21.1	10.4	21.2	25.7	26.0	24.7	91.4	92.3	88.0
		E3	25.7	99.0	92.2	21.3	10.9	21.4	25.7	27.0	25.3	92.2	97.0	90.9
		F3	25.7	99.0	92.2	21.1	10.2	21.3	25.7	26.7	25.0	90.3	93.9	87.9
		Mean	25.7	99.0	92.2	21.3	10.7	21.4	25.69	26.16	24.46	84.0	85.6	79.9
		Std. Dev	0.0	0.0	0.0	0.3	0.5	0.2	0.00	0.52	0.83	11.2	12.3	11.1
	108	A4	25.7	99.0	92.2	19.4	12.2	20.4	25.7	26.5	25.5	89.2	91.9	88.5
		B4	25.7	99.0	92.2	19.8	11.5	20.3	25.7	26.1	21.7	93.3	94.7	78.8
		C4	25.7	99.0	92.2	19.7	11.9	20.0	25.7	27.4	25.6	94.9	101.2	94.8
		D4	25.7	99.0	92.2	19.6	11.4	20.4	25.7	27.9	25.6	83.3	90.4	83.0
		E4	25.7	99.0	92.2	19.4	11.3	19.9	25.7	26.0	25.2	88.2	89.3	86.4
		F4	25.7	99.0	92.2	19.7	10.8	20.3	25.7	26.6	25.1	88.2	91.1	86.1
		Mean	25.7	99.0	92.2	19.6	11.5	20.2	25.69	26.73	24.78	89.5	93.1	86.3
		Std. Dev	0.0	0.0	0.0	0.2	0.4	0.2	0.00	0.68	1.39	3.8	4.0	4.9
	126	A5	27.5	96.8	94.0	18.7	13.0	19.9	27.5	29.4	27.5	95.5	100	95.4
		B5	27.5	96.8	94.0	18.7	12.1	19.7	27.5	28.4	27.3	99.8	100	99.2
		C5	27.5	96.8	94.0	18.8	12.9	19.5	27.5	28.0	27.4	100	100	100
		D5	27.5	96.8	94.0	18.0	9.8	19.4	27.5	29.6	27.4	89.1	95.9	88.8
		E5	27.5	96.8	94.0	18.6	12.6	19.6	27.5	29.2	27.3	94.3	100.0	93.8
		F5	27.5	96.8	94.0	18.1	11.2	19.3	27.5	28.9	27.4	79.9	84.1	79.8
		Mean	27.5	96.8	94.0	18.5	11.9	19.6	27.48	28.91	27.38	93.4	98.1	93.0
		Std. Dev	0.0	0.0	0.0	0.3	1.1	0.2	0.00	0.55	0.05	7.2	6.8	7.1
		Mean	26.3	98.3	92.8	19.8	11.4	20.4	26.29	27.27	25.54	88.9	92.3	86.4
		Std. Dev	0.8	1.0	0.8	1.2	0.9	0.8	0.85	1.33	1.61	8.9	9.9	9.7

Table 9.2. Notation Representing Sensor Data

Sensor No.	Location	Clay/Sublayer	Depth (z) (in.)
1	A1….. F1	Dupont	35
2	A2….. F2	Dupont	77
3	A3….. F3	County	89
4	A4….. F4	County	108
5	A5….. F5	County	126

Three specific scenarios representing the variation in temperature and moisture content will be discussed in this study: Scenario 1: Average temperature and moisture variation at a particular depth; Scenario 2: Maximum variation of temperature at a particular depth; Scenario 3: Maximum moisture variation at a particular depth. Table 9.3 shows the variation of temperature and moisture content with depth for the three cases mentioned above. The general trend of temperature and moisture content changes, as a function of depth within the clay layers, is readily observed in Figure 9.1. Changes in temperature are greater at shallow depths and decreases with depth, while moisture content changes are greater at the top of Dupont clay, but it is variable within County clay.

Table 9.3. Variation of Temperature, Moisture Content and Degree of Saturation in NAPTF

Soil Type	Depth	Sensor	Min. temp	Max. temp	Max. w/c	Min. w/c	Max. S	Min. S	ΔTemp	Δw/c
	in.		°C	°C	%	%	%	%	%	%
Scenario 1: Average of all sensors at the same depth										
Du	35	A1…F1	5.55	25.55	29.07	26.51	98	90	20.00	2.56
	77	A1…F2	10.12	22.68	37.46	35.69	96	91	12.57	1.76
Co	89	A3…F3	10.70	21.40	26.16	24.46	94	88	10.70	1.70
	108	A4…F4	11.52	20.22	26.73	24.78	96	89	8.70	1.95
	126	A5…F5	11.93	19.57	28.91	27.38	98	90	7.63	1.53
Scenario 2: Max. temperatures observed at a particular depth										
Du	35	C1	5.00	25.80	28.93	25.90	98	88	20.80	3.03
	77	B2	9.40	24.30	37.29	35.37	96	91	14.90	1.93
Co	89	B3	10.00	21.30	25.78	24.99	93	90	11.30	0.79
	108	F4	10.80	20.30	26.55	25.09	95	90	9.50	1.47
	126	D5	9.80	19.40	29.56	27.37	100	94	9.60	2.19
Scenario 3: Max. moisture contents observed at a particular depth										
Du	35	F1	5.20	25.10	29.35	25.68	99	87	19.90	3.67
	77	D2	10.20	22.30	37.36	34.90	96	89	12.10	2.45
Co	89	A3	11.40	21.90	25.73	23.03	92	83	10.50	2.70
	108	B4	11.50	20.30	26.08	21.71	94	78	8.80	4.37
	126	D5	9.80	19.40	29.56	27.37	100	94	9.60	2.19

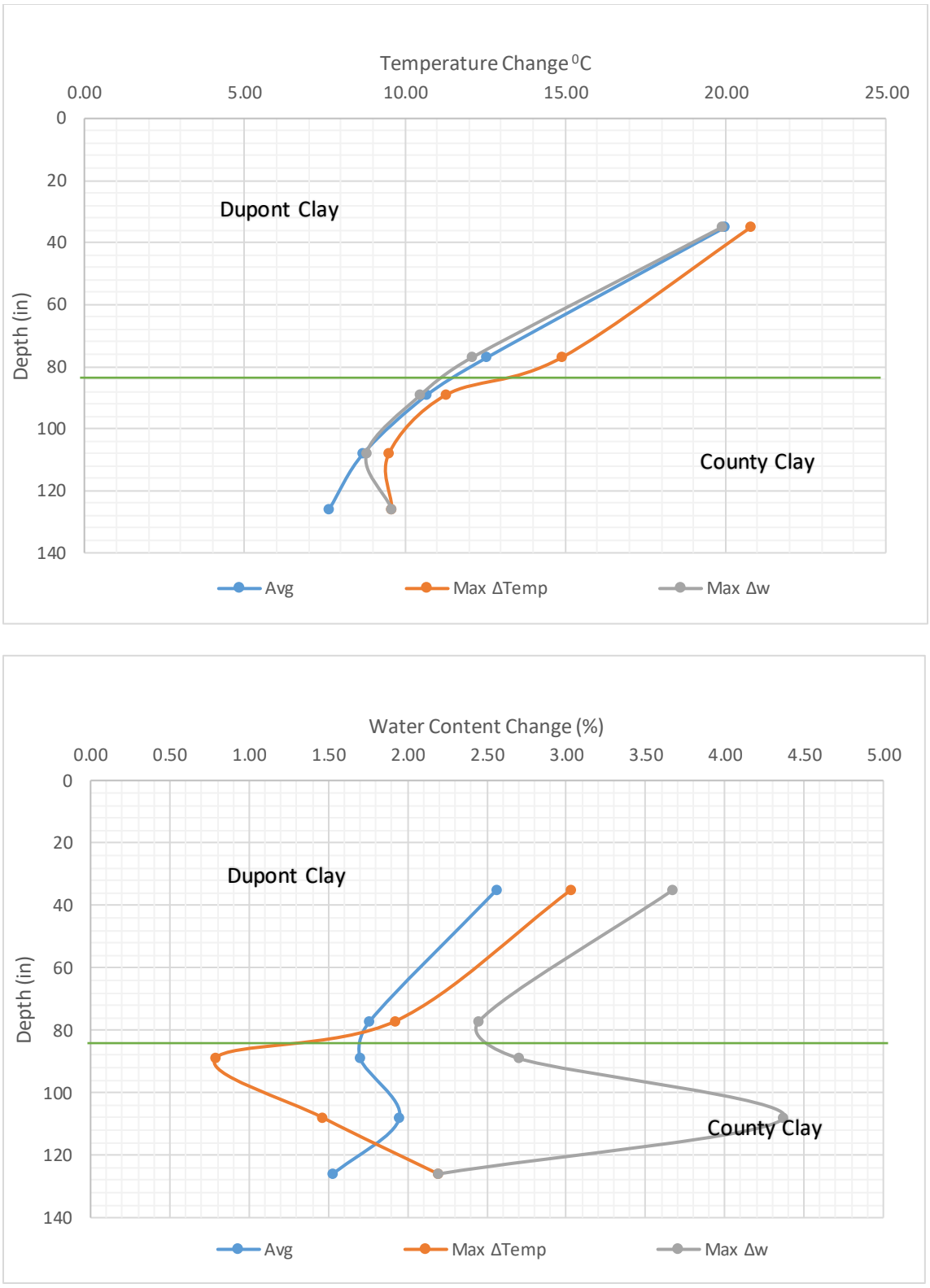

Figure 9.1. Range of Temperature and Moisture Content for Different Depths

EFFECT OF MOISTURE AND TEMPERATURE VARIATION ON HYDRAULIC AND STRENGTH SOIL PROPERTIES

It is well established that changes in moisture content influence the hydraulic and thermal properties of the soil. (Lu, 2015). In turn, the strength parameters of the soil are majorly influenced by the moisture content or the degree of saturation of the soil. As discussed in previous chapters, non-isothermal conditions can cause changes in soil properties that in turn affects the strength of the soil. Temperature gradients also trigger moisture flow. In the following sections, the influence of temperature and moisture content fluctuations on strength/stiffness of the material are studied in detail. The strength properties include the soil CBR and Vane shear strength, and the stiffness as measured by the resilient modulus (M_r). Table 9.3 shows a summary of the organization of the study: the first part of the study considered the range in water contents observed at a particular location in the test section under isothermal conditions. Based on the moisture content range observed, the range in soil suction and the range in hydraulic conductivity values were estimated. The moisture content range was used to estimate CBR and Vss variability, while the suction range was used to estimate M_r variation. The second part of the study considered changes in moisture content under non-isothermal conditions. In this case, the suction variability, together with the effect of temperature on the stress state variables representing the external loading conditions were used to estimate the variability of the M_r. Three scenarios were considered: Scenario 1, using the average values obtained at a particular depth; Scenario 2, using the max change in temperature (ΔTemp) observed at a particular location; and Scenario 3, using the maximum change in water content (Δw) observed at a particular location.

Table 9.4. Effect of Variation in Temperature and Moisture Content on Soil Properties

Analysis	Case 1- Isothermal Moisture Variability (Hydraulic Gradient)	Case 2 – Non-isothermal Moisture and Temperature Variability (Hydro-Thermal Gradient)
Properties	$\Delta\Psi$ f(Δw/c) Δk_{unsat} f($\Delta\Psi$) ΔCBR f(Δw/c) ΔV_{SS} f(Δw/c) ΔM_r f($\Delta\Psi$)	Δw/c f(ΔT) $\Delta\Psi$ f(Δw/c, ΔT) Δk_{unsat} f($\Delta\Psi$) $\Delta\theta$ f(ΔT,E_{sg}, P) $\Delta\tau_{oct}$ f(ΔT,load) ΔM_r f($\Delta\Psi$, θ, τ_{oct})

VARIATION IN MATRIC SUCTION

As presented in Chapter 4, the temperature was found to affect the moisture retention properties of the soils considered in this study. This finding allowed for the development of a family of SWCC curves at a range of temperatures found in the field, as shown in figures 9.2 and 9.3 for County soil and Dupont soil, respectively. Based on the laboratory results and the moisture content changes observed in the field, the changes in moisture retention potential (suction stress) were evaluated at isothermal conditions (Case 1). Table 9.5 shows the initial suction measured in the NAPTF and the results are presented din the next section.

Case 1. Matric Suction Range Corresponding to Variation of Moisture Content Observed in Test Facility

SWCC for 25^0C was used to find a range of matric suction value with the degree of saturation measured in the facility. Table 9.6 and Figure 9.4 shows the range of matric suction in the subgrade in NAPTF estimated from the moisture content range observed in

the field. After analyzing all three scenarios, a maximum variation in suction of 635 kPa (92 psi) was observed at a depth of 35 in. for Dupont clay. For County clay, the maximum variation was estimated to be 330 kPa (47.8 psi) at 108 in. in depth. These maximum values were estimated from the maximum variation in moisture content measured by individual sensors located at particular depths.

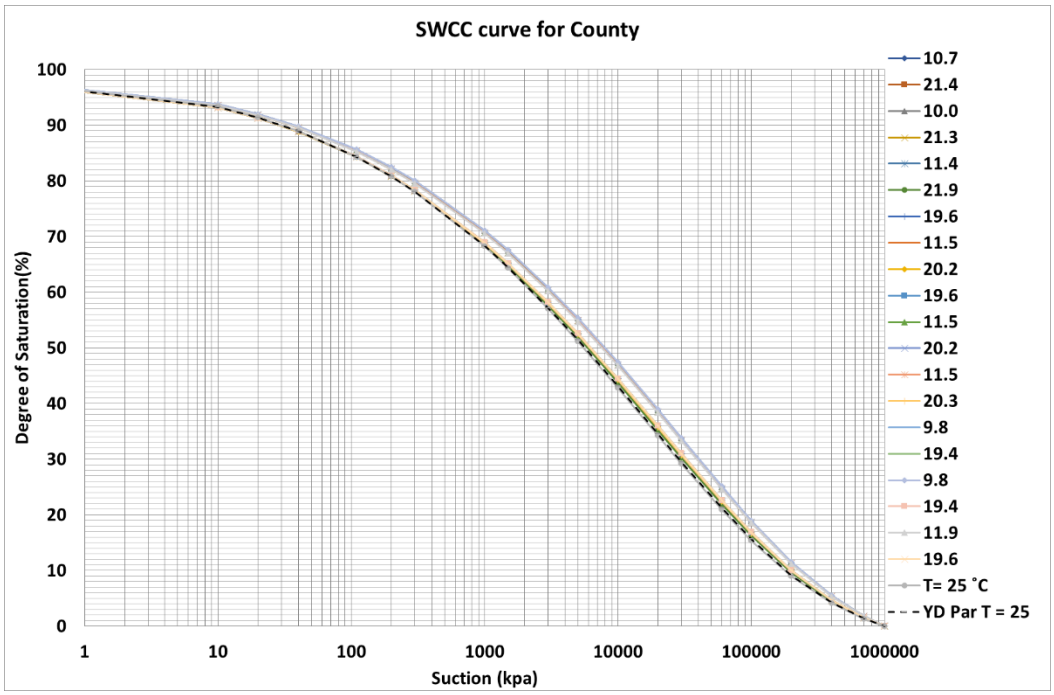

Figure 9.2. County Clay SWCCs for a Range of Temperatures Observed in the NAPTF

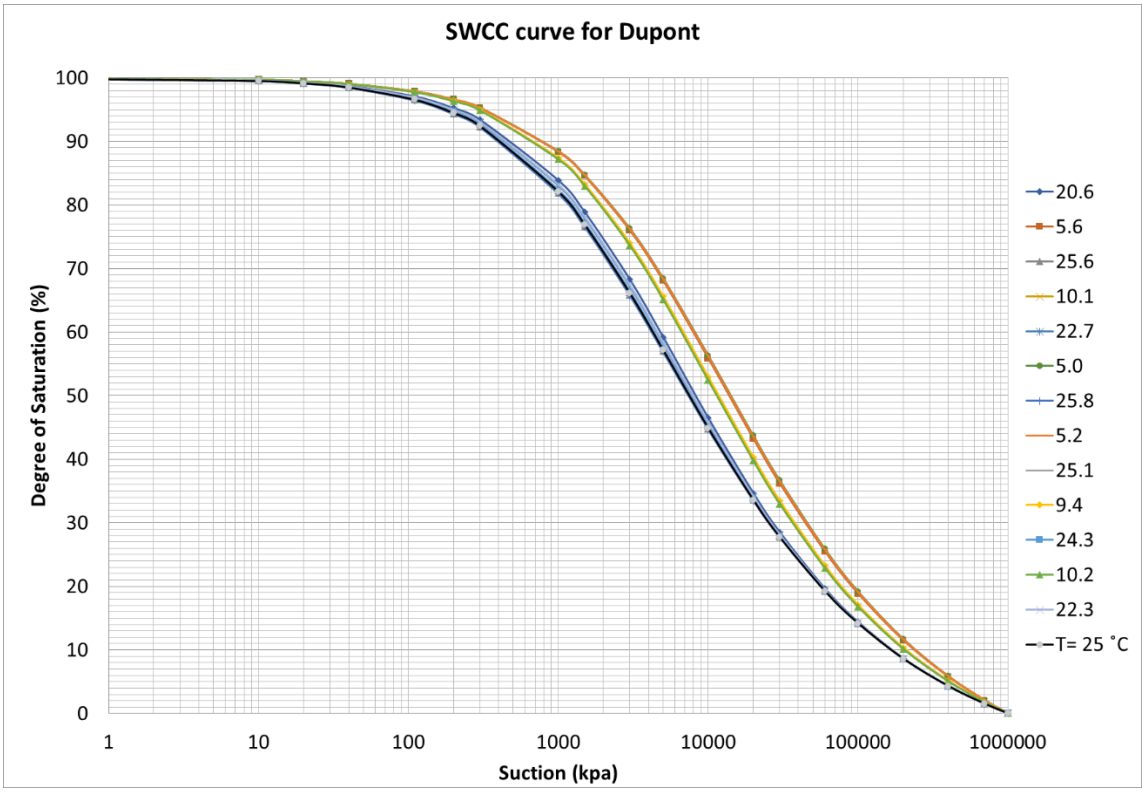

Figure 9.3. Dupont Clay SWCCs for a Range of Temperatures Observed in the NAPTF

Table 9.5. Estimated Initial Matric Suction in the NAPTF at Different Depths

Type of Soil	Sensor	Depth	Initial Dry Density	Initial Temp.	Initial w/c	Initial S	Initial Suction
		in.	pcf	°C	%	%	psi
Dupont soil	A1….F1	35	95.47	19.58	27.02	91.54	44.96
	A1….F2	77	83.36	22.13	37.25	95.49	26.11
County soil	A3….F3	89	98.98	21.28	25.69	92.29	2.76
	A4….F4	108	98.98	19.60	25.69	92.29	2.76
	A5….F5	126	96.83	18.48	27.48	94.02	1.16

Table 9.6. Estimated Matric Suction Variation due to Changes in Moisture Content Observed at NAPTF with Depth for All Scenarios

Type of Soil	Sensor	Depth	Min temp	Max temp	Max S	Min S	Min Suction	Max Suction	$\Delta\psi$
		in	^{0}C	^{0}C	%	%	psi	psi	psi
Scenario 1: Average of All Sensor Measurements at a Particular Depth									
Dupont	A1….F1	35			98.5	89.8	7.0	59.5	52.5
	A1….F2	77			96.0	91.5	17.4	45.0	27.6
County	A3….F3	89			94.0	87.9	1.2	10.2	9.0
	A4….F4	108			96.0	89.0	0.1	4.4	4.2
	A5….F5	126			98.9	93.7	0.1	1.5	1.3
Scenario 3: Considering the Maximum Difference in Water Content									
Dupont	F1	35			99.4	87.0	2.2	94.3	92.1
	D2	77			95.8	89.5	17.4	60.9	43.5
County	A3	89			92.4	82.7	1.7	26.1	24.4
	B4	108			93.7	78.0	1.5	49.3	47.8
	D5	126			100	93.6	0.0	1.5	1.4

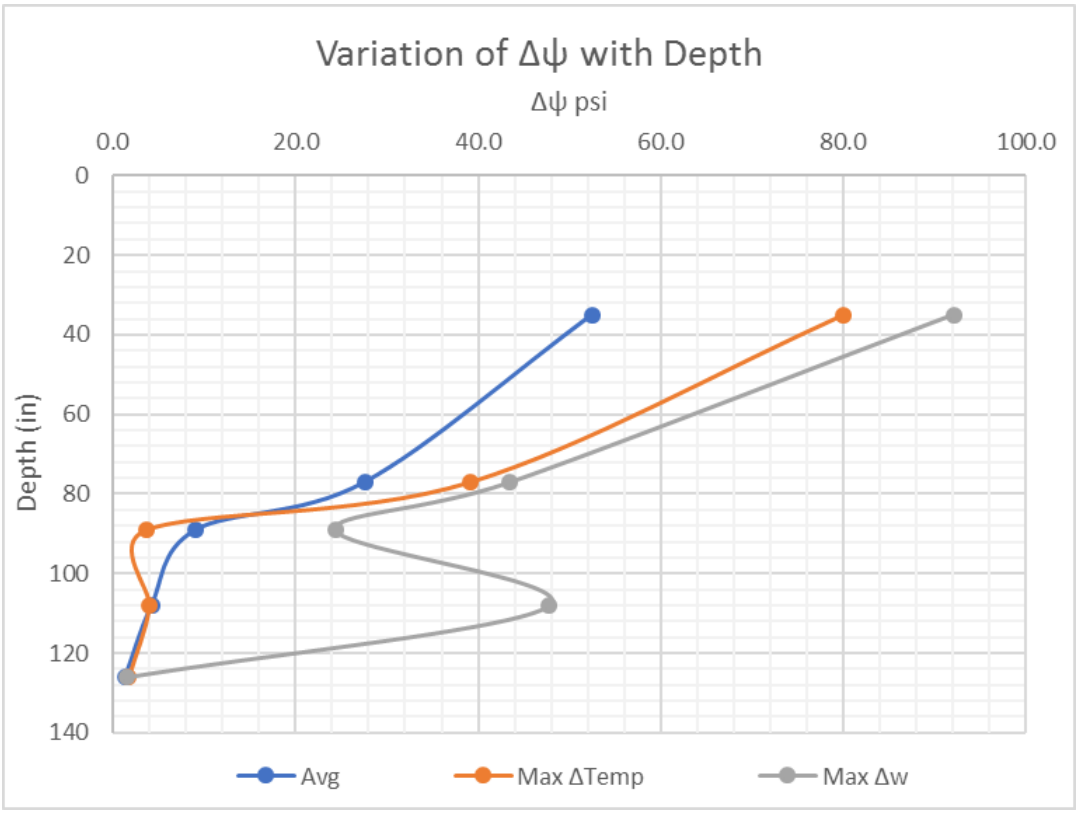

Figure 9.4. Variation of Matric Suction in NAPTF due to Moisture Content Changes with Depth for All Cases

Case 2. Change in Matric Suction due to Both Moisture and Temperature Changes

For Case 2, a range in matric suction was obtained based on the SWCCs for different temperatures at the moisture content values observed in the NAPTF. Table 9.7and Figure 9.5 shows the variation of suction observed. Though the pattern of the change in the matric suction is the same and the maximum variation is observed at the same depths and locations as Case 1, the magnitude of the variation is different. A combined effect of moisture and temperature changes will estimate a range in matric suction variation, which is 1.2 times greater for County clay and 1.6 times greater for Dupont clay than that observed for Case

1. Figure 9.6 explains the ratio of variation between the hydraulic and hydro-thermal gradients.

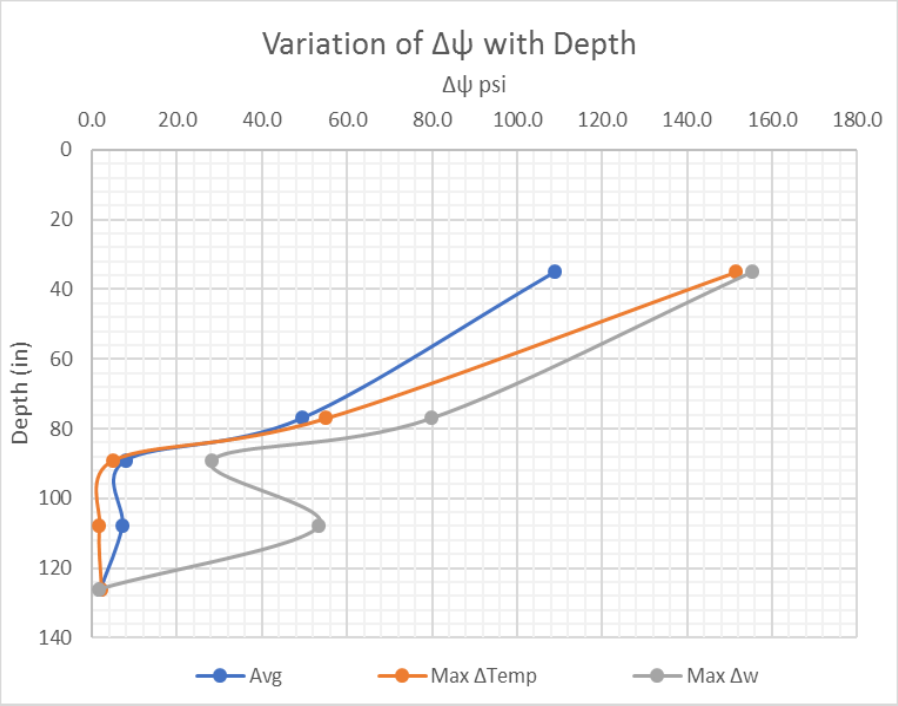

Figure 9.5. Variation of Matric Suction in NAPTF due to Combined Effect of Moisture and Temperature Changes

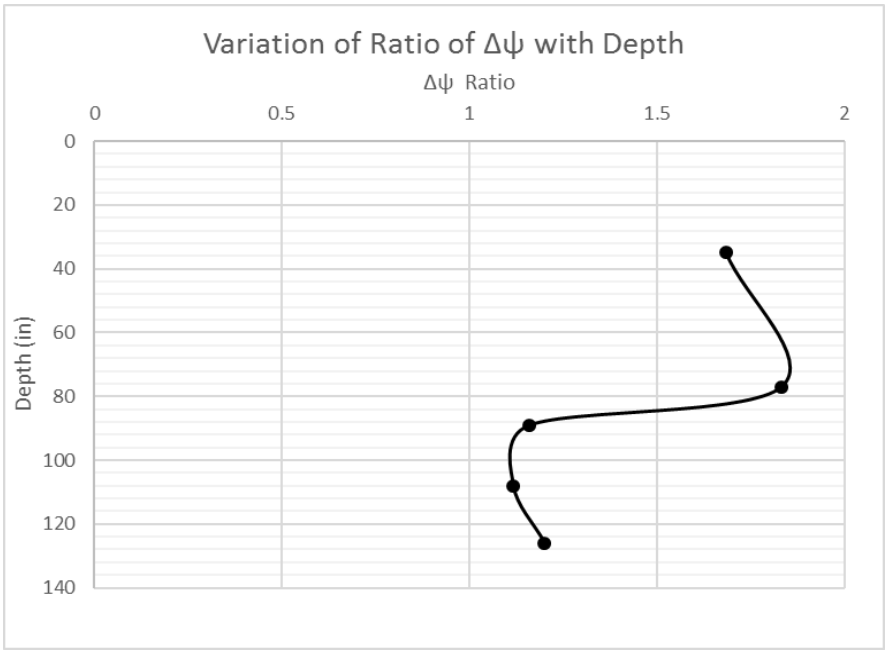

Figure 9.6. Ratio of Variation of Matric Suction in NAPTF due to Hydraulic to Hydro-Thermal Gradients with Depth.

Table 9.7. Variation of Matric Suction in NAPTF due to Combined Effect of Changes in Moisture Content and Temperature for the Three Scenarios

Type of Soil	Sensor	Depth	Min temp	Max temp	Max S	Min S	Change in Matric Suction			
							Min Temperature		Min Temperature	
							Suction for Min S	Suction for Max S	Suction for Min S	Suction for Max S
		in	^{0}C	^{0}C	%	%	psi	psi	psi	psi
Scenario 1: Suction Range Considering Average Temperature/Degree of Saturation Values										
Du	A1 to F1	35	5.6	25.6	98.49	89.81	116.0	11.6	58.0	7.3
	A2 to F2	77	10.1	22.7	96.01	91.49	79.8	30.5	58.0	30.5
Co	A3 to F3	89	10.7	21.4	93.97	87.86	8.7	0.7	7.3	1.0
	A4 to F4	108	11.5	20.2	96.03	89.03	5.8	0.1	7.3	0.1
	A5 to F5	126	11.9	19.6	98.91	93.67	1.7	0.0	2.0	0.0
Scenario 2: Suction Range from Maximum Difference in Temperature										
Du	C1	35	5	25.8	98.02	87.75	15.2	159.5	8.0	84.1
	B2	77	9.4	24.3	95.58	90.65	46.4	84.1	29.0	57.3
Co	B3	89	10	21.3	92.61	89.78	2.9	7.3	2.2	5.8
	F4	108	10.8	20.3	95.39	90.12	3.6	4.6	2.9	4.4
	D5	126	9.8	19.4	100.00	93.62	0.0	2.2	0.0	1.6
Scenario 3: Suction Range from Maximum Difference in Water Content										
Du	F1	35	5.2	25.1	99.43	86.98	5.8	159.5	4.4	85.6
	D2	77	10.2	22.3	95.75	89.47	46.4	69.6	31.9	111.7
Co	A3	89	11.4	21.9	92.45	82.74	2.9	30.5	2.2	21.8
	B4	108	11.5	20.3	93.70	77.99	2.2	55.1	1.7	45.0
	D5	126	9.8	19.4	100.00	93.62	0.0	1.7	0.0	1.5

VARIATION IN k_{unsat}

A similar analysis was performed on k_{unsat} based on the results obtained in Chapter 4. The equations used to predict the k_{unsat} from the matric suction. The matric suction predicted from the previous section is used for this analysis. The equations used to predict the kunsat are as follows:

For County Clay, $k_{unsat} = (5\times10^{-13}T + 1\times10^{-11})\psi^{-(-0.00015T^2+0.00293T+0.93905)}$

For Dupont Clay, $k_{unsat} = (1.77\times10^{-12}T + 3.12\times10^{-11})\psi^{-(0.000132T^2-0.00467T+0.916)}$

Table 9.8 shows the initial k_{unsat} in the field.

Table 9.8. Initial k_{unsat} in NAPTF

Type of Soil	Sensor	Depth	Initial Dry density	Initial temp	Initial w/c	Initial S	Initial Suction	Initial k_{unsat}
		in	pcf	^{0}C	%	%	psi	m/s
	A1….F1	35	95.47	19.58	27.02	91.54	44.96	4.92E-13
Dupont	A1….F2	77	83.36	22.13	37.25	95.49	26.11	8.49E-13
	A3….F3	89	98.98	21.28	25.69	92.29	2.76	5.75E-12
	A4….F4	108	98.98	19.60	25.69	92.29	2.76	5.46E-12
County	A5….F5	126	96.83	18.48	27.48	94.02	1.16	1.11E-11

Change in k_{unsat} due to Hydraulic Gradient

Table 9.9 shows the range of k_{unsat} in the subgrade in NAPTF influenced by the hydraulic gradient. After analyzing all the three cases, the maximum variation in kunsat of 3.28E-12 m/s was observed in depth of 35" for Dupont clay. For County clay, the maximum variation was observed in 126" depth for 1.55E-08 m/s. Both of the maximum values were observed when there was a maximum variation in moisture content case.

Table 9.9. Variation of k_{unsat} in NAPTF due to Hydraulic Gradients with Depth for All Cases

Type of Soil	Sensor	Depth	Max S	Min S	Min Suction	Max Suction	k_{unsat} for at Max w/c	k_{unsat} for Min w/c	Δk_{unsat}
		in	%	%	psi	psi	m/s	m/s	m/s
Average of All locations									
Dupont	A1 to F1	35	98.5	89.8	7.0	59.5	1.30E-12	4.56E-13	8.40E-13
	A2 to F2	77	96.0	91.5	17.4	45.0	7.48E-13	5.40E-13	2.08E-13
County	A3 to F3	89	94.0	87.9	1.2	10.2	4.51E-11	9.89E-12	3.52E-11
	A4 to F4	108	96.0	89.0	0.1	4.4	2.87E-10	1.98E-11	2.67E-10
	A5 to F5	126	98.9	93.7	0.1	1.5	2.91E-10	5.02E-11	2.41E-10
Max difference in Temperature									
Dupont	C1	35	98.0	87.7	87.0	12.6	1.25E-12	3.30E-13	9.21E-13
	B2	77	95.6	90.6	59.5	8.6	6.29E-13	4.43E-13	1.86E-13
County	B3	89	92.6	89.8	5.8	0.8	1.07E-11	8.42E-11	-7.36E-11
	F4	108	95.4	90.1	4.4	0.6	1.42E-11	1.05E-10	-9.08E-11
	D5	126	101.1	93.6	1.7	0.3	3.05E-11	2.26E-10	-1.95E-10
Max difference in w/c									
Dupont	F1	35	99.4	87.0	2.2	94.3	3.59E-12	3.04E-13	3.28E-12
	D2	77	95.8	89.5	17.4	60.9	7.52E-13	4.11E-13	3.40E-13
County	A3	89	92.4	82.7	1.7	26.1	3.25E-11	4.45E-12	2.81E-11
	B4	108	93.7	78.0	1.5	49.3	3.67E-11	2.45E-12	3.42E-11
	D5	126	101.1	93.6	0.0	1.5	1.56E-08	4.99E-11	1.55E-08

Change in k_{unsat} due to Both Hydraulic and Temperature Gradient

Using the SWCC for different temperatures and the moisture content observed in the NAPTF, a range of Matric suction was found in previous section. This was used to predict the k_{unsat} change due to hydro-thermal gradient. Table 9.10 shows the variation of k_{unsat} observed. Though the pattern of the change in the k_{unsat} is the same and the maximum variation is observed in the same depths and locations as before, the magnitude of the variation is different. A combined effect of hydraulic and temperature produced matric k_{unsat} variation of 0.2 to 0.9 times lower than the k_{unsat} variation due to hydraulic gradient. Figure 9.7 explains the ratio of variation between the hydraulic and hydro-thermal gradients.

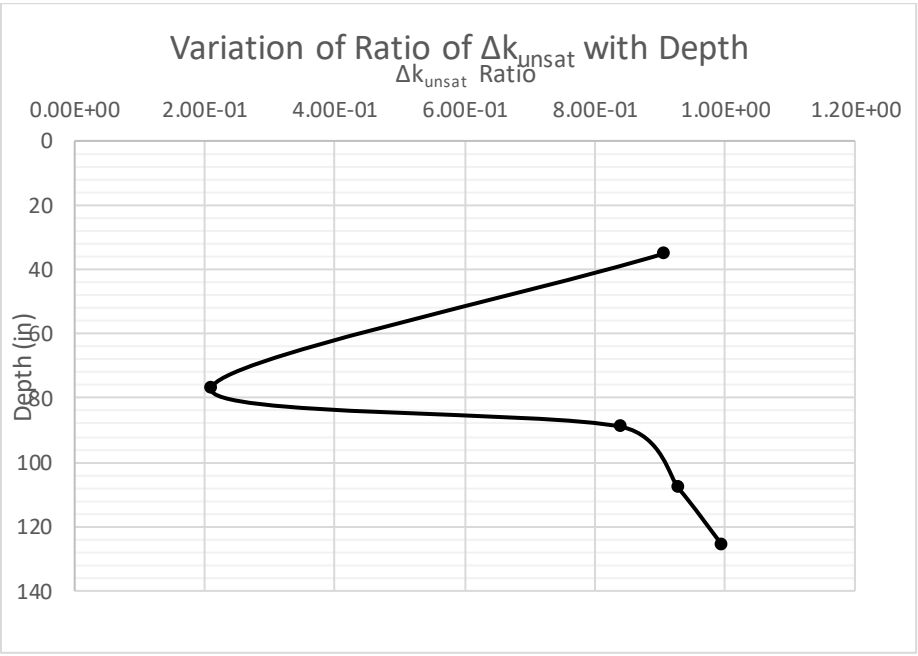

Figure 9.7: Ratio of Variation of k_{unsat} in NAPTF due to Hydraulic to Hydro-Thermal Gradients with Depth.

Table 9.10: Variation of Matric Suction in NAPTF due to Hydro-Thermal Gradients with Depth for All Cases

					Change in Matric Suction				Change in Kunsat				
					Min Temperature		Max Temperature		Min Temp	Max Temp	Min Temp	Max Temp	
Type of Soil	Sensor	Depth	Min temp	Max temp	Suction for Min S	Suction for Max S	Suction for Min S	Suction for Max S	k_{unsat} for at Max w/c	k_{unsat} for Min w/c	k_{unsat} for at Max w/c	k_{unsat} for Min w/c	Δk_{unsat}
		in	°C	°C	psi	psi	psi	psi	m/s	m/s	m/s	m/s	psi
Average of all Locations													
Dupont	A1 to F1	35	5.6	25.6	116	12	58	7	1.05E-13	1.86E-12	1.95E-13	2.79E-12	2.69E-12
	A2 to F2	77	10.1	22.7	80	30	58	30	1.96E-13	7.55E-13	2.60E-13	7.55E-13	5.59E-13
County	A3 to F3	89	10.7	21.4	9	1	7	1	1.42E-12	1.82E-11	1.66E-12	1.36E-11	1.68E-11
	A4 to F4	108	11.5	20.2	6	0	7	0	2.10E-12	7.04E-11	1.73E-12	7.04E-11	6.87E-11
	A5 to F5	126	11.9	19.6	2	0	2	0	6.14E-12	1.25E-09	5.36E-12	1.25E-09	1.24E-09
Max difference in Temperature													
Dupont	C1	35	5	25.8	15	160	8	84	6.21E-13	1.96E-13	1.11E-12	3.40E-13	9.12E-13
	B2	77	9.4	24.3	46	84	29	57	3.04E-13	3.29E-13	4.59E-13	4.57E-13	1.56E-13
County	B3	89	10	21.3	3	7	2	6	3.59E-12	2.50E-12	4.63E-12	3.03E-12	2.13E-12
	F4	108	10.8	20.29999924	4	5	3	4	3.07E-12	3.56E-12	3.73E-12	3.77E-12	6.98E-13
	D5	126	9.800000191	19.4	0	2	0	2	2.85E-09	6.66E-12	2.85E-09	8.70E-12	2.84E-09
Max difference in w/c													
Dupont	F1	35	5.2	25.1	6	160	4	86	1.49E-12	1.93E-13	1.93E-12	3.30E-13	1.74E-12
	D2	77	10.2	22.3	46	70	32	112	3.18E-13	3.67E-13	4.41E-13	2.44E-13	1.97E-13
County	A3	89	11.4	21.9	3	30	2	22	3.83E-12	7.39E-13	4.93E-12	9.87E-13	4.19E-12
	B4	108	11.5	20.29999924	2	55	2	45	4.95E-12	4.22E-13	6.02E-12	5.03E-13	5.60E-12
	D5	126	9.800000191	19.4	0	2	0	1	2.85E-09	8.07E-12	2.85E-09	9.44E-12	2.84E-09

VARIATION IN CBR AND VANE SHEAR STRENGTH

The models used to predict the CBR and Vane shear strength used in Chapter 5 will be used to predict the changes in the CBR and Vane shear strength of the subgrade soils. The analysis of the change in CBR and Vane shear strength are performed only for hydraulic gradients since the models developed does not incorporate any parameter that is affected by temperature.

Change in CBR and Vane Shear Strength due to Hydraulic Gradient

Table 9.12 and Figure 9.8 shows the range of CBR in the subgrade in NAPTF influenced by the hydraulic gradient. After analyzing all the three cases, the maximum variation in CBR of 2.35% was found in depth of 35" for Dupont clay. For County clay, the maximum variation was observed in 108" depth for 2.88%. Both of the maximum values were observed when there was a maximum variation in moisture content case. The results of Vane shear strength is also presented in Table 9.12. The maximum variation of Vss was found in depth of 35" for Dupont clay and in Depth 108" for County clay. Dupont clay noticed a maximum variation of 0.0065 tsf whereas a variation of 0.0131 tsf was noticed in County clay. Figure 9.9 shows the range of variation of Vss with depth.

Table 9.11: Variation of Matric Suction in NAPTF due to Hydraulic Gradients with Depth for All Cases

Sensor	Depth	Initial Dry density	Max w/c	Min w/c	CBR For Max w/c	CBR For Min w/c	ΔCBR	Vss For Max w/c	Vss For Min w/c	ΔVss
	in	pcf	%	%	%	%		tsf	tsf	
Average of all Locations										
1	35	95.47	29.07	26.51	6.97	8.71	1.75	0.039	0.044	0.0049
2	77	83.36	37.46	35.69	1.11	1.17	0.07	0.014	0.015	0.0005
3	89	98.98	26.16	24.46	1.72	2.21	0.48	0.019	0.021	0.0027
4	108	98.98	26.73	24.78	1.69	2.07	0.38	0.018	0.020	0.0022
5	126	96.83	28.91	27.38	0.01	1.12	1.11		0.014	0.0145
Max difference in Temperature										
1	35	95.47	28.93	25.90	7.03	9.09	2.05	0.040	0.045	0.0057
2	77	83.36	37.29	35.37	1.12	1.17	0.05	0.014	0.015	0.0003
3	89	98.98	25.78	24.99	1.78	1.99	0.21	0.019	0.020	0.0012
4	108	98.98	26.55	25.09	1.69	1.96	0.26	0.018	0.020	0.0016
5	126	96.83	29.56	27.37	0.00	1.12	1.12		0.014	0.0145
Max difference in w/c										
1	35	95.47	29.35	25.68	6.86	9.21	2.35	0.039	0.046	0.0065
2	77	83.36	37.36	34.90	1.12	1.18	0.06	0.014	0.015	0.0004
3	89	98.98	25.73	23.03	1.79	3.14	1.35	0.019	0.026	0.0068
4	108	98.98	26.08	21.71	1.73	4.62	2.88	0.019	0.032	0.0131
5	126	96.83	29.56	27.37	0.00	1.12	1.12		0.014	0.01

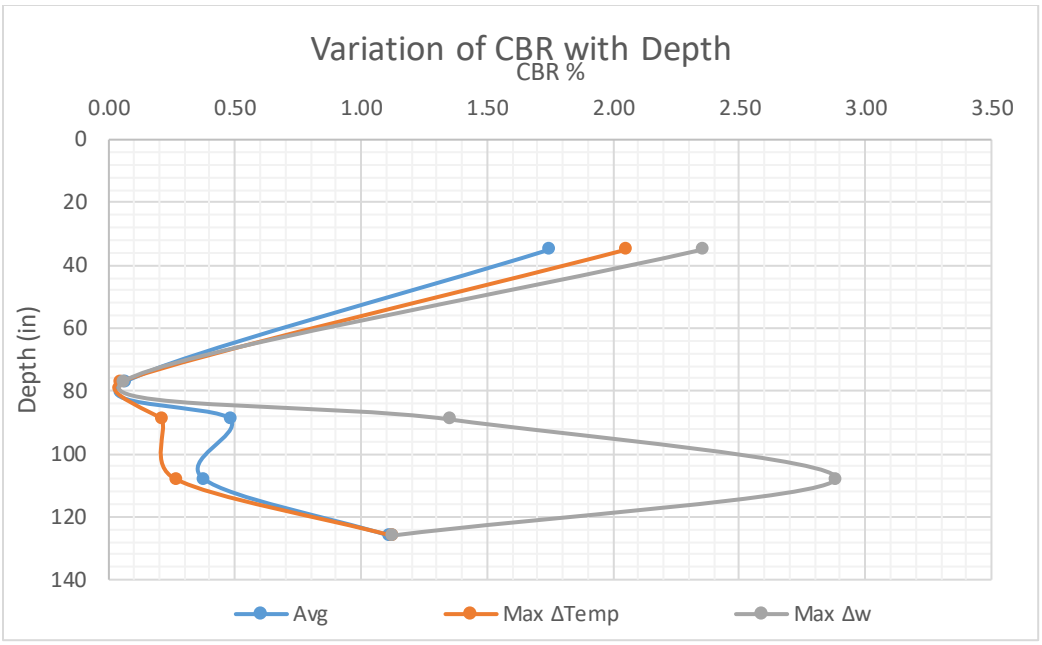

Figure 9.8. Variation of Matric Suction in NAPTF due to Hydraulic Gradients with Depth for All Cases

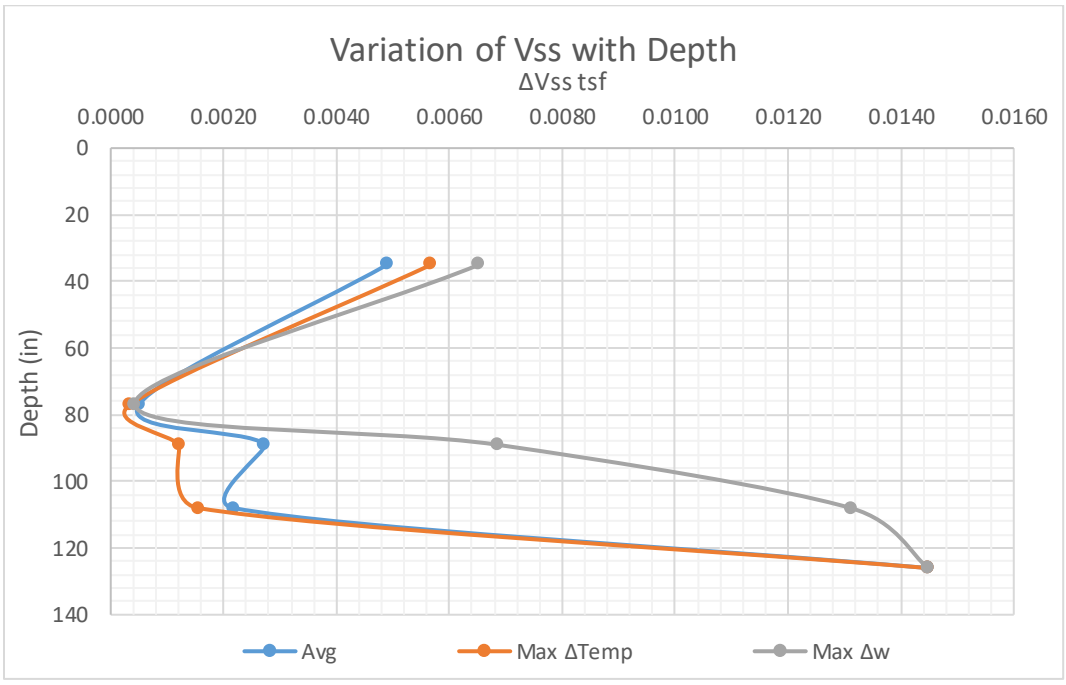

Figure 9.9. Variation of Vss in NAPTF due to Hydraulic Gradients with Depth for All Cases

VARIATION IN THE RESILIENT MODULUS OF SUBGRADE

The variation in the resilient modulus of the soil can be attributed to both hydraulic and the thermal function. The factors used to calculate M_r are bulks stress, octahedral stress and matric suction. Since all these factors have an influence on the temperature, the M_r calculated seems to have a significant effect with temperature. Additionally, different gear types such as Dual gear, Dual Tandem and Triple tandem is used in the analysis to calculate bulk stress and octahedral stress. Models developed in Chapter 6 and Chapter 7 are used in the analysis. Table 9.12 shows the initial stress state parameters and the M_r of the subgrade with depth.

Dual Gear

Due to Hydraulic gradient

Table 9.13 shows the variation of the stress state parameters and the M_r of the soil for the three cases considered. Similar to the other properties, the maximum variation of the M_r was found when there is maximum variation of water content. The maximum variation of M_r recorded was 7.4 ksi in Dupont clay at 35" and 6.8 ksi in County clay at 108". The maximum bulk and octahedral stress was recorded in the top of the subgrade. The combination of the load stress applied and the moisture content present influenced the change in the M_r. Figure 9.10 shows the variation of M_r with respect to depth. .

Table 9.12. Initial Stress State and M_r of Subgrades

Depth	Initial Temp		Initial S	Initial Suction	Bulk Stress	Oct Stress	Mr
in	0F	0F	%	psi	psi	psi	psi
Dual							
35	67.25	67.25	91.54	44.96	30.09	7.83	17999.65
77	71.84	71.84	95.49	26.11	10.24	2.89	19855.07
89	70.31	70.31	92.29	2.76	7.91	2.12	9597.57
108	67.28	67.28	92.29	2.76	6.27	1.67	9561.98
126	65.27	65.27	94.02	1.16	5.24	1.37	9110.79
Dual Tandem							
35	67.25	67.25	91.54	44.96	28.79	8.11	16936.08
77	71.84	71.84	95.49	26.11	15.36	4.31	19380.24
89	70.31	70.31	92.29	2.76	11.45	3.41	8855.72
108	67.28	67.28	92.29	2.76	8.20	2.87	8611.26
126	65.27	65.27	94.02	1.16	5.69	2.48	7793.99
Triple Tandem							
35	67.25	67.25	91.54	44.96	34.97	8.30	18286.05
77	71.84	71.84	95.49	26.11	18.84	5.00	19353.76
89	70.31	70.31	92.29	2.76	14.49	3.98	8800.77
108	67.28	67.28	92.29	2.76	10.78	3.47	8605.47
126	65.27	65.27	94.02	1.16	7.89	3.09	7910.68

Table 9.13. Variation of M_r Due to Hydraulic Gradient For Dual Gear

					Matric Suction		Mr		Change in Mr
Depth	Initial S	Initial Suction	Bulk Stress	Oct Stress	Min	Max	Max Suction	Min Suction	

in	%	psi	psi	psi	psi	psi	psi	psi	
35	91.54	44.96	30.09	7.83	6.96	59.47	14127.76	18960.70	4832.95
77	95.49	26.11	10.24	2.89	17.40	44.96	18748.60	21742.31	2993.71
89	92.29	2.76	7.91	2.12	1.16	10.15	9235.47	11059.06	1823.59
108	92.29	2.76	6.27	1.67	0.15	4.35	8960.19	9903.47	943.28
126	94.02	1.16	5.24	1.37	0.15	1.45	8872.12	9177.29	305.16
For Max Temperature Difference									
35	91.54	44.96	30.09	7.83	6.96	87.02	14127.76	20448.10	6320.34
77	95.49	26.11	10.24	2.89	20.31	59.47	19140.36	22903.20	3762.84
89	92.29	2.76	7.91	2.12	2.18	5.80	9468.28	10237.29	769.01
108	92.29	2.76	6.27	1.67	0.36	4.35	9012.65	9903.47	890.82
126	94.02	1.16	5.24	1.37	0.00	1.74	8837.59	9243.07	405.48
For Max W/c Difference									
35	91.54	44.96	30.09	7.83	2.18	94.27	13308.94	20787.46	7478.52
77	95.49	26.11	10.24	2.89	17.40	60.92	18748.60	23009.47	4260.87
89	92.29	2.76	7.91	2.12	1.74	26.11	9369.56	13492.89	4123.33
108	92.29	2.76	6.27	1.67	1.52	49.31	9285.06	16103.36	6818.31
126	94.02	1.16	5.24	1.37	0.00	1.45	8837.59	9177.29	339.70

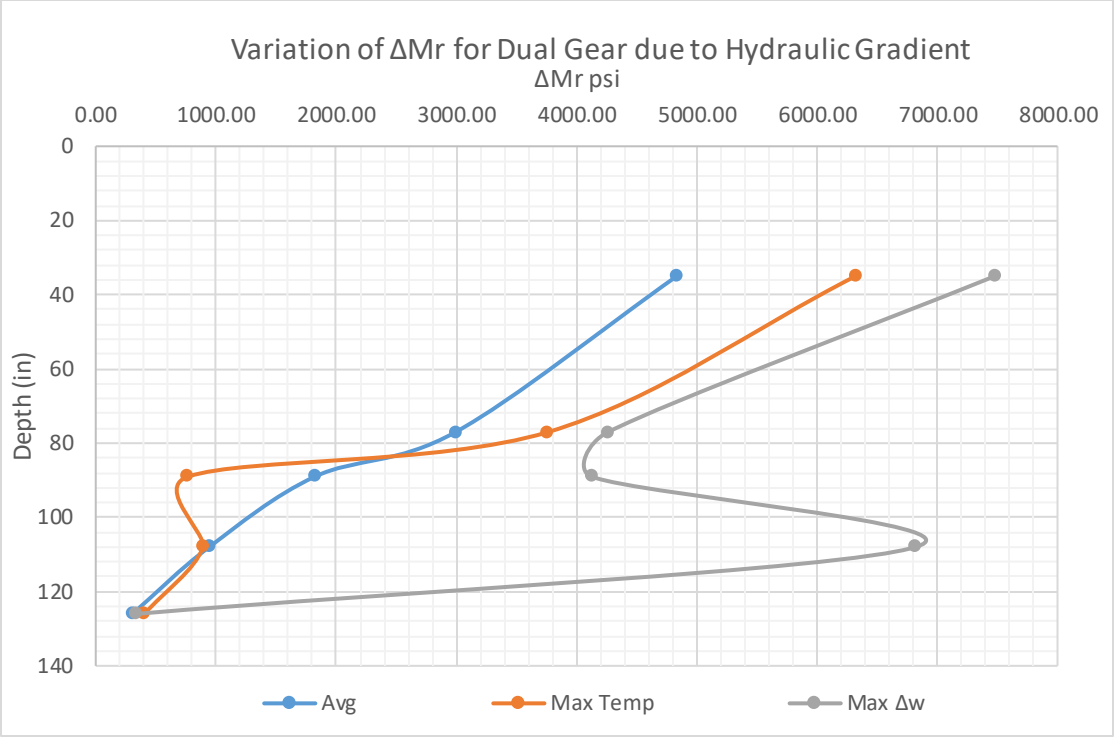

Figure 9.10. Variation of M_r Due to Hydraulic Gradient for Dual Gear

Due to Hydro-Thermal Gradient

Table 9.14 shows the variation of the stress state parameters and the M_r of the soil for the three cases considered. The variation of the both the load stresses and the suction stress changes were considered and the M_r value was found. The maximum variation of the M_r was found when there is maximum variation of water content. The maximum variation of M_r recorded was 18 ksi in Dupont clay at 35" and 10 ksi in County clay at 108". The maximum bulk and octahedral stress was recorded in the top of the subgrade. The combination of the load stress applied and the moisture content present influenced the change in the M_r. Figure 9.11 shows the variation of M_r with respect to depth due to Hydro-thermal gradients.

Table 9.14. Variation of M_r Due to Hydro-Thermal Gradient for Dual Gear

							M_r				
			Bulk Stress		Oct Stress		Min Temperature		Max Temperature		
Depth	Min temp	Max temp	For Min Temp	For Max Temp	For Min Temp	For Max Temp	Suction for Min w/c	Suction for Max w/c	Suction for Min w/c	Suction for Max w/c	ΔM_r
in	^0F	^0F	psi	psi	psi	psi	psi	psi	psi	psi	
35	42	78	27.59	31.26	7.53	4.69	21618	14735	30282	22742	15547
77	50	73	9.82	10.25	2.83	1.41	23990	20110	29758	26555	9648
89	51	71	7.58	7.91	2.07	0.60	10727	9075	13644	11932	4569
108	53	68	6.10	6.28	1.65	0.44	10144	8911	12998	11110	4087
126	53	67	5.14	5.26	1.36	0.33	9202	8799	11200	10635	2401
For Max Temperature Difference											
35	41	78	27.54	31.30	7.52	4.77	15194	23150	22657	32212	17018
77	49	76	9.80	10.27	2.83	1.45	21592	24220	26205	29525	7934
89	50	70	7.56	7.91	2.07	0.61	9562	10448	12249	13244	3683
108	51	69	6.08	6.28	1.64	0.45	9691	9903	11876	12260	2569
126	50	67	5.11	5.25	1.36	0.35	8781	9280	10588	11035	2254
For Max W/c Difference											
35	41	77	27.56	31.18	7.52	4.73	13881	23152	21834	32476	18595
77	50	72	9.82	10.24	2.83	1.41	21621	23350	26769	33977	12356
89	53	71	7.60	7.93	2.07	0.59	9575	13973	12309	16766	7191
108	53	69	6.10	6.28	1.65	0.44	9382	16582	11575	19412	10030
126	50	67	5.11	5.25	1.36	0.35	8781	9184	10588	10995	2215

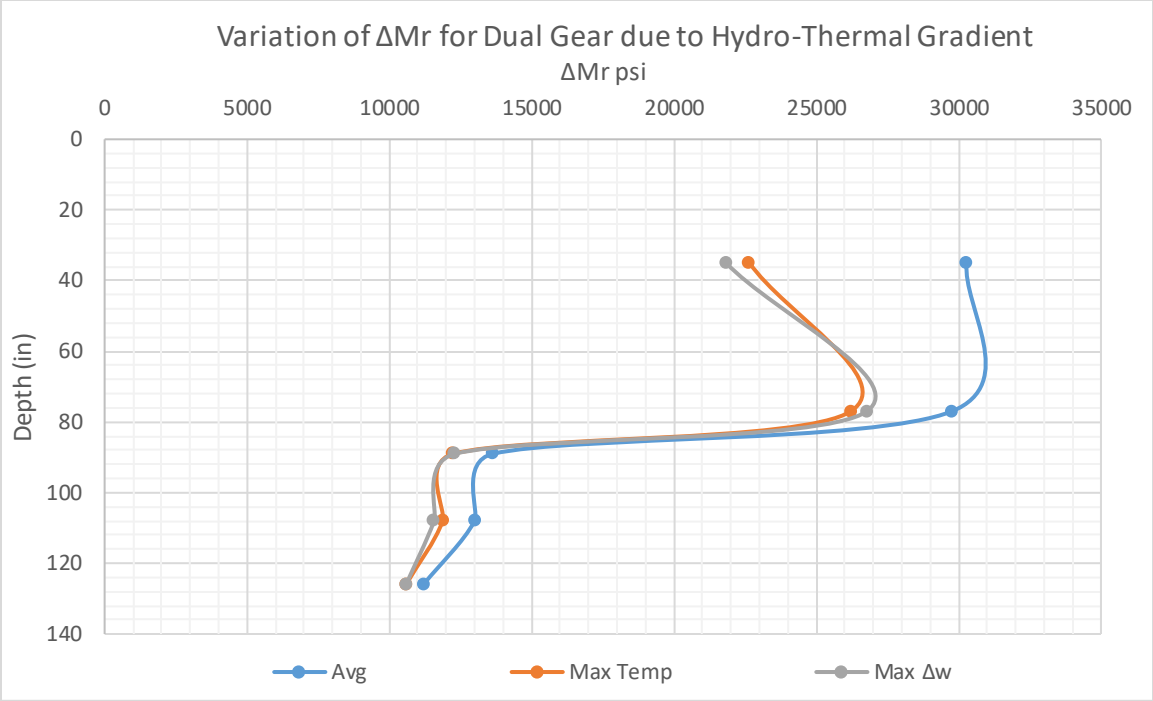

Figure 9.11 Variation of M_r Due to Hydro-Thermal Gradient For Dual Gear

Dual Tandem Gear

Due to Hydraulic gradient

Table 9.15 shows the variation of the stress state parameters and the M_r of the soil for the three cases considered. The maximum variation of the M_r was found when there is maximum variation of water content. The maximum variation of M_r recorded was 7.5 ksi in Dupont clay at 35" and 6.13 ksi in County clay at 108". The maximum bulk and octahedral stress was recorded in the top of the subgrade. The combination of the load stress applied and the moisture content present influenced the change in the M_r. Figure 9.12 shows the variation of M_r with respect to depth.

Table 9.15. Variation of M_r Due to Hydraulic Gradient for Dual Tandem Gear

			Dual Tandem		Matric Suction		Mr		
Depth	Initial S	Initial Suction	Bulk Stress	Oct Stress	Min	Max	min	Max	Change in Mr
in	%		psi	psi	psi	psi	psi	psi	
Average of all Locations									
35	91.54	44.96	28.79	8.11	6.96	59.47	13292.97	17840.34	4547.37
77	95.49	26.11	15.36	4.31	17.40	44.96	18300.23	21222.35	2922.12
89	92.29	2.76	11.45	3.41	1.16	10.15	8521.61	10204.25	1682.64
108	92.29	2.76	8.20	2.87	0.15	4.35	8069.31	8918.80	849.49
126	94.02	1.16	5.69	2.48	0.15	1.45	7589.82	7850.88	261.06
For Max Temperature Difference									
35	91.54	44.96	28.79	8.11	6.96	87.02	13292.97	19239.85	5946.88
77	95.49	26.11	15.36	4.31	20.31	59.47	18682.62	22355.47	3672.85
89	92.29	2.76	11.45	3.41	2.18	5.80	8736.43	9446.00	709.57
108	92.29	2.76	8.20	2.87	0.36	4.35	8116.56	8918.80	802.25
126	94.02	1.16	5.69	2.48	0.00	1.74	7560.28	7907.16	346.88
For Max W/c Difference									
35	91.54	44.96	28.79	8.11	2.18	94.27	12522.53	19559.16	7036.63
77	95.49	26.11	15.36	4.31	17.40	60.92	18300.23	22459.20	4158.97
89	92.29	2.76	11.45	3.41	1.74	26.11	8645.34	12449.96	3804.62
108	92.29	2.76	8.20	2.87	1.52	49.31	8361.88	14502.26	6140.39
126	94.02	1.16	5.69	2.48	0.00	1.45	7560.28	7850.88	290.60

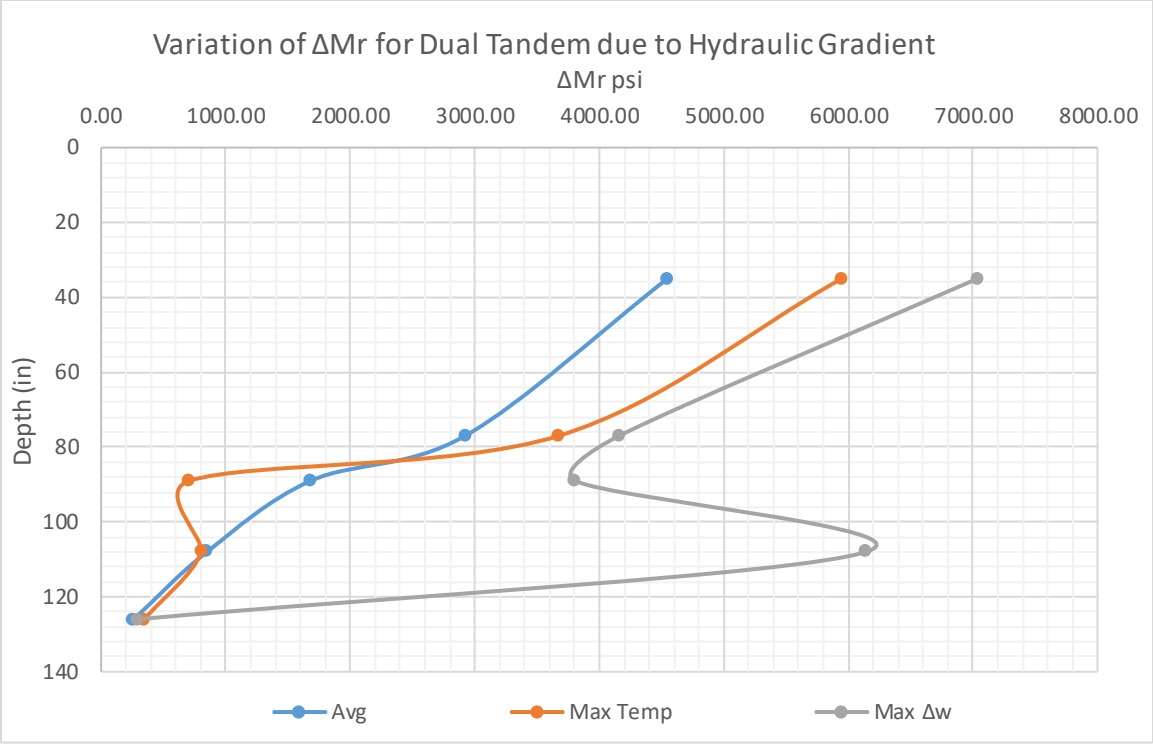

Figure 9.12. Variation of M_r Due to Hydraulic Gradient for Dual Tandem Gear

Due to Hydro-Thermal Gradient

Table 9.16 shows the variation of the stress state parameters and the M_r of the soil for the three cases considered for a dual Tandem gear for hydro-thermal gradient. The variation of the both the load stresses and the suction stress changes were considered and the M_r value was found. As previous sections, the maximum variation of the M_r was found when there is maximum variation of water content. The maximum variation of M_r recorded was 11.6 ksi in Dupont clay at 77" and 6.8 ksi in County clay at 108". The maximum bulk and octahedral stress was recorded in the top of the subgrade. The combination of the load stress applied and the moisture content present influenced the change in the M_r. Figure 9.13 shows the variation of M_r with respect to depth due to Hydro-thermal gradients.

Table 9.16. Variation of M_r Due to Hydro-Thermal Gradient for Dual Tandem Gear

			Dual Tandem				Mr				
			Bulk Stress		Oct Stress		Min Temperature		Max Temperature		
Depth	Min temp	Max temp	For Min Temp	For Max Temp	For Min Temp	For Max Temp	Suction for Min w/c	Suction for Max w/c	Suction for Min w/c	Suction for Max w/c	Change in M_r
in	^{0}F	^{0}F	psi	psi	psi	psi	psi	psi	psi	psi	
Average of all Locations											
28.79	42	78	26.51	30.42	7.10	8.59	22447	15300	17162	12889	9557
77	50	73	14.12	15.43	3.84	4.33	24448	20493	22228	19836	4612
89	51	71	10.65	11.46	3.09	3.42	10221	8647	9706	8488	1733
108	53	68	7.78	8.24	2.66	2.89	9331	8197	9432	8062	1370
126	53	67	5.47	5.74	2.33	2.51	7992	7642	7952	7551	441
For Max Temperature Difference											
35	42	78	26.51	30.42	7.10	8.59	15780	24042	12990	18468	11052
77	50	73	14.12	15.43	3.84	4.33	22030	24712	19681	22175	5031
89	51	71	10.65	11.46	3.09	3.42	9117	9962	8734	9444	1227
108	53	68	7.78	8.24	2.66	2.89	8920	9116	8632	8910	484
126	53	67	5.47	5.74	2.33	2.51	7642	8077	7550	7869	526
For Max W/c Difference											
35	41	77	26.48	30.29	7.08	8.55	22506	15341	17205	12921	9585
77	50	72	14.13	15.38	3.85	4.32	24441	20487	22243	19849	4591
89	53	71	10.68	11.51	3.11	3.43	10200	8629	9697	8480	1720
108	53	69	7.78	8.25	2.66	2.89	9332	8198	9431	8061	1370
126	50	67	5.42	5.73	2.29	2.51	8029	7678	7954	7553	477

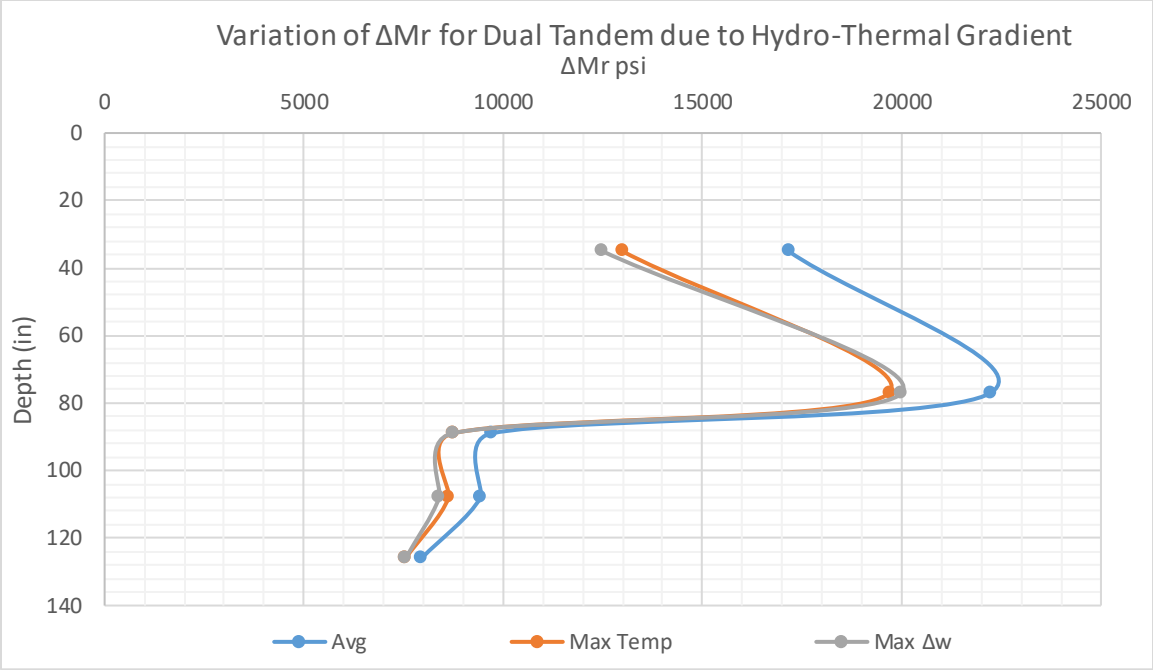

Figure 9.13. Variation of M_r due to Hydro-Thermal Gradient for Dual Tandem Gear

Triple Tandem Gear

Due to Hydraulic Gradient

Table 9.17 shows the variation of the stress state parameters and the M_r of the soil for the three cases considered. The maximum variation of the M_r was found when there is maximum variation of water content. The maximum variation of M_r recorded was 7.6 ksi in Dupont clay at 35" and 6.4 ksi in County clay at 108". The maximum bulk and octahedral stress was recorded in the top of the subgrade. The combination of the load stress applied and the moisture content present influenced the change in the M_r. Figure 9.14 shows the variation of M_r with respect to depth.

Table 9.17. Variation of M_r Due to Hydraulic Gradient for Triple Tandem Gear

					Matric Suction		M_r		
Depth	Initial S	Initial Suction	Bulk Stress	Oct Stress	Min	Max	min	Max	Change in M_r
in	%		psi	psi	psi	psi	psi	psi	
Average of all Locations									
35	91.54	44.96	34.97	8.30	6.96	59.47	14352.55	19262.40	4909.84
77	95.49	26.11	18.84	5.00	17.40	44.96	18275.23	21193.35	2918.13
89	92.29	2.76	14.49	3.98	1.16	10.15	8468.74	10140.94	1672.20
108	92.29	2.76	10.78	3.47	0.15	4.35	8063.88	8912.80	848.92
126	94.02	1.16	7.89	3.09	0.15	1.45	7703.46	7968.42	264.96
For Max Temperature Difference									
35	91.54	44.96	34.97	8.30	6.96	87.02	14352.55	20773.45	6420.90
77	95.49	26.11	18.84	5.00	20.31	59.47	18657.09	22324.93	3667.83
89	92.29	2.76	14.49	3.98	2.18	5.80	8682.22	9387.39	705.17
108	92.29	2.76	10.78	3.47	0.36	4.35	8111.09	8912.80	801.71
126	94.02	1.16	7.89	3.09	0.00	1.74	7673.47	8025.54	352.07
For Max W/c Difference									
35	91.54	44.96	34.97	8.30	2.18	94.27	13520.70	21118.22	7597.52
77	95.49	26.11	18.84	5.00	17.40	60.92	18275.23	22428.52	4153.29
89	92.29	2.76	14.49	3.98	1.74	26.11	8591.70	12372.71	3781.01
108	92.29	2.76	10.78	3.47	1.52	49.31	8356.25	14492.50	6136.25
126	94.02	1.16	7.89	3.09	0.00	1.45	7673.47	7968.42	294.95

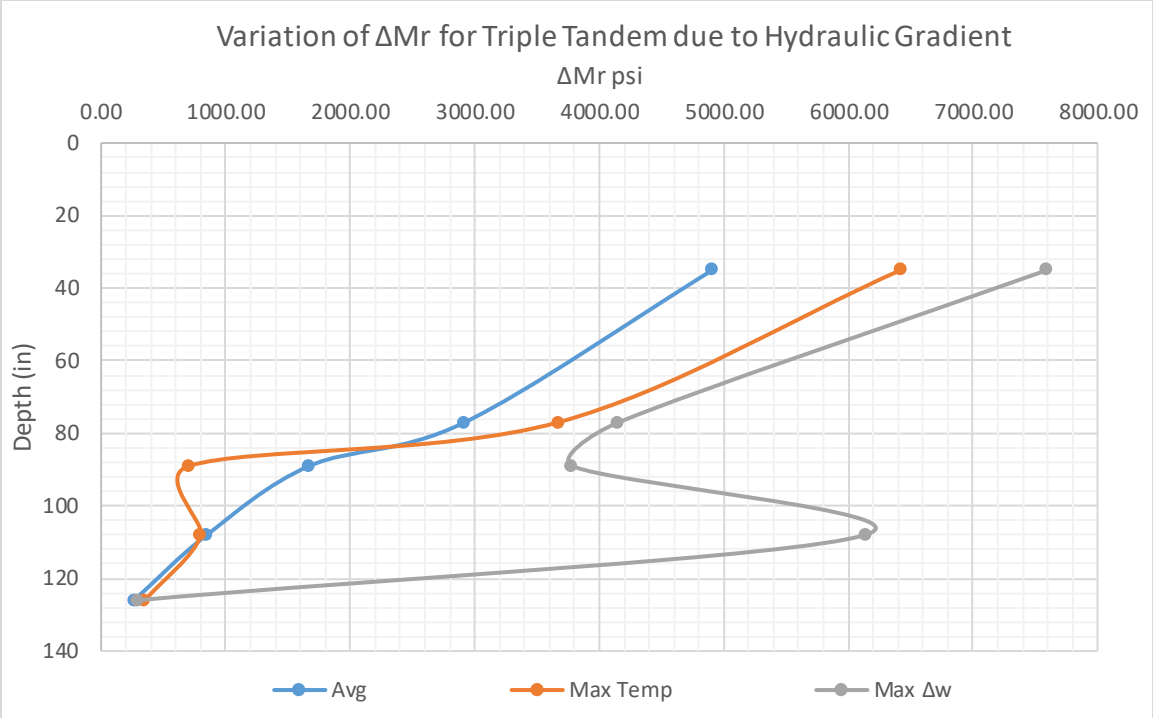

Figure 9.14. Variation of M_r Due to Hydraulic Gradient for Triple Tandem Gear

Due to Hydro-Thermal Gradient

Table 9.18 shows the variation of the stress state parameters and the M_r of the soil for the three cases considered for a Triple Tandem gear for hydro-thermal gradient. The variation of the both the load stresses and the suction stress changes were considered and the M_r value was found. The maximum variation of M_r recorded was 12.4 ksi in Dupont clay at 77" and 7.0 ksi in County clay at 108". The maximum bulk and octahedral stress was recorded in the top of the subgrade. Both maximum variations of the M_r was found when there is maximum variation of water content. The combination of the load stress applied and the moisture content present influenced the change in the M_r. Figure 9.15 shows the variation of M_r with respect to depth due to Hydro-thermal gradients.

Table 9.18. Variation of M_r Due to Hydro-Thermal Gradient for Triple Tandem Gear

							Mr				
			Bulk Stress		Oct Stress		Min Temperature		Max Temperature		
Depth	Min temp	Max temp	For Min Temp	For Max Temp	For Min Temp	For Max Temp	Suction for Min w/c	Suction for Max w/c	Suction for Min w/c	Suction for Max w/c	Change in M_r
in	^{0}F	^{0}F	psi	psi	psi	psi	psi	psi	psi	psi	
Average of all Locations											
35	42	78	32.85	36.34	7.42	8.75	24025	16376	18428	13840	10185
77	50	73	17.87	18.90	4.52	5.02	24793	20783	22170	19784	5009
89	51	71	13.87	14.49	3.64	3.99	10256	8676	9644	8434	1822
108	53	68	10.49	10.81	3.24	3.49	9412	8268	9415	8048	1368
126	53	67	7.76	7.92	2.92	3.12	8186	7828	8054	7648	538
For Max Temperature Difference											
35	42	78	32.85	36.34	7.42	8.75	16889	25733	13948	19830	11785
77	50	73	17.87	18.90	4.52	5.02	22342	25061	19630	22117	5431
89	51	71	13.87	14.49	3.64	3.99	9148	9996	8679	9384	1317
108	53	68	10.49	10.81	3.24	3.49	8998	9194	8617	8895	578
126	53	67	7.76	7.92	2.92	3.12	7827	8272	7647	7970	625
For Max W/c Difference											
35	41	77	32.82	36.23	7.40	8.72	24073	16408	18485	13882	10191
77	50	72	17.88	18.86	4.52	5.00	24785	20776	22205	19815	4971
89	53	71	13.90	14.53	3.66	4.00	10233	8657	9627	8419	1814
108	53	69	10.49	10.81	3.24	3.49	9412	8269	9413	8046	1367
126	50	67	7.73	7.91	2.88	3.11	8236	7875	8059	7652	584

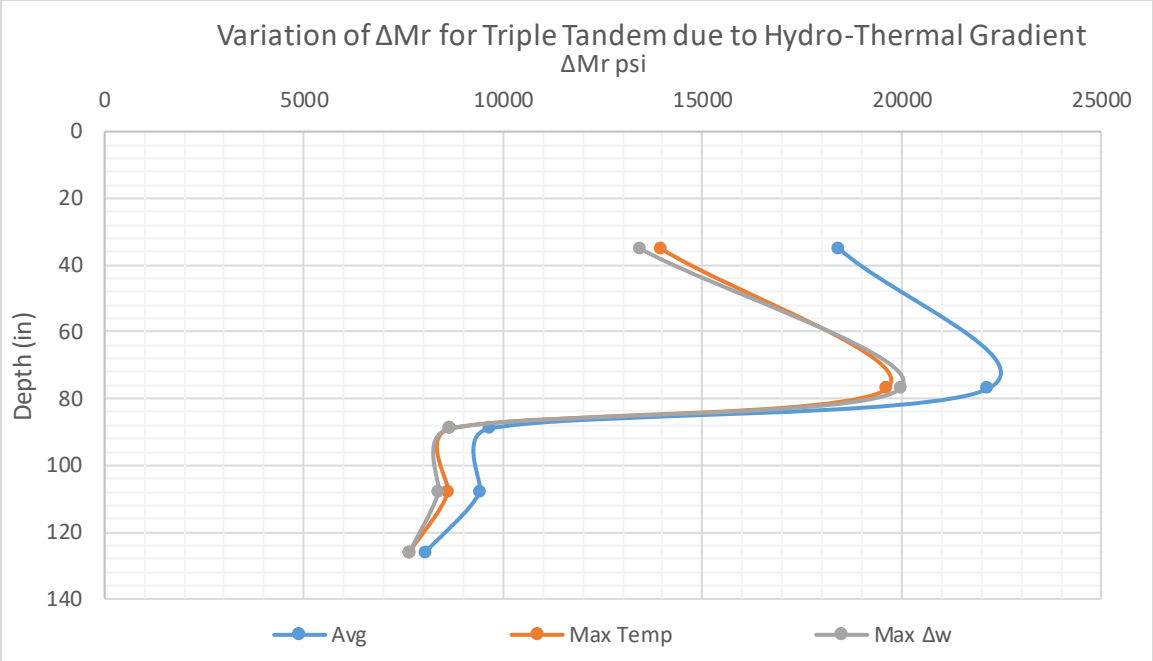

Figure 9.15. Variation of M_r Due to Hydro-Thermal Gradient for Triple Tandem Gear

Comparison of Gear Types

The Gear types are compared in this section to study the influence of the change in the gear type on the Mr of the subgrade. Since, it was observed that the maximum variations of Mr occurred when the change in the moisture content is maximum. A comparison of the three gear types have been performed for the ΔMr when there is a maximum change in moisture content. Figure 9.16 and Figure 9.17 shows the comparison of the ΔM_r for Dual gear with Dual tandem and triple tandem gear for Hydraulic gradients and Hydro-thermal gradients respectively. The figures clearly show that Dual gear which exhibits less amount of load compared to other two exhibits higher resilient modulus. When considering as a whole for all the gear types, the change in M_r that can be expected is 22ksi when considering both Hydro-thermal gradients whereas when you consider just the hydraulic gradients, a M_r

change of 15 ksi is observed. Hence it is foremost important that the impact of thermal gradients along with the hydraulic gradients should be considered when determining the strength of the subgrade soil and leads to accurate prediction of the design.

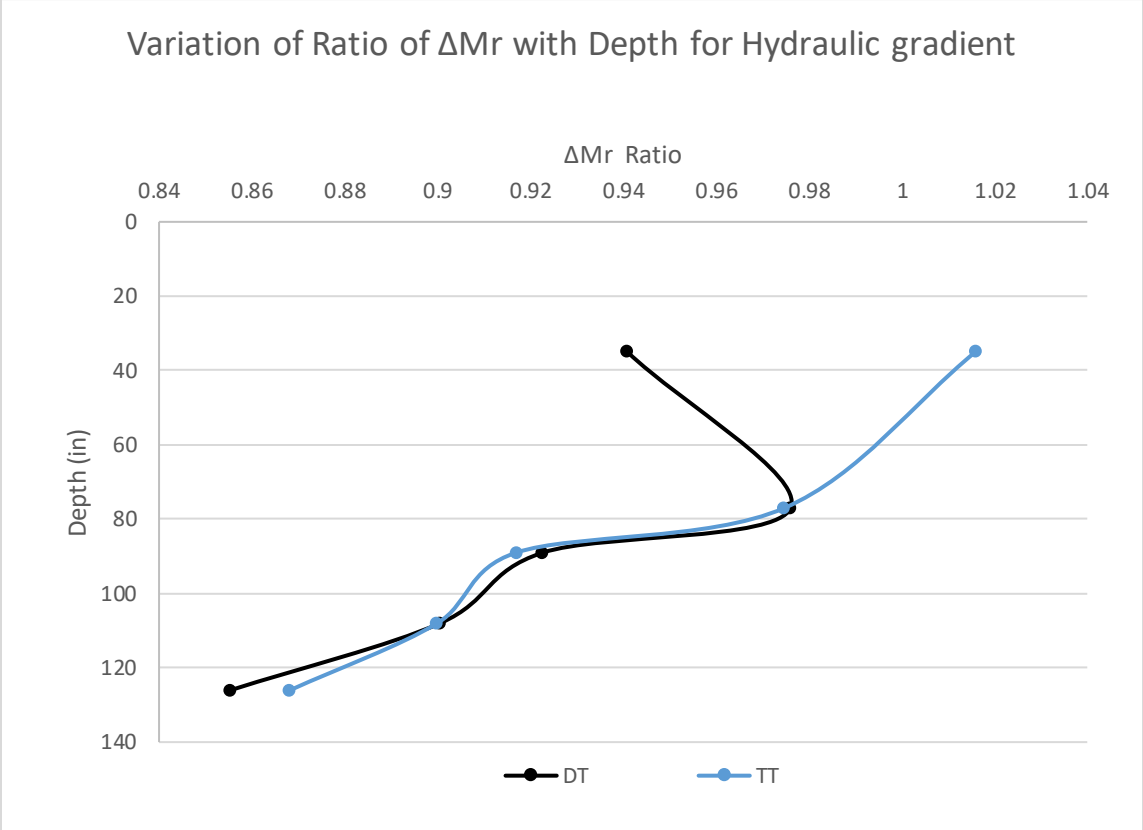

Figure 9.16. Ratio of Variation of M_r in NAPTF for Dual Gear Compared to Dual Tandem and Triple Tandem Gear Type Due to Hydraulic Gradients with Depth

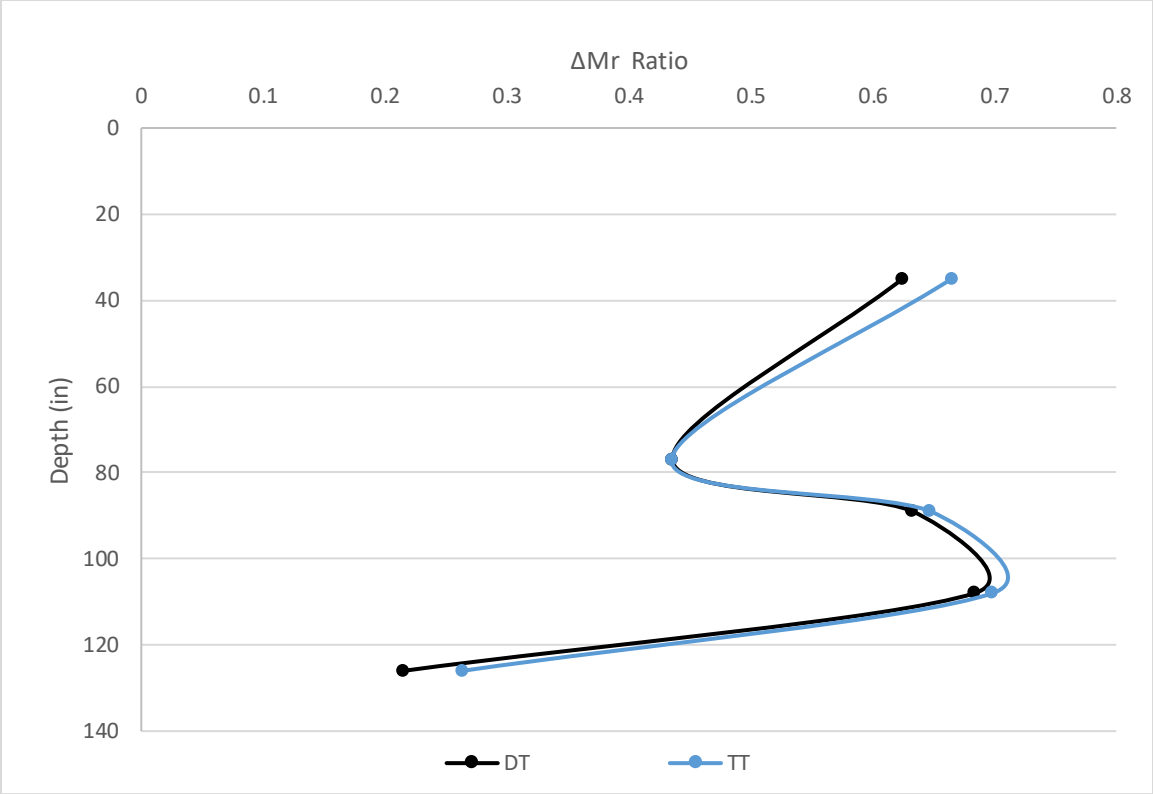

Figure 9.17. Ratio of Variation of Mr in NAPTF for Dual Gear Compared to Dual Tandem and Triple Tandem Gear Type Due to Hydro-Thermal Gradients With Depth

FINAL SUMMARY

This chapter has presented the results of the potential influence, upon both clay layers, of thermo-hydraulic moisture changes upon the CBR, Vss (vane shear) and M_r (resilient moduli) estimated from two widely used empirical models relating CBR to M_r.

As has been previously stated, the changes in moisture content within the clays caused by this several thermal influence are not considered significantly large, by an absolute measure standard. The range was found to decrease with depth into NAPTF pavement section and varied from a difference (w_{max}-w_{min}) of approximately 2.0% for upper Dupont Sublayer No. 1 to approximately 1.5% for the lowest County Sublayer No. 2. These numbers are

based upon difference between the average seasonal extremes, at all location for a given depth. If one considers the extreme difference at a given sensor set and location these values change to 4.3% and 2.3%.

Thus, for the upper Dupont No.1 layer, the mean sublayer moisture of w= 27.0% will range, on average, between w= 25.9% and w= 28.1%, throughout an annual cycle of testing at the NAPTF facility.

Nonetheless, while the moisture changes may appear to be inconsequential (or small); it is extremely important that they should be viewed relative to their respective changes in strength and resilient moduli that will be occurring at the facility. This situation is indeed magnified by the fact that the FAA NAPTF facility has been purposely constructed to maintain very low CBR/M_r populations during the history of performance testing at the facility. thus, what may be viewed as an insignificant measure moisture content variation of w=25.9% to w= 28.1%, may lead to annual mean variations (for the upper part Dupont clay layer) of CBR= 4.1% to CBR= 6.3%. Because of the highly sensitive drop in performance with thickness, caused by lower CBR strengths; the impact of these thermally induced changes in soil strength and resilient modulus should not be overlooked in any performance.

The model representing the resilient modulus which incorporates bulk stress, octahedral stress and suction stress parameters which are influenced by temperature shows that thermally induced changes can cause a wide effect in the performance of the subgrade. The change in the strength of the soil can be underestimated as 7.5 ksi due to just the hydraulic gradients when the actual change in the modulus can be as big as 18 ksi.

Chapter 10. : Modeling Temperature and Moisture Flow in NAPTF due to Changes in Hydraulic and Thermal Properties due to Temperature Variability

The goal of this study was to investigate the influence of temperature on the hydraulic and thermal properties and how it affects moisture and thermal flows in two different subgrade layers. This numerical study is comprised of three sensitivity analysis using different unsaturated hydraulic and thermal properties obtained at 20°C, at 5°C (low temperature measured in the NAPTF facility) and 26°C (highest temperature observed in the facility). All material properties and boundary conditions were kept constant except for the unsaturated hydraulic and thermal properties. The laboratory-obtained SWCC and unsaturated hydraulic conductivity functions at the three temperatures were used for these models. This analysis allowed to indirectly consider the thermal effect using a coupled hydro-thermal model.

Based upon the data recorded and investigated in Chapter 8. The temperature and the moisture content data obtained from the modeling is compared with the actual data obtained from 5TM Decagon sensor.

INTRODUCTION TO CODE BRIGHT GID

The Code Bright program is a tool designed to handle coupled problems in geological media. The program has been generalized for modelling thermo-hydro-mechanical (THM) processes in a coupled way in geological media. Basically, the code couples mechanical, hydraulic and thermal problems in geological media. The theoretical approach consists in a set of governing equations, a set of constitutive laws and a special computational approach. CODE_BRIGHT uses GiD system for preprocessing and post-processing. GiD is developed by the International Center for Numerical Methods in Engineering (CIMNE).

GiD is an interactive graphical user interface that is used for the definition, preparation and visualisation of all the data related to numerical simulations. This data includes the definition of the geometry, materials, conditions, solution information and other parameters. The program can also generate the finite element mesh and write the information for a numerical simulation program in its adequate format for CODE_BRIGHT. It is also possible to run the numerical simulation directly from the system and to visualize the resulting information without transfer of files.

The governing equations for non-isothermal multiphase flow of water and gas through media have been presented by Olivella et al. (1994). The procedure used to seek the solution process is as follows:

- Define geometry - points, lines, surfaces, volumes.
- Define attributes and conditions.
- Generate mesh.
- Carry out simulation.
- View results

The following sections describes the step by step procedure to obtain the temperature and liquid saturation of the subgrade with time.

GEOMETRY

Figure 10.1 shows the geometry used for the NAPTF. The model consists of a base , base, two layers of Dupont subgrade and two layers of County subgrade. All measurements are shown in inches.

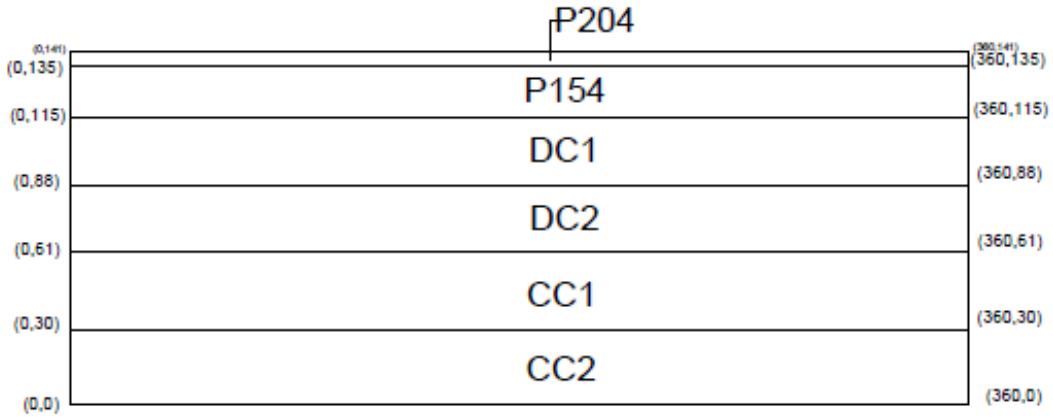

Figure 10.1. Geometry and Coordinates Entered for Pavement Layers in NAPTF

MATERIAL PROPERTIES

The properties of the material entered into the program can be divided into three categories: mechanical properties, Hydraulic Properties, Thermal Properties and Solid phase properties. For this study, hydraulic properties, thermal properties and solid phase properties are used for this study. Table 10.1 shows the in-situ compaction properties and soil index properties of the different layers of the pavement.

Table 10.1. Compaction Properties of Pavement Subgrade Layer.

Property	P 209	P 154	DC 1	DC 2	CC 1	CC2
Gs	2.65	2.7	2.79	2.79	2.84	2.84
dry density(pcf)	124.32	146.06	95.50	83.40	99.00	96.80
Dry Density (kg/m^3)	1991.61	2339.88	1529.91	1336.07	1585.98	1550.74
Gravimteric Moisture Content (%)	1.86	3.80	27.00	37.20	25.70	27.50
Volumteric Moisture content (%)	3.71	8.89	41.32	49.72	40.77	42.66
void ratio	0.330	0.153	0.823	1.087	0.790	0.831
density of water (pcf)	62.4	62.4	62.4	62.4	62.4	62.4
porosity	0.248	0.133	0.451	0.521	0.441	0.454

Hydraulic Properties

The hydraulic properties entered into the Code Bright GiD includes the retention curve, intrinsic permeability, and liquid relative permeability.

The retention curve used is Van Genuchten model

$$S_l = S_{rl} + \frac{S_{ls} - S_{rl}}{\left(1 + \left(\frac{P_g - P_l}{P}\right)^{\frac{1}{1-\lambda}}\right)^{\lambda}}$$

Where P is the related to air entry value, λ related to the shape of the curve, S_{rl} is residual saturation and S_{ls} is the maximum saturation.

The intrinsic permeablity of the soil is caluclted using Kozeny's model for the continuous medium.

$$k = k_0 \frac{\varphi^3}{(1-\varphi)^2} \frac{(1-\varphi_0)^2}{{\varphi_0}^3}$$

Where φ_0 is refrence porpsity and k_0 is the intrinsic permeability for φ_0.

Liquid phase permeability used the Van Genuchten model

$$k_{rl} = \sqrt{S_e}\left(1 - \left(1 - S_e^{\frac{1}{\lambda}}\right)^{\lambda}\right)^2$$

Table 10.2 shows the hydraulic properties of the soil for the three temperatures used in the model.

Thermal Properties of Pavement Layers

The thermal properties of the soil entered include the thermal conductivity of the dry porous medium, thermal conductivity of saturated porous medium, solid phase specific cheat capacity and solid phase density. Table 10.3 shows the thermal properties of the pavement layers.

Table 10.2. Hydraulic Properties of Pavement Layers

Property		P 209	P 154	DC 1			DC 2			CC 1			CC 2		
Temp ^{0}C				Normal	High	Low	Normal	High	Low	Normal	High	Low	Normal	High	Low
				20	26.8	5	20	26.8	5	20	26.8	5	20	26.8	5
Retention Curve															
ITYCL		Van Genuchten													
P 1	P_0 (MPa)	1.70 E-04	4.50 E-04	0.8197	0.6705	0.9236	0.8197	0.6705	0.9236	0.0262	0.0373	0.0245	0.0262	0.0373	0.0245
P 2	σ_0 (Nm^{-1})	0.072	0.072	0.072	0.072	0.075	0.072	0.072	0.074	0.073	0.073	0.074	0.072	0.072	0.074
P 3	λ	0.643	0.648	0.227	0.216	0.251	0.227	0.216	0.251	0.136	0.110	0.110	0.110	0.110	0.120
P 4	S_{rl}	0	0	0	0	0	0	0	0	0	0	0	0	0	0
P 5	S_{ls}	1	1	1	1	1	1	1	1	1	1	1	1	1	1
P 9	Φ_0	0.248	0.133	0.451			0.521			0.441			0.454		
Intrinsic Permeability															
ITYCL		Kozeny's Model 1													
P 1	(k_{11}) m^2_0	1.00 E-12	1.00 E-12	4.10159 E-16	4.1531E -16	1.18024 E-15	5.21791 E-16	4.92017 E-16	6.81573 E-16	2.22E -15	1.70833 E-15	7.55576 E-15	7.28717 E-14	3.42126 E-15	4.83078 E-14
P 2	(k_{22}) $_0$ m^2	1.00 E-12	1.00 E-12	4.10159 E-16	4.1531E -16	1.18024 E-15	5.21791 E-16	4.92017 E-16	6.81573 E-16	2.22E -15	1.70833 E-15	7.55576 E-15	7.28717 E-14	3.42126 E-15	4.83078 E-14
P 3	(k_{33}) $_0$ m^2	1.00 E-12	1.00 E-12	4.10159 E-16	4.1531E -16	1.18024 E-15	5.21791 E-16	4.92017 E-16	6.81573 E-16	2.22E -15	1.70833 E-15	7.55576 E-15	7.28717 E-14	3.42126 E-15	4.83078 E-14
P 4	φ_0	0.248	0.133	0.451	0.451	0.451	0.521	0.521	0.521	0.441	0.441	0.441	0.454	0.454	0.454
P 5	Φ_{min}	0.001	0.001	0.001	0.001	0.001	0.001	0.001	0.001	0.001	0.001	0.001	0.001	0.001	0.001

Table 10.3. Liquid Phase Relative Permeability Parameters of Pavement Layers

Property		P 209	P 154	DC 1			DC 2			CC 1			CC 2		
Temperature ^0C				Normal	High	Low	Normal	High	Low	Normal	High	Low	Normal	High	Low
				25	26.8	5	25	24.3	9.3	25	21.9	10	25	19.9	9.8
Liquid Phase Relative Permeability															
ITYCL		1	1	1	1	1	1	1	1	1	1	1	1	1	1
P1	Void														
P2	Void														
P3	λ	0.643	0.648	0.219	0.216	0.251	0.219	0.220	0.244	0.136	0.110	0.110	0.110	0.110	0.120
P4	Srl	0	0	0	0	0	0	0	0	0	0	0	0	0	0
P5	Sls	1	1	1	1	1	1	1	1	1	1	1	1	1	1

Table 10.4. Thermal Properties of Pavement Layers

Property		P 209	P 154	DC 1			DC 2			CC 1			CC2		
Conductive Heat Flux 1															
Temperature ^{0}C				Normal	High	Low	Normal	High	Low	Normal	High	Low	Normal	High	Low
				20	26.8	5	20	26.8	5	20	26.8	5	20	26.8	5
ITYCL		1	1	1			1			1			1		
P1	Thermal Conductivity at dry porous medium (W m K^{-1})	5.03	4.44	1.347	1.33	1.36	1.347	1.33	1.36	1.592	1.54	1.61	1.592	1.54	1.61
P2	Thermal Conductivity at saturated porous medium (W m K^{-1})	5.03	4.44	1.402	1.38	1.42	1.402	1.38	1.42	1.834	1.82	1.85	1.834	1.82	1.85
Solid Phase Properties															
ITYCL		1	1	1			1			1			1		
P1	Solid Phase Specific Heat (Jkg^{-1} K^{-1})	1270	1175	1402.57	1390	1408	1607	1598	1612	1437.74	1428	1444	1470.4	1466	1475
P2	Solid Phase Density (kg m^{-3})	1991.61	2339.88	1529.91			1336.07			1585.98			1550.74		

CONDITIONS

The conditions applied to the pavement layer system are of three types:

Boundary Condition

The boundary conditions applied to the system are of two types. The atmospheric temperature variation which is measured as pavement temperature and collected from NAPTF. The data collected from Chapter 8 is used for the pavement temperature which is applied on top of the geometry. The second is the temperature fluctuation on the edges of the system. Data collected from location B,D and F are used for extreme side of the pavement system are used on the sides of the geometry. Table 10.4 shows the boundary condition used.

Initial Unknowns

The initial unknows entered into the program is initial temperature and initial suction which is entered as liquid pressure. The value are shown in Table 10.5.

Table 10.5. Initial Unknowns of Pavement System

Layer	Depth	Initial Dry density	Initial temp	Initial w/c	Initial S	Initial Suction
	in	pcf	^{0}C	%	%	MPa
P 209	6	124.32	26	1.86	3.7	3.00E-03
P 154	19	146.06	24.75	3.8	9.1	1.50E-02
Dupont	35	95.46	19.6	27.02	91.54	0.31
	77	83.35	22.1	37.25	95.49	0.18
County	89	98.97	21.3	25.69	92.29	0.019
	108	98.97	19.6	25.69	92.29	0.008
	126	96.83	18.5	27.48	94.02	3.00E-03

Initial Porosity

The initial porosity values are entered as shown in Table 10.2.

INTERVAL DATA

Once the material properties are entered, the interval data is entered in such way that the program runs for 33 months. The program was asked to record the data for each and every day all throughout the three years.

POST PROCESSING AND ANALYSIS

The Final process is to create the mesh and then to simulate the program. The program was run for three case of soil properties: 1) Normal Temperature of 20 ^{0}C; 2) High Temperature 26.8 ^{0}C; 3) Low temperature of 5 ^{0}C.

Four graphs were obtained for each case showing the temperature and Liquid saturation degree for near the corner and near the middle of the pavement. Figure 10.2.

The post processing analysis clearly shows that there is a higher variation of temperature and S near the edges (Location B,D and F) rather than the center (Location A, C and E). The lowest point of temperature is found near center of the pavement at the depth of 144" while the highest is at the top of pavement near the edge. All the three cases provide the same analysis.

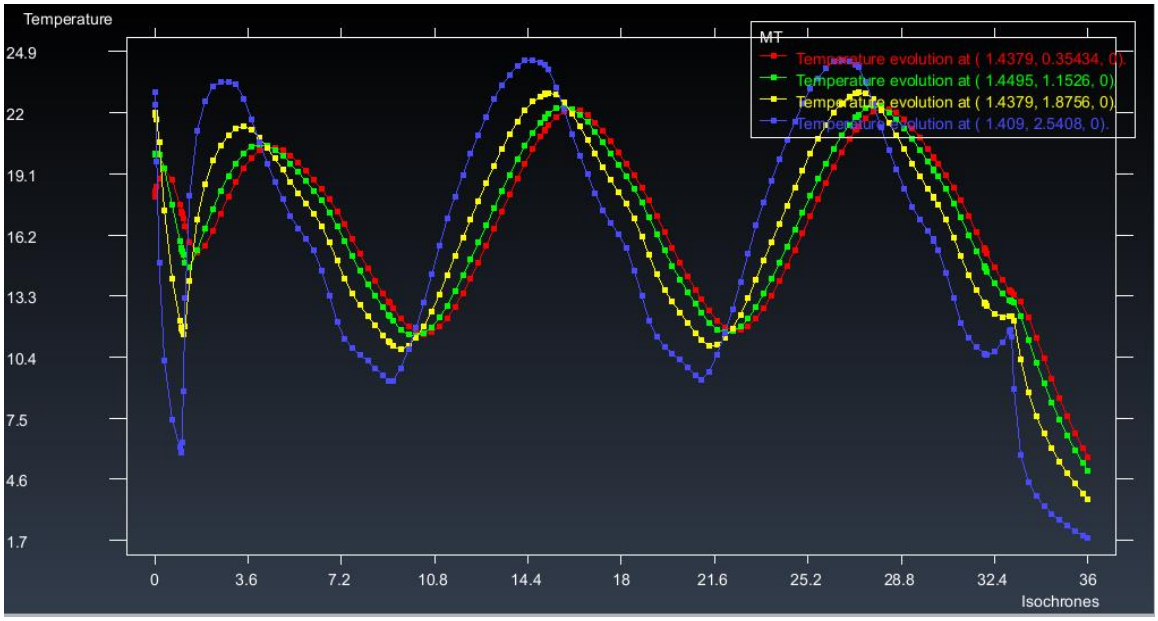

Figure 10.2. Temperature Variation Near Center of Pavement for Normal Temperature Analysis

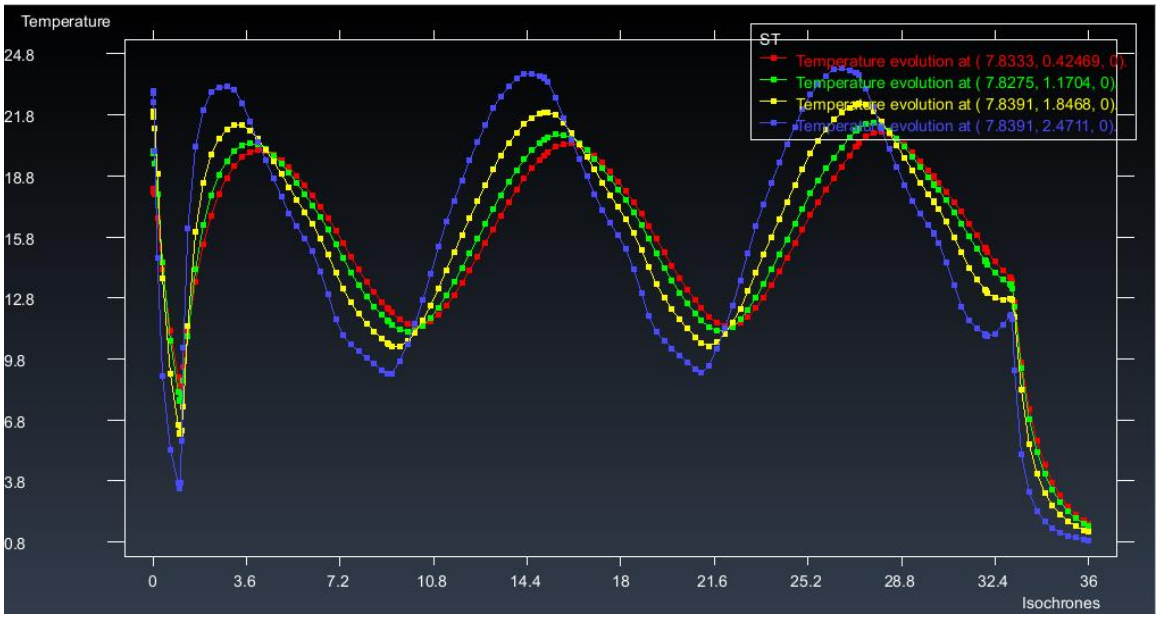

Figure 10.3. Temperature Variation Near Edge of Pavement for Normal Temperature Analysis

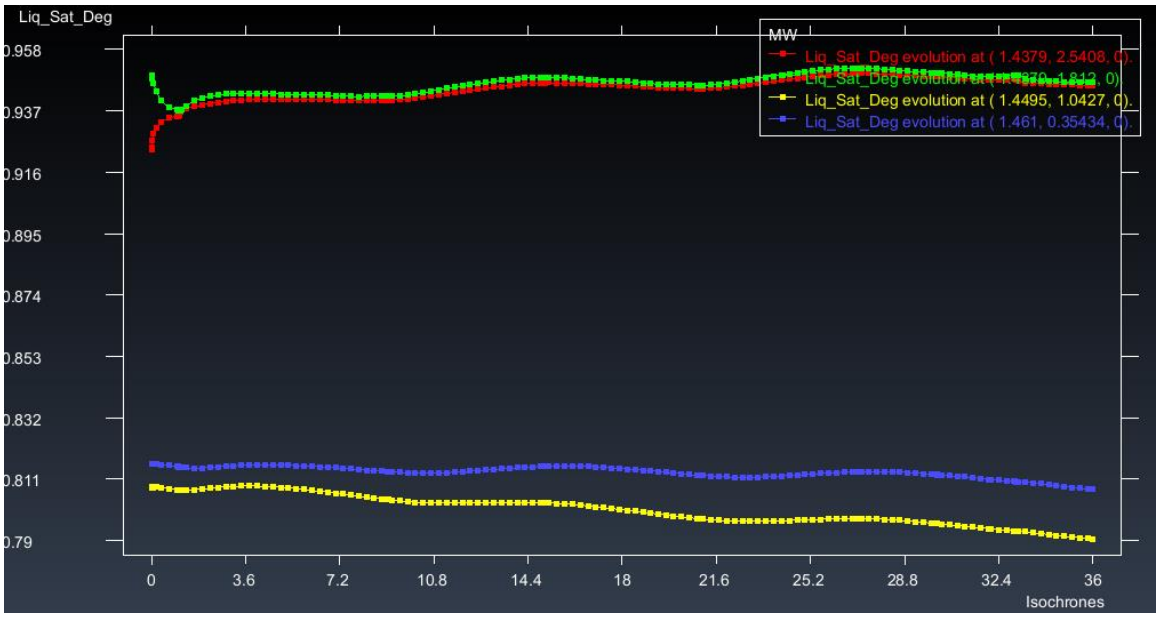

Figure 10.4.Liquid Saturation Degree Variation Near Centre of Pavement for Normal Temperature Analysis

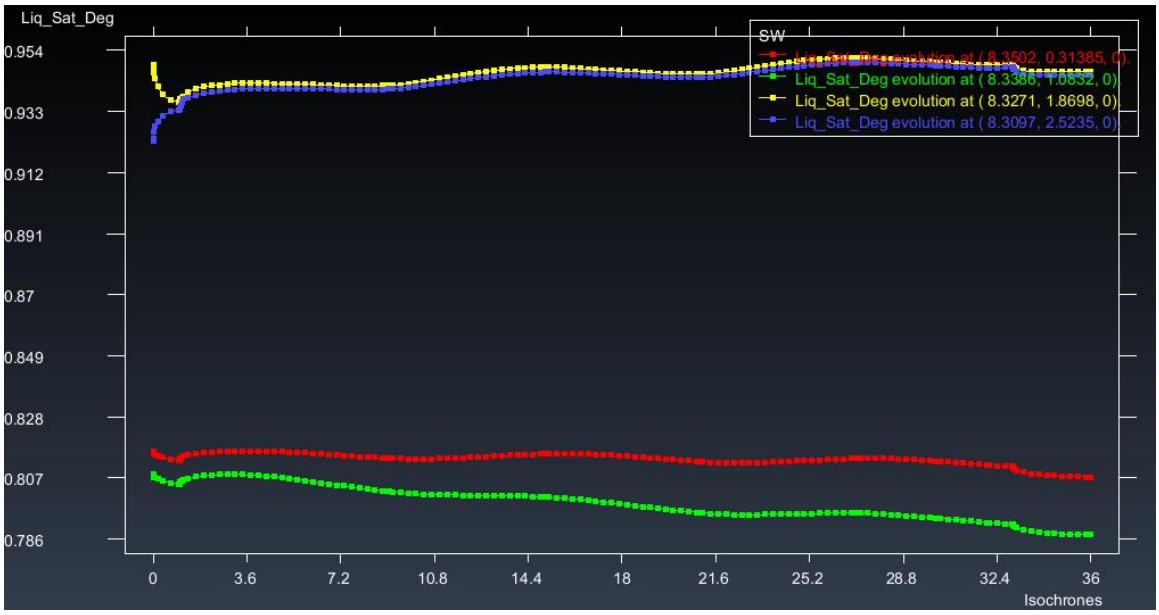

Figure 10.5. Liquid Saturation Degree Variation Near Edge of Pavement for Normal Temperature Analysis

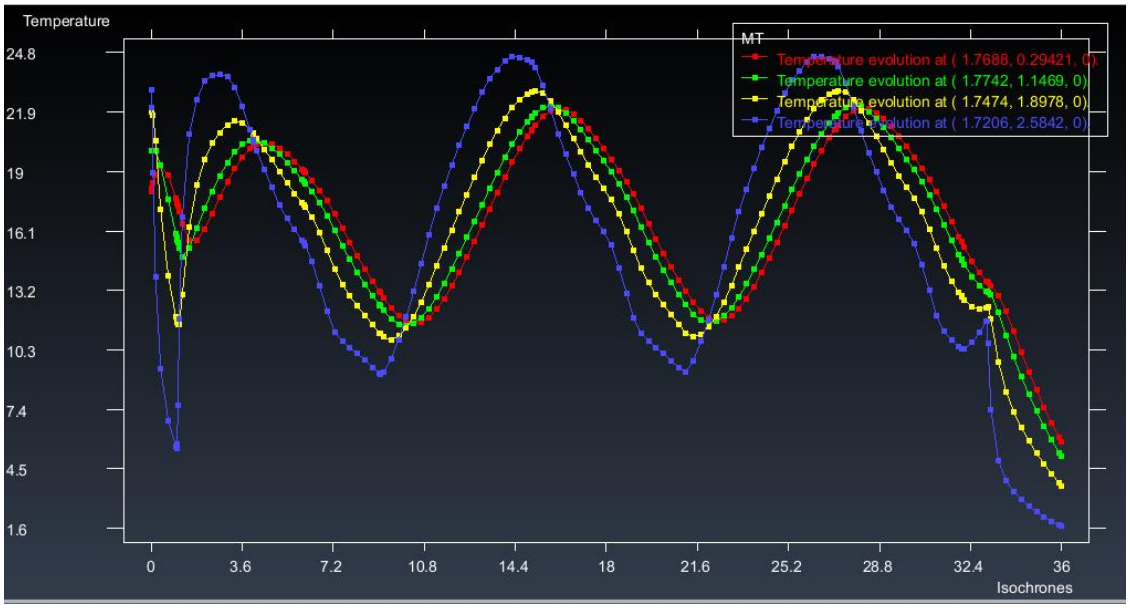

Figure 10.6. Temperature Variation Near Center of Pavement for High Temperature Analysis

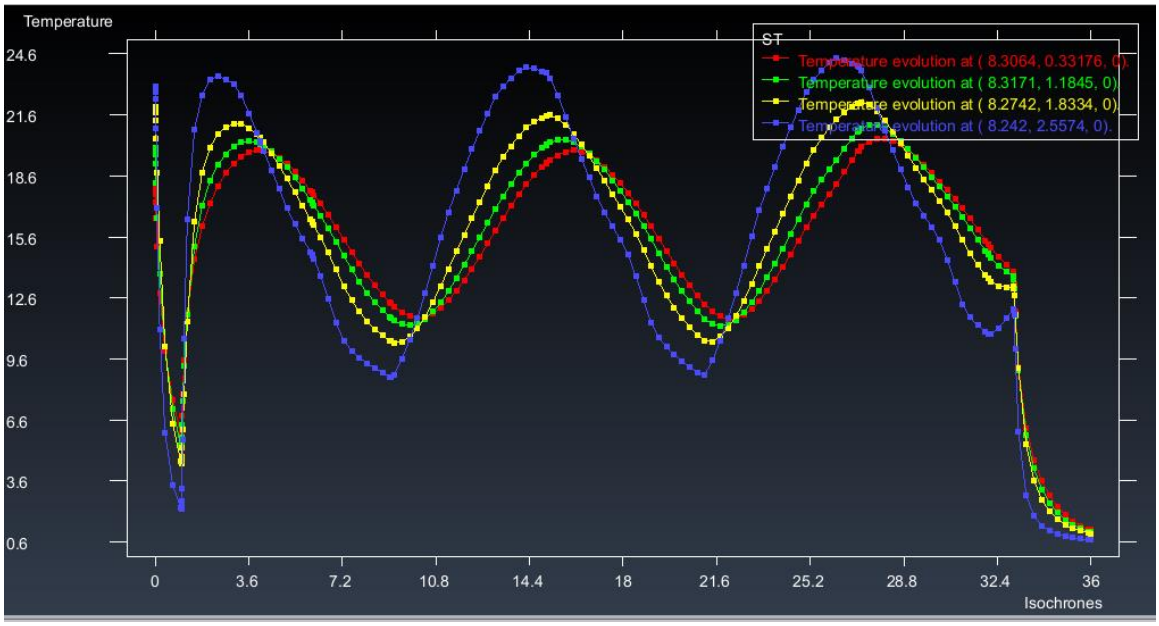

Figure 10.7. Temperature Variation Near Edge of Pavement for High Temperature Analysis

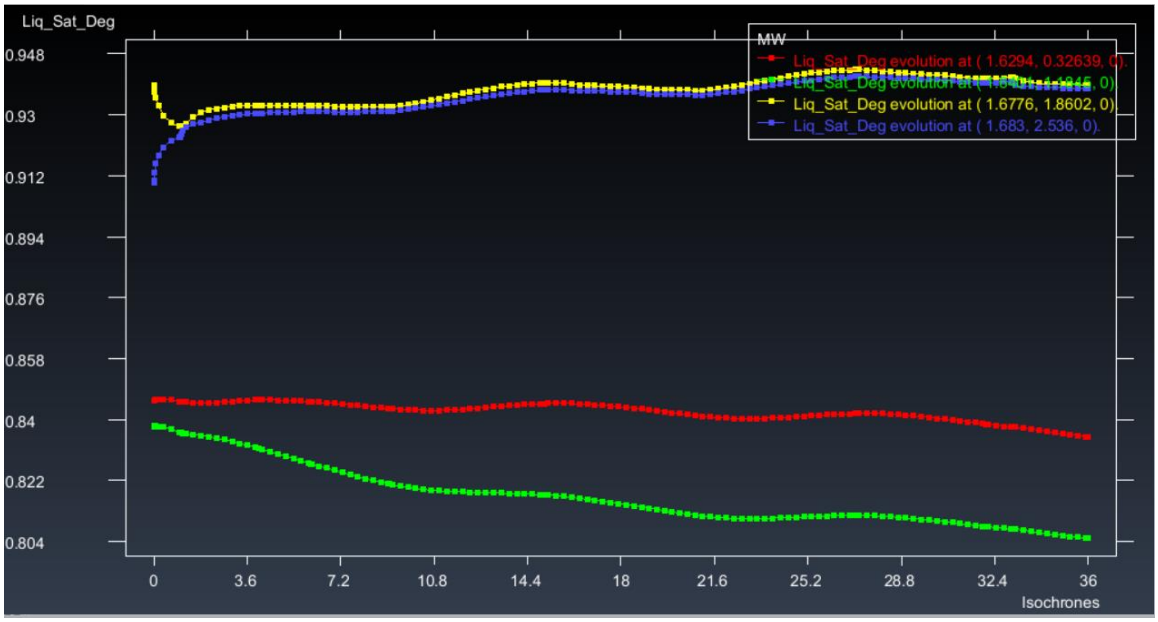

Figure 10.8. Liquid Saturation Degree Variation Near Centre of Pavement for High Temperature Analysis

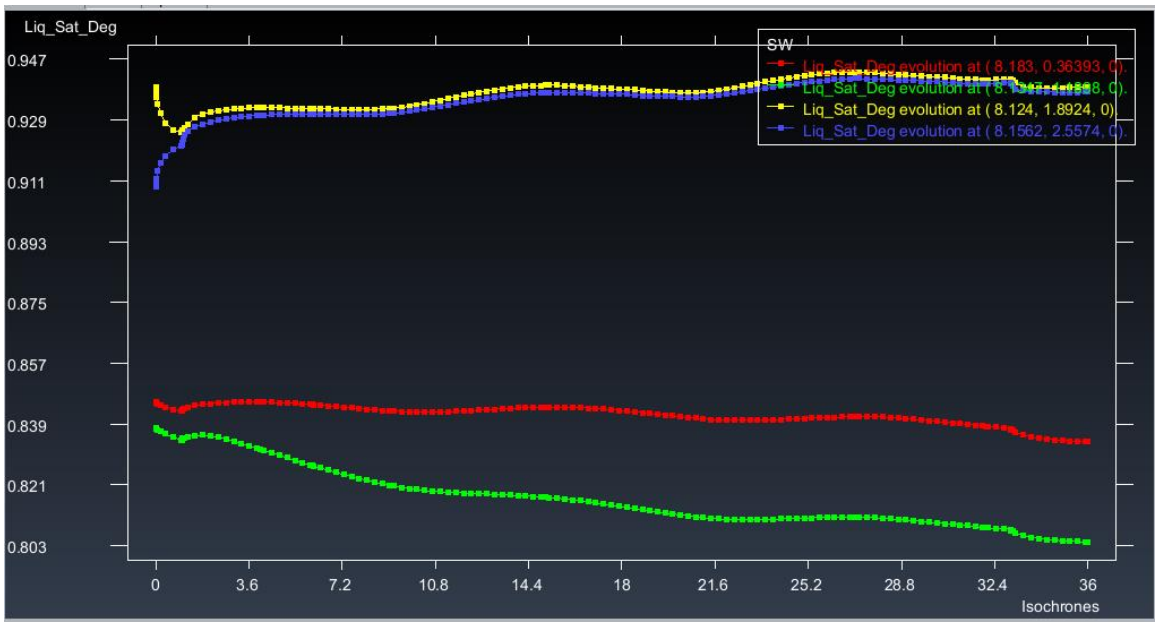

Figure 10.9. Liquid Saturation Degree Variation Near Edge of Pavement for High Temperature Analysis

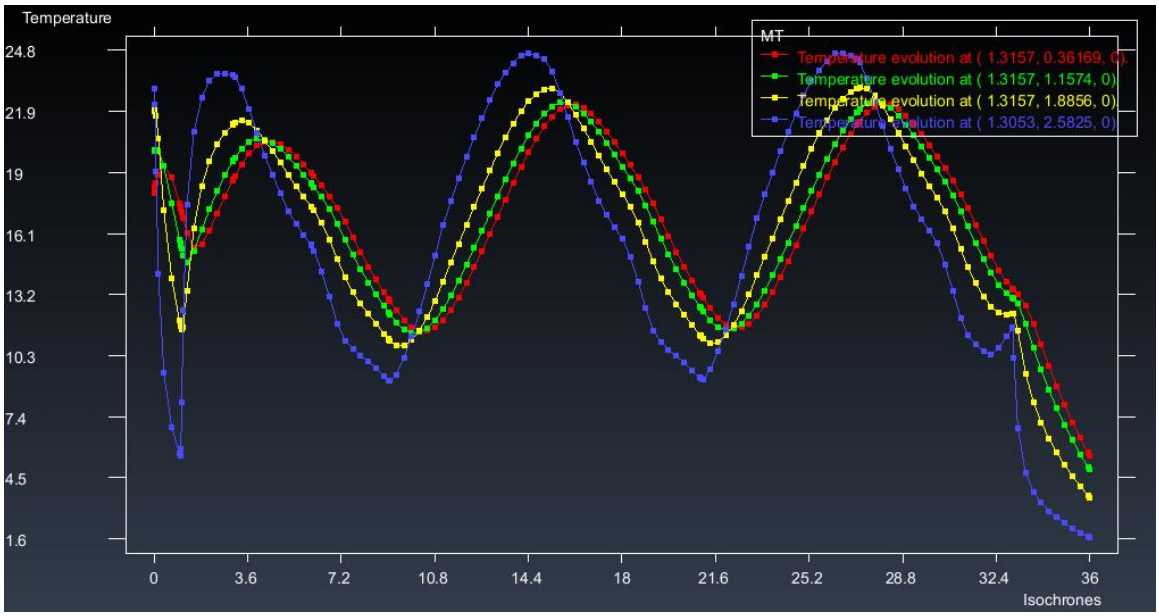

Figure 10.10. Temperature Variation Near Center of Pavement for Low Temperature Analysis

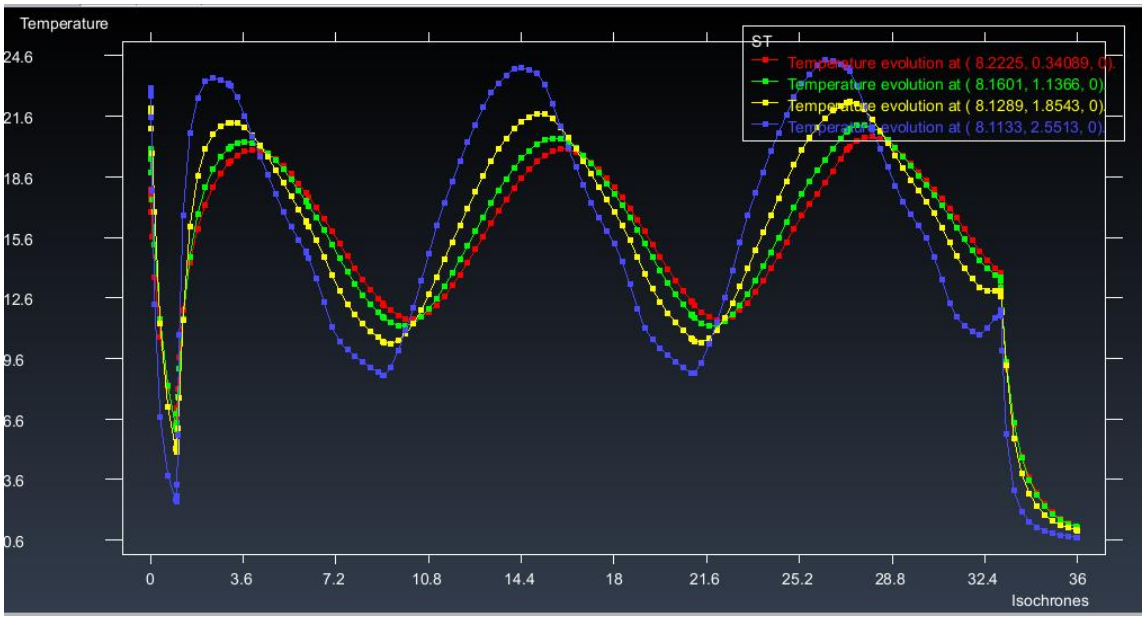

Figure 10.11. Temperature Variation Near Edge of Pavement for Low Temperature Analysis

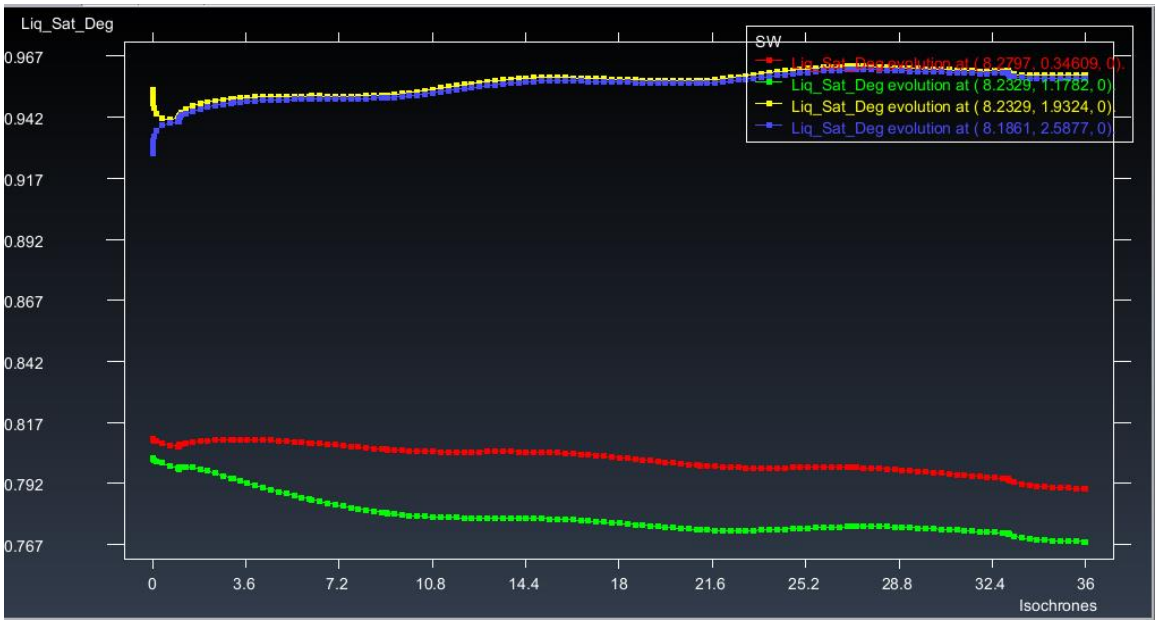

Figure 10.12. Liquid Saturation Degree Variation Near Edge of Pavement for Low Temperature Analysis

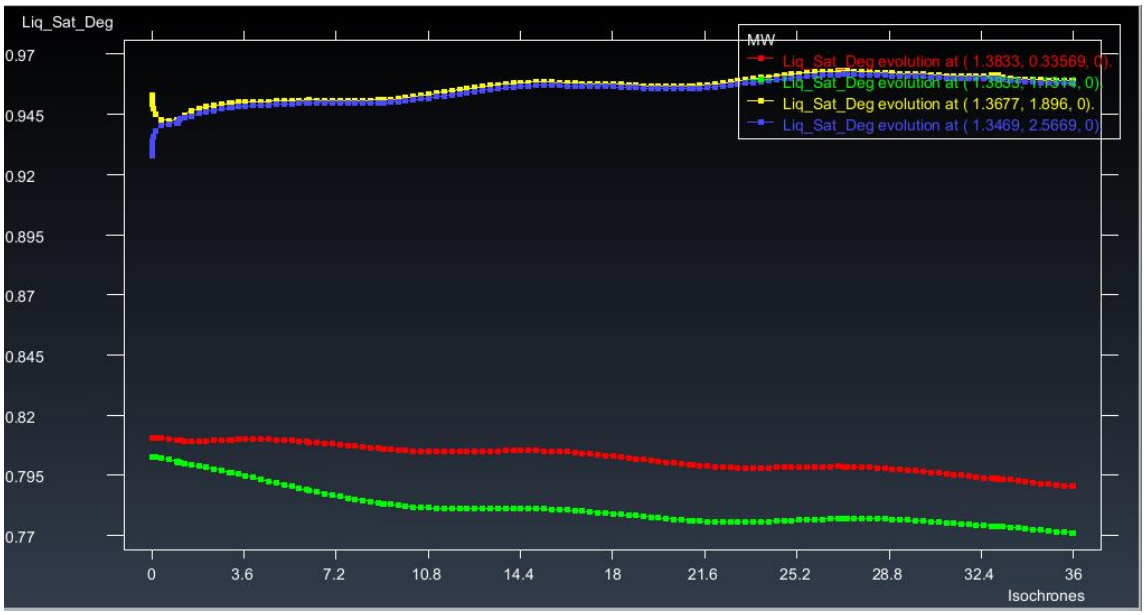

Figure 10.13. Liquid Saturation Degree Variation Near Center of Pavement for Low Temperature Analysis

ANALYSIS OF RESULTS

A comparison of the data collected from the three data sets were analyzed. The data set was then compared with the data measured using the five sensors. The measured temperature and degree of saturation measured after 33 months were plotted against the data predicted using Code-Bright. The three data sets (average, high and low temperature data sets) are shown in Figures 10.14 and 10.15. Figure 10.14 shows the temperature data comparison obtained from the sensors at locations A, C and E. From this graph, it can be seen that the comparison follows the same trend independently of the temperature dataset use in the prediction. It can also be observed that the measured temperature is generally higher than the predicted data. However, it is a good correspondence between the measured and the predicted results, as evidenced by an R^2 of 79%. Variation of thermal conductivity and specific heat capacity due to temperature may have affected the predicted results obtained by Code-Bright, and more investigation is necessary optimize the model.

Figure 10.15 shows the comparison between the measured degree of saturation obtained from sensor at three locations and the data predicted when considering hydraulic and thermal properties obtained at three different temperatures (average, low and high temperatures). It can be observed that the model was not able to accurately predict the changes in the degree of saturation. The prediction of S for Average, low and high temperature dataset was found to be varying. From graph observations, it looks like the predicted results using the properties for the highest temperature yields slightly better results than the other two sets. However, it cannot be claimed that the predicted results are accurate. For most of the predictions, Code-Bright seems to under predict the degree of

saturation. The calibration of the model by varying unsaturated hydraulic and thermal properties might result in more accurate prediction.

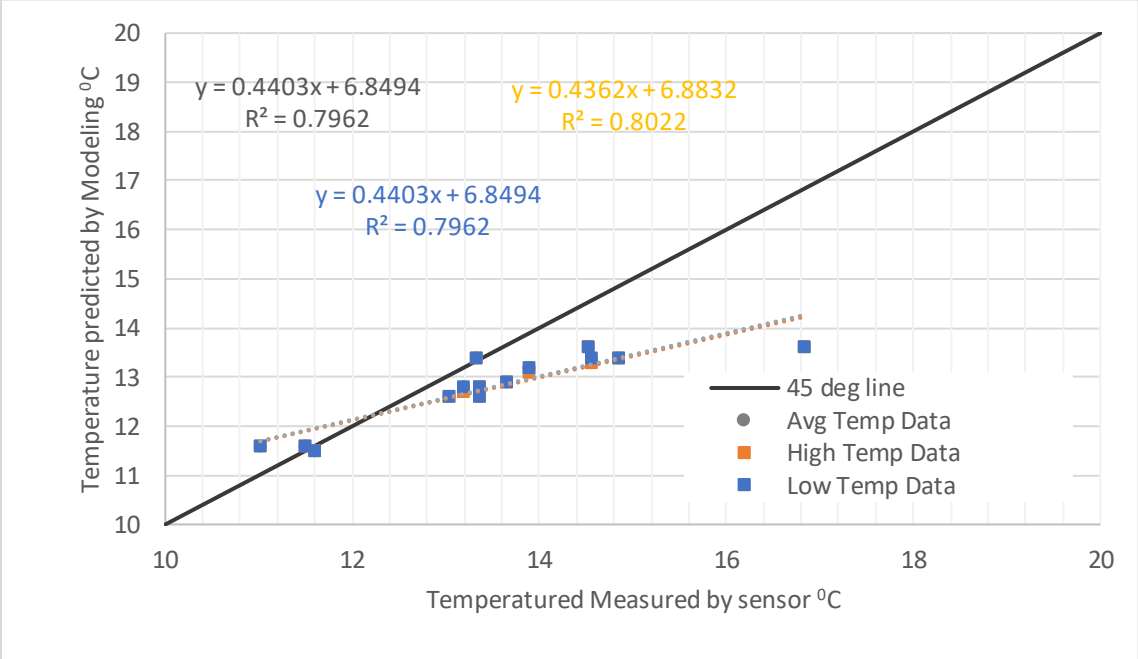

Figure 10.14. Measured Temperature using Sensor versus Temperature Predicted Using Modeling Using Highest, Lowest and Average Temperatures

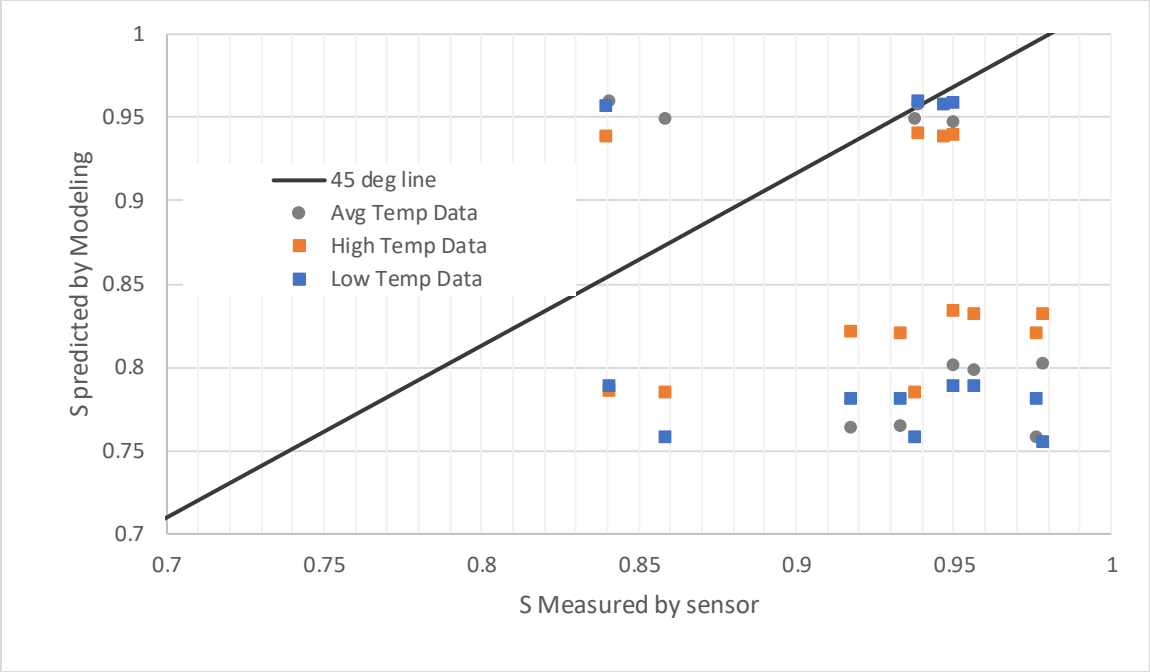

Figure 10.15. Measured S Using Sensor versus S Predicted Using Highest, Lowest and Average Temperatures Soil Properties

SUMMARY

An analysis of the modeling was performed for three cases of soil properties of high temperature, low temperature and normal temperature. The unsaturated hydraulic and thermal properties were varied during the simulation.

The value of temperature and degree of saturation was compared on the edge and center of the pavement. The prediction of temperature and degree of saturation of saturation was not found to be same as the actual values measured in NAPTF. The equations developed to predict the models may need to be recalibrated to attain the values closer to actual values. The variation in the soil properties entered for the three cases showed little variation in the temperature output whereas the variation of the degree of saturation output was found to be noticeable.

Chapter 11. : Summary and Conclusion

The evaluation of the modulus and change in the strength of the subgrade induced due the change in the temperature was investigated in this study. This research study has been conducted to explain the influence of the temperature on the unsaturated hydraulic and thermal properties of the soil. The study also incorporated the measurement of the change in temperature and the moisture content in NAPTF. The change in the moisture content was then related to the change in the CBR and the M_r values which was predicted using the models developed. This report provides the experimental procedure developed to analyze the unsaturated hydraulic properties, thermal properties, CBR, change in the modulus of the bound and unbound materials. A summary of the research conducted is presented in this Chapter along with the conclusions arrived based upon this study.

SUMMARY

The practical problems experienced in the NAPTF and the study required to address the problem were established in Chapter 1. The background for this study along with the introduction was outlined. The objectives required to address the problem were clearly set for this research study. The temperature effects on the various characteristics of the soil pose a threat to the change in the strength of the soil. The main purpose of this research study is to investigate the existence of subgrade soil moisture changes that may have arisen due to thermal and hydraulic gradients at the Atlantic City NAPTF and to evaluate their effect on the resilient modulus (material stiffness) and the California Bearing Ratio (CBR) strength parameter of the clay subgrade materials used at the facility.

Based upon the objectives set in Chapter 1, a brief literature review was performed in all topics helpful for this study and were presented in Chapter 2. The literature review was

started with the studies that were performed showing the change in the hydraulic properties of the soil with temperature change. The hydraulic properties that were studied are SWCC and unsaturated hydraulic conductivity of the soils. The literature review was then performed on the effect of temperature changes on the hydraulic properties. A brief review of the past studies performed on the effect of the change in moisture content on the resilient modulus and the CBR results. Then a study was performed on the past studies which dealt with the influence of the temperature on the flow of the moisture within the soil and the empirical models developed based on these studies.

Chapter 3 explains the past study performed in the NAPTF and the data collected the test section layout and the properties of the soil along with the dry density and moisture content of the soil compacted in the facility were collected. The CBR tests performed in the facility

Chapter 4 explains the preliminary test that were performed on the two soils to compile the index properties of the soil. The characterization of the soil materials was presented and the experiment procedures were introduced. County soil was classified as low Plasticity silt (ML) and DuPont soil was classified as high Plasticity silt (MH). The basic soil properties such as grain size distribution, Atterberg limits, specific gravity, Proctor Compaction tests and consolidation testing results were showed. Chapter 4 also explains model developed to predict the unsaturated hydraulic and thermal properties of the soil with a variation in Temperature.

Chapter 5 explains the CBR tests performed for both County and Dupont soil at various dry density, moisture content and compaction energy. A vane shear test was also performed

along with CBR tests. The vane shear test results and CBR were equated using a model. Using the model developed, the CBR and the vane shear for the variation of moisture content in the field was predicted. A model was created to relate the CBR, moisture content, dry density and compaction energy. The model relating the dry density dn the moisture content of the two clay soils was in the form of the polynomial function.

$$\gamma_d = (f_1 E_c + f_2)w^3 + (g_1 E_c + g_2)w^2 + (j_1 E_c + j_2)w + (k_1 E_c + k_2)$$

The values of f_i, g_i, j_i, and k_i, depends upon the type of the soil. Then a model was developed to relate the log CBR with the moisture content with a sigmoidal function as shown below:

$$Log\ CBR = (q) + \frac{(p-q)}{\left[1 + EXP\ (\frac{w-r}{s}\right]}$$

The values of p_i, q_i, r_i and s_i depend on the type of soil. The value of CBR for a particular dry density and moisture content was obtained by simultaneously solving the two equations.

In order to predict the vane shear strength of the soil, the vane shear strength of the soil was directly related to the CBR value in the form of another polynomial function as shown below.

$$CBR = p_1 {V_s}^2 + p_2 V_s + p_3$$

p_1, p_2 and p_3 depends on the type of the soil.

An analysis of the CBR data measured in the NAPTF with the dry density and moisture content collected from the FAA was analyzed. It was observed that there was a noticeable variation in the CBR tests results performed in the lab and in NAPTF historic data.

Chapter 6 evaluates the potential critical stress states, caused by any given load cart, on the unbound (base, subbase and subgrade) layers of the NAPTF pavement cross sections. An in-depth study of the stress state in the subgrade Dupont and County clay layers was performed. An analysis of the distribution of stresses on the subgrade materials of the pavement due to the loading of the pavement with the change in the properties of the Asphalt layer due to a variation of the pavement temperature. The stress analysis was performed by the JULEA program. Empirical models were developed to predict the stress on the subgrade material with respect to depth and change in temperature. The variation of the octahedral stress and bulk stress was related to the moduli of the subgrade and the temperature. Three relations were established for different types of loading gear.

For Dual gear,

$$\tau_{oct} = c_1 {E_{sg}}^{c_2} c_5 e^{c_6 T} \, z^{-(c_3 {E_{sg}}^{c_4})\,(c_7 T^2 + c_8 T + c_9)}$$

For Dual Tandem and Triple Tandem analysis,

$$\tau_{oct} = (c_1 {E_{sg}}^{c_2})\,(c_3 T^2 + c_4 T + c_5) z^{(c_6 {E_{sg}}^{c_7})\,(c_8 T^2 + c_9 T + c_{10})}$$

$$\tau_{oct} = (c_1 {E_{sg}}^{c_2})\,(c_3 T^2 + c_4 T + c_5) z^{(c_6 {E_{sg}}^{c_7})\,(c_8 T^2 + c_9 T + c_{10})}$$

The values of c_i varies with the type of gear and the load.

A model was developed for bulk stress in a similar way.

For Dual gear in the subgrade,

$$\theta = (c_1 {E_{sg}}^{c_2})\,(c_3 T^2 + c_4 T + c_5)\, z^{-(c_6 {E_{sg}}^{c_7})\,(c_8 T^2 + c_9 T + c_{10})}$$

For Dual Tandem and Triple Tandem in subgrade,

$$\theta = -(c_1 {E_{sg}}^{c_2})\,(c_3 T^2 + c_4 T + c_5)\ln z + (c_6 {E_{sg}}^{c_7})\,(c_8 T^2 + c_9 T + c_{10})$$

The models developed for the prediction of bulk and octahedral stress can be used to predict the non-linear resilient modulus of the base, subbase and the subgrade materials using the Witczak and Uzan, Universal model as shown below:

$$M_r = k_1 p_a \left(\frac{\theta}{p_a}\right)^{k_2} \left(\frac{\tau_{oct}}{p_a} + 1\right)^{k_3}$$

The testing and the evaluation of the resilient modulus tests were discussed in Chapter 7. The resilient modulus was performed in a range of moisture contents near the moisture contents found in the NAPTF. The M_r tests were performed to the NCHRP 128A protocol. All tests were performed. Th e equipment used and the specimen preparation were addressed. Using the test results, obtained for the two soils, the relation of k_1, k_2 and k_3, in the Witczak and Uzan Universal model, with the moisture content was analyzed and predicted. Another regression model of Cary and Zapata model was analyzed. The model was changed in Modified Cary and Zapata model which was used in the analysis. The regression parameters of the Modified Cary and Zapata model were found.The influence of each of these parameters are explained in detail in Chapter 9. during the compaction of the soil in the facility were also collected.

Chapter 8 involves the collection of data from the FAA and NAPTF, related to the project performed for this study. The location of the 30 sensors in the NAPTF has been shown in the plan and section view. The data collected by the 30 sensors were obtained and were analyzed. The data obtained from the sesnors included Volumetric Moisture Content and Temperature in ^{0}C. The VMC data calculated by the sensors did not include the effect of the temperature involvement in the measurement of VMC by the Decagon Sensors. Hence

the sensor data was calibrated to incorporate the effect of temperature on the raw data recorded. In order to understand the effect of variation in moisture content and to compare the VMC data obtained from the sensor with the VMC data compacted in the field during the construction., a data of the compacted field dry density and moisture content throughout the facility was obtained. A compilation of dry density and moisture content measured at 120 locations in Dupont clay and 24 locations in County clay was obtained.

The temperature and the moisture data collected from the field were calibrated to incorporate the variation of temperature into the raw data. The VMC and Temperature collected in all 30 locations of the NAPTF for a duration of 2.5 years was analyzed. A temperature variation was observed in the all 30 locations of the facility. This variation in the temperature was noticed to be decreasing with an increasing depth. As the temperature in the subgrade varied, a variation in the VMC was also observed. The change in the temperature and moisture content in the field at different depths were analyzed and presented.

Chapter 9 evaluated the variation in the temperature and moisture content in the NAPTF. Using the range of moisture contents observed in the NAPTF, the CBR, vane shear strength and the Mr of the subgrade soil was found. The models obtained in Chapter 4,5 ,6, 7 and 8 were used to predict the variation of CBR, stress states and the Mr with the change in moisture content in the NAPTF.

Chapter 10 discusses the modeling performed for NAPTF using Code Bright GID. The unsaturated hydraulic and thermal properties of the soil used as inputs were discussed along with the boundary conditions applied, initial unknowns and the initial porosity of the layers. The theoretical concepts and equations used in the prediction of the model were also

discussed. The results were analyzed for three scenarios of: Soil properties at average temperature in NAPTF, soil properties at high temperature and soil properties at low temperature. The results were obtained near the center of the pavement (Location A,C and E) and were compared with the actual values measured by the sensor in the field.

CONCLUSIONS

Calibration of the sensors

The initial analysis of the temperature and moisture data obtained from the field showed that the sensor was not incorporating the effect of temperature on the measurement of the voltage acquired by sensor. Since the sensor measurement depends on the di-electric permittivity of the soil which can be affected by temperature, a calibration was performed to incorporate the effect of temperature.

Based upon the experiment results, Topp's equation was recalibrated to the soil conditions of this study. The equation obtained after calibration are:

For DuPont soil:

$$VWC = 0.698144 \times \left[0.818814 - 0.992436^{\left(\frac{R}{T^{0.5}+2} \right)} + 0.0145732 \right]$$

For County soil:

$$VWC = 0.796544 \times \left[0.372384 - 0.99673^{\left(\frac{R}{T^{0.6}+2} \right)} + 0.422945 \right]$$

Where θ is the volumetric water content of testing material, R is the raw data the output of the sensor and T is the temperature in Celsius.

The R^2 of Dupont Clay calibration model and County Clay calibration model is 0.89 and 0.98 separately. The standard error of Dupont Clay calibration model is 0.0467600 and County Clay calibration model is 0.0180355.

Variation of moisture and temperature recorded in NAPTF

The sensors in shallow depth of 35" below the top of pavement had a temperature variation of 18.3^0 C with the average temperature being 15.86^0 C considering all locations. It also showed a variation of 0.0247 in the volumetric water content. At depth of 77", the sensors recorded an average temperature of 17^0 C while the variation in temperature was found to be 12.8^0 C. The temperature variation at the depth of 89" was 10.3^0 C and the average temperature at this depth was found to be 16.63^0 C The variation of temperature at the depth of 108" was 8.3^0 C. At the depth of 126", the variation in temperature was found to be 7.1^0 C

The sensors at a depth of 35" measured an average volumetric moisture content of 0.423 for the 2.5-year duration. The variation of moisture content during the 2.5 years in depth 35" was found to be 0.0247. In depth 77", the average VMC measured for 2.5 years was 0.489 and the variation of this moisture content through different seasons was found to be 0.0165. In depth 89", the variation of VMC was found to be 0.0162. At depth of 108", the variation of VMC for the 2.5-year duration was found to be 0.0206. At a depth of 126", the variation of VMC was measured as 0.0212.

Unsaturated hydraulic properties of the soil

To analyze the temperature effect on the SWCC and unsaturated hydraulic conductivity of two soils, results from three temperatures were compared. According to the results obtained, it was found that the SWCC of County soil was affected by temperature when

suction was higher than about 1,000 kPa. The SWCC at 5°C was slightly higher than the SWCC at 25°C and 40°C, which indicates that the County soil retained more water at lower temperatures. The three curves at 5˚C, 25˚C and 40˚C overlapped when the suction was lower than 1,000 kPa and not significant differences were observed. As for DuPont soil, the differences in temperature also had an effect on the SWCC. When comparing the results at the same degree of saturation, it was found that the suction increased as temperature decreased for suction values lower than about 10,000 kPa. In other words, the DuPont soil tended to hold more water at lower temperatures. A model was developed to predict the change in SWCC regression parameters and the k_{unsat} value with temperature.

Various theories have been proposed to explain the temperature effect on SWCC. One of the theories consider the soil water composed of continuous water and isolated packets of water, where the continuous water is the only water that can flow freely in and out of soil. As temperature increases, the interfacial tension will decrease so the capillary tube will not be able to hold all entrapped water, which will release isolated water into continuous water. In addition, the attractive force between soil solid surfaces will decrease as temperature increases. A reduction in the attractive force will release isolated water into continuous water, which will result in lower water content at lower temperatures when the same matric suction is applied (Hopmans and Dane, 1986). Therefore, the results obtained are well aligned with the findings from Hopmans and Dane.

The unsaturated hydraulic conductivity functions results obtained at three temperatures varied for the two soils used in this study. For County soil, the unsaturated hydraulic conductivity at 40˚C was found to be definitely higher than values obtained at 25˚C and 5˚C, at all suction levels. For DuPont soil, the temperature effect on the unsaturated

hydraulic conductivity was less obvious, but a slightly lower conductivity was observed for the function obtained at 5°C. From these results, it can be said that an increase in temperature increases the conductivity of the soils of this study. This finding can be explained by invoking the viscosity of water concept. The hydraulic conductivity is inversely proportional to water viscosity; which in turn is inversely proportional to temperature (Hopmans and Dane, 1986). Thus, a temperature increase will induce an increase in hydraulic conductivity.

CBR and vane shear test

CBR and vane shear tests were performed in three different energy levels. A model was obtained relating the dry density, moisture content and the CBR test result. The model was further improved to predict the CBR result more accurately. Hence CBR was found to be a function of dry density, moisture content and the compaction energy. Another model relating the CBR and the vane shear strength value was also created. A distinct variation in the CBR measured in the facility and in the lab was observed. While no firm conclusions are possible to establish the change in the CBR test results between NAPTF and ASU lab, based upon current information available to ASU; a finite possibility does exist that differences (small) may have been simply due to normal variations in sampling from a supposedly identical population.

Developing model to measure the bulk and octahedral stress on unbound materials affected by temperature

The variation of temperature causes a change in the properties of the asphalt layer. This change of properties of the soil leads to a change on the transfer of loads by the wheel cart which produces stress on the base, subbase and subgrade materials. The FAA AC 150/5320-6E were not able to accurately predict the changes of the stress caused in the

pavement layers. The empirical models developed showed a higher variation of the stress transferred and a change in moduli than the charts used by U.S army corps of Engineers or FAA AC 150.

Table 6.29 shows the summary of all models developed/presented in this chapter that can be used to accurately predict the τ_{oct} shear stress values within any depth of the Dupont and County clay subgrade. These equations predicts τ_{oct} as a function of:

- Gear type: Dual, Dual Tandem, Triple Tandem.
- Depth within subgrade: z inches from pavement surface
- Subgrade Modulus: E_{sg} (ksi)
- AC Temperature: T (deg F)
- Single wheel loads: P_i (kips)

Table 6.30 shows the summary of all bulk stress (θ) shear stress values within any depth of the Dupont and County clay subgrade. These equations allow for the prediction of θ as a function of:

- Gear type: Dual, Dual Tandem, Triple Tandem.
- Subgrade Modulus: E_{sg} (ksi)
- AC Temperature: T (deg F)
- Single wheel loads: P_i (kips)

Resilient modulus of subgrade

An analysis of the influence of the octahedral stress parameter and the bulk stress parameters separately showed that the inclusion of the k2 parameter yielded a much more accurate prediction of the M_r. Then an analysis was performed on the CZ model with the inclusion of $\Delta\psi$ value and modified CZ without the inclusion of $\Delta\psi$ value. The results yielded that modified CZ model leads to a more accurate prediction of M_r with the three stress parameters of bulk, octahedral and suction. Hence, it was decided that modified CZ

model will be used in the analysis of the prediction of M_r in the NAPTF. The regression parameters of the Modified CZ model were obtained for the two soils.

Assessment in the variation of subgrade moduli and strength due to thermos-hydraulic moisture movement

The changes in moisture content within the clays caused by several thermal influences are not considered significantly large, by an absolute measure standard. The range was found to decrease with depth into NAPTF pavement section and varied from a difference (w_{max}-w_{min}) of approximately 2.0% for upper Dupont Sublayer No. 1 to approximately 1.5% for the lowest County Sublayer No. 2. These numbers are based upon difference between the average seasonal extremes, at all location for a given depth. If one considers the extreme difference at a given sensor set and location these values change to 4.3% and 2.3%.

Thus, for the upper Dupont No.1 layer, the mean sublayer moisture of w= 27.0% will range, on average, between w= 25.9% and w= 28.1%, throughout an annual cycle of testing at the NAPTF facility.

The Temperature variation can affect the properties of the soil directly or by indirectly when the thermal gradients induce a moisture flow. Using all the models developed, the variation of the properties of the subgrade were studied. The variation in the matric suction of the Dupont Clay was from 94.3 psi due to just hydraulic gradient caused by temperature to 155 psi due to hydro-thermal gradients. For County clay, the variation in matric suction varied from 47.8 psi due to hydraulic gradients to 53.4 cos of the hydro-thermal gradients.

The unsaturated hydraulic conductivity of the subgrade can also be directly influenced by temperature. The change in k_{unsat} can vary from 3.28E-12 to 1.74E-12 for Dupont clay and from 1.55 E-08 to 2.84 E-09 for County clay.

The variation of the CBR and the vane shear strength can be as high as 3% and 0.0065 tsf for both clays. Nonetheless, while the moisture changes may appear to be inconsequential (or small); it is extremely important that they should be viewed relative to their respective changes in strength and resilient moduli that will be occurring at the facility. This situation is indeed magnified by the fact that the FAA NAPTF facility has been purposely constructed to maintain very low CBR/M_r populations during the history of performance testing at the facility. thus, what may be viewed as an insignificant measure moisture content variation of w=25.9% to w= 28.1%, may lead to annual mean variations (for the upper part Dupont clay layer) of CBR= 4.1% to CBR= 6.3%. Because of the highly sensitive drop in performance with thickness, caused by lower CBR strengths; the impact of these thermally induced changes in soil strength and resilient modulus (CBR, Vss and M_r) should not be overlooked in any performance.

Resilient Modulus of the soil was studied with most utmost importance. The Resilient Modulus of the soil have a direct and indirect influence on the temperature. The parameters used to calculate the resilient modulus such as bulk stress, octahedral stress and matric suction are directly influence by temperature. The bulk stress and the octahedral stress decreases with depth but the matric suction of the soil is influenced by the water content of the soil. On top of that the amount of load applied to the soil using the gear type also affects the resilient modulus of the subgrade.

The model representing the resilient modulus which incorporates bulk stress, octahedral stress and suction stress parameters which are influenced by temperature shows that thermally induced changes can cause a wide effect in the performance of the subgrade. The change in the strength of the soil can be underestimated as 7.5 ksi due to just the hydraulic

gradients when the actual change in the modulus can be as big as 18 ksi for Dupont clay. For County clay, the variation can be underestimated as 6.8 ksi when the change in modulus can be 10 ksi.

When the gear type is incorporated into the analysis, Dupont clay can exhibit a high Mr of 22 ksi when dual gear load is applied to as low as 13 ksi for Triple Tandem gear type. County clay had a M_r as high as 16 ksi for Dual gear load to 7 ksi for triple tandem gear type.

In conclusion, variation in CBR and Vss was influenced by the moisture movement in subgrade. The prediction of variation in M_r was influenced by both moisture and temperature changes. The variation of M_r was caused due to stress state parameters such as bulk, octahedral and matric suction. Ignoring Non-isothermal condition can cause a M_r prediction error of upto 150%.

Chapter 12. Future Recommendations

The comprehensive study detailed in this study has led to a set of future recommendations. The specific recommendations to further build a more comprehensive database of these thermo-hydraulic properties of pavement layers, along with further studies using advanced hydro-thermal-mechanical (HTM) moisture movement models are presented in the following paragraphs.

Although the ASU study served to re-calibrate the sensors, the calibration was limited to the two subgrade soils used in the NAPTF and also limited to three temperatures. It is therefore a major recommendation, that a revision to Topp's equation be performed, which would be valuable not only to future FAA data analysis but also to any sensor that employs permittivity as the main predictor of water content. It is recommended that this soil testing program be expanded to include 3-6 more typical subgrade soils found at US airports, to assess the relative significance of soil type (classification) properties for future engineering simulation studies.

It is recommended that a research study be developed to assess the applicability of such a coupled HTM model for use in the predicted assessment of the potential soil moisture changes that may occur in actual airfield pavement systems due to seasonal temperature changes as well as suction gradients brought about by typical variations in layer material compaction properties and types.

Though initially suction and thermal conductivity measuring sensors were installed in the NAPTF. They were found to be not working during the period of the evaluation. Hence, having actual sensors working in the field might help in prediction of the suction and thermal conductivity variation in field for the 33 months.

As a result, it is highly recommended that a research study be undertaken to establish a series of equivalent subgrade volume cells, defined by longitudinal, horizontal and vertical (depth) borders that would subdivide the entire subgrade area at NAPTF into a series of data collection and measurement cells. For example, borders at 100 ft stations; 20 ft lateral intervals and the mid depths of each clay type; would lead to a series of 36 separate data collection units, relative to subgrade physical properties.

The initial effort used to establish CBR-w%-γ_d relationships for the Dupont and County clays, principally focused on defining relationships over a very broad range of moisture contents, from dry of optimum to wet of optimum. All CBR tests were also conducted at "as molded" conditions and incorporated compaction energies ranging from standard to modified efforts. It is recommended that additional CBR tests be conducted on both clays to evaluate the CBR at very small moisture increments (Δw%=1.0%), ranging between 25% to 35% for the County clay and 30% to 40% for the Dupont clay. CBR tests should be evaluated at the three levels of compaction, previously used. The specific goal of this effort should be to develop the most accurate relationship possible between CBR and w%, for the typical in-situ moisture content ranges occurring at the test facility.

It is recommended that a "field" vane shear device be employed, rather than the "pocket" vane shear used in this study. This "field" device should have vane heights that are approximately 1.5 in to 2.0 in, to insure that the greatest accuracy and precision can be obtained with these measurements. This study should be completed in conjunction with the CBR study recommended.

Future research should be conducted to evaluate the feasibility of using the field vane shear device as an accurate, rapid, simple procedure to establish and monitor field quality

control measurements to achieve compaction of future subgrades to a specific "target" CBR value for a test section. The possibility of controlling the subgrade compaction to achieve a unique target CBR value by a simple hand held device yielding a "CBR correlation" in 30 seconds would appear to be of enormous benefit and time, cost savings, compared to evaluating in-situ moisture and density tests, combined with in-place or "undisturbed" lab CBR tests during the subgrade compaction/construction process.

As a consequence, the results of this research study suggest that the best possible compaction QC methodology may be to directly control the moisture content as closely as possible and also directly control the in-situ CBR strength through the use of the field vane shear device.

It is highly recommended that a software program be developed that would allow temperature sensor readings to be directly read as input, so that the analysis of temperature frequency distributions, at a given depth, can be computed in the NAPTF sections. Such a program would be of enormous benefit to the data processing capability at the facility.

The Modified CZ model developed was based on the variation of the matric suction during NCHRP 1-28A test protocol was small. This should be verified with granular base and sandy materials.

The soil compacted in the NAPTF had soils on the wet side of the compaction curve and mostly consisted of soils of 90% degree of saturation. The study was not able to include the soils with water contents on the dry side. The study could be extended to soils compacted on the dry side or maximum dry density to explore the variation of modulus of the soil when the water content is low.

REFERENCES

Åkesson, M., Jacinto, A.C., Gatabin, C., Sanchez, M. and Ledesma, A. (2009). Bentonite THM Behaviour at High Temperatures: Experimental and Numerical Analysis. *Géotechnique, Symposium in Print - Thermal Behaviour of the Ground: Part 2*, 59(4), 307-318.

Alonso, E., Gens, A. and Josa, A. (1990). A Constitutive Model for Partially Saturated Soils. *Geotechnique*. 40(3), 405-430.

Andrei, D. (2003). Development of a Predictive Model for the Resilient Modulus of Unbound Materials. *Doctoral Dissertation*. Arizona State University, Tempe, Arizona.

Assouline, S. and Tartakovsky, D.M. (2001). Unsaturated Hydraulic Conductivity Function based on a Fragmentation Process. *Water Resources Research*, 37(5), 1309-1312.

ASTM D693-98, Standard Specification for Crushed Aggregate for Macadam Pavements, ASTM International, West Conshohocken, PA, 1998.

STM D698-12e2, Standard Test Methods for Laboratory Compaction Characteristics of Soil Using Standard Effort (12 400 ft-lbf/ft^3 (600 kN-m/m^3)), ASTM International, West Conshohocken, PA, 2012.

ASTM D854-14, Standard Test Methods for Specific Gravity of Soil Solids by Water Pycnometer, ASTM International, West Conshohocken, PA, 2014.

ASTM D1557-12e1, Standard Test Methods for Laboratory Compaction Characteristics of Soil Using Modified Effort (56,000 ft-lbf/ft^3 (2,700 kN-m/m^3)), ASTM International, West Conshohocken, PA, 2012.

ASTM D1587 / D1587M-15, Standard Practice for Thin-Walled Tube Sampling of Fine-Grained Soils for Geotechnical Purposes, ASTM International, West Conshohocken, PA, 2015.

ASTM D1883-16, Standard Test Method for California Bearing Ratio (CBR) of Laboratory-Compacted Soils, ASTM International, West Conshohocken, PA, 2016.

ASTM D2435 / D2435M-11, Standard Test Methods for One-Dimensional Consolidation Properties of Soils Using Incremental Loading, ASTM International, West Conshohocken, PA, 2011.

ASTM D2937-17e1, Standard Test Method for Density of Soil in Place by the Drive-Cylinder Method, ASTM International, West Conshohocken, PA, 2017.

ASTM D4318-17, Standard Test Methods for Liquid Limit, Plastic Limit, and Plasticity Index of Soils, ASTM International, West Conshohocken, PA, 2017

ASTM D6836-16, Standard Test Methods for Determination of the Soil Water Characteristic Curve for Desorption Using Hanging Column, Pressure Extractor, Chilled Mirror Hygrometer, or Centrifuge, ASTM International, West Conshohocken, PA, 2016.

ASTM D6951 / D6951M-09(2015), Standard Test Method for Use of the Dynamic Cone Penetrometer in Shallow Pavement Applications, ASTM International, West Conshohocken, PA, 2015.

ASTM D7664-10, Standard Test Methods for Measurement of Hydraulic Conductivity of Unsaturated Soils, ASTM International, West Conshohocken, PA, 2010.

Barbour, S. L., Fredlund, D. G., Gan, J. K. M., and Wilson, G. W. (1995). Moisture Movement in Highway Subgrade Soils, Prediction and Measurement. *Symposium on Unsaturated Soil Behavior and Applications*, Nairobi, Kenya, August, pp. 21-40.

Barbour, S.L. (1998). The Soil-Water Characteristic Curve: A Historical Perspective. *19th Canadian Geotechnical Colloquium: Canadian Geotechnical Journal*, 35, 873-894.

Brooks, R. H., and Corey, A. T. (1964) Hydraulic properties of porous media, *Colorado State University Hydrology Paper*, No. 3. Fort Collins, CO.

Campbell, G. S. (1974). A simple method for determining unsaturated conductivity from moisture retention data, *Soil Science Journal*, Vol. 117, No. 6, pp. 311–314.

Carslaw, H. S. and Jaeger, J. C. (1959) Conduction of Heat in Solids, *2nd edn. Oxford: Clarendon Press*

Cary, J.W. (1966). Soil Moisture Transport due to Thermal Gradients. *Soil Science Society of America Journal*, 30, 428-433.

Cary, C. E. (2008). Resilient Modulus Testing for Unsaturated Unbound Materials. *Master Thesis*. Arizona State University, Tempe, Arizona.

Chandler, R.J, and Gutierrez. C.I (1986) "The filter paper method of suction measurement." Geotechnique, 36, pp 265-268.

Childs, E. C., and Collis-George, N. (1950). The permeability of porous materials, *Proceedings of the Royal Society*, London, Series A, Vol. 201A, pp. 392–405.

Cho, W. J., Lee, J. O. and Chun, K. S. (1999) The temperature effects on hydraulic conductivity of compacted bentonite, *Applied Clay Science*, 14, 47-58.

Coccia, C.J.R. and McCartney, J.S. (2013). Impact of Heat Exchange on the Thermo-Hydro-Mechanical Response of Reinforced Embankments. *Proceedings of GeoCongress 2013*. ASCE. San Diego, CA. pp. 343-352.

Dakshanamurthy, V., and Fredlund, D. G. (1981) A mathematical model for predicting moisture flow in an unsaturated soil under hydraulics and temperature gradients, *Water Resources Research*, Vol. 17, No. 3, pp. 714–722.

Darcy, H. (1856) *Histoire des Foundataines Publique de Dijon, Dalmont,* Paris, pp. 590–594.

Das, Braja M. (2008) Advanced Soil Mechanics. New York, NY: Taylor & Francis.

De Vries, D. A. (1975) Heat transfer in soils, in *Heat and Mass Transfer* in the Biosphere, Vol. 1, *Transfer Processes in Plant Environment*, Scripta, Washington, DC, pp. 5–28.

Delage, P, Sultan, N. and Cui, Y. J. (2000) On the thermal consolidation of Boomclay, *Can.Geotech.* J., 37, 343-354.

Dempsey, B.J., Herlach, W.A. and Patel, A.J. (1985). The Climatic-Material-Structural Pavement Analysis Program. *FHWA/RD-84/115, Vol.3, Final Report*, Federal Highway Administration, Washington D.C.

Deryaguin, B. V. and Melnikova, M. K. (1956): Experimental Study of the Migration of Water Through the Soil under the Influence of Salt Concentration, Temperature, And Moisture Gradients, In: *Int. Congr. Soil Sci.*, Trans. 6th (Paris), pp. 305–314.

El-Kehsky, M. (2011) Temperature effect on the Soil Water Retention Characteristic. Master Thesis, Arizona State University.

Farouki, O. T., 1986: Thermal Properties of Soils. Series on Rock and Soil Mechanics, *Vol. 11, Trans Tech*, 136 pp.

Farouki, O.T. (1981). Thermal Properties of Soils. *CRREL Monograph, Cold Region Res. Eng. Lab.*, Hanover, NH.

Fayer, M.J. (2000). UNSAT-H, Version 3.0: Unsaturated Soil Water and Heat Flow Model. *Pacific Northwest National Laboratory,* Richland, WA.

Fayer, M.J. and Jones, T.L. (1990). UNSAT-H Version 2.0: Unsaturated Soil Water and Heat Flow Model Prepared for United States Department of Energy, *Pacific Northwest National Laboratory*, Richland, WA.

Federal Aviation Administration (FAA), FAA AC 150/5320-6E, *Pavement Design and Evaluation*, 2009.

Fredlund, D.G., and Houston, S.L. Interpretation of soil-water characteristic curves when volume change occurs as soil suction is changed. Advances in Unsaturated Soils, London, Taylor and Francis Group.

Fredlund, D. G., and N. R. Began (1977). Stress State Variables for Unsaturated Soils. *ASCE Journal of the Geotechnical Engineering Division*, Vol. 103, No. 5, pp. 447-466.
Fredlund, D. (2006). Unsaturated Soil Mechanics in Engineering Practice. *ASCE Journal of Geotechnical and Geoenvironmental Engineering*, Vol. 132, No. 3, pp. 286-321.

Fredlund, D.G., Xing, A., and Huang, S. 1994. Predicting the permeability function for unsaturated soils using the soil-water characteristic curve. *Canadian Geotechnical Journal*, 31(4): 533–546. doi:10.1139/t94-062

Fredlund, D. G., and Xing, A. (1994) Equations for the soil-water characteristic curve, *Canadian Geotechnical Journal*, Vol. 31, No. 3, pp. 521–532.

Fredlund, D.G. and Rahardjo, H. (2012) Unsaturated Soil mechanics in Engineering Practice. New York, NY: John Wiley and Sons, Inc.

Geo-Slope International Ltd. (2005). Vadose/W User's Manual, Version 1.10. Copyright 1991-2005. *Geo-Slope Ltd*., Calgary, Alberta, Canada.

Gitirana Jr., G., Fredlund, M.D. and Fredlund, D.G. (2006). Numerical Modelling of Soil-Atmosphere Interaction for Unsaturated Surfaces. Unsaturated Soils 2006. *Geotechnical Special Publication No. 147. The Geo-Institute of the ASCE. Proceedings of the 4th International Conference on Unsaturated Soils*. April 2-6, Carefree, AZ, 658-669.

Gitirana Jr., G. (2005). Weather-Related Goe-Hazard Assessment Model for Railway Embankment Stability. *Ph.D. Thesis*. University of Saskatchewan, Saskatoon, SK, Canada.

Grant, S. and Salehzadeh, A. (1996) Calculation of temperature effects on wetting coefficients of porous solids and their capillary pressure functions, *Water Resour. Res.*, 32(2), 261-270.

Gui, J., Phelan, P., Kaloush, K., and J. Golden. (2007). Impact of Pavement Thermo-Physical Properties on Surface Temperatures. *ASCE Journal of Materials in Civil Engineering*. 19(8), 683-690.

Gurr, C. G., Marshall, T. J. and Hutton, J.T. (1952). Movement of Water in Soil due to a Temperature Gradient. *Soil Science Journal*, Vol. 72, No.5, pp.335–344.

Guymon, G.L., Berg, R.L., and Johnson, T.C (1986). Mathematical Model of Frost Heave and Thaw Settlement in Pavement. *Report, U. S. Army Cold Region Research and Engineering Laboratory*.

Hamilton, J. M., Daniel, D. E., and Olson, R. E. (1981) Measurement of hydraulic conductivity of partially saturated soils, in T. F. Zimmie and C. O. Riggs (Eds.), *Permeability and Groundwater Contaminant Transport*, ASTM Special Technical Publication 746, American Society for Testing and Materials, Philadelphia, PA, pp. 182–196.

Hooper, F. C., And Lepper, F. R. (1950) Transient heat flow apparatus for the determination of thermal conductivities. *ASHVE Transactions 56*, pp. 309-324.

Hopmans, J. W and Dane, J. H. (1986) Temperature dependence of soil hydraulic properties, *Soil Sci. Soc. Am. J.*, 50, 4-9.

Hossain, M., Romanoschi, S. and Gisi, A. J. (2000). Seasonal and Spatial Variation of Subgrade Response. Pavement, Subgrade, Unbound Materials, and Nondestructive Testing, *Geotechnical Special Publication*. 98 edition, ASCE, pp. 150-166.

Houston, S.L., Houston, W.N., Zapata, C.E. and Lawrence, C. (2001). Geotechnical Engineering Practice for Collapsible Soils. *Geotechnical and Geological Engineering Journal*. 19(3-4).

Hutcheon, N. B., And Paxton, J. A. (1952) Moisture migration in a closed guarded hot plate. *ASHVE Journal Section. Heatino piping and Air Conditioning*, pp". 113-122.

Hutson, J.L. and Wagenet, R.J. (1992). Leaching Estimation and Chemistry Model, LEACHM. *New York State College of Agriculture and Life Sciences*, Cornell University, Ithaca, New York.

Hveem, F. N., and R. M. Carmany (1948). The Factors Underlying the Rational Design of Pavements. In *Highway Research Record 28*, HRB, National Research Council, Washington, D.C., pp. 101-136.

Hveem, F. N. (1955). Pavement Deflections and Fatigue Failures. In *Highway Research Record 114*, HRB, National Research Council, Washington, D.C., pp. 43-87.

IAPWC, (2008), International Association for Properties of Water and Steam, Release on the IAPWS Formulation 2008 for the Viscosity of Ordinary Water Substance, IAPWS R12-08, IAPWS, Witney, UK, September 2008.

Jacquemin, S.C. (2011) Laboratory Determination of Hydraulic Conductivity Functions for Unsaturated Cracked Fine Grained Soil, Arizona University, March 2011.

Kestin, J., Sokolov, M. and Wakeham, W.A. (1978) Viscosity of Liquid Water in the Range 10^0C to 150^0C. Journal of Physical Chemistry, 7, 941-948.

Khoury, N. N., and M. Zaman. (2004). Correlation among Resilient Modulus, Moisture Variation and Soil Suction for Subgrade Soils. In *Transportation Research Record. 1874*, TRB, National Research Council, Washington, D.C., pp. 99-107.

Klute, A. (1972) The determination of the hydraulic conductivity and diffusivity of unsaturated soils, *Soil Science Journal*, Vol. 113, pp. 264–276.

Krisdani, H., Rahardjo, H., and Leong, E. C. (2009) Use of instantaneous profile and statistical methods to determine permeability functions of unsaturated soils, *Canadian Geotechnical Journal*, Vol. 46, No. 7, pp. 869–874.

Lin, L. and Benson, C.H. (2000). Effect of Wet-Dry Cycling on Swelling and Hydraulic Conductivity of GCLs. *ASCE Journal of Geotechnical and Geoenvironmental Engineering*, 126(1), 40-49.

Lloret, A., and Alonso, E. E. (1980) Consolidation of unsaturated soils including swelling and collapse behaviour, *Geotechnique,* Vol. 30, No. 4, pp. 449–477.

Lu, Y. (2015). Temperature Effects on the Unsaturated Hydraulic Properties of Two Fine-Grained Soils and Their Influence on Moisture Movement under an Airfield Test Facility. *Master Thesis*. Arizona State University, Tempe, Arizona.

Maher,A., and Bennert, T. (2008). Evaluation of Poisson's Ratio for Use in the Mechanistic Empirical Pavement Design Guide (MEPDG), Federal Highway Administration U.S. Department of Transportation Washington, D.C, FHWA-NJ-2008-004.

Marshall, T. J. (1958) A relation between permeability and size distribution of pores, *Soil Science Journal*, Vol. 9, pp. 1–8.

McKee, C. R., and Bumb, A. C. (1987) Flow-testing coalbed methane production wells in the presence of water and gas, *Society of Petroleum Engineers Formation Evaluation,* Vol. 2, No. 4, pp. 599–608.

Milly, P.C.D (1982) Moisture and heat transport in hysteretic, inhomogeneous porous media: A matric head-based formulation and a numerical model, water resources research, 18(3), 489-498, 1982.

Mitchell, J.K. and Soga, K. (2005). Fundamentals of Soil Behavior. 3rd Ed., *John Wiley & Sons, Inc*. New York.

Miyazaki T (2006) Water flow in soils, 2nd edn. Taylor and Francis, London.

Mualem, Y. (1986) Hydraulic conductivity of unsaturated soils: Prediction and formulas, in *Methods of Soil Analysis*, Part 1: Physical and mineralogical methods, Second edition, Agronomy, Madison, WI, pp. 799–823.

National Cooperative Highway Research Program (NCHRP). *Guide for Mechanistic Empirical Design of New and Rehabilitated Pavement Structures*, NCHRP 1-37 A, Final Report, TRB, National Research Council, Washington, D.C., 2004.

National Cooperative Highway Research Program. *NCHRP 1-28. Laboratory Determination of Resilient Modulus for Flexible Pavement Design*, NCHRP 1-28 Draft Final Report. 1996.

Nimmo, J. R. and Miller, E. E. (1986) The temperature dependence of isothermal moisture vs. potential characteristics of soils, *Soil Sci. Soc. Am. J.*, 50, 1105-1113.

Olivella, S., Gens, A., Carrera, J. and Alonso, E.E. (1996). Numerical Formulation for Simulator (Code-Bright) for Coupled Analysis of Saline media. *Engineering Computation*, 13(7), 87-112.

Padilla, J.M., Perera. Y.Y., Houston, W.N. and Fredlund, D.G. (2005) A New Soil-Water Characteristic Curve Device *Proceedings of Advanced Experimental Unsaturated Soil Mechanics-an International Symposiums*, EXPERUS 2005, Trento, Italy. pp. 15-22 June 27-29.2005.

Palanivelu, P. T., Zapata, C. E., & Underwood, S. (2016). Effect of As-Compacted Moisture Content and Density on Pavement Performance in Different Climatic Regimes. In *Geotechnical and Structural Engineering Congress 2016 - Proceedings of the Joint Geotechnical and Structural Engineering Congress 2016* (pp. 1303-1316).

Philip, J. R., and de Vries, D. A. (1957) Moisture movement in porous materials under temperature gradients, Transactions, *American Geophysical Union*, Vol. 38. No. 2, pp. 222–232.

Pruess, K., and J. S. Y. Wang (1987), Numerical modeling of isothermal and nonisothermal flow in unsaturated fractured rock—A review, in *Flow and Transport Through Unsaturated Fractured Rock*, Geophys. Monogr. Ser., vol. **42**, edited by D. Evans, and T. Nicholson, pp. 11–21, AGU, Washington, D. C.

Rada G. and Witczak M.W. (1981). Comprehensive Evaluation of Laboratory Resilient Moduli Results for Granular Material. *Transportation Research Record 810*, TRB, National Research Council, 1981, Washington, D.C., pp. 23-33.

Romero, E. Gens. A. and Lloret, A. (2001) Temperature effects on the hydraulic behavior of an unsaturated clay. *Geotechnical and Geology Engineering* 19:331-332.

Sakai, M., Toride, N. and Simunek, J. (2009). Water and Vapor Movement with Condensation and Evaporation in a Sandy Column. *Soil Science Society of America Journal*, 73(3), 707 – 717.

Schroeder, P.R., Aziz, N.M. Lloyd, C.M. and Zappi, P.A. (1994). The Hydrologic Evaluation of Landfill Performance (HELP) Model: User's Guide for Version 3.

EPA/600/9-94/xxx, United States Environmental Protection Agency Risk Reduction Engineering Laboratory, Cincinnati, OH.

Sánchez, M., Gens, A., Olivella, S. (2016). Fully Coupled Thermo-Hydro-Mechanical ouble-Porosity Formulation for Unsaturated Soils, International Journal of Geomechanics, 10.1061/(ASCE)GM.1943-5622.0000728

She, H. Y. and Sleep, B. E. (1998) The effect of temperature on capillary pressure-saturation relationships for air-water and perchloroethylene-water systems, *Water Resources. Res.*, 34(10), 2587-2597

Seed H. B., C. K. Chan, and C. E. Lee (1962). Resilience Characteristics of Subgrade Soils and their Relation to Fatigue Failures in Asphalt Pavements. *Conference Proceedings: International Conference on Structural Design of Asphalt Pavements*, Vol. 1, Ann Arbor, USA, pp. 611-636.

Shonder, J. A. and J. V. Beck. 2000. Field test of a new method for determining soil formation thermal conductivity and borehole resistance. *ASHRAE Transactions* 106(1): 843-850. Morgensen (1983)

Šimůnek, J., M. Šejna, H. Saito, M. Sakai, and M. Th. van Genuchten, (2013), The Hydrus-1D Software Package for Simulating the Movement of Water, Heat, and Multiple Solutes in Variably Saturated Media, Version 4.17, HYDRUS Software Series 3, Department of Environmental Sciences, University of California Riverside, Riverside, California, USA, pp. 342.

SoilVision Systems Ltd. (2005). SVFlux User's and Theory Guide. Version 5.55. Saskatoon, SK, Canada.

Taylor. S.A., and Cary, J.W (1964). Linear Equations for the Simultaneous Flow of Matter and Energy in a Continuous Soil System. *Soil Sci.Soc. Am. Proc. 28*, 167-172.

Thirthar Palanivelu, P., And Zapata, C. (2017) "Evaluation of a Resilient Modulus Model For Unsaturated Soil Conditions" International Conference On The Bearing Capacity Of Roads, Railways And Airfields 2017, 1-15

Thomas, H.R., Siddiqua, S. and Seetharam, S.C. (2009). Inclusion of Higher-Temperature Effects in a Soil Behavior Model. Geotechnique. Symposium in Print - *Thermal Behavior of the Ground: Part 1*. 59(3), 279-282.

Topp, J.C., Davis, J. L. and Annan, A.P. (1980).Electromagnetic Determination of Soil Water Content: Measurements in Coaxial Transmission lines. *Water Resources Research.* Vol. 16 No.3. Pages 574-582.

Toll, D.G. (1990). *A Framework for Unsaturated Soil Behaviour. Geotechnique*. 40(1), 31-44

Towhata, I., Kuntiwattanakul, P., Seko, I. and Ohishi, K. (1993) Volume change of clays induced by heating as observed in consolidation tests, *Soils and Foundations*, 33(4),170-183.

Uchaipichat, A. and Khalili, N. (2009). Experimental Investigation of Thermo-Hydro-Mechanical Behaviour of an Unsaturated Silt. *Geotechnique. Symposium in Print - Thermal Behaviour of the Ground: Part 2*. 59(4), 339-353.

University of California Riverside. (2005). The Hydrus-1D Software Package for Simulating the One-Dimensional Movement of Water, Heat, and Multiple Solutes in Variably-Saturated Media. Version 3, Department of Environmental Sciences, Riverside, CA.

U.S. Army Corps of Engineers (USACE) *Engineer Manual for Laboratory Soil Testing*, 1970.

U.S. Army Corps of Engineers (USACE), UFC 3-260-02 *Pavement Design for Airfields*, 2007.

Uzan. J, Witczak M.W., Scullion. T, and Lytton R. L. (1992). Development and Validation of Realistic Pavement Response Models. *Proceedings of the 7th International Conference on Asphalt Pavements, Nottingham. International Society for Asphalt Pavements (ISAP)*, Philadelphia, PA, USA, vol. 1, pp. 334– 350.

Van Genuchten, M.T. (1980). A Closed-Form Equation for Predicting the Hydraulic Conductivity of Unsaturated Soils. *Soil Science Society of America Journal*, 44, 892-898.

Van Rooyen, M. and H.F. Winterkorn (1957). Structural and Textural Influences on Thermal Conductivity of Soils. Highway Research

Vanapalli, S. K., Fredlund, D. G., Pufahl, D. E., and Clifton, A. W. (1996) Model for the prediction of shear strength with respect to soil suction, *Canadian Geotechnical Journal*, Vol. 33, No.3, pp. 379–392

Vanapalli, S. K., Sillers, W. S., and Fredlund, M. D. (1998) The meaning and relevance of residual state to unsaturated soils, *Proceedings of the Fifty-First Canadian Geotechnical Conference*, Edmonton, AB, October 4–7, pp. 1–8.

Wan, A. W. L. (1996) *The use of thermocouple psychrometers to measure in situ suctions and water contents in compacted clays*. PhD Thesis, University of Manitoba.

Wang, X., Shao, H., Hesser, He, Zhang, C., and Wang, W. (2004) Numerical analysis of thermal impact on hydro-mechanical properties of clay. *Journal of Rock Mechanics and Geotechnical Engineering* 6 .405-416

Wilson, G.W. (1990). Soil Evaporative Fluxes for Geotechnical Engineering Problems. Ph.D. *Dissertation,* University of Saskatchewan, Saskatoon.

Witczak, M.W., and C. E. Zapata. (2000). Development of Bulk and Octahedral Shear Stress Relationships Between Equivalent Pavement Depths. *Development of the 2002 Guide for the Development of New and Rehabilitated Pavement Structures, NCHRP 1-37 A, Inter Team Technical Report,* Arizona State University, Tempe, Arizona.

Witczak M.W., W.N. Houston, and D. Andrei. (2000). Resilient Modulus as Function of Soil Moisture – A Study of the Expected Changes in Resilient Modulus of the Unbound Layers with Changes in Moisture for 10 LTPP Sites. *Development of the 2002 Guide for the Development of New and Rehabilitated Pavement Structures, NCHRP 1-37 A,* Inter Team Technical Report (Seasonal 2). Arizona State University, Tempe, Arizona.

Witczak M.W., X. Qi, and W.M. Mirza (1995). Use of Nonlinear Subgrade Modulus in AASHTO Design Procedure. *ASCE Journal of Transportation Engineering*, Vol. 123, No. 3, 1995, pp. 273-282.
Witczak, M. Wnseca, O. A. (1996) Revised Predictive Model for Dynamic (Complex) Modulus of Asphalt Mixtures, *Transportation Research Record* 1540, 15-23.

Woodside, W., And Cliffe, J. B. 1959 Heat and moisture transfer in closed systems of two granular materials. Soil Sci. 87: 75-82.

Yoder, E. J., Witczak, M. W. (1975). Principles of Pavement Design, John Wiley & Sons, 1975

Zhang, M., Zhang, H., Zhou, L., Jia, L. Temperature effects on unsaturated hydraulic property of bentonite-sand buffer backfilling mixtures, J*ournal of Wuhan University of Technology-Mater. Sci. Ed. June 2013* pp 487-494.

Zapata, C.E., Andrei, D., Witczak, M.W. and Houston, W.N. (2007). Incorporation of Environmental Effects in Pavement Design. *International Journal of Road Materials and Pavement Design,* 8(4), 667-693.

Zapata, C.E., Perera, Y.Y. and Houston, W.N. (2009). Matric Suction Prediction Model in New AASHTO Mechanistic-Empirical Pavement Design Guide. Transportation Research Record: *Journal of the Transportation Research Board*, No. 2101, Geology and Properties of Earth Materials, 53-62.

Zapata, C.E., Palanivelu, P.T., Lu, Y., Contreras, J. and Gowda, R.P.C. (2017). Investigation of Subgrade Moisture Flow in an Airfield Pavement System. *Federal Aviation Administration. Research Project No. 13-G-008 Final Report*. Tempe, AZ.

Zapata, C.E., Witczak, M.W. and Palanivelu, P.T. (2017). “Evaluation of the Federal Aviation Administration Methodology for Characterizing the Nonlinear Behavior of Granular Base and Subbase Materials”. *Transportation Geotechnics Online Publication*. DOI information: 10.1016/j.trgeo.2017.06.004.

APPENDIX A

CBR TESTING DATA SET

ID	CCM510USO	Volume of the Mold	2118.49	cm^3
Type of Soil	County	Dry Density of the soil	108.70	pcf
Category	Modified	Water content	11.42	%
No. of Layers	5	Dry Mass of Soil	3690.51	g
No. of blows	26	Wet Mass of Soil and Mold	12208.60	g
		Mold Mass	8096.70	g
CBR	38	Height of Specimen	11.62	cm
Vane shear result	23.2	Diameter of Mold	15.24	cm

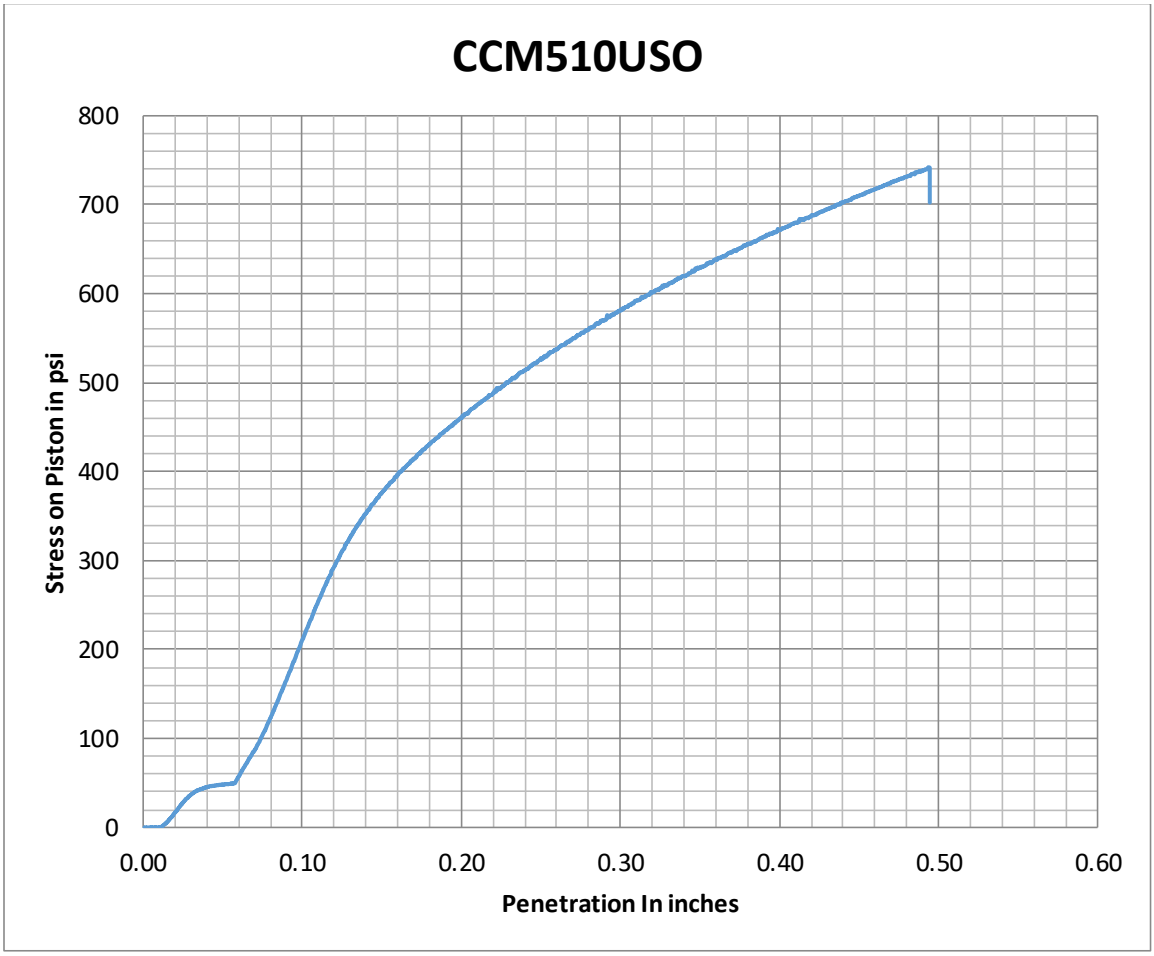

ID	CCS315USO	Volume of the Mold	2118.49	cm^3
Type of Soil	County	Dry Density of the soil	96.92	pcf
Category	Standard	Water content	17.01	%
No. of Layers	3	Dry Mass of Soil	3290.33	g
No. of blows	56	Wet Mass of Soil and Mold	11945.80	g
		Mold Mass	8095.90	g
CBR	14	Height of Specimen	11.62	cm
Vane shear result	10.6	Diameter of Mold	15.24	cm

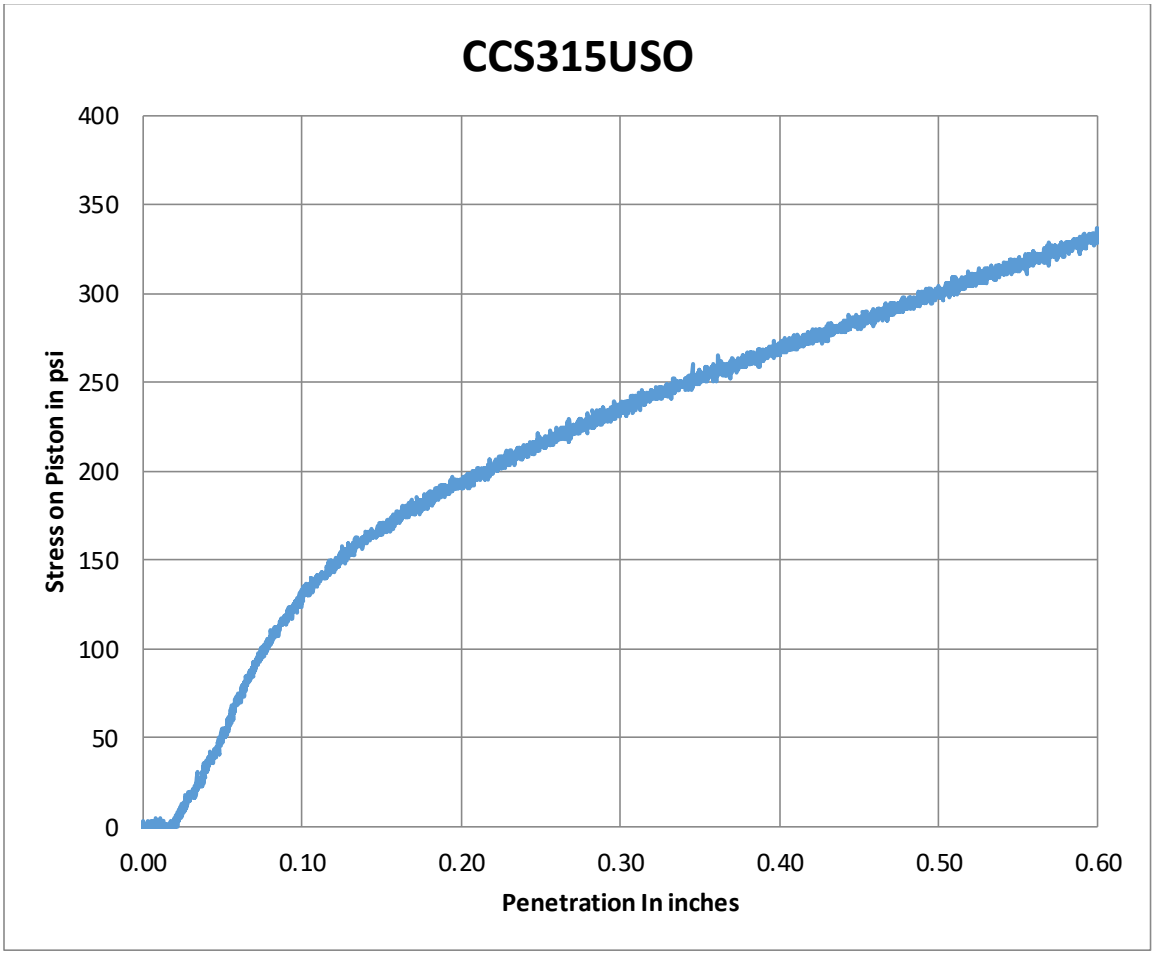

ID	CCI515USO	Volume of the Mold	2118.49	cm^3
Type of Soil	County	Dry Density of the soil	99.73	pcf
Category	Intermediate	Water content	16.08	%
No. of Layers	5	Dry Mass of Soil	3385.97	g
No. of blows	56	Wet Mass of Soil and Mold	11220.50	g
		Mold Mass	7290.20	g
CBR	21	Height of Specimen	11.62	cm
Vane shear result	12.3	Diameter of Mold	15.24	cm

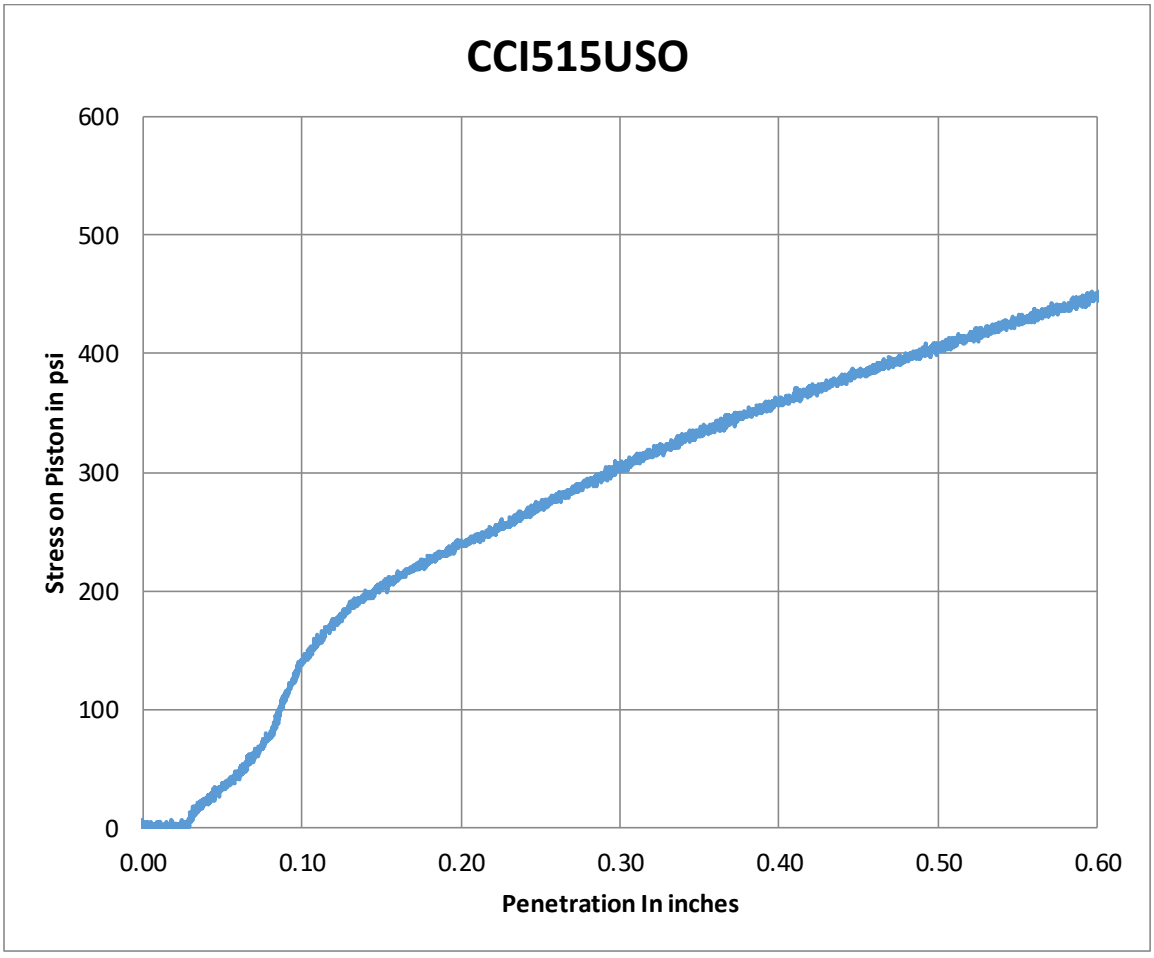

ID	CCM515USO	Volume of the Mold	2118.49	cm^3
Type of Soil	County	Dry Density of the soil	113.30	pcf
Category	Modified	Water content	16.53	%
No. of Layers	5	Dry Mass of Soil	3846.55	g
No. of blows	26	Wet Mass of Soil and Mold	11770.70	g
		Mold Mass	7288.20	g
CBR	48	Height of Specimen	11.62	cm
Vane shear result	21.6	Diameter of Mold	15.24	cm

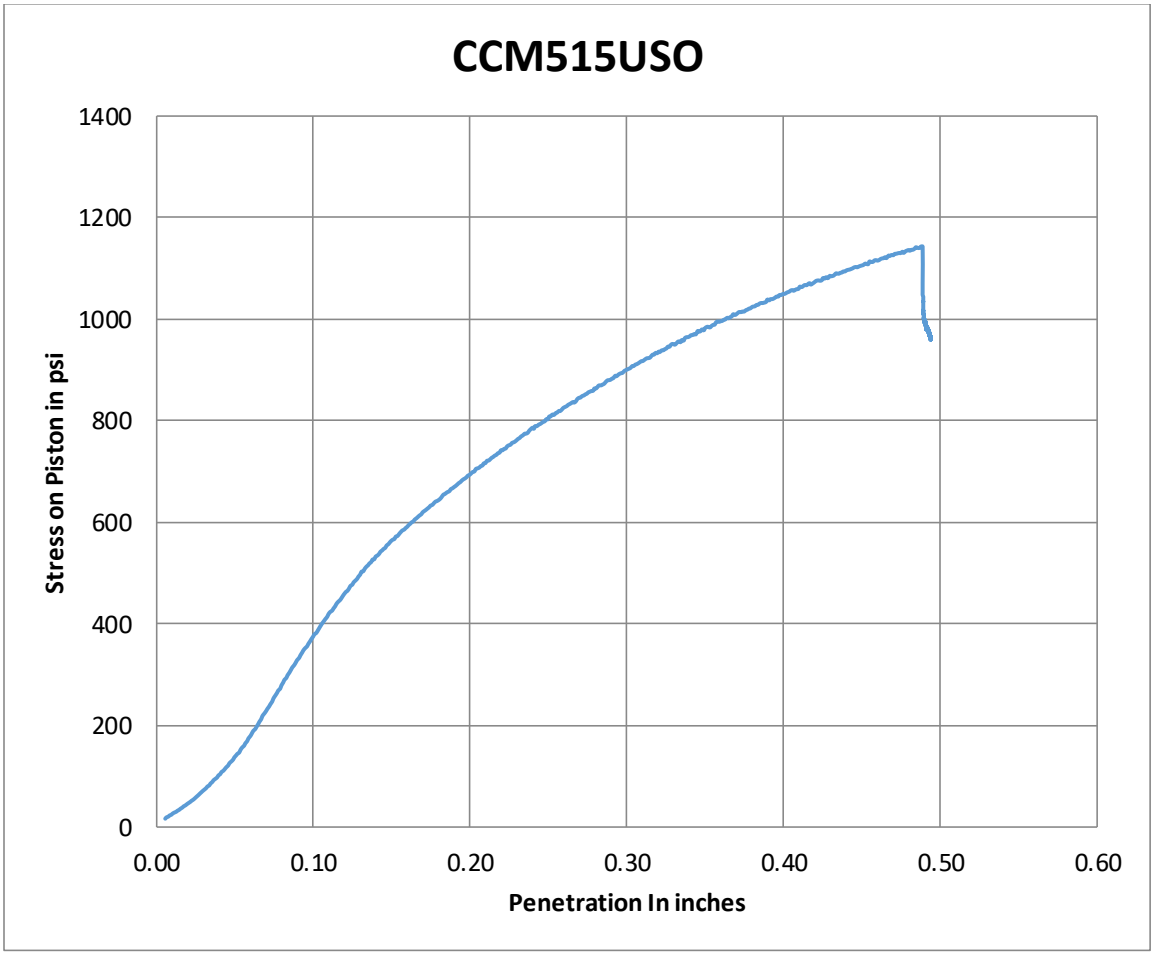

ID	CCS320USO	Volume of the Mold	2118.49	cm^3
Type of Soil	County	Dry Density of the soil	100.17	pcf
Category	Standard	Water content	20.58	%
No. of Layers	3	Dry Mass of Soil	3400.72	g
No. of blows	56	Wet Mass of Soil and Mold	11467.60	g
		Mold Mass	7366.90	g
		Height of Specimen	11.62	cm
CBR	12.0			
Vane shear result	7.3	Diameter of Mold	15.24	cm

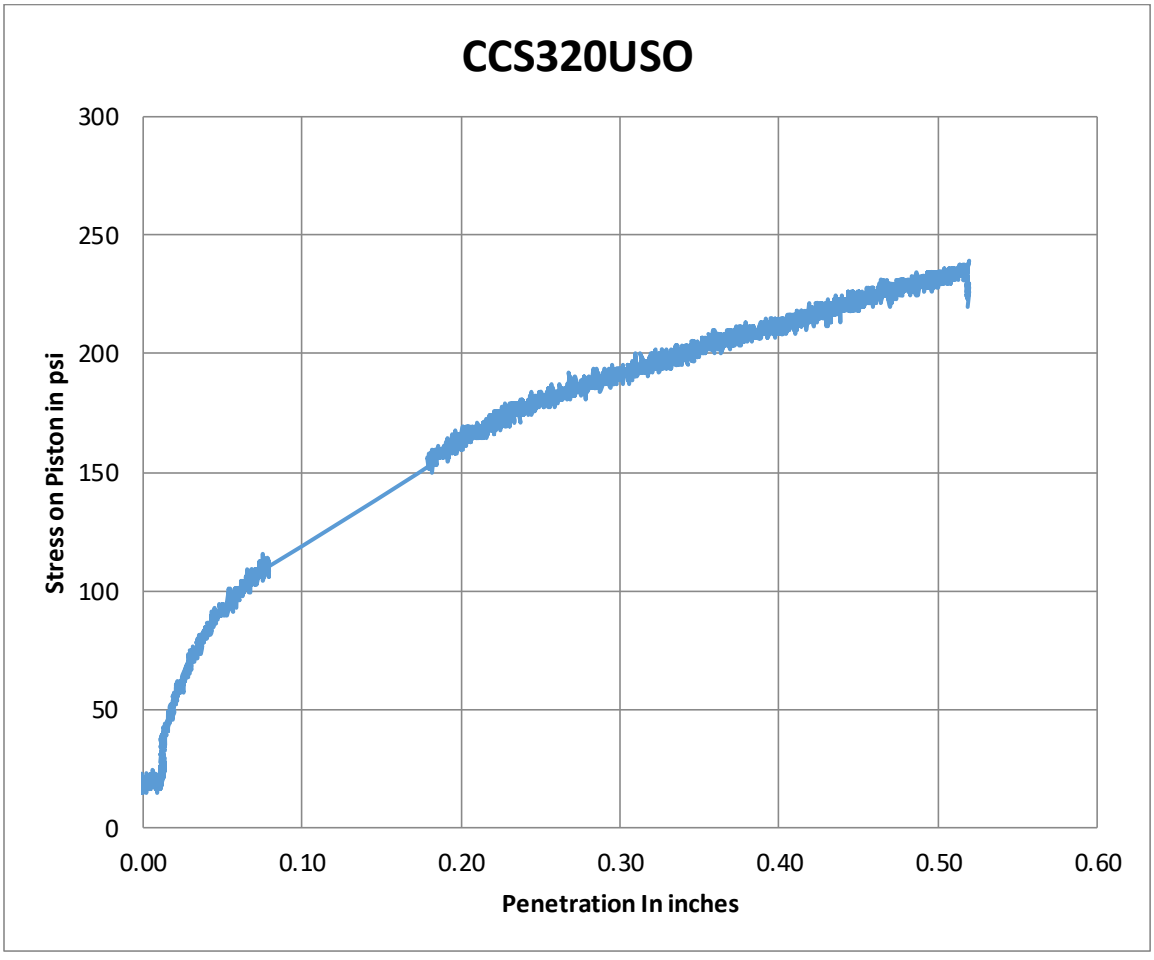

ID	CCI520USO	Volume of the Mold	2118.49	cm^3
Type of Soil	County	Dry Density of the soil	104.40	pcf
Category	Intermediate	Water content	18.88	%
No. of Layers	5	Dry Mass of Soil	3544.46	g
No. of blows	56	Wet Mass of Soil and Mold	11412.40	g
		Mold Mass	7198.90	g
CBR	10.3	Height of Specimen	11.62	cm
Vane shear result	7.01	Diameter of Mold	15.24	cm

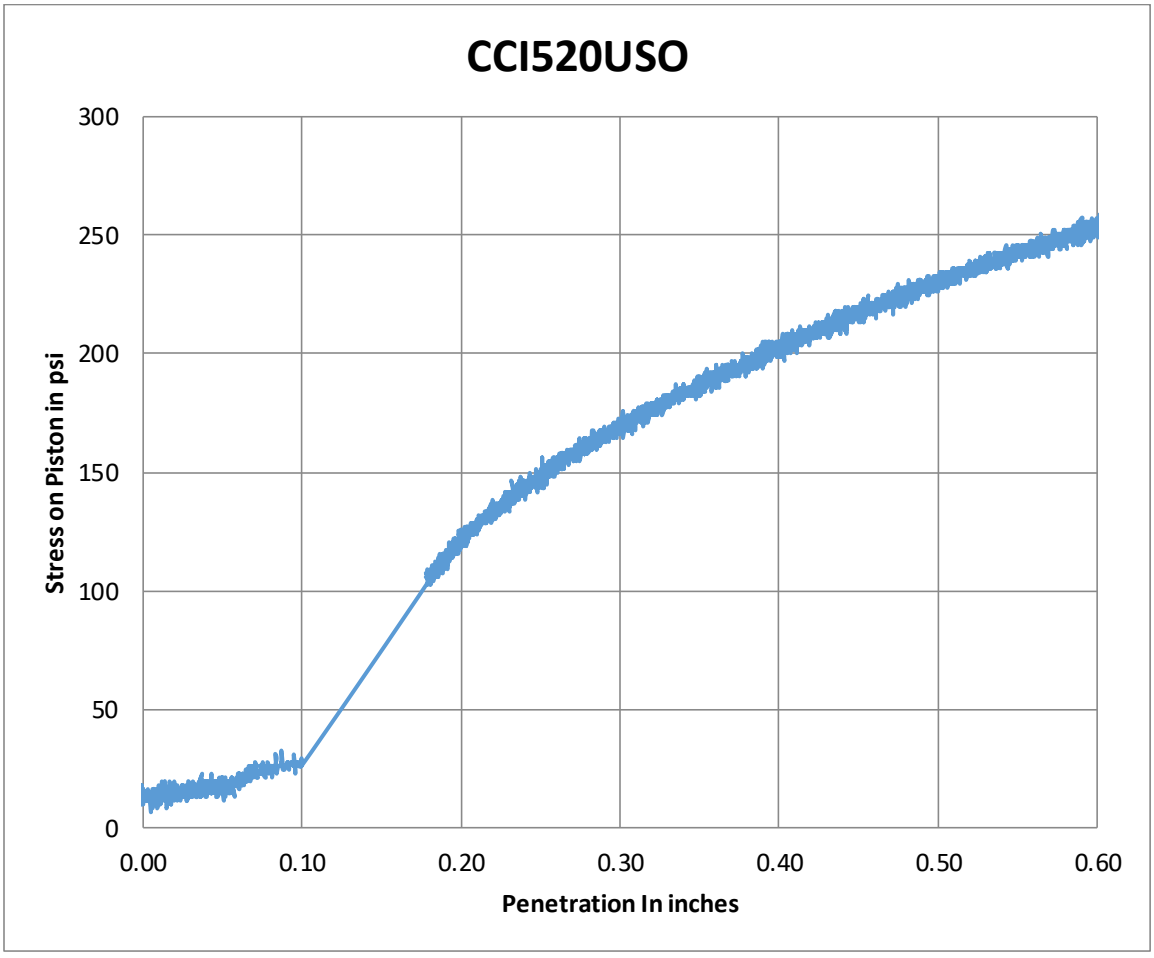

ID	CCS325USO		Volume of the Mold	2118.49	cm^3
Type of Soil	County		Dry Density of the soil	100.82	pcf
Category	Standard		Water content	22.22	%
No. of Layers		3	Dry Mass of Soil	3422.77	g
No. of blows		56	Wet Mass of Soil and Mold	11432.00	g
			Mold Mass	7248.80	g
			Height of Specimen	11.62	cm
CBR		3.1			
Vane shear result		5.98	Diameter of Mold	15.24	cm

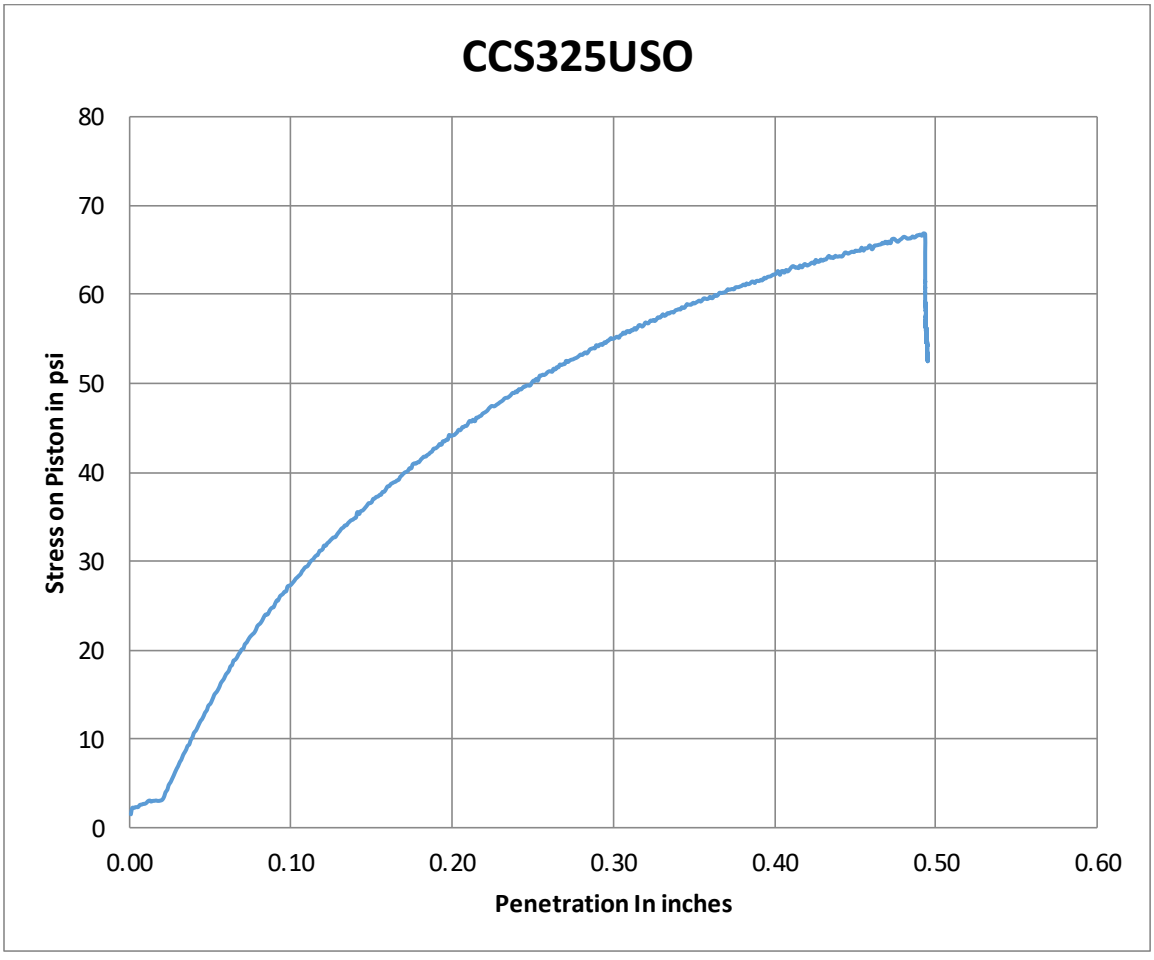

ID	CCI525USO		Volume of the Mold	2118.49	cm^3
Type of Soil	County		Dry Density of the soil	102.00	pcf
Category	Intermediate		Water content	22.50	%
No. of Layers		5	Dry Mass of Soil	3463.03	g
No. of blows		56	Wet Mass of Soil and Mold	11504.60	g
			Mold Mass	7262.30	g
CBR		11.5	Height of Specimen	11.62	cm
Vane shear result		10.6	Diameter of Mold	15.24	cm

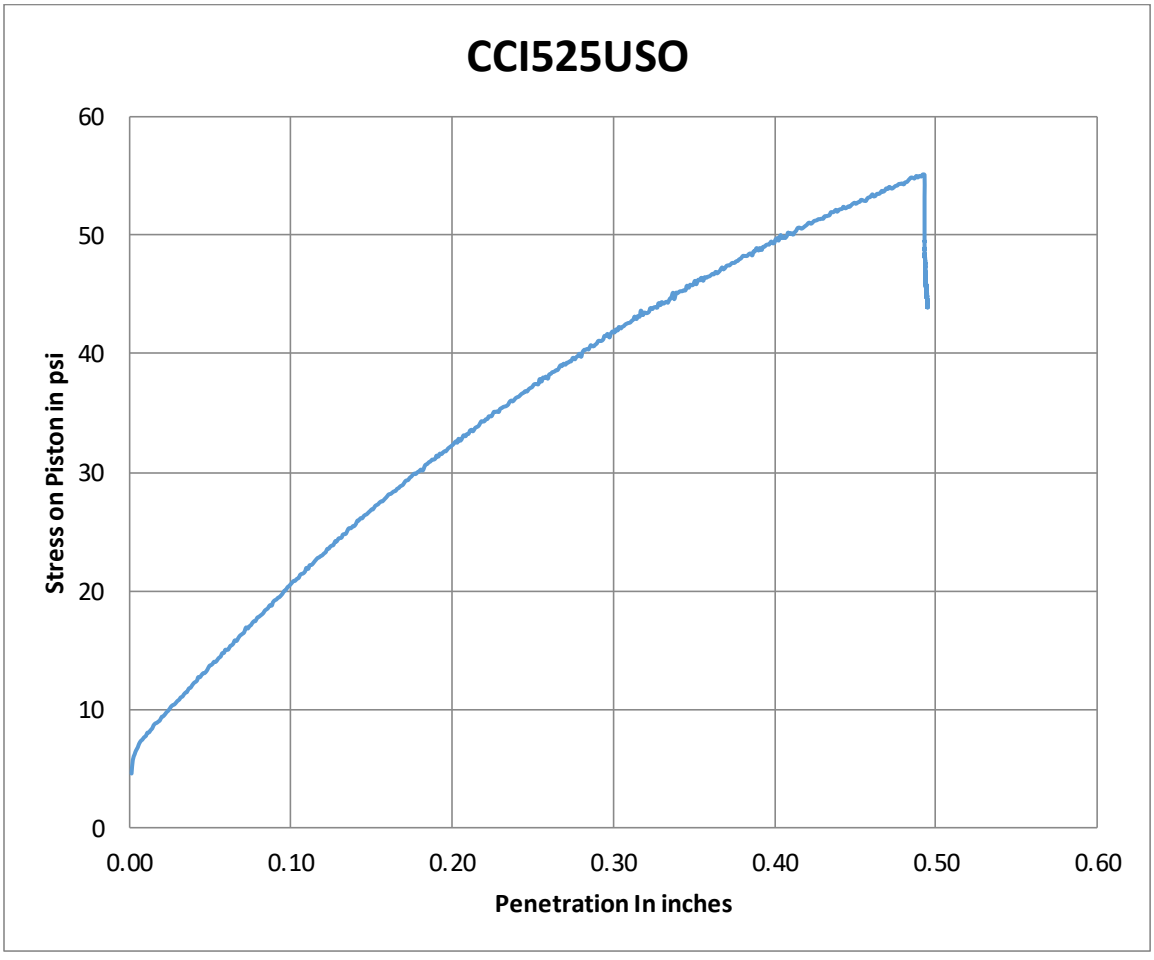

ID	CCM525USO	Volume of the Mold	2118.49	cm^3
Type of Soil	County	Dry Density of the soil	105.51	pcf
Category	Modified	Water content	22.36	%
No. of Layers	5	Dry Mass of Soil	3582.17	g
No. of blows	26	Wet Mass of Soil and Mold	12639.60	g
		Mold Mass	8256.40	g
CBR	16.3	Height of Specimen	11.62	cm
Vane shear result	20.4	Diameter of Mold	15.24	cm

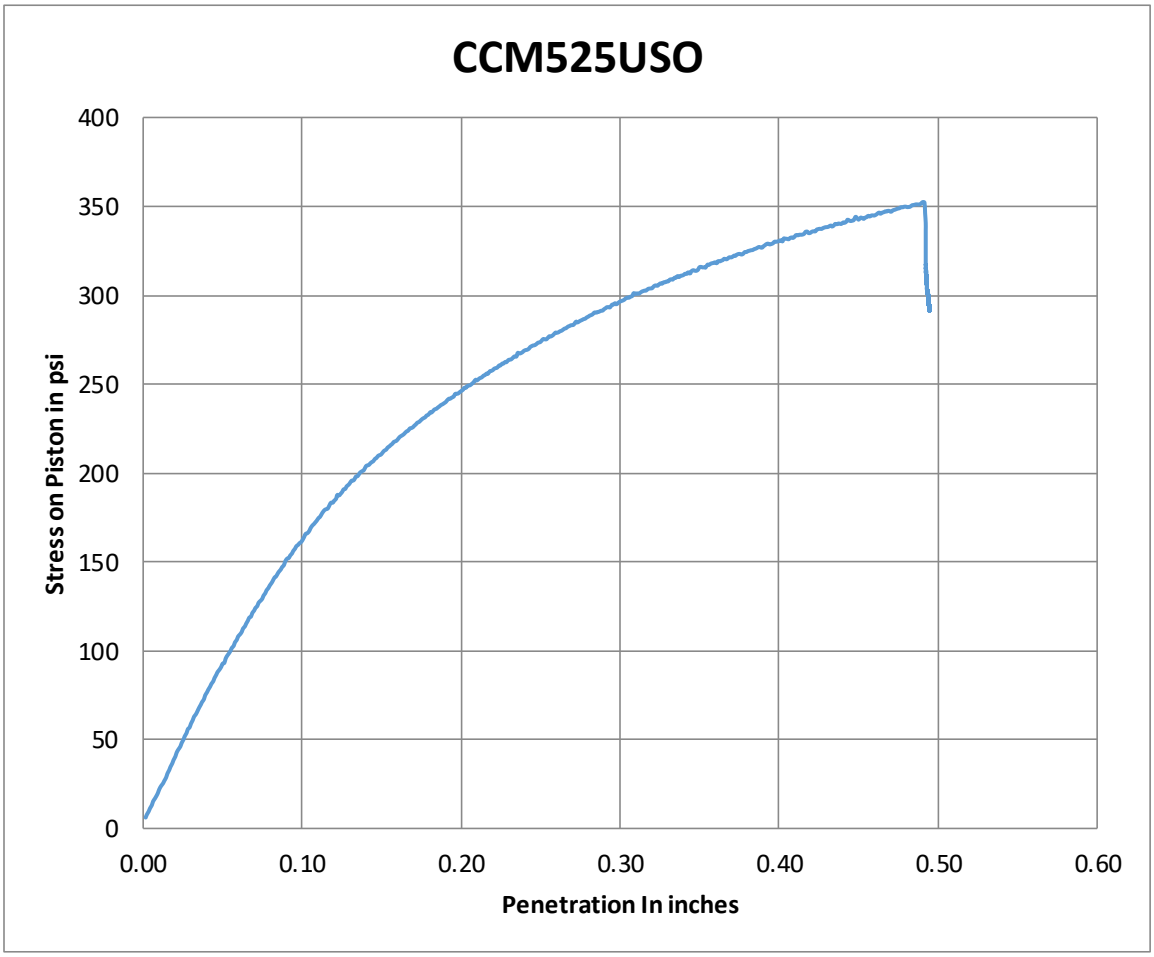

ID	CCS327USO		Volume of the Mold	2118.49	cm^3
Type of Soil	County		Dry Density of the soil	93.82	pcf
Category	Standard		Water content	26.14	%
No. of Layers		3	Dry Mass of Soil	3185.26	g
No. of blows		56	Wet Mass of Soil and Mold	12115.10	g
			Mold Mass	8097.10	g
CBR		0.35	Height of Specimen	11.62	cm
Vane shear result		0.85	Diameter of Mold	15.24	cm

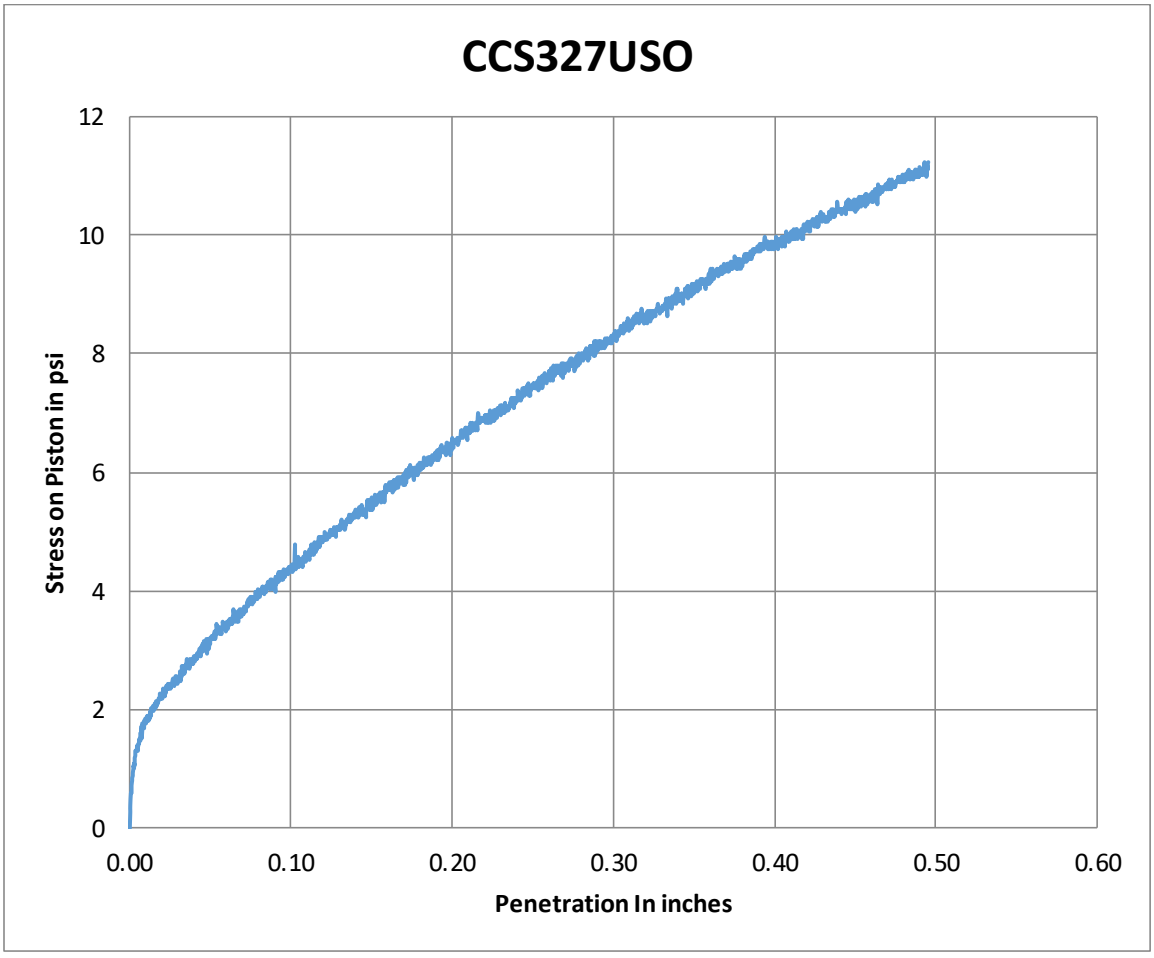

ID	CCI527USO		Volume of the Mold	2118.49	cm^3
Type of Soil	County		Dry Density of the soil	96.23	pcf
Category	Intermediate		Water content	26.24	%
No. of Layers		5	Dry Mass of Soil	3266.97	g
No. of blows		56	Wet Mass of Soil and Mold	11475.10	g
			Mold Mass	7350.90	g
			Height of		
CBR		0.46	Specimen	11.62	cm
Vane shear					
result		0.2	Diameter of Mold	15.24	cm

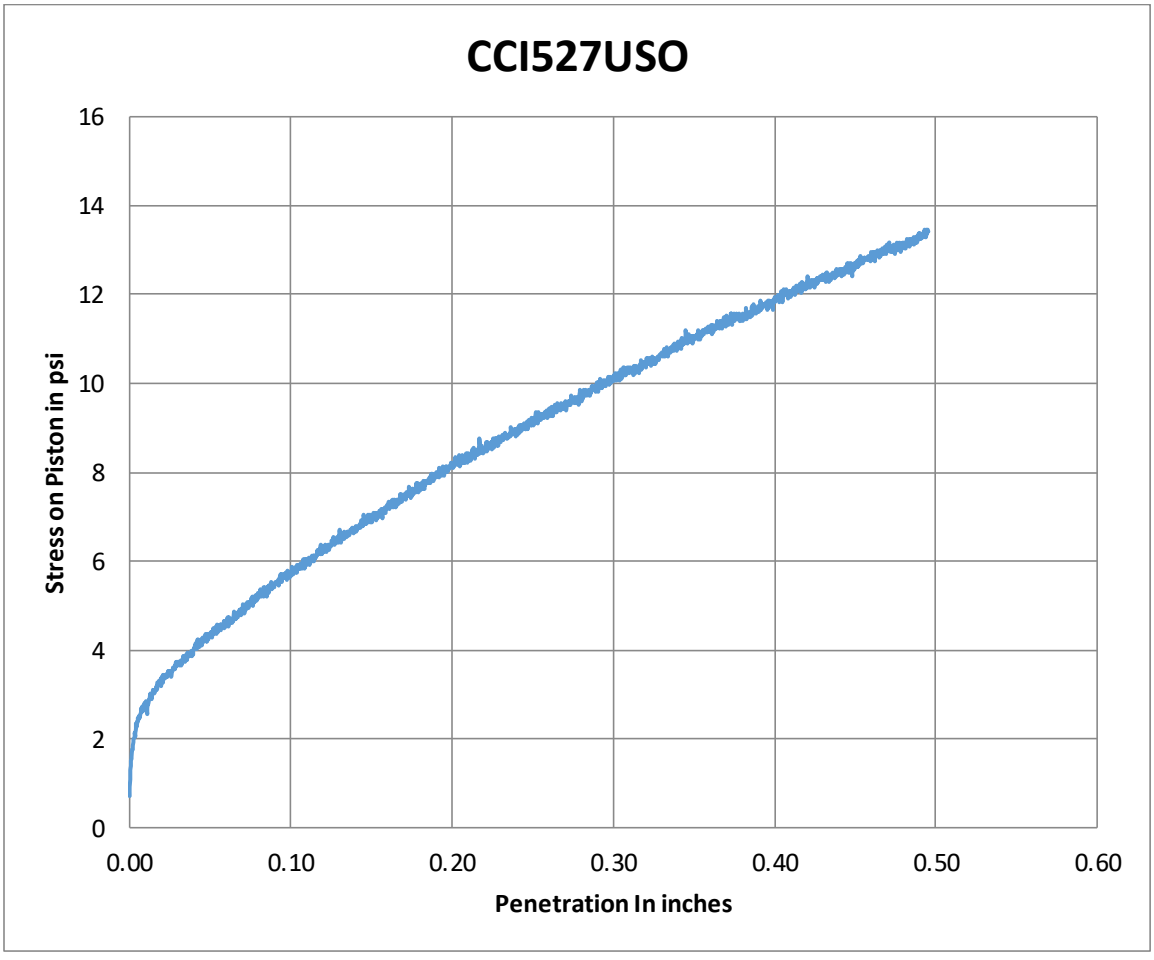

ID	CCM527USO	Volume of the Mold	2118.49	cm^3
Type of Soil	County	Dry Density of the soil	98.08	pcf
Category	Modified	Water content	26.51	%
No. of Layers	5	Dry Mass of Soil	3329.96	g
No. of blows	26	Wet Mass of Soil and Mold	11611.20	g
		Mold Mass	7398.50	g
CBR	0.73	Height of Specimen	11.62	cm
Vane shear result	4.21	Diameter of Mold	15.24	cm

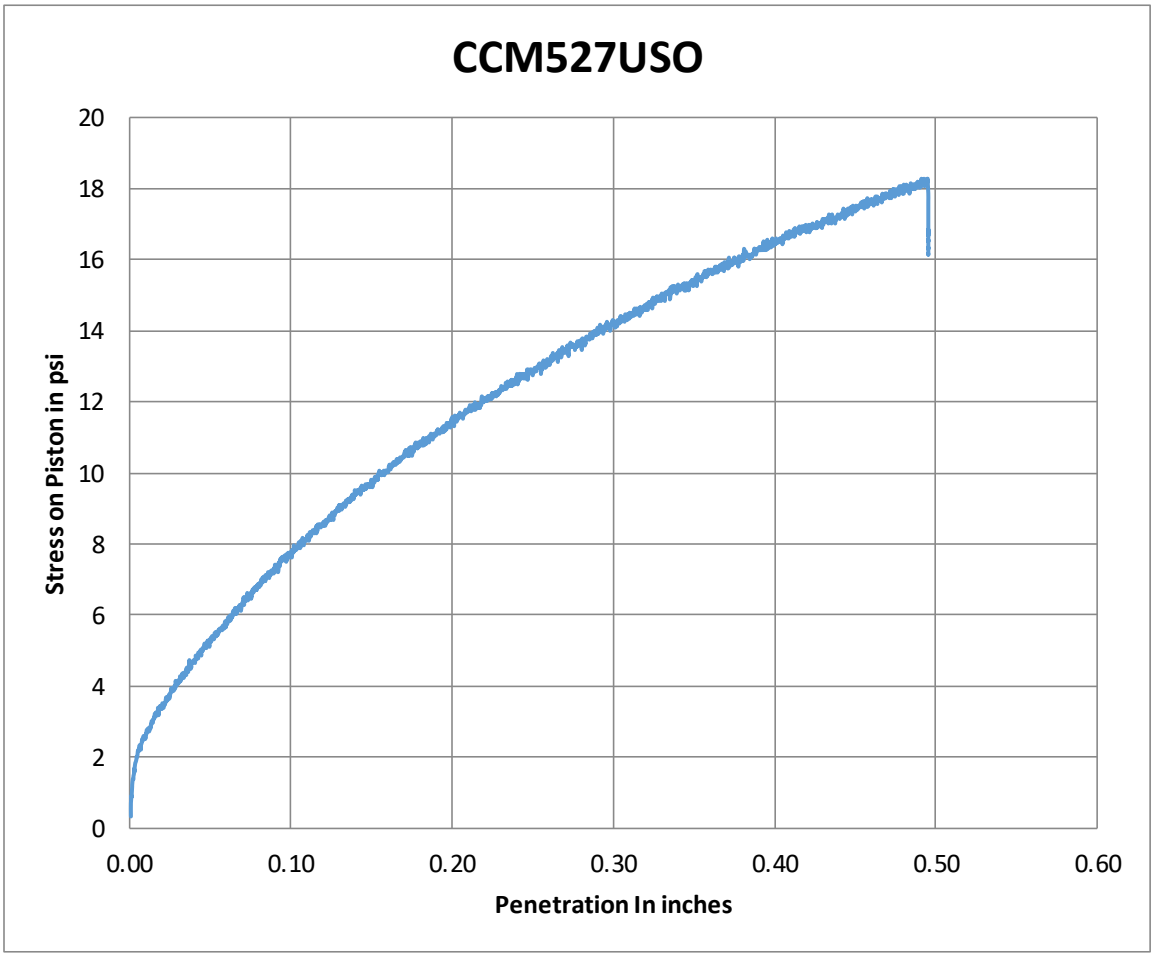

ID	CCS330USO		Volume of the Mold	2118.49	cm^3
Type of Soil	County		Dry Density of the soil	84.95	pcf
Category	Standard		Water content	31.80	%
No. of Layers		3	Dry Mass of Soil	3329.96	g
No. of blows		56	Wet Mass of Soil and Mold	11128.90	g
			Mold Mass	7398.50	g
			Height of Specimen	11.62	cm
CBR		0.22			
Vane shear result		0.50	Diameter of Mold	15.24	cm

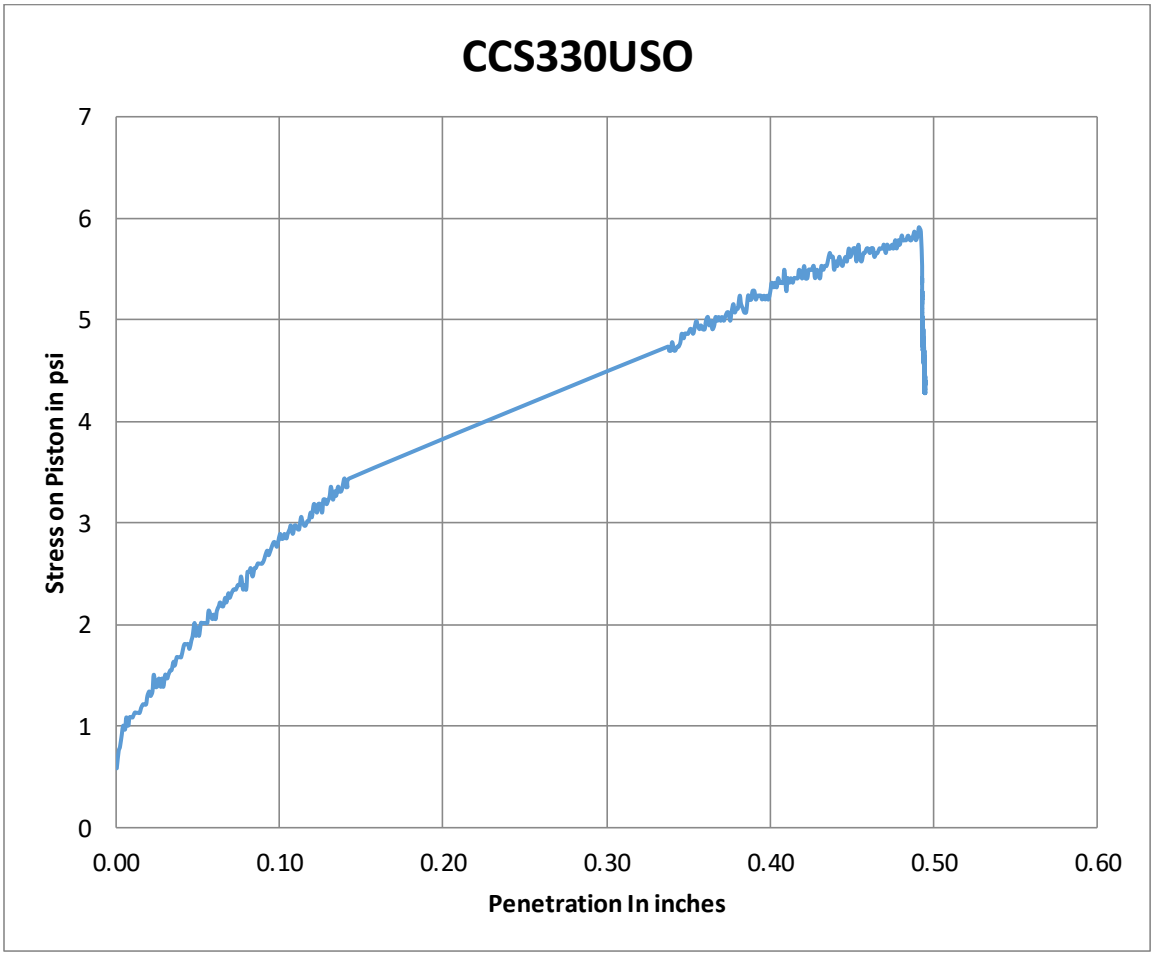

ID	CCS335USO		Volume of the Mold	2118.49	cm^3
Type of Soil	County		Dry Density of the soil	83.72	pcf
Category	Standard		Water content	34.46	%
No. of Layers		3	Dry Mass of Soil	2842.34	g
No. of blows		56	Wet Mass of Soil and Mold	11178.20	g
			Mold Mass	7356.30	g
			Height of		
CBR		0.05	Specimen	11.62	cm
Vane shear					
result		0.2	Diameter of Mold	15.24	cm

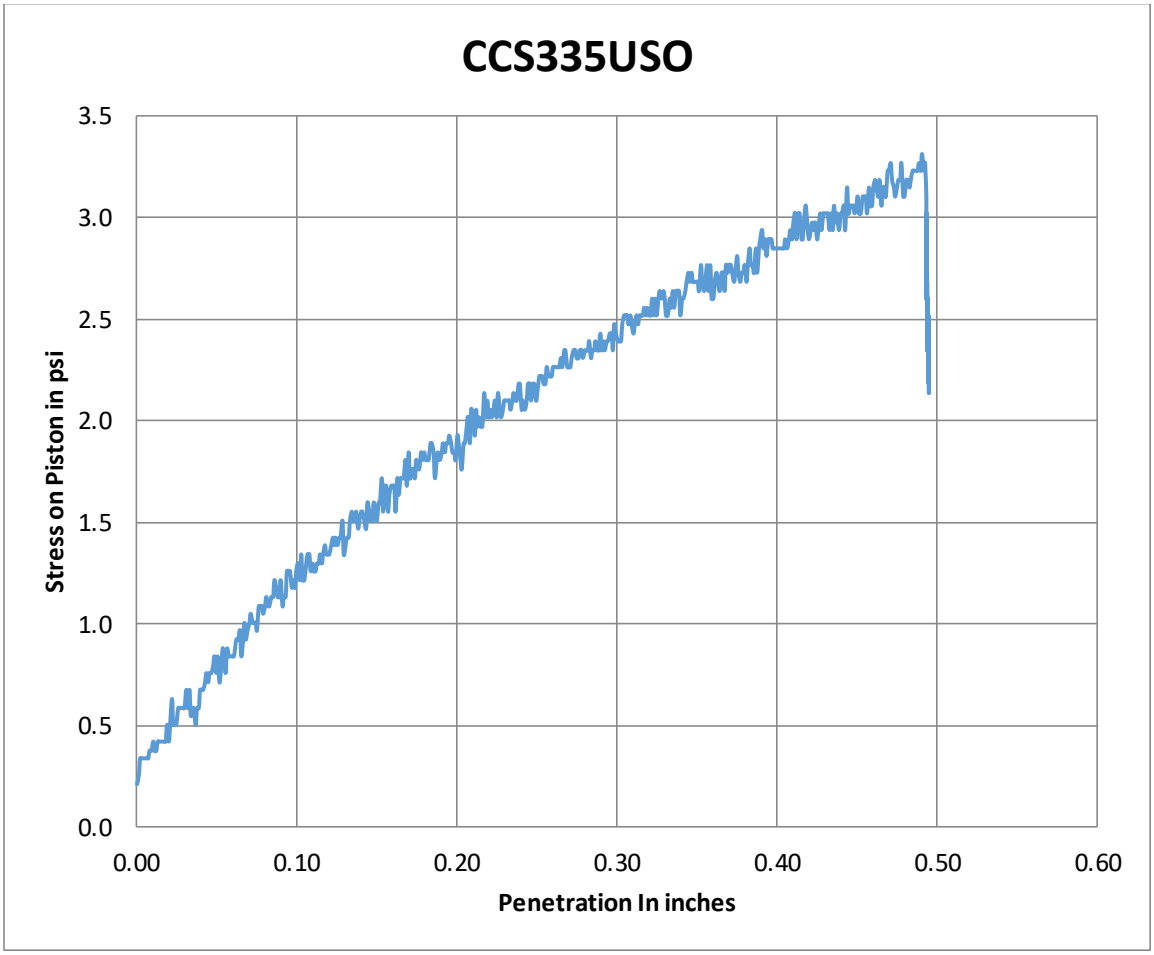

ID	CCI535USO		Volume of the Mold	2118.49	cm^3
Type of Soil	County		Dry Density of the soil	84.78	pcf
Category	Intermediate		Water content	34.46	%
No. of Layers		5	Dry Mass of Soil	2878.26	g
No. of blows		56	Wet Mass of Soil and Mold	11275.30	g
			Mold Mass	7405.10	g
			Height of		
CBR		0.06	Specimen	11.62	cm
Vane shear					
result		0.2	Diameter of Mold	15.24	cm

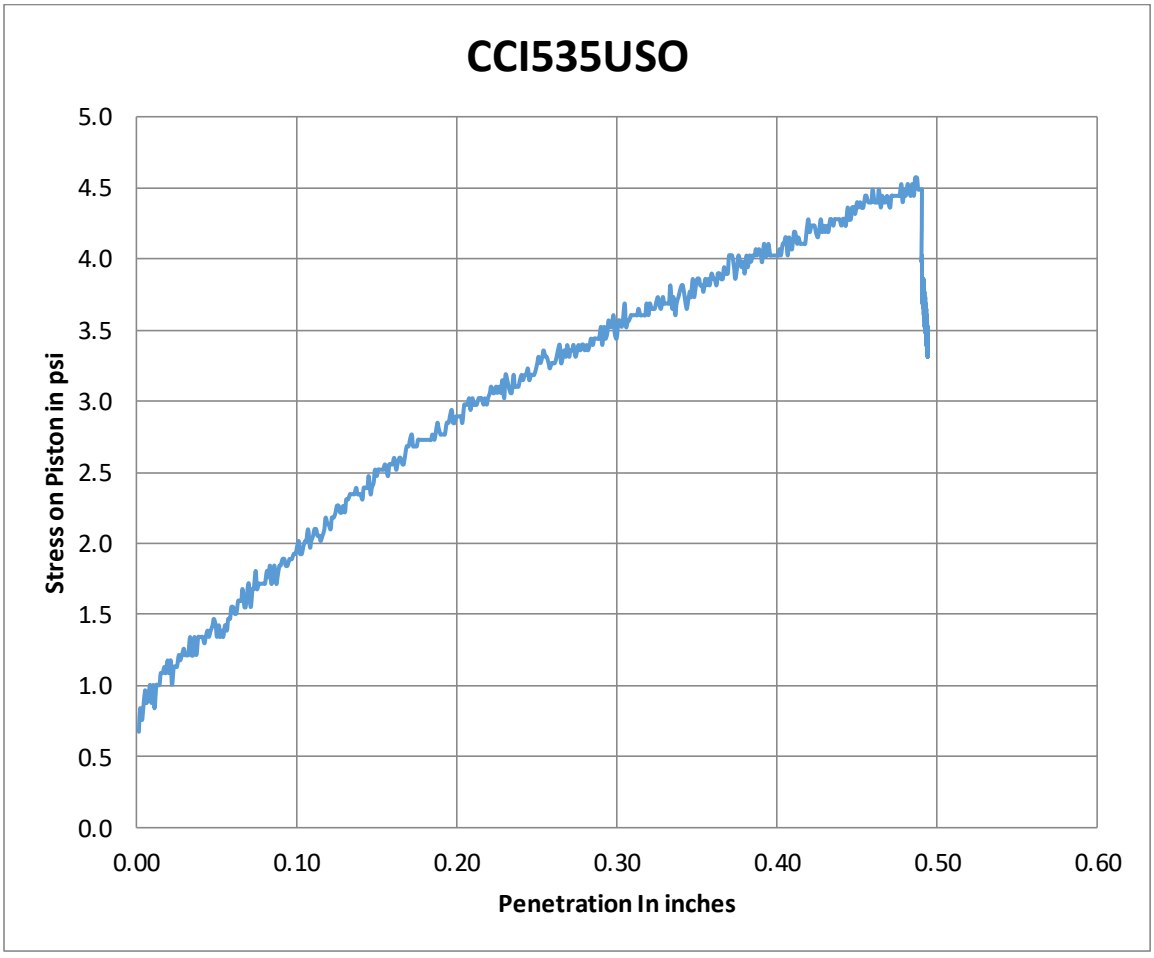

ID	CCM535USO	Volume of the Mold	2118.49	cm^3
Type of Soil	County	Dry Density of the soil	85.60	pcf
Category	Modified	Water content	33.13	%
No. of Layers	5	Dry Mass of Soil	2906.19	g
No. of blows	56	Wet Mass of Soil and Mold	11198.00	g
		Mold Mass	7328.90	g
CBR	0.09	Height of Specimen	11.62	cm
Vane shear result	0.5	Diameter of Mold	15.24	cm

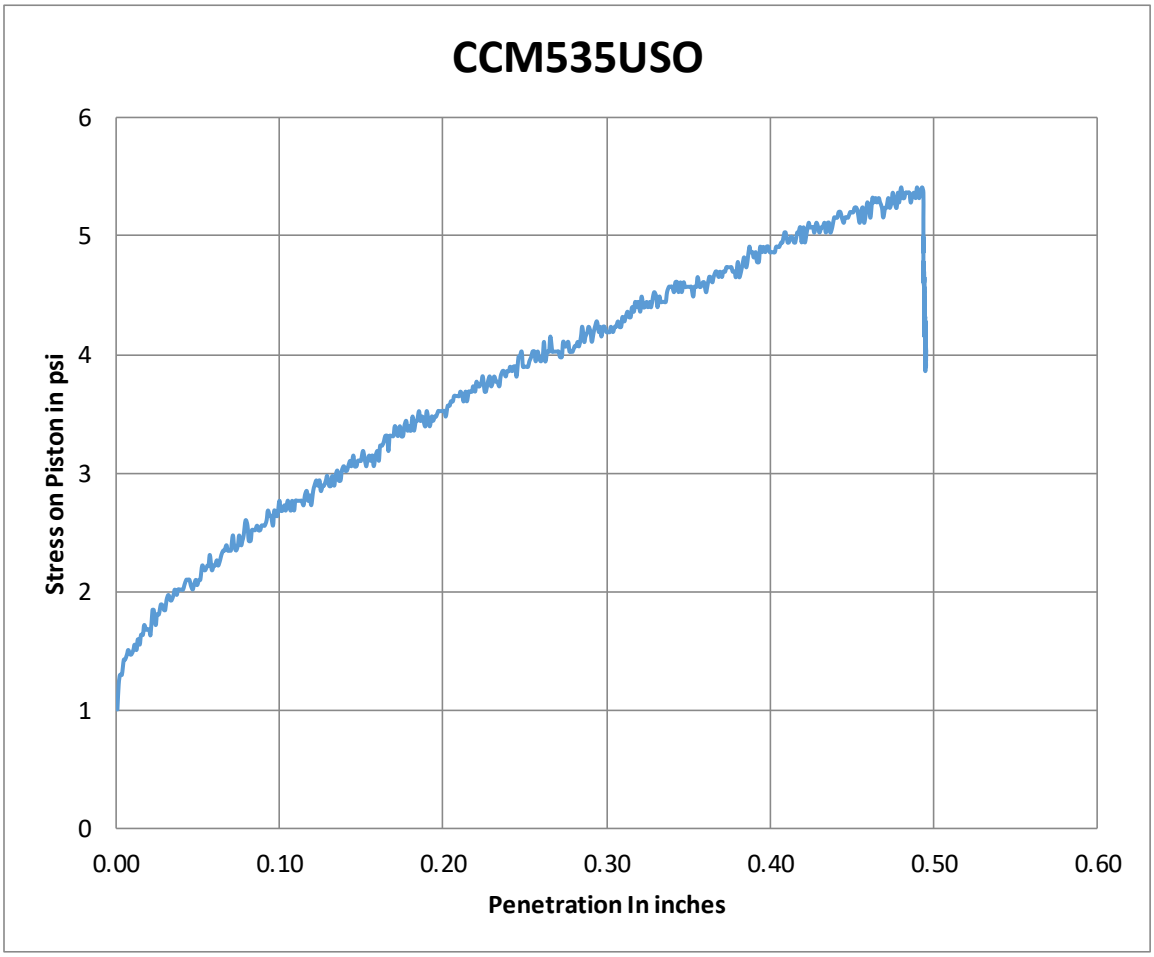

ID	CCM508USO	Volume of the Mold	2118.49	cm^3
Type of Soil	County	Dry Density of the soil	106.90	pcf
Category	Modified	Water content	9.64	%
No. of Layers	5	Dry Mass of Soil	3664.98	g
No. of blows	56	Wet Mass of Soil and Mold	11302.80	g
		Mold Mass	7284.40	g
CBR	52	Height of Specimen	11.62	cm
Vane shear result	-	Diameter of Mold	15.24	cm

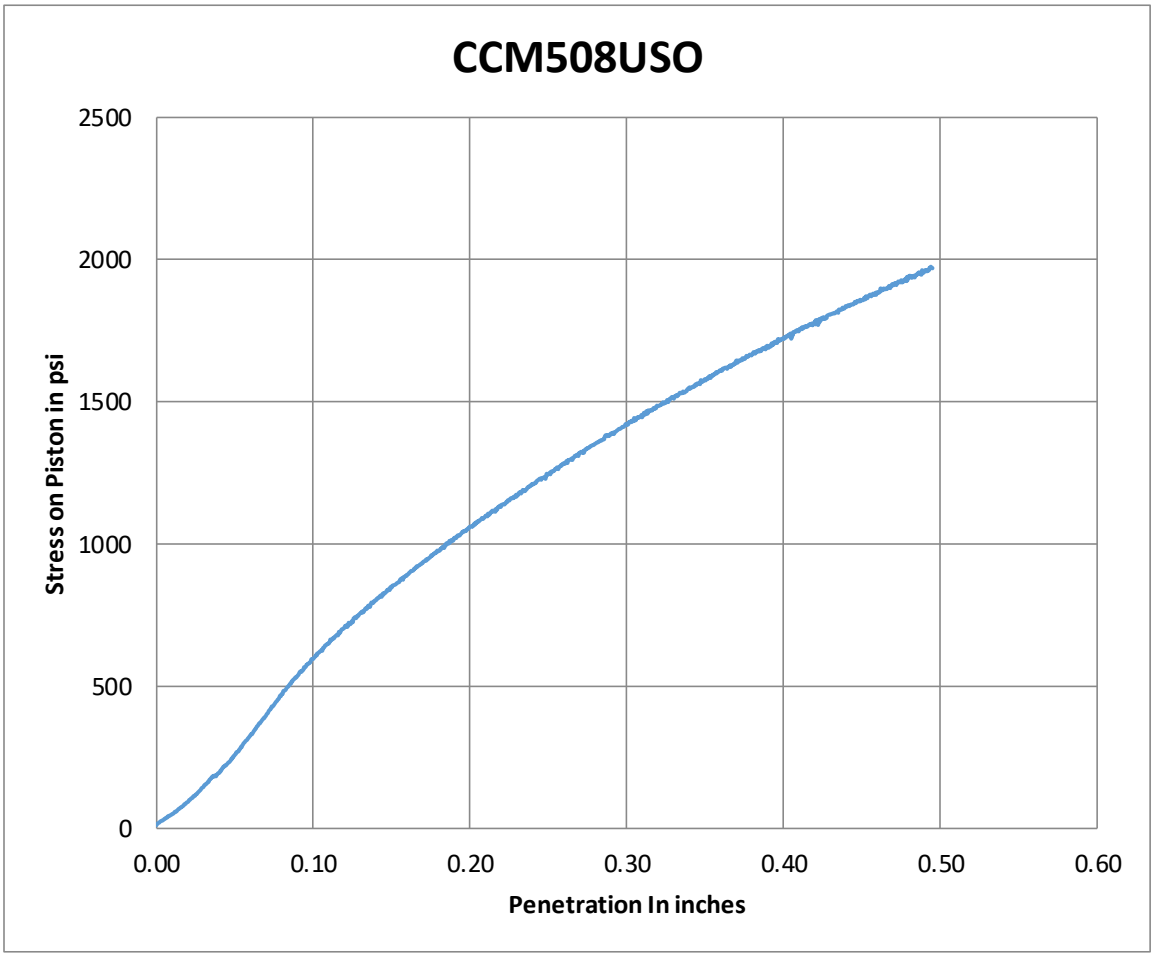

ID	CCI514USO		Volume of the Mold	2118.49	cm^3
Type of Soil	County		Dry Density of the soil	97.53	pcf
Category	Intermediate		Water content	14.53	%
No. of Layers		5	Dry Mass of Soil	3311.30	g
No. of blows		56	Wet Mass of Soil and Mold	11142.80	g
			Mold Mass	7350.50	g
			Height of		
CBR		21.8	Specimen	11.62	cm
Vane shear					
result		-	Diameter of Mold	15.24	cm

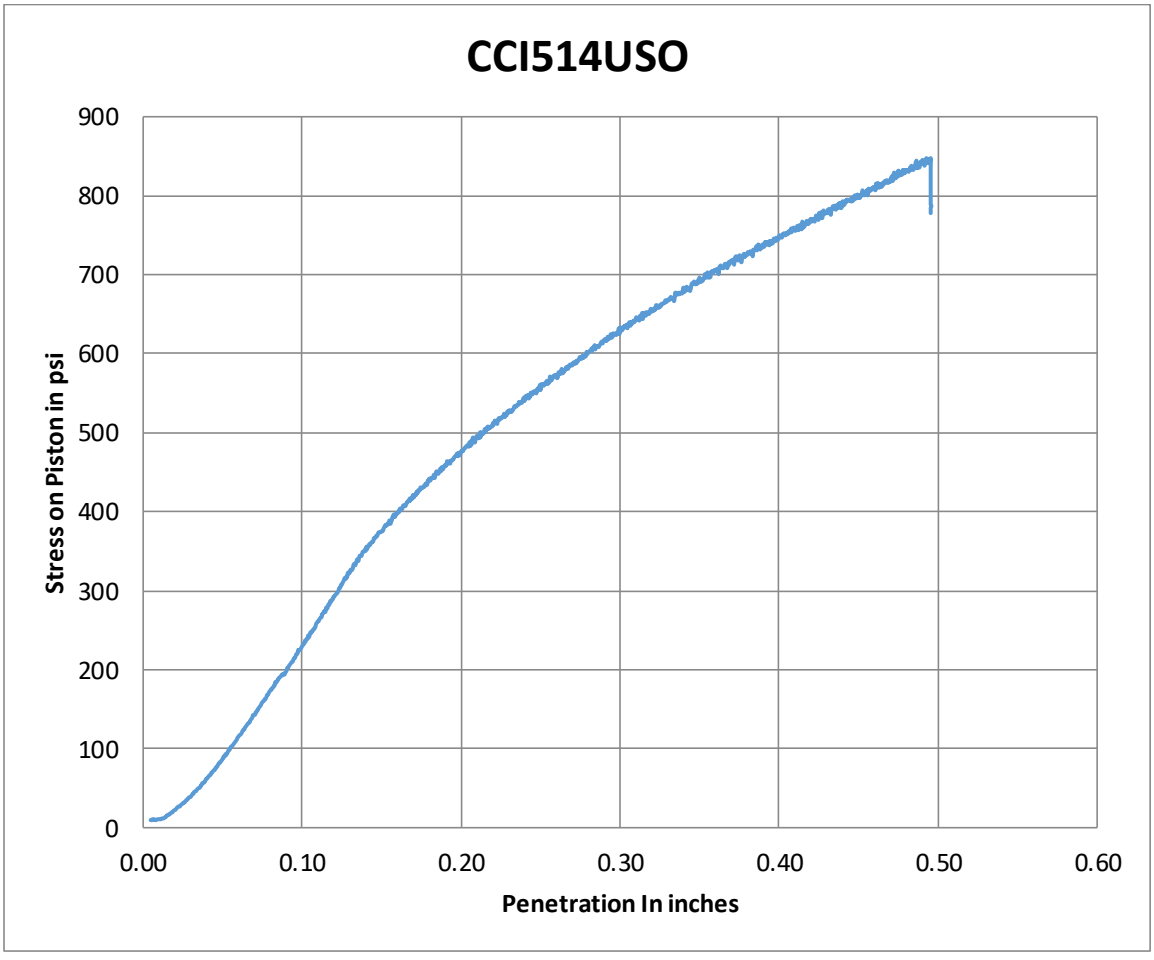

ID	CCM517USO		Volume of the Mold	2118.49	cm^3
Type of Soil	County		Dry Density of the soil	111.98	pcf
Category	Modified		Water content	17.01	%
No. of Layers		5	Dry Mass of Soil	3801.87	g
No. of blows		56	Wet Mass of Soil and Mold	11733.40	g
			Mold Mass	7284.80	g
			Height of		
CBR		11.2	Specimen	11.62	cm
Vane shear result			Diameter of Mold	15.24	cm

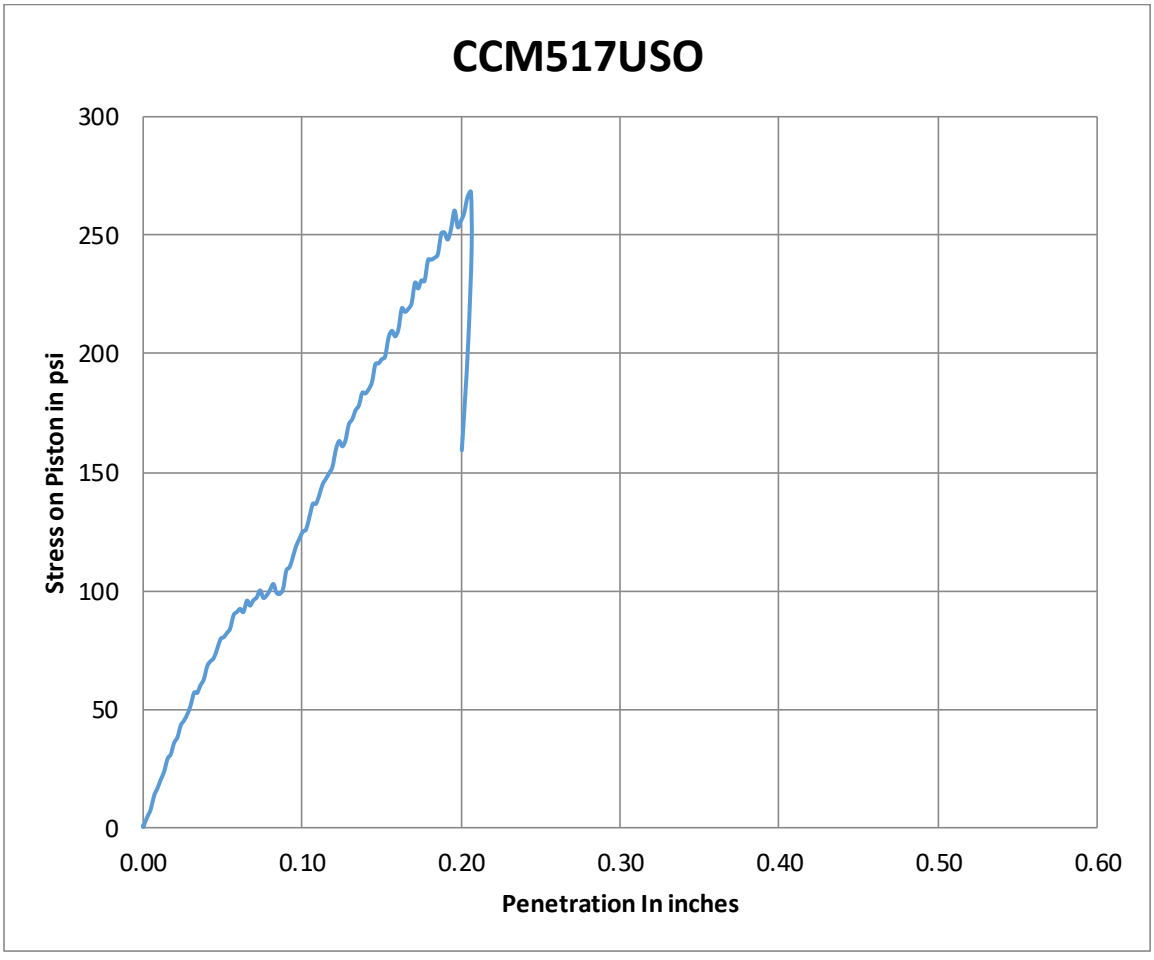

ID	DCS313USO	Volume of the Mold	2118.49	cm^3
Type of Soil	Dupont	Dry Density of the soil	89.20	pcf
Category	Standard	Water content	14.07	%
No. of Layers	3	Dry Mass of Soil	3028.30	g
No. of blows	56	Wet Mass of Soil and Mold	10852.60	g
		Mold Mass	7398.10	g
CBR	12.5	Height of Specimen	11.62	cm
Vane shear result	13.5	Diameter of Mold	15.24	cm

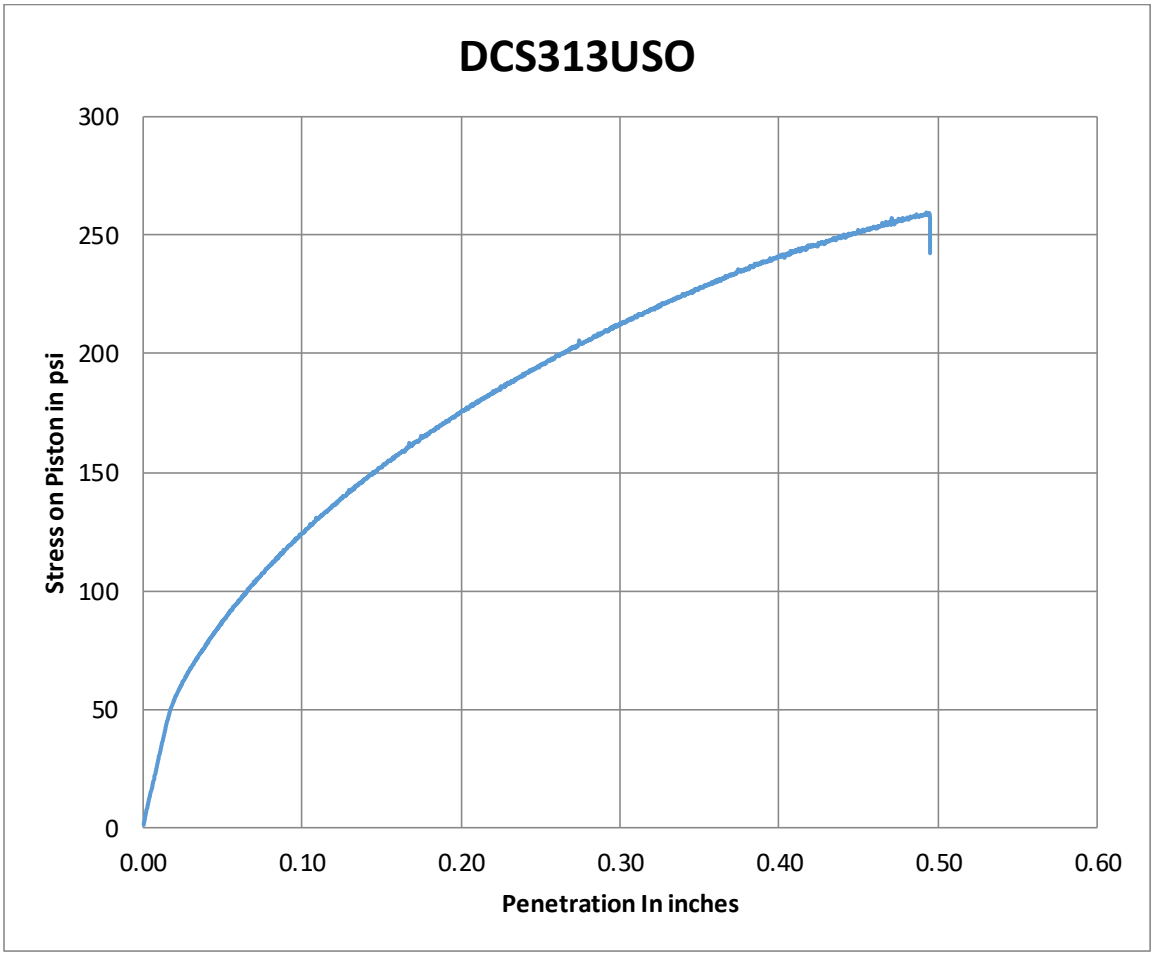

ID	DCI513USO	Volume of the Mold	2118.49	cm^3
Type of Soil	Dupont	Dry Density of the soil	93.89	pcf
Category	Intermediate	Water content	14.07	%
No. of Layers	5	Dry Mass of Soil	3187.50	g
No. of blows	56	Wet Mass of Soil and Mold	10986.30	g
		Mold Mass	7350.20	g
		Height of		
CBR	13.4	Specimen	11.62	cm
Vane shear				
result	15	Diameter of Mold	15.24	cm

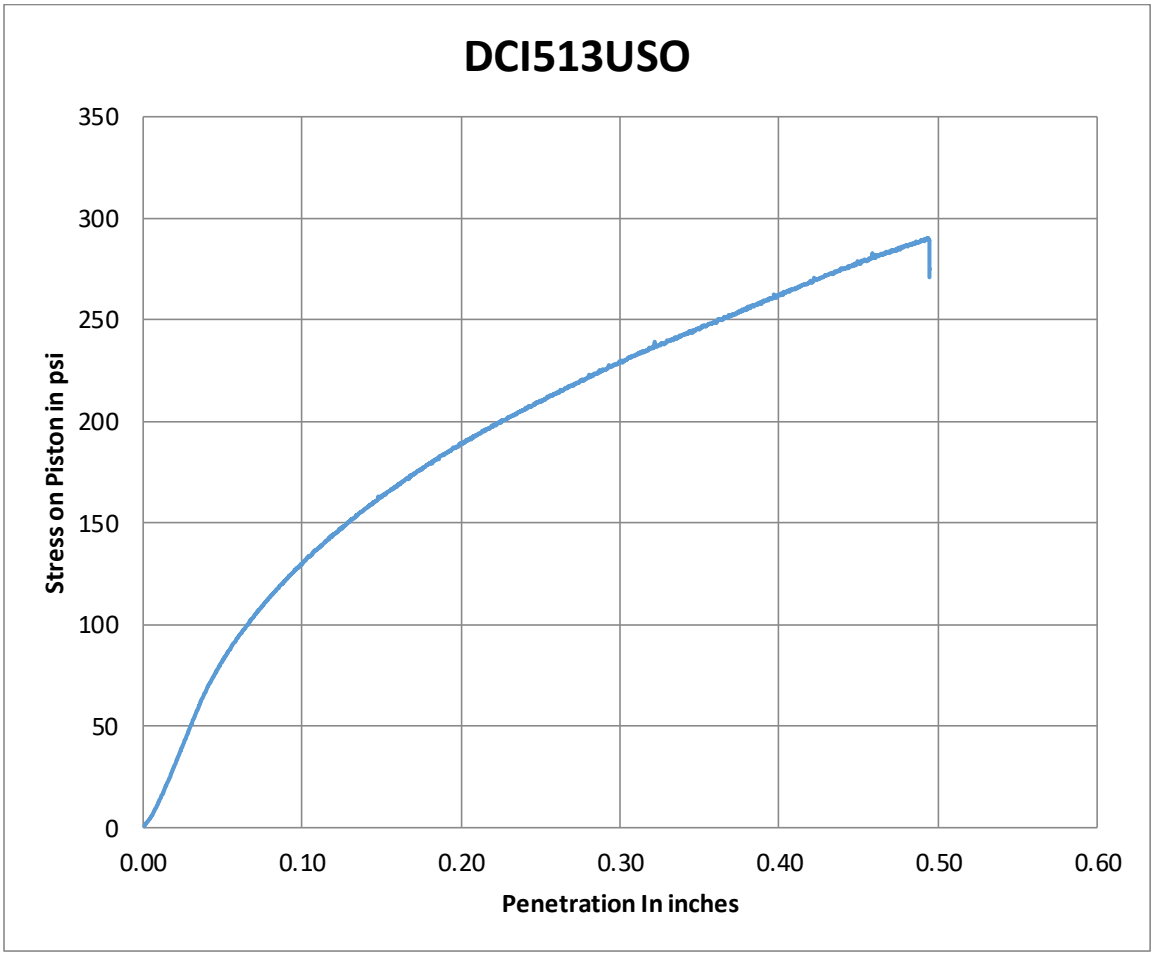

ID	DCM513USO	Volume of the Mold	2118.49	cm^3
Type of Soil	Dupont	Dry Density of the soil	103.18	pcf
Category	Modified	Water content	13.63	%
No. of Layers	5	Dry Mass of Soil	3502.94	g
No. of blows	56	Wet Mass of Soil and Mold	11265.10	g
		Mold Mass	7284.80	g
		Height of Specimen	11.62	cm
CBR	27.6			
Vane shear result	-	Diameter of Mold	15.24	cm

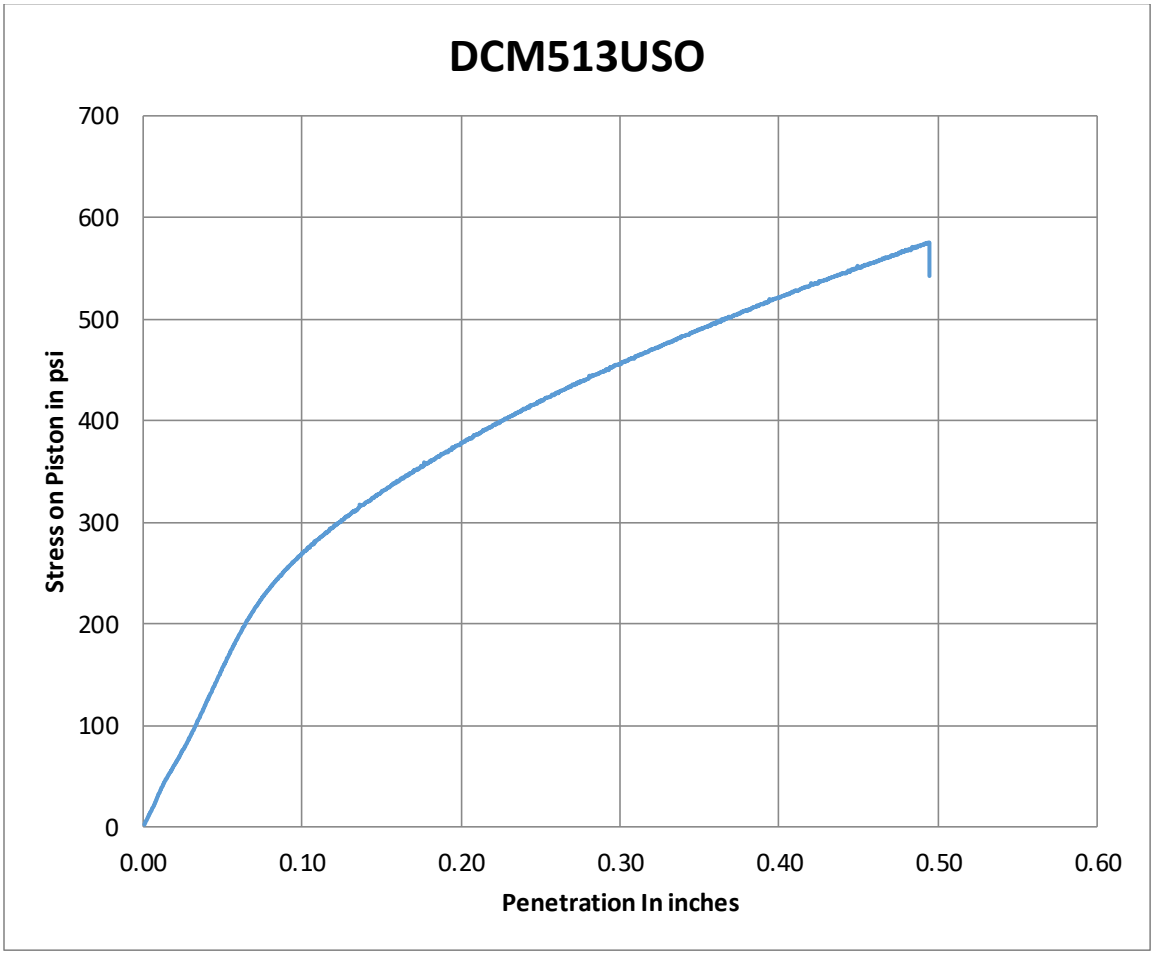

ID	DCS318USO	Volume of the Mold	2118.49	cm^3
Type of Soil	Dupont	Dry Density of the soil	91.79	pcf
Category	Standard	Water content	17.35	%
No. of Layers	3	Dry Mass of Soil	3116.17	g
No. of blows	56	Wet Mass of Soil and Mold	10941.30	g
		Mold Mass	7284.40	g
CBR	7.8	Height of Specimen	11.62	cm
Vane shear result	10.7	Diameter of Mold	15.24	cm

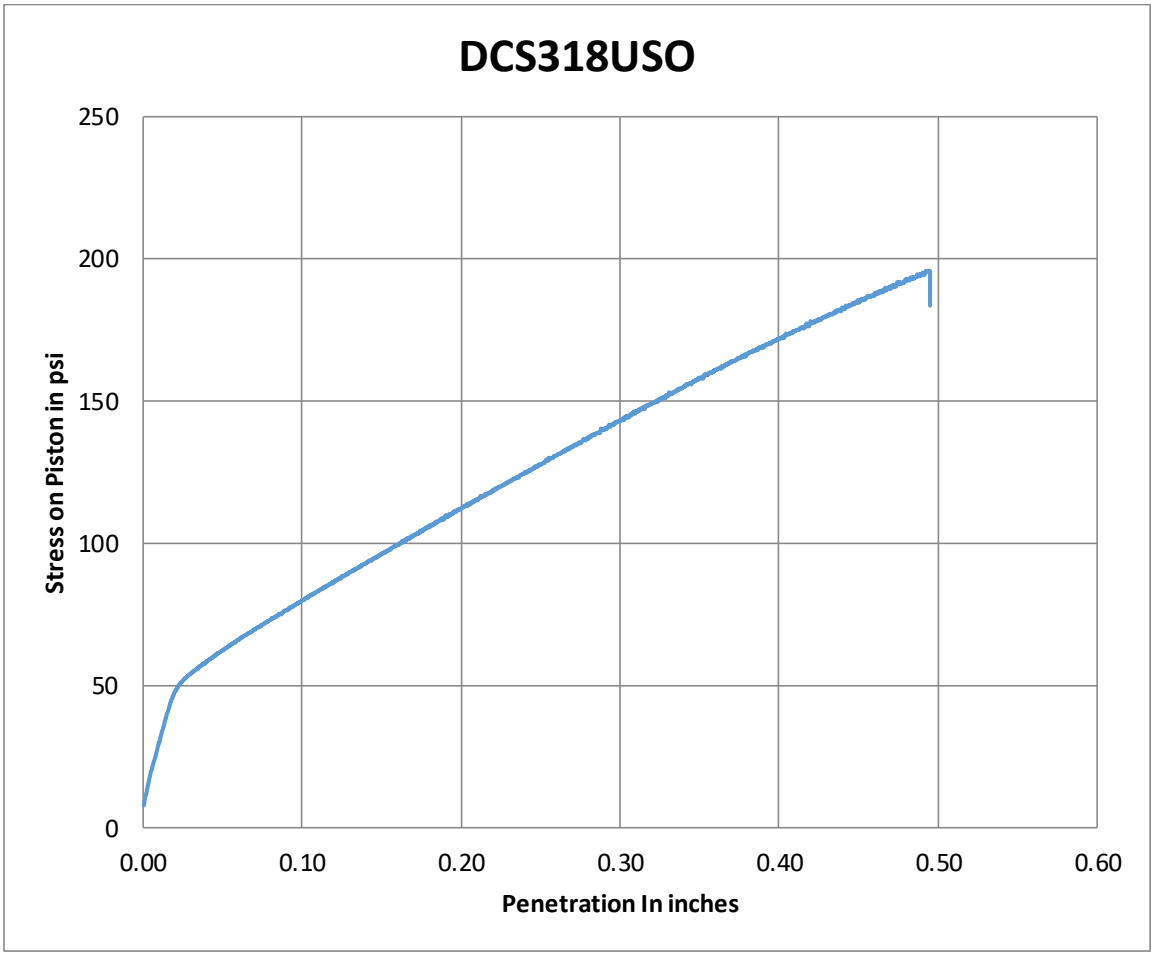

ID	DCI518USO	Volume of the Mold	2118.49	cm^3
Type of Soil	Dupont	Dry Density of the soil	97.83	pcf
Category	Intermediate	Water content	18.30	%
No. of Layers	5	Dry Mass of Soil	3321.40	g
No. of blows	56	Wet Mass of Soil and Mold	11284.80	g
		Mold Mass	7355.60	g
CBR	12.5	Height of Specimen	11.62	cm
Vane shear result	13.7	Diameter of Mold	15.24	cm

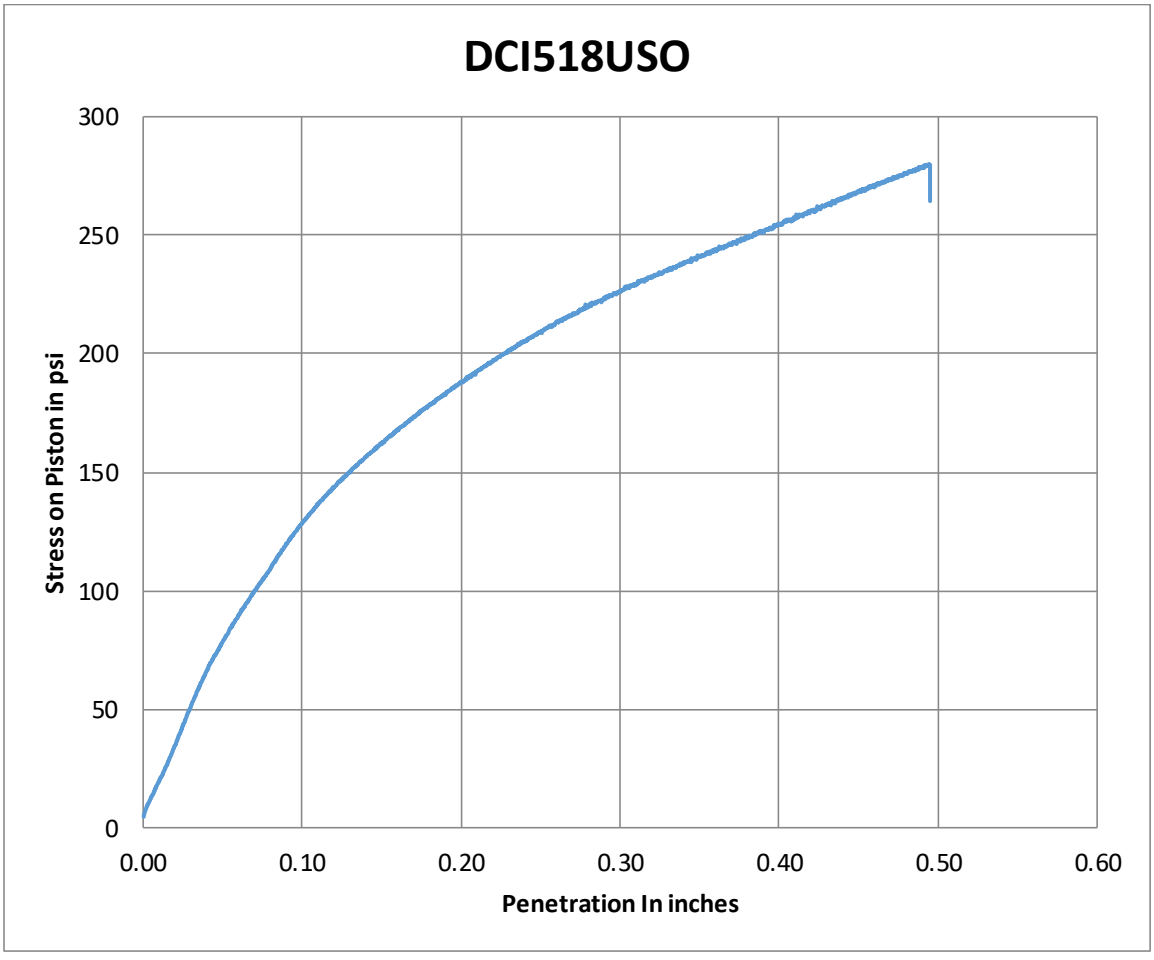

ID	DCM518USO	Volume of the Mold	2118.49	cm^3
Type of Soil	Dupont	Dry Density of the soil	107.19	pcf
Category	Modified	Water content	17.50	%
No. of Layers	5	Dry Mass of Soil	3639.04	g
No. of blows	56	Wet Mass of Soil and Mold	11668.00	g
		Mold Mass	7392.00	g
CBR	21	Height of Specimen	11.62	cm
Vane shear result	20.25	Diameter of Mold	15.24	cm

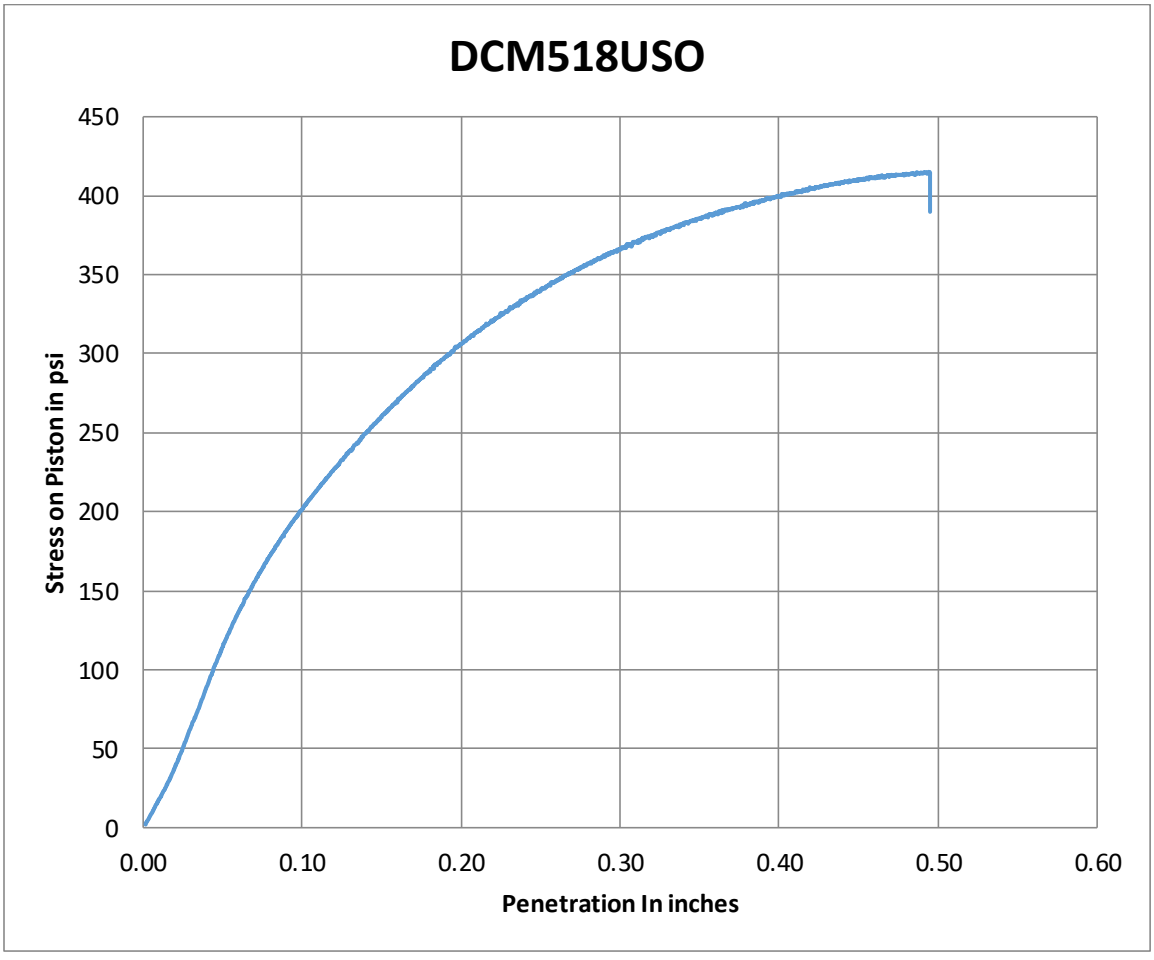

ID	DCS322USO		Volume of the Mold	2118.49	cm^3
Type of Soil	Dupont		Dry Density of the soil	92.29	pcf
Category	Standard		Water content	25.82	%
No. of Layers		3	Dry Mass of Soil	3133.35	g
No. of blows		56	Wet Mass of Soil and Mold	11139.70	g
			Mold Mass	7197.40	g
			Height of		
CBR		12	Specimen	11.62	cm
Vane shear					
result		6.1	Diameter of Mold	15.24	cm

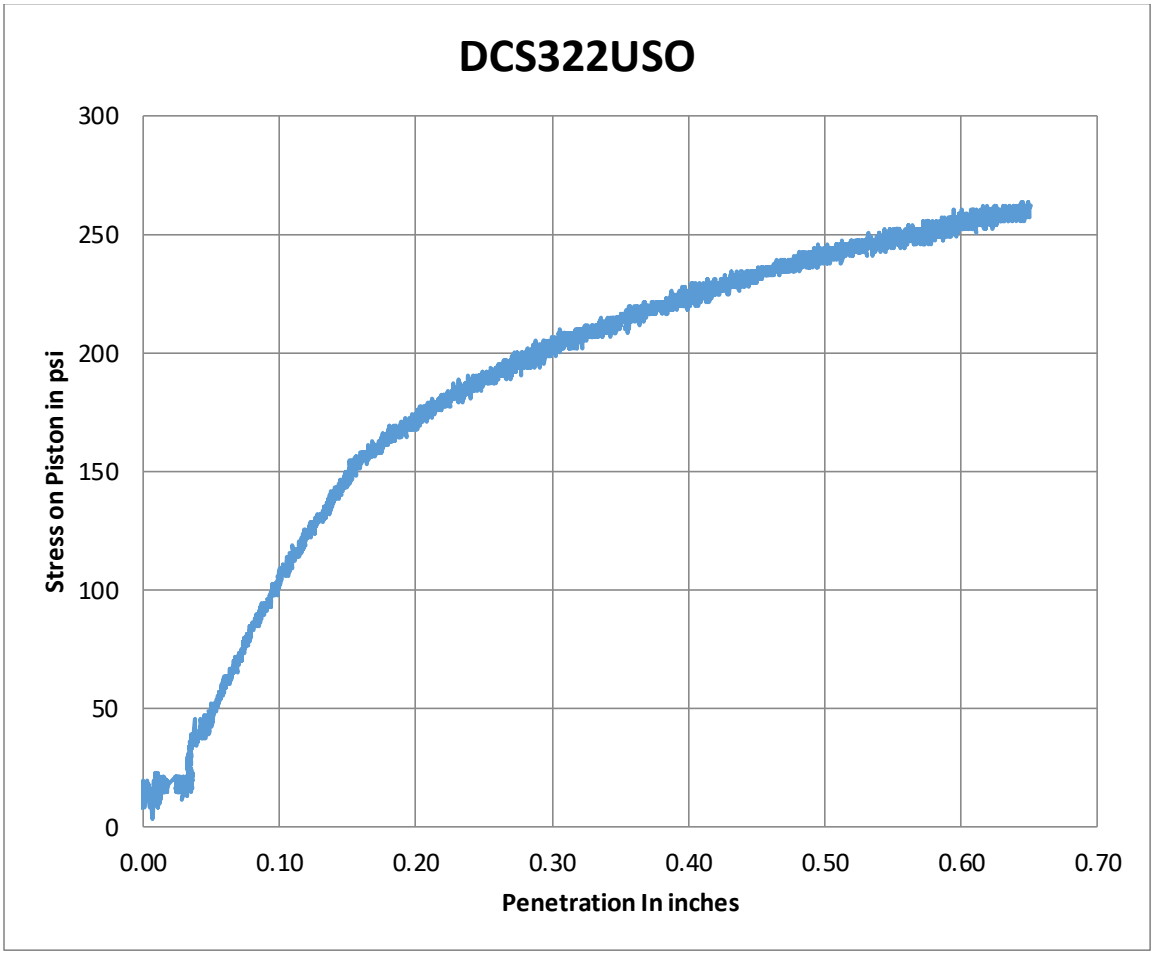

ID	DCI522USO	Volume of the Mold	2118.49	cm^3
Type of Soil	Dupont	Dry Density of the soil	95.77	pcf
Category	Intermediate	Water content	25.43	%
No. of Layers	5	Dry Mass of Soil	3251.54	g
No. of blows	56	Wet Mass of Soil and Mold	11369.00	g
		Mold Mass	7290.50	g
		Height of		
CBR	12.2	Specimen	11.62	cm
Vane shear				
result	13.79	Diameter of Mold	15.24	cm

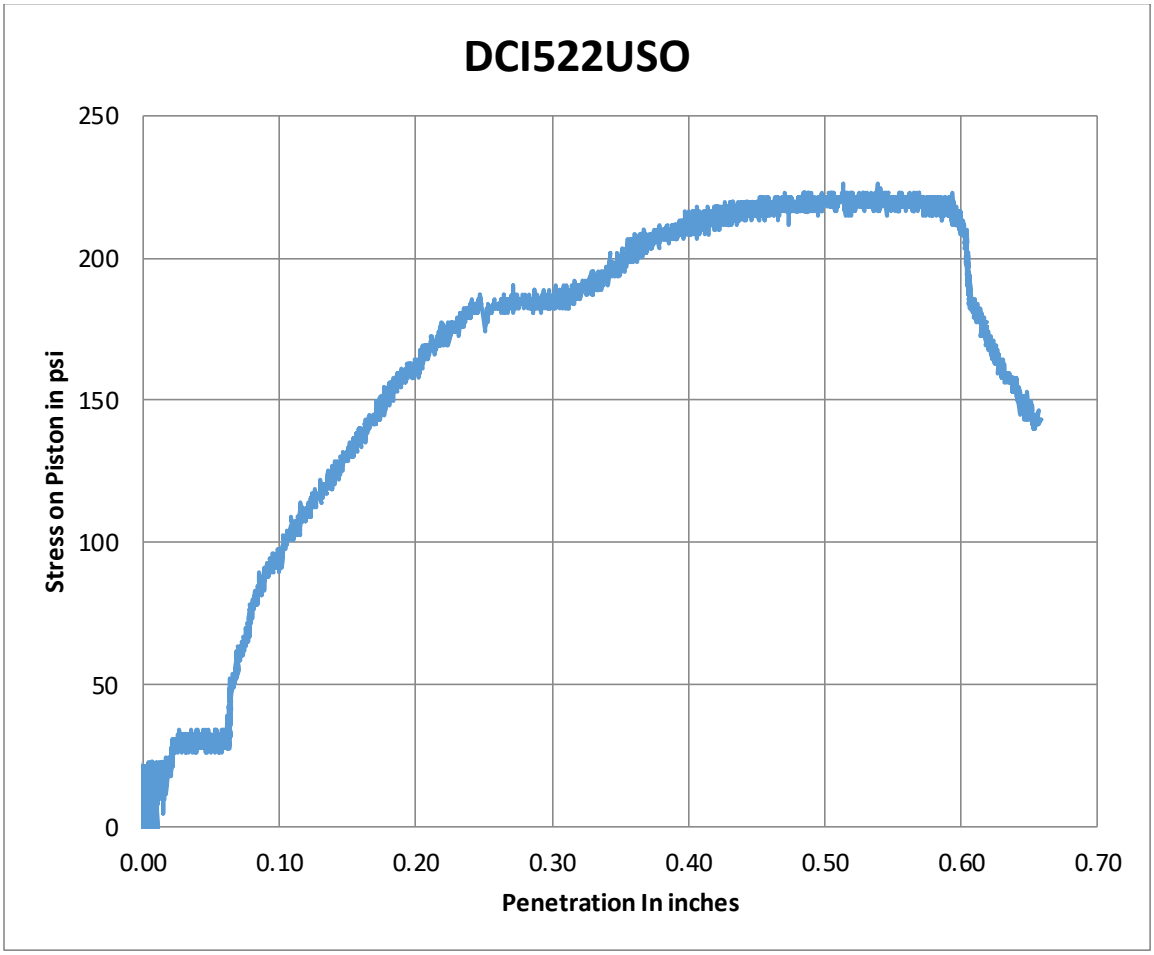

ID	DCM522USO		Volume of the Mold	2118.49	cm^3
Type of Soil	Dupont		Dry Density of the soil	100.77	pcf
Category	Modified		Water content	23.72	%
No. of Layers		5	Dry Mass of Soil	3421.32	g
No. of blows		56	Wet Mass of Soil and Mold	11430.10	g
			Mold Mass	7197.40	g
			Height of		
CBR		21	Specimen	11.62	cm
Vane shear					
result		21.18	Diameter of Mold	15.24	cm

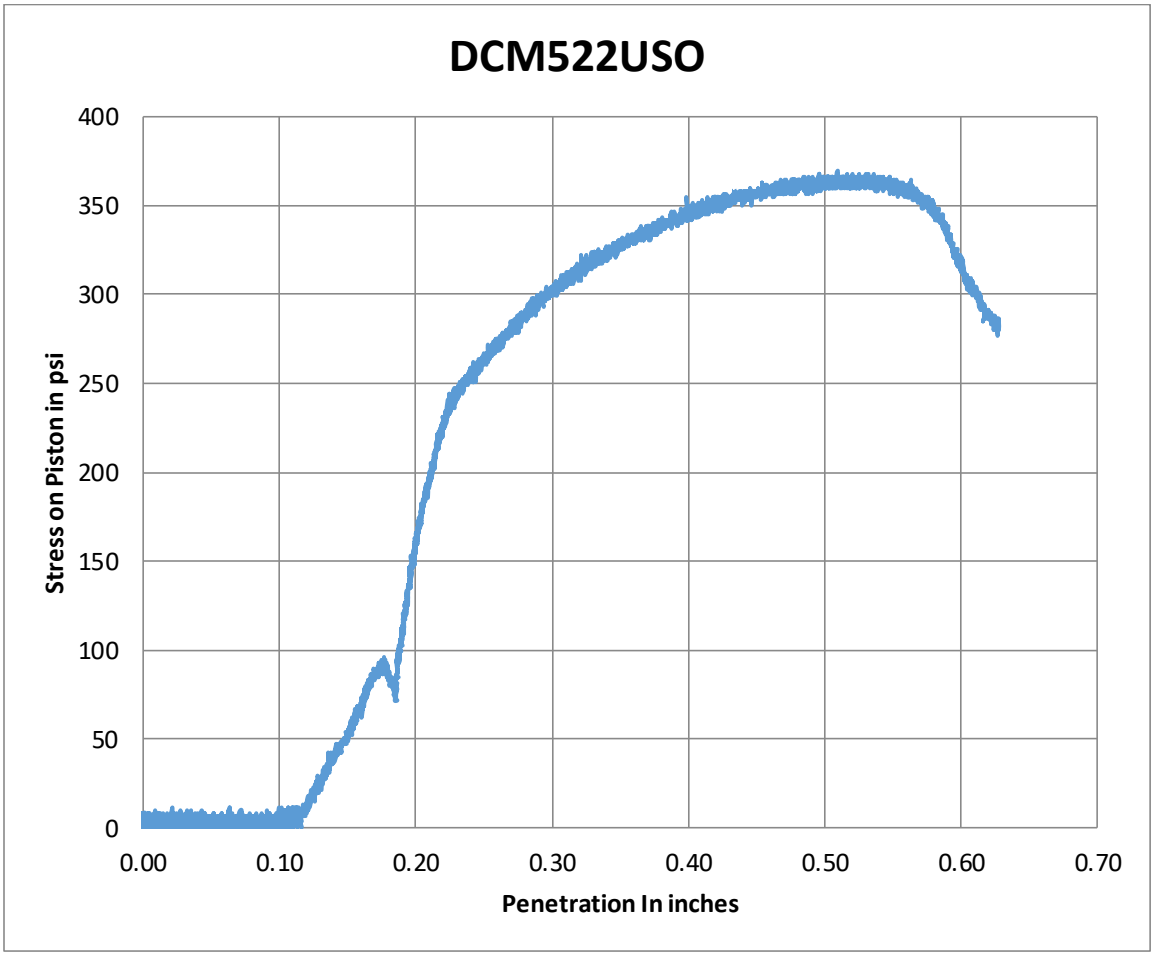

ID	DCS327USO		Volume of the Mold	2118.49	cm^3
Type of Soil	Dupont		Dry Density of the soil	88.65	pcf
Category	Standard		Water content	29.57	%
No. of Layers		3	Dry Mass of Soil	3009.57	g
No. of blows		56	Wet Mass of Soil and Mold	11304.80	g
			Mold Mass	7405.30	g
CBR		3.1	Height of Specimen	11.62	cm
Vane shear result		6.36	Diameter of Mold	15.24	cm

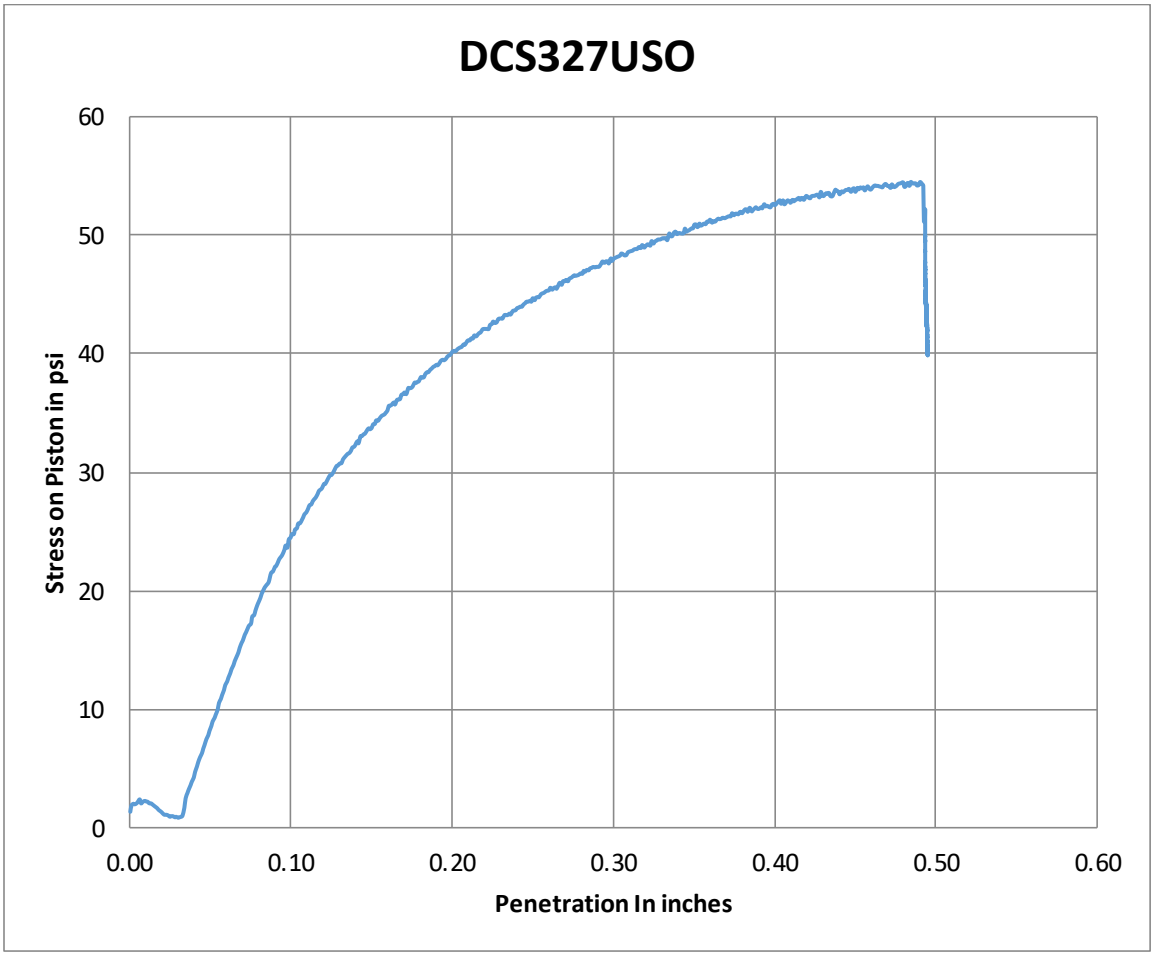

ID	DCI527USO		Volume of the Mold	2118.49	cm^3
Type of Soil	Dupont		Dry Density of the soil	90.24	pcf
Category	Intermediate		Water content	29.90	%
No. of Layers		5	Dry Mass of Soil	3063.50	g
No. of blows		56	Wet Mass of Soil and Mold	11238.70	g
			Mold Mass	7259.20	g
CBR		1.48	Height of Specimen	11.62	cm
Vane shear result		5.75	Diameter of Mold	15.24	cm

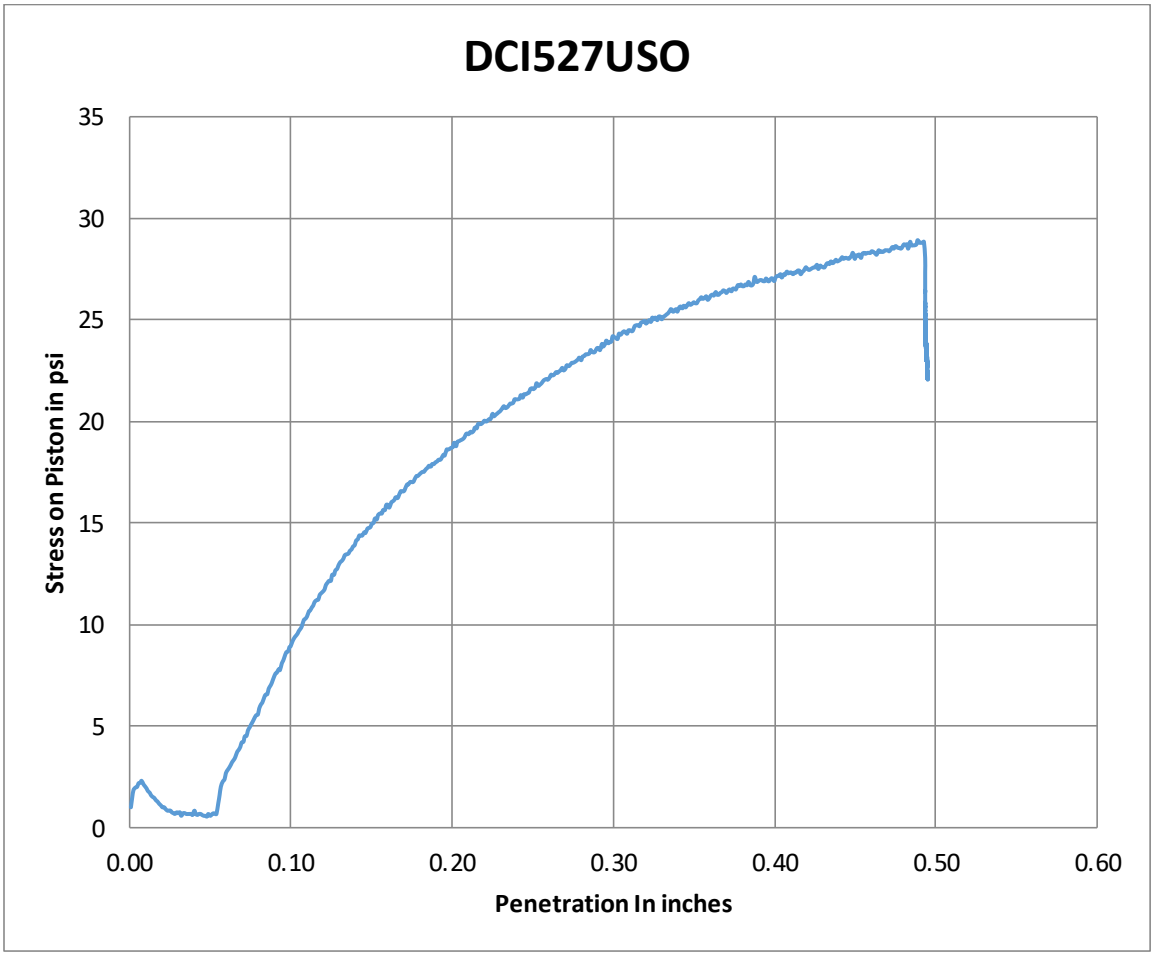

ID	DCM527USO		Volume of the Mold	2118.49	cm^3
Type of Soil	Dupont		Dry Density of the soil	93.16	pcf
Category	Modified		Water content	28.65	%
No. of Layers		5	Dry Mass of Soil	3162.89	g

No. of blows	56	Wet Mass of Soil and Mold	11474.80	gm
		Mold Mass	7405.60	g
		Height of		
CBR	2.87	Specimen	11.62	cm
Vane shear				
result	8.84	Diameter of Mold	15.24	cm

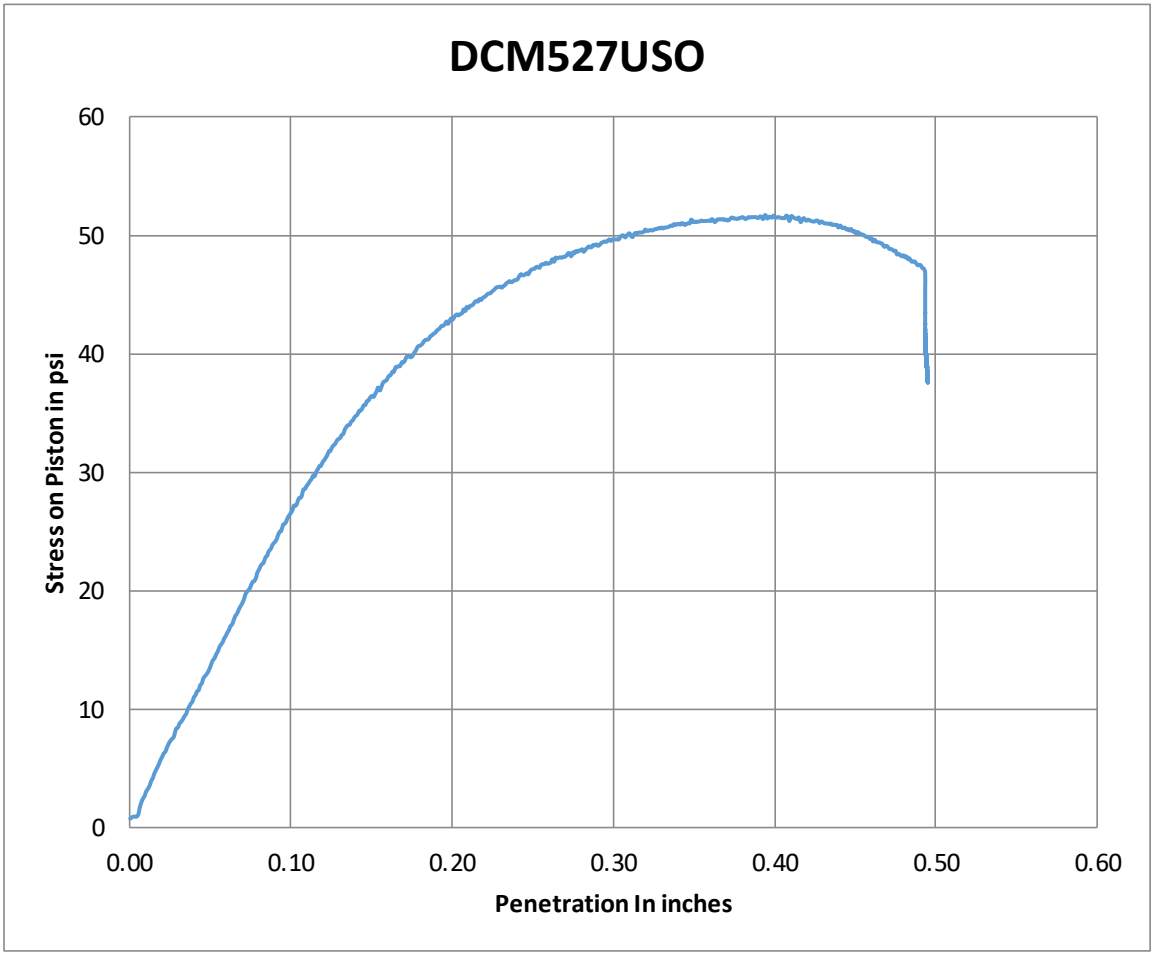

ID	DCS337USO		Volume of the Mold	2118.49	cm^3
Type of Soil	Dupont		Dry Density of the soil	77.89	pcf
Category	Standard		Water content	39.89	%
No. of Layers		3	Dry Mass of Soil	2644.31	g
No. of blows		56	Wet Mass of Soil and Mold	11104.20	g
			Mold Mass	7405.20	g
			Height of		
CBR		0.29	Specimen	11.62	cm
Vane shear					
result		1.54	Diameter of Mold	15.24	cm

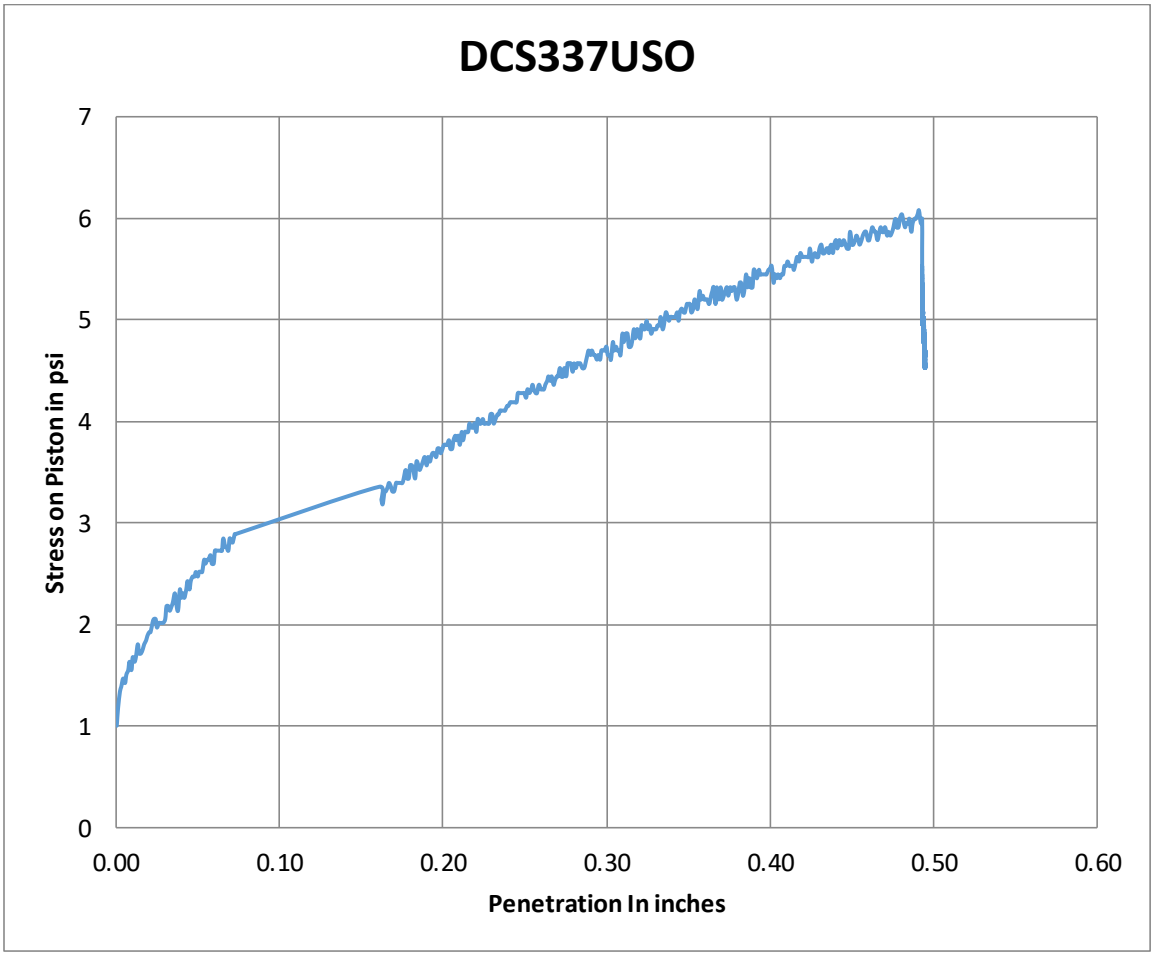

ID	DCI537USO		Volume of the Mold	2118.49	cm^3
Type of Soil	Dupont		Dry Density of the soil	78.02	pcf
Category	Intermediate		Water content	39.56	%
No. of Layers		5	Dry Mass of Soil	2648.84	g
No. of blows		56	Wet Mass of Soil and Mold	11048.80	g
			Mold Mass	7352.10	g
CBR		0.4	Height of Specimen	11.62	cm
Vane shear result		2.07	Diameter of Mold	15.24	cm

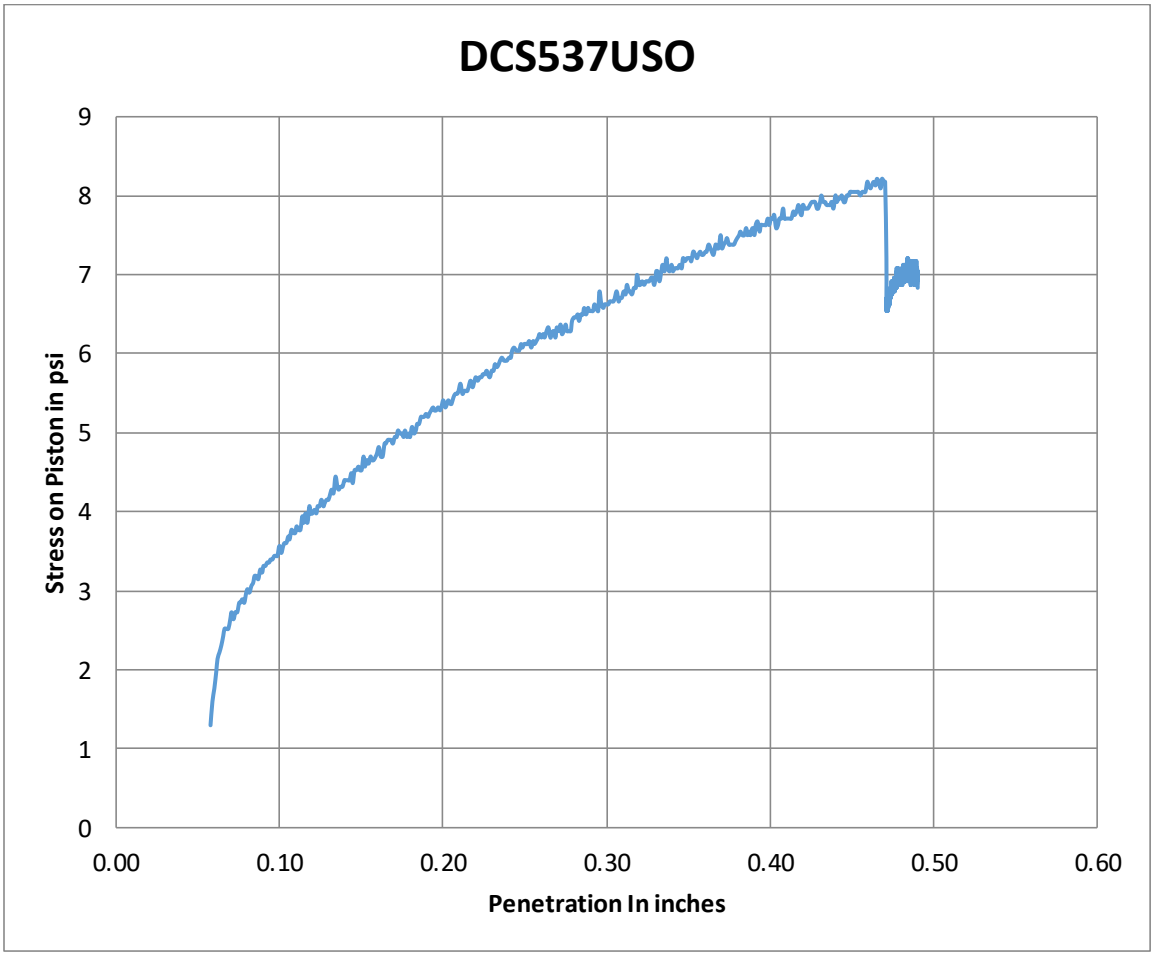

ID	DCM537USO		Volume of the Mold	2118.49	cm^3
Type of Soil	Dupont		Dry Density of the soil	79.24	pcf
Category	Modified		Water content	39.20	%
No. of Layers		5	Dry Mass of Soil	2690.34	g
No. of blows		56	Wet Mass of Soil and Mold	11887.80	g
			Mold Mass	8142.80	g
			Height of		
CBR		5.4	Specimen	11.62	cm
Vane shear					
result		3.33	Diameter of Mold	15.24	cm

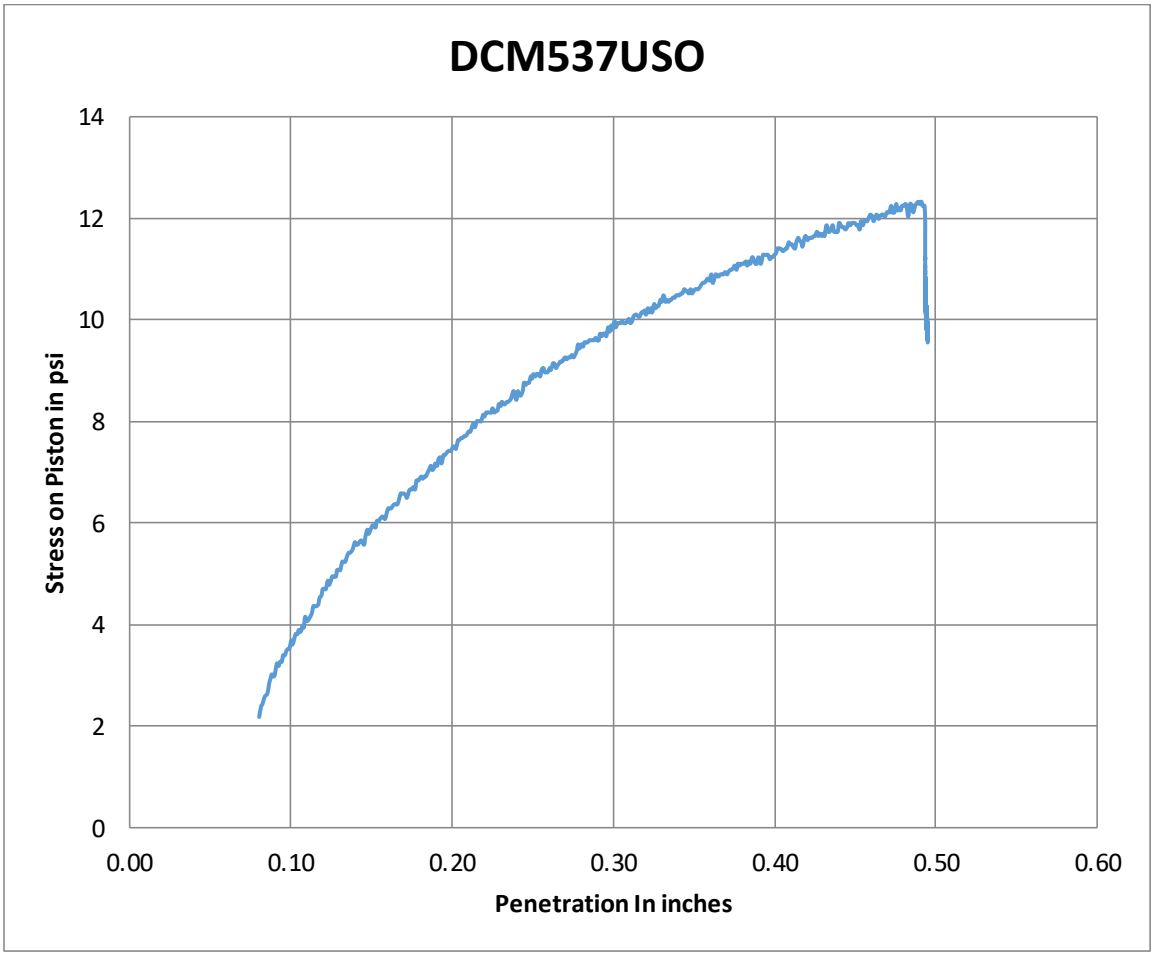

ID	DCS342USO		Volume of the Mold	2118.49	cm^3
Type of Soil	Dupont		Dry Density of the soil	75.74	pcf
Category	Standard		Water content	43.25	%
No. of Layers		3	Dry Mass of Soil	2571.22	g
No. of blows		56	Wet Mass of Soil and Mold	10932.00	g
			Mold Mass	7248.80	g
			Height of		
CBR		0.01	Specimen	11.62	cm
Vane shear					
result		1.3	Diameter of Mold	15.24	cm

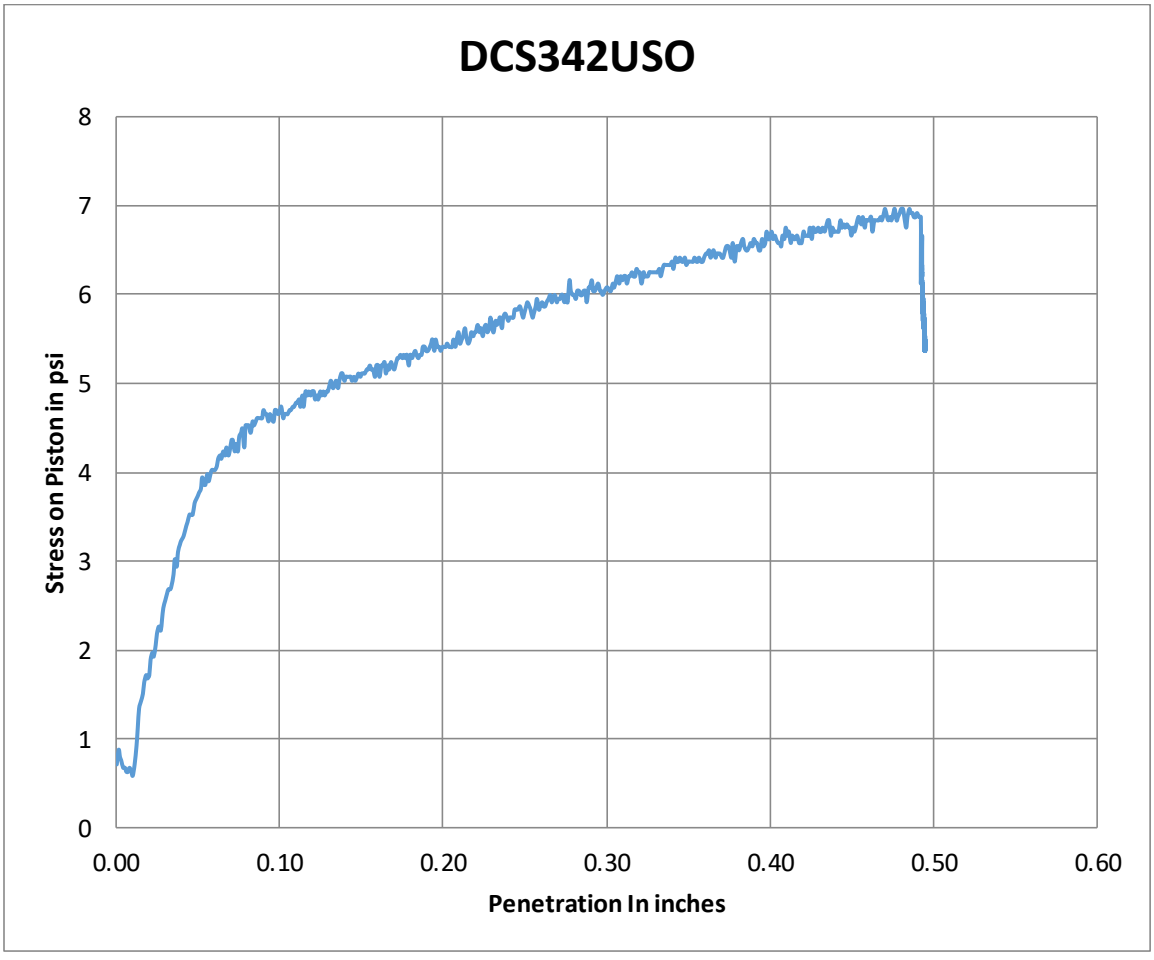

ID	DCI542USO		Volume of the Mold	2118.49	cm^3
Type of Soil	Dupont		Dry Density of the soil	76.71	pcf
Category	Intermediate		Water content	40.80	%
No. of Layers		5	Dry Mass of Soil	2604.21	g
No. of blows		56	Wet Mass of Soil and Mold	10927.00	g
			Mold Mass	7260.20	g
			Height of		
CBR		0.51	Specimen	11.62	cm
Vane shear					
result		1.5	Diameter of Mold	15.24	cm

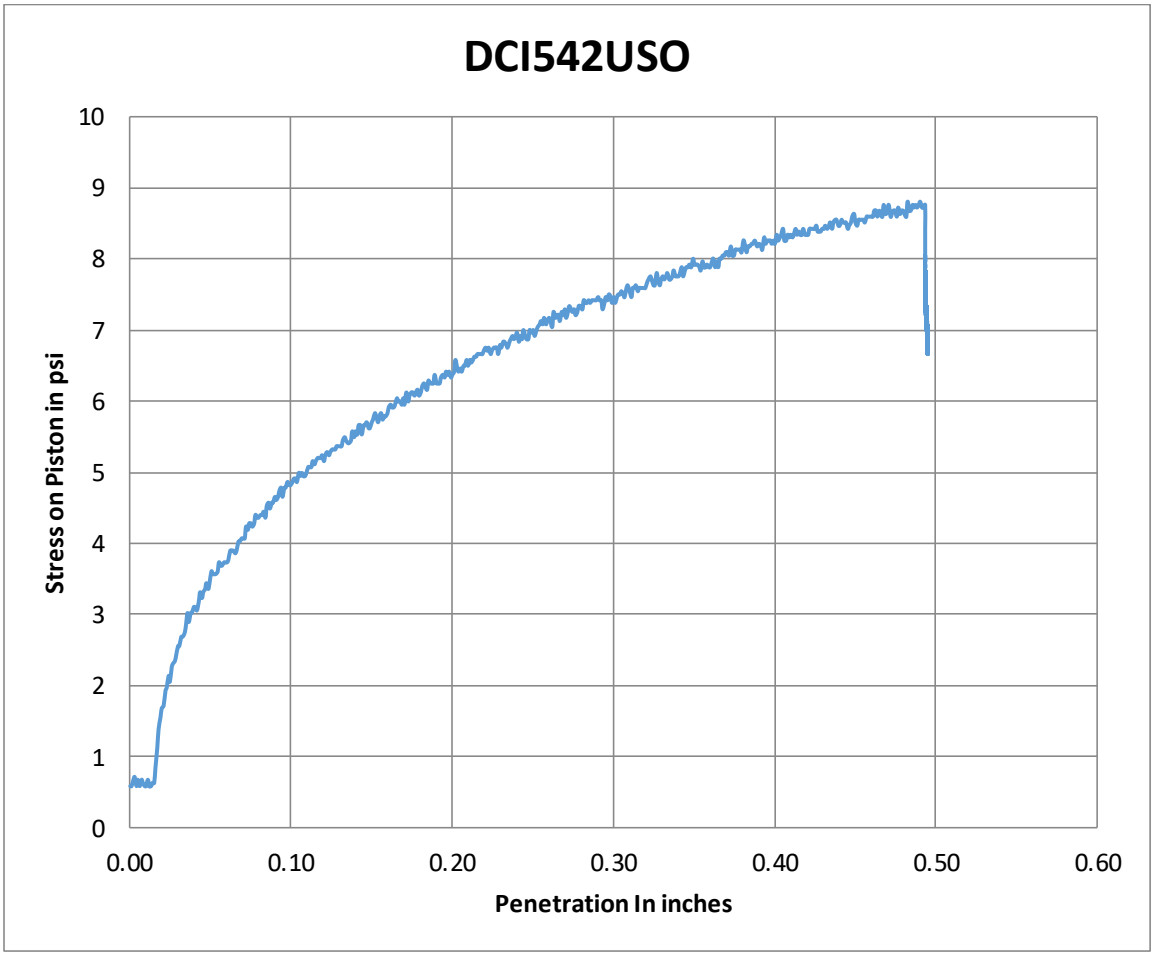

ID	DCM542USO		Volume of the Mold	2118.49	cm^3
Type of Soil	Dupont		Dry Density of the soil	77.48	pcf
Category	Modified		Water content	40.50	%
No. of Layers		5	Dry Mass of Soil	2630.45	g
No. of blows		56	Wet Mass of Soil and Mold	10954.90	g
			Mold Mass	7259.20	g
			Height of		
CBR		0.57	Specimen	11.62	cm
Vane shear					
result		3.58	Diameter of Mold	15.24	cm

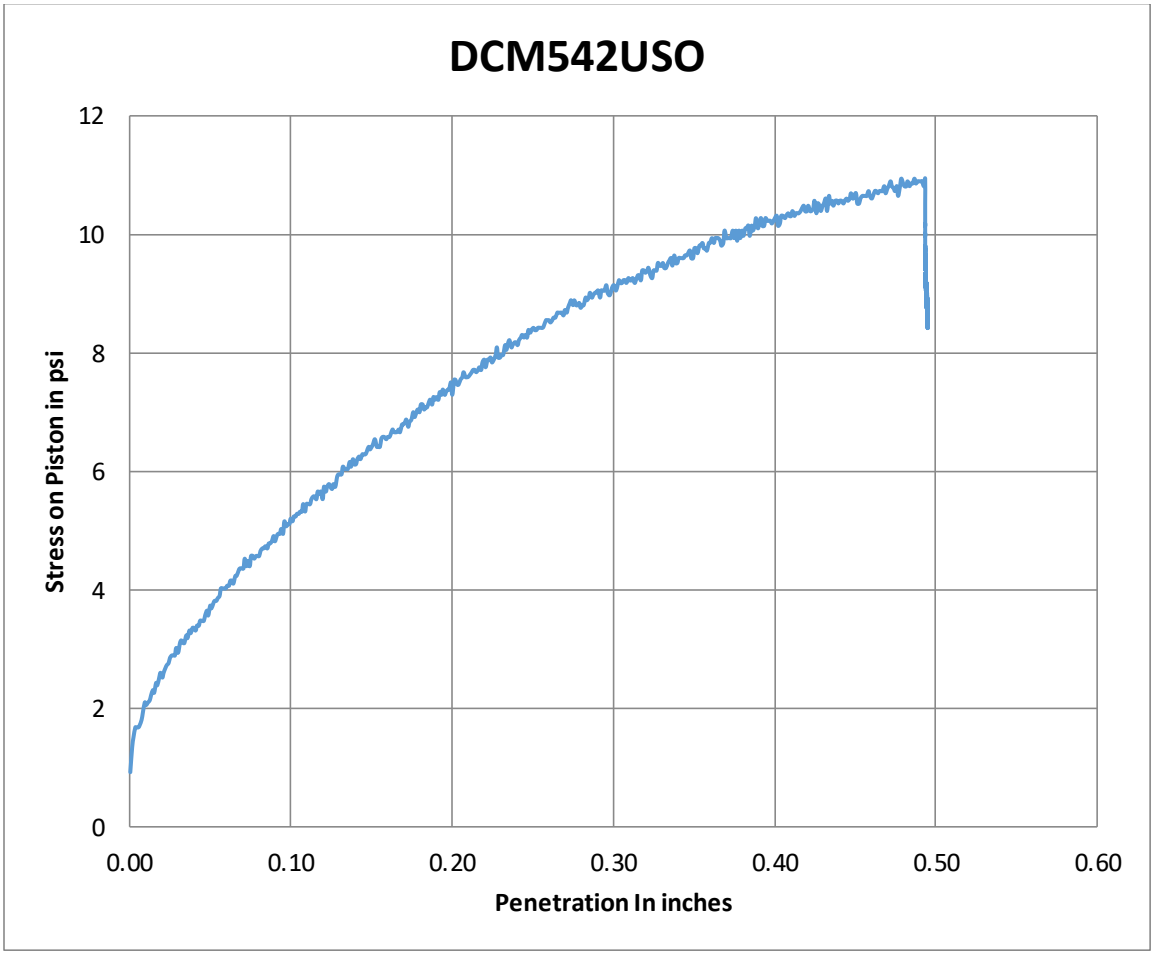

ID	DCM508USO		Volume of the Mold	2118.49	cm^3
Type of Soil	Dupont		Dry Density of the soil	96.92	pcf
Category	Modified		Water content	8.62	%
No. of Layers		5	Dry Mass of Soil	3289.10	g
No. of blows		56	Wet Mass of Soil and Mold	10857.10	g
			Mold Mass	7284.40	g
			Height of		
CBR		48.8	Specimen	11.62	cm
Vane shear result		-	Diameter of Mold	15.24	cm

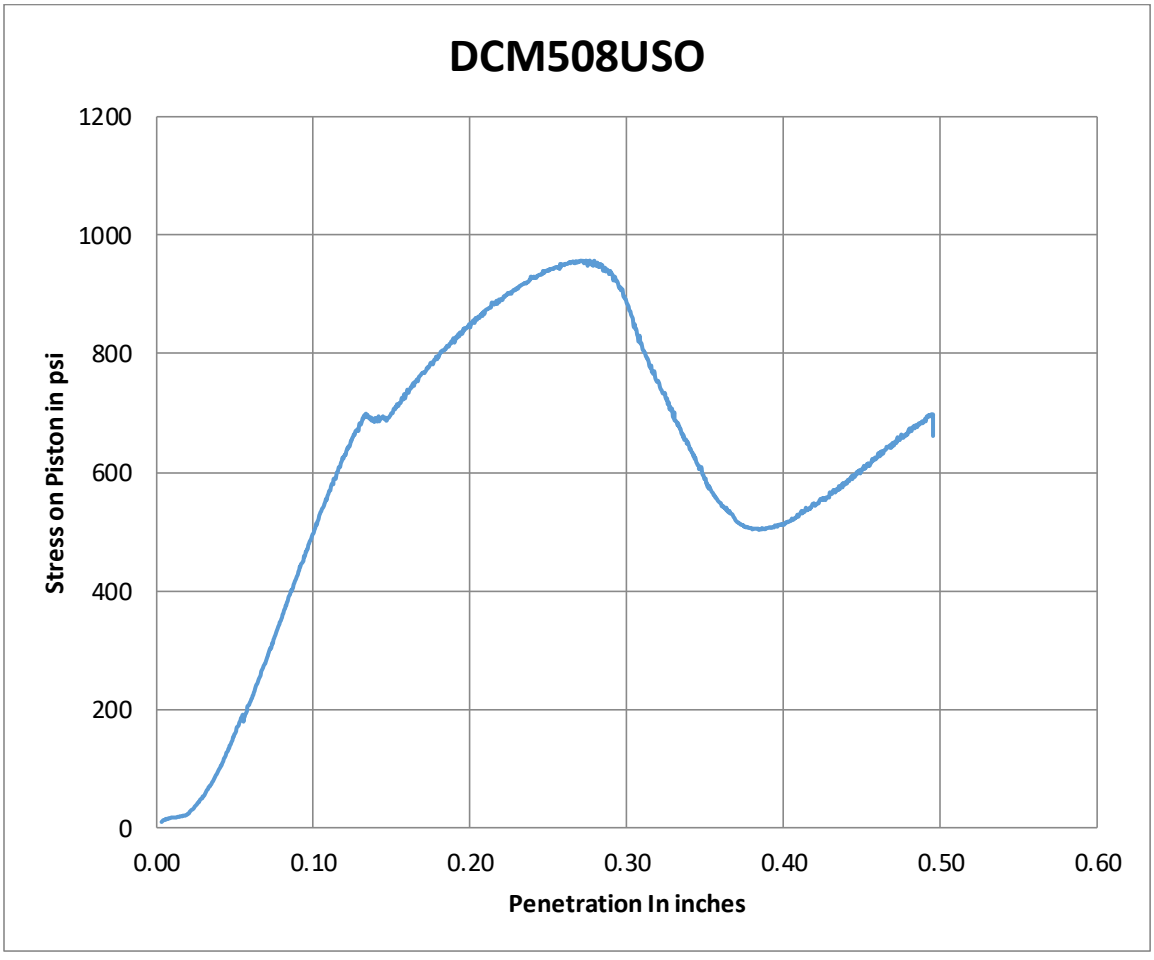

ID	DCM511USO		Volume of the Mold	2118.49	cm^3
Type of Soil	Dupont		Dry Density of the soil	106.7	pcf
Category	Modified		Water content	12.56	%
No. of Layers		5	Dry Mass of Soil	3679.25	g
No. of blows		56	Wet Mass of Soil and Mold	11425.70	g
			Mold Mass	7284.40	g
CBR		62	Height of Specimen	11.62	cm
Vane shear result		-	Diameter of Mold	15.24	cm

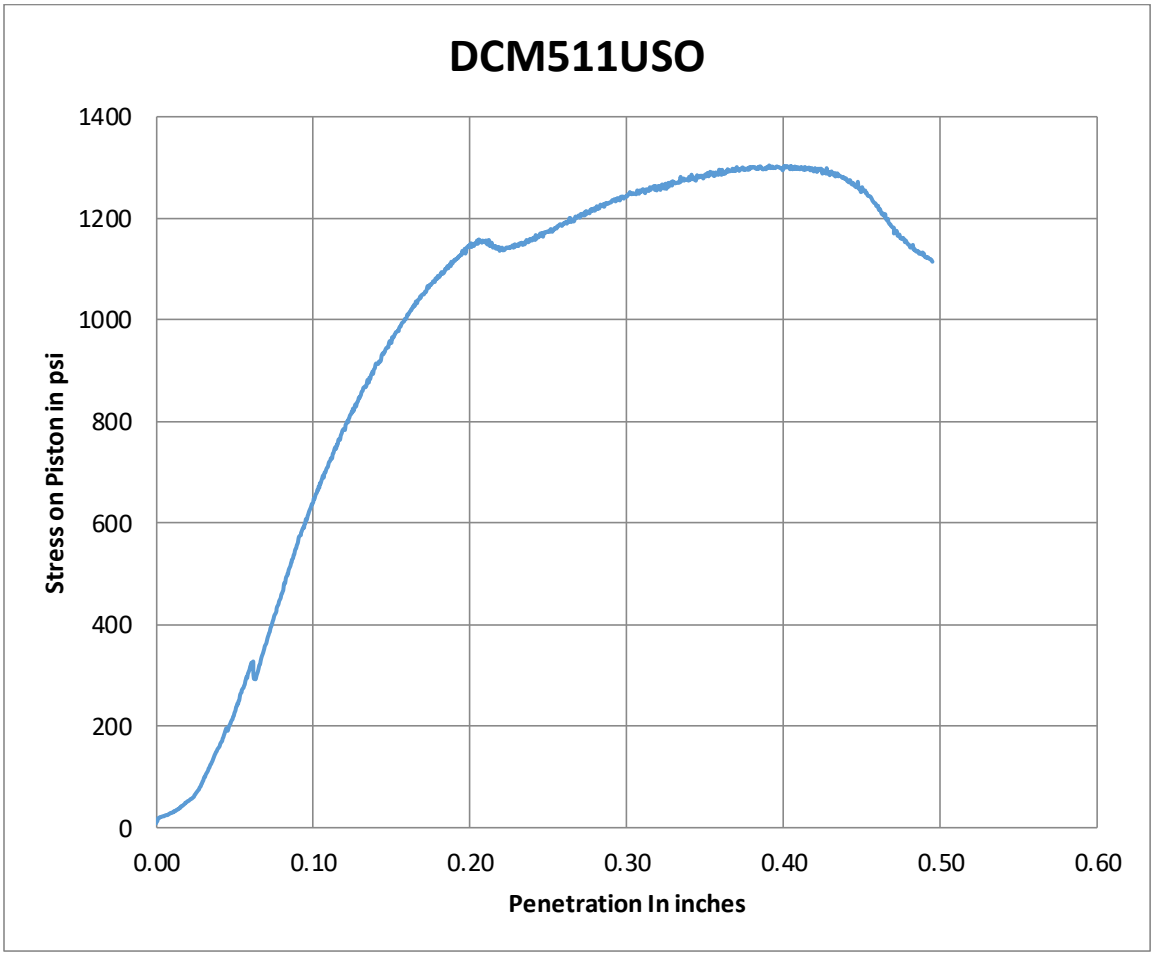

ID	DCM525USO		Volume of the Mold	2118.49	cm^3
Type of Soil	Dupont		Dry Density of the soil	97.79	pcf
Category	Modified		Water content	25.22	%
No. of Layers		5	Dry Mass of Soil	3318.41	g
No. of blows		56	Wet Mass of Soil and Mold	11439.70	g
			Mold Mass	7284.40	g
			Height of		
CBR		4.6	Specimen	11.62	cm
Vane shear					
result		-	Diameter of Mold	15.24	cm

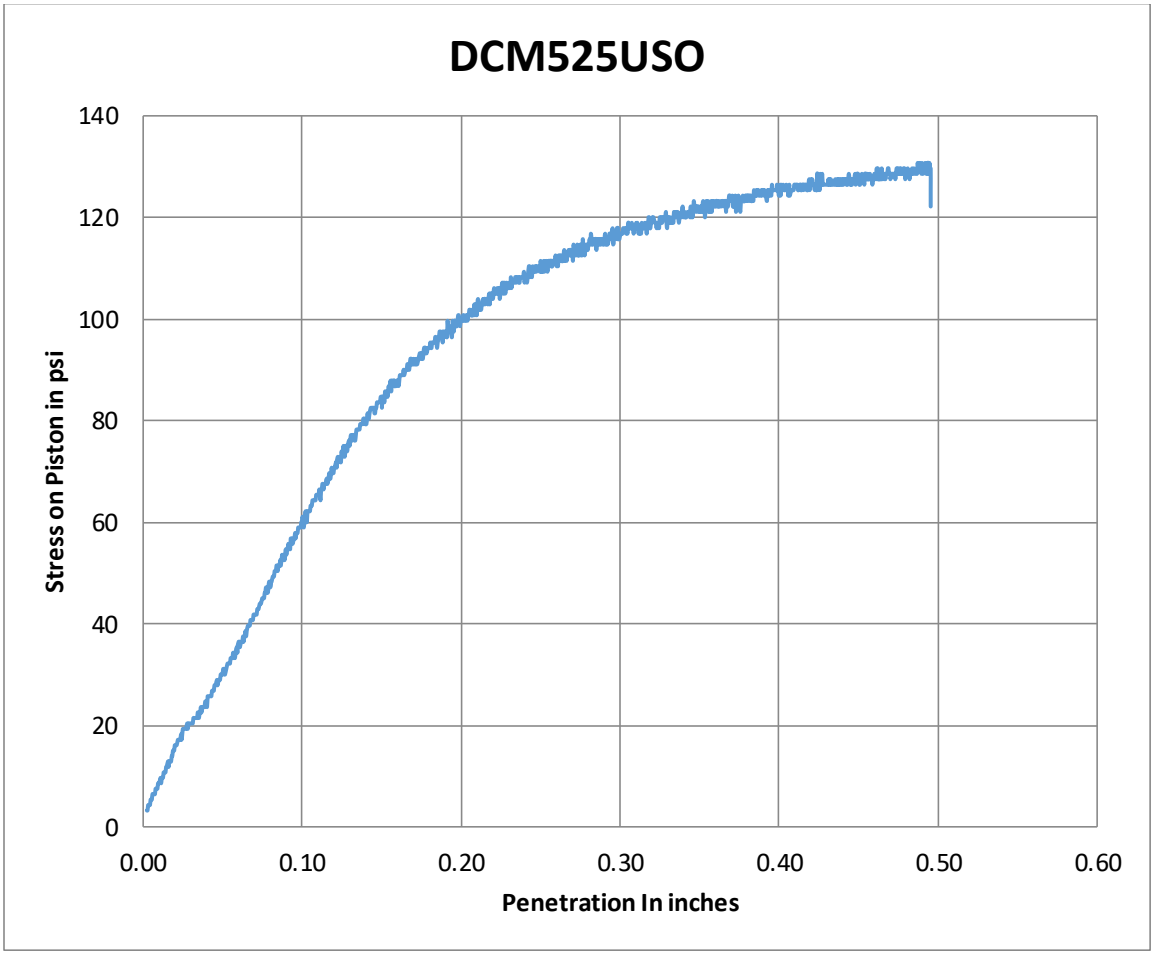

ID	DCS342USO		Volume of the Mold	2118.49	cm^3
Type of Soil	Dupont		Dry Density of the soil	87.83	pcf
Category	Standard		Water content	31.00	%
No. of Layers		3	Dry Mass of Soil	2981.98	g
No. of blows		56	Wet Mass of Soil and Mold	11191.00	g
			Mold Mass	7284.60	g
			Height of		
CBR		2.17	Specimen	11.62	cm
Vane shear					
result		-	Diameter of Mold	15.24	cm

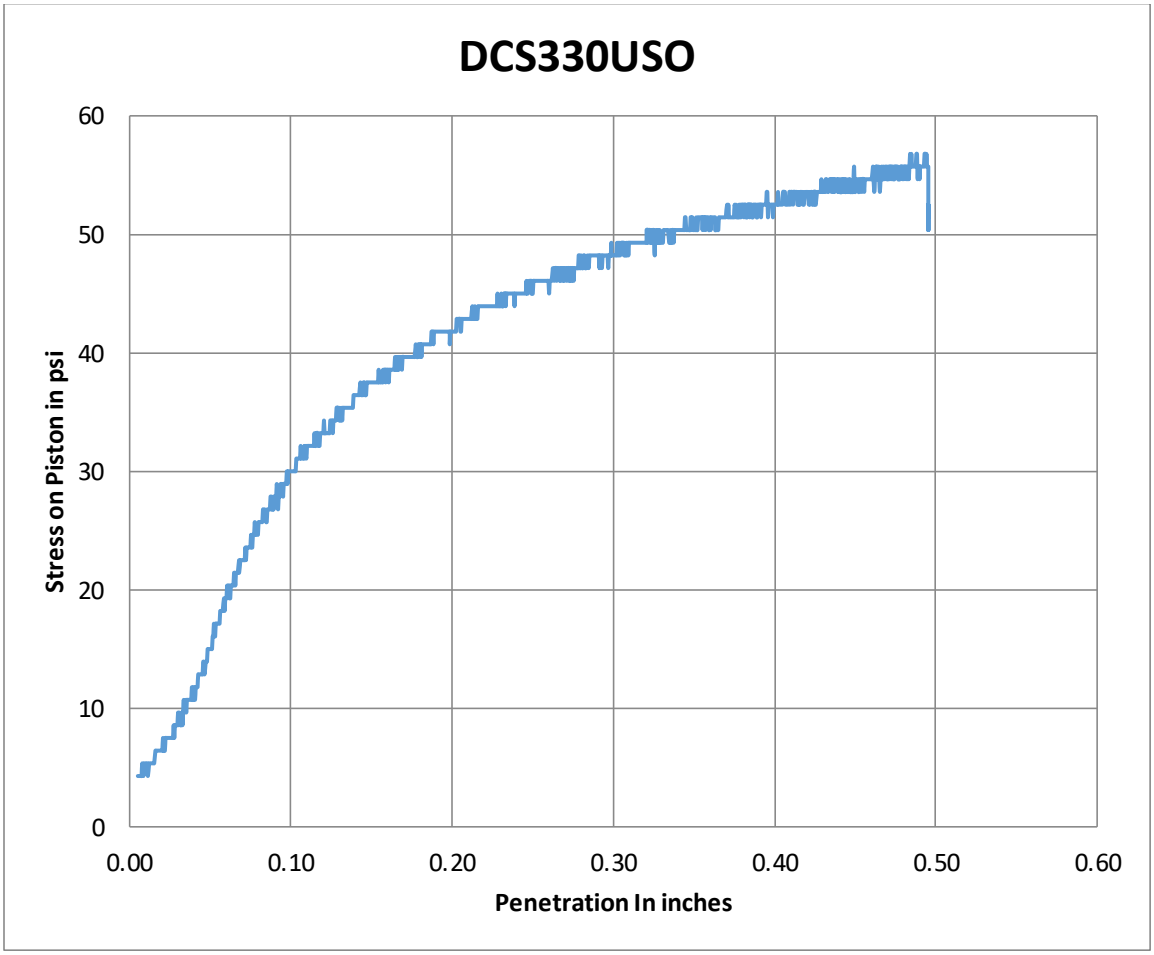

ID	DCI532USO		Volume of the Mold	2118.49	cm^3
Type of Soil	Dupont		Dry Density of the soil	88.77	pcf
Category	Intermediate		Water content	30.52	%
No. of Layers		5	Dry Mass of Soil	3013.69	g
No. of blows		56	Wet Mass of Soil and Mold	11284.10	g
			Mold Mass	7350.50	g
			Height of		
CBR		2.4	Specimen	11.62	cm
Vane shear					
result		-	Diameter of Mold	15.24	cm

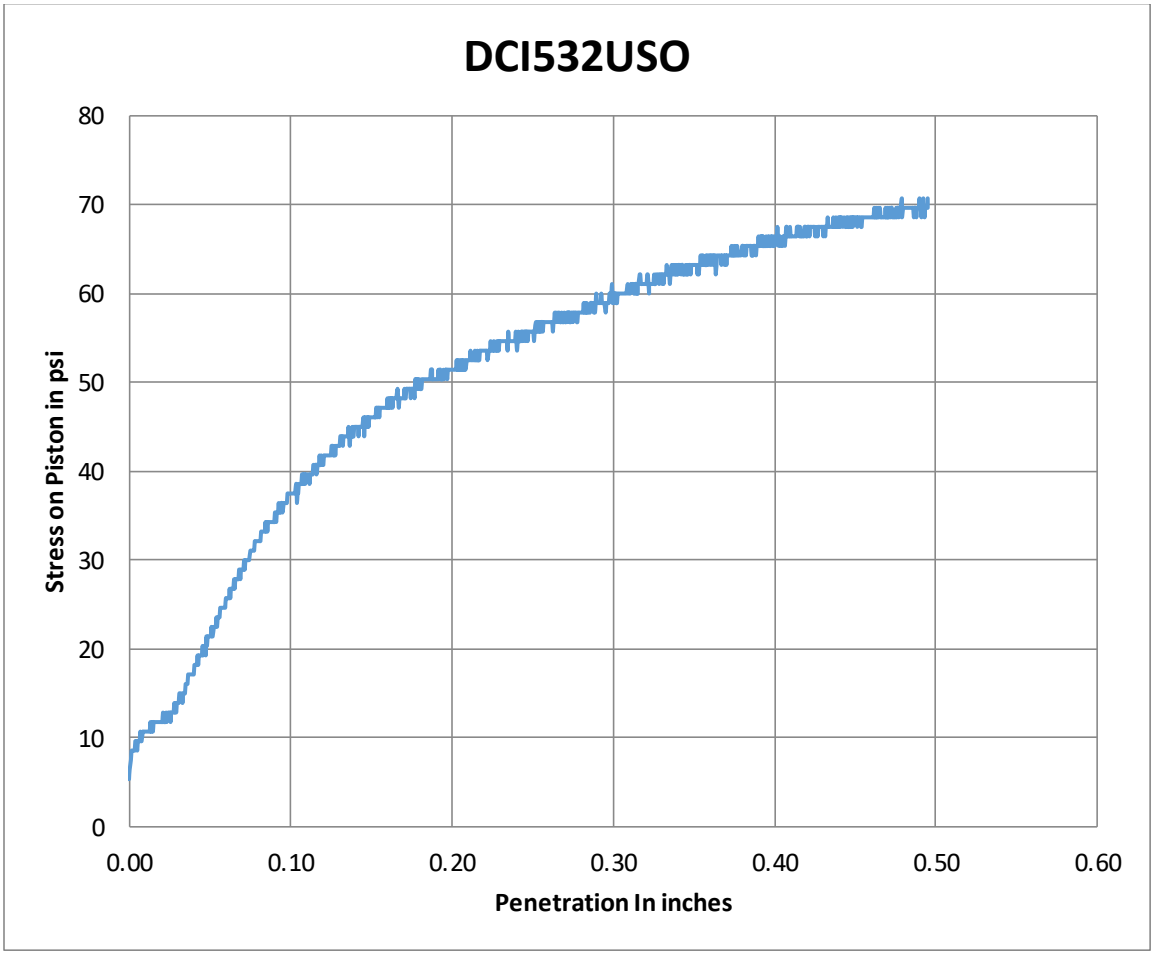

ID	DCM532USO		Volume of the Mold	2118.49	cm^3
Type of Soil	Dupont		Dry Density of the soil	93.15	pcf
Category	Modified		Water content	28.46	%
No. of Layers		5	Dry Mass of Soil	3162.39	g
No. of blows		56	Wet Mass of Soil and Mold	11346.70	g
			Mold Mass	7284.40	g
			Height of		
CBR		3.1	Specimen	11.62	cm
Vane shear					
result		-	Diameter of Mold	15.24	cm

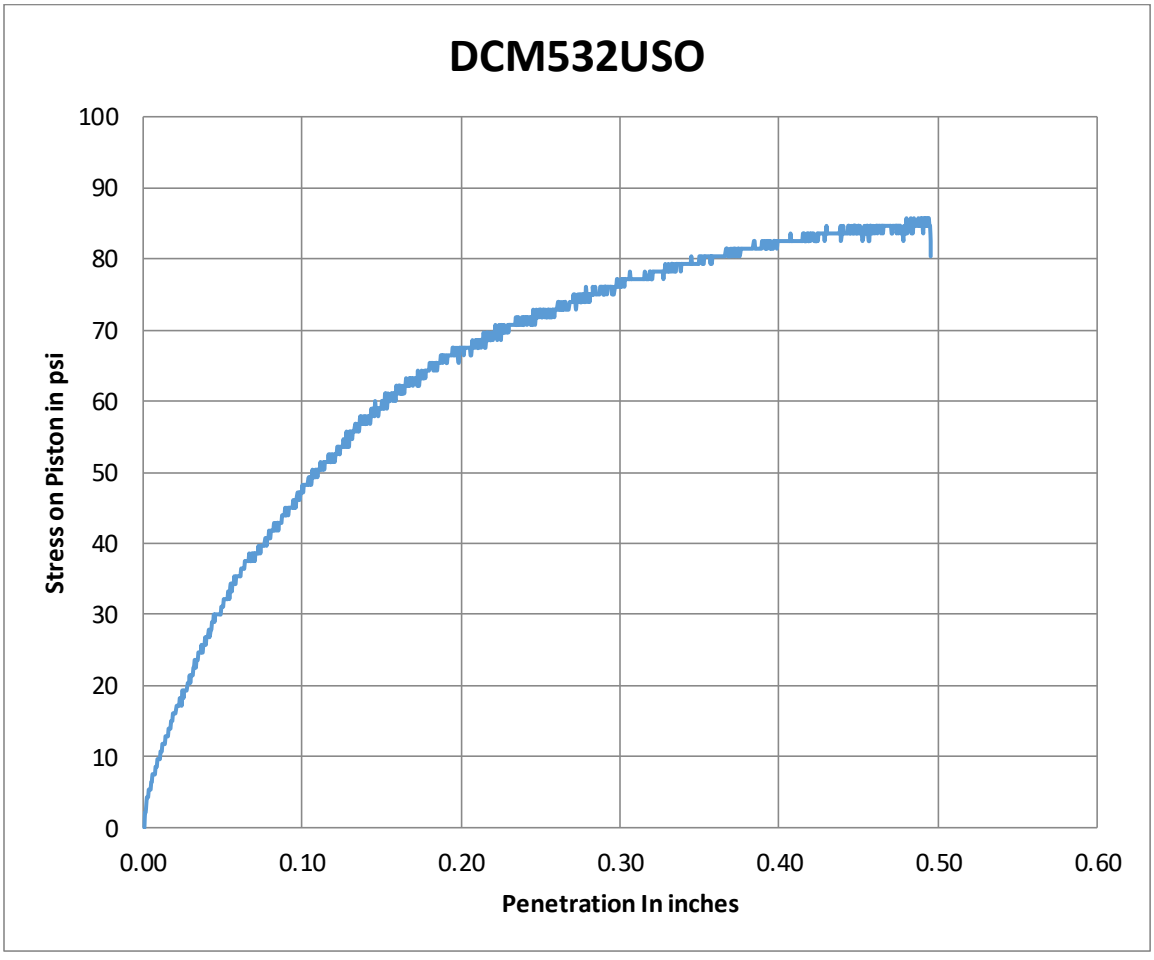

APPENDIX B

RESILIENT MODULUS TESTING DATA SET

STRESS AND STRAIN DATA OBTAINED DURING MR TEST

Test ID CC19 1
Dry Density 106.9 pcf
Water Content 18.7 %

Sequence	Nominal Cell Pressure	Actual Cell Pressure	Nominal Max Deviator Stress	Actual Max Load	Actual Cyclic Load	Actual Contact Load	Actual Max Deviator Stress	Cyclic Stress	Recoverable Deformation 1	Recoverable Deformation 2	Recoverable Deformation Average	Vertical Displacement Ratio	Resilient Strain Average	Resilient Modulus Avg
	NCP	ACP	$S_{d\,max}$	P_{max}	P_{Cyclic}	$P_{Contact}$	$S_{d\,Max}$	$S_{d\,Cyclic}$	ΔH_1	ΔH_2	H_{avg}	H2/H1	$\varepsilon_{r\,avg}$	M_r
	(kPa)	(kPa)	(kPa)	(N)	(N)	(N)	(kPa)	(kPa)	(mm)	(mm)	(mm)		(%)	(psi)
0	29	29	54	442	387	55	55	49	5	0.0016	0.0253	0.0134	0.008	N/A
1	55	55	39	339	223	116	39	28	11	0.0006	0.0083	0.0044	0.003	162118
2	38	38	36	293	207	86	35	26	8	0.0011	0.0099	0.0055	0.003	122405
3	26	26	33	263	207	57	32	26	6	0.001	0.0108	0.0059	0.003	113256
4	12	12	30	233	205	29	29	26	3	0.0009	0.0117	0.0063	0.004	105318
5	56	56	59	498	385	114	60	49	11	0.0013	0.0177	0.0095	0.005	131219
6	42	42	57	459	373	86	56	47	8	0.0017	0.0218	0.0117	0.007	102538
7	28	28	54	431	373	58	53	47	5	0.0018	0.0237	0.0127	0.007	94670
8	15	15	51	398	369	29	50	47	3	0.0016	0.0238	0.0127	0.007	93888
9	56	56	80	666	551	114	81	70	11	0.0024	0.0302	0.0163	0.009	109053
10	38	38	77	617	532	85	76	68	8	0.0026	0.0343	0.0184	0.011	93199
11	28	28	75	592	536	55	74	68	5	0.0024	0.0359	0.0192	0.011	90273
12	14	14	72	564	535	29	71	68	3	0.0026	0.0372	0.0199	0.011	86920
13	56	56	108	889	775	114	110	99	11	0.0048	0.041	0.0229	0.013	109417
14	39	39	105	844	757	88	105	96	8	0.0045	0.0449	0.0247	0.014	98903
15	24	102	814	757	57	102	97	6	0.0227	0.0365	0.0296	0.03	24	24439
16	14	99	776	747	30	98	95	3	0.0233	0.037	0.0302	0.03	14	23470

Test ID CC19 2

Dry Density 105.8 pcf

Water Content 17.2 %

Sequence	Nominal Cell Pressure	Actual Cell Pressure	Nominal Max Deviator Stress	Actual Max Load	Actual Cyclic Load	Actual Contact Load	Actual Max Deviator Stress	Cyclic Stress	Recoverable Deformation 1	Recoverable Deformation 2	Recoverable Deformation Average	Vertical Displacement Ratio	Resilient Strain Average	Resilient Modulus Avg
	NCP	ACP	$S_{d\,max}$	P_{max}	P_{Cyclic}	$P_{Contact}$	$S_{d\,Max}$	$S_{d\,Cyclic}$	ΔH_1	ΔH_2	H_{avg}	H2/H1	$\varepsilon_{r\,avg}$	M_r
	(kPa)	(kPa)	(kPa)	(N)	(N)	(N)	(kPa)	(kPa)	(mm)	(mm)	(mm)		(%)	(psi)
0	28	54	494	435	59	61	55	6	0.0071	0.0179	0.0125	0.013	29	N/A
1	55	39	330	215	114	38	27	11	0.0028	0.0064	0.0046	0.005	55	1118058
2	41	36	293	210	83	35	27	8	0.0028	0.0064	0.0046	0.005	38	844170
3	28	33	264	207	57	32	26	6	0.0028	0.0061	0.0044	0.004	26	781073
4	14	30	233	204	29	29	26	3	0.0026	0.0061	0.0043	0.004	12	726332
5	55	59	482	367	115	58	47	11	0.0056	0.0127	0.0092	0.009	56	904958
6	41	57	461	375	86	56	48	8	0.0057	0.0135	0.0096	0.01	42	707162
7	28	54	430	374	56	53	48	5	0.0058	0.0135	0.0097	0.01	28	652897
8	14	51	397	368	28	50	47	3	0.0059	0.0138	0.0099	0.01	15	647501
9	55	80	649	535	114	79	68	11	0.01	0.0222	0.0161	0.016	56	752092
10	41	77	615	530	85	76	68	8	0.0105	0.0226	0.0165	0.017	38	642751
11	28	75	593	535	58	74	68	6	0.0111	0.0232	0.0172	0.017	28	622574
12	14	72	563	533	29	71	68	3	0.0113	0.0237	0.0175	0.018	14	599448
13	55	108	875	762	114	108	97	11	0.0199	0.0348	0.0273	0.027	56	754598
14	41	105	838	751	87	104	96	9	0.0207	0.0344	0.0276	0.028	39	682087
15	28	102	814	757	57	102	97	6	0.0227	0.0365	0.0296	0.03	24	24439
16	14	99	776	747	30	98	95	3	0.0233	0.037	0.0302	0.03	14	23470

Test ID CC19 3

Dry Density 106.9 pcf

Water Content 18.7 %

Sequence	Nominal Cell Pressure	Actual Cell Pressure	Nominal Max Deviator Stress	Actual Max Load	Actual Cyclic Load	Actual Contact Load	Actual Max Deviator Stress	Cyclic Stress	Recoverable Deformation 1	Recoverable Deformation 2	Recoverable Deformation Average	Vertical Displacement Ratio	Resilient Strain Average	Resilient Modulus Avg
	NCP	ACP	$S_{d\,max}$	P_{max}	P_{Cyclic}	$P_{Contact}$	$S_{d\,Max}$	$S_{d\,Cyclic}$	ΔH_1	ΔH_2	H_{avg}	H2/H1	$\varepsilon_{r\,avg}$	M_r
	(kPa)	(kPa)	(kPa)	(N)	(N)	(N)	(kPa)	(kPa)	(mm)	(mm)	(mm)		(%)	(psi)
0	28	28	54	417	371	46	53	47	6	0.0165	0.0091	0.0128	0.013	
1	55	55	39	302	215	87	38	27	11	0.0076	0.0043	0.0059	0.006	66880
2	41	41	36	279	213	66	35	27	8	0.0069	0.0041	0.0055	0.005	71721
3	28	28	33	251	206	45	32	26	5	0.0067	0.0041	0.0054	0.005	70622
4	14	14	30	229	206	23	29	26	3	0.0071	0.0041	0.0056	0.006	68415
5	55	55	59	455	367	89	58	47	11	0.0143	0.0088	0.0115	0.012	58745
6	41	41	57	441	373	68	56	48	8	0.0156	0.0091	0.0123	0.012	55827
7	28	28	54	417	371	46	53	47	6	0.0159	0.0094	0.0127	0.013	54115
8	14	14	51	397	371	26	50	47	3	0.0157	0.0095	0.0126	0.013	54499
9	55	55	80	620	531	90	79	68	11	0.0246	0.0154	0.02	0.02	48966
10	41	41	77	601	531	71	76	68	9	0.026	0.0161	0.0211	0.021	46538
11	28	28	75	586	537	49	74	68	6	0.027	0.0168	0.0219	0.022	45280
12	14	14	72	582	553	29	74	70	3	0.0287	0.0183	0.0235	0.023	43472
13	55	55	108	866	770	95	110	98	12	0.0396	0.0266	0.0331	0.033	42910
14	41	41	105	823	750	74	105	95	9	0.0391	0.0258	0.0325	0.032	42631
15	28	28	102	798	747	51	101	95	6	0.0405	0.0278	0.0341	0.034	40385
16	14	14	99	780	749	31	99	95	4	0.0415	0.0291	0.0353	0.035	39230

Test ID C22 1

Dry Density 105.8 pcf

Water Content 17.2 %

Sequence	Nominal Cell Pressure	Actual Cell Pressure	Nominal Max Deviator Stress	Actual Max Load	Actual Cyclic Load	Actual Contact Load	Actual Max Deviator Stress	Cyclic Stress	Recoverable Deformation 1	Recoverable Deformation 2	Recoverable Deformation Average	Vertical Displacement Ratio	Resilient Strain Average	Resilient Modulus Avg
	NCP	ACP	$S_{d\,max}$	P_{max}	P_{Cyclic}	$P_{Contact}$	$S_{d\,Max}$	$S_{d\,Cyclic}$	ΔH_1	ΔH_2	H_{avg}	H2/H1	$\varepsilon_{r\,avg}$	M_r
	(kPa)	(kPa)	(kPa)	(N)	(N)	(N)	(kPa)	(kPa)	(mm)	(mm)	(mm)		(%)	(psi)
0	28	28	54	507	379	129	54	48	6	0.1342	0.1342	0.1342	0.056	N/A
1	55	55	39	397	218	179	39	28	11	0.0593	0.0593	0.0593	0.025	16315
2	41	41	36	366	213	153	36	27	9	0.0624	0.0624	0.0624	0.026	15120
3	28	28	33	333	211	122	33	27	6	0.0643	0.0643	0.0643	0.027	14563
4	14	14	30	303	211	92	29	27	2	0.065	0.065	0.065	0.027	14384
5	55	55	59	555	376	180	59	48	11	0.1152	0.1152	0.1152	0.048	14442
6	41	41	57	528	378	150	57	48	8	0.1264	0.1264	0.1264	0.053	13264
7	28	28	54	498	373	125	53	47	6	0.1301	0.1301	0.1301	0.054	12696
8	14	14	51	470	377	93	51	48	3	0.136	0.136	0.136	0.057	12282
9	55	55	80	715	534	181	79	68	11	0.1719	0.1719	0.1719	0.072	13770
10	41	41	77	687	534	153	77	68	9	0.1875	0.1875	0.1875	0.078	12610
11	28	28	75	663	536	126	74	68	6	0.198	0.198	0.198	0.082	12002
12	14	14	72	629	539	91	71	69	3	0.2097	0.2097	0.2097	0.087	11387
13	55	55	108	945	763	182	108	97	11	0.2674	0.2674	0.2674	0.111	12649
14	41	41	105	906	754	152	105	96	9	0.29	0.29	0.29	0.121	11515
15	28	28	102	875	754	122	102	96	6	0.3041	0.3041	0.3041	0.127	10980

Test ID CC22 2

Dry Density 99.2 pcf

Water Content 18.3 %

Sequence	Nominal Cell Pressure	Actual Cell Pressure	Nominal Max Deviator Stress	Actual Max Load	Actual Cyclic Load	Actual Contact Load	Actual Max Deviator Stress	Cyclic Stress	Recoverable Deformation 1	Recoverable Deformation 2	Recoverable Deformation Average	Vertical Displacement Ratio	Resilient Strain Average	Resilient Modulus Avg
	NCP	ACP	$S_{d\,max}$	P_{max}	P_{Cyclic}	$P_{Contact}$	$S_{d\,Max}$	$S_{d\,Cyclic}$	ΔH_1	ΔH_2	H_{avg}	H2/H1	$\varepsilon_{r\,avg}$	M_r
	(kPa)	(kPa)	(kPa)	(N)	(N)	(N)	(kPa)	(kPa)	(mm)	(mm)	(mm)		(%)	(psi)
0	28	23	54	401	343	58	50	44	6	0.016	0.0015	0.0088	0.004	
1	55	54	39	335	220	115	39	28	11	0.0065	0.0008	0.0037	0.002	221415
2	41	38	36	296	211	85	35	27	8	0.0065	0.0005	0.0035	0.002	222866
3	28	24	33	267	209	58	32	27	6	0.008	0.001	0.0045	0.002	172400
4	14	14	30	236	205	31	29	26	3	0.009	0.0008	0.0049	0.002	153979
5	55	55	59	501	385	117	60	49	11	0.0136	0.0013	0.0074	0.004	194947
6	41	36	57	460	374	87	56	48	9	0.0148	0.0018	0.0083	0.004	166127
7	28	29	54	436	375	61	54	48	6	0.0161	0.0015	0.0088	0.004	157698
8	14	15	51	402	370	32	50	47	3	0.0194	0.0018	0.0106	0.005	128792
9	55	55	80	669	552	116	82	70	11	0.0207	0.0024	0.0115	0.006	177567
10	41	40	77	620	533	87	76	68	9	0.0208	0.0025	0.0117	0.006	168524
11	28	26	75	595	536	59	74	68	6	0.0239	0.0029	0.0134	0.007	147873
12	14	15	72	574	546	28	72	70	3	0.0281	0.0031	0.0156	0.008	129296
13	55	55	108	891	774	117	110	98	11	0.0321	0.0056	0.0189	0.009	151793
14	41	37	105	852	766	86	106	97	9	0.0322	0.0065	0.0193	0.01	146218
15	28	25	102	823	763	59	103	97	6	0.0349	0.0065	0.0207	0.01	136036
16	14	15	99	796	763	33	100	97	3	0.0396	0.0064	0.023	0.011	122425

Test ID CC22 3

Dry Density 101.1 pcf
Water Content 19.8 %

Sequence	Nominal Cell Pressure	Actual Cell Pressure	Nominal Max Deviator Stress	Actual Max Load	Actual Cyclic Load	Actual Contact Load	Actual Max Deviator Stress	Cyclic Stress	Recoverable Deformation 1	Recoverable Deformation 2	Recoverable Deformation Average	Vertical Displacement Ratio	Resilient Strain Average	Resilient Modulus Avg
	NCP	ACP	$S_{d\,max}$	P_{max}	P_{Cyclic}	$P_{Contact}$	$S_{d\,Max}$	$S_{d\,Cyclic}$	ΔH_1	ΔH_2	H_{avg}	H2/H1	$\varepsilon_{r\,avg}$	M_r
	(kPa)	(kPa)	(kPa)	(N)	(N)	(N)	(kPa)	(kPa)	(mm)	(mm)	(mm)		(%)	(psi)
0	28	21	54	394	352	42	49	45	4	0.0055	0.0086	0.0071	0.003	
1	55	46	39	331	219	111	39	28	11	0.0023	0.0033	0.0028	0.001	349316
2	41	34	36	303	219	84	36	28	8	0.0025	0.0035	0.003	0.001	326891
3	28	21	33	265	209	56	32	27	6	0.0027	0.0037	0.0032	0.001	294935
4	14	10	30	49	36	13	6	5	1	0.0002	0.0003	0.0002	0	667622
5	55	46	59	500	383	117	61	49	12	0.0052	0.0062	0.0057	0.002	297863
6	41	35	57	481	400	81	59	51	8	0.0055	0.0071	0.0063	0.003	281111
7	28	19	54	441	402	38	55	51	4	0.0054	0.0098	0.0076	0.003	234971
8	14	10	51	442	409	33	56	52	4	0.0064	0.0123	0.0094	0.004	193404
9	55	45	80	663	550	113	81	70	11	0.008	0.01	0.009	0.004	271342
10	41	32	77	625	543	82	77	69	8	0.0082	0.011	0.0096	0.004	250918
11	28	20	75	536	489	48	67	62	5	0.0074	0.0123	0.0098	0.004	220275
12	14	7	72	673	586	87	85	75	11	0.0146	0.0194	0.017	0.007	152268
13	55	49	108	882	765	116	109	97	11	0.0184	0.0186	0.0185	0.008	183220

Test ID C25 1
Dry Density 99.2 pcf
Water Content 24.0 %

Sequence	Nominal Cell Pressure	Actual Cell Pressure	Nominal Max Deviator Stress	Actual Max Load	Actual Cyclic Load	Actual Contact Load	Actual Max Deviator Stress	Cyclic Stress	Recoverable Deformation 1	Recoverable Deformation 2	Recoverable Deformation Average	Vertical Displacement Ratio	Resilient Strain Average	Resilient Modulus Avg
	NCP	ACP	$S_{d\,max}$	P_{max}	P_{Cyclic}	$P_{Contact}$	$S_{d\,Max}$	$S_{d\,Cyclic}$	ΔH_1	ΔH_2	H_{avg}	H2/H1	$\varepsilon_{r\,avg}$	M_r
	(kPa)	(kPa)	(kPa)	(N)	(N)	(N)	(kPa)	(kPa)	(mm)	(mm)	(mm)		(%)	(psi)
0	28	28	54	548	488	60	68	62	6	0.0636	0.0598	0.0617	0.026	N/A
1	55	56	39	332	216	116	39	28	11	0.0146	0.0113	0.013	0.005	73773
2	41	41	36	295	208	86	35	27	8	0.0185	0.0115	0.015	0.006	61384
3	28	30	33	263	206	58	32	26	5	0.0187	0.0117	0.0152	0.006	59991
4	14	20	30	235	203	31	29	26	3	0.0144	0.0111	0.0127	0.005	70681
5	55	58	59	487	369	117	58	47	11	0.0277	0.0271	0.0274	0.011	59785
6	41	42	57	460	373	87	56	47	8	0.0369	0.0306	0.0337	0.014	49007
7	28	31	54	431	372	59	53	47	6	0.0435	0.0323	0.0379	0.016	43516
8	14	23	51	404	369	35	50	47	3	0.0464	0.0336	0.04	0.017	40906
9	55	58	80	652	532	120	79	68	12	0.0407	0.054	0.0474	0.02	49852
10	41	42	77	622	531	91	77	68	9	0.0465	0.0616	0.054	0.023	43557
11	28	34	75	609	544	65	75	69	6	0.0541	0.0646	0.0593	0.025	40681
12	14	24	72	577	539	38	72	69	3	0.0615	0.0695	0.0655	0.027	36560
13	55	58	108	917	784	133	113	100	13	0.0883	0.0897	0.089	0.037	39052
14	41	42	105	866	766	99	108	98	10	0.0879	0.0869	0.0874	0.036	38864
15	28	34	102	844	772	72	105	98	7	0.0904	0.0905	0.0904	0.038	37791

Test ID CC25 2

Dry Density 97.3 pcf

Water Content 22.0 %

Sequence	Nominal Cell Pressure	Actual Cell Pressure	Nominal Max Deviator Stress	Actual Max Load	Actual Cyclic Load	Actual Contact Load	Actual Max Deviator Stress	Cyclic Stress	Recoverable Deformation 1	Recoverable Deformation 2	Recoverable Deformation Average	Vertical Displacement Ratio	Resilient Strain Average	Resilient Modulus Avg
	NCP	ACP	$S_{d\,max}$	P_{max}	P_{Cyclic}	$P_{Contact}$	$S_{d\,Max}$	$S_{d\,Cyclic}$	ΔH_1	ΔH_2	H_{avg}	H2/H1	$\varepsilon_{r\,avg}$	M_r
	(kPa)	(kPa)	(kPa)	(N)	(N)	(N)	(kPa)	(kPa)	(mm)	(mm)	(mm)		(%)	(psi)
0	28	22	54	497	443	54	62	56	5	0.0232	0.0007	0.0119	0.005	
1	55	50	39	329	216	112	39	27	11	0.0063	0.0003	0.0033	0.001	291755
2	41	34	36	291	209	82	35	27	8	0.0065	0.0004	0.0034	0.001	268995
3	28	26	33	263	207	56	32	26	5	0.0072	0.0004	0.0038	0.002	243562
4	14	8	30	230	205	25	29	26	3	0.0101	0.0004	0.0052	0.002	173014
5	55	51	59	498	386	112	60	49	11	0.0136	0.0003	0.007	0.003	245877
6	41	34	57	463	381	83	57	48	8	0.0146	0.0003	0.0075	0.003	226269
7	28	25	54	429	373	56	53	47	5	0.0167	0.0003	0.0085	0.004	194771
8	14	11	51	398	370	27	50	47	3	0.0222	0.0003	0.0112	0.005	146016
9	55	52	80	666	552	114	81	70	11	0.0206	0.002	0.0113	0.005	217247
10	41	34	77	615	531	83	76	68	8	0.0215	0.0005	0.011	0.005	213355
11	28	26	75	596	539	56	74	69	5	0.0246	0.0005	0.0126	0.005	190314
12	14	10	72	566	537	29	71	68	3	0.0346	0.0003	0.0175	0.007	136286
13	55	52	108	886	772	114	109	98	11	0.032	0.0084	0.0202	0.008	169956
14	41	40	105	839	752	87	104	96	9	0.0336	0.0068	0.0202	0.008	164752
15	28	23	102	806	750	56	101	95	6	0.0376	0.0071	0.0224	0.009	148555
16	14	12	99	783	752	31	99	96	3	0.045	0.0071	0.0261	0.011	127726

Test ID CC25 3

Dry Density 97.7 pcf

Water Content 20.8 %

Sequence	Nominal Cell Pressure	Actual Cell Pressure	Nominal Max Deviator Stress	Actual Max Load	Actual Cyclic Load	Actual Contact Load	Actual Max Deviator Stress	Cyclic Stress	Recoverable Deformation 1	Recoverable Deformation 2	Recoverable Deformation Average	Vertical Displacement Ratio	Resilient Strain Average	Resilient Modulus Avg
	NCP	ACP	$S_{d\,max}$	P_{max}	P_{Cyclic}	$P_{Contact}$	$S_{d\,Max}$	$S_{d\,Cyclic}$	ΔH_1	ΔH_2	H_{avg}	H2/H1	$\varepsilon_{r\,avg}$	M_r
	(kPa)	(kPa)	(kPa)	(N)	(N)	(N)	(kPa)	(kPa)	(mm)	(mm)	(mm)		(%)	(psi)
0	28	26	54	468	413	55	58	53	5	0.0071	0.0202	0.0136	0.006	
1	55	47	39	330	220	110	39	28	11	0.0029	0.0065	0.0047	0.002	208682
2	41	31	36	293	213	80	35	27	8	0.0027	0.0071	0.0049	0.002	192472
3	28	23	33	269	213	55	33	27	6	0.0028	0.0073	0.0051	0.002	186944
4	14	12	30	251	224	28	31	28	3	0.0034	0.0099	0.0066	0.003	149785
5	55	49	59	489	377	112	59	48	11	0.0076	0.0153	0.0114	0.005	146467
6	41	37	57	466	381	86	57	48	8	0.0072	0.0166	0.0119	0.005	141812
7	28	24	54	440	386	54	54	49	5	0.0073	0.0192	0.0132	0.006	129125
8	14	13	51	413	384	29	52	49	3	0.0075	0.0213	0.0144	0.006	118239
9	55	51	80	665	552	112	81	70	11	0.0193	0.028	0.0237	0.01	103624
10	41	36	77	623	538	85	77	68	8	0.0202	0.0298	0.025	0.01	95082
11	28	24	75	594	537	57	74	68	6	0.0205	0.0318	0.0261	0.011	90913
12	14	16	72	574	544	31	72	69	3	0.0203	0.0365	0.0284	0.012	84814
13	55	52	108	878	762	115	108	97	11	0.0451	0.052	0.0486	0.02	69559

Test ID DC23 1

Dry Density 95.1 pcf

Water Content 25.0 %

Sequence	Nominal Cell Pressure	Actual Cell Pressure	Nominal Max Deviator Stress	Actual Max Load	Actual Cyclic Load	Actual Contact Load	Actual Max Deviator Stress	Cyclic Stress	Recoverable Deformation 1	Recoverable Deformation 2	Recoverable Deformation Average	Vertical Displacement Ratio	Resilient Strain Average	Resilient Modulus Avg
	NCP	ACP	$S_{d\,max}$	P_{max}	P_{Cyclic}	$P_{Contact}$	$S_{d\,Max}$	$S_{d\,Cyclic}$	ΔH_1	ΔH_2	H_{avg}	H2/H1	$\varepsilon_{r\,avg}$	M_r
	(kPa)	(kPa)	(kPa)	(N)	(N)	(N)	(kPa)	(kPa)	(mm)	(mm)	(mm)		(%)	(psi)
0	28	34	54	525	467	58	65	60	5	0.0174	0.0053	0.0113	0.005	
1	55	49	39	322	210	112	38	27	11	0.0057	0.0018	0.0038	0.002	251235
2	41	34	36	296	213	83	36	27	8	0.0057	0.002	0.0038	0.002	247976
3	28	28	33	274	219	55	33	28	5	0.0065	0.0021	0.0043	0.002	228860
4	14	10	30	241	214	27	30	27	3	0.0073	0.002	0.0046	0.002	206182
5	55	51	59	499	387	112	60	49	11	0.0126	0.0036	0.0081	0.003	212142
6	41	34	57	457	375	82	56	48	8	0.0124	0.0038	0.0081	0.003	206086
7	28	22	54	441	386	55	55	49	6	0.0142	0.0042	0.0092	0.004	186478
8	14	14	51	393	361	32	49	46	3	0.014	0.0038	0.0089	0.004	181634
9	55	49	80	660	547	112	81	70	11	0.02	0.0055	0.0128	0.005	190733
10	41	33	77	618	534	84	77	68	8	0.0213	0.0061	0.0137	0.006	173570
11	28	27	75	598	540	58	75	69	6	0.023	0.0059	0.0145	0.006	166122
12	14	12	72	593	561	32	75	72	3	0.025	0.006	0.0155	0.006	160802
13	55	50	108	871	753	119	108	96	12	0.0338	0.0087	0.0212	0.009	157437
14	41	42	105	858	768	91	107	98	9	0.0351	0.009	0.0221	0.009	154436
15	28	23	102	783	722	61	98	92	6	0.0348	0.0079	0.0213	0.009	150556
16	14	14	99	776	740	35	98	94	4	0.0371	0.0077	0.0224	0.009	146591

Test ID DC23 2

Dry Density 97.2 pcf

Water Content 20.1 %

Sequence	Nominal Cell Pressure	Actual Cell Pressure	Nominal Max Deviator Stress	Actual Max Load	Actual Cyclic Load	Actual Contact Load	Actual Max Deviator Stress	Cyclic Stress	Recoverable Deformation 1	Recoverable Deformation 2	Recoverable Deformation Average	Vertical Displacement Ratio	Resilient Strain Average	Resilient Modulus Avg
	NCP	ACP	$S_{d\,max}$	P_{max}	P_{Cyclic}	$P_{Contact}$	$S_{d\,Max}$	$S_{d\,Cyclic}$	ΔH_1	ΔH_2	H_{avg}	H2/H1	$\varepsilon_{r\,avg}$	M_r
	(kPa)	(kPa)	(kPa)	(N)	(N)	(N)	(kPa)	(kPa)	(mm)	(mm)	(mm)		(%)	(psi)
0	28	26	54	492	432	59	60	54	6	0.0163	0.0281	0.0222	0.011	
1	55	51	39	340	226	115	39	28	11	0.0048	0.0075	0.0062	0.003	133741
2	41	35	36	303	219	85	36	27	8	0.005	0.0078	0.0064	0.003	124711
3	28	28	33	279	218	61	33	27	6	0.006	0.0105	0.0083	0.004	96443
4	14	16	30	245	215	30	30	27	3	0.0092	0.0167	0.0129	0.006	60954
5	55	53	59	508	390	118	60	49	11	0.0098	0.0158	0.0128	0.006	110713
6	41	36	57	470	386	84	57	48	8	0.0111	0.0184	0.0147	0.007	95362
7	28	26	54	432	374	58	52	47	6	0.0128	0.023	0.0179	0.009	76194
8	14	13	51	881	749	132	109	93	16	0.0484	0.0723	0.0603	0.03	44836
9	55	52	80	674	558	116	81	70	11	0.0133	0.0217	0.0175	0.009	115279
10	41	38	77	629	541	89	76	67	9	0.0148	0.0247	0.0198	0.01	98697
11	28	23	75	613	555	58	75	69	6	0.0216	0.0384	0.03	0.015	66860
12	14	14	72	545	514	31	67	64	3	0.0296	0.0481	0.0389	0.019	47885
13	55	51	108	900	783	117	109	97	11	0.0199	0.0332	0.0265	0.013	106507
14	41	35	105	881	794	87	107	99	9	0.025	0.0451	0.0351	0.018	81755
15	28	25	102	826	772	54	101	96	5	0.0306	0.053	0.0418	0.021	66653
16	14	11	99	787	760	27	97	95	3	0.0461	0.0724	0.0593	0.03	46304

Test ID DC23 3

Dry Density 995.0 pcf

Water Content 19.8 %

Sequence	Nominal Cell Pressure	Actual Cell Pressure	Nominal Max Deviator Stress	Actual Max Load	Actual Cyclic Load	Actual Contact Load	Actual Max Deviator Stress	Cyclic Stress	Recoverable Deformation 1	Recoverable Deformation 2	Recoverable Deformation Average	Vertical Displacement Ratio	Resilient Strain Average	Resilient Modulus Avg
	NCP	ACP	$S_{d\,max}$	P_{max}	P_{Cyclic}	$P_{Contact}$	$S_{d\,Max}$	$S_{d\,Cyclic}$	ΔH_1	ΔH_2	H_{avg}	H2/H1	$\varepsilon_{r\,avg}$	M_r
	(kPa)	(kPa)	(kPa)	(N)	(N)	(N)	(kPa)	(kPa)	(mm)	(mm)	(mm)		(%)	(psi)
0	28	28	54	430	375	56	53	48	6	0.0242	0.0106	0.0174	0.009	
1	55	0	39	332	217	115	39	28	11	0.0083	0.0035	0.0059	0.003	135487
2	41	0	36	297	214	83	36	27	8	0.012	0.0043	0.0081	0.004	97353
3	28	0	33	265	211	55	32	27	5	0.0144	0.0046	0.0095	0.005	82010
4	14	14	30	256	227	29	32	29	3	0.0188	0.0058	0.0123	0.006	68304
5	55	0	59	491	376	115	59	48	11	0.0138	0.01	0.0119	0.006	116337
6	41	0	57	468	386	82	57	49	8	0.0214	0.0107	0.0161	0.008	88669
7	28	0	54	439	382	57	54	49	6	0.0284	0.0113	0.0199	0.01	70924
8	14	14	51	409	380	30	52	48	3	0.0322	0.0121	0.0222	0.011	63141
9	55	0	80	662	547	115	81	69	11	0.0183	0.0199	0.0191	0.01	105338
10	41	0	77	622	539	83	77	68	8	0.0255	0.0194	0.0224	0.011	88490
11	28	0	75	622	562	60	78	71	6	0.0379	0.0218	0.0299	0.015	69292
12	14	0	72	566	537	30	71	68	3	0.0393	0.0213	0.0303	0.015	65333
13	55	0	108	899	779	120	111	99	12	0.025	0.0344	0.0297	0.015	96432
14	41	0	105	869	782	86	108	99	9	0.033	0.0365	0.0347	0.017	82733
15	28	0	102	829	771	58	103	98	6	0.0412	0.0372	0.0392	0.02	72228
16	14	0	99	758	734	24	95	93	2	0.0447	0.0372	0.0409	0.02	65852

Test ID DC27 1

Dry Density 91.1 pcf

Water Content 29.1 %

Sequence	Nominal Cell Pressure	Actual Cell Pressure	Nominal Max Deviator Stress	Actual Max Load	Actual Cyclic Load	Actual Contact Load	Actual Max Deviator Stress	Cyclic Stress	Recoverable Deformation 1	Recoverable Deformation 2	Recoverable Deformation Average	Vertical Displacement Ratio	Resilient Strain Average	Resilient Modulus Avg
	NCP	ACP	$S_{d\,max}$	P_{max}	P_{Cyclic}	$P_{Contact}$	$S_{d\,Max}$	$S_{d\,Cyclic}$	ΔH_1	ΔH_2	H_{avg}	H2/H1	$\varepsilon_{r\,avg}$	M_r
	(kPa)	(kPa)	(kPa)	(N)	(N)	(N)	(kPa)	(kPa)	(mm)	(mm)	(mm)		(%)	(psi)
0	28	27	54	442	382	60	55	49	6	0.0228	0.028	0.0254	0.011	N/A
1	55	50	39	335	222	114	39	28	11	0.0094	0.0109	0.0102	0.004	96911
2	41	33	36	303	221	82	36	28	8	0.0097	0.0113	0.0105	0.004	93804
3	28	27	33	278	221	56	34	28	5	0.0101	0.0119	0.011	0.005	88874
4	14	14	30	242	211	30	30	27	3	0.0103	0.0121	0.0112	0.005	83493
5	55	51	59	487	373	114	59	47	11	0.0198	0.0236	0.0217	0.009	76158
6	41	34	57	468	384	84	57	49	9	0.0218	0.0268	0.0243	0.01	69993
7	28	26	54	435	377	58	54	48	6	0.0226	0.0275	0.025	0.01	66835
8	14	14	51	414	384	30	52	49	3	0.0241	0.0301	0.0271	0.011	62951
9	55	51	80	661	542	119	81	69	12	0.0412	0.0484	0.0448	0.019	53643
10	41	39	77	625	537	89	77	68	9	0.0418	0.0492	0.0455	0.019	52354
11	28	24	75	609	546	63	76	70	6	0.0477	0.0551	0.0514	0.021	47101
12	14	14	72	562	532	31	71	68	3	0.0498	0.0563	0.0531	0.022	44436
13	55	50	108	872	753	119	108	96	12	0.1058	0.1151	0.1105	0.046	30328
14	41	35	105	866	771	95	108	98	10	0.1027	0.1165	0.1096	0.046	31163
15	28	22	102	824	761	63	103	97	7	0.0992	0.1167	0.108	0.045	31149
16	14	12	99	855	819	35	108	104	4	0.1238	0.1499	0.1369	0.057	26463

Test ID	DC27 2	
Dry Density	93.1	pcf
Water Content	24.1	%

Sequence	Nominal Cell Pressure	Actual Cell Pressure	Nominal Max Deviator Stress	Actual Max Load	Actual Cyclic Load	Actual Contact Load	Actual Max Deviator Stress	Cyclic Stress	Recoverable Deformation 1	Recoverable Deformation 2	Recoverable Deformation Average	Vertical Displacement Ratio	Resilient Strain Average	Resilient Modulus Avg
	NCP	ACP	$S_{d\,max}$	P_{max}	P_{Cyclic}	$P_{Contact}$	$S_{d\,Max}$	$S_{d\,Cyclic}$	ΔH_1	ΔH_2	H_{avg}	H2/H1	$\varepsilon_{r\,avg}$	M_r
	(kPa)	(kPa)	(kPa)	(N)	(N)	(N)	(kPa)	(kPa)	(mm)	(mm)	(mm)		(%)	(psi)
0	28	22	54	447	393	55	55	50	6	0.0156	0.0133	0.0145	0.006	N/A
1	55	49	39	334	223	111	39	28	11	0.0057	0.0052	0.0055	0.002	181054
2	41	37	36	299	213	86	36	27	8	0.0053	0.0048	0.005	0.002	188377
3	28	26	33	267	209	58	32	27	6	0.0059	0.0052	0.0055	0.002	167926
4	14	15	30	240	209	31	30	27	3	0.0074	0.0059	0.0067	0.003	139043
5	55	50	59	499	386	112	60	49	11	0.0117	0.0091	0.0104	0.004	164559
6	41	35	57	462	377	85	56	48	9	0.0119	0.0097	0.0108	0.005	153925
7	28	26	54	440	382	58	54	49	6	0.0142	0.0111	0.0127	0.005	133751
8	14	13	51	402	373	30	50	47	3	0.0158	0.0121	0.0139	0.006	118446
9	55	47	80	660	549	111	81	70	11	0.0171	0.0143	0.0157	0.007	154385
10	41	35	77	621	537	84	77	68	8	0.0183	0.0146	0.0165	0.007	144577
11	28	22	75	599	545	55	75	69	5	0.0217	0.0175	0.0196	0.008	122828
12	14	15	72	572	541	31	72	69	3	0.0247	0.0192	0.022	0.009	108918
13	55	50	108	884	770	114	109	98	11	0.0269	0.0225	0.0247	0.01	137722
14	41	34	105	836	754	83	104	96	8	0.0279	0.0232	0.0255	0.011	130571
15	28	25	102	807	750	58	101	95	6	0.0295	0.0242	0.0268	0.011	123708
16	14	10	99	782	752	29	99	96	3	0.0376	0.0285	0.0331	0.014	100654

Test ID	DC27 3	
Dry Density	96.7	pcf
Water Content	23.1	%

Sequence	Nominal Cell Pressure	Actual Cell Pressure	Nominal Max Deviator Stress	Actual Max Load	Actual Cyclic Load	Actual Contact Load	Actual Max Deviator Stress	Cyclic Stress	Recoverable Deformation 1	Recoverable Deformation 2	Recoverable Deformation Average	Vertical Displacement Ratio	Resilient Strain Average	Resilient Modulus Avg
	NCP	ACP	$S_{d\,max}$	P_{max}	P_{Cyclic}	$P_{Contact}$	$S_{d\,Max}$	$S_{d\,Cyclic}$	ΔH_1	ΔH_2	H_{avg}	H2/H1	$\varepsilon_{r\,avg}$	M_r
	(kPa)	(kPa)	(kPa)	(N)	(N)	(N)	(kPa)	(kPa)	(mm)	(mm)	(mm)		(%)	(psi)
0	28	22	54	436	381	56	54	48	6	0.0036	0.0119	0.0078	0.003	N/A
1	55	51	39	331	217	114	39	28	11	0.0021	0.0052	0.0037	0.002	261844
2	41	35	36	297	214	83	35	27	8	0.0022	0.0052	0.0037	0.002	254843
3	28	24	33	272	216	56	33	27	6	0.002	0.0054	0.0037	0.002	256057
4	14	12	30	242	214	28	30	27	3	0.002	0.006	0.004	0.002	236260
5	55	51	59	491	379	112	59	48	11	0.0042	0.0101	0.0071	0.003	235176
6	41	36	57	464	381	83	57	48	8	0.004	0.0105	0.0073	0.003	231457
7	28	28	54	443	386	58	54	49	6	0.004	0.011	0.0075	0.003	225925
8	14	12	51	404	374	29	50	47	3	0.0042	0.0115	0.0078	0.003	210999
9	55	52	80	663	550	113	81	70	11	0.0071	0.015	0.0111	0.005	219439
10	41	36	77	628	544	84	77	69	8	0.0072	0.0151	0.0112	0.005	215294
11	28	25	75	602	545	57	75	69	6	0.0074	0.0161	0.0117	0.005	205080
12	14	15	72	567	536	31	71	68	3	0.0073	0.0176	0.0125	0.005	189901
13	55	52	108	890	775	115	110	98	11	0.0117	0.0234	0.0176	0.007	194832
14	41	36	105	842	759	84	105	96	8	0.0116	0.0233	0.0174	0.007	192098
15	28	27	102	820	763	57	102	97	5	0.012	0.0247	0.0183	0.008	183966
16	14	12	99	795	764	31	100	97	3	0.0135	0.0281	0.0208	0.009	162004

Test ID	DC30 1
Dry Density	88.5 pcf
Water Content	29.9 %

Sequence	Nominal Cell Pressure	Actual Cell Pressure	Nominal Max Deviator Stress	Actual Max Load	Actual Cyclic Load	Actual Contact Load	Actual Max Deviator Stress	Cyclic Stress	Recoverable Deformation 1	Recoverable Deformation 2	Recoverable Deformation Average	Vertical Displacement Ratio	Resilient Strain Average	Resilient Modulus Avg
	NCP	ACP	$S_{d\,max}$	P_{max}	P_{Cyclic}	$P_{Contact}$	$S_{d\,Max}$	$S_{d\,Cyclic}$	ΔH_1	ΔH_2	H_{avg}	H2/H1	$\varepsilon_{r\,avg}$	M_r
	(kPa)	(kPa)	(kPa)	(N)	(N)	(N)	(kPa)	(kPa)	(mm)	(mm)	(mm)		(%)	(psi)
0	28	28	54	443	384	59	54	49	6	0.0232	0.0229	0.023	0.01	N/A
1	55	53	39	331	217	115	39	27	11	0.0087	0.0091	0.0089	0.004	107182
2	41	35	36	294	211	83	35	27	8	0.0079	0.0087	0.0083	0.003	112606
3	28	27	33	269	211	58	32	27	6	0.0079	0.0088	0.0083	0.003	112380
4	14	14	30	238	209	29	29	27	3	0.0077	0.009	0.0084	0.003	110664
5	55	52	59	487	373	115	58	47	11	0.0203	0.0207	0.0205	0.009	80621
6	41	36	57	462	377	85	56	48	8	0.0213	0.021	0.0211	0.009	78788
7	28	22	54	431	374	57	53	47	6	0.0208	0.022	0.0214	0.009	77275
8	14	15	51	409	376	33	51	48	3	0.0221	0.0231	0.0226	0.009	73297
9	55	47	80	663	541	121	81	69	12	0.0468	0.0587	0.0528	0.022	45957
10	41	39	77	627	534	93	77	68	9	0.0451	0.0566	0.0509	0.021	46196
11	28	28	75	605	540	64	75	68	6	0.0493	0.0621	0.0557	0.023	42701
12	14	12	72	577	542	36	72	68	4	0.0511	0.0649	0.058	0.024	41103
13	55	50	108	896	772	124	109	97	12	0.0903	0.7011	0.3957	0.165	8704
14	41	38	105	864	768	96	105	96	10	0.0865	0.7519	0.4192	0.175	8014
15	28	27	102	799	740	59	98	92	6	0.0885	0.8788	0.4837	0.202	6655
16	14	11	99	723	662	61	88	81	7	0.0797	0.9249	0.5023	0.209	5877

Test ID	DC30 2

Dry Density 86.0 pcf

Water Content 26.2 %

Sequence	Nominal Cell Pressure	Actual Cell Pressure	Nominal Max Deviator Stress	Actual Max Load	Actual Cyclic Load	Actual Contact Load	Actual Max Deviator Stress	Cyclic Stress	Recoverable Deformation 1	Recoverable Deformation 2	Recoverable Deformation Average	Vertical Displacement Ratio	Resilient Strain Average	Resilient Modulus Avg
	NCP	ACP	$S_{d\,max}$	P_{max}	P_{Cyclic}	$P_{Contact}$	$S_{d\,Max}$	$S_{d\,Cyclic}$	ΔH_1	ΔH_2	H_{avg}	H2/H1	$\varepsilon_{r\,avg}$	M_r
	(kPa)	(kPa)	(kPa)	(N)	(N)	(N)	(kPa)	(kPa)	(mm)	(mm)	(mm)		(%)	(psi)
0	28	20	54	462	407	54	58	52	6	0.0095	0.019	0.0142	0.006	N/A
1	55	45	39	326	218	108	39	28	11	0.003	0.0062	0.0046	0.002	209741
2	41	34	36	293	211	83	35	27	8	0.0034	0.0066	0.005	0.002	188213
3	28	22	33	267	211	56	33	27	6	0.0037	0.0078	0.0058	0.002	162813
4	14	11	30	231	203	28	29	26	3	0.004	0.0092	0.0066	0.003	135931
5	55	43	59	486	377	109	59	48	11	0.007	0.0139	0.0104	0.004	160235
6	41	33	57	459	376	83	56	48	8	0.0078	0.0159	0.0119	0.005	140487
7	28	23	54	430	375	56	53	48	6	0.0084	0.0177	0.013	0.005	127536
8	14	12	51	403	374	29	51	48	3	0.0088	0.0185	0.0136	0.006	121942
9	55	47	80	657	547	110	81	70	11	0.0132	0.0204	0.0168	0.007	144295
10	41	34	77	611	527	84	76	67	9	0.0127	0.0221	0.0174	0.007	134395
11	28	23	75	605	548	57	76	70	6	0.0142	0.0256	0.0199	0.008	122239
12	14	11	72	577	545	31	73	69	3	0.0152	0.0277	0.0215	0.009	112655
13	55	46	108	877	764	113	109	97	11	0.0229	0.0312	0.027	0.011	125477
14	41	35	105	847	760	88	106	97	9	0.0249	0.0326	0.0288	0.012	117175
15	28	24	102	822	761	61	103	97	6	0.0272	0.0354	0.0313	0.013	107831
16	14	11	99	786	754	32	99	96	3	0.0276	0.038	0.0328	0.014	102059

Test ID DC30 3

Dry Density 88.7 pcf

Water Content 27.3 %

Sequence	Nominal Cell Pressure	Actual Cell Pressure	Nominal Max Deviator Stress	Actual Max Load	Actual Cyclic Load	Actual Contact Load	Actual Max Deviator Stress	Cyclic Stress	Recoverable Deformation 1	Recoverable Deformation 2	Recoverable Deformation Average	Vertical Displacement Ratio	Resilient Strain Average	Resilient Modulus Avg
	NCP	ACP	$S_{d\,max}$	P_{max}	P_{Cyclic}	$P_{Contact}$	$S_{d\,Max}$	$S_{d\,Cyclic}$	ΔH_1	ΔH_2	H_{avg}	H2/H1	$\varepsilon_{r\,avg}$	M_r
	(kPa)	(kPa)	(kPa)	(N)	(N)	(N)	(kPa)	(kPa)	(mm)	(mm)	(mm)		(%)	(psi)
0	28	15	54	452	400	51	57	51	6	0.0127	0.0131	0.0129	0.005	N/A
1	55	44	39	327	218	109	39	28	11	0.0051	0.0052	0.0052	0.002	187804
2	41	32	36	296	215	81	36	27	8	0.0056	0.0052	0.0054	0.002	177011
3	28	21	33	271	218	53	33	28	5	0.0057	0.0052	0.0055	0.002	176929
4	14	8	30	235	208	27	29	26	3	0.0057	0.005	0.0054	0.002	171463
5	55	44	59	484	376	108	59	48	11	0.0104	0.0112	0.0108	0.004	154788
6	41	33	57	456	375	82	56	48	8	0.0107	0.0112	0.0109	0.005	152161
7	28	21	54	432	378	54	54	48	5	0.0115	0.0114	0.0115	0.005	146229
8	14	10	51	412	383	28	52	49	3	0.0128	0.0114	0.0121	0.005	140995
9	55	45	80	654	544	110	80	69	11	0.017	0.0202	0.0186	0.008	129826
10	41	34	77	620	536	83	77	68	8	0.0174	0.0205	0.019	0.008	125285
11	28	21	75	596	541	55	75	69	6	0.0195	0.0195	0.0195	0.008	123057
12	14	9	72	570	544	26	72	69	3	0.0213	0.0173	0.0193	0.008	124887
13	55	45	108	879	766	113	109	98	11	0.031	0.0322	0.0316	0.013	107431
14	41	34	105	840	754	86	105	96	9	0.032	0.0316	0.0318	0.013	105268
15	28	22	102	814	755	59	102	96	6	0.033	0.0314	0.0322	0.013	103998
16	14	15	54	452	400	51	57	51	6	0.0127	0.0131	0.0129	0.005	99527

STRESS STATE PARAMETERS FOR M_R TESTS

Test ID CC19 1
Dry Density 106.9 pcf
Water Content 18.7 %

Cycle	Deviator Stress	Confining Pressure+pore air pressure	σ_1	$\sigma_2=\sigma_3$	Pore water pressure	Pore air pressure	Bulk Stress	Octahedral stress	Measured Resilient Modulus
	psi	psi	psi	psi	psi	psi	psi	psi	psi
	σ_d	σ_3	$\sigma d+\sigma 3$		u_w	u_a	θ	τ_{oct}	$M_{r\ avg}$
0	7.83	3.50							
1	5.66	7.97	13.63	7.98	0.00	1.98	29.58	2.67	67549.34
2	5.22	7.54	11.17	5.95	-1.59	2.07	23.06	2.46	51001.94
3	4.79	4.05	8.85	4.06	0.01	2.09	16.97	2.26	47189.83
4	4.35	2.02	6.38	2.03	0.01	2.16	10.44	2.05	43882.56
5	8.56	7.98	16.53	7.98	0.00	2.21	32.48	4.03	54674.55
6	8.27	5.95	14.21	5.95	-0.01	2.23	26.10	3.90	42724.37
7	7.83	4.08	11.89	4.06	-0.02	2.26	20.01	3.69	39445.86
8	7.40	2.02	9.43	2.03	0.01	2.35	13.49	3.49	39119.85
9	11.60	7.98	19.58	7.98	0.00	2.39	35.53	5.47	45438.89
10	11.17	5.95	17.11	5.95	-0.01	2.40	29.00	5.26	38832.87
11	10.88	4.07	14.94	4.06	-0.01	2.41	23.06	5.13	37613.85
12	10.44	2.02	12.47	2.03	0.01	2.49	16.53	4.92	36216.65
13	15.66	7.97	23.64	7.98	0.00	2.52	39.59	7.38	45590.30
14	15.23	5.95	21.17	5.95	0.00	2.53	33.06	7.18	41209.42
15	14.79	4.08	18.85	4.06	-0.02	2.54	26.97	6.97	42516.42

Test ID CC19 2
Dry Density 105.8 pcf
Water Content 17.2 %

Cycle	Deviator Stress	Confining Pressure+pore air pressure	σ_1	$\sigma_2=\sigma_3$	Pore water pressure	Pore air pressure	Bulk Stress	Octahedral stress	Measured Resilient Modulus
	psi	psi	psi	psi	psi	psi	psi	psi	psi
	σ_d	σ_3	$\sigma d+\sigma 3$		u_w	u_a	θ	τ_{oct}	$M_{r\ avg}$
0	7.83	4.42							
1	5.66	8.28	13.63	7.98	-0.31	1.28	29.58	2.67	86572.54
2	5.22	6.20	11.17	5.95	-0.26	1.27	23.06	2.46	84920.99
3	4.79	4.34	8.85	4.06	-0.28	1.23	16.97	2.26	86208.45
4	4.35	2.25	6.38	2.03	-0.22	1.20	10.44	2.05	86908.22
5	8.56	8.47	16.53	7.98	-0.50	1.18	32.48	4.03	74131.83
6	8.27	6.23	14.21	5.95	-0.28	1.16	26.10	3.90	72243.21
7	7.83	4.33	11.89	4.06	-0.27	1.12	20.01	3.69	71351.02
8	7.40	2.36	9.43	2.03	-0.33	1.09	13.49	3.49	69085.40
9	11.60	8.41	19.58	7.98	-0.44	1.06	35.53	5.47	61429.40
10	11.17	6.15	17.11	5.95	-0.21	1.03	29.00	5.26	59211.19
11	10.88	4.37	14.94	4.06	-0.31	1.00	23.06	5.13	57596.03
12	10.44	2.38	12.47	2.03	-0.35	0.94	16.53	4.92	56299.88
13	15.66	8.46	23.64	7.98	-0.49	0.92	39.59	7.38	51502.26
14	15.23	6.25	21.17	5.95	-0.30	0.89	33.06	7.18	50329.36
15	14.79	4.34	18.85	4.06	-0.28	0.85	26.97	6.97	47246.95

Test ID CC19 3

Dry Density 106.9 pcf

Water Content 15.4 %

Cycle	Deviator Stress	Confining Pressure+pore air pressure	σ_1	$\sigma_2=\sigma_3$	Pore water pressure	Pore air pressure	Bulk Stress	Octahedral stress	Measured Resilient Modulus
	psi	psi	psi	psi	psi	psi	psi	psi	psi
	σ_d	σ_3	$\sigma d+\sigma 3$		u_w	u_a	θ	τ_{oct}	$M_{r\ avg}$
0	7.69	3.87							
1	5.51	7.97	13.49	7.98	0.00	-0.16	29.44	2.60	66879.51
2	5.08	5.82	11.02	5.95	0.12	-0.18	22.91	2.39	71721.06
3	4.64	4.05	8.70	4.06	0.01	-0.19	16.82	2.19	70621.96
4	4.21	1.94	6.24	2.03	0.09	-0.22	10.30	1.98	68415.21
5	8.41	7.89	16.39	7.98	0.08	-0.23	32.34	3.96	58744.72
6	8.12	5.79	14.07	5.95	0.15	-0.23	25.96	3.83	55827.47
7	7.69	4.01	11.75	4.06	0.05	-0.26	19.87	3.62	54115.02
8	7.25	1.92	9.28	2.03	0.11	-0.26	13.34	3.42	54498.54
9	11.46	7.84	19.43	7.98	0.14	-0.27	35.38	5.40	48966.36
10	11.02	5.91	16.97	5.95	0.03	-0.27	28.86	5.19	46537.75
11	10.73	3.87	14.79	4.06	0.19	-0.29	22.91	5.06	45279.73
12	10.73	1.90	12.76	2.03	0.13	-0.29	16.82	5.06	43471.87
13	15.95	7.83	23.93	7.98	0.15	-0.30	39.88	7.52	42909.71
14	15.23	5.81	21.17	5.95	0.14	-0.33	33.06	7.18	42631.16
15	14.65	3.88	18.71	4.06	0.18	-0.31	26.83	6.90	40384.53

Test ID CC22 1

Dry Density 100.4 pcf

Water Content 22.3 %

Cycle	Deviator Stress	Confining Pressure+pore air pressure	σ_1	$\sigma_2=\sigma_3$	Pore water pressure	Pore air pressure	Bulk Stress	Octahedral stress	Measured Resilient Modulus
	psi	psi	psi	psi	psi	psi	psi	psi	psi
	σ_d	σ_3	$\sigma d+\sigma 3$		u_w	u_a	θ	τ_{oct}	$M_{r\ avg}$
0	7.83	26.07							
1	5.66	27.92	33.58	27.92	19.95	9.75	89.43	2.67	6797.90
2	5.22	26.99	32.21	26.99	21.04	10.22	86.19	2.46	6300.19
3	4.79	24.84	29.63	24.84	20.78	11.13	79.32	2.26	6067.89
4	4.21	23.00	27.20	23.00	20.97	11.64	73.20	1.98	5993.33
5	8.56	25.63	34.19	25.63	17.66	12.15	85.45	4.03	6017.56
6	8.27	26.12	34.38	26.12	20.17	12.44	86.61	3.90	5526.49
7	7.69	24.92	32.60	24.92	20.86	13.17	82.43	3.62	5289.96
8	7.40	22.95	30.35	22.95	20.92	13.60	76.26	3.49	5117.35
9	11.46	25.76	37.21	25.76	17.78	14.10	88.73	5.40	5737.53
10	11.17	26.10	37.26	26.10	20.15	14.35	89.46	5.26	5254.08
11	10.73	24.83	35.56	24.83	20.77	14.66	85.23	5.06	5000.99
12	10.30	22.46	32.76	22.46	20.43	14.75	77.68	4.85	4744.76
13	15.66	25.00	40.66	25.00	17.02	15.17	90.65	7.38	5270.27
14	15.23	26.05	41.27	26.05	20.10	15.39	93.37	7.18	4798.05
15	14.79	24.29	39.08	24.29	20.23	15.49	87.67	6.97	4575.11
16	14.36	22.72	37.07	22.72	20.69	15.54	82.50	6.77	4371.57

Test ID CC22 2

Dry Density 99.2 pcf

Water Content 18.3 %

Cycle	Deviator Stress	Confining Pressure+pore air pressure	σ_1	$\sigma_2=\sigma_3$	Pore water pressure	Pore air pressure	Bulk Stress	Octahedral stress	Measured Resilient Modulus
	psi	psi	psi	psi	psi	psi	psi	psi	psi
	σ_d	σ_3	$\sigma d+\sigma 3$		u_w	u_a	θ	τ_{oct}	$M_{r\ avg}$
0	7.25	4.06							
1	5.66	7.97	13.63	7.98	0.00	0.73	29.58	2.67	92256.43
2	5.08	5.94	11.02	5.95	0.00	0.72	22.91	2.39	92860.90
3	4.64	4.06	8.70	4.06	0.00	0.73	16.82	2.19	71833.18
4	4.21	2.03	6.24	2.03	0.00	0.73	10.30	1.98	64157.97
5	8.70	7.94	16.68	7.98	0.03	0.73	32.63	4.10	81227.97
6	8.12	5.91	14.07	5.95	0.03	0.73	25.96	3.83	69219.56
7	7.83	4.03	11.89	4.06	0.03	0.73	20.01	3.69	65707.35
8	7.25	2.00	9.28	2.03	0.03	0.73	13.34	3.42	53663.47
9	11.89	7.91	19.87	7.98	0.07	0.73	35.82	5.60	73986.07
10	11.02	5.88	16.97	5.95	0.07	0.73	28.86	5.19	70218.43
11	10.73	3.99	14.79	4.06	0.07	0.72	22.91	5.06	61613.94
12	10.44	1.96	12.47	2.03	0.07	0.73	16.53	4.92	53873.42
13	15.95	7.86	23.93	7.98	0.12	0.74	39.88	7.52	63247.01
14	15.37	5.83	21.32	5.95	0.12	0.73	33.21	7.25	60924.35
15	14.94	3.94	19.00	4.06	0.12	0.73	27.12	7.04	56681.47
16	14.50	1.92	16.53	2.03	0.11	0.74	20.59	6.84	51010.28

Test ID CC22 3

Dry Density 101.1 pcf

Water Content 19.8 %

Cycle	Deviator Stress	Confining Pressure+pore air pressure	σ_1	$\sigma_2=\sigma_3$	Pore water pressure	Pore air pressure	Bulk Stress	Octahedral stress	Measured Resilient Modulus
	psi	psi	psi	psi	psi	psi	psi	psi	psi
	σ_d	σ_3	$\sigma d+\sigma 3$		u_w	u_a	θ	τ_{oct}	$M_{r\ avg}$
0	7.11	4.06							
1	5.66	7.97	13.63	7.98	0.00	2.46	29.58	2.67	145548.22
2	5.22	5.94	11.17	5.95	0.00	1.94	23.06	2.46	136204.78
3	4.64	4.06	8.70	4.06	0.00	2.60	16.82	2.19	122889.55
4	0.87	2.03	2.90	2.03	0.00	1.60	6.96	0.41	278175.98
5	8.85	7.97	16.82	7.98	0.00	2.18	32.77	4.17	124109.43
6	8.56	5.94	14.50	5.95	0.00	0.97	26.39	4.03	117129.67
7	7.98	4.06	12.04	4.06	0.00	2.17	20.16	3.76	97904.79
8	8.12	2.03	10.15	2.03	0.00	2.30	14.21	3.83	80585.08
9	11.75	7.97	19.72	7.98	0.00	2.77	35.67	5.54	113059.28
10	11.17	5.94	17.11	5.95	0.00	2.66	29.00	5.26	104549.29
11	9.72	4.06	13.78	4.06	0.00	3.32	21.90	4.58	91781.13
12	12.33	2.01	14.36	2.03	0.02	2.19	18.42	5.81	63444.93
13	15.81	7.96	23.78	7.98	0.02	0.65	39.73	7.45	76341.47
14	15.37	5.93	21.32	5.95	0.02	2.56	33.21	7.25	76827.53
15	14.65	4.04	18.71	4.06	0.02	2.87	26.83	6.90	73785.30
16	31.76	1.97	33.79	2.03	0.06	3.37	37.85	14.97	32889.44

Test ID CC25 1

Dry Density 99.2 pcf

Water Content 24.0 %

Cycle	Deviator Stress	Confining Pressure+pore air pressure	σ_1	$\sigma_2=\sigma_3$	Pore water pressure	Pore air pressure	Bulk Stress	Octahedral stress	Measured Resilient Modulus
	psi	psi	psi	psi	psi	psi	psi	psi	psi
	σ_d	σ_3	$\sigma d+\sigma 3$		u_w	u_a	θ	τ_{oct}	$M_{r\ avg}$
0	9.86	4.01							
1	5.66	7.92	13.63	7.98	0.06	0.01	29.58	2.67	30738.91
2	5.08	5.89	11.02	5.95	0.05	0.02	22.91	2.39	25576.85
3	4.64	4.01	8.70	4.06	0.05	0.01	16.82	2.19	24996.43
4	4.21	1.98	6.24	2.03	0.05	0.00	10.30	1.98	29450.41
5	8.41	7.92	16.39	7.98	0.06	0.00	32.34	3.96	24910.52
6	8.12	5.89	14.07	5.95	0.05	0.00	25.96	3.83	20419.50
7	7.69	4.01	11.75	4.06	0.05	0.00	19.87	3.62	18131.71
8	7.25	1.98	9.28	2.03	0.05	0.02	13.34	3.42	17044.33
9	11.46	7.92	19.43	7.98	0.06	0.00	35.38	5.40	20771.67
10	11.17	5.89	17.11	5.95	0.06	0.01	29.00	5.26	18148.86
11	10.88	4.00	14.94	4.06	0.06	0.00	23.06	5.13	16950.56
12	10.44	1.97	12.47	2.03	0.06	0.01	16.53	4.92	15233.52
13	16.39	7.90	24.36	7.98	0.07	0.01	40.31	7.72	16271.48
14	15.66	5.87	21.61	5.95	0.07	0.01	33.50	7.38	16193.18
15	15.23	3.99	19.29	4.06	0.07	-0.20	27.41	7.18	15746.09
16	14.65	1.96	16.68	2.03	0.07	-0.05	20.74	6.90	15454.70

Test ID CC25 2

Dry Density 97.3 pcf

Water Content 22.0 %

Cycle	Deviator Stress	Confining Pressure+pore air pressure	σ_1	$\sigma_2=\sigma_3$	Pore water pressure	Pore air pressure	Bulk Stress	Octahedral stress	Measured Resilient Modulus
	psi	psi	psi	psi	psi	psi	psi	psi	psi
	σ_d	σ_3	$\sigma d+\sigma 3$		u_w	u_a	θ	τ_{oct}	$M_{r\ avg}$
0	8.99	4.05							
1	5.66	7.96	13.63	7.98	0.01	-0.22	29.58	2.67	121564.38
2	5.08	5.93	11.02	5.95	0.01	-0.22	22.91	2.39	112081.44
3	4.64	4.05	8.70	4.06	0.01	-0.23	16.82	2.19	101483.99
4	4.21	2.02	6.24	2.03	0.01	-0.27	10.30	1.98	72089.11
5	8.70	7.96	16.68	7.98	0.02	-0.29	32.63	4.10	102448.90
6	8.27	5.93	14.21	5.95	0.02	-0.28	26.10	3.90	94278.64
7	7.69	4.05	11.75	4.06	0.01	-0.30	19.87	3.62	81154.57
8	7.25	2.02	9.28	2.03	0.01	-0.33	13.34	3.42	60839.89
9	11.75	7.95	19.72	7.98	0.03	-0.34	35.67	5.54	90519.45
10	11.02	5.92	16.97	5.95	0.03	-0.36	28.86	5.19	88898.11
11	10.73	4.04	14.79	4.06	0.02	-0.38	22.91	5.06	79297.60
12	10.30	2.01	12.33	2.03	0.02	-0.43	16.39	4.85	56785.99
13	15.81	7.92	23.78	7.98	0.05	-0.41	39.73	7.45	70815.10
14	15.08	5.89	21.03	5.95	0.05	-0.46	32.92	7.11	68646.56
15	14.65	4.01	18.71	4.06	0.05	-0.52	26.83	6.90	61897.96
16	14.36	1.98	16.39	2.03	0.05	-0.57	20.45	6.77	53219.23

Test ID CC25 3

Dry Density 97.7 pcf

Water Content 20.8 %

Cycle	Deviator Stress	Confining Pressure+pore air pressure	σ_1	$\sigma_2=\sigma_3$	Pore water pressure	Pore air pressure	Bulk Stress	Octahedral stress	Measured Resilient Modulus
	psi	psi	psi	psi	psi	psi	psi	psi	psi
	σ_d	σ_3	$\sigma d+\sigma 3$		u_w	u_a	θ	τ_{oct}	$M_{r\ avg}$
0	8.41	4.06							
1	5.66	7.97	13.63	7.98	0.00	2.22	29.58	2.67	86950.88
2	5.08	5.95	11.02	5.95	0.00	2.20	22.91	2.39	80196.54
3	4.79	4.06	8.85	4.06	0.00	2.12	16.97	2.26	77893.15
4	4.50	2.03	6.53	2.03	0.00	1.82	10.59	2.12	62410.48
5	8.56	7.97	16.53	7.98	0.00	1.72	32.48	4.03	61027.84
6	8.27	5.94	14.21	5.95	0.00	1.62	26.10	3.90	59088.29
7	7.83	4.06	11.89	4.06	0.00	0.79	20.01	3.69	53802.01
8	7.54	2.03	9.57	2.03	0.00	0.98	13.63	3.55	49266.05
9	11.75	7.97	19.72	7.98	0.00	0.61	35.67	5.54	43176.59
10	11.17	5.94	17.11	5.95	0.00	0.98	29.00	5.26	39617.56
11	10.73	4.06	14.79	4.06	0.00	0.44	22.91	5.06	37880.22
12	10.44	2.03	12.47	2.03	0.00	0.22	16.53	4.92	35339.16
13	15.66	7.96	23.64	7.98	0.02	0.81	39.59	7.38	28982.90
14	15.23	5.93	21.17	5.95	0.02	1.27	33.06	7.18	26947.95
15	14.94	4.04	19.00	4.06	0.02	0.88	27.12	7.04	25058.05
16	14.50	2.01	16.53	2.03	0.02	0.99	20.59	6.84	22825.42

Test ID DC 23 1

Dry Density 95.1 pcf

Water Content 25.0 %

Cycle	Deviator Stress	Confining Pressure+pore air pressure	σ_1	$\sigma_2=\sigma_3$	Pore water pressure	Pore air pressure	Bulk Stress	Octahedral stress	Measured Resilient Modulus
	psi	psi	psi	psi	psi	psi	psi	psi	psi
	σ_d	σ_3	$\sigma d+\sigma 3$		u_w	u_a	θ	τ_{oct}	$M_{r\ avg}$
0	9.43	4.05							
1	5.51	7.97	13.49	7.98	0.01	1.74	29.44	2.60	104681.18
2	5.22	5.94	11.17	5.95	0.01	1.06	23.06	2.46	103323.38
3	4.79	4.06	8.85	4.06	0.00	0.60	16.97	2.26	95358.40
4	4.35	2.03	6.38	2.03	0.00	0.67	10.44	2.05	85909.36
5	8.70	7.97	16.68	7.98	0.01	1.35	32.63	4.10	88392.36
6	8.12	5.94	14.07	5.95	0.01	1.81	25.96	3.83	85869.00
7	7.98	4.06	12.04	4.06	0.00	1.70	20.16	3.76	77699.16
8	7.11	2.03	9.14	2.03	0.00	0.78	13.20	3.35	75680.94
9	11.75	7.97	19.72	7.98	0.01	2.31	35.67	5.54	79471.96
10	11.17	5.94	17.11	5.95	0.01	1.80	29.00	5.26	72320.68
11	10.88	4.05	14.94	4.06	0.01	1.05	23.06	5.13	69217.50
12	10.88	2.03	12.91	2.03	0.00	0.52	16.97	5.13	67000.94
13	15.66	7.96	23.64	7.98	0.01	1.82	39.59	7.38	65598.73
14	15.52	5.93	21.46	5.95	0.01	0.00	33.35	7.31	64348.22
15	14.21	4.05	18.27	4.06	0.01	1.09	26.39	6.70	62731.77
16	14.21	2.02	16.24	2.03	0.01	1.10	20.30	6.70	61079.44

Test ID DC 23 2

Dry Density 97.2 pcf

Water Content 20.1 %

Cycle	Deviator Stress	Confining Pressure+pore air pressure	σ_1	$\sigma_2=\sigma_3$	Pore water pressure	Pore air pressure	Bulk Stress	Octahedral stress	Measured Resilient Modulus
	psi	psi	psi	psi	psi	psi	psi	psi	psi
	σ_d	σ_3	$\sigma d+\sigma 3$		u_w	u_a	θ	τ_{oct}	$M_{r\ avg}$
0	8.70	4.05							
1	5.66	7.97	13.63	7.98	0.01	1.51	29.58	2.67	55725.49
2	5.22	5.94	11.17	5.95	0.01	1.51	23.06	2.46	51963.11
3	4.79	4.05	8.85	4.06	0.01	1.49	16.97	2.26	40184.45
4	4.35	2.03	6.38	2.03	0.00	1.46	10.44	2.05	25397.41
5	8.70	7.96	16.68	7.98	0.01	1.60	32.63	4.10	46130.48
6	8.27	5.93	14.21	5.95	0.01	1.55	26.10	3.90	39734.05
7	7.54	4.05	11.60	4.06	0.01	1.53	19.72	3.55	31747.39
8	15.81	2.02	17.84	2.03	0.01	1.56	21.90	7.45	18681.62
9	11.75	7.96	19.72	7.98	0.02	1.54	35.67	5.54	48033.00
10	11.02	5.93	16.97	5.95	0.02	1.63	28.86	5.19	41123.69
11	10.88	4.04	14.94	4.06	0.02	1.58	23.06	5.13	27858.13
12	9.72	2.02	11.75	2.03	0.01	1.55	15.81	4.58	19952.06
13	15.81	7.95	23.78	7.98	0.02	1.62	39.73	7.45	44377.79
14	15.52	5.93	21.46	5.95	0.02	1.59	33.35	7.31	34064.49
15	14.65	4.04	18.71	4.06	0.02	1.61	26.83	6.90	27771.97
16	14.07	2.02	16.10	2.03	0.01	1.61	20.16	6.63	19293.40

Test ID DC 23 3

Dry Density 95.0 pcf

Water Content 19.8 %

Cycle	Deviator Stress	Confining Pressure+pore air pressure	σ_1	$\sigma_2=\sigma_3$	Pore water pressure	Pore air pressure	Bulk Stress	Octahedral stress	Measured Resilient Modulus
	psi	psi	psi	psi	psi	psi	psi	psi	psi
	σ_d	σ_3	$\sigma d+\sigma 3$		u_w	u_a	θ	τ_{oct}	$M_{r\ avg}$
0	7.69	4.06							
1	5.66	7.21	13.63	7.98	0.76	0.68	29.58	2.67	56452.85
2	5.22	5.08	11.17	5.95	0.86	0.63	23.06	2.46	40563.63
3	4.64	3.00	8.70	4.06	1.06	-0.14	16.82	2.19	34170.64
4	4.64	1.12	6.67	2.03	0.91	0.95	10.73	2.19	28460.00
5	8.56	6.81	16.53	7.98	1.16	0.57	32.48	4.03	48473.68
6	8.27	4.78	14.21	5.95	1.17	0.71	26.10	3.90	36945.34
7	7.83	2.96	11.89	4.06	1.10	0.64	20.01	3.69	29551.54
8	7.54	0.81	9.57	2.03	1.22	0.71	13.63	3.55	26308.74
9	11.75	6.56	19.72	7.98	1.41	0.72	35.67	5.54	43890.90
10	11.17	4.46	17.11	5.95	1.49	0.55	29.00	5.26	36870.66
11	11.31	2.50	15.37	4.06	1.56	-0.01	23.49	5.33	28871.49
12	10.30	0.48	12.33	2.03	1.55	0.51	16.39	4.85	27222.00
13	16.10	6.14	24.07	7.98	1.83	0.06	40.02	7.59	40179.80
14	15.66	4.10	21.61	5.95	1.84	0.15	33.50	7.38	34472.18
15	14.94	2.33	19.00	4.06	1.73	0.02	27.12	7.04	30094.87
16	0.00	0.00	0.00	0.00	0.00	0.00	0.00	0.00	0.00

Test ID DC 27 1

Dry Density 91.1 pcf

Water Content 29.1 %

Cycle	Deviator Stress	Confining Pressure+pore air pressure	σ_1	$\sigma_2=\sigma_3$	Pore water pressure	Pore air pressure	Bulk Stress	Octahedral stress	Measured Resilient Modulus
	psi	psi	psi	psi	psi	psi	psi	psi	psi
	σ_d	σ_3	$\sigma d+\sigma 3$		u_w	u_a	θ	τ_{oct}	$M_{r\ avg}$
0	7.69	4.06							
1	5.66	7.21	13.63	7.98	0.76	0.68	29.58	2.67	56452.85
2	5.22	5.08	11.17	5.95	0.86	0.63	23.06	2.46	40563.63
3	4.64	3.00	8.70	4.06	1.06	-0.14	16.82	2.19	34170.64
4	4.64	1.12	6.67	2.03	0.91	0.95	10.73	2.19	28460.00
5	8.56	6.81	16.53	7.98	1.16	0.57	32.48	4.03	48473.68
6	8.27	4.78	14.21	5.95	1.17	0.71	26.10	3.90	36945.34
7	7.83	2.96	11.89	4.06	1.10	0.64	20.01	3.69	29551.54
8	7.54	0.81	9.57	2.03	1.22	0.71	13.63	3.55	26308.74
9	11.75	6.56	19.72	7.98	1.41	0.72	35.67	5.54	43890.90
10	11.17	4.46	17.11	5.95	1.49	0.55	29.00	5.26	36870.66
11	11.31	2.50	15.37	4.06	1.56	-0.01	23.49	5.33	28871.49
12	10.30	0.48	12.33	2.03	1.55	0.51	16.39	4.85	27222.00
13	16.10	6.14	24.07	7.98	1.83	0.06	40.02	7.59	40179.80
14	15.66	4.10	21.61	5.95	1.84	0.15	33.50	7.38	34472.18
15	14.94	2.33	19.00	4.06	1.73	0.02	27.12	7.04	30094.87
16	0.00	0.00	0.00	0.00	0.00	0.00	0.00	0.00	0.00

Test ID DC 27 2

Dry Density 93.1 pcf

Water Content 24.1 %

Cycle	Deviator Stress	Confining Pressure+pore air pressure	σ_1	$\sigma_2=\sigma_3$	Pore water pressure	Pore air pressure	Bulk Stress	Octahedral stress	Measured Resilient Modulus
	psi	psi	psi	psi	psi	psi	psi	psi	psi
	σ_d	σ_3	$\sigma d+\sigma 3$		u_w	u_a	θ	τ_{oct}	$M_{r\ avg}$
0	7.98	4.05							
1	5.66	7.97	13.63	7.98	0.01	0.77	29.58	2.67	75439.03
2	5.22	5.94	11.17	5.95	0.01	0.80	23.06	2.46	78490.49
3	4.64	4.05	8.70	4.06	0.01	0.77	16.82	2.19	69969.33
4	4.35	2.02	6.38	2.03	0.01	0.73	10.44	2.05	57934.45
5	8.70	7.96	16.68	7.98	0.01	0.82	32.63	4.10	68566.27
6	8.12	5.93	14.07	5.95	0.01	0.83	25.96	3.83	64135.25
7	7.83	4.05	11.89	4.06	0.01	0.81	20.01	3.69	55729.42
8	7.25	2.02	9.28	2.03	0.01	0.86	13.34	3.42	49352.62
9	11.75	7.96	19.72	7.98	0.02	0.93	35.67	5.54	64327.20
10	11.17	5.93	17.11	5.95	0.02	0.89	29.00	5.26	60240.25
11	10.88	4.04	14.94	4.06	0.02	0.87	23.06	5.13	51178.17
12	10.44	2.01	12.47	2.03	0.02	0.84	16.53	4.92	45382.52
13	15.81	7.95	23.78	7.98	0.03	0.96	39.73	7.45	57384.35
14	15.08	5.92	21.03	5.95	0.03	0.96	32.92	7.11	54404.73
15	14.65	4.04	18.71	4.06	0.02	0.93	26.83	6.90	51545.20
16	14.36	2.01	16.39	2.03	0.02	0.92	20.45	6.77	41939.26

Test ID DC 27 3

Dry Density 96.7 pcf

Water Content 23.1 %

Cycle	Deviator Stress	Confining Pressure+pore air pressure	σ_1	$\sigma_2=\sigma_3$	Pore water pressure	Pore air pressure	Bulk Stress	Octahedral stress	Measured Resilient Modulus
	psi	psi	psi	psi	psi	psi	psi	psi	psi
	σ_d	σ_3	$\sigma d+\sigma 3$		u_w	u_a	θ	τ_{oct}	$M_{r\ avg}$
0	0.00	4.06							
1	0.15	7.98	7.91	13.63	7.98	0.07	57.94	29.58	0.39
2	0.29	5.95	5.78	11.17	5.95	0.17	58.31	23.06	0.36
3	0.44	4.06	3.82	8.70	4.06	0.24	58.70	16.82	0.32
4	0.58	2.03	1.80	6.38	2.03	0.23	58.77	10.44	0.30
5	0.73	7.98	7.73	16.68	7.98	0.24	58.33	32.63	0.59
6	0.87	5.95	5.70	14.07	5.95	0.24	58.48	25.96	0.56
7	1.02	4.06	3.63	11.89	4.06	0.43	59.23	20.01	0.54
8	1.16	2.03	1.70	9.28	2.03	0.33	58.87	13.34	0.50
9	1.31	7.98	7.58	19.72	7.98	0.39	58.68	35.67	0.80
10	1.45	5.95	5.51	17.11	5.95	0.43	58.84	29.00	0.76
11	1.60	4.06	3.59	14.94	4.06	0.47	59.06	23.06	0.74
12	1.74	2.03	1.53	12.47	2.03	0.50	59.31	16.53	0.71
13	1.89	7.98	7.48	23.78	7.98	0.49	58.80	39.73	1.08
14	2.03	5.95	5.53	21.03	5.95	0.42	58.46	32.92	1.03
15	2.18	4.06	3.62	18.71	4.06	0.44	58.59	26.83	1.00
16	2.32	2.03	1.49	16.39	2.03	0.54	59.29	20.45	0.98

Test ID DC 30 1

Dry Density 88.5 pcf

Water Content 29.9 %

Cycle	Deviator Stress	Confining Pressure+pore air pressure	σ_1	$\sigma_2=\sigma_3$	Pore water pressure	Pore air pressure	Bulk Stress	Octahedral stress	Measured Resilient Modulus
	psi	psi	psi	psi	psi	psi	psi	psi	psi
	σ_d	σ_3	$\sigma d+\sigma 3$		u_w	u_a	θ	τ_{oct}	$M_{r\ avg}$
0	7.83	4.05							
1	5.66	7.96	13.63	7.98	0.01	2.20	29.58	2.67	44659.09
2	5.08	5.93	11.02	5.95	0.01	2.56	22.91	2.39	46919.28
3	4.64	4.05	8.70	4.06	0.01	2.25	16.82	2.19	46825.15
4	4.21	2.02	6.24	2.03	0.01	2.52	10.30	1.98	46109.94
5	8.41	7.96	16.39	7.98	0.02	2.81	32.34	3.96	33591.97
6	8.12	5.93	14.07	5.95	0.02	2.70	25.96	3.83	32828.36
7	7.69	4.04	11.75	4.06	0.02	3.09	19.87	3.62	32198.10
8	7.40	2.02	9.43	2.03	0.01	2.34	13.49	3.49	30540.38
9	11.75	7.95	19.72	7.98	0.03	2.68	35.67	5.54	19148.76
10	11.17	5.92	17.11	5.95	0.03	2.48	29.00	5.26	19248.51
11	10.88	4.03	14.94	4.06	0.03	2.31	23.06	5.13	17791.92
12	10.44	2.01	12.47	2.03	0.02	2.40	16.53	4.92	17126.43
13	15.81	7.93	23.78	7.98	0.04	3.11	39.73	7.45	3626.69
14	15.23	5.90	21.17	5.95	0.04	2.94	33.06	7.18	3338.99
15	14.21	4.02	18.27	4.06	0.04	2.81	26.39	6.70	2772.82
16	12.76	1.98	14.79	2.03	0.05	2.51	18.85	6.02	2448.93

Test ID DC 30 2

Dry Density 86.0 pcf

Water Content 26.2 %

Cycle	Deviator Stress	Confining Pressure+pore air pressure	σ_1	$\sigma_2=\sigma_3$	Pore water pressure	Pore air pressure	Bulk Stress	Octahedral stress	Measured Resilient Modulus
	psi	psi	psi	psi	psi	psi	psi	psi	psi
	σ_d	σ_3	$\sigma d+\sigma 3$		u_w	u_a	θ	τ_{oct}	$M_{r\ avg}$
0	8.41	4.06							
1	5.66	7.97	13.63	7.98	0.00	0.98	29.58	2.67	87392.23
2	5.08	5.94	11.02	5.95	0.00	0.88	22.91	2.39	78422.22
3	4.79	4.06	8.85	4.06	0.00	0.94	16.97	2.26	67838.73
4	4.21	2.03	6.24	2.03	0.00	1.12	10.30	1.98	56638.03
5	8.56	7.97	16.53	7.98	0.00	1.94	32.48	4.03	66764.40
6	8.12	5.94	14.07	5.95	0.00	1.67	25.96	3.83	58536.44
7	7.69	4.06	11.75	4.06	0.00	0.91	19.87	3.62	53140.20
8	7.40	2.03	9.43	2.03	0.00	0.53	13.49	3.49	50809.03
9	11.75	7.97	19.72	7.98	0.01	0.85	35.67	5.54	60122.92
10	11.02	5.94	16.97	5.95	0.01	1.15	28.86	5.19	55997.85
11	11.02	4.05	15.08	4.06	0.01	0.85	23.20	5.19	50933.00
12	10.59	2.03	12.62	2.03	0.00	0.80	16.68	4.99	46939.70
13	15.81	7.96	23.78	7.98	0.01	1.16	39.73	7.45	52282.11
14	15.37	5.93	21.32	5.95	0.01	0.73	33.21	7.25	48822.83
15	14.94	4.05	19.00	4.06	0.01	0.46	27.12	7.04	44929.76
16	14.36	2.02	16.39	2.03	0.01	0.66	20.45	6.77	42524.57

Test ID DC 30 3

Dry Density 88.7 pcf

Water Content 27.3 %

Cycle	Deviator Stress	Confining Pressure+pore air pressure	σ_1	$\sigma_2=\sigma_3$	Pore water pressure	Pore air pressure	Bulk Stress	Octahedral stress	Measured Resilient Modulus
	psi	psi	psi	psi	psi	psi	psi	psi	psi
	σ_d	σ_3	$\sigma d+\sigma 3$		u_w	u_a	θ	τ_{oct}	$M_{r\ avg}$
0	8.27	4.05							
1	5.66	7.97	13.63	7.98	0.01	-0.18	29.58	2.67	78251.55
2	5.22	5.94	11.17	5.95	0.01	-0.19	23.06	2.46	73754.55
3	4.79	4.05	8.85	4.06	0.01	-0.90	16.97	2.26	73720.54
4	4.21	2.03	6.24	2.03	0.00	-0.50	10.30	1.98	71443.01
5	8.56	7.96	16.53	7.98	0.01	0.19	32.48	4.03	64494.91
6	8.12	5.94	14.07	5.95	0.01	-0.31	25.96	3.83	63400.46
7	7.83	4.05	11.89	4.06	0.01	-0.63	20.01	3.69	60928.58
8	7.54	2.02	9.57	2.03	0.01	-1.01	13.63	3.55	58748.02
9	11.60	7.95	19.58	7.98	0.02	-0.27	35.53	5.47	54094.18
10	11.17	5.93	17.11	5.95	0.02	-0.59	29.00	5.26	52201.93
11	10.88	4.04	14.94	4.06	0.02	-0.29	23.06	5.13	51273.75
12	10.44	2.01	12.47	2.03	0.02	-0.32	16.53	4.92	52036.15
13	15.81	7.78	23.78	7.98	0.20	-0.17	39.73	7.45	44762.89
14	15.23	5.71	21.17	5.95	0.24	-0.07	33.06	7.18	43861.53
15	14.79	3.81	18.85	4.06	0.25	-0.14	26.97	6.97	43332.59
16	14.50	1.77	16.53	2.03	0.26	-0.74	20.59	6.84	41469.40